

A Final Report Submitted to the
U.S. Department of Energy
Nuclear Engineering and Education Research (NEER)
Program

by the

Office of Research and Graduate Programs
University of Florida
Gainesville, Florida 32611

For a project entitled

***An Image-Based Computational System for the Design
of Radionuclide Therapies for Skeletal Tumors
DE-FG07-02ID14327***

Wesley Bolch, PhD, PE, CHP, Principal Investigator
Department of Nuclear and Radiological Engineering
University of Florida

November 2005

Table of Contents

A. Summary of Research Accomplishments (Published Journal Articles)	2
B. Summary of Research Accomplishments (Articles to be Submitted)	5
C. List of Presentations Given at Scientific Meetings	8
D. Journal Articles – Published Reprints	11
1. Shah et al. <i>JNM</i> 46 344-353 (2005)	12
2. Shah et al. <i>MP</i> 32 1354-1366 (2005)	22
3. Shah et al. <i>HP</i> 89 199-215 (2005)	35
4. Watchman et al. <i>JNM</i> 46 1171-1185 (2005)	52
5. Shah et al. <i>MP</i> 32 3151-3159 (2005)	90
E. Journal Articles – In Preparation for Submission	99
6. Watchman et al. <i>JNM</i> (cortical bone model – alpha particles)	100
7. Watchman et al. <i>JNM</i> (cortical bone model – electrons)	135
8. Watchman et al. <i>JNM</i> (individual variabilities in alpha particle dosimetry)	165
9. Watchman et al. <i>PMB</i> (skeletal tissue masses)	189
10. Watchman et al. <i>PMB</i> (alpha-particle dosimetry with revised ICRP skeletal targets)	217
11. Watchman et al. <i>CBR</i> (spatial distribution of CD34+ marrow cells in the skeleton) ...	251

Note: Page numbers listed above correspond to those given by Adobe Acrobat / Reader

Summary of Research Accomplishments

Abstracts of Published Journal Articles

1. AP Shah, **WE Bolch**, DA Rajon, PW Patton, and DW Jokisch, "A paired-image radiation transport (PIRT) model for skeletal dosimetry" *J Nucl Med* **46** 344-353 (2005).

Toxicity of the hematopoietically active bone marrow continues to be a primary limitation in radionuclide therapies of cancer. Improved techniques for patient-specific skeletal dosimetry are thus crucial to the development of dose-response relationships needed to optimize these therapies (i.e., avoid both marrow toxicity and tumor under-dosing). Current clinical methods of skeletal dose assessment rely heavily on a single set of bone and marrow cavity chord-length distributions in which particle energy deposition is tracked within an infinite extent of trabecular spongiosa, with no allowance for particle escape to cortical bone. In the present study, we introduce a paired-image radiation transport (PIRT) model which can provide a more realistic 3D geometry for particle transport of the skeletal site at both microscopic and macroscopic levels of its histology. **Methods:** Ex-vivo CT scans were acquired of the lumbar vertebra and right proximal femur excised from a 66-year male cadaver (BMI of 22.7 kg m⁻²). For both skeletal sites, regions of trabecular spongiosa and cortical bone were identified and segmented. Physical sections of interior spongiosa were then taken and subjected to NMR microscopy. Voxels within the resulting NMR microimages were segmented and labeled into regions of bone trabeculae, endosteum, active marrow, and inactive marrow. The PIRT methodology was then implemented within the EGSnrc radiation transport code whereby electrons of various initial energies are simultaneously tracked within both the ex-vivo CT macroimage and the NMR microimage of the skeletal site. **Results:** At electron initial energies greater than 50 – 200 keV, a divergence in absorbed fractions to active marrow are noted between PIRT model simulations and those estimated under infinite spongiosa transport techniques. Calculations of radionuclide S values under both methodologies imply that current chord-based models used in clinical skeletal dosimetry can over-estimate dose to active bone marrow in these two skeletal sites by ~4% to 23% for low-energy beta emitters (³³P, ¹⁶⁹Er, and ¹⁷⁷Lu), by ~4% to 25% for intermediate-energy beta emitters (¹⁵³Sm, ¹⁸⁶Re, and ⁸⁹Sr), and by ~11% to 30% for high-energy beta emitters (³²P, ¹⁸⁸Re, and ⁹⁰Y). **Conclusion:** The PIRT methodology allows for detailed modeling of the 3D macrostructure of individual marrow-containing bones within the skeleton thus permitting improved estimates of absorbed fractions and radionuclide S values for intermediate-to-high beta emitters.

-
2. AP Shah, **WE Bolch**, DA Rajon, PW Patton, and DW Jokisch, "Beta-particle energy loss to cortical bone via paired-image radiation transport (PIRT): Corrections to clinical models of skeletal tissue dose" *Med Phys* **32** 1354-1366 (2005).

Current methods of skeletal dose assessment in both medical physics (radionuclide therapy) and health physics (dose reconstruction and risk assessment) rely heavily on a single set of bone and marrow cavity chord-length distributions in which particle energy deposition is tracked within an infinite extent of trabecular spongiosa, with no allowance for particle escape to cortical bone. In the present study, we introduce a paired-image radiation transport (PIRT) model which can provide a more realistic 3D geometry for particle transport of the skeletal site at both microscopic and macroscopic levels of its histology. **Methods:** Ex-vivo CT scans were acquired of the pelvis, cranial cap, and individual ribs excised from a 66-year male cadaver (BMI of 22.7 kg m⁻²). For both skeletal sites, regions of trabecular spongiosa and cortical bone were identified and segmented. Physical sections of interior spongiosa were then taken and

subjected to μ CT imaging. Voxels within the resulting μ CT microimages were segmented and labeled into regions of bone trabeculae, endosteum, active marrow, and inactive marrow. The PIRT methodology was then implemented within the EGSnrc radiation transport code whereby electrons of various initial energies are simultaneously tracked within both the ex-vivo CT macroimage and the μ CT microimage of the skeletal site. **Results:** At electron initial energies greater than 50 – 200 keV, a divergence in absorbed fractions to active marrow are noted between PIRT model simulations and those estimated under infinite spongiosa transport techniques. Calculations of radionuclide S values under both methodologies imply that current chord-based models used in clinical skeletal dosimetry can over-estimate dose to active bone marrow in these skeletal sites by ~2% to 28% for low-energy beta emitters (^{33}P , ^{169}Er , and ^{177}Lu), by ~4% to 48% for intermediate-energy beta emitters (^{153}Sm , ^{186}Re , and ^{89}Sr), and by ~14% to 76% for high-energy beta emitters (^{32}P , ^{188}Re , and ^{90}Y). **Conclusion:** The PIRT methodology allows for detailed modeling of the 3D macrostructure of individual marrow-containing bones within the skeleton thus permitting improved estimates of absorbed fractions and radionuclide S values for intermediate-to-high beta emitters.

-
3. AP Shah, DA Rajon, PW Patton, DW Jokisch, and **WE Bolch**, “A comparison of skeletal chord-length distributions in the adult male” *Health Phys* **89** (3): 199-215 (2005).

In radiation protection, skeletal dose estimates are required for the tissues of the hematopoietically active bone marrow and the osteogenic cells of the trabecular and cortical endosteum. Similarly, skeletal radiation dose estimates are required in therapy nuclear medicine in order to develop dose-response functions for myelotoxicity where active bone marrow is generally the dose-limiting organ in cancer radioimmunotherapy. At the present time, skeletal dose models in both radiation protection and medical dosimetry are fundamentally reliant on a single set of chord-length distribution measurements performed at the University of Leeds in the late 1970s for a 44-year male subject. These distributions describe the relative frequency at which linear pathlengths are seen across both the marrow cavities and bone trabeculae in seven individual bone sites: vertebrae (cervical and lumbar), proximal femur (head and neck), ribs, cranium (parietal bone), and pelvis (iliac crest). In the present study, we present an alternative set of chord-length distribution data acquired within a total of 14 skeletal sites of a 66-year male subject. The UF distributions are assembled via 3D image processing of microCT scans of physical sections of trabecular spongiosa at each skeletal site. In addition, a tri-linear interpolation Marching Cube algorithm is employed to smooth the digital surfaces of the bone trabeculae while chord-length measurements are performed. A review of mean chord lengths indicate that larger marrow cavities are noted on average in the UF individual for the cervical vertebrae (1038 vs. 910 μm), lumbar vertebrae (1479 vs. 1233 μm), ilium (1508 vs. 904 μm), and parietal bone (812 vs. 389 μm), while smaller marrow cavities are noted in the UF individual for the femoral head (1043 μm vs. 1157 μm), the femoral neck (1454 μm versus 1655 μm), and the ribs (1630 μm vs. 1703 μm). The mean chord-lengths for the bone trabeculae show close agreement for both individuals in the ilium (~240 μm) and cervical vertebrae (~280 μm). Thicker trabeculae were seen on average in the UF individual for the femoral head (ratio of 1.50), femoral neck (ratio 1.10), lumbar vertebrae (ratio of 1.29), and ribs (ratio 1.14), while thinner trabeculae were seen on average in the UF individual for the parietal bone of the cranium (ratio of 0.92). In two bone sites, prominent discrepancies in chord distribution shape were noted between the Leeds 44-year male and the UF 66-year male: (1) the bone trabeculae in the ribs and (2) the marrow cavities and bone trabeculae within the cranium.

-
4. CJ Watchman, **WE Bolch**, PW Patton, DA Rajon, and G Sgouros, "Absorbed fractions for alpha particles in tissues of trabecular bone – considerations of marrow cellularity" (*J Nucl Med*)

Introduction: Alpha particles are of current interest for radionuclide therapies due to their short range and high rates of energy deposition to target tissues. When detailed histological data are not available to identify source and target tissues for alpha-particle therapy, the MIRD dosimetry schema may be employed, particularly for administrations at high specific activity. Values of absorbed fraction needed under the MIRD schema are generally available only from skeletal models presented in ICRP Publication 30. The ICRP 30 alpha-particle absorbed fractions, however, are designed to conservatively estimate energy deposition to target tissues as needed for radiological protection, and are given with no consideration for their variations with alpha emission energy, skeletal site, or marrow cellularity – all features of potentially high importance in alpha-emitter radionuclide therapy. **Methods:** In this study, a radiation transport model (3D-CBIST) is presented which combines (1) chord-based techniques for tracking alpha particles across bone trabeculae, endosteum, and marrow cavities, and (2) a spatial model of the marrow tissues which explicitly considers the presence of marrow adipose tissue across a broad range of marrow cellularities. Chord-length distributions are taken from studies performed at the University of Leeds at seven skeletal sites within a single 44-year male subject, and are identical to those used currently for clinical dose estimates for beta-emitters in the skeleton. **Results:** ICRP 30 alpha-particle absorbed fractions are found to significantly over-estimate energy deposition to active marrow given by the 3D-CBIST model for all source regions. A single exception is for high-energy alpha particles emitted from the bone surfaces irradiating marrow at high cellularity. These deviations become more and more prominent as marrow cellularity decreases further from 100%. In contrast, the ICRP 30 bone model significantly under-estimates energy deposition to skeletal endosteum as predicted under the 3D-CBIST model. Exceptions are noted for $\phi(\text{TBE} \leftarrow \text{TBE})$ and $\phi(\text{TBE} \leftarrow \text{TBS})$ at high energies (>5 MeV and >6.5 MeV, respectively), and for $\phi(\text{TBE} \leftarrow \text{TBV})$ at low energies (i.e., 3 MeV for ribs and cervical vertebra). For active marrow sources, the ICRP 30 model predicts no energy deposition to trabecular endosteum; however, our calculations indicate that a few percent of the alpha energy emitted within the TAM is deposited in TBE at an amount that is influenced modestly by marrow cellularity. **Conclusion:** Improvements in patient-specific dosimetry of skeletal tissues require explicit consideration of not only tissue mass changes with marrow cellularity (i.e., active marrow), but their corresponding changes in values of the absorbed fraction. The data given in this study will provide a more firm basis for application of the MIRD schema to patient-specific dosimetry in newly developing therapies using alpha-particle emitters.

-
5. AP Shah, DW Jokisch, CJ Watchman, DA Rajon, PW Patton, and **WE Bolch**, "Chord-based versus voxel-based methods of electron transport in the skeletal tissues" *Med Phys* **32** (10) 3151-3159 (2005).

Anatomic models needed for internal dose assessment have traditionally been developed using mathematical surface equations to define organ boundaries, shapes, and their positions within the body. Many researchers, however, are now advocating the use of tomographic models created from segmented patient CT or MR scans. In the skeleton, however, the tissue structures of the bone trabeculae, marrow cavities, and endosteal layer are exceedingly small and of complex shape, and thus do not lend themselves easily to either stylistic representations or in-vivo CT imaging. Historically, the problem of modeling the skeletal tissues has been

addressed through the development of chord-based methods of radiation particle transport, as given by studies at the University of Leeds using a 44-year male subject. We have proposed an alternative approach to skeletal dosimetry in which excised sections of marrow-intact cadaver spongiosa are imaged directly via microCT scanning. The cadaver selected for initial investigation of this technique was a 66-year male subject of nominal body mass index (22.7 kg m^{-2}). The objectives of the present study were to compare chord-based versus voxel-based methods of skeletal dosimetry using data from the UF 66-year male subject. Good agreement between chord-based and voxel-based transport was noted for marrow irradiation by either bone surface or bone volume sources up to 500 - 1000 keV (depending upon the skeletal site). In contrast, chord-based models of electron transport yielded consistently lower values of the self-absorbed fraction to marrow tissues than seen under voxel-based transport at energies above 100 keV, a feature directly attributed to the inability of chord-based models to account for non-linear electron trajectories. Significant differences were also noted in the dosimetry of the endosteal layer (for all source tissues), with chord-based transport predicting a higher fraction of energy deposition than given by voxel-based transport (average factor of about 1.6). The study supports future use of voxel-based skeletal models which (1) permit non-linear electron trajectories across the skeletal tissues, (2) do not rely on mathematical algorithms for treating the endosteal tissue layer, and (3) do not implicitly assume independence of marrow and bone trajectories as is the case for chord-based skeletal models.

Abstracts of Journal in Preparation for Submission

6. CJ Watchman and **WE Bolch**, "Absorbed fractions for alpha particles in tissues of cortical bone" *J Nucl Med* (to be submitted).

A chord-based model for charged-particle transport in the cortical bone has been presented that incorporates microstructural data (individual target energy deposition). The model incorporates the transverse chord-length distributions obtained by Beddoe for three cortical bone sites. This data set is limited to three long bone sites for microstructural data. Absorbed fractions obtained in this model provide an improved data set for alpha emitters and may be used in therapeutic applications as well as health physics applications. Over the energy range studied, the effective alpha particle ranges are less than a maximum of $\sim 120 \text{ }\mu\text{m}$ and thus cross-osteon irradiation and bone volume escape are negligible. For therapeutic applications, use of these absorbed fractions, especially the CHS source, may lead to a better estimate of endosteal dose due to the short-lived nature of the alpha emitters proposed for therapy. In radiation protection applications, an improved dose estimate will also be achieved since the current ICRP 30 values are energy independent and values given in the 2003 Eckerman model do not account for the relative fraction of the haversian cavity associated with the endosteal layer.

-
7. CJ Watchman and **WE Bolch**, "Absorbed fractions for electrons in tissues of cortical bone" *J Nucl Med* (to be submitted).

A chord-based model for charged-particle transport in the cortical bone has been presented that incorporates microstructural data (individual target energy deposition) and macrostructural (particle escape) data. The model incorporates the transverse chord-length distributions obtained by Beddoe for three cortical bone sites. This data set is limited to three long bone sites for microstructural data. The primary limitation of this model with respect to electrons lies in the assumption of linear pathlengths in cortical bone. Electrons as they travel through a medium undergo angular deflections that result in different amounts of energy along their tracks when compared to our CSDA range methodology. While the cortical model of Bouchet and

Bolch does take these nonlinear pathlengths into account, this model also does not allow for irradiation of neighboring osteons, and thus neither model fully accounts for all factors relevant for high-energy emitters in the cortical bone microstructure. It is recommended that perhaps microCT images of cortical bone may be used in future to construct a more accurate transport geometry for cortical bone similar to that provided by the PIRT model for trabecular bone. Absorbed fractions obtained in this model provide an improved data set that may be used in therapeutic applications as well as health physics applications. With respect to electrons, this method more effectively accounts for electron escape from the diaphysis of the long bones. For therapeutic applications, use of absorbed fractions, especially the CHS source, should lead to a better estimate of endosteal dose due to the short-lived nature of the alpha emitters proposed for therapy. In radiation protection applications, an improved dose estimate will also be achieved since the ICRP 30 model presents only two absorbed fraction values and values given in the 2003 Eckerman model do not account for the relative fraction of the haversian cavity associated with the endosteal layer.

-
8. CJ Watchman and **WE Bolch**, "Age and Individual Variability in Alpha-Particle Absorbed Fractions to the Skeletal Tissues" *Med Phys* (to be submitted).

Introduction: A previous study of α -particle absorbed fractions using chord distribution data from the ICRP reference male (Leeds 44-year male) demonstrated their dependence on marrow cellularity, skeletal site, and particle energy. In this study, we extend our analysis to include a series of 6 adults and 2 pediatric subjects. Currently, there are no published values of α -particle absorbed fractions in the skeletal tissues that account marrow cellularity by skeletal site. **Methods:** Using the 3D-CBIST computer code published by Watchman et al. [JNM 46 1171-1185 (2005)], absorbed fractions were calculated for the Leeds 1.7-y male (5 bone sites) and 9-y male (6 bone sites) in the iliac crest and ribs. Lumbar vertebrae sites were also investigated for a 55-y, 70-y and 85-y female, as well as a 25-y and 66-y male. Each calculation was performed over the energy range of 3 – 10 MeV for marrow cellularities ranging from 10% to 100%, and for α -emitting radiopharmaceuticals localized to the active marrow (TAM), bone surfaces (TBS) and bone trabeculae volumes (TBV). Comparisons of absorbed fractions were made at 100% cellularity and at an age-dependant reference cellularity for active marrow and endosteum targets. **Results:** Variations in $\phi(\text{active marrow} \leftarrow \text{active marrow})$ are less than 1% among the six adults in the lumbar vertebrae at 100% marrow cellularity, but are between 12-15% for values of $\phi(\text{endosteum} \leftarrow \text{active marrow})$. While observable differences were seen α -particle absorbed fractions as a function of age at 100% cellularity, significantly higher age variations were seen when age-dependent marrow cellularity was explicitly considered during particle transport. For example, at an energy of 7 MeV, the ratio of $\phi(\text{active marrow} \leftarrow \text{active marrow})$ and $\phi(\text{endosteum} \leftarrow \text{active marrow})$ in the iliac crest of the 1.7-y to their corresponding values in the 66-y male are 1.87 and 0.32, respectively. **Conclusion:** The largest source of uncertainty in patient-specific α -particle dosimetry in molecular radiotherapy continues to be the neglect of marrow cellularity in the assignment of absorbed fractions to the skeletal tissues. The assumption of unity for values of $\phi(\text{TAM} \leftarrow \text{TAM})$ as given in existing skeletal dosimetry models can lead to significant errors in marrow dose assessment, particularly in older patients with high skeletal fat fractions and high α -particle energies (5 to 9 MeV).

-
9. CJ Watchman and **WE Bolch**, "Derivation of Skeletal Masses within the Current ICRP Age Series: Considerations of a 10- μm and a 50- μm Endosteum " *Phys Med Biol* (to be submitted).

Dosimetry calculations in skeletal tissues are routinely performed using tissue masses provided in publications from the International Commission on Radiological Protection. These values include gross tissue masses as a function of age, and are not generally broken down by individual skeletal site. Recent studies have demonstrated site-specific variations in absorbed fraction calculations. Consequently, site-specific bone tissue masses are required to properly determine skeletal-averaged absorbed fractions and specific absorbed fractions. Assignment of values for these reference masses is based upon several different data sources. These sources are not necessarily be consistent with one another. To assess the validity and limitations of the ICRP values, a methodology has been developed, using data from the various ICRP publications, to determine bone-site-specific skeletal tissue masses for the entire ICRP age series. Active marrow masses have been calculated and differences have been shown with respect to ICRP Publication 70 and ICRP Publication 89 values. Mineral bone and endosteal masses have also been calculated and shown to follow similar growth patterns. A series of tables are provided with age-dependant and bone-site-specific masses for all members of the ICRP age series other than the newborn.

-
10. CJ Watchman and **WE Bolch**, "Alpha Particle Absorbed Fractions in the Skeletal Tissues: Consideration of a 50- μ m Endosteum Target" *Phys Med Biol* (to be submitted).

In response to the increasing body of evidence that irradiation of osteoprogenitor cells within a distance of 50 μ m from bone surfaces is relevant to bone cancer induction, this study into the dosimetry consequences of this tissue definition has been presented. This study has shown results for absorbed fractions calculated using 3D-CBIST for a 50 μ m endosteum target. Results obtained for both the UF 66-y male subject and five third lumbar vertebrae from the University of Leeds were presented. Data obtained in this study has demonstrated significant differences in alpha particle absorbed fractions for the TBE₅₀ in comparison to the TBE₁₀ as a function of bone site, individual, marrow cellularity and changes endosteum thickness. Results from this study also show that using the current definition of endosteum results in over-estimates of the total dose to sensitive tissues with respect to bone cancer induction. Further research is warranted in better describing the spatial distribution of osteoprogenitor tissues within the marrow cavities.

-
11. CJ Watchman and **WE Bolch**, "Spatial distribution of CD34+ primitive hematopoietic cells and blood vessels within the marrow cavities of trabecular bone" *Phys Med Biol* (to be submitted).

Data has been presented that contradicts the homogenous distribution of hematopoietic progenitor cells within the marrow cavities of trabecular bone. These results indicate that the current disparity between dose calculations and clinical response in molecular radiotherapy may be due in part to incorrectly estimating the dose to the most radiosensitive cells in bone marrow. A weighting method has been presented which will allow for incorporation of the PHC frequency data into current dosimetry methods. Use of this data in dosimetry modeling may result in improved dose-response relationships. Further work is warranted due to the spatial limitations resulting from the use of bone marrow core biopsies. Development of 3D models that allow for multiple whole marrow cavities may further improve our knowledge of the location of PHC and the marrow vasculature. Potentially greater delineation of cell types is possible if additional immunohistochemical agents are used to directly differentiate between cell types, i.e. using CD34 and CD38 to distinguish between HSC (CD38⁺) and other progenitor cells (CD38⁺). Additional investigation is also merited in looking at how pathology may change the spatial

distribution of PHC in the marrow. Improved description of each cell type, with respect to normal and pathological bone marrow, along the hematopoietic lineage may allow for other weighting schemes that further improve dose-response relationships with respect to marrow toxicity and clinical effect.

List of Presentations Given at Scientific Meetings

1. DA Rajon^{*}, AP Shah^{*}, CJ Watchman^{*}, JM Brindle^{*}, and WE Bolch, “Chord length distribution measurements through polygonal representations of trabecular bone samples”, 2002 Annual Meeting of the Health Physics Society, Tampa, Florida, June 16-20, 2002 [Supplement to *Health Phys.* **82** (6) S128 (2002)].
2. D Rajon^{*}, A Shah^{*}, C Watchman^{*}, J Brindle^{*}, and W Bolch, “Polygonal representation of trabecular bone samples for chord length distribution measurements”, 2002 Annual Meeting of the American Association of Medical Physicists, Montreal, Canada, July 14-18, 2002.
3. CJ Watchman^{*}, AP Shah^{*}, JM Brindle^{*}, DA Rajon, and WE Bolch “A 3D chord length based model of alpha particle dosimetry in bone marrow”, 2003 Annual Meeting of the Health Physics Society, San Diego, California, July 20-24, 2003. [Supplement to *Health Phys.* **84** (6) S197-198 (2003)].
4. AP Shah, DA Rajon, PW Patton, RW Howell, WE Bolch, “Skeletal dosimetry: establishment of dose gradients for cellular components across the marrow cavity”, 2003 Annual Meeting of the American Association for Physicists in Medicine, San Diego, California, August 10-14, 2003. [Supplement of *Medical Phys.* **30** (6): 1400 (2003)].
5. CW Watchman^{*} and WE Bolch, “Absorbed fractions for skeletal dosimetry of alpha particles”, 2004 Annual Meeting of the American Association of Physicists in Medicine, Pittsburgh, Pennsylvania, July 25-29, 2004. [Supplement to *Med Phys* **31** (6): 1756-1757 (2004)].
6. WE Bolch , Amish Shah, James Brindle, Phillip Patton, Derek Jokisch, and George Sgouros, “A reference skeletal dosimetry model of the adult male radionuclide therapy patient based on 3D microimaging and radiation transport”, 2004 Annual Meeting of the European Association of Nuclear Medicine, 1st International Symposium on Radionuclide Therapy and Radiopharmaceutical Dosimetry”, Helsinki, Finland, September 4-8, 2004.
7. WE Bolch and AP Shah^{*}, “Skeletal dose estimates via a Paired-Image Radiation Transport (PIRT) model”, *Transactions of the 2004 Winter Meeting of the American Nuclear Society*, Washington, DC, November 14-18, 2004.
8. CJ Watchman^{*}, and WE Bolch, “Age and individual variability of absorbed fractions for alpha particle emissions in the tissues of trabeculae bone” 2005 Annual Meeting of the Society of Nuclear Medicine, Toronto, Canada, June 19-22, 2005. [Supplement to *J Nucl Med* **46** (5): 341-342 (2005)].

9. WE Bolch, “An-imaged based skeletal reference model of the adult male radionuclide therapy patient”, 2005 Annual Meeting of the Society of Nuclear Medicine, Toronto, Canada, June 19-22, 2005. [Supplement to *J Nucl Med* **46** (5): 193-194 (2005)]
10. KN Kielar^{*}, D Hasenauer^{*}, AP Shah^{*}, and WE Bolch, “A skeletal reference dosimetry model for the adult female”, 2005 Annual Meeting of the Health Physics Society, Spokane, Washington, July 10-14, 2005. [Supplement to *Health Phys* **89** (1): S20 (2005)].
11. D Hasenauer^{*}, CW Watchman^{*}, AP Shah^{*}, and WE Bolch, “Skeletal reference models for pediatric patients”, 2005 Annual Meeting of the Health Physics Society, Spokane, Washington, July 10-14, 2005. [Supplement to *Health Phys* **89** (1): S56 (2005)].

Journal Articles – Published

A Paired-Image Radiation Transport Model for Skeletal Dosimetry

Amish P. Shah, PhD¹; Wesley E. Bolch, PhD^{1,2}; Didier A. Rajon, PhD³; Phillip W. Patton, PhD⁴; and Derek W. Jokisch, PhD⁵

¹Department of Biomedical Engineering, University of Florida, Gainesville, Florida; ²Department of Nuclear and Radiological Engineering, University of Florida, Gainesville, Florida; ³Department of Neurosurgery, University of Florida, Gainesville, Florida; ⁴Department of Health Physics, University of Nevada–Las Vegas, Las Vegas, Nevada; and ⁵Department of Physics and Astronomy, Francis Marion University, Florence, South Carolina

Toxicity of the hematopoietically active bone marrow continues to be a primary limitation in radionuclide therapies of cancer. Improved techniques for patient-specific skeletal dosimetry are thus crucial to the development of dose–response relationships needed to optimize these therapies (i.e., avoid both marrow toxicity and tumor underdosing). Current clinical methods of skeletal dose assessment rely heavily on a single set of bone and marrow cavity chord-length distributions in which particle energy deposition is tracked within an infinite extent of trabecular spongiosa, with no allowance for particle escape to cortical bone. In the present study, we introduce a paired-image radiation transport (PIRT) model that can provide a more realistic 3-dimensional geometry for particle transport of the skeletal site at both microscopic and macroscopic levels of its histology.

Methods: Ex vivo CT scans were acquired of the lumbar vertebra and right proximal femur excised from a 66-y male cadaver (body mass index, 22.7 kg m⁻²). For both skeletal sites, regions of trabecular spongiosa and cortical bone were identified and segmented. Physical sections of interior spongiosa were then taken and subjected to nuclear magnetic resonance (NMR) microscopy. Voxels within the resulting NMR microimages were segmented and labeled into regions of bone trabeculae, endosteum, active marrow, and inactive marrow. The PIRT methodology was then implemented within the EGSnrc radiation transport code, whereby electrons of various initial energies are simultaneously tracked within both the ex vivo CT macroimage and the NMR microimage of the skeletal site. **Results:** At electron initial energies greater than 50–200 keV, a divergence in absorbed fractions to active marrow is noted between PIRT model simulations and those estimated under infinite spongiosa transport techniques. Calculations of radionuclide S values under both methodologies imply that current chord-based models used in clinical skeletal dosimetry can overestimate dose to active bone marrow in these 2 skeletal sites by ~4%–23% for low-energy β -emitters (³³P, ¹⁶⁹Er, and ¹⁷⁷Lu), by ~4%–25% for intermediate-energy β -emitters (¹⁵³Sm, ¹⁸⁶Re, and ⁸⁹Sr), and by ~11%–30% for high-energy β -emitters (³²P, ¹⁸⁸Re, and ⁹⁰Y).

Conclusion: The PIRT methodology allows for detailed modeling of the 3D macrostructure of individual marrow-containing

bones within the skeleton, thus permitting improved estimates of absorbed fractions and radionuclide S values for intermediate-to-high β -emitters.

Key Words: skeletal dosimetry; marrow dose; nuclear magnetic resonance microscopy; radionuclide S value; absorbed fraction

J Nucl Med 2005; 46:344–353

The skeletal system represents one of the more complex challenges in internal dosimetry. This distributed organ, with its wide variety of bone sizes and configurations, encompasses the hematopoietic tissues of the active (red) bone marrow as well as the osteogenic tissues of the endosteum, both of which are relevant targets for short-term deterministic and long-term probabilistic radiation effects. Of primary importance is the 3-dimensional (3D) microscopic architecture of the bone trabeculae, which separate and define the marrow cavities. For short-ranged radiations (α -particles and lower-energy β -particles), knowledge of this 3D microstructure is necessary and sufficient for accurate computation of particle transport through these skeletal tissues. For longer-ranged radiations (such as intermediate-to high-energy β -particles), further consideration should be given to the 3D macrostructure of the skeletal site, including the location and extent of cortical bone into which escaping particles may penetrate.

The vast majority of initial studies in skeletal dosimetry were conducted at the University of Leeds by Spiers and his students (1–6). Spiers was the first to recognize that the anisotropic structure of trabecular bone required a unique method for characterizing the trabecular geometry as needed for accurate skeletal dosimetry of β -emitters (2,4). Consequently, he and his students constructed an optical bone-scanning system that measured linear chord-length distributions across 2-dimensional radiographs of excised bone tissue slices. Using these frequency distributions of linear chord lengths through both bone trabeculae and marrow cavities, the fraction of a particle's kinetic energy deposited in each tissue type was estimated. Spiers and his students obtained chord-length distributions in the lumbar

Received Jul. 6, 2004; revision accepted Sep. 13, 2004.

For correspondence or reprints contact: Wesley E. Bolch, PhD, Advanced Laboratory for Radiation Dosimetry Studies, Department of Nuclear and Radiological Engineering, University of Florida, Gainesville, FL 32611-8300.

E-mail: wbolch@ufl.edu

vertebrae for several subjects, as well as at several skeletal sites of a 1.7-y child (5 sites), a 9-y child (5 sites), and a 44-y man (7 sites) (7–10). In many ways, the chord-length distribution data measured for the 44-y man has served to define many of the skeletal attributes of Reference Man as defined by the International Commission on Radiological Protection (ICRP) (11,12). Furthermore, all skeletal dosimetry models published and presently used in clinical dose assessment are fundamentally reliant on this single set of adult chord-length distributions (13–17).

In this technique, radiation particles are effectively transported within an infinite region of trabecular spongiosa (defined as the combined tissues of the bone trabeculae, endosteum, and marrow cavities). Models of skeletal dosimetry used in current clinical practice, such as the Eckerman and Stabin model (16) of MIRDose3 and its successor codes (18), belong to a class of models called CBIST (Chord-Based Infinite Spongiosa Transport) and do not account for particle escape to cortical bone. Consequently, absorbed fractions to skeletal tissues are potentially overestimated in CBIST models for higher-energy β -emitters.

One of the first attempts to account for energy loss to cortical bone was made by Spiers' doctoral student J.R. Whitwell (9,10). She introduced a trabecular equilibrium factor, Q_{trab} , to account for the finite extent of the spongiosa. This correction factor was determined for several radionuclides of interest in radiation protection and for each of the 7 skeletal sites for which chord-length distributions were obtained in the 44-y male subject. For ^{90}Y , the highest correction noted by Whitwell was for the parietal bone ($Q_{\text{trab}} = 0.672$), whereas the lowest was for the head of the femur ($Q_{\text{trab}} = 0.980$). Nevertheless, these values of Q_{trab} were determined using simplified geometries for both spongiosa and cortical bone (e.g., planes and spheres).

In a more recent study by Patton et al. (19), nuclear magnetic resonance (NMR) microscopy was applied to the study of the 3D microstructure of bone trabeculae within the femoral and humeral heads of 3 subjects: a 51-y man, an 82-y woman, and a 89-y woman. To account for energy lost to cortical bone, an ex vivo CT scan of the excised femoral or humeral head was obtained before spongiosa sectioning. From spatial measurements on the CT images, a spheric region of spongiosa was constructed surrounded by a spheric shell of cortical bone. Electrons of various initial energies were thus transported (via the ESG4 radiation transport code) simultaneously within the NMR microimage (constructed of voxels of bone and marrow) and within a stylized model of the femoral or humeral head. Comparisons were subsequently made between energy-weighted absorbed fractions to active marrow under particle transport in either (a) an infinite extent of spongiosa or (b) the stylized model of the bone site. Patton et al. demonstrated that, without explicit consideration of energy loss to cortical bone, radionuclide S values for ^{32}P and ^{90}Y could potentially overestimate active marrow dose by 6% and 11%, respectively, in the femoral head—values that exceeded the 2%

corrections predicted by Whitwell. This tendency to overestimate dose to active marrow under infinite spongiosa transport had also been demonstrated by Jokisch et al. (20) for the thoracic vertebra, in which the physical extent of the vertebral spongiosa was delineated in a stylized model of the vertebral body (e.g., truncated circular cylinder). Due to their geometric complexity, however, no attempt was made to include the vertebral processes in the stylized vertebral model (which account for up to ~25% of vertebral spongiosa).

In the present study, we significantly extend the skeletal modeling approach originally explored by Jokisch et al. (20) and Patton et al. (19) to fully account for the 3D macrostructural dimensions of skeletal sites within which dose estimates are desired. A Paired-Image Radiation Transport or PIRT model for skeletal dosimetry is introduced, in which radiation particles are tracked simultaneously within 2 different segmented digital images: (a) an ex vivo CT image of the entire skeletal site outlining regions of trabecular spongiosa, cortical bone, and surrounding tissues and (b) an ex vivo NMR microscopy image of the interior bone trabeculae and marrow cavity microstructure representative of that found in spongiosa volumes of the larger CT image. The PIRT model is demonstrated within 2 skeletal sites obtained from a single male cadaver: the L4 vertebra and the right proximal femur. In addition, representative site-specific S values are calculated and compared with those obtained under particle transport within infinite regions of spongiosa for a variety of radionuclides of interest in skeletal imaging and therapy.

MATERIALS AND METHODS

Cadaver Selection

Candidate subjects for study were obtained through the State of Florida Anatomic Board located on the University of Florida (UF) campus. Cadaver selection criteria included (a) an age between 50 and 75 y (representative of typical radionuclide therapy patients), (b) a body mass index (BMI) of 18.5–25 kg m⁻² (Centers for Disease Control and Prevention—recommended healthy range), and (c) a cause of death that would preclude significant skeletal deterioration. The subject identified was a 66-y male, approximately 68 kg in total mass and 173 cm in total height at the time of death (BMI, 22.7 kg m⁻²). The subject died suddenly of complications associated with cardiomyopathy.

In Vivo CT

Before bone harvesting, the male cadaver was subjected to whole-body imaging via multislice helical CT at a pitch necessary to reconstruct contiguous 1-mm axial slices. The images were acquired on a Siemens Sensation 16 unit within the Department of Radiology at UF Shands Hospital. Image reconstruction was performed with a bone filter at an in-plane pixel resolution of 977 × 977 μm . The CT image sets were then transferred to workstations within the Advanced Laboratory for Radiation Dosimetry Studies (ALRADs) in the UF Department of Nuclear and Radiological Engineering for image processing and data storage. The in vivo CT scans provided image data for (a) selecting the anatomic region from which the bone site would be harvested and (b) constructing

3D anatomic models of skeletal sites where bone harvesting (and thus ex vivo CT) might be incomplete (e.g., facial bones of the skull).

Bone Harvesting and Ex Vivo CT

After detailed review of the whole-body in vivo CT images, bone harvesting was conducted. Thirteen major skeletal sites were taken from the male cadaver, including the entire vertebral column and both proximal femora. Once each skeletal site was excised, it was cleaned of excess tissue, bagged, labeled, and stored frozen until ex vivo CT could be scheduled. After harvest, ex vivo CT was conducted at higher resolution (1.0-mm slice thickness with an in-plane resolution of 0.3×0.3 mm) than permitted for in vivo scans. The ex vivo CT scans provided image data for (a) identifying the location and extent of trabecular spongiosa to be sectioned for NMR microscopy, (b) quantifying volumes of trabecular spongiosa and cortical bone within the bone site, and (c) constructing 3D anatomic models of the bone site for subsequent PIRT simulations.

After detailed review of the ex vivo CT scans, physical sections of trabecular spongiosa were taken from each bone site. Sections represented as large a region of spongiosa as possible, given the constraints of the bone shape and the NMR imaging system (e.g., cuboidal samples taken from a spherically shaped femoral head). Marrow-intact sections of spongiosa were bagged, labeled, and kept frozen until NMR microimaging sessions could be arranged. For the lumbar vertebra, 2 cuboidal sections (roughly, $1.25 \times 1.25 \times 2.5$ cm on edge) were cut from the vertebral body representing ~24% of the total vertebral body spongiosa. For the right proximal femur, 4 cuboidal sections were cut from the femoral head (~20% of total spongiosa within the head) and 4 sections were cut from the femoral neck (~16% of the total spongiosa within the neck).

Image Segmentation of Spongiosa and Cortical Bone Regions

To create tomographic anatomic models for use in internal dosimetry, radiation transport codes must be able to decipher the boundaries of each tissue region for which an independent dose assessment is to be made. Limitations of CT image acquisition can result in an overlap of gray-scale values for tissues of interest, thus precluding the use of simple automated methods of boundary definition. In the present study, the program CT_Contours was adopted for use in segmenting spongiosa and cortical bone within each ex vivo CT image set (21). This program is based on Interactive Data Language version 5.5 and can output labeled contour files in a variety of formats, including binary files for EGSnrc (22) and ASCII text for MCNP (23). CT_Contours displays the current CT information as well as a color overlay of the contours being edited. The contours can be created using a variety of tools, including basic thresholding, pixel growing, voxel growing, region growing, and manual segmentation. The voxels contained in the individual contours are filled with the desired segmentation value, generating volumes of voxels with identical tag values. In the present study, these volumes represent individual regions of either trabecular spongiosa or cortical bone within the skeletal site. CT_Contours was written to have the option of displaying the images using 15 different filters, including gaussian smoothing (3×3 , 5×5 , or 7×7), median (3×3 , 5×5 , or 7×7), Roberts edge detection, Sobel edge detection, Prewitt edge detection, isotropic edge detection, histogram equalization, adaptive histogram equalization, sharpening, and Kuwahara (3×3 or 5×5) filtering.

By altering regions of a separate contour dataset, the desired segmentation can be performed. CT_Contours was designed so that ROI creation or modification can be performed in the transverse, sagittal, or coronal plane.

NMR Microscopy of Trabecular Spongiosa

NMR microscopy of trabecular bone for the purposes of skeletal dosimetry has been discussed previously (20,24–27). NMR imaging requires physical sectioning of the excised sample and digestion of the marrow tissues. Samples of trabecular bone sections are first immersed and suspended within a circulating solution of sodium hypochlorite for ~3 h. The samples are then rinsed in water and reimmersed in a new solution. This process is repeated up to 3 times depending on the size of the sample. Visual inspection is used to determine the number of repetitions needed. To ensure that water completely fills all marrow cavities, each sample is placed in a container filled with Gd-doped water under vacuum. While immersed, the sample is placed in a smaller container needed for insertion into the magnet. This imaging container is then sealed and taken to the Advanced Magnetic Resonance Imaging and Spectroscopy facility at the UF McKnight Brain Institute for NMR microscopy.

NMR microscopy images in the present study were acquired on a Bruker 40-cm wide-bore imaging spectrometer, operated at a 470-MHz proton resonance frequency (11-T magnetic field strength). The system is fitted with a small gradient set (for microimaging), consisting of 3-axes magnetic-field gradients, with a maximum gradient amplitude of 22 G/cm in all 3 orthogonal directions. A 35-mm-diameter quadrature birdcage coil of 45-mm length is used to obtain the best signal-to-noise ratio (SNR). For all imaging sessions, a 3D RARE (rapid acquisition with relaxation enhancement) spin-echo pulse sequence is used to obtain fully 3D images of the samples. Fields of view are typically $3.2 \times 3.2 \times 3.2$ cm with matrix dimensions of $512 \times 512 \times 512$. The resulting spatial resolution of the 3D images is thus $63 \times 63 \times 63$ μ m. Smaller voxel dimensions can be achieved at UF (~58 μ m), but at the cost of smaller sample sizes and increased imaging time (to preserve SNR). Postacquisition image processing, including gray-level thresholding, voxel segmentation, and 3D median filtering, have been reported previously (24,28). For use in radiation transport simulations, interior ROIs are taken to avoid physical distortions (bone saw tearing) or imaging distortions (NMR aliasing) at the edges of the sectioned specimen.

Voxel-Based Infinite Spongiosa Transport (VBIST) Model

After NMR microscopy of our skeletal samples, a series of VBIST models were created to approximate (via 3D transport) the results of current CBIST models. First, marrow voxels within the binary NMR microscopy image are further labeled into voxels of active (red) marrow and inactive (yellow) marrow at a predetermined value of marrow cellularity. This process has been outlined previously by Shah et al. and is based on microscopy measurements of the spatial distribution of adipocytes within normal bone marrow biopsies covering a broad range of marrow cellularities (25). Skeletal endosteum is further defined as a 10- μ m tissue layer at the bone-marrow interface as previously described by Jokisch et al. (20). The resulting 4-tissue 3D model of trabecular spongiosa is coupled to the EGSnrc radiation transport code (22) for electron and β -particle transport simulations. Source tissues include the trabecular active marrow (TAM), trabecular bone surfaces (TBS), and trabecular bone volume (TBV). Bone surface sources are

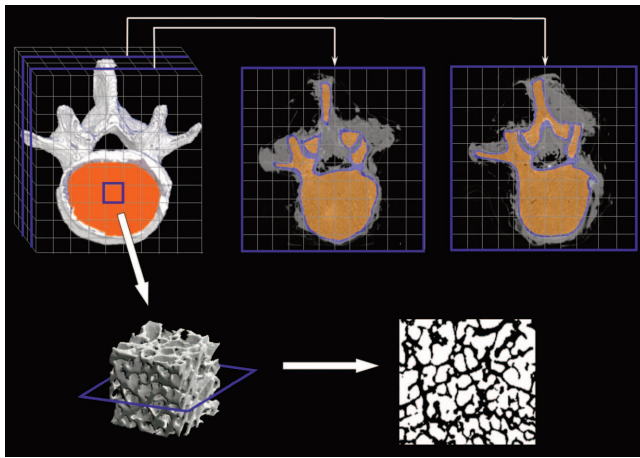


FIGURE 1. Schematic of PIRT model constructed for L4 vertebra.

approximated as a 0.1- μm layer on the marrow side of the bone-marrow voxel interface. Target tissues include the TAM and the trabecular bone endosteum (TBE). Once a given electron reaches the physical edge of the 3D NMR microscopy image, that particle is reintroduced to the image at a corresponding location at its opposing edge. The processes of particle transport within the image of spongiosa and its reintroduction are continued until all initial kinetic energy is expended. Particle histories are continued (50,000–2,000,000) until coefficients of variation on the absorbed fraction are $<1\%$. It is noted, however, that results given here for our voxel-based Infinite Spongiosa Transport (IST) model are only approximate to those given from chord-based IST models. In previous studies by Jokisch et al. (20,29), the authors question the sampling independence of the marrow and bone chord-length distributions within existing CBIST models and suggest a 3D joint distribution might be more appropriate to describing the full 3D microarchitecture of particle transport within the spongiosa regions of trabecular bone.

PIRT Model: L4 Vertebra

In contrast to the VBIST model, the PIRT model supplements the 3D microscopic histology provided by the NMR microscopy image with the 3D macroscopic histology given in the corresponding ex vivo CT image. The latter provides additional data for

particle transport, including (a) the spatial extent of the trabecular spongiosa (e.g., vertebral processes and body) and (b) the spatial extent of the surrounding cortical bone (which laterally encompasses the vertebral body, forms the lamina separating the vertebral processes, and is absent at the superior and inferior body-disk interfaces).

A schematic of the PIRT model for the L4 vertebra of the 66-y man is given in Figure 1. The ex vivo CT image is shown in the top left, in which segmented regions of spongiosa and cortical bone surfaces are highlighted in orange and white, respectively. Two representative transverse slices are shown (top middle and top right), where regions of spongiosa (orange) and cortical bone (light blue) are again differentiated. Superimposed over the entire ex vivo CT image is a 3D array of the replicate cuboidal NMR microscopy images, each representing the 3D microstructure of the individual bone trabeculae and marrow cavities. A 3D rendering of the NMR microimage is thus shown in the bottom left of Figure 1. Finally, a single transverse slice through the NMR microimage is shown in the bottom right, displaying individual voxels of bone (black) and total marrow (white).

In the EGSnrc implementation of the vertebral PIRT model, individual electrons are tracked simultaneously within the coordinates of the NMR microimage (indicating locations in TBV, TBE, TAM, or trabecular inactive marrow [TIM]) and the coordinates of the CT macroimage (indicating locations in spongiosa, cortical bone volume [CBV], or surrounding tissues—muscle, soft tissue, or vertebral disks). Elemental compositions and mass densities assumed within the PIRT model were taken from Report 46 of the International Commission on Radiation Units and Measurements (30) (see Table 1). When the particle is shown to leave the spongiosa of the CT macroimage, tracking within the NMR microimage is halted and the particle is transported within a homogeneous region of cortical bone defined only by the larger voxels of the ex vivo CT macroimage. Upon particle escape from outer surface of the bone site, particle tracking is terminated. In cases in which the particle leaves cortical bone and reenters the interior spongiosa, particle tracking in the NMR microimage is resumed. The PIRT model is thus far more anatomically realistic than is the geometry provided by either the CBIST or VBIST model, especially for higher-energy, longer-ranged electrons and β -particles.

The principal approximation inherent within the PIRT model is that the trabecular microstructure given by the physical section of spongiosa (as imaged via NMR) is uniform across all CT-seg-

TABLE 1
Elemental Tissue Compositions (% by Mass) and Mass Densities Used in Either VBIST or PIRT Model of Skeletal Dosimetry

Tissue or region	H	C	N	O	Trace	Mass density (g cm ⁻³)
TAM	10.5	41.4	3.4	43.9	0.1 P, 0.2 S, 0.2 C, 0.2 K, 0.1 Fe	1.03
TIM	11.5	64.4	0.7	23.1	0.1 Na, 0.1 S, 0.1 C	0.98
TBE	10.5	25.6	2.7	60.2	0.1 Na, 0.2 P, 0.3 S, 0.2 C, 0.2 K	1.03
TBV	3.4	15.5	4.2	43.5	0.1 Na, 0.2 Mg, 10.3 P, 0.3 S, 22.5 Ca	1.92
CBV	3.4	15.5	4.2	43.5	0.1 Na, 0.2 Mg, 10.3 P, 0.3 S, 22.5 Ca	1.92
Surrounding tissues	10.5	25.6	2.7	60.2	0.1 Na, 0.2 P, 0.3 S, 0.2 C, 0.2 K	1.03

TAM = “adult red marrow”; TIM = “adult yellow marrow”; TBE = “adult ICRU-44 soft tissue (male)”; TBV = “adult cortical bone”; CBV = “adult cortical bone” (Appendix A of ICRU Report 46) (30).

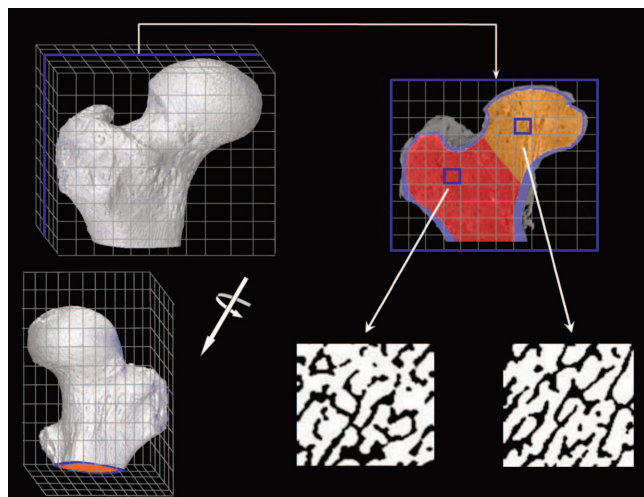


FIGURE 2. Schematic of PIRT model constructed for right proximal femur.

mented regions of spongiosa within the skeletal site. As a result, the trabecular microstructures of the various vertebral processes (spinal, superior articular, and transverse) are implicitly assumed to be approximated by that imaged within the vertebral body. In cases in which more than one physical section of spongiosa has been imaged by NMR, the PIRT model can be rerun using different NMR microimages. The resulting microimage-specific absorbed fraction profiles can thus be averaged either uniformly or weighted by the volume of spongiosa sectioned. Finally, it is noted that the PIRT model permits explicit consideration of a cortical bone volume (CBV) as a potential radioactivity source—a feature not permitted within the CBIST or VBIST model of skeletal dose.

PIRT Model: Proximal Femur

A corresponding schematic of the PIRT model for the right proximal femur of the 66-y male subject is shown in Figure 2. In adults, hematopoiesis occurs primarily within the proximal epiphysis of the femur and, thus, the macrostructural model (shown in the top right of Fig. 2 and given by the ex vivo CT) is terminated inferiorly at the point where the lesser trochanter merges anatomically with the femoral diaphysis. As with the University of Leeds chord-length measurements for their 44-y man, the biomechanics and, thus, the trabecular microstructure are notably different within the femoral head and femoral neck; consequently, 3D NMR microscopy images were taken separately from the head and neck regions of the proximal femur. Representative transverse NMR

image slices are shown in the bottom middle and bottom right of Figure 2. For each tissue source region in the model (TAM, TBV, or TBS), 2 different transport simulations are performed—one in which electrons are started within the spongiosa of the femoral head (orange voxels of the ex vivo CT transverse slice) and one in which electrons are started within the spongiosa of the femoral neck (red voxels of the ex vivo CT transverse slice). In each case, only the corresponding NMR microscopy image is used within the PIRT model (head or neck microimage). Final absorbed fraction results for the entire proximal femur are taken as mass weighted averages of results from the head-only and neck-only spongiosa source transport calculations. Table 2 displays the various source and target tissue masses for both the proximal femur and lumbar vertebra PIRT dosimetry models (given as the product of their segmented volume and the reference densities of Table 1). The bottom row of Table 2 gives values of marrow volume fraction (MVF) defined as the fraction of all voxels within the NMR microimage that are assigned to marrow tissues after image thresholding. Here it is noted that the MVF of the femoral head is 64.5%, whereas it is 75.5% within the femoral neck. The MVF within the L4 vertebral body, however, was measured at 87%.

RESULTS

Absorbed Fractions to Active Marrow Within L4 Vertebra

Figure 3 displays values of electron-absorbed fraction to active (red) bone marrow within the L4 vertebra of the 66-y male subject. Figure 3A corresponds to an assumption of 100% marrow cellularity (no voxels of adipose tissue are labeled within the NMR microimage), whereas Figure 3B corresponds to an assumed marrow cellularity of 70% (reference value in both ICRP Publications 70 and 89 (12,31)). In each graph, solid lines indicate energy-dependent absorbed fractions obtained from PIRT model simulations, whereas dashed lines indicate those derived from VBIST model simulations. For either model and at both cellularities, 3 source tissues are considered: TAM (diamonds), TBS (triangles), and TBV (circles).

At source energies below ~100 keV, the 2 model types yield essentially equivalent results, as boundary effects at the spongiosa–cortical bone interface (within the PIRT model) play a negligible role in modifying the pattern of energy deposition to active marrow voxels (as seen within the VBIST model). Model equivalency is noted to extend to

TABLE 2
Tissues Masses Used in PIRT Model (100% Marrow Cellularity)

Tissue region or quantity	L4 vertebra	Femoral head	Femoral neck	Proximal femur
TAM (g)	153.3	15.80	26.30	42.1
TBE (g)	3.2	0.68	1.12	1.8
TBV (g)	117.0	4.55	7.55	12.1
CBV (g)	74.4			26.6
MVF* (%)	87	64.5	75.5	

*MVF = marrow volume fraction: ratio of total marrow voxels to total voxels in binary 3D NMR microscopy images of excised cube of trabecular spongiosa.

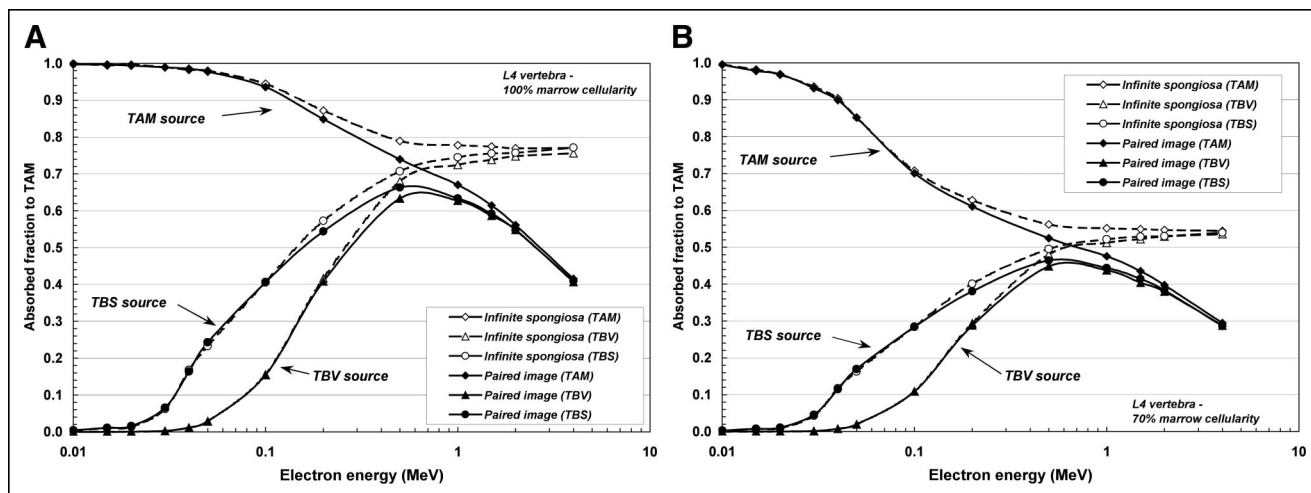


FIGURE 3. Electron-absorbed fractions to active bone marrow within L4 vertebrae for 3 source tissues: TAM, TBV, and TBS. Data shown by solid lines are from PIRT model, whereas those given by dashed lines are from VBIST model. Data for A correspond to 100% marrow cellularity, whereas those for B correspond to ICRP 70 reference cellularity of 70% (31).

electrons of ~ 200 -keV initial energy when emitted within the volume of the bone trabeculae (TBV sources).

As the electron initial energy increases above 100–200 keV, energy deposition to active marrow as predicted under VBIST model simulations increasingly overpredicts that given by the more anatomically realistic PIRT model. As previously noted for chord-based skeletal models under either CBIST or VBIST simulations, absorbed fractions asymptotically approach a limited value independent of the source tissue (13,15,20). At 100% cellularity, the VBIST model absorbed fraction to active marrow approaches a value of 0.76 at high electron energies, whereas it approaches a limiting value of 0.53 at 70% cellularity (70% of 0.76). Similarly, absorbed fractions to active marrow predicted under PIRT model simulations also converge in a source-independent manner, but this convergence value is

energy dependent as more and more electron energy is lost to the surrounding cortical bone (and potentially surrounding tissues). With the PIRT model results serving as the local standard, percentage errors in the self-absorbed fraction to active marrow given by the VBIST model are 7% at 500 keV, 16% at 1 MeV, and 85% at 4 MeV. Corresponding percentage errors are 7%, 16%, and 88% for TBS sources and 7%, 18%, and 89% for TBV sources. These percentage errors are roughly equivalent at both marrow cellularities.

Absorbed Fractions to Active Marrow Within Proximal Femur

Figure 4 displays values of electron-absorbed fraction to active marrow for TAM, TBS, and TBV sources located within the spongiosa of the right proximal femur of the 66-y male subject. Figures 4A and 4B correspond to marrow

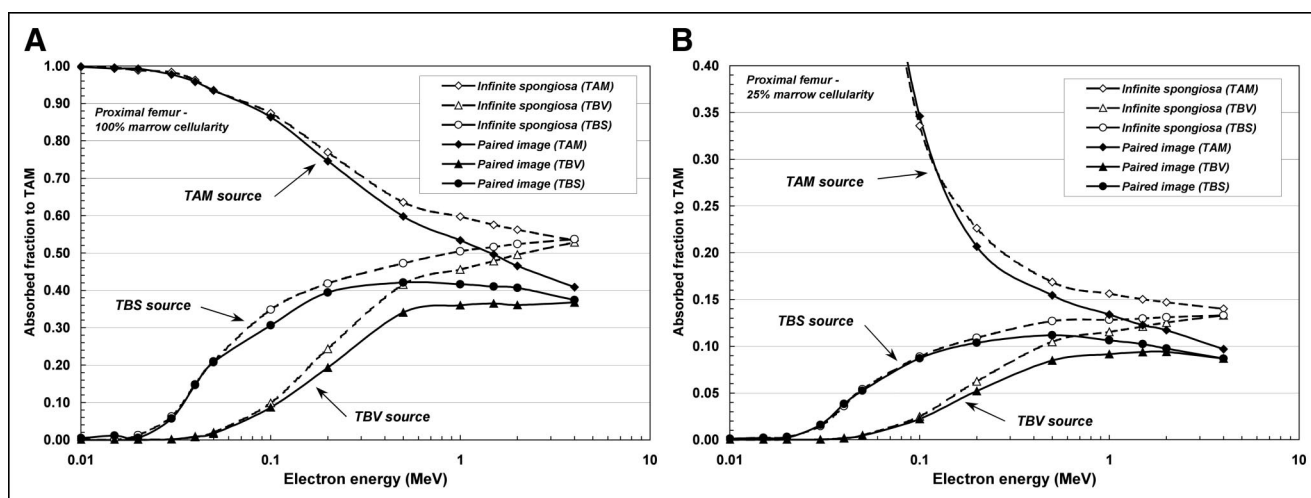


FIGURE 4. Electron-absorbed fractions to active bone marrow within proximal femur for 3 source tissues: TAM, TBV, and TBS. Data shown by solid lines are from PIRT model, whereas those given by dashed lines are from VBIST model. Data for A correspond to 100% marrow cellularity, whereas those for B correspond to ICRP 70 reference cellularity of 25% (31).

cellularities of 100% and 25%, respectively, where the latter is the default cellularity for the upper femur given in ICRP Publications 70 and 89 (12,31). In each graph, the individual absorbed fraction profiles for electron sources in the femoral head and in the femoral neck have been averaged according to the total mass of source tissue in the head and neck regions of the proximal femur, respectively. In Figure 4B, the ordinate has been expanded to better view differences in modeling results at high electron energies. At the lowest energy considered (10 keV), a value of $\phi(\text{TAM} \leftarrow \text{TAM}) = 0.98$ is seen under both VBIST and PIRT simulations.

Patterns of divergence between the 2 modeling approaches (VBIST vs. PIRT) in the proximal femur are seen to occur at lower energies compared with those found within the L4 vertebra (~ 100 keV for TAM sources, ~ 50 keV for TBS sources, and ~ 100 keV for TBV sources). Furthermore, it is seen that at 4 MeV (the highest energy considered), full convergence of the absorbed fraction to active marrow under both VBIST and PIRT model simulations has not yet been reached for the 3 source regions. Nevertheless, the energy-independent (VBIST) and energy-dependent (PIRT) patterns of convergence are still evident at electron initial energies of >1 MeV. With the PIRT model results serving as the local standard, percentage errors in self-absorbed fraction to active marrow (100% cellularity) given by the VBIST model are 6% at 500 keV, 12% at 1 MeV, and 31% at 4 MeV. Corresponding percentage errors are 22%, 27%, and 44% for TBS sources and 12%, 21%, and 44% for TBV sources. These percentage errors are $\sim 20\%$ – 50% higher when the marrow cellularity of the proximal femur is reduced to 25% (fat fraction of $\sim 75\%$).

Absorbed Fractions to Endosteal Tissues

Figure 5 displays values of absorbed fraction to the trabecular endosteal tissues defined as a 10- μm layer of soft tissue on the marrow side of the bone–marrow interface

within the NMR microimages. Figure 5A gives results for TBS, TBV, and TAM electron sources emitted within the L4 vertebra containing bone marrow at 70% cellularity. Figure 5B shows data for these same source tissues within the right proximal femur at 25% marrow cellularity. In both graphs, the ordinate scale is expanded to a maximum value of 0.16 to facilitate viewing model differences at higher energies. At the lowest energy considered (10 keV), a value of $\phi(\text{TBE} \leftarrow \text{TBS}) = 0.5$ is seen under both VBIST and PIRT simulations.

At each energy for each model, higher absorbed fractions are noted for electron sources on the trabecular surfaces, whereas lower absorbed fractions are seen for electron sources emitted within the active bone marrow. Intermediate absorbed fractions are shown for bone volume sources that peak in value at a source energy of ~ 100 keV in both skeletal sites. As expected, VBIST model simulations approach energy- and source-independent convergence values at high electron initial energies (0.032 in the L4 vertebra, and 0.045 in the proximal femur), whereas source-independent convergence values for the PIRT model are shown to continually decline with increasing source energy above 1 MeV. This decline is slightly more prominent in the L4 vertebra than seen in the proximal femur and is accountable in part by cortical bone losses within the vertebral processes. In these anatomic regions of the vertebra (which encompass $\sim 25\%$ of total vertebral spongiosa), the surface-to-volume ratio of trabecular spongiosa is higher than that found in the vertebral body and, thus, electron escape to cortical bone is greater for individual electron emissions.

DISCUSSION

As a further means of comparing the VBIST and PIRT model results, radionuclide S values were calculated for a wide range of β -particle emitters of interest in skeletal

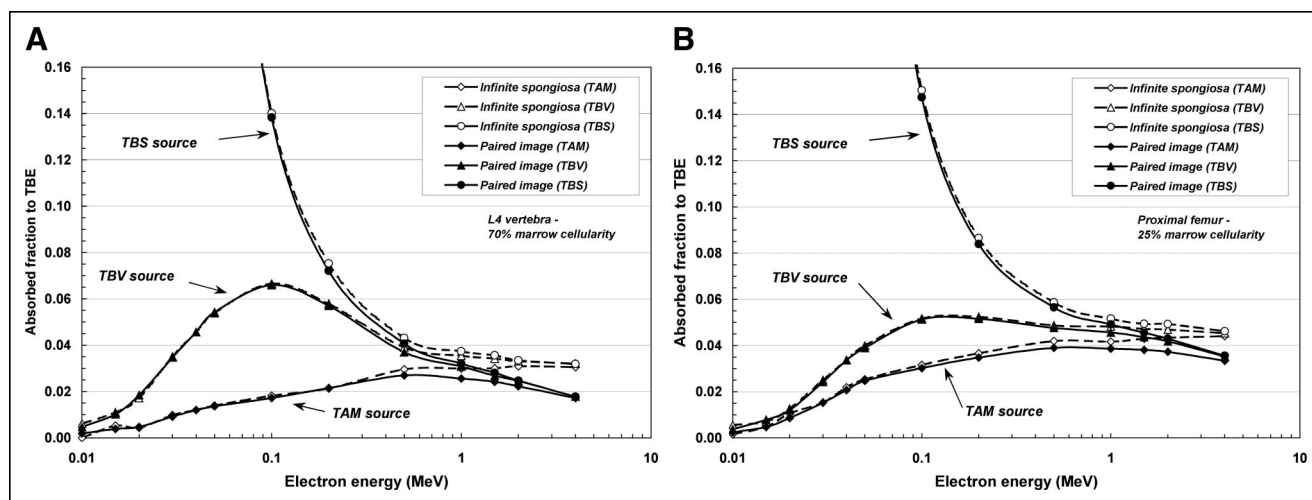


FIGURE 5. Electron-absorbed fractions to trabecular bone endosteum within L4 vertebra (A) and proximal femur (B) for 3 source tissues: TAM, TBV, and TBS. Data shown by solid lines are from PIRT model, whereas those given by dashed lines are from VBIST model.

TABLE 3
Ratio of Radionuclide S Value for Active Marrow (TAM) Target as Given by Voxel-Based VBIST Model to That Given by PIRT Model

Radionuclide	E_{ave} (keV)	E_{max} (keV)	L4 vertebra: 100% cellularity			Proximal femur: 100% cellularity		
			TAM source	TBS source	TBV source	TAM source	TBS source	TBV source
³³ P	77	239	1.01	1.02	1.02	1.02	1.09	1.21
¹⁶⁹ Er	100	351	1.02	1.04	1.03	1.02	1.08	1.23
¹⁷⁷ Lu	133	498	1.03	1.05	1.04	1.03	1.09	1.23
¹⁵³ Sm	225	809	1.05	1.06	1.06	1.04	1.10	1.23
¹⁸⁶ Re	323	1,075	1.08	1.09	1.09	1.06	1.13	1.24
⁸⁹ Sr	583	1,492	1.13	1.14	1.13	1.10	1.18	1.26
³² P	695	1,854	1.15	1.16	1.15	1.11	1.19	1.26
¹⁸⁸ Re	764	2,000	1.17	1.19	1.18	1.12	1.21	1.28
⁹⁰ Y	934	2,282	1.21	1.23	1.22	1.14	1.23	1.30

Radionuclide	E_{ave} (keV)	E_{max} (keV)	L4 vertebra: 70% cellularity			Proximal femur: 25% cellularity		
			TAM source	TBS source	TBV source	TAM source	TBS source	TBV source
³³ P	77	239	1.01	1.02	1.01	1.00	1.03	1.17
¹⁶⁹ Er	100	351	1.02	1.04	1.02	1.02	1.05	1.19
¹⁷⁷ Lu	133	498	1.03	1.05	1.04	1.04	1.07	1.21
¹⁵³ Sm	225	809	1.05	1.06	1.06	1.07	1.10	1.22
¹⁸⁶ Re	323	1,075	1.08	1.09	1.09	1.09	1.13	1.24
⁸⁹ Sr	583	1,492	1.13	1.14	1.14	1.13	1.18	1.25
³² P	695	1,854	1.15	1.16	1.16	1.15	1.19	1.26
¹⁸⁸ Re	764	2,000	1.18	1.19	1.20	1.16	1.21	1.27
⁹⁰ Y	934	2,282	1.22	1.23	1.24	1.19	1.24	1.28

tissue imaging and radionuclide therapy. Absorbed fractions to active bone marrow given in Figures 3A and 3B and Figures 4A and 4B, along with tissue mass data of Table 2 and β -particle energy spectra from Eckerman et al. (32), were used to calculate S values under the MIRD schema for 9 different radionuclides. Ratios of the S value based on VBIST-model absorbed fractions to that using PIRT-model absorbed fractions are displayed in Table 3 for both skeletal sites and at both 100% and ICRP reference marrow cellularities. For low-energy β -emitters such as ³³P, ¹⁶⁹Er, and ¹⁷⁷Lu, absorbed fractions given by the VBIST model simulations overestimate radionuclide S values for TAM, TBS, and TBV sources by only 1%–5% in the L4 vertebra. Higher errors are noted in the proximal femur, particularly for bone trabeculae volume sources (ratios of 1.17–1.23). For radionuclides at intermediate β -energies (E_{ave} of 225–583 keV), S value ratios range from 1.05 to 1.14 in the L4 vertebra and from 1.04 to 1.26 in the proximal femur. For radionuclides in the highest β -energy range (E_{ave} of 695–934 keV), S value ratios range from 1.15 to 1.24 in the L4 vertebra and from 1.11 to 1.30 in the proximal femur. It is reasonable to assume that similar errors are also present in radionuclide S values derived from chord-based models (14,16), which, as in the VBIST simulations of the present study, assume an infinite region of spongiosa during particle transport.

Before the full development of the PIRT methodology given here, the UF ALRADS research group had attempted to correct for energy loss to cortical bone by applying a stylized model of the skeletal site macrostructure. For ex-

ample, in the study by Patton et al. (19), a spheric region of spongiosa surrounded by a spheric shell of cortical bone was applied to the femoral heads of 3 different individuals based on CT image analysis. In that study, it was demonstrated that infinite spongiosa transport yielded radionuclide S values for ³²P that were ~5%–8% higher than those in which cortical bone energy loss was accounted for via stylistic modeling of the femoral head. For the higher-energy ⁹⁰Y, the infinite spongiosa transport results gave S values 8%–11% higher. In the present study, however, the full 3D histologic macrostructure of the proximal femur (head as well as neck and trochanter regions) is treated within the PIRT model simulations. Corresponding corrections to infinite spongiosa transport are shown in the present study (by the PIRT model) to be significantly higher (up to 1.26 for ³²P and up to 1.30 for ⁹⁰Y) than indicated previously by Patton et al. (19) for the femoral head. These larger corrections are attributed to enhanced particle energy loss at 3 spongiosa regions of the PIRT femur model: the femoral neck, the trochanters, and the bottom interface of the model (where particles are lost to inactive marrow of the femoral diaphysis; Fig. 2). These regions of enhanced electron escape were not present within the spheric femoral head model of the Patton et al. study.

Improved macrostructural modeling of the skeleton via the PIRT model methodology will potentially lead to improvements in correlations between marrow dose estimates and observed patient myelotoxicity. For example, clinical studies of the bone pain palliation agents ¹⁵³Sm-ethylenedi-

aminetetramethylene phosphonate (^{153}Sm -EDTMP) (33–35) and ^{186}Re -hydroxyethylidene diphosphonate (^{186}Re -HEDP) (36–38) have shown patient marrow toxicities that were lower than expected based on marrow dose estimates from standard CBIST skeletal dose models (e.g., MIRDSE2 and MIRDSE3). Although various studies have been initiated to explain these discrepancies, including improvements in activity uptake quantification (39,40), the data of Table 3 indicate that perhaps values of marrow dose were simply overestimated in these studies, as the standard clinical models do not properly account for particle escape from marrow-filled regions of spongiosa. For both bone surface and volume sources, infinite spongiosa transport is shown in Table 3 to overestimate the femoral marrow self-dose by 10%–22% for ^{153}Sm and 13%–24% for ^{186}Re , whereas the vertebral marrow self-dose is overestimated by 6% for ^{153}Sm and 9% for ^{186}Re .

CONCLUSION

A PIRT model for skeletal dosimetry is presented in which electrons and β -particles are tracked simultaneously within 2 different segmented digital images: (a) an ex vivo CT image of the skeletal site with segmented regions of trabecular spongiosa, cortical bone, and surrounding tissues and (b) an ex vivo NMR microscopy image of the interior bone trabeculae and marrow cavity microstructure representative of that found within spongiosa regions of the ex vivo CT image. Example dose calculations under the PIRT methodology within the L4 vertebra and right proximal femur of an adult 66-y male subject demonstrate a divergence from standard infinite spongiosa transport (VBIST) methods at energies as low as 50–200 keV, depending on the source tissue and skeletal site. Calculations of radionuclide S values under both methodologies imply that current chord-based models used in clinical skeletal dosimetry may overestimate dose to active bone marrow in these 2 skeletal sites by ~4%–23% for low-energy β -emitters (^{33}P , ^{169}Er , and ^{177}Lu), by ~4%–25% for intermediate-energy β -emitters (^{153}Sm , ^{186}Re , and ^{89}Sr), and by ~11%–30% for high-energy β -emitters (^{32}P , ^{188}Re , and ^{90}Y). Higher errors are noted for bone-volume seekers, whereas lower errors are seen for source emissions within the active bone marrow. Though the proximal femur and lumbar vertebra are investigated in the present study, potentially larger errors in skeletal dosimetry are presumed to exist in skeletal sites with disproportionately smaller volumes of spongiosa (e.g., ribs, cranium, and sternum).

The PIRT methodology supersedes previous stylized modeling attempts by the UF ALRADS research group to account for the finite spatial extent of trabecular spongiosa and the presence of cortical bone. This approach thus renders obsolete any need for mathematic modeling of the either simple or complex bone site geometries. Furthermore, the technique increases the prospects for expanded availability of reference skeletal dosimetry models for both gen-

ders and of individuals of varying stature and skeletal size for use in radionuclide therapy treatment planning of cancer in which marrow toxicity is of concern.

ACKNOWLEDGMENTS

This work was supported in part by grant CA96441 from the National Cancer Institute and grant DE-FG07-02ID14327 from the U.S. Department of Energy with the University of Florida.

REFERENCES

1. Spiers FW. Radiotherapeutic physics. II. Dosage in irradiated soft tissue and bone. *Br J Radiol.* 1951;24:365–370.
2. Spiers FW. Dose to trabecular bone from internal beta-emitters. In: Snyder WS, ed. *First International Congress of Radiation Protection*. Vol. 1. Rome, Italy: Pergamon Press; 1966:165–172.
3. Spiers FW. A review of the theoretical and experimental methods of determining radiation dose in bone. *Br J Radiol.* 1966;39:216–221.
4. Spiers FW. Beta particle dosimetry in trabecular bone. In: Mays CW, Jee WSS, Lloyd RD, Stover BJ, Dougherty JH, Taylor GN, eds. *Delayed Effects of Bone-Seeking Radionuclides*. Salt Lake City, UT: University of Utah Press; 1967:95–108.
5. Spiers FW. Dosimetry at interfaces with special reference to bone. In: Booz J, Ebert HG, eds. *Symposium on Microdosimetry*. Report EUR 3747. Ispra, Italy: European Atomic Energy Commission; 1968:473–508.
6. Spiers FW. Determination of absorbed dose to bone and red bone marrow. In: Cloutier R, Edwards C, Snyder W, eds. *Medical Radionuclides: Radiation Dose and Effects*. AEC Symposium Series 20. Oak Ridge, TN: U.S. Atomic Energy Commission; 1969:347–367.
7. Beddoe AH. *The Microstructure of Mammalian Bone in Relation to the Dosimetry of Bone-Seeking Radionuclides* [thesis]. Leeds, U.K.: Department of Medical Physics, University of Leeds; 1976.
8. Beddoe AH, Darley PJ, Spiers FW. Measurements of trabecular bone structure in man. *Phys Med Biol.* 1976;21:589–607.
9. Whitwell JR. *Theoretical Investigations of Energy Loss by Ionizing Particles in Bone* [thesis]. Leeds, U.K.: Department of Medical Physics, University of Leeds; 1973.
10. Whitwell JR, Spiers FW. Calculated beta-ray dose factors for trabecular bone. *Phys Med Biol.* 1976;21:16–38.
11. ICRP. *Report on the Task Group on Reference Man*. ICRP Publication 23. Oxford, UK: International Commission on Radiological Protection; 1975:62–98.
12. ICRP. *Basic Anatomical and Physiological Data for Use in Radiological Protection: Reference Values*. Publication 89. New York, NY: International Commission on Radiological Protection; 2002:167–190.
13. Eckerman KF. Aspects of the dosimetry of radionuclides within the skeleton with particular emphasis on the active marrow. In: Schlafke-Stelson AT, Watson EE, eds. *Proceedings of the Fourth International Radiopharmaceutical Dosimetry Symposium*. CONF-85113. Oak Ridge, TN: Oak Ridge Associated Universities; 1985:514–534.
14. Bouchet LG, Bolch WE, Howell RW, Rao DV. S values for radionuclides localized within the skeleton. *J Nucl Med.* 2000;41:189–212.
15. Bouchet LG, Jokisch DW, Bolch WE. A three-dimensional transport model for determining absorbed fractions of energy for electrons in trabecular bone. *J Nucl Med.* 1999;40:1947–1966.
16. Eckerman KF, Stabin MG. Electron absorbed fractions and dose conversion factors for marrow and bone by skeletal regions. *Health Phys.* 2000;78:199–214.
17. Stabin MG, Eckerman KF, Bolch WE, Bouchet LG, Patton PW. Evolution and status of bone and marrow dose models. *Cancer Biother Radiopharm.* 2002;17:427–445.
18. Stabin MG. MIRDSE: personal computer software for internal dose assessment in nuclear medicine. *J Nucl Med.* 1996;37:538–546.
19. Patton PW, Rajon DA, Shah AP, Jokisch DW, Inglis B, Bolch WE. Site-specific variability in trabecular bone dosimetry: considerations of energy loss to cortical bone. *Med Phys.* 2002;29:6–14.
20. Jokisch DW, Bouchet LG, Patton PW, Rajon DA, Bolch WE. Beta-particle dosimetry of the trabecular skeleton using Monte Carlo transport within 3D digital images. *Med Phys.* 2001;28:1505–1518.
21. Nipper J, Williams J, Bolch W. Creation of two tomographic voxel models of pediatric patients in the first year of life. *Phys Med Biol.* 2002;47:3143–3164.

22. Kawrakow I. Accurate condensed history Monte Carlo simulation of electron transport. I. EGSnrc, the new EGS4 version. *Med Phys.* 2000;27:485–498.
23. Briesmeister JF. *MCNP: A General Monte Carlo N-Particle Transport Code*. LA-12625-M. Los Alamos, NM: Los Alamos National Laboratory; 1997.
24. Patton PW, Jokisch DW, Rajon DA, Shah AP, Myers SL, Bolch WE. Skeletal dosimetry via NMR microscopy: investigations of sample reproducibility and signal source. *Health Phys.* 2002;82:316–326.
25. Shah AP, Patton PW, Rajon DA, Bolch WE. Adipocyte spatial distributions in bone marrow: implications for skeletal dosimetry models. *J Nucl Med.* 2003;44:774–783.
26. Bolch WE, Patton PW, Shah AP, Rajon DA. Considerations of anthropomorphic, tissue volume, and tissue mass scaling for improved patient specificity of skeletal S values. *Med Phys.* 2002;29:1054–1070.
27. Bolch WE, Patton PW, Rajon DA, Shah AP, Jokisch DW, Inglis B. Considerations of marrow cellularity in 3D dosimetric models of the trabecular skeleton. *J Nucl Med.* 2002;43:97–108.
28. Jokisch DW, Patton PW, Inglis BA, et al. NMR microscopy of trabecular bone and its role in skeletal dosimetry. *Health Phys.* 1998;75:584–596.
29. Jokisch DW, Patton PW, Rajon DA, Inglis BA, Bolch WE. Chord distributions across 3D digital images of a human thoracic vertebra. *Med Phys.* 2001;28:1493–1504.
30. ICRU. *Photon, Electron, Proton and Neutron Interaction Data for Body Tissues*. Report 46. Bethesda, MD: International Commission on Radiation Units and Measurements; 1992.
31. ICRP. *Basic Anatomical and Physiological Data for Use in Radiological Protection: The Skeleton*. ICRP Publication 70. Oxford, U.K.: International Commission on Radiological Protection; 1995:1–80.
32. Eckerman KF, Westfall RJ, Ryman JC, Cristy M. Availability of nuclear decay data in electronic form, including beta spectra not previously published. *Health Phys.* 1994;67:338–345.
33. Turner H, Claringbold P. A phase II study of treatment of painful multifocal skeletal metastases with single and repeated dose samarium-153-EDTMP. *Eur J Cancer.* 1991;27:1084–1086.
34. Collins C, Eary JF, Donaldson G, et al. Samarium-153-EDTMP in bone metastases of hormone refractory prostate carcinoma: a phase I/II trial. *J Nucl Med.* 1993;34:1839–1844.
35. Farhanghi M, Holmes RA, Volkert WA, Logan KW, Singh A. Samarium-153-EDTMP: pharmacokinetic, toxicity and pain response using an escalating dose schedule in treatment of metastatic bone cancer. *J Nucl Med.* 1992;33:1451–1458.
36. Kucuk NO, Ibis E, Aras G, et al. Palliative analgesic effect of Re-186 HEDP in various cancer patients with bone metastases. *Ann Nucl Med.* 2000;14:239–245.
37. Giannakenas C, Kalofonos HP, Apostolopoulos DJ, Zarakovitis J, Kosmas C, Vassilakos PJ. Preliminary results of the use of Re-186-HEDP for palliation of pain in patients with metastatic bone disease. *Am J Clin Oncol.* 2000;23:83–88.
38. Breitz HB, Fisher DR, Wessels BW. Marrow toxicity and radiation absorbed dose estimates from rhenium-186-labeled monoclonal antibody. *J Nucl Med.* 1998;39:1746–1751.
39. van Rensburg AJ, Alberts AS, Louw WK. Quantifying the radiation dosage to individual skeletal lesions treated with samarium-153-EDTMP. *J Nucl Med.* 1998;39:2110–2115.
40. Brenner W, Kampen WU, Kampen AM, Henze E. Skeletal uptake and soft-tissue retention of ^{186}Re -HEDP and ^{153}Sm -EDTMP in patients with metastatic bone disease. *J Nucl Med.* 2001;42:230–236.



Accounting for beta-particle energy loss to cortical bone via paired-image radiation transport (PIRT)

Amish P. Shah

Department of Biomedical Engineering and Department of Nuclear & Radiological Engineering,
University of Florida, Gainesville, Florida 32611

Didier A. Rajon

Department of Neurosurgery, University of Florida, Gainesville, Florida 32611

Phillip W. Patton

Department of Health Physics, University of Nevada-Las Vegas, Las Vegas, Nevada

Derek W. Jokisch

Department of Physics and Astronomy, Francis Marion University, Florence, South Carolina 29501-0547

Wesley E. Bolch^{a)}

Department of Biomedical Engineering and Department of Nuclear & Radiological Engineering,
University of Florida, Gainesville, Florida 32611

(Received 5 October 2004; revised 29 January 2005; accepted for publication 8 March 2005;
published 18 April 2005)

Current methods of skeletal dose assessment in both medical physics (radionuclide therapy) and health physics (dose reconstruction and risk assessment) rely heavily on a single set of bone and marrow cavity chord-length distributions in which particle energy deposition is tracked within an infinite extent of trabecular spongiosa, with no allowance for particle escape to cortical bone. In the present study, we introduce a paired-image radiation transport (PIRT) model which provides a more realistic three-dimensional (3D) geometry for particle transport in the skeletal site at both microscopic and macroscopic levels of its histology. *Ex vivo* CT scans were acquired of the pelvis, cranial cap, and individual ribs excised from a 66-year male cadaver (BMI of 22.7 kg m⁻²). For the three skeletal sites, regions of trabecular spongiosa and cortical bone were identified and segmented. Physical sections of interior spongiosa were taken and subjected to microCT imaging. Voxels within the resulting microCT images were then segmented and labeled as regions of bone trabeculae, endosteum, active marrow, and inactive marrow through application of image processing algorithms. The PIRT methodology was then implemented within the EGSNRC radiation transport code whereby electrons of various initial energies are simultaneously tracked within both the *ex vivo* CT macroimage and the CT microimage of the skeletal site. At initial electron energies greater than 50–200 keV, a divergence in absorbed fractions to active marrow are noted between PIRT model simulations and those estimated under existing techniques of infinite spongiosa transport. Calculations of radionuclide *S* values under both methodologies imply that current chord-based models may overestimate the absorbed dose to active bone marrow in these skeletal sites by 0% to 27% for low-energy beta emitters (³³P, ¹⁶⁹Er, and ¹⁷⁷Lu), by ~4% to 49% for intermediate-energy beta emitters (¹⁵³Sm, ¹⁸⁶Re, and ⁸⁹Sr), and by ~14% to 76% for high-energy beta emitters (³²P, ¹⁸⁸Re, and ⁹⁰Y). The PIRT methodology allows for detailed modeling of the 3D macrostructure of individual marrow-containing bones within the skeleton thus permitting improved estimates of absorbed fractions and radionuclide *S* values for intermediate-to-high energy beta emitters. © 2005 American Association of Physicists in Medicine. [DOI: 10.1118/1.1898463]

Key words: skeletal dosimetry, marrow dose, NMR microscopy, radionuclide *S* value, absorbed fraction

I. INTRODUCTION

Accurate models of absorbed dose to skeletal tissue are needed in both radiation protection (e.g., predicting risks for leukemia and bone cancer induction following inhalation of long-lived bone-seeking radionuclides) and in radionuclide therapy (e.g., correlations of marrow absorbed dose and toxicity for radiopharmaceuticals subject to either specific or nonspecific skeletal uptake). Ideally these models must take into account both the microscopic structure of the bone tra-

beculae and marrow cavities, as well as the macroscopic structure of the bone site itself (shape and volume of the trabecular spongiosa and the exterior cortex of cortical bone). For alpha emitters and low-energy beta emitters, only the microscopic characterization of the bone site is needed in the dosimetry model, as these shorter-ranged particles typically expend their full emission energy within the trabecular spongiosa. For intermediate- to high-energy beta emitters, however, energy loss to the exterior cortical bone is to be

expected, especially at those skeletal sites with high spongiosa surface-to-volume ratios (e.g., flat bones such as the cranium and ribs).

Current models of skeletal dosimetry used in both health physics and medical physics track alpha and beta particles within the skeleton through an infinite region of trabecular spongiosa, thus neglecting effects introduced by the bone's three-dimensional (3D) macrostructure. These IST, or infinite spongiosa transport, models use as their input either (1) linear chord-length distributions measured across the trabeculae and marrow cavities,^{1,2} or (2) 3D digital images of that microstructure.^{3,4} Subsequently, we refer to these two modeling approaches as CBIST (chord-based IST) or VBIST (voxel-based IST) skeletal dosimetry models, respectively. The skeletal dosimetry model used in current clinical practice, the Eckerman and Stabin model⁵ of MIRDOSE3⁶ and its successor code, belongs to the CBIST model classification.

In the present study, we discuss a new approach to skeletal dosimetry using paired-image radiation transport (PIRT). In the PIRT skeletal model, radiation particles are tracked simultaneously within two different segmented digital images: (1) an *ex vivo* CT image of the skeletal site outlining regions of trabecular spongiosa and cortical bone, and (2) an *ex vivo* microCT image of the spongiosa microstructure (bone trabeculae and marrow cavities). In Shah *et al.*,⁷ we compare dosimetry results between VBIST and PIRT model transport simulations for electron and beta-particle emitters within the proximal femur and lumbar vertebrae of a 66-year adult male. In the current study, we extend this comparison to include three other skeletal sites with high percentages of active bone marrow: the pelvis, cranium, and ribs.

Microimaging of trabecular spongiosa: NMR microscopy vs microCT. Our research group has previously reported on the use of NMR microscopy to obtain 3D microimages of the trabecular micro-architecture for skeletal dosimetry.^{3,4,7-12} Optimal images from NMR microscopy require physical samples of spongiosa be subjected to marrow digestion. Marrow digestion is efficient for those skeletal sites with relatively large and externally accessible marrow cavities (e.g., femur head/neck and vertebra). In contrast, marrow digestion can be incomplete for skeletal sites with inaccessible and relatively small marrow cavities (e.g., cranium, sternum, etc.). Alternatively, sectioned pieces of trabecular spongiosa may be imaged directly via NMR as marrow-intact samples. Problems with this approach, however, include poor signal-to-noise ratios and corresponding difficulties in image segmentation and thresholding. For both marrow-digested and marrow-intact samples, one must also contend with limitations in sample size considering the small imaging bore of high-field NMR systems. An attractive alternative to NMR microscopy for skeletal dosimetry is the use of microCT imaging of physical samples of spongiosa.¹³⁻¹⁵ MicroCT imaging of marrow-intact samples is an option that requires little sample preparation and thus is achievable at all skeletal sites regardless of the ability to fully digest the marrow tissues.

II. MATERIALS AND METHODS

A. Cadaver selection

Candidate subjects for study were obtained through the State of Florida Anatomical Board located on the University of Florida (UF) campus. Cadaver selection criteria included (1) an age between 50 and 75 years (representative of typical radionuclide therapy patients), (2) a body mass index of 18.5–25 kg m⁻² (CDC recommended healthy range¹⁶), and (3) a cause of death that would preclude significant skeletal deterioration. The subject identified was a 66-year male approximately 68 kg in total mass and 173 cm in total height at the time of death (BMI of 22.7 kg m⁻²). The subject died suddenly of complications associated with cardiomyopathy.

B. *In vivo* computed tomography scanning

Prior to bone harvesting, the male cadaver was subjected to whole-body imaging via multi-slice helical CT at a pitch necessary to reconstruct contiguous 1 mm axial slices. The images were acquired on a Siemens Sensation 16 unit within the Department of Radiology at UF Shands Hospital. Image reconstruction was performed with a bone filter at an in-plane pixel resolution of 977 μ m \times 977 μ m. The CT image sets were then transferred to workstations within the *Advanced Laboratory for Radiation Dosimetry Studies (ALRADS)* in the UF Department of Nuclear & Radiological Engineering for image processing and data storage. The *in vivo* CT scans provided image data in order to (1) select the anatomical region from which the bone site would be harvested, and (2) construct 3D anatomic models of skeletal sites where bone harvesting (and thus *ex vivo* CT scanning) might be incomplete (e.g., rib cage).

C. Bone harvesting and *ex vivo* computed tomography scanning

Following detailed review of the whole-body *in vivo* CT images, bone harvesting was conducted. Fourteen major skeletal sites were taken from the male cadaver including the pelvis (pelvis), the cranium (cranial cap), and several ribs from both the right and left side of the rib cage. Once each skeletal site was excised, it was cleaned of excess tissue, bagged, labeled, and stored frozen until *ex vivo* CT imaging could be scheduled. Post-harvest, *ex vivo* CT imaging was conducted at the highest resolution permitted based on sample size (1.0 mm slice thickness with an in-plane resolution of 0.65 mm \times 0.65 mm for the pelvis, 0.23 mm \times 0.23 mm for the ribs). The *ex vivo* CT scans provided image data for (1) identifying the location and extent of trabecular spongiosa to be sectioned for microCT imaging; (2) quantifying both trabecular spongiosa and cortical bone volumes within the bone site; and (3) constructing 3D anatomic models of the bone site for subsequent paired-image radiation transport simulations.

Following detailed review of the *ex vivo* CT scans; physical sections of trabecular spongiosa were taken from each bone site. Sections representing as large a region of spon-

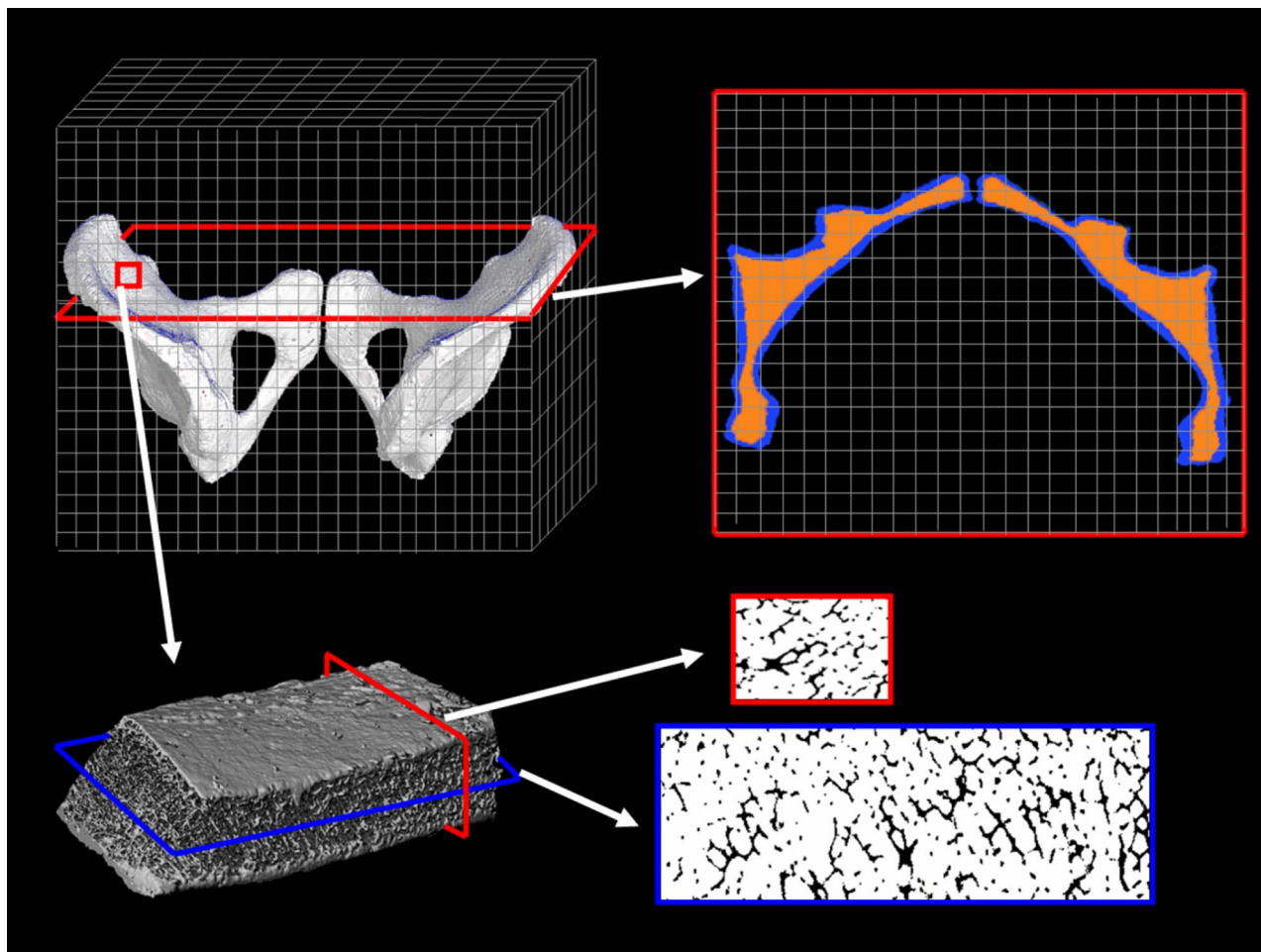


FIG. 1. Schematic of the PIRT model constructed for the pelvis. Regions of spongiosa (interior) and cortical bone (exterior) are shown in the CT macroimage (upper right).

giosa as possible were taken, given the constraints of the bone shape and the microimaging system (e.g., cuboidal samples taken from a spherically shaped femoral head). Marrow-intact sections of spongiosa were bagged, labeled, and kept frozen until microimaging sessions were arranged. For the left parietal bone, two cuboidal sections (roughly $4.9\text{ cm} \times 2.8\text{ cm} \times 1.3\text{ cm}$ on edge) were cut from the cranial section representing $\sim 10\%$ of the total spongiosa within the cranial cap. For the left middle rib, four cylindrical sections were cut ($\sim 12\%$ of total spongiosa within the left side of the rib cage), and six sections were cut from different bones of the pelvis ($\sim 25\%$ of the total spongiosa within the entire pelvis). These physical sections of trabecular spongiosa were originally intended to be imaged via NMR microscopy, and thus they were cut at sizes less than those permitted by microCT imaging.

D. Image segmentation of spongiosa and cortical bone regions

To create tomographic anatomic models for use in internal dosimetry, radiation transport codes must be able to decipher the boundaries of each tissue region for which an independent dose assessment is to be made. Limitations of CT image

acquisition can result in an overlap of grayscale values for tissues of interest, thus precluding the use of simple automated methods of boundary definition. In the present study, the program CT_CONTOURS was adopted for use in segmenting spongiosa and cortical bone within each *ex vivo* CT image set.¹⁷ This program is based upon Interactive Data Language (IDL) version 5.5 and can output labeled contour files in a variety of formats including binary files for EGSNRC¹⁸ and ASCII text for MCNP.¹⁹ CT_CONTOURS displays the current CT information, as well as a color overlay of the contours being edited. The contours can be created using a variety of tools including: basic thresholding, pixel growing, voxel growing, region growing, and manual segmentation. The voxels contained in the individual contours are filled with the desired segmentation tag value, generating volumes of voxels with identical tag values. In the present study, segmentation was performed via manual drawing using the features of CT_CONTOURS and tablet hardware for the computer, which allows for physical drawing of the contour overlay. Segmentation was performed while continuously controlling the contrast window and constantly changing the display of the images using several different filters, including Gaussian (3×3 , 5×5 , or 7×7) and median (3×3 , 5×5 , or 7×7)

filters. CT_CONTOURS was designed so that ROI creation or modification can be performed in either the transverse, sagittal, or coronal plane.

E. Micro-computed tomography of trabecular spongiosa

Micro-tomographic imaging of cuboidal samples of spongiosa was performed on desktop cone-beam μ CT40 or μ CT80 scanners (Scanco Medical AG, Bassersdorf, Switzerland) yielding 3D image data sets at a voxel resolution of $60\ \mu\text{m} \times 60\ \mu\text{m} \times 60\ \mu\text{m}$. Although a resolution of $30\ \mu\text{m}$ on edge could be obtained at an equivalent sample size, the higher resolution images exceed the maximum allowable binary array size of both the image processing and radiation transport codes. Postacquisition image processing steps included (1) selection of a volume of interest for radiation transport simulation, (2) gray-level thresholding, (3) voxel segmentation, and (4) 3D median filtering, all of which have been previously reported in Jokisch *et al.*⁸ and Patton *et al.*⁹

F. Voxel-based infinite spongiosa transport (VBIST) model

Following microCT imaging of our skeletal samples, a series of VBIST models were created to approximate (via 3D transport) the results of current CBIST models. First, marrow voxels within the binary microCT image are further labeled into voxels of active (red) marrow and inactive (yellow) marrow at a predetermined value of marrow cellularity. This process has been outlined previously by Shah *et al.*,¹⁰ and is based upon microscopy measurements of the spatial distribution of adipocytes within normal bone marrow biopsies covering a broad range of marrow cellularities. The trabecular bone endosteum (TBE) is further defined as a $10\ \mu\text{m}$ tissue layer at the bone–marrow interface as previously described by Jokisch.³ The resulting four-tissue 3D model of trabecular spongiosa is coupled to the EGSNRC radiation transport code for electron (beta particle) transport simulations. Source tissues include the trabecular active marrow (TAM), trabecular bone surfaces (TBS), and trabecular bone volume (TBV). TBS sources are approximated as a $0.1\ \mu\text{m}$ layer on the marrow side of the bone–marrow voxel interface. Target tissues include both the active marrow and bone endosteum. Once a given electron reaches the physical edge of the 3D microimage, that particle is re-introduced to the image at a corresponding location at its opposing edge. The processes of particle transport within the image of spongiosa and its reintroduction are continued until all initial kinetic energy is expended. Particle histories are continued (50 000 to 2 000 000) until coefficients of variation on the absorbed fraction are below 1%. VBIST models for the pelvis, cranium, and ribs are shown in the bottom rows of Figs. 1–3, respectively. Elemental compositions and mass densities used within the VBIST model were taken from ICRU Report 46 (see Table I).²⁰

G. Paired image radiation transport (PIRT) model

The paired-image radiation transport or PIRT model supplements the 3D *microscopic* histology provided by the microCT image with the 3D *macroscopic* histology given in the corresponding *ex vivo* CT image. The latter provides additional data for particle transport including (1) the spatial extent of the trabecular spongiosa (e.g., ilium, pubis, and ischium bones of the pelvis) and (2) the spatial extent of the surrounding cortical bone (which laterally encompasses the entire pelvis).

A schematic of the PIRT model of the pelvis from the 66-year male is given in Fig. 1, where the *ex vivo* CT image is shown in the upper left. A representative transverse slice is shown in the upper right where regions of spongiosa (orange) and cortical bone (blue) are differentiated. Superimposed over the entire *ex vivo* CT image is a 3D array of replicate cuboidal microCT images each representing the 3D microstructure of the individual bone trabeculae and corresponding marrow cavities. A 3D rendering of the microCT image is thus shown in the lower left of Fig. 1. Finally, transverse and sagittal slices through the microCT image are shown in the lower right displaying individual voxels of bone (black) and total marrow (white), a pattern inverted from that within the original microCT image.

In the EGSNRC implementation of the PIRT model, individual electrons are tracked simultaneously within the coordinates of the infinite array of microCT images (indicating locations in TBV, TBE, TAM, or trabecular inactive marrow—TIM), and the coordinates of the single CT macroimage (indicating locations in either spongiosa, cortical bone volume—CBV, or surrounding tissues—muscle or soft tissue). Elemental compositions and mass densities used within the PIRT model were taken from ICRU Report 46 (see Table I).²⁰ When the particle is shown to leave the spongiosa of the CT macroimage, tracking within the microCT image is halted and the particle is transported within a homogeneous region of cortical bone defined only by the larger voxels of the *ex vivo* CT macroimage. Upon particle escape from the outer surface of the bone site, particle tracking is terminated. In cases where the particle leaves cortical bone and re-enters the interior spongiosa, particle tracking within the array of microCT images is resumed. The PIRT model is thus far more anatomically realistic than is the geometry provided by the VBIST model, especially when accounting for higher-energy, longer-ranged electrons.

The principle approximation inherent within the PIRT model is that the trabecular microstructure given by the physical section of spongiosa (as imaged via microCT) is uniform across all CT-segmented regions of spongiosa within an individual skeletal site. As a result, the trabecular microstructures of the various other regions of the pelvis (pubis and ischium) are implicitly assumed to be approximated by that imaged within the ilium. In cases where more than one physical section of spongiosa has been imaged by microCT, the PIRT model can be re-run using different microimages representative of different spongiosa regions of the bone site. The resulting microimage-specific absorbed fraction profiles

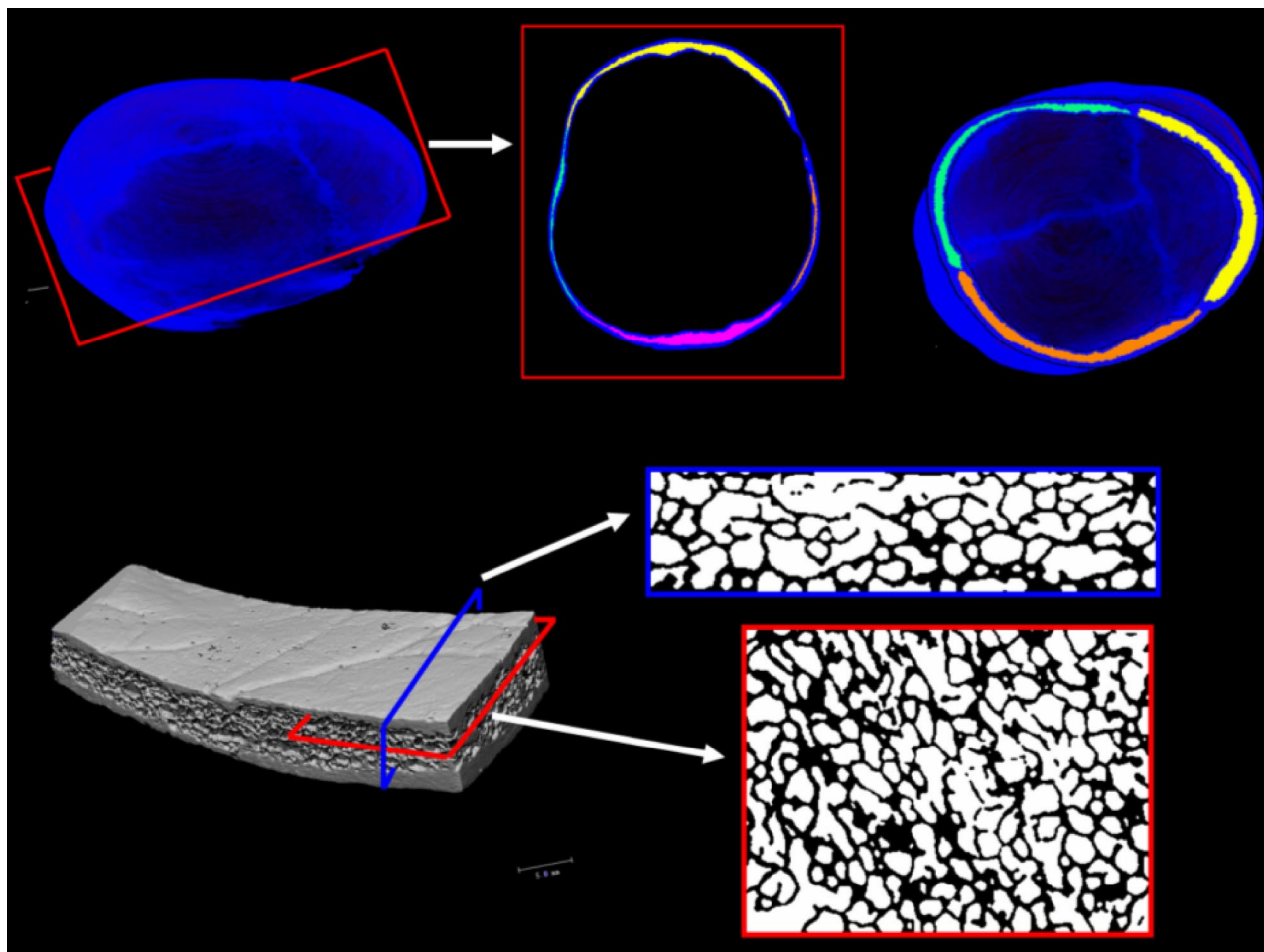


FIG. 2. Schematic of the PIRT model constructed for the cranium. Segmented regions of spongiosa are shown for the frontal, right parietal, left parietal, and occipital bones of the cranial cap.

can thus be averaged either uniformly or weighted by the volume of spongiosa sectioned. In the case of the pelvis, the microstructure of the pubis and ischium can be sampled, utilized, and the resulting transport data can be averaged (not as yet performed in the present study). Finally, it is noted that the PIRT model permits explicit consideration of a cortical bone volume (CBV) as a potential radioactivity source for active marrow irradiation—a feature not permitted within chord-based models of skeletal dose (CBIST).

In this study, two other bone sites representative of flat bones in the human body were subjected to electron transport within the PIRT model: the ribs and the cranium. As with the pelvis, the cranium and ribs have several regions in which sampling of the trabecular structure can be performed. In the case of the cranium, final dosimetry data can be averaged from sampling of the frontal, occipital, left parietal and right parietal bones. In the present study, we focus on the microstructure of the left parietal bone as shown in Fig. 2. The upper left corner of Fig. 2 shows the *ex vivo* image of the cranial cap. Only the outer cortex of the cranium can be seen with the coronal suture, nearly transverse in direction, between the frontal and parietal bones, and the sagittal sutures, medially placed, between the right and left parietal bones.

Two representative transverse slices are shown (upper middle and upper right) where regions of spongiosa (occipital, frontal, right parietal, left parietal) and cortical bone are again differentiated. A 3D rendering of the microCT image of the parietal bone is thus shown in the lower left of Fig. 2. Finally, one transverse and one coronal slice through the microCT image are shown in the lower right displaying individual voxels of bone (black) and total marrow (white).

The need for multiple spongiosa sampling sites also occurs in the ribs, in which the left and right rib cages each contain twelve individual rib bones. To accurately sample the trabecular microstructure of the rib cage, three ribs were chosen from both the right and left side. In the present study (Fig. 3), we focus only on a single rib—the middle or seventh rib of the left rib cage. The upper left image in Fig. 3 shows the spongiosa regions in the middle portions of both the left and right rib cage. Differentiation of spongiosa and cortical bone within the left middle rib are shown in the upper right. A 3D rendering of the microCT image for the middle left rib is shown in the lower left of Fig. 3, along with transverse and coronal slices displaying individual voxels of bone (black) and total marrow (white).

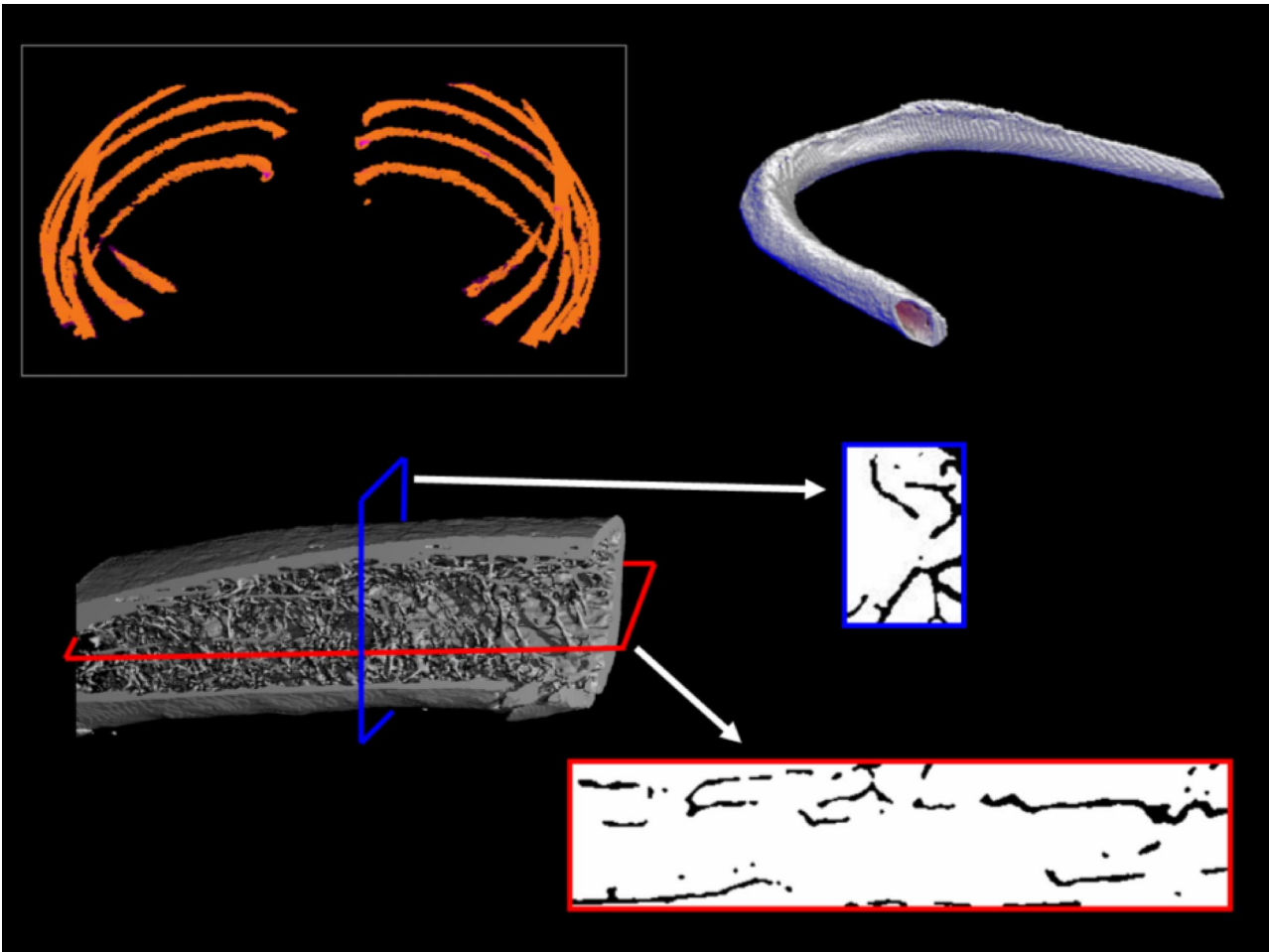


FIG. 3. Schematic of the PIRT model constructed for the ribs.

Table II displays the various source and target tissues masses for the pelvis, cranium, and left rib cage of the 66-year male subject. Values for cortical bone mass are estimated as the product of the tissue density (1.92 g cm^{-3} from Table I) and their cortical volumes from either the *in vivo* CT image (left rib cage) or *ex vivo* CT image (pelvis and cranium). Mass estimates for total marrow, bone endosteum, and bone trabeculae in each skeletal site are calculated as the product of (1) the total spongiosa volume from the CT macroimage (*in vivo* or *ex vivo*), (2) the tissue volume fraction taken from the microCT image, and (3) the tissue density (values given in Table I). As an example, values of the mar-

row volume fraction (MVf)—the fraction of tissue volume assigned to marrow in the segmented microCT image—are given at the bottom of Table II for the left ilium (85.3%), left parietal bone (60.0%), and left middle rib (88.8%), respectively.

III. RESULTS AND DISCUSSION

A. Absorbed fractions to active marrow within the pelvis

Figure 4 displays values of electron absorbed fraction to active (red) bone marrow within the pelvis of the 66-year

TABLE I. Tissue compositions (% by mass) and mass densities used in both the VBIST and PIRT models of skeletal dosimetry.

Tissue or Region ^a	H	C	N	O	Trace	Mass density(g cm^{-3})
Trabecular active marrow (TAM)	10.5	41.4	3.4	43.9	0.1 P, 0.2 S, 0.2 Cl, 0.2 K, 0.1 Fe	1.03
Trabecular inactive marrow (TIM)	11.5	64.4	0.7	23.1	0.1 Na, 0.1 S, 0.1 Cl	0.98
Trabecular bone endosteum (TBE)	10.5	25.6	2.7	60.2	0.1 Na, 0.2 P, 0.3 S, 0.2 Cl, 0.2 K	1.03
Trabecular bone volume (TBV)	3.4	15.5	4.2	43.5	0.1 Na, 0.2 Mg, 10.3 P, 0.3 S, 22.5 Ca	1.92
Cortical bone volume (CBV)	3.4	15.5	4.2	43.5	0.1 Na, 0.2 Mg, 10.3 P, 0.3 S, 22.5 Ca	1.92
Surrounding tissues	10.5	25.6	2.7	60.2	0.1 Na, 0.2 P, 0.3 S, 0.2 Cl, 0.2 K	1.03

^aTAM—“adult red marrow,” TIM—“adult yellow marrow,” TBE—“adult ICRU-44 soft tissue (male).” TBV—“adult cortical bone,” CBV—“adult cortical bone” (Appendix A of ICRU Report 46) (ICRU 1992).

TABLE II. Tissues masses used in the paired-image radiation transport (PIRT) model (100% marrow cellularity). The marrow volume fractions are taken from the 3D microCT images of excised sections of spongiosa.

Tissue/quantity	Pelvis	Cranium	Left rib cage
Trabecular active marrow (TAM)	471.40 g	67.80 g	87.42 g
Trabecular bone endosteum (TBE)	19.30 g	4.91 g	1.49 g
Trabecular bone volume (TBV)	157.50 g	90.48 g	25.76 g
Cortical bone volume (CBV)	392.50 g	361.95 g	140.15 g
Marrow volume fraction (MVF) ^a	85.3% (left ilium)	60.0% (left parietal)	88.8% (left seventh rib)

^aRatio of total marrow voxels to total voxels within the 3D microCT images of trabecular spongiosa.

male subject. The upper graph corresponds to an assumption of 100% marrow cellularity (no voxels of adipose tissue are labeled within the microCT image), while the lower graph corresponds to an assumed marrow cellularity of 48% (reference adult value in both ICRP Publications 70 and 89).^{21,22} In each graph, solid lines indicate energy-dependent absorbed fractions obtained from PIRT model simulations, while dashed lines indicate those derived from VBIST model simulations. For either model and at both cellularities, three source tissues are considered: active marrow (diamonds), bone surfaces (triangles), and bone trabeculae (circles).

The two model types yield essentially equivalent results only at electron energies below ~ 50 keV where boundary effects at the spongiosa-cortical bone interface (within the PIRT model) play a negligible role in modifying the pattern of energy deposition to active marrow voxels (as seen within the VBIST model). Model equivalency is noted to extend to electrons of ~ 80 – 100 keV initial energy when emitted along the surfaces of the bone trabeculae (TBS sources).

As the electron initial energy increases above 50–100 keV, energy deposition to active marrow as predicted under VBIST model simulations increasingly overpredicts that given by the more anatomically realistic PIRT model. As previously noted for skeletal models under either CBIST or VBIST simulations, absorbed fractions asymptotically approach a limiting value independent of the source tissue.^{3,23,24} At 100% cellularity, the VBIST model absorbed fraction to active marrow approaches a value of ~ 0.75 at high electron energies, while it approaches a limiting value of 0.36 at 48% cellularity (48% of 0.75). Similarly, absorbed fractions to active marrow predicted under PIRT model simulations also converge in a source-independent manner, but this convergence value is noted to be energy-dependent as more and more electron energy is lost to the surrounding cortical bone (and potentially surrounding tissues). With the PIRT model results serving as the local standard, percent errors in self-absorbed fraction to active marrow given by the VBIST model are 17% at 500 keV, 34% at 2 MeV, and 70% at 4 MeV. Corresponding percent errors are 8%, 30%, and 68% for TBS sources, and 22%, 36%, and 72% for TBV sources. These percent errors are roughly equivalent at both marrow cellularities.

B. Absorbed fractions to active marrow within the cranium

Figure 5 displays values of electron absorbed fraction to active marrow for TAM, TBS, and TBV sources located

within the spongiosa of the cranium of the 66-year male subject. The upper and lower graphs of Fig. 5 correspond to marrow cellularities of 100% and 38%, respectively, where the latter is the default cellularity for the cranium given in ICRP Publications 70 and 89. In the lower graph, the ordinate has been expanded to better view differences in modeling results at high electron energies. At the lowest energy considered (10 keV), a value of unity for $\phi(\text{TAM} \leftarrow \text{TAM})$ is seen under both VBIST and PIRT simulations.

Patterns of divergence between the two modeling approaches (VBIST versus PIRT) in the cranium are seen to occur at higher energies compared to those found within the pelvis (~ 100 keV for TAM and TBS sources). Model equivalency is noted to extend to electrons of ~ 200 keV when emitted within the volume of the bone trabeculae (TBV sources). At 100% cellularity, the VBIST model absorbed fraction to active marrow approaches a value of 0.44 at high electron energies, while it approaches a limiting value of 0.17 at 38% cellularity (38% of 0.44). Similarly, absorbed fractions to active marrow predicted under PIRT model simulations also converge in a source-independent manner, but again this convergence value is energy dependent. With the PIRT model results serving as the local standard, percent errors in self-absorbed fraction to active marrow (100% cellularity) given by the VBIST model are 18% at 500 keV, 88% at 2 MeV, and 200% at 4 MeV. Corresponding percent errors are 22%, 93%, and 208% for TBS sources, and 21%, 93%, and 208% for TBV sources. As shown similarly in the pelvis, these percent errors are roughly equivalent when the marrow cellularity of the cranium is reduced to 38% (fat fraction of $\sim 62\%$).

C. Absorbed fractions to active marrow within the rib cage

Figure 6 displays values of electron absorbed fraction to active marrow for TAM, TBS, and TBV sources located within the spongiosa of the left rib cage of the 66-year male subject. The upper and lower graphs of Figure 6 correspond to marrow cellularities of 100% and 70%, respectively, where the latter is the default cellularity for the ribs given in ICRP Publications 70 and 89. In each graph, solid lines indicate energy-dependent absorbed fractions obtained from PIRT model simulations, while dashed lines indicate those derived from VBIST model simulations. At the lowest en-

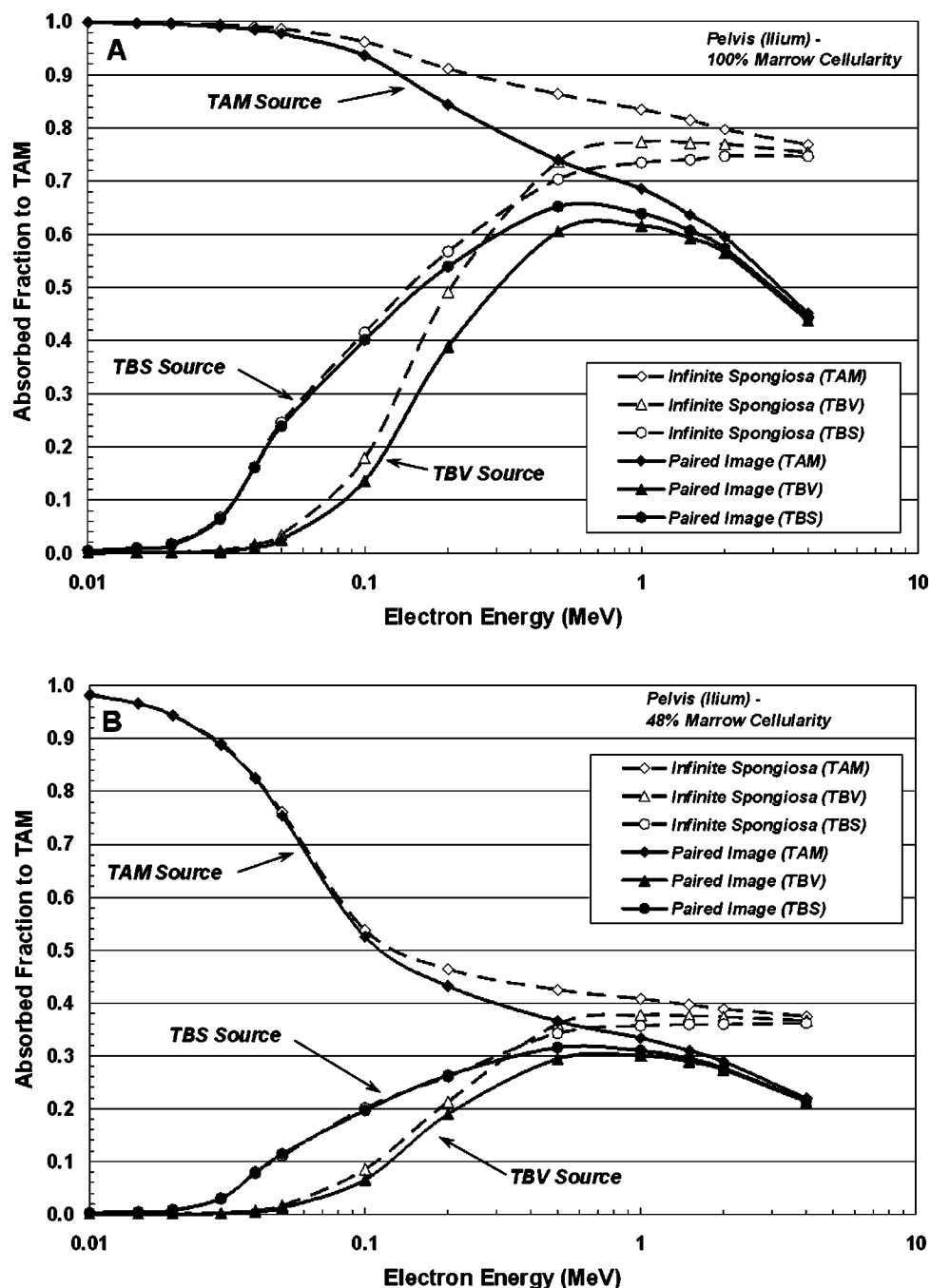


FIG. 4. Electron absorbed fractions to active bone marrow within the pelvis for three source tissues—TAM, TBV, and TBS. Data shown by solid lines are from the PIRT model, while those given by dashed lines are from VBIST simulations. Two marrow cellularities are assumed: (a) 100% active marrow and (b) the ICRP reference cellularity of 48%.

ergy considered (10 keV), a value of $\phi(\text{TAM} \leftarrow \text{TAM}) = 1.0$ is seen under both VBIST and PIRT simulations, as expected.

Patterns of divergence between the two modeling approaches (VBIST versus PIRT) in the ribs are seen to mirror those seen in the cranium (both flat bones of the axial skeleton). At 4 MeV (the highest energy considered), full convergence of the absorbed fraction to active marrow under VBIST model simulations has not yet been reached for the three source regions. Nevertheless, the energy-independent

(VBIST) and energy-dependent (PIRT) patterns of convergence are still evident at electron initial energies exceeding 1 MeV. At 100% cellularity, the VBIST model absorbed fraction to active marrow approaches a value of ~ 0.82 at high electron energies. With the PIRT model results serving as the local standard, percent errors in self-absorbed fraction to active marrow (100% cellularity) given by the VBIST model are 21% at 500 keV, 124% at 2 MeV, and 313% at 4 MeV. Corresponding percent errors are 16%, 136%, and 327% for TBS sources, and 31%, 55%, and 337% for TBV

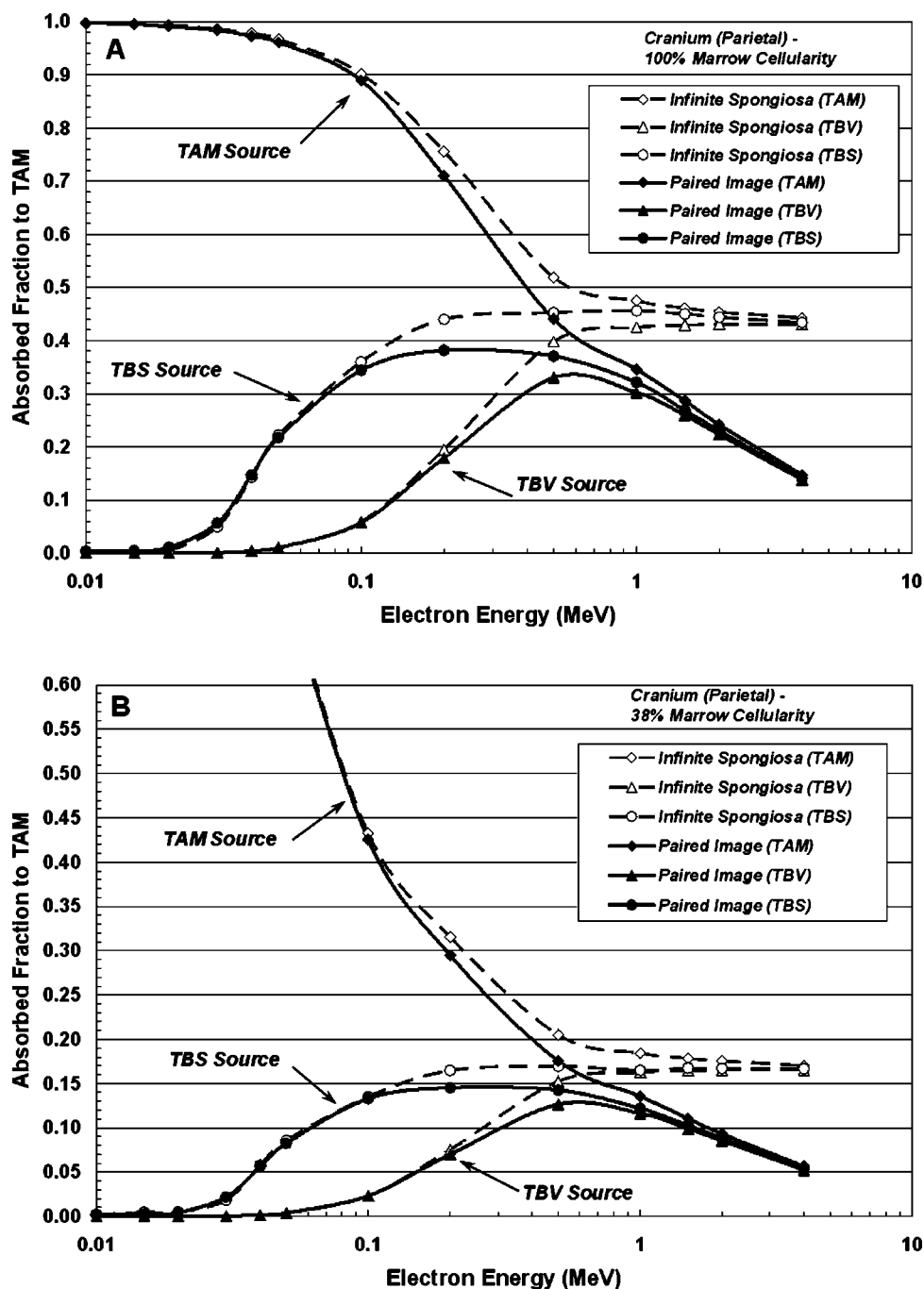


FIG. 5. Electron absorbed fractions to active bone marrow within the cranium for three source tissues—TAM, TBV, and TBS. Data shown by solid lines are from the PIRT model, while those given by dashed lines are from VBIST simulations. Two marrow cellularities are assumed: (a) 100% active marrow and (b) the ICRP reference cellularity of 38%.

sources. These percent errors are roughly equivalent when the marrow cellularity of the rib cage is reduced to 70% (fat fraction of $\sim 30\%$). The higher errors in dosimetry for the ribs under VBIST simulations are not unexpected, considering that this bone site has both a high surface-to-volume ratio of spongiosa (higher chance for electron escape to cortical bone), as well as a high marrow volume fraction within its spongiosa (lesser chance for energy absorption within the bone trabeculae).

D. Absorbed fractions to endosteal tissues

Figure 7 displays values of absorbed fraction to the trabecular endosteal tissues defined as a $10\ \mu\text{m}$ layer of soft tissue on the marrow-side of the bone–marrow interface within the microCT images. Figure 7(a) gives results for TBS, TBV, and TAM electron sources emitted within the pelvis containing bone marrow at 48% cellularity. Figures 7(b) and 7(c) show corresponding values within the cranium and left rib

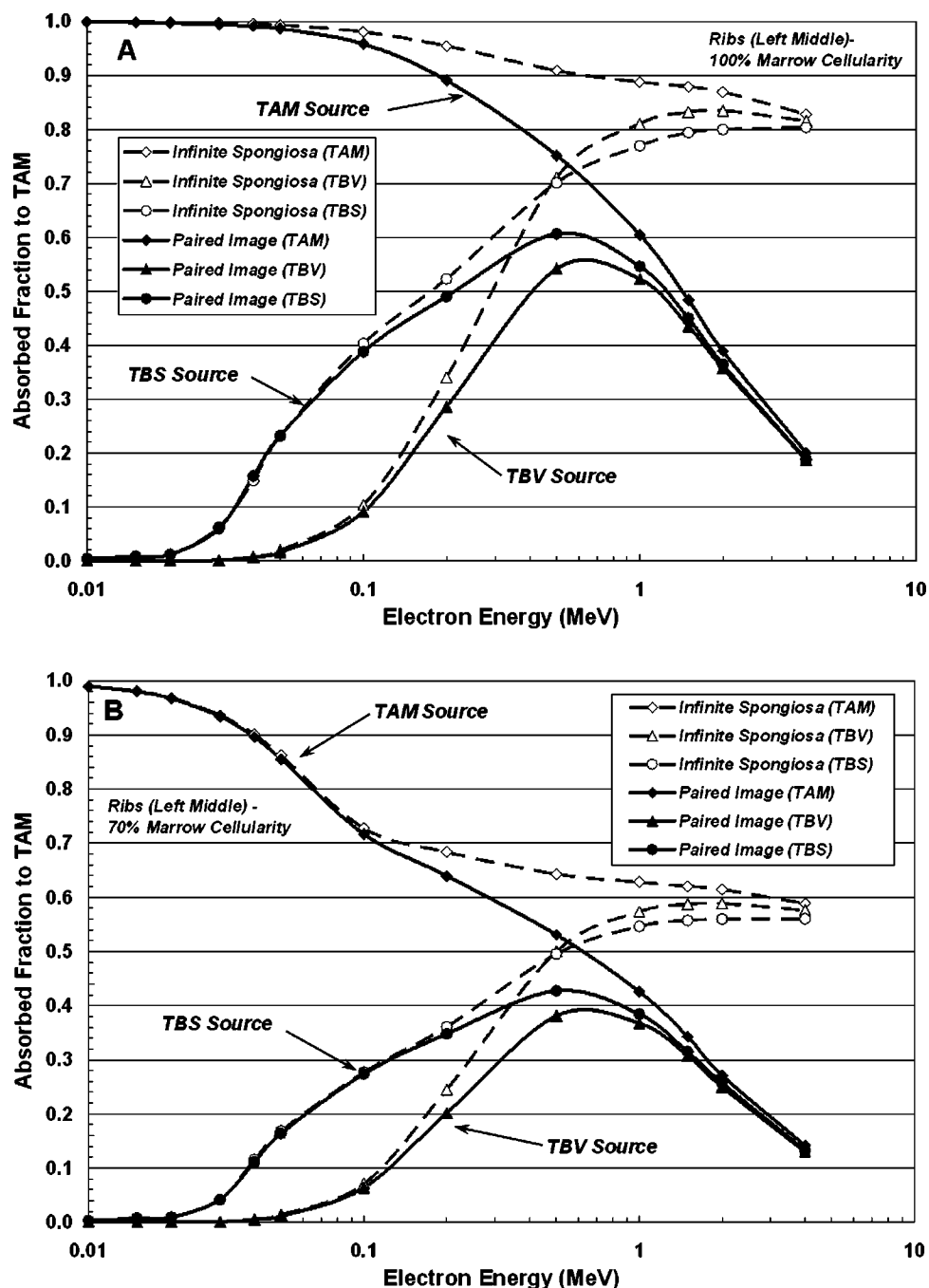


FIG. 6. Electron absorbed fractions to active bone marrow within the ribs for three source tissues—TAM, TBV, and TBS. Data shown by solid lines are from the PIRT model, while those given by dashed lines are from VBIST simulations. Two marrow cellularities are assumed: (a) 100% active marrow and (b) the ICRP reference cellularity of 70%.

cage, respectively, also at reference marrow cellularities (38% for cranium and 70% for the ribs). In all three graphs, the ordinate scale is expanded to a maximum value of 0.10 to facilitate viewing model differences at higher energies. At the lowest energy considered (10 keV), a value of $\phi(\text{TBE} \leftarrow \text{TBS}) = 0.5$ is seen under both VBIST and PIRT simulations (half-space source-target geometry for all bone sites). Also, changes in the marrow cellularity at each bone site have no direct effect on the absorbed fraction to the en-

dosteal tissues.¹⁰ Consequently, reported in this investigation are only the absorbed fraction values at the reference cellularity for each bone site.

At each energy and for each model, higher absorbed fractions are noted for electron sources on the trabecular surfaces, while lower absorbed fractions are seen for electron sources emitted within the active bone marrow. Intermediate absorbed fractions are shown for bone volume sources which peak in value at a source energy of ~ 100 keV in the pelvis

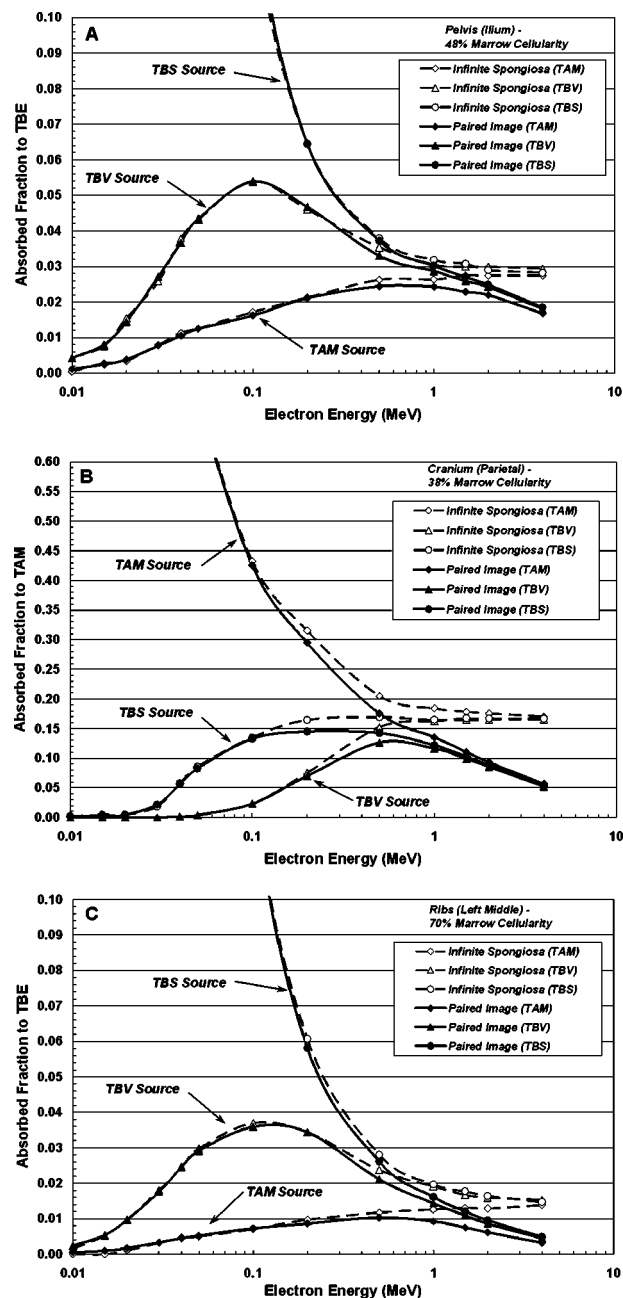


FIG. 7. Electron absorbed fractions to the trabecular bone endosteum within (a) the pelvis, (b) the cranium, and (c) the ribs for three source tissues—TAM, TBV, and TBS. Data shown by solid lines are from the PIRT model, while those given by dashed lines are from VBIST simulations.

and rib skeletal sites. Within the cranium, values of $\phi(\text{TBE} \leftarrow \text{TBV})$ peak in value at a source energy of ~ 200 keV. As expected, VBIST model simulations approach energy- and source-independent convergence values at high electron initial energies (0.028 in the pelvis, 0.030 in the cranium, and 0.015 in the left rib cage), while source-independent convergence values under PIRT are shown to continually decline with increasing source energy above 1 MeV. This decline is more prominent in the cranium and the ribs than seen in the pelvis (ratios of 3.0 versus 1.5 at high energies), and is accountable in part by cortical bone losses and particle escape from these two flat bones.

TABLE III. Ratio of the radionuclide S value for an active marrow (TAM) target as given by the voxel-based infinite spongiosa transport (VBIST) model to that given by the paired-image radiation transport (PIRT) model.

Radionuclide	E_{ave} (keV)	Pelvis—48% cellularity		
		TAM source	TBS source	TBV source
P-33	77	1.03	1.01	1.27
Er-169	100	1.04	1.01	1.26
Lu-177	133	1.06	1.02	1.25
Sm-153	225	1.08	1.04	1.24
Re-186	323	1.13	1.08	1.24
Sr-89	583	1.19	1.12	1.25
P-32	695	1.20	1.14	1.25
Re-188	764	1.22	1.16	1.27
Y-90	934	1.25	1.19	1.29

Radionuclide	E_{ave} (keV)	Cranium—38% Cellularity		
		TAM source	TBS source	TBV source
P-33	77	1.02	1.06	1.05
Er-169	100	1.03	1.09	1.08
Lu-177	133	1.05	1.11	1.11
Sm-153	225	1.06	1.14	1.16
Re-186	323	1.13	1.19	1.22
Sr-89	583	1.26	1.30	1.34
P-32	695	1.30	1.33	1.38
Re-188	764	1.34	1.39	1.44
Y-90	934	1.45	1.49	1.53

Radionuclide	E_{ave} (keV)	Ribs—70% cellularity		
		TAM source	TBS source	TBV source
P-33	77	1.03	1.00	1.18
Er-169	100	1.04	1.02	1.21
Lu-177	133	1.06	1.05	1.24
Sm-153	225	1.10	1.10	1.29
Re-186	323	1.19	1.18	1.35
Sr-89	583	1.35	1.33	1.49
P-32	695	1.41	1.38	1.54
Re-188	764	1.48	1.46	1.63
Y-90	934	1.62	1.59	1.76

E. Radionuclide S values between VBIST and PIRT model simulations

As a further means of comparing the VBIST and PIRT model results, radionuclide S values were calculated for a wide range of beta-particle emitters of interest in skeletal tissue imaging and radionuclide therapy. Absorbed fractions to active bone marrow given in Figs. 4–6, along with both the tissue mass data of Table II and the beta-particle energy spectra,²⁵ were used to calculate radionuclide S values under the MIRD schema for ten different radionuclides. Ratios of the S value based on VBIST-model absorbed fractions to those using PIRT-model absorbed fractions are displayed in Table III for all three skeletal sites and at ICRP-reference marrow cellularities. For low-energy beta-emitters such as ³³P, ¹⁶⁹Er, and ¹⁷⁷Lu, absorbed fractions given by the VBIST model simulations overestimate radionuclide S values for TAM, TBS, and TBV sources by only 2% to 11% in the

cranium. Higher errors are noted in the ribs (ratios of 1.03 to 1.24) and in the pelvis (ratios of 1.03 to 1.25). In both cases, the greater discrepancies between VBIST and PIRT are shown to occur for bone volume sources (all three skeletal sites). For radionuclides at intermediate beta energies (E_{ave} of 192–583 keV), S value ratios range from 1.06 to 1.34 in the cranium, from 1.10 to 1.49 in the ribs, and from 1.04 to 1.25 in the pelvis. For radionuclides in the highest beta-energy range (E_{ave} of 695–934 keV), S value ratios range from 1.30 to 1.53 in the cranium, from 1.38 to 1.76 in the ribs, and from 1.14 to 1.29 in the pelvis. It is reasonable to assume that similar errors are also present in radionuclide S values derived from chord-based models^{5,26} which, as does the VBIST simulations of the present study, assume an infinite region of spongiosa during particle transport.

IV. CONCLUSIONS

A paired-image radiation transport (PIRT) model for skeletal dosimetry is presented in which electrons (beta particles) are tracked simultaneously within two different segmented digital images: (1) an *ex vivo* CT image of the skeletal site with segmented regions of trabecular spongiosa, cortical bone, and surrounding tissues, and (2) an *ex vivo* microCT image of the interior bone trabeculae and marrow cavity microstructure representative of that found within spongiosa regions of the macroscopic CT image. Example absorbed dose calculations under the PIRT methodology within the cranium, ribs, and pelvis of an adult 66-year male subject demonstrate a divergence from standard infinite spongiosa transport (VBIST) methods at energies as low as 50–200 keV depending upon the source tissue and skeletal site. Calculations of radionuclide S values under both methodologies imply that current chord-based models used in clinical skeletal dosimetry may over estimate absorbed dose to active bone marrow in these three skeletal sites by 0% to 27% for low-energy beta emitters (^{33}P , ^{169}Er , and ^{177}Lu), by ~4% to 49% for intermediate-energy beta emitters (^{131}I , ^{153}Sm , ^{186}Re , and ^{89}Sr), and by ~14% to 76% for high-energy beta emitters (^{32}P , ^{188}Re , and ^{90}Y). Higher errors are noted for bone-volume seekers, while lower errors are seen for source emissions within the active bone marrow. These findings are consistent with those investigated previously in the proximal femur and lumbar vertebrae of the same 66-year male subject.⁷ The PIRT model thus supersedes previous stylized modeling attempts by the UF ALRADS research group to account for the infinite spatial extent of trabecular spongiosa and cortical bone,^{3,4,11,12} and provides a method for expanding the availability of reference models needed for clinical bone-marrow dose estimates in radionuclide therapy patients.

ACKNOWLEDGMENTS

This work was supported in part by Grant No. CA96441 from the National Cancer Institute and Grant No. DE-FG07-02ID14327 from the U.S. Department of Energy with the University of Florida. We would also like to thank Scanco

Medical AG for their assistance with the use of their commercial scanning service.

^aElectronic mail: wbolch@ufl.edu

¹J. R. Whitwell and F. W. Spiers, "Calculated beta-ray dose factors for trabecular bone," *Phys. Med. Biol.* **21**, 16–38 (1976).

²A. H. Beddoe, P. J. Darley, and F. W. Spiers, "Measurements of trabecular bone structure in man," *Phys. Med. Biol.* **21**, 589–607 (1976).

³D. W. Jokisch, L. G. Bouchet, P. W. Patton, D. A. Rajon, and W. E. Bolch, "Beta-particle dosimetry of the trabecular skeleton using Monte Carlo transport within 3D digital images," *Med. Phys.* **28**, 1505–1518 (2001).

⁴P. W. Patton, D. A. Rajon, A. P. Shah, D. W. Jokisch, B. Inglis, and W. E. Bolch, "Site-specific variability in trabecular bone dosimetry: considerations of energy loss to cortical bone," *Med. Phys.* **29**, 6–14 (2002).

⁵K. F. Eckerman and M. G. Stabin, "Electron absorbed fractions and dose conversion factors for marrow and bone by skeletal regions," *Health Phys.* **78**, 199–214 (2000).

⁶M. G. Stabin, "MIRDose: Personal computer software for internal dose assessment in nuclear medicine," *J. Nucl. Med.* **37**, 538–546 (1996).

⁷A. Shah, W. Bolch, D. Rajon, P. Patton, and D. Jokisch, "A paired-image radiation transport (PIRT) model for skeletal dosimetry," *J. Nucl. Med.* **46**, 344–353 (2005).

⁸D. W. Jokisch, P. W. Patton, B. A. Inglis, L. G. Bouchet, D. A. Rajon, J. Rifkin, and W. E. Bolch, "NMR microscopy of trabecular bone and its role in skeletal dosimetry," *Health Phys.* **75**, 584–596 (1998).

⁹P. W. Patton, D. W. Jokisch, D. A. Rajon, A. P. Shah, S. L. Myers, and W. E. Bolch, "Skeletal dosimetry via NMR microscopy: Investigations of sample reproducibility and signal source," *Health Phys.* **82**, 316–326 (2002).

¹⁰A. P. Shah, P. W. Patton, D. A. Rajon, and W. E. Bolch, "Adipocyte spatial distributions in bone marrow: Implications for skeletal dosimetry models," *J. Nucl. Med.* **44**, 774–783 (2003).

¹¹W. E. Bolch, P. W. Patton, D. A. Rajon, A. P. Shah, D. W. Jokisch, and B. Inglis, "Considerations of marrow cellularity in 3D dosimetric models of the trabecular skeleton," *J. Nucl. Med.* **43**, 97–108 (2002).

¹²W. E. Bolch, P. W. Patton, A. P. Shah, and D. A. Rajon, "Considerations of anthropomorphic, tissue volume, and tissue mass scaling for improved patient specificity of skeletal S values," *Med. Phys.* **29**, 1054–1070 (2002).

¹³R. Muller, H. Van Campenhout, B. Van Damme, G. Van Der Perre, J. Dequeker, T. Hildebrand, and P. Rueggsegger, "Morphometric analysis of human bone biopsies: A quantitative structural comparison of histological sections and micro-computed tomography," *Bone (N.Y.)* **23**, 59–66 (1998).

¹⁴P. Rueggsegger, B. Koller, and R. Müller, "A microtomographic system for the nondestructive evaluation of bone architecture," *Calcif. Tissue Int.* **58**, 24–29 (1996).

¹⁵T. Dufresne, "Segmentation techniques for analysis of bone by three-dimensional computed tomographic imaging," *Technol. Health Care* **6**, 351–359 (1998).

¹⁶V. H. Heyward and L. M. Stolarczyk, *Applied Body Composition Assessment* (Human Kinetics, Champaign, IL, 1996).

¹⁷J. Nipper, J. Williams, and W. Bolch, "Creation of two tomographic voxel models of pediatric patients in the first year of life," *Phys. Med. Biol.* **47**, 3143–3164 (2002).

¹⁸I. Kawrakow, "Accurate condensed history Monte Carlo simulation of electron transport. I. EGSnrc, the new EGS4 version," *Med. Phys.* **27**, 485–498 (2000).

¹⁹J. F. Briesmeister, "MCNP-A general Monte Carlo N-particle transport code," LA-12625-M, Los Alamos National Laboratory, Los Alamos, NM, 1997.

²⁰ICRU, *Photon, Electron, Proton and Neutron Interaction Data for Body Tissues*, Report 46 (International Commission on Radiation Units and Measurements, Bethesda, MD, 1992).

²¹ICRP, *Basic Anatomical and Physiological Data for Use in Radiological Protection: The Skeleton*, ICRP Publication 70 (International Commission on Radiological Protection, Oxford, UK, 1995).

²²ICRP, *Basic Anatomical and Physiological Data for Use in Radiological Protection: Reference Values*, Publication 89 (International Commission on Radiological Protection, New York, 2002).

²³K. F. Eckerman, "Aspects of the dosimetry of radionuclides within the skeleton with particular emphasis on the active marrow," in *Proceedings*

- of the Fourth International Radiopharmaceutical Dosimetry Symposium, edited by A. T. Schlafke-Stelson and E. E. Watson (Oak Ridge Associated Universities, Oak Ridge, TN, 1985), pp. 514–534.
- ²⁴L. G. Bouchet, D. W. Jokisch, and W. E. Bolch, “A three-dimensional transport model for determining absorbed fractions of energy for electrons in trabecular bone,” *J. Nucl. Med.* **40**, 1947–1966 (1999).
- ²⁵K. F. Eckerman, R. J. Westfall, J. C. Ryman, and M. Cristy, “Availability of nuclear decay data in electronic form, including beta spectra not previously published,” *Health Phys.* **67**, 338–345 (1994).
- ²⁶L. G. Bouchet, W. E. Bolch, R. W. Howell, and D. V. Rao, “S values for radionuclides localized within the skeleton,” *J. Nucl. Med.* **41**, 189–212 (2000).

A COMPARISON OF SKELETAL CHORD-LENGTH DISTRIBUTIONS IN THE ADULT MALE

Amish P. Shah,* Didier A. Rajon,[†] Derek W. Jokisch,[‡] Phillip W. Patton,[§]
and Wesley E. Bolch**

Abstract—In radiation protection, skeletal dose estimates are required for the tissues of the hematopoietically active bone marrow and the osteogenic cells of the trabecular and cortical endosteum. Similarly, skeletal radiation dose estimates are required in therapy nuclear medicine in order to develop dose-response functions for myelotoxicity where active bone marrow is generally the dose-limiting organ in cancer radioimmunotherapy. At the present time, skeletal dose models in both radiation protection and medical dosimetry are fundamentally reliant on a single set of chord-length distribution measurements performed at the University of Leeds in the late 1970's for a 44-y-old male subject. These distributions describe the relative frequency at which linear pathlengths are seen across both the marrow cavities and bone trabeculae in seven individual bone sites: vertebrae (cervical and lumbar), proximal femur (head and neck), ribs, cranium (parietal bone), and pelvis (iliac crest). In the present study, we present an alternative set of chord-length distribution data acquired within a total of 14 skeletal sites of a 66-y-old male subject. The University of Florida (UF) distributions are assembled via 3D image processing of microCT scans of physical sections of trabecular spongiosa at each skeletal site. In addition, a tri-linear interpolation Marching Cube algorithm is employed to smooth the digital surfaces of the bone trabeculae while chord-length measurements are performed. A review of mean chord lengths indicate that larger marrow cavities are noted on average in the UF individual for the cervical vertebrae (1,038 vs. 910 μm), lumbar vertebrae (1,479 vs. 1,233 μm), ilium (1,508 vs. 904 μm), and parietal bone (812 vs. 389 μm), while smaller marrow cavities are noted in the UF individual for the femoral head (1,043 μm vs. 1,157 μm), the femoral neck (1,454 μm vs. 1,655 μm), and the ribs (1,630 μm vs. 1,703 μm). The mean chord-lengths for the bone trabeculae show close agreement for both individuals in the ilium ($\sim 240 \mu\text{m}$)

and cervical vertebrae ($\sim 280 \mu\text{m}$). Thicker trabeculae were seen on average in the UF individual for the femoral head (ratio of 1.50), femoral neck (ratio of 1.10), lumbar vertebrae (ratio of 1.29), and ribs (ratio of 1.14), while thinner trabeculae were seen on average in the UF individual for the parietal bone of the cranium (ratio of 0.92). In two bone sites, prominent discrepancies in chord distribution shape were noted between the Leeds 44-y-old male and the UF 66-y-old male: (1) the bone trabeculae in the ribs, and (2) the marrow cavities and bone trabeculae within the cranium.

Health Phys. 89(3):199–215; 2005

Key words: skeleton; radiation therapy; bone marrow; Reference Man

INTRODUCTION

THE ACTIVE (red) bone marrow of the trabecular regions of the adult skeleton, as well as the endosteal tissues aligning the interior bone surfaces, are important target tissues in radiation protection (e.g., induction of leukemia and bone cancer, respectively, following long-term internal exposure). In radioimmunotherapy (RIT) the active marrow has been identified as the dose-limiting organ in these treatments, thus placing increased importance on methods of marrow dosimetry that are patient-specific (Sgouros 1993; Sgouros et al. 2000). The need to avoid myelotoxicity in radionuclide therapy can, in many cases, result in suboptimal therapy of the targeted lesion by the radioimmunoconjugate.

ICRP skeletal model for the adult male radiation worker

At present, modeling techniques for estimating skeletal tissue dose in both radiation protection and in therapy nuclear medicine are fundamentally based upon research conducted by F.W. Spiers and his students at the University of Leeds in the late 1960's to late 1970's (Spiers 1966; Spiers et al. 1978, 1981). The Leeds research group developed a novel optical scanning system from which chord-length distributions were acquired in the lumbar vertebrae for several subjects, as well as at several skeletal sites of a 1.7-y-old child (5 sites), a 9-y-old child (5 sites), and a 44-y-old male (7 sites)

* Department of Biomedical Engineering, University of Florida, Gainesville, FL 32611-8300; [†] Department of Nuclear & Radiological Engineering, University of Florida, Gainesville, FL 32611-8300; [‡] Department of Physics and Astronomy, Francis Marion University, Florence, SC 29501-0547; [§] Department of Health Physics, University of Nevada-Las Vegas, Las Vegas, NV 89154-3037; ** Department of Nuclear & Radiological Engineering and Department of Biomedical Engineering, University of Florida, Gainesville, FL 32611-8300.

For correspondence or reprints contact: Wesley E. Bolch, Director, Advanced Laboratory for Radiation Dosimetry Studies (ALRADs), Department of Nuclear and Radiological Engineering, University of Florida, Gainesville, FL 32611-8300, or email at wbolch@ufl.edu.

(Manuscript received 2 November 2004; revised manuscript received 26 February 2005, accepted 8 May 2005)

0017-9078/05/0

Copyright © 2005 Health Physics Society

(Beddoe 1976; Beddoe et al. 1976; Whitwell 1973; Whitwell and Spiers 1976). These chord-length distributions were used by Whitwell to derive dose factors (marrow and endosteal doses per unit skeletal activity burden) for several radionuclides of interest in radiation protection (Whitwell 1973; Whitwell and Spiers 1976). Fig. 1 demonstrates schematically the measurement of bone and marrow chords at scanning angle θ across a representative physical section of trabecular bone.

The skeletal microstructure implicitly embodied within the current International Commission on Radiological Protection (ICRP) reference male (ICRP 1995, 2002) can be traced to the chord-length distributions constructed at the University of Leeds for their 44-y-old male subject. In 1985, the Leeds distributions were used by Eckerman to determine electron absorbed fractions as a function of particle energy (Eckerman 1985). These values were subsequently used to establish fluence-to-dose response functions for use in photon dosimetry of the skeleton (Cristy and Eckerman 1987). The Eckerman electron transport model was later updated in 2000 (Eckerman and Stabin 2000) and in 2002 (Stabin et al. 2002) and is the basis for the skeletal tissue model in both the MIRDose (Stabin 1996) and OLINDA (Stabin and Sparks 2003) computer codes.

University of Florida (UF) skeletal model for the adult male radionuclide therapy patient

While the current ICRP skeletal reference model provides tissue dose estimates adequate for use in prospective radiation protection, the model can be considered limited in its ability to provide either

individual-specific skeletal doses in retrospective dose-reconstruction studies, or patient-specific skeletal doses in radionuclide cancer therapy beyond simply total (or lean) body mass scaling of reference tissue masses. These limitations include (1) lack of consideration of energy loss to cortical bone for intermediate-to-high energy beta sources (Patton et al. 2002b; Shah et al. 2005), (2) reliance on fixed reference values of marrow cellularity (Cristy 1981; Custer and Ahlfeldt 1932), (3) use of multiple data sources for skeletal tissue masses different from those used to establish values of absorbed fraction (Mechanik 1926; Trotter and Hixon 1974), and (4) lack of bone site-specific data on spongiosa volumes, cortical bone volumes, and marrow volume fractions—data needed for improvements in patient-specific scaling of reference doses (ICRP 1995).

To address the need for a more comprehensive model for skeletal tissue dose, we have performed a variety of in-vivo and ex-vivo CT imaging studies of the skeleton of a 66-y-old male cadaver—an age more representative of those considered for radionuclide cancer therapy. In addition, sections of trabecular spongiosa were imaged under micro-computed tomography revealing high-resolution details of the individual bone marrow cavities and bone trabeculae in 14 skeletal sites within the UF 66-y-old adult male radionuclide therapy patient (AMRTP). In the present study, we evaluate differences in the trabecular microstructures of these two individuals through side-by-side comparisons of their marrow cavity and bone trabeculae chord distributions. A companion study of dosimetry results (e.g., electron absorbed fractions) between the Leeds 44-y-old male and the UF 66-y-old male at equivalent bone sites of the skeleton is reported separately (Shah 2004). The UF 66-y-old male is offered as an alternative to the Leeds individual for use in medical dosimetry, and can serve as a basis for patient-specific scaling of skeletal dose estimates. Based on age considerations alone, however, the Leeds individual at 44 years of age is still perhaps more representative of the skeletal structure of the ICRP reference male defined as between 20 to 30 years of age.

MATERIALS AND METHODS

Bone specimen selection

Candidate subjects for study were obtained through the State of Florida Anatomical Board located on the UF campus. Cadaver selection criteria included (1) an age between 50–75 y (representative of typical radionuclide therapy patients), (2) a body mass index of 18.5–25 kg m⁻² (Centers for Disease Control recommended healthy range) (Heyward and Stolarczyk 1996), and (3) a cause

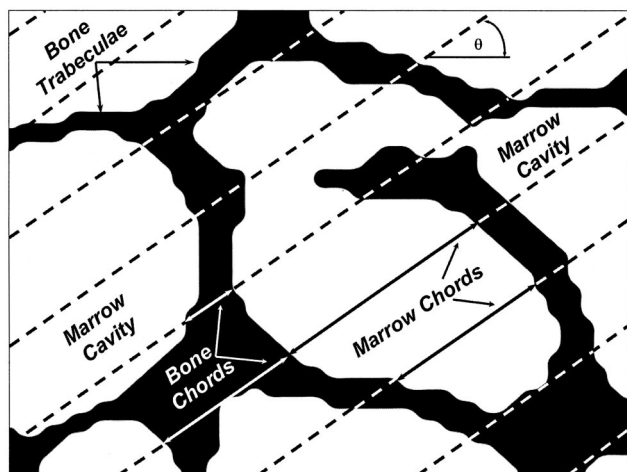


Fig. 1. Schematic demonstrating the acquisition of chord-lengths across bone trabeculae and marrow cavities at scanning angle θ . Two chord-lengths are shown for the bone trabeculae (white arrows) and the marrow cavities (black arrows).

of death that would preclude significant skeletal deterioration. The subject identified was a 66-y-old male approximately 68 kg in total mass and 173 cm in total height at the time of death (BMI of 22.7 kg m^{-2}). The subject died suddenly of complications associated with cardiomyopathy. Over forty bone samples were removed from the cadaver. After removal, the samples were stored frozen at -17°C until imaging sessions could be scheduled.

Microimaging of trabecular spongiosa

Physical sectioning was performed on all excised skeletal sites. For example, cuboidal sections of spongiosa were cut from the vertebral body of C3, C6, T3, T6, T11, L2, and L4 to assess the trabecular microstructure of various regions of the spine. Micro-tomographic imaging of the samples was performed using desktop cone-beam $\mu\text{CT}40$ or $\mu\text{CT}80$ scanners (Scanco Medical AG, Bassersdorf, Switzerland) yielding 3D image data sets at a voxel resolution of $60 \mu\text{m} \times 60 \mu\text{m} \times 60 \mu\text{m}$. Previous studies by Rajon et al. using mathematical models of trabecular bone had indicated that accurate estimates of marrow dose can be achieved at this resolution over a broad range of electron energies (Rajon et al. 2002). Post-acquisition image processing steps included (1) selection of the volume of interest, (2) gray-level thresholding, (3) voxel segmentation, and (4) 3D median filtering, all of which have been previously reported by Jokisch et al. (1998) and by Patton et al. (2002a).

Measurement of chord-length distributions

The problems associated with acquiring chord distributions across digital images were first identified by Jokisch et al. (2001). The stair-stepped representation of bone/marrow interfaces within digital images gives rise to voxel effects when measuring pathlengths across these regions. Accurate techniques for both the generation (Rajon and Bolch 2003) and measurement (Rajon et al. 2003) of μ -random chords^{††} through any 3D object were subsequently explored. These investigators further addressed issues relating to voxel effects imposed on the measured chord-length distributions. Rajon et al. showed that voxel effects increase the frequency of short chords and consequently reduce the mean chord-length by $\sim 30\%$ at resolutions of $\sim 60 \mu\text{m}$. These investigators further expressed the need for a smoother representation of the bone-marrow interface within the 3D digital image. The method recommended was an extension of the Marching Cube (MC) algorithm (Lorensen and Cline 1987) offering a bone-marrow interface surface that is

reasonably smooth and continuous. Through the application of their Trilinear Interpolation MC (TLI-MC) algorithm at an image resolution of $60 \mu\text{m}$, Rajon et al. showed significant improvements to the true distribution found within a mathematical simulation model of trabecular bone (Rajon et al. 2003). In the present study, all chord-length distributions through the 33 spongiosa physical sections (as taken from the 14 major skeletal sites) were constructed using the TLI-MC technique.

Averaging of chord-length distributions

In the present study, several bone regions were sampled in order to determine representative chord-length distribution for a particular bone site. For example, four different bones were sampled within the cranium: left parietal, right parietal, frontal, and occipital bones. For each cranial bone, physical sections were imaged under microCT and the resulting images were used to generate chord-length distributions for that bone site. To report a single distribution for the cranium of the UF 66-y-old male, it is necessary to take into account each of the four separate distributions. Probability densities within each bin of the chord distributions for the individual cranium bones were averaged based on weighting schemes defined by the volume of each physical bone section at each particular skeletal site. This average distribution was then renormalized across the entire range of chord lengths. In this study, bone trabeculae and marrow cavity chord distributions were tabulated in $20\text{-}\mu\text{m}$ and $100\text{-}\mu\text{m}$ bin widths, respectively, and out to a maximum value of $2,000 \mu\text{m}$ (bone trabeculae) and $10,000 \mu\text{m}$ (marrow cavities), values equivalent to those reported in the Leeds studies.

Reference skeletal sites

In the University of Leeds studies, optical scanning measurements were performed on contact radiographs of trabecular bone sections taken from seven skeletal sites of a 44-y-old male subject. These skeletal sites included the lumbar vertebra (L3), the cervical vertebra (C4), the ribs, the iliac crest, the femur head, the femur neck, and the parietal bone of the cranium. In the present study, chord-length distributions taken from 3D microCT images of spongiosa in these same seven skeletal sites within the UF 66-y-old male are shown for comparison. For the lumbar vertebra, chord distributions were obtained from vertebral body spongiosa microimages of L2 and L4, whereas chord distributions from C3 and C6 were averaged to report a single distribution for the cervical vertebrae. The 2nd, 7th, and 11th ribs from the right and left rib cage (total of 6) were all averaged to generate chord-distributions for the ribs of the UF 66-y-old male. All three bones of the pelvis (ilium, ischium,

^{††} μ -random chords are those generated across an object or region from trajectories externally and isotropically incident to the object or region.

and pubis), and all four bones of the cranium (right and left parietal bones, frontal bone, and occipital bone) were averaged to develop the pelvis and cranium chord distributions, respectively. Lastly, both femoral heads and necks from the right and left proximal epiphysis of the femur were averaged to construct the femoral head and neck data. Additionally, several bones sites were sampled in this study from regions not present in the Leeds data. These include the scapulae (right/left), clavicles (right/left), humerus (right/left), sacrum, mandible, sternum and thoracic vertebra (T3, T6, and T11).

RESULTS

In this study, microCT imaging was used to expand the original University of Leeds chord-length distribution data presently available for models of skeletal tissue dose. Differences in the chord distributions from the Leeds and UF studies may be attributed to two items. First, there might exist physical differences in the trabecular microstructure of these two individuals—one a 44-y-old male and one a 66-y-old male. Age-dependent bone thinning (osteopenia) is just one example. As cancer patients treated with radionuclide therapy are generally in the age range of 50 to 75 y, the trabecular microstructure of the UF 66-y-old individual might better resemble that of individual patients requiring marrow dose estimates, particularly for male patients.

Second, differences in the measured chord-length distributions might exist that are attributable to the acquisition method. In the case of the Leeds data, the chord-lengths were measured on 2D physical sections and by light absorption/transmission timing measurements. Careful selection of cut angles when preparing the 2D physical sections provided justification for reporting the Leeds chord-length distributions as omni-directional (i.e., representing the 3D structure). For this present study, 3D digital images were acquired using microCT scanning on marrow-intact samples, and chord-length measurements were acquired using 3D ray-trace techniques within these images. As a result, the method of chord measurement is very different in the Leeds and UF studies, and these differences might further contribute to a divergence of distribution shapes.

Figs. 2 to 7 display normalized chord-length distributions across both bone trabeculae and marrow cavities in the UF samples as measured through microCT imaging and image analysis. In addition, these figures show the respective chord distributions for each bone site as measured by the Leeds optical bone scanner and reported in Appendix C of Whitwell's thesis (Whitwell 1973). Values of mean chord lengths are given in Table 1 for both the Leeds 44-y-old male and the UF 66-y-old male

subject. Finally, it is noted that further omni-directional refinements in the Whitwell distributions were made by Beddoe (Beddoe 1976); unfortunately, these revised distributions were never published in numerical format (e.g., graphical format only). As a result, only the more approximate distributions by Whitwell have been utilized in past and current studies of bone dosimetry (Eckerman 1985; Eckerman and Stabin 2000).

DISCUSSION

Femoral head and neck

In Fig. 2a, chord-length distributions across the marrow cavities of the femoral head and neck are compared between the Leeds 44-y-old male and the UF 66-y-old male. For both individuals, marrow cavities are shown to be generally larger in the femoral neck than in the femoral head. For the femoral head, the chord distributions of the two individuals have similar shapes, both peak at a marrow chord-length of $\sim 650 \mu\text{m}$, and both show very similar frequencies for chords exceeding $1,300 \mu\text{m}$. In both regions of the femur, the distributions of the UF 66-y-old male show a higher frequency of smaller marrow chords as compared to the Leeds 44-y-old male. We further note that the Leeds femoral head and neck distributions in Fig. 2a show an upward excursion within the first $100\text{--}300 \mu\text{m}$. A continuous and smooth distribution of marrow chord-lengths is seen in both femoral regions of the UF 66-y-old male. The mean marrow chord is $1,043 \mu\text{m}$ in the femoral head and $1,454 \mu\text{m}$ in the femoral neck of the UF 66-y-old male (see Table 1). Comparable averages in the Leeds individual are slightly higher at $1,157 \mu\text{m}$ and $1,655 \mu\text{m}$, respectively.

Corresponding distributions across the bone trabeculae of the femoral head and neck of both individuals are shown in Fig. 2b. Modest agreement is seen in the femoral neck data for the two subjects with both distributions peaking in chord frequency at $\sim 180\text{--}220 \mu\text{m}$. However, a smaller secondary frequency peak is observed at $\sim 30 \mu\text{m}$ in the Leeds distribution. While the data of Fig. 2b indicate that bone chord-lengths are comparable in the femoral head and neck of the UF 66-y-old male (mean bone chords of 348 and $347 \mu\text{m}$, respectively), greater differences are noted for bone chords in these femoral regions of the Leeds 44-y-old male (mean values of $232 \mu\text{m}$ and $314 \mu\text{m}$, respectively). For the latter, a very prominent peak in chord frequency is noted in the Leeds femoral head distribution at $\sim 140 \mu\text{m}$.

Cervical and lumbar vertebrae

Fig. 3a compares marrow chord distributions within the cervical and lumbar vertebrae of both the UF and

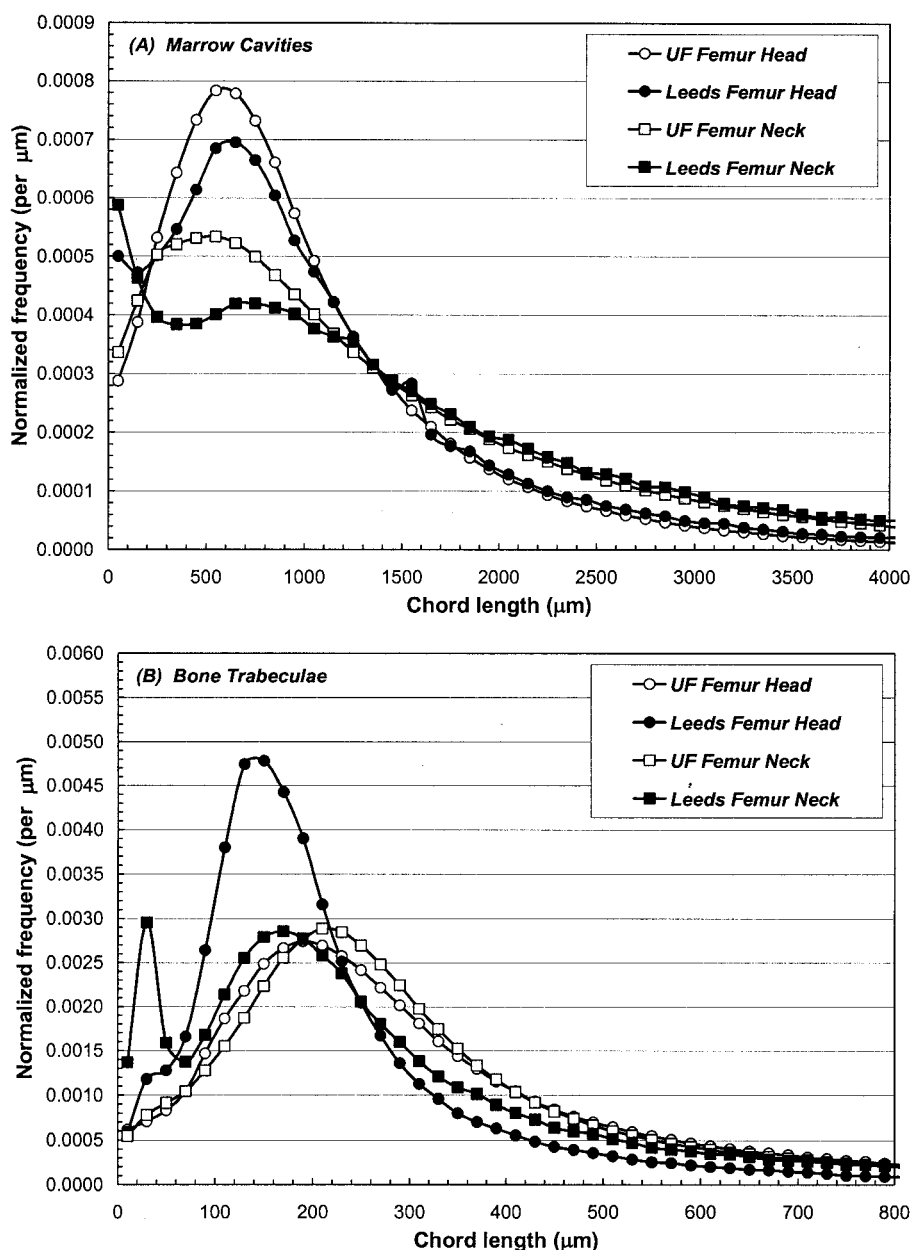


Fig. 2. Normalized, omnidirectional chord-length distributions through the (a) marrow cavities and (b) bone trabeculae of the femoral head and neck as measured with physical sectioning and automated light microscopy (Whitwell 1973) and via microCT imaging, image processing, and the trilinear Marching Cube technique for surface smoothing (present study).

Leeds individuals.^{‡‡} In addition, the marrow chord distribution of the thoracic vertebrae is shown for the UF subject (a site not reported in the Leeds data). In general, marrow chord distributions seen in both bone sites are

^{‡‡} In the preparation of Figs. 3a and 3b, it was noted that the tables of chord distributions across the marrow cavities and trabeculae within the lumbar vertebra were mislabeled on p. C.5 of Whitwell's thesis. This error is easily verified by integrating the normalized probability density functions for each region and comparing the result to unity. The labeling error, however, does not seem to have been carried over to the reported mean chord lengths in Table 5.1 of the thesis or in Table 2 of Whitwell and Spiers (1976).

reasonably comparable between the two individuals. For marrow chords in the range of 0–1,000 μm , the UF distributions rise to a peak frequency (~ 550 μm for the CV, ~ 700 μm for the TV, and ~ 650 μm for the LV) and then decline. In contrast, peak distributions are noted only at extremely low chord-lengths for the Leeds 44-y-old male in both the cervical and lumbar vertebrae. Mean marrow chord-lengths are 1,038 μm (CV) and 1,479 μm (LV) for the UF 66-y-old male, while they are 910 μm (CV) and 1,233 μm (LV), respectively, in the

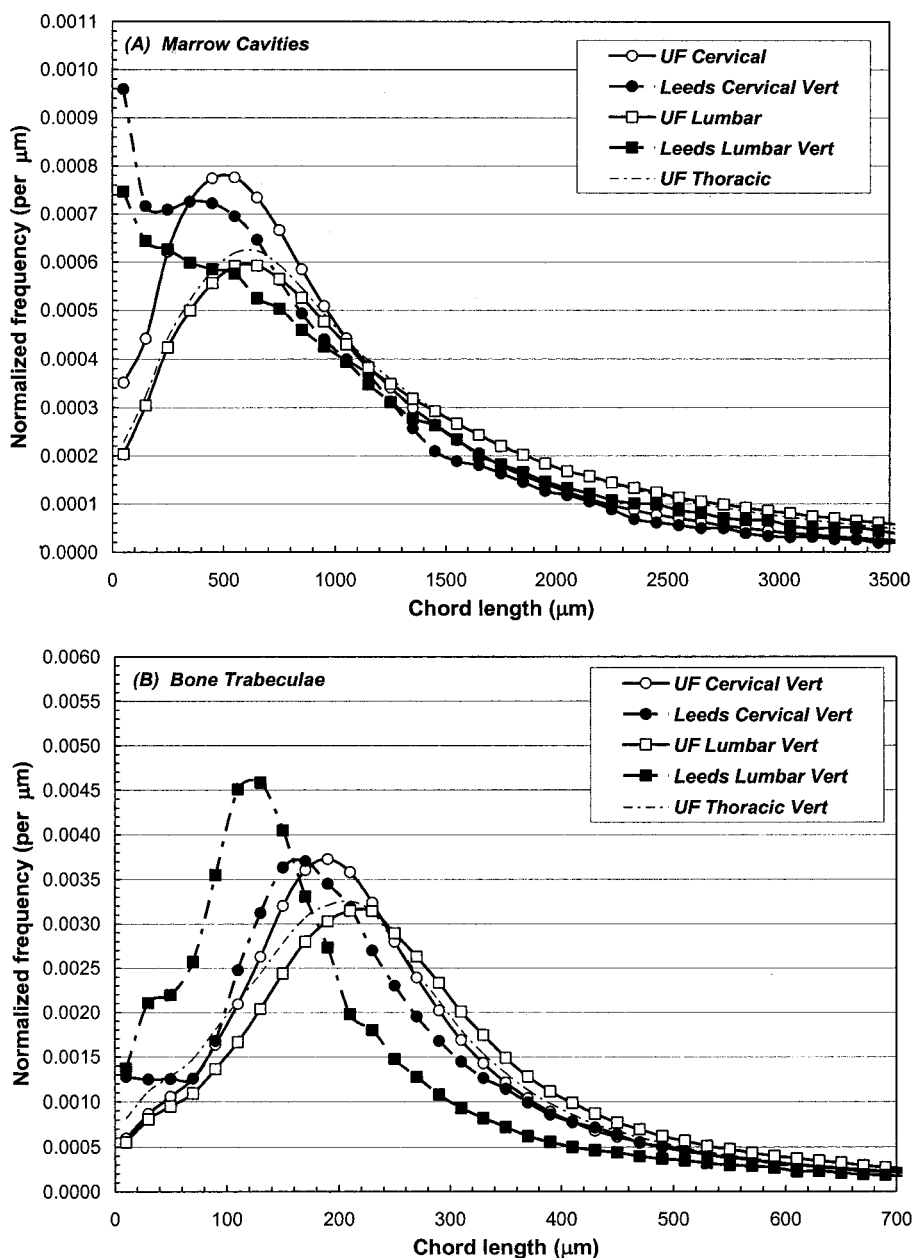


Fig. 3. Chord-length distributions through (a) marrow cavities and (b) bone trabeculae of the cervical and lumbar vertebra.

Leeds 44-y-old male. The mean marrow chord-length in the UF thoracic vertebrae is 1,368 μm .

Fig. 3b displays the corresponding chord distributions across bone trabeculae within the spinal column of both the Leeds and UF individuals. Here, we note that very comparable distributions are shown in the cervical vertebra of the UF and Leeds subjects (mean bone chords of 282 μm and 279 μm , respectively). Larger differences are shown in the distribution of bone chords in the lumbar vertebrae, where a higher frequency of smaller bone chords is seen in the Leeds subject (frequency peak at ~ 110 μm). The mean LV bone chord-length in the UF

individual is 316 μm , but is 246 μm in the Leeds individual. In the UF subject, microCT images of the trabecular structure of the cervical (C3 and C6) and thoracic (T3, T6, and T11) vertebrae showed relatively consistent shapes in their bone chord-length distributions. Greater inter-vertebral differences, however, were noted in the bone chord-length distributions of the lumbar region of the spine (L2 vs. L4) (data not shown).

Ribs

Fig. 4a and b displays chord distributions across the marrow cavities and bone trabeculae, respectively, in the

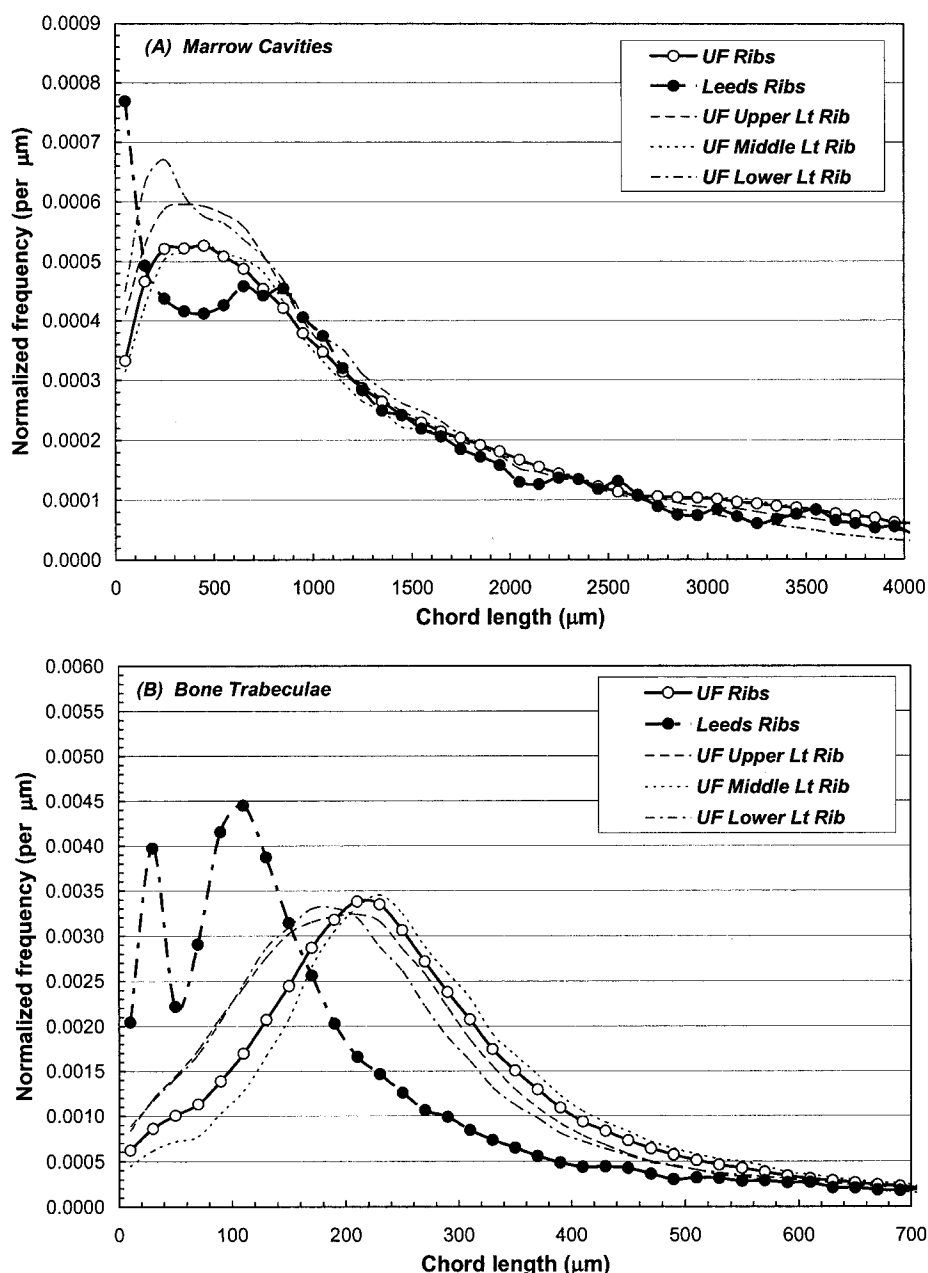


Fig. 4. Chord-length distributions through (a) marrow cavities and (b) bone trabeculae of the ribs. Values for individual rib bones used to compute the UF average are shown for the upper left rib (dashed line), middle left rib (dotted line), and lower left rib (dot-dash line).

ribs. For the UF data, lighter dashed, dotted, and dash-dot lines are used to indicate the individual rib distributions, which were then averaged to create the composite rib distribution (open circles). For marrow chords exceeding $\sim 900 \mu\text{m}$, close agreement is seen between the Leeds and UF individuals. While the UF marrow chords in the ribs peak in frequency around $400\text{--}500 \mu\text{m}$, the Leeds distribution is slightly depressed from 200 to $700 \mu\text{m}$, and then increases steeply at chords lengths below ~ 200

μm . A greater divergence in distribution shape is evident for the bone chord-lengths as shown in Fig. 4b. Here, the UF distribution shows a gradual increase in chord frequency peaking at $\sim 200\text{--}300 \mu\text{m}$, and then a steady decline until it matches the frequency of the Leeds data at bone chords exceeding $\sim 600 \mu\text{m}$. The Leeds data, however, show a bimodal distribution of bone chords in a manner similar to that found in the Leeds femoral head data. Mean values of marrow and bone chord lengths in

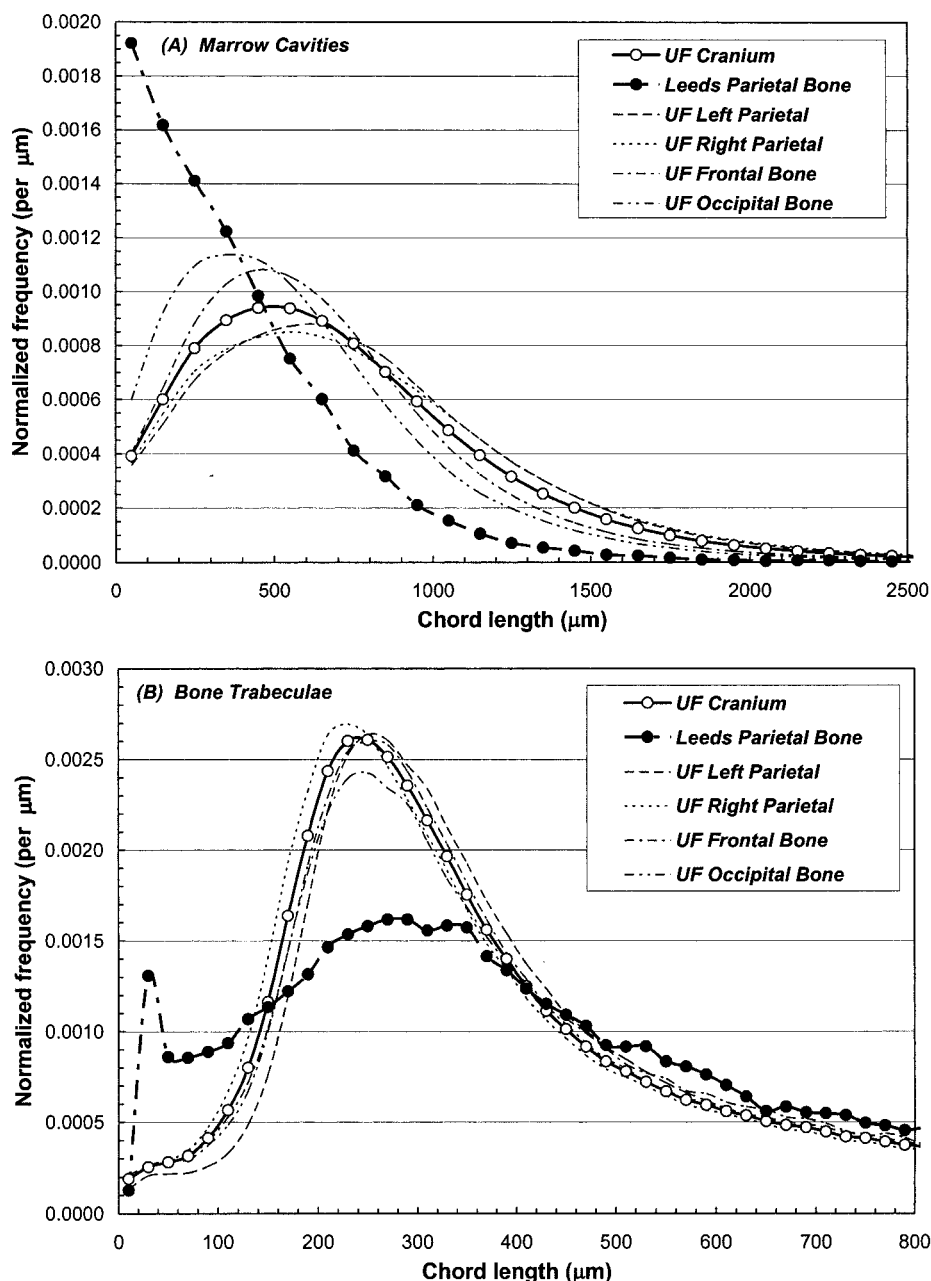


Fig. 5. Chord-length distributions through (a) marrow cavities and (b) bone trabeculae of the cranium. Values for individual bones of the cranium in the UF male subject are shown as well.

the ribs of the UF 66-y-old male are 1,630 μm and 302 μm , respectively. Corresponding values for the Leeds subject are 1,703 μm and 266 μm , as given in Table 1.

Cranium

Fig. 5a and b displays chord-length distributions across the marrow cavities and bone trabeculae in the cranial bones of the skeletal. For the UF data, individual distributions are given for the left and right parietal bones, the frontal bone, and the occipital bone, along

with an average distribution representing the entire cranium. For the Leeds data, distributions are only given for the parietal bone of their 44-y-old male subject. Dramatically different shapes are seen in the chord distributions between the UF and Leeds subjects for both spongiosa tissues. For the marrow cavities, the UF cranial averaged chords rise and peak in frequency at ~ 450 μm , while the Leeds chords increase in frequency almost linearly for chords below ~ 600 – 700 μm , with very low frequencies observed for chords exceeding ~ 1500 μm . The UF

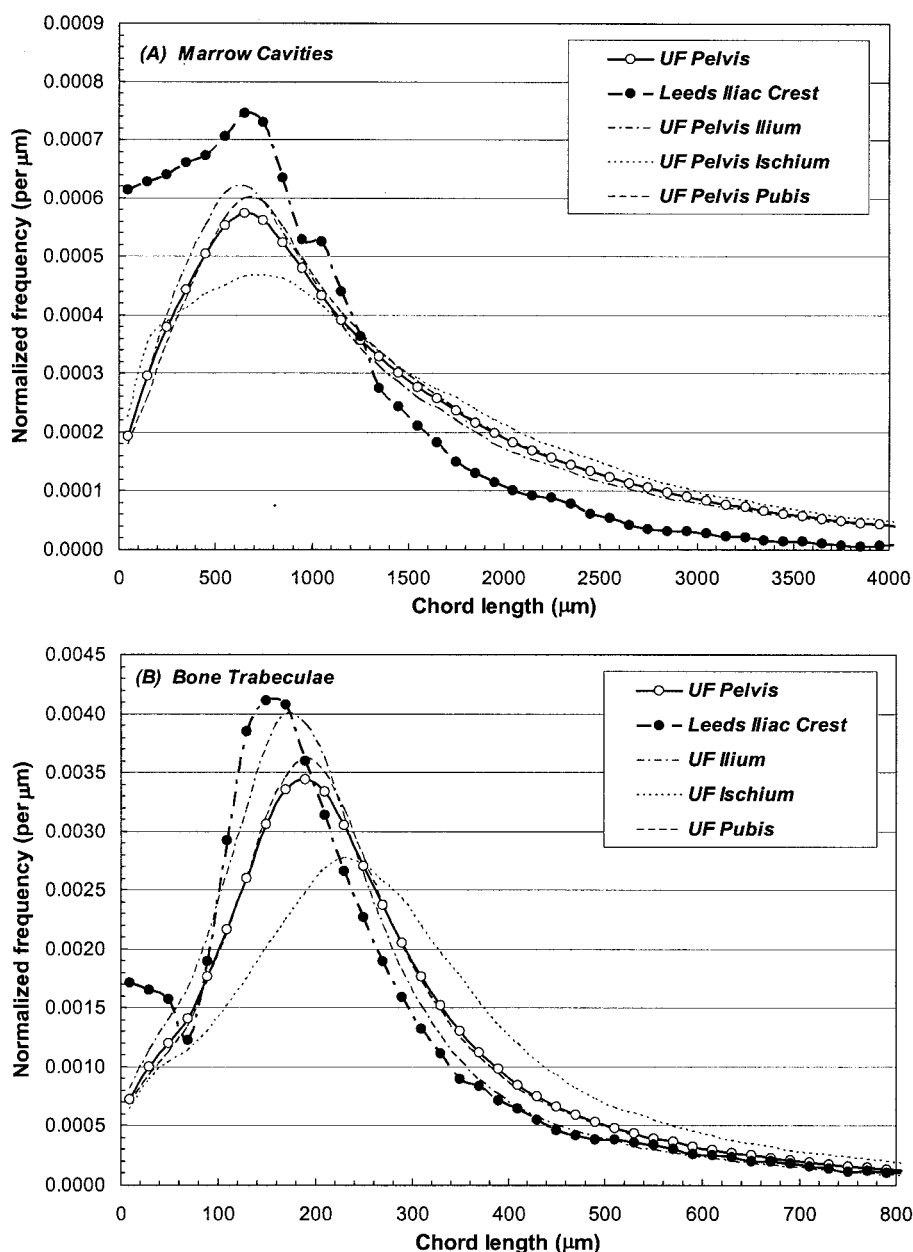


Fig. 6. Chord-length distributions through (a) marrow cavities and (b) bone trabeculae of the pelvis. Values for individual bones of the pelvis in the UF male subject are shown as well.

average marrow chord-length for the cranium is $751 \mu\text{m}$, while the Leeds parietal average marrow chord-length is only $389 \mu\text{m}$. For the bone trabeculae, the UF chord distributions again rise to a peak frequency at $\sim 250 \mu\text{m}$, after which the frequency distribution declines and approaches that of the Leeds parietal distribution at bone chords exceeding $\sim 400 \mu\text{m}$. In contrast, the Leeds bone chord distribution also rises to a peak ($\sim 300 \mu\text{m}$), but this peak is much broader. Also, a small spike in frequency is noted in the 2nd chord bin of the Leeds distribution at $40 \mu\text{m}$. The mean bone chord-lengths in

the UF cranial data and in the Leeds parietal bone data are $465 \mu\text{m}$ and $511 \mu\text{m}$, respectively. While these distributions differ in shape and frequency, the UF data confirms the observation made in the Leeds studies that the smallest marrow cavities in the skeleton are indeed located in the cranial spongiosa.

Pelvis

The final skeletal site for which direct comparisons can be made between the UF 66-y-old male and the Leeds 44-y-old male is the pelvis (Fig. 6a and b). For the

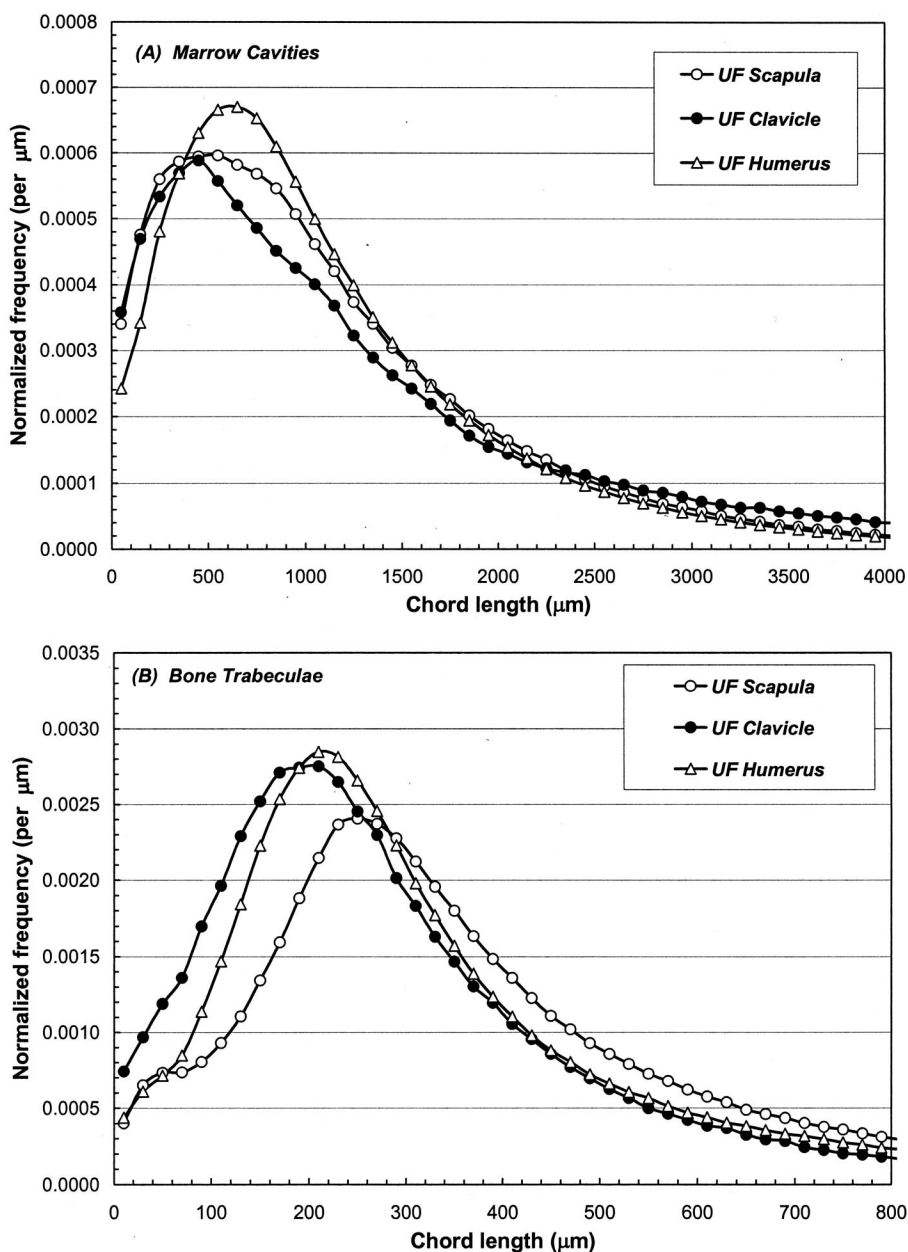


Fig. 7. Chord-length distributions through (a) marrow cavities and (b) bone trabeculae of the scapula, clavicle, and humerus in the UF male subject.

Leeds individual, marrow and bone chords distributions were acquired across samples of the iliac crest. For the UF individual, however, several cuboidal sections of spongiosa were taken and imaged from each of the three major bones comprising the pelvis—the ilium, the ischium, and the pubis. In Fig. 6a, frequencies in both the UF and Leeds chord distributions rise for decreasing marrow chords and peak in frequency at ~ 600 – 700 μm . However, the distribution of iliac crest marrow chords shown in the Leeds subject are shifted in favor of smaller marrow cavities in comparison to the UF individual.

While the mean marrow chord-length in the iliac crest of the Leeds individual is 904 μm , the UF individual shows mean marrow chord-lengths of 1,508, 1,593, and 1,493 μm in the ilium, ischium, and pubis (pelvic average of 1,523 μm). For the bone trabeculae, the UF data display a very similar distributional shape to the Leeds iliac crest distribution (except at small bone chords). The peak frequency for the Leeds data is located at ~ 150 μm , while peak frequencies are shown in the UF individual at 170 μm (ilium), 190 μm (ischium), and 240 μm (pubis). Nevertheless, mean chord lengths for bone trabeculae in

Table 1. Comparison of measured mean chord lengths with values published from the University of Leeds (Whitwell 1973).

		Mean marrow cavity chord length (μm)		Mean bone trabeculae chord length (μm)	
	Description of UF study	UF (present study) ^a	Whitwell (1973) ^a	UF (present study) ^b	Whitwell (1973) ^b
Femoral head	average of left, right	1043	1157	348	232
Femoral neck	average of left, right	1454	1655	347	314
Cervical vertebra	average of C3, C6	1038	910	282	279
Thoracic vertebra	average of T3, T6, T11	1368	* ^c	282	*
Lumbar vertebrae	average of L2, L4	1479	1233	316	246
Sacrum	single bone site	1116	*	330	*
Pelvis	average of 3 pelvic bones	1523	*	280	*
Ilium	single iliac crest	1508	904	245	242
Ischium	single bone site	1593	*	330	*
Pubic bone	single bone site	1493	*	280	*
Cranium	average of 4 cranial bones	751	*	465	*
Frontal bone	single bone site	676	*	470	*
Parietal bone	average left, right	812	389	469	511
Occipital bone	single bone site	598	*	491	*
Mandible	single bone site	1273	*	335	*
Ribs	average of 6 ribs	1630	1703	302	266
Humerus	average of left, right	1169	*	357	*
Scapula	average of left, right	1179	*	417	*
Sternum	single bone site	1404	*	273	*
Clavicle	average of left, right	1535	*	315	*

^a Normalized distribution out to 10,000 μm .^b Normalized distribution out to 2,000 μm .^c Note: * indicates values not reported in Whitwell (1973).

the ilium within the UF and Leeds individuals are very similar (245 and 242 μm , respectively).

Remaining marrow-containing bones of the skeleton

There are six remaining bone sites that contain active marrow in the adult skeleton for which chord-length distribution data for marrow cavities and bone trabeculae are not available for the Leeds 44-y-old male subject. These include the scapulae, clavicles, humeri, sacrum, sternum, and mandible. Fig. 7a and b displays chord distribution data in the UF individual for the marrow cavities and bone trabeculae, respectively, within the scapulae, clavicles, and humeri. Each curve in Fig. 7 represents the average chord distribution for both the left and right skeletal sites of this individual. Marrow chord distributions in Fig. 7a for these three upper torso skeletal sites are remarkably similar, all peaking in frequency at chord-lengths 500–700 μm . Bone trabeculae are shown in Fig. 7b to be slightly larger in the scapula (mean bone chord of 417 μm) and slightly smaller in the clavicles (mean bone chord of 315 μm). Marrow and bone chord distributions for the three remaining bone sites are shown in Fig. 8a and b, respectively. The mean marrow chord-length in the sacrum (1,116 μm) is shown to fall intermediate to that in the cervical (1,038 μm) and thoracic and lumbar (1,368 and 1,479 μm) vertebrae. The bone trabeculae of the sacrum are shown to be thicker on average (mean

bone chord of 330 μm) than seen in the other regions of the spine (282, 282, and 316 μm in the cervical, thoracic, and lumbar vertebrae, respectively). Furthermore, the mandible (mean marrow chord of 1,273 μm) is shown to display larger marrow cavities than seen in the cranium (mean marrow chord of 751 μm). In contrast, the bone trabeculae of the mandible (mean bone chord of 335 μm) were seen to be slightly thinner than found throughout the cranium (mean bone chord of 465 μm).

Weighting schemes for non-imaged bone sites in the Leeds data

As noted earlier, the Leeds chord-length distribution data for their 44-y-old male subject have been used extensively in both bone dosimetry in radiation protection and in nuclear medicine. However, since the Leeds data are limited to only measurements in seven skeletal sites (two of which are needed for the proximal femur), weighting schemes have been proposed by which chord-length distributions and dosimetry data at other non-imaged skeletal sites can be approximated. The larger and more extensive set of chord distributions assembled for the UF individual thus provides a unique opportunity to assess semi-quantitatively these weighting schemes. Table 8 of Bouchet et al. (2000) displays the various skeletal weighting schemes as originally proposed by Whitwell (Whitwell 1973). Three of these schemes are evaluated in the present study as shown in Figs. 9 to 11.

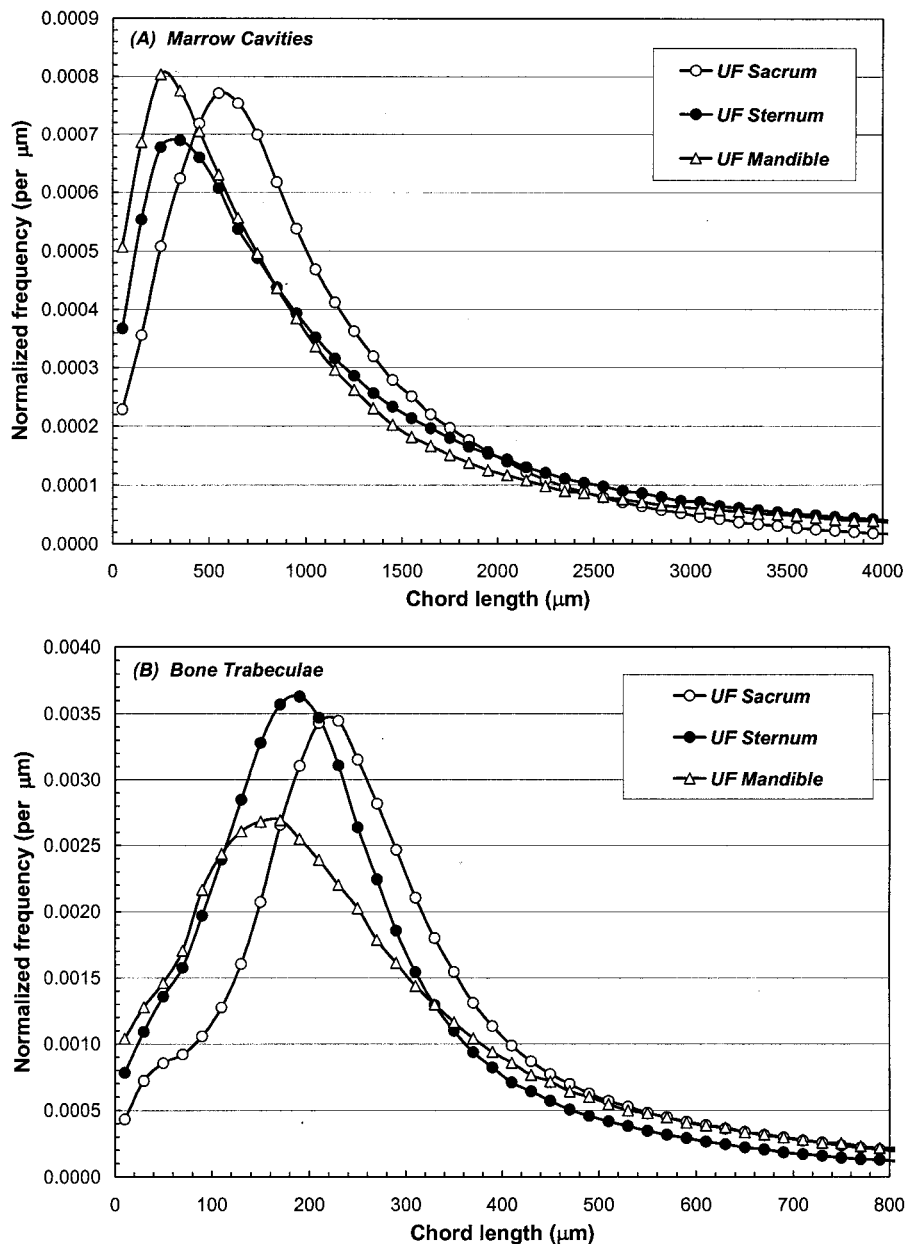


Fig. 8. Chord-length distributions through (a) marrow cavities and (b) bone trabeculae of the sacrum, sternum, and mandible in the UF male subject.

In the Leeds data, chord distributions were acquired in the cervical and lumbar regions of the spine, but not in the thoracic region (at least the data were not reported in Whitwell's dissertation). Consequently, it was proposed that the spongiosa microstructure of the thoracic vertebrae could be estimated as a 50:50 weighting of the cervical and lumbar chord distributions for both the marrow cavities and bone trabeculae. This 50:50 weighting scheme is shown in Fig. 9a and b as open circles. Data shown as closed circles are the microCT measured chord-length distributions as averaged across T3, T6, and T11. Relatively good agreement is shown in both tissue

regions, particularly for the bone trabeculae. For comparison, the estimated thoracic vertebrae distributions using the Leeds data are shown as dot-dashed lines in both figures.

A second approximation involves a weighting of 60% iliac crest and 40% lumbar vertebra to approximate the spongiosa microstructure of the sacrum. As shown in Fig. 10a, this scheme is fairly accurate in predicting the true sacral distribution of marrow chords in the UF individual. The same scheme applied to the Leeds data slightly underpredicts the peak frequency of bone trabeculae chord-lengths as seen in the sacrum of the UF individual.

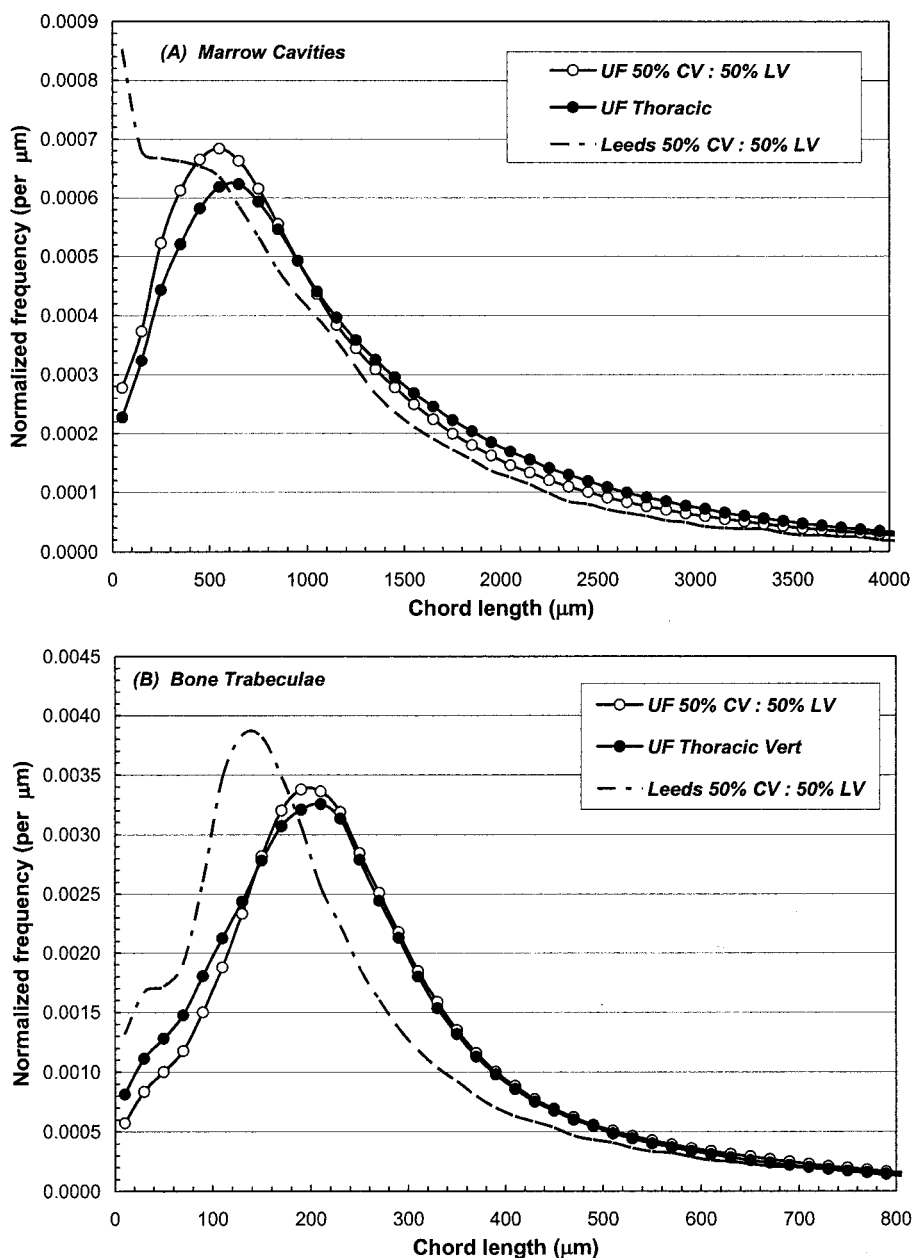


Fig. 9. Chord-length distributions through (a) marrow cavities and (b) bone trabeculae of the thoracic vertebra (present study) as approximated using a weighted average of the cervical and lumbar vertebrae.

Finally, the weighting scheme proposed by Whitwell to approximate the spongiosa microstructure of the humerus involved an 80:20 weighting of the femoral head and femoral neck, respectively. As shown in Fig. 11a and b, this technique (as applied only to the UF data) provides an excellent approximation of the true chord-length distributions measured across the marrow cavities and bone trabeculae of the proximal humerus. Differences between the Leeds estimate and the UF measurements of the bone chord-length distribution of the proximal humerus shown in Fig. 11b are directly attributed to

the differences seen earlier in the bone chord distribution of the femoral heads in these two individuals (see Fig. 2b).

CONCLUSION

In this study, we present 3D chord-length probability distributions across the marrow cavities and bone trabeculae at multiple skeletal sites of a 66-y-old male subject. These distributions are then compared to those assembled at the University of Leeds in the late 1970's,

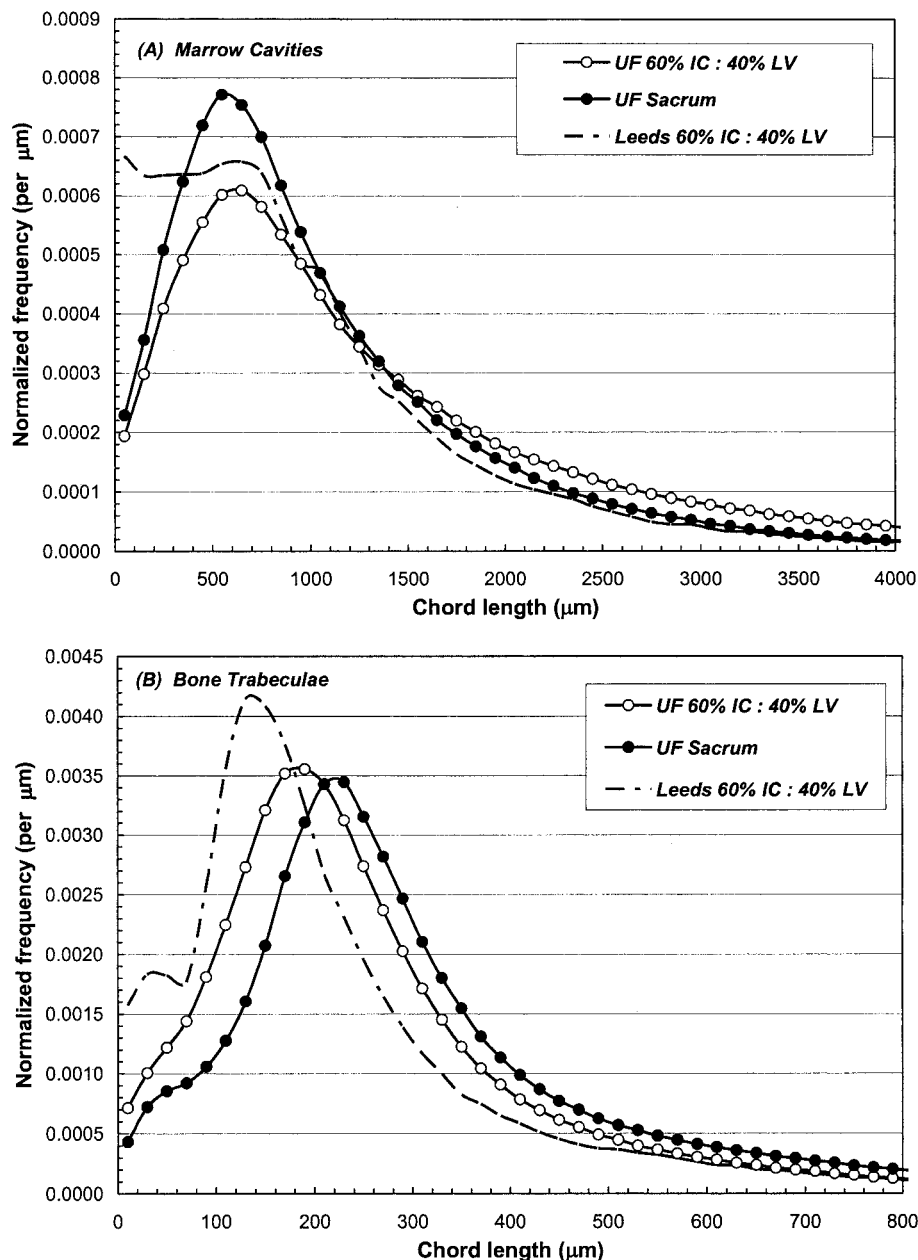


Fig. 10. Chord-length distributions through (a) marrow cavities and (b) bone trabeculae of the sacrum (present study) as approximated using a weighted average of the iliac crest and lumbar vertebrae.

which form the microstructural basis for current ICRP reference male skeletal models used in both radiation protection and medical dosimetry. A review of mean chord lengths given in Table 1 indicate that larger marrow cavities are noted on average in the UF individual for the cervical vertebrae (1,038 vs. 910 μm), lumbar vertebrae (1,479 vs. 1,233 μm), ilium (1,508 vs. 904 μm), and parietal bone (812 vs. 389 μm), while smaller marrow cavities are noted in the UF individual for the femoral head (1,043 μm vs. 1,157 μm), the femoral neck (1,454 μm vs. 1,655 μm), and the ribs (1,630 μm vs.

1,703 μm). The mean chord-lengths for the bone trabeculae show close agreement for the two subjects within the ilium (~ 240 μm) and cervical vertebrae (~ 280 μm). Thicker trabeculae were seen on average in the UF individual for the femoral head (ratio of 1.50), femoral neck (ratio of 1.10), lumbar vertebrae (ratio of 1.29), and ribs (ratio of 1.14), while thinner trabeculae were seen on average in the UF individual for the parietal bone of the cranium (ratio of 0.92). In three cases, prominent discrepancies in chord-distributional shape were noted between the two subjects: the bone trabeculae in the ribs

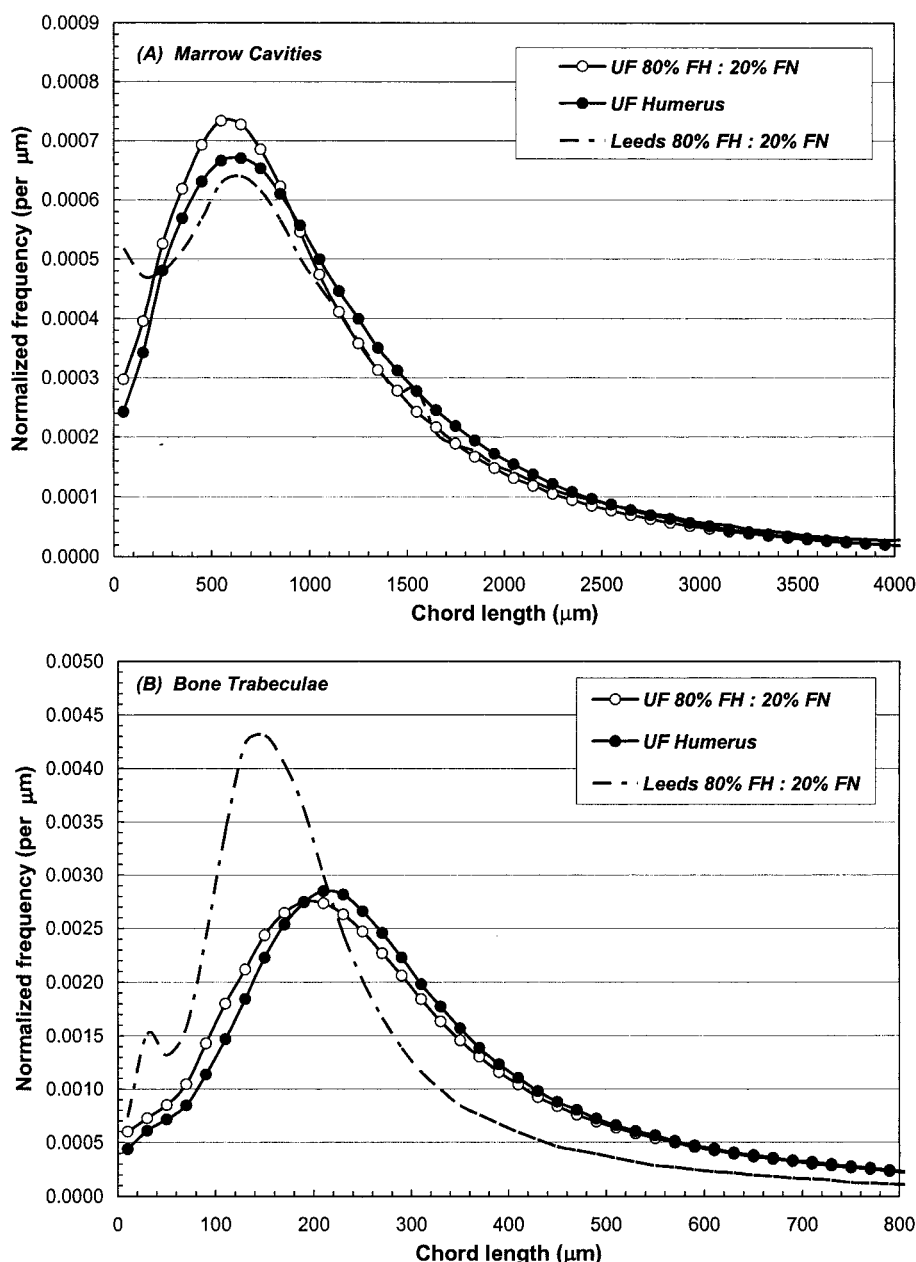


Fig. 11. Chord-length distributions through (a) marrow cavities and (b) bone trabeculae of the humerus (present study) as approximated using a weighted average of the femoral head and neck.

(Fig. 4b) and the marrow cavities and bone trabeculae in the cranium (Fig. 5a and b). Overall, the distributional shapes for all UF measurements were fairly consistent across skeletal site where a moderate-to-steep rise in chord frequency is seen for small chords, followed by a peak in the chord frequency (300–700 μm for marrow cavity chords and 100–300 μm for the bone trabeculae) and gradual decline in chord frequency thereafter.

While the data provided in this study greatly expand one's ability to assess bone-specific skeletal tissue dose

in individuals more representative of those undergoing radionuclide and other radiation therapies, further research is clearly warranted. First, the 3D imaging techniques presented here should be extended to studies of both the male and female trabecular microstructure as a function of patient age, and perhaps more importantly, as a function of skeletal health. An age-dependent catalog of microCT images can be envisioned spanning normal to osteopenic to osteoporotic skeletal microstructures. Pairing of images/dosimetry with the patient could then be made through CT-based assessments of volumetric

bone mineral density (BMD_v) (Lang et al. 2002). Second, both the Leeds and UF individuals represent subjects of declining skeletal characteristics. Imaging data from the mature skeleton of young adults (~25 y) would be of high interest as the ICRP reference individuals are between 20–30 years of age. Finally, extremely limited data exist on the skeletal microstructure of children. In all cases, however, access to tissue samples becomes increasingly difficult at younger ages. Nevertheless, the information provided would potentially enhance our ability to individualize skeletal dosimetry as needed for risk assessment and predictions of marrow toxicity and cancer risk in both radiation and radionuclide therapy.

Acknowledgments—This work was supported in part by Grant CA96441 from the National Cancer Institute and Grant DE-FG07-02ID14327 from the U.S. Department of Energy with the University of Florida.

We would also like to thank Scanco Medical AG for their assistance with their commercial scanning service. Finally, we wish to thank Keith Eckerman for his helpful thoughts and comments on this manuscript.

REFERENCES

- Beddoe AH. The microstructure of mammalian bone in relation to the dosimetry of bone-seeking radionuclides. Leeds, UK: University of Leeds; 1976. Thesis.
- Beddoe AH, Darley PJ, Spiers FW. Measurements of trabecular bone structure in man. *Phys Med Biol* 21:589–607; 1976.
- Bouchet LG, Bolch WE, Howell RW, Rao DV. S values for radionuclides localized within the skeleton. *J Nucl Med* 41:189–212; 2000.
- Cristy M. Active bone marrow distribution as a function of age in humans. *Phys Med Biol* 26:389–400; 1981.
- Cristy M, Eckerman KF. Specific absorbed fractions of energy at various ages from internal photon sources. Oak Ridge: Oak Ridge National Laboratory; ORNL/TM-8381/Volumes I–VII; 1987.
- Custer RP, Ahlfeldt FE. Studies on the structure and function of bone marrow variations in cellularity in various bones with advancing years of life and their relative response to stimuli. *J Laboratory Clinical Med* 17:951–962; 1932.
- Eckerman KF. Aspects of the dosimetry of radionuclides within the skeleton with particular emphasis on the active marrow. In: Schlafke-Stelson AT, Watson EE, eds. *Proceedings of the Fourth International Radiopharmaceutical Dosimetry Symposium*. Oak Ridge, TN: Oak Ridge Associated Universities; 1985: 514–534.
- Eckerman KF, Stabin MG. Electron absorbed fractions and dose conversion factors for marrow and bone by skeletal regions. *Health Phys* 78:199–214; 2000.
- Heyward VH, Stolarczyk LM. Applied body composition assessment. Champaign, IL: Human Kinetics; 1996.
- International Commission on Radiological Protection. Basic anatomical and physiological data for use in radiological protection: the skeleton. Oxford, UK: International Commission on Radiological Protection; ICRP Publication 70; 1995.
- International Commission on Radiological Protection. Basic anatomical and physiological data for use in radiological protection: reference values. New York: International Commission on Radiological Protection; Publication 89; 2002.
- Jokisch DW, Patton PW, Inglis BA, Bouchet LG, Rajon DA, Rifkin J, Bolch WE. NMR microscopy of trabecular bone and its role in skeletal dosimetry. *Health Phys* 75:584–596; 1998.
- Jokisch DW, Patton PW, Rajon DA, Inglis BA, Bolch WE. Chord distributions across 3D digital images of a human thoracic vertebra. *Med Phys* 28:1493–1504; 2001.
- Lang TF, Guglielmi G, van Kuijk C, De Serio A, Cammisa M, Genant HK. Measurement of bone mineral density at the spine and proximal femur by volumetric quantitative computed tomography and dual-energy X-ray absorptiometry in elderly women with and without vertebral fractures. *Bone* 30:247–250; 2002.
- Lorensen WE, Cline HE. Marching Cubes: a high-resolution 3D surface construction algorithm. *Computer Graphics* 21:163–169; 1987.
- Mechanik N. Studies of the weight of bone marrow in man. *Zeitschrift für die Gest. Anatomy* 79:58–99; 1926.
- Patton PW, Jokisch DW, Rajon DA, Shah AP, Myers SL, Bolch WE. Skeletal dosimetry via NMR microscopy: investigations of sample reproducibility and signal source. *Health Phys* 82:316–326; 2002a.
- Patton PW, Rajon DA, Shah AP, Jokisch DW, Inglis B, Bolch WE. Site-specific variability in trabecular bone dosimetry: considerations of energy loss to cortical bone. *Med Phys* 29:6–14; 2002b.
- Rajon DA, Bolch WE. Interactions within 3D isotropic and homogeneous radiation fields: A Monte Carlo simulation algorithm. *Comput Methods Programs Biomed* 70:167–177; 2003.
- Rajon DA, Patton PW, Shah AP, Watchman CJ, Bolch WE. Surface area overestimation within three-dimensional digital images and its consequence for skeletal dosimetry. *Med Phys* 29:682–693; 2002.
- Rajon DA, Shah AP, Watchman CJ, Brindle JA, Bolch WE. A hyperboloid representation of the bone-marrow interface within 3D NMR images of trabecular bone: Applications to skeletal dosimetry. *Phys Med Biol* 48:1721–1740; 2003.
- Sgouros G. Bone marrow dosimetry for radioimmunotherapy: Theoretical considerations. *J Nucl Med* 34:689–694; 1993.
- Sgouros G, Stabin M, Erdi Y, Akabani G, Kwok C, Brill AB, Wessels B. Red marrow dosimetry for radiolabeled antibodies that bind to marrow, bone, or blood components. *Med Phys* 27:2150–2164; 2000.
- Shah A. Reference skeletal dosimetry model for an adult male radionuclide therapy patient based on 3D imaging and paired-image radiation transport [Dissertation]. Gainesville, FL: University of Florida; 2004.
- Shah A, Bolch W, Rajon D, Patton P, Jokisch D. A paired-image radiation transport (PIRT) model for skeletal dosimetry. *J Nucl Med* 46:344–353; 2005.
- Shah A, Jokisch D, Watchman C, Rajon D, Patton P, Bolch W. Chord-based versus voxel-based methods of electron transport in the skeletal tissues. *Med Phys*; in press.
- Spiers FW. A review of the theoretical and experimental methods of determining radiation dose in bone. *Br J Radiol* 39:216–221; 1966.
- Spiers FW, Beddoe AH, Whitwell JR. Mean skeletal dose factors for beta-particle emitters in human bone. Part I: Volume-seeking radionuclides. *Br J Radiol* 51:622–627; 1978.
- Spiers FW, Beddoe AH, Whitwell JR. Mean skeletal dose factors for beta-particle emitters in human bone. Part II:

- Surface-seeking radionuclides. *Br J Radiol* 54:500–504; 1981.
- Stabin MG. MIRDOSE—Personal computer software for internal dose assessment in nuclear medicine. *J Nucl Med* 37:538–546; 1996.
- Stabin M, Sparks R. OLINDA—PC-based software for biokinetic analysis and internal dose calculations in nuclear medicine [Abstract]. *J Nucl Med* 44:103P; 2003.
- Stabin MG, Eckerman KF, Bolch WE, Bouchet LG, Patton PW. Evolution and status of bone and marrow dose models. *Cancer Biother Radiopharm* 17:427–445; 2002.
- Trotter M, Hixon B. Sequential changes in weight, density, and percentage ash weight of human skeletons from an early fetal period through old age. *Anat Rec* 179:1–18; 1974.
- Whitwell JR. Theoretical investigations of energy loss by ionizing particles in bone. Leeds, UK: University of Leeds; 1973. Thesis.
- Whitwell JR, Spiers FW. Calculated beta-ray dose factors for trabecular bone. *Phys Med Biol* 21:16–38; 1976. ■ ■

Absorbed Fractions for α -Particles in Tissues of Trabecular Bone: Considerations of Marrow Cellularity Within the ICRP Reference Male

Christopher J. Watchman, MS¹; Derek W. Jokisch, PhD²; Phillip W. Patton, PhD³; Didier A. Rajon, PhD⁴; George Sgouros, PhD⁵; and Wesley E. Bolch, PhD^{1,6}

¹Department of Nuclear and Radiological Engineering, University of Florida, Gainesville, Florida; ²Department of Physics and Astronomy, Francis Marion University, Florence, South Carolina; ³Department of Health Physics, University of Nevada–Las Vegas, Las Vegas, Nevada; ⁴Department of Neurosurgery, University of Florida, Gainesville, Florida; ⁵Department of Radiology, Johns Hopkins University, Baltimore, Maryland; and ⁶Department of Biomedical Engineering, University of Florida, Gainesville, Florida

α -Particles are of current interest in radionuclide therapy due to their short range and high rates of energy transfer to target tissues. Published values of α -particle absorbed fraction ϕ in the skeletal tissues, as needed for patient-specific dosimetry under the MIRD schema, do not generally account for its variation with particle energy or skeletal site. Furthermore, variations in α -particle absorbed fraction with marrow cellularity have yet to be fully considered. **Methods:** In this study, a 3-dimensional (3D) chord-based radiation transport model (or 3D-CBIST) is presented, which combines (a) chord-based techniques for tracking α -particles across bone trabeculae, endosteum, and marrow cavities and (b) a spatial model of the marrow tissues that explicitly considers the presence of marrow adipocytes. Chord-length distributions are taken from a 44-y male subject (ICRP [International Commission on Radiological Protection] Reference Male) and are identical to those used currently for clinical dose estimates for β -particle emitters. **Results:** Values of ϕ (active marrow \leftarrow active marrow) given by the 3D-CBIST model are shown to be considerably lower than $\phi = 1.0$ assumed under the ICRP Publication 30 and 2003 Eckerman bone models. For example, values of absorbed fraction for the self-dose to active bone marrow in the ribs, cervical vertebra, and parietal bone are 0.81, 0.80, and 0.55 for 6-MeV α -particles and are 0.74, 0.72, and 0.43 for 9-MeV α -particles, where each is evaluated at ICRP reference cellularities in the 3D-CBIST model (72%, 72%, and 42%, respectively, at age 25 y). **Conclusion:** Improvements in patient-specific dosimetry of skeletal tissues require explicit consideration of not only changes in target mass with variable patient marrow cellularity (i.e., active marrow) but also corresponding changes in values of the absorbed fraction. The data given in this study provide a more-firm basis for application of the MIRD schema to patient-specific dosimetry for newly developing therapies using α -particle emitters.

Key Words: radionuclide therapy; α -particles; absorbed fraction; marrow cellularity; bone dosimetry.

J Nucl Med 2005; 46:1171–1185

Beta-particle emitters have played a prominent role in the development of radionuclide-based cancer therapy. More recently, increased interest has been shown in the potential of α -emitters for radioimmunotherapy, particularly for leukemia and micrometastases (1–4). α -Particles provide an attractive alternative to β -particles owing to their higher collisional stopping power (providing increased absorbed dose to tumor cells) and correspondingly shorter range (providing increased sparing of nontargeted tissues). Examples of α -emitters under clinical investigation for radionuclide therapy are listed in Table 1 (5). When α -emitters are localized at low-activity concentrations in targeted tissues, techniques of microdosimetry are generally required to characterize the frequency distribution of absorbed dose to individual target cells. At high-activity concentrations, as would be expected in clinical α -particle radioimmunotherapy, the variation in cellular dose is small, and macroscopic dosimetry techniques may be applied as formulated under the MIRD schema (6).

At present, standardized values of absorbed fraction (ϕ) for α -particles in the skeletal tissues are limited to two principal sources: the International Commission on Radiological Protection (ICRP) in their Publication 30 (7) and the 2003 Eckerman model as published by Stabin and Siegel (8) for use in the OLINDA (Organ Level Internal Dose Assessment) code (9). Although the ICRP has provided many important updates to both physiologic and anatomic reference values for the skeleton (10,11), no fundamental updates to its skeletal dosimetry model have been issued. The ICRP Publication 30 bone model, developed to provide a conservative dosimetric framework for radiation protection of the skeletal tissues, gives values of α -particle absorbed fraction that are independent of both particle energy and skeletal site. Literature sources cited as references for the ICRP 30 model include studies by Thorne (12,13) and by Mays and Sears (14), in which simple geometric configurations were adopted such as infinite parallel planes (repre-

Received Aug. 1, 2004; revision accepted Mar. 18, 2005.

For correspondence or reprints contact: Wesley E. Bolch, PhD, Advanced Laboratory for Radiation Dosimetry Studies, Department of Nuclear and Radiological Engineering, University of Florida, Gainesville, FL 32611-8300.
E-mail: wbolch@ufl.edu

TABLE 1
Candidate α -Particle Emitters for Radionuclide Therapy

Radionuclide daughters	Half-life	Yield* (%)	Emission particle	Particle energy†
^{213}Bi	45.6 min	2	α	5.9 MeV
		98	β^-	444 keV
		17	γ	440 keV
^{213}Po	4.2 μs	98	α	8.4 MeV
^{209}Tl	2.2 min	2	β^-	659 keV
^{209}Pb	3.25 h	100	β^-	198 keV
^{209}Bi	Stable			
^{212}Bi	1.0 h	36	α	6.0 MeV
		64	β^-	492 keV
^{212}Po	298 ns	64	α	8.8 MeV
^{208}Tl	3.05 min	36	β^-	560 keV
		8	γ	510 keV
		31	γ	580 keV
		36	γ	2.6 MeV
^{208}Pb	Stable			
^{211}At	7.21 h	42	α	5.9 MeV
		19	γ	80 keV
^{211}Po	516 ms	58	α	7.4 MeV
^{207}Bi	32 y	24	γ	70 keV
		41	γ	570 keV
		31	γ	1 MeV
^{207}Pb	Stable			
^{225}Ac	10 d	100	α	5.8 MeV
^{211}Fr	4.9 min	100	α	6.4 MeV
		10	γ	218 keV
^{217}At	32.3 ms	100	α	7.1 MeV
^{213}Bi	See ^{213}Bi			
^{223}Ra	11.4 d	100	α	5.7 MeV
		40	γ	80 keV
		14	γ	270 keV
^{219}Rn	4 s	100	α	6.8 MeV
		10	γ	270 keV
^{215}Po	1.8 ms	100	α	7.4 MeV
^{211}Pb	36.1 min	100	β^-	447 keV
^{211}Bi	2.1 min	16	α	6.3 MeV
		84	α	6.6 MeV
		13	γ	350 keV
^{207}Tl	4.8 min	100	β^-	493 keV
^{207}Pb	Stable			

*Percent emitted per decay of parent radionuclide.

†Mean β -energy and approximate α - and γ -energies are listed.

senting the bone–marrow interface) and spheres (representing the marrow space with an endosteum layer on its surface). The β -particle results of Whitwell and Spiers (15) are also used as reference values for α -particles irradiating the active marrow from bone volume sources. In the 2003 Eckerman model, an energy dependence is introduced for some source–target tissue combinations, whereas for others, values from the ICRP 30 model are adopted.

In the present study, an expanded model of α -particle transport in the skeletal tissues is given that explicitly ac-

counts for absorbed fraction variations with not only particle energy but also with skeletal site and marrow cellularity. Each parameter is potentially important in improving the patient specificity of the skeletal dose estimate. As shown in Table 1, α -energies of clinically relevant radionuclides range from ~ 5.5 to 9 MeV. In contrast, those of interest in occupational radiation protection (for which the ICRP 30 model was established) range from only ~ 4 to 5.5 MeV. Furthermore, when bone-site-specific radionuclide therapies are applied, variations in the trabecular microarchitecture (bone trabeculae and marrow cavity sizes) may alter patterns of α -energy deposition beyond that predicted by a single skeletal-averaged set of absorbed fractions. Finally, marrow cellularity can vary greatly among different patients (16) and is not considered in either of the two existing models. As shown in Figure 1, adipocytes localized along the trabecular surfaces at low marrow cellularities can significantly reduce the α -particle energy available for deposition to active bone marrow.

MATERIALS AND METHODS

In this study, α -particle transport in the skeletal tissues is accomplished using techniques similar to those developed for electrons in models published by Eckerman and Stabin (17) and by Bouchet et al. (18). The 3-dimensional (3D) microstructure of individual bone trabeculae and marrow cavities are taken from the chord-length distributions published by Whitwell and Spiers (15) and Whitwell (19) at the University of Leeds for 7 skeletal sites from a 44-y male subject. The unique feature of the present model, however, is the use of a supplemental 3D spatial model of the active and inactive tissues within the marrow space. Through the use of range–energy relationships, absorbed fractions to active marrow, as well as bone endosteum and bone trabeculae, are calculated for α -particle emissions up to 10 MeV. The details of this 3D chord-based infinite spongiosa transport (3D-CBIST)

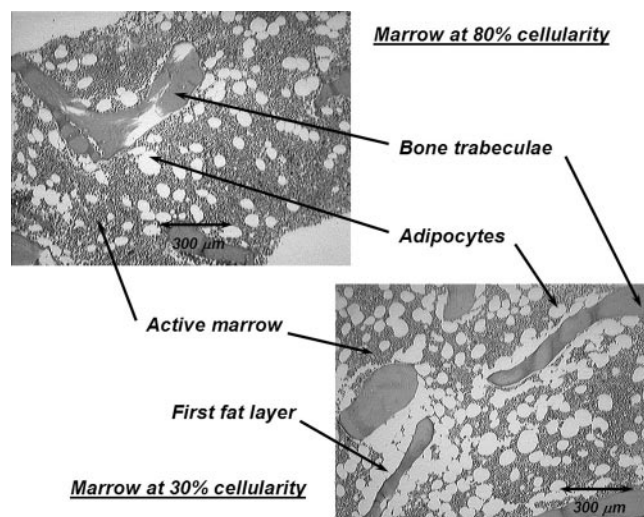


FIGURE 1. Histology slides of normal human bone marrow at 2 different marrow cellularities. At lower cellularity, a greater proportion of bone trabecula surface is covered by adipocytes (i.e., the first fat layer).

TABLE 2
Elemental Composition (% by Mass) of Tissues
of Skeletal Spongiosa

Element	Tissues of trabecular spongiosa			
	Active marrow (TAM)*	Inactive marrow (TIM)†	Endosteum (TBE)‡	Trabeculae (TBV)§
H	10.5	11.5	10.5	3.4
C	41.4	64.4	25.6	15.5
N	3.4	0.7	2.7	4.2
O	43.9	23.1	60.2	43.5
Na	—	0.1	0.1	0.1
Mg	—	—	—	0.2
P	0.1	—	0.2	10.3
S	0.2	0.1	0.3	0.3
Cl	0.2	0.1	0.2	—
K	0.2	—	0.2	—
Ca	—	—	—	22.5
Fe	0.1	—	—	—
Mass density (g cm ⁻³)	1.03	0.98	1.03	1.92

*TAM = “adult red marrow.”

†TIM = “adult yellow marrow.”

‡TBE = “adult soft tissue (male).”

§TBV = “adult cortical bone.”

Data taken from ICRU Report 46, Appendix A (21).

model for skeletal dosimetry are outlined below. In the model, we adopt the following nomenclature to define various source and target tissues: TBV, trabecular bone volume; TBE, trabecular bone endosteum; TBS, trabecular bone surfaces; TAM, trabecular active (“red”) marrow; and TIM, trabecular inactive (“yellow”) marrow. The modifying phrase “infinite spongiosa transport” indicates that we are only considering α -transport within the tissues of trabecular spongiosa (marrow, endosteum, and bone trabeculae). Any cross-fire from cortical bone to the interior spongiosa regions of the skeletal site is thus ignored. Though this assumption is rarely valid for higher-energy β -particles in the skeleton (20), the model is considered to be quite adequate for α -particles even at energies approaching 10 MeV. For TBV sources, the radiopharmaceutical is assumed to be distributed uniformly within the volume of the bone trabeculae. Future extensions of the model may accommodate its variation with depth when the physical half-life exceeds bone remodeling half-times. Generally, however, TBS and TBE sources would be more appropriate for bone-seeking agents in radionuclide therapy. The former would correspond to agents initially incorporated in the osseous tissues at bone-remodeling sites, whereas the latter would correspond to agents directly targeting osteoblasts or osteoclasts.

Tissue Composition and Range–Energy Data

Elemental compositions and mass densities for the tissues of trabecular spongiosa were taken from Report 46 of the International Commission on Radiation Units and Measurements (ICRU) (21) (Table 2). Range–energy functions were calculated for active (red) marrow, inactive (yellow) marrow, and trabecular endosteum using the Bragg–Kleeman rule (22) with liquid water (23) as the reference media for range scaling:

$$R_T = R_{H_2O} \frac{\rho_{H_2O}}{\rho_T} \sqrt{\frac{A_T}{A_{H_2O}}}, \quad \text{Eq. 1}$$

where R_T is the CSDA (continuous slow-down approximation) range in the desired tissue (TAM, TIM, or TBE), R_{H_2O} is the corresponding linear range in water, and ρ_T and ρ_{H_2O} are their respective mass densities. In Equation 1, the effective atomic number of these tissues, A_T (as well as A_{H_2O}), is calculated as:

$$\sqrt{A_T} = \left(\sum_i \frac{w_i}{\sqrt{A_i}} \right)^{-1}, \quad \text{Eq. 2}$$

where w_i is the mass fraction for the i th element within that tissue. Trabecular bone was similarly scaled using ICRU Report 49 compact bone as the reference tissue (23). Tabular data for the CSDA range versus particle energy were thus created for all tissues for use by the transport code. Ranges at intermediate energies were assessed via interpolation of tabular values.

Spatial Model for Marrow Tissue Transport

As previously noted by Bolch et al. (24), the chord-based skeletal models of both Eckerman and Stabin (17) and of Bouchet et al. (18) were constructed in such a fashion that considerations of marrow cellularity could not be made explicitly during particle transport (only via energy-independent scaling of absorbed fractions after particle transport). To permit such considerations during α -particle transport, a spatial model of the marrow tissues was created as demonstrated schematically in Figure 2. Each model consists of 2 regions: (a) an inner sphere of marrow in which randomly selected marrow chords are started (each representing the potential trajectory of an α -particle track emitted within the active marrow or emerging from the endosteal layer into the marrow space), and (b) a buffer region in which marrow chords (and, thus, the α -particle tracks) may terminate, but not begin. The

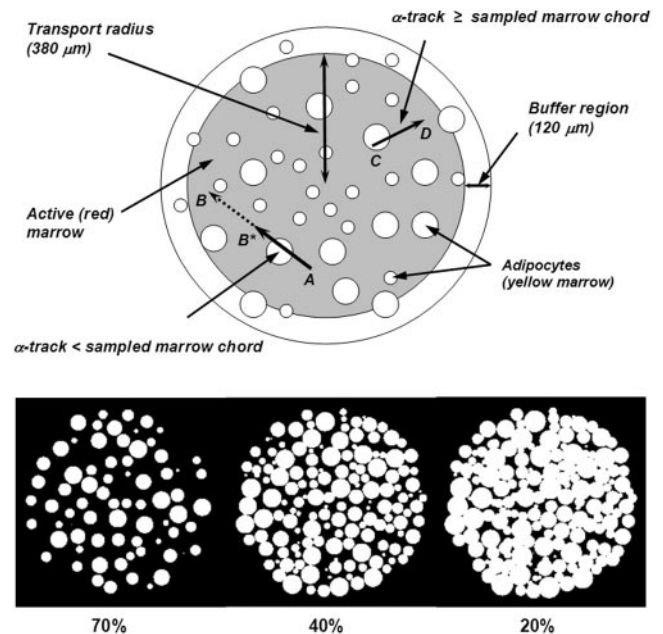


FIGURE 2. Geometric model used to partition sampled marrow cavity chords into subtrajectories of α -particle through active (red) marrow and inactive (yellow) marrow, the latter represented by individual adipocytes (white spheres).

buffer region (scaled to the active marrow range of 10-MeV α -particles) thus ensures that the sampled marrow-cavity chord will always fully lie within tissues of the marrow spatial model. The 1,000- μm diameter of the marrow spatial model corresponds roughly to the nominal chord-length seen for marrow cavities in the Leeds 44-y male.

As shown in Figure 2, regions of inactive (or yellow) marrow are simulated as a series of randomly placed spheric fat cells (adipocytes). Adipocyte diameters are randomly sampled from a 5-bin histogram (92, 72, 56, 40, and 20 μm) that approximate the gaussian distribution of sizes reported by Reverter et al. (25) in normal human bone marrow (mean diameter, $56.7 \pm 5.6 \mu\text{m}$). Marrow models of varying marrow cellularity (from 10% to 100%) are generated by increasing the number of randomly placed adipocytes within the marrow sphere. For marrow cellularities greater than 50%, adipocyte overlap is prohibited as cell clustering is only prominent at cellularities below 50% (26).

For marrow cellularities below 50%, the 50% cellularity model is modified through stepwise increases in adipocyte diameter (5% each) and by abandoning the restriction on adipocyte overlap. Adipocyte diameter increases (representing multicellular adipocyte clusters) are continued until the desired overall marrow cellularity is achieved. Transverse views through marrow models at cellularities of 70% (no cell clusters), 40% (few cell clusters), and 20% (multiple cell clusters) are shown in the lower portion of Figure 2. Note that in all 3D spatial models of the marrow space, neither of the bone trabeculae for the trabecular endosteum are represented; their influence on particle transport is handled separately by chord-based techniques as described.

Chord-Based Model for Spongiosa Tissue Transport

α -Particle transport in the present study is performed through random and alternate sampling of cumulative density functions (CDFs) for μ -random (external) chord-lengths across bone trabeculae (d_T) and the marrow cavities (d_{MC}) in each of the 7 skeletal sites of the Leeds 44-y male. Corresponding distributions under I-randomness (interior) are applied in regions of α -particle source emissions (27). For consistency with the sample preparation and scanning methods of the Leeds studies, we make a distinction between the marrow cavity (MC, total volume of tissue between bone trabeculae inclusive of the endosteal layer) and the marrow space (MS, total marrow tissue volume between bone trabeculae exclusive of the endosteal layer). Explicit treatment of the endosteal layer, as well as the active and inactive tissues of the bone marrow, is discussed below.

The transport methodology is best described by first considering an α -emitter uniformly distributed within the tissues of the bone trabeculae (i.e., TBV source). The transport code first randomly samples a bone chord-length d_T^{max} from the I-random $CDF_I(d_T^{max})$ for the skeletal site of interest (e.g., cervical vertebra). This sampled chord-length is treated as the maximum possible distance that an α -particle may travel within its bone trabecula before entering the endosteal layer. The transport distance actually taken, d_T , is thus uniformly sampled across this interval: $[0, d_T^{max}]$. The range-energy function for α -particles in bone tissue is then used to determine the total energy expended by the particle within that bone trabecula. If residual kinetic energy remains, the particle is further transported into (and potentially across) the adjacent endosteal layer.

For the α -particle emerging from a bone trabecula, a random marrow-cavity chord-length d_{MC} is sampled under μ -randomness

(CDF_μ) for the same skeletal site. The value of d_{MC} is at most composed of 2 endosteal chord-lengths (near and far side of the marrow cavity) and an intervening chord-length across the marrow space:

$$d_{MC} = d_{E1} + d_{MS} + d_{E2}. \quad \text{Eq. 3}$$

Values of d_{E1} and d_{E2} (and thus d_{MS}) are determined through uniform sampling of the cosine of the entry angle (η) across each 10- μm endosteal layer:

$$\begin{aligned} \eta_1 &\in [0:1] \quad \text{with} \quad d_{E1} = (10 \mu\text{m})/\eta_1 \quad \text{and} \\ \eta_2 &\in [0:1] \quad \text{with} \quad d_{E2} = (10 \mu\text{m})/\eta_2 \quad \text{and} \\ (d_{E1} + d_{E2}) &\leq d_E^{max}. \end{aligned} \quad \text{Eq. 4}$$

The assignment of d_E^{max} in this and in other chord-based skeletal models is discussed in Appendix A. If $(d_{E1} + d_{E2}) < d_E^{max}$, then:

$$d_{MS} = d_{MC} - (d_{E1} + d_{E2}) \quad \text{with} \quad d_{MS} \geq 0. \quad \text{Eq. 5}$$

If, however, $(d_{E1} + d_{E2}) \geq d_E^{max}$, then both near and far endosteal chord-lengths are iteratively rescaled:

$$\begin{aligned} d_{E1} &= \left(\frac{d_{E1}}{d_{E1} + d_{E2}} \right) d_E^{max} \quad \text{and} \\ d_{E2} &= d_E^{max} - d_{E1} \quad \text{and} \\ d_{MS} &= d_{MC} - (d_{E1} + d_{E2}). \end{aligned} \quad \text{Eq. 6}$$

The α -particle range-energy function in endosteal tissues is then used to determine the kinetic energy lost within the first endosteal layer. If residual kinetic energy still exists, and $d_{MS} > 0$, the α -particle is further transported within the tissues of the marrow space.

At this point, the chord-length d_{MS} is placed at a random location and direction within the transport region of the marrow spatial model (Fig. 2). Consider for the moment that d_{MS} is given as chord A-B. This marrow space chord thus represents the potential trajectory of the α -particle emerging from the surface of the bone endosteum in which the first tissue encountered is active marrow. In this particular case, however, the particle has only sufficient kinetic energy to carry it from starting point A to point B* in the marrow tissues. During its traversal, the α -particle traverses a single adipocyte. Consequently, the particle trajectory A-B* can be divided into 3 marrow subtrajectories: d_{M1} (distance from point A to the adipocyte entry point), d_{M2} (distance across the adipocyte), and d_{M3} (distance from the adipocyte exit point to the particle termination point B*). Energy deposition to active marrow for this particle would be recorded only across active-marrow subtrajectories d_{M1} and d_{M3} .

As another example, another sampled chord-length d_{MS} might be positioned at chord C-D in Figure 2. In this case, the α -particle "sees" an adipocyte immediately on its emergence from the bone endosteum and must expend some kinetic energy within that fat cell before it enters (and then stops) within the active marrow tissues. As the fat fraction of the geometric model increases (marrow cellularity decreases), this scenario becomes more and more prevalent, thus simulating the presence and increased loss of α -particle energy in the first-fat layer for particles emerging from the trabecular endosteum. Furthermore, the α -particle in this example is able to fully travel the sampled chord-length d_{MS} . In this case, residual kinetic energy still remains at point D and the

particle is then transported across the endosteal chord-length d_{E2} on the far side of the marrow space (via methods described previously).

For a TAM source, transport calculations are performed as described above except that the starting value of d_{MC} is selected from an I-random $CDF_I(d_{MC})$. The corresponding marrow-space chord, d_{MS} , is then placed within the marrow spatial model at a point external to the adipocytes and partitioned into subtrajectories as described earlier. For TBE sources, a transport chord-length is selected uniformly across the interval $[0, d_{EI}]$ followed by transport in either bone (d_T) or marrow tissues (d_{MS}), depending on the emission angle. Similarly, for TBS sources of α -particles, they may be directed either within the adjacent bone trabeculae (d_T) or across the full chord-length of the endosteal layer (d_{EI}). If residual energy is still present at various tissue interfaces, the transport techniques described above are continued.

RESULTS

Tabulated values of absorbed fraction are presented in supplemental Appendix B (Tables 1B–12B) (available online only at <http://jnm.snmjournals.org>). A representative tabulation of these data is given in Table 3 for α -particle emissions within the various source tissues of the lumbar vertebrae of the Leeds 44-y male subject. For each source–target combination, energy deposition is tracked within the primary tissue (e.g., TAM←TAM), secondary tissue (e.g., TAM←TBE or TBS), or tertiary tissue (e.g., TAM←TBV) depending on the emission energy (and the resulting CSDA range) of the α -particle. Coefficients of variation (COVs) are $\leq 1\%$ for primary targets and $\leq 5\%$ for secondary targets. Errors in absorbed fractions to tertiary targets vary according to the source–target geometry and marrow cellularity selected. Values of COV for $\phi(\text{TAM} \leftarrow \text{TBV})$ and $\phi(\text{TBV} \leftarrow \text{TAM})$ (both separated by the bone endosteum) are below 20% for α -particle energies of > 2.5 MeV. Endosteal and surface sources for α -particle emission yield absorbed fractions with COVs below 3% for both secondary and tertiary target tissues. For each source region, computation times for the 100% cellularity model are noted to be only ~ 5 min on a 1-GHz Dell Dimension Pentium V workstation and are ~ 1 h on the same system at low cellularities approaching 10%.

DISCUSSION

Absorbed Fractions to Active Bone Marrow

Figures 3A–3D display values of absorbed fraction to active bone marrow as a function of α -particle energy within 3 of the 7 skeletal sites of the Leeds 44-y male. Although the energy range of clinical interest extends down to only ~ 5.5 MeV, values at very low energies are displayed as well for visual confirmation of the model (e.g., values of ϕ should approach unity when the source and target tissue are the same). In each case, the marrow cellularity is set to 100% and, thus, differences in energy dependence of the absorbed fraction are strictly related to differences in the trabecular microstructure of these bone sites.

Their dependence on marrow cellularity is discussed separately.

The absorbed fraction for self-irradiation of the active bone marrow, $\phi(\text{TAM} \leftarrow \text{TAM})$, is shown in Figure 3A for the ribs, cervical vertebra, and parietal bone. At low energies, the absorbed fraction in each bone site is ~ 1.0 and, thus, is closely approximated by the energy-independent value assumed under both the ICRP Publication 30 and 2003 Eckerman bone models. As the particle energy increases, however, an increasing amount of kinetic energy is lost to the bone trabeculae and endosteum, leaving less energy available for deposition to bone marrow. The parietal bone demonstrates the greatest divergence from the ICRP Publication 30 and 2003 Eckerman models at all energies (~ 0.90 at 6 MeV and ~ 0.80 at 10 MeV), as this particular bone site is characterized by relatively small marrow cavities and thick bone trabeculae (28).

Energy-dependent absorbed fractions to active bone marrow (100% cellular) are shown in Figure 3B for α -particles emitted uniformly within the 10- μm tissue layer of the bone endosteum (a source region not considered in the other 2 bone models). For this source tissue, the absorbed fraction to bone marrow is shown to be 0.043 at the lowest energy considered (500 keV) and increases to values of 0.48, 0.46, and 0.45 at 10 MeV in the ribs, cervical vertebra, and parietal bone, respectively. When the α -emitter is localized within the surfaces of the bone trabeculae (Fig. 3C), values of absorbed fraction to the marrow tissues are reduced at all energies as compared with a TBE source. In this case, the α -particle must exceed ~ 2 MeV for it to have sufficient energy to penetrate the endosteal layer.

In contrast, the ICRP Publication 30 and 2003 Eckerman bone models assign a value of 0.5 to $\phi(\text{TAM} \leftarrow \text{TBS})$ independent of the α -particle emission energy (based on a planar half-space transport geometry). Furthermore, these models do not explicitly treat the endosteum and bone marrow as independent target tissues. At an emission energy of 6 MeV, for example, the ICRP Publication 30 and 2003 Eckerman bone models predict an α -particle dose to bone marrow 1.9, 1.9, and 2.1 times higher in the ribs, cervical vertebra, and parietal bone, respectively, than that given in the present study. However, when energy deposition to the endosteal layer is separately accounted for in the 2003 Eckerman model (dashed curve in Fig. 3C), excellent agreement is noted between the 2 model predictions.

Finally, energy-dependent values of $\phi(\text{TAM} \leftarrow \text{TBV})$ are shown in Figure 3D for α -particles emitted uniformly within the volume of the bone trabeculae. The ICRP Publication 30 model applies an energy-independent value, 0.05, to this source–target combination. Our 3D-CBIST model predicts values of $\phi(\text{TAM} \leftarrow \text{TBV})$ less than 0.05 at α -energies below ~ 8 MeV in the ribs and cervical vertebra, with higher absorbed fractions to bone marrow seen at energies exceeding 8 MeV. The ICRP Publication 30 model is shown to be overly conservative with regard to values of $\phi(\text{TAM} \leftarrow \text{TBS})$ in the parietal bone at all energies consid-

TABLE 3
Absorbed Fractions to Active Bone Marrow (TAM) for α -Emissions Within Lumbar Vertebrae
of Leeds 44-Year Male for Various Source Tissues and Marrow Cellularities

Energy (MeV)	$\phi(\text{TAM} \leftarrow \text{TAM})$ Cellularity									
	100%	90%	80%	70%	60%	50%	40%	30%	20%	10%
3.0	9.90E-01	9.72E-01	9.46E-01	9.19E-01	8.83E-01	8.47E-01	8.11E-01	7.65E-01	7.18E-01	6.45E-01
3.5	9.88E-01	9.64E-01	9.33E-01	8.99E-01	8.54E-01	8.12E-01	7.69E-01	7.13E-01	6.60E-01	5.77E-01
4.0	9.86E-01	9.57E-01	9.18E-01	8.78E-01	8.25E-01	7.75E-01	7.25E-01	6.62E-01	6.03E-01	5.15E-01
4.5	9.83E-01	9.49E-01	9.02E-01	8.55E-01	7.94E-01	7.38E-01	6.82E-01	6.13E-01	5.49E-01	4.57E-01
5.0	9.80E-01	9.40E-01	8.87E-01	8.34E-01	7.66E-01	7.03E-01	6.42E-01	5.67E-01	5.00E-01	4.05E-01
5.5	9.77E-01	9.32E-01	8.72E-01	8.13E-01	7.38E-01	6.69E-01	6.04E-01	5.25E-01	4.55E-01	3.59E-01
6.0	9.74E-01	9.23E-01	8.57E-01	7.93E-01	7.14E-01	6.40E-01	5.70E-01	4.87E-01	4.15E-01	3.20E-01
6.5	9.70E-01	9.14E-01	8.43E-01	7.75E-01	6.91E-01	6.15E-01	5.41E-01	4.55E-01	3.82E-01	2.87E-01
7.0	9.67E-01	9.07E-01	8.31E-01	7.59E-01	6.74E-01	5.93E-01	5.16E-01	4.27E-01	3.53E-01	2.60E-01
7.5	9.62E-01	8.99E-01	8.19E-01	7.45E-01	6.61E-01	5.76E-01	4.96E-01	4.05E-01	3.30E-01	2.37E-01
8.0	9.59E-01	8.93E-01	8.09E-01	7.34E-01	6.49E-01	5.63E-01	4.81E-01	3.87E-01	3.10E-01	2.18E-01
8.5	9.55E-01	8.85E-01	8.01E-01	7.25E-01	6.41E-01	5.52E-01	4.69E-01	3.74E-01	2.96E-01	2.03E-01
9.0	9.50E-01	8.79E-01	7.94E-01	7.18E-01	6.35E-01	5.44E-01	4.60E-01	3.63E-01	2.84E-01	1.92E-01
9.5	9.46E-01	8.74E-01	7.88E-01	7.13E-01	6.30E-01	5.38E-01	4.52E-01	3.54E-01	2.75E-01	1.82E-01
10.0	9.41E-01	8.68E-01	7.82E-01	7.08E-01	6.26E-01	5.33E-01	4.45E-01	3.47E-01	2.67E-01	1.74E-01

Energy (MeV)	$\phi(\text{TAM} \leftarrow \text{TBE})$ Cellularity									
	100%	90%	80%	70%	60%	50%	40%	30%	20%	10%
3.0	2.62E-01	2.38E-01	2.10E-01	1.87E-01	1.64E-01	1.35E-01	1.09E-01	7.79E-02	5.42E-02	2.70E-02
3.5	3.01E-01	2.72E-01	2.42E-01	2.15E-01	1.88E-01	1.54E-01	1.24E-01	8.94E-02	6.14E-02	3.09E-02
4.0	3.30E-01	2.98E-01	2.66E-01	2.37E-01	2.06E-01	1.70E-01	1.36E-01	9.80E-02	6.80E-02	3.38E-02
4.5	3.52E-01	3.20E-01	2.84E-01	2.52E-01	2.21E-01	1.81E-01	1.46E-01	1.05E-01	7.24E-02	3.62E-02
5.0	3.72E-01	3.36E-01	2.99E-01	2.66E-01	2.32E-01	1.92E-01	1.53E-01	1.11E-01	7.60E-02	3.84E-02
5.5	3.87E-01	3.52E-01	3.12E-01	2.77E-01	2.42E-01	2.00E-01	1.61E-01	1.15E-01	7.99E-02	3.99E-02
6.0	4.00E-01	3.62E-01	3.21E-01	2.86E-01	2.50E-01	2.07E-01	1.65E-01	1.19E-01	8.22E-02	4.13E-02
6.5	4.12E-01	3.73E-01	3.32E-01	2.95E-01	2.57E-01	2.12E-01	1.70E-01	1.22E-01	8.45E-02	4.23E-02
7.0	4.21E-01	3.81E-01	3.39E-01	3.01E-01	2.63E-01	2.17E-01	1.74E-01	1.25E-01	8.63E-02	4.31E-02
7.5	4.29E-01	3.89E-01	3.45E-01	3.08E-01	2.69E-01	2.22E-01	1.78E-01	1.28E-01	8.84E-02	4.42E-02
8.0	4.39E-01	3.98E-01	3.53E-01	3.14E-01	2.74E-01	2.26E-01	1.81E-01	1.30E-01	9.01E-02	4.50E-02
8.5	4.45E-01	4.05E-01	3.59E-01	3.19E-01	2.78E-01	2.29E-01	1.84E-01	1.33E-01	9.16E-02	4.60E-02
9.0	4.53E-01	4.10E-01	3.64E-01	3.24E-01	2.83E-01	2.33E-01	1.87E-01	1.35E-01	9.29E-02	4.64E-02
9.5	4.60E-01	4.17E-01	3.69E-01	3.30E-01	2.86E-01	2.37E-01	1.90E-01	1.36E-01	9.42E-02	4.72E-02
10.0	4.66E-01	4.23E-01	3.75E-01	3.35E-01	2.92E-01	2.41E-01	1.93E-01	1.39E-01	9.56E-02	4.79E-02

Energy (MeV)	$\phi(\text{TAM} \leftarrow \text{TBS})$ Cellularity									
	100%	90%	80%	70%	60%	50%	40%	30%	20%	10%
3.0	5.91E-02	5.34E-02	4.76E-02	4.25E-02	3.70E-02	3.07E-02	2.44E-02	1.77E-02	1.21E-02	6.16E-03
3.5	1.05E-01	9.46E-02	8.41E-02	7.50E-02	6.52E-02	5.40E-02	4.31E-02	3.10E-02	2.15E-02	1.07E-02
4.0	1.46E-01	1.33E-01	1.18E-01	1.05E-01	9.18E-02	7.55E-02	6.11E-02	4.37E-02	3.04E-02	1.52E-02
4.5	1.84E-01	1.67E-01	1.48E-01	1.32E-01	1.15E-01	9.48E-02	7.60E-02	5.48E-02	3.83E-02	1.89E-02
5.0	2.16E-01	1.96E-01	1.74E-01	1.55E-01	1.35E-01	1.12E-01	8.96E-02	6.45E-02	4.45E-02	2.21E-02
5.5	2.42E-01	2.19E-01	1.95E-01	1.74E-01	1.52E-01	1.26E-01	1.01E-01	7.24E-02	5.02E-02	2.49E-02
6.0	2.63E-01	2.39E-01	2.12E-01	1.89E-01	1.65E-01	1.37E-01	1.10E-01	7.90E-02	5.42E-02	2.73E-02
6.5	2.82E-01	2.56E-01	2.28E-01	2.03E-01	1.77E-01	1.47E-01	1.18E-01	8.42E-02	5.84E-02	2.93E-02
7.0	2.99E-01	2.71E-01	2.42E-01	2.15E-01	1.88E-01	1.56E-01	1.25E-01	8.95E-02	6.24E-02	3.11E-02
7.5	3.16E-01	2.86E-01	2.55E-01	2.27E-01	1.98E-01	1.64E-01	1.31E-01	9.50E-02	6.55E-02	3.28E-02
8.0	3.30E-01	2.99E-01	2.66E-01	2.37E-01	2.07E-01	1.71E-01	1.38E-01	9.88E-02	6.80E-02	3.41E-02
8.5	3.42E-01	3.10E-01	2.76E-01	2.47E-01	2.15E-01	1.78E-01	1.42E-01	1.03E-01	7.09E-02	3.53E-02
9.0	3.54E-01	3.21E-01	2.86E-01	2.55E-01	2.22E-01	1.84E-01	1.47E-01	1.06E-01	7.31E-02	3.66E-02
9.5	3.66E-01	3.32E-01	2.95E-01	2.63E-01	2.30E-01	1.90E-01	1.53E-01	1.09E-01	7.56E-02	3.75E-02
10.0	3.76E-01	3.42E-01	3.03E-01	2.70E-01	2.36E-01	1.95E-01	1.57E-01	1.13E-01	7.79E-02	3.89E-02

TABLE 3 (Continued)

Energy (MeV)	$\phi(\text{TAM} \leftarrow \text{TBV})$ Cellularity									
	100%	90%	80%	70%	60%	50%	40%	30%	20%	10%
3.0	9.75E-04	8.49E-04	7.90E-04	6.99E-04	6.09E-04	5.09E-04	3.91E-04	3.10E-04	1.97E-04	1.03E-04
3.5	2.52E-03	2.32E-03	2.09E-03	1.85E-03	1.61E-03	1.31E-03	1.08E-03	7.68E-04	5.25E-04	2.53E-04
4.0	5.24E-03	4.73E-03	4.14E-03	3.72E-03	3.19E-03	2.64E-03	2.14E-03	1.57E-03	1.07E-03	5.51E-04
4.5	8.96E-03	8.11E-03	7.11E-03	6.34E-03	5.51E-03	4.58E-03	3.59E-03	2.62E-03	1.81E-03	9.05E-04
5.0	1.36E-02	1.22E-02	1.08E-02	9.58E-03	8.36E-03	7.06E-03	5.59E-03	4.00E-03	2.81E-03	1.43E-03
5.5	1.90E-02	1.72E-02	1.54E-02	1.35E-02	1.19E-02	9.82E-03	7.93E-03	5.71E-03	3.90E-03	1.94E-03
6.0	2.53E-02	2.30E-02	2.03E-02	1.81E-02	1.59E-02	1.31E-02	1.05E-02	7.55E-03	5.22E-03	2.63E-03
6.5	3.23E-02	2.95E-02	2.62E-02	2.35E-02	2.03E-02	1.69E-02	1.36E-02	9.64E-03	6.75E-03	3.36E-03
7.0	3.97E-02	3.64E-02	3.24E-02	2.88E-02	2.52E-02	2.06E-02	1.67E-02	1.20E-02	8.37E-03	4.18E-03
7.5	4.86E-02	4.40E-02	3.93E-02	3.48E-02	3.05E-02	2.53E-02	2.02E-02	1.46E-02	1.00E-02	5.04E-03
8.0	5.76E-02	5.24E-02	4.66E-02	4.16E-02	3.62E-02	2.99E-02	2.41E-02	1.72E-02	1.18E-02	6.05E-03
8.5	6.71E-02	6.10E-02	5.42E-02	4.83E-02	4.21E-02	3.46E-02	2.81E-02	2.02E-02	1.40E-02	7.06E-03
9.0	7.74E-02	7.07E-02	6.29E-02	5.61E-02	4.87E-02	4.03E-02	3.23E-02	2.33E-02	1.59E-02	8.01E-03
9.5	8.87E-02	8.02E-02	7.13E-02	6.39E-02	5.55E-02	4.62E-02	3.69E-02	2.66E-02	1.82E-02	9.24E-03
10.0	9.98E-02	9.10E-02	8.05E-02	7.17E-02	6.27E-02	5.19E-02	4.14E-02	2.99E-02	2.06E-02	1.04E-02

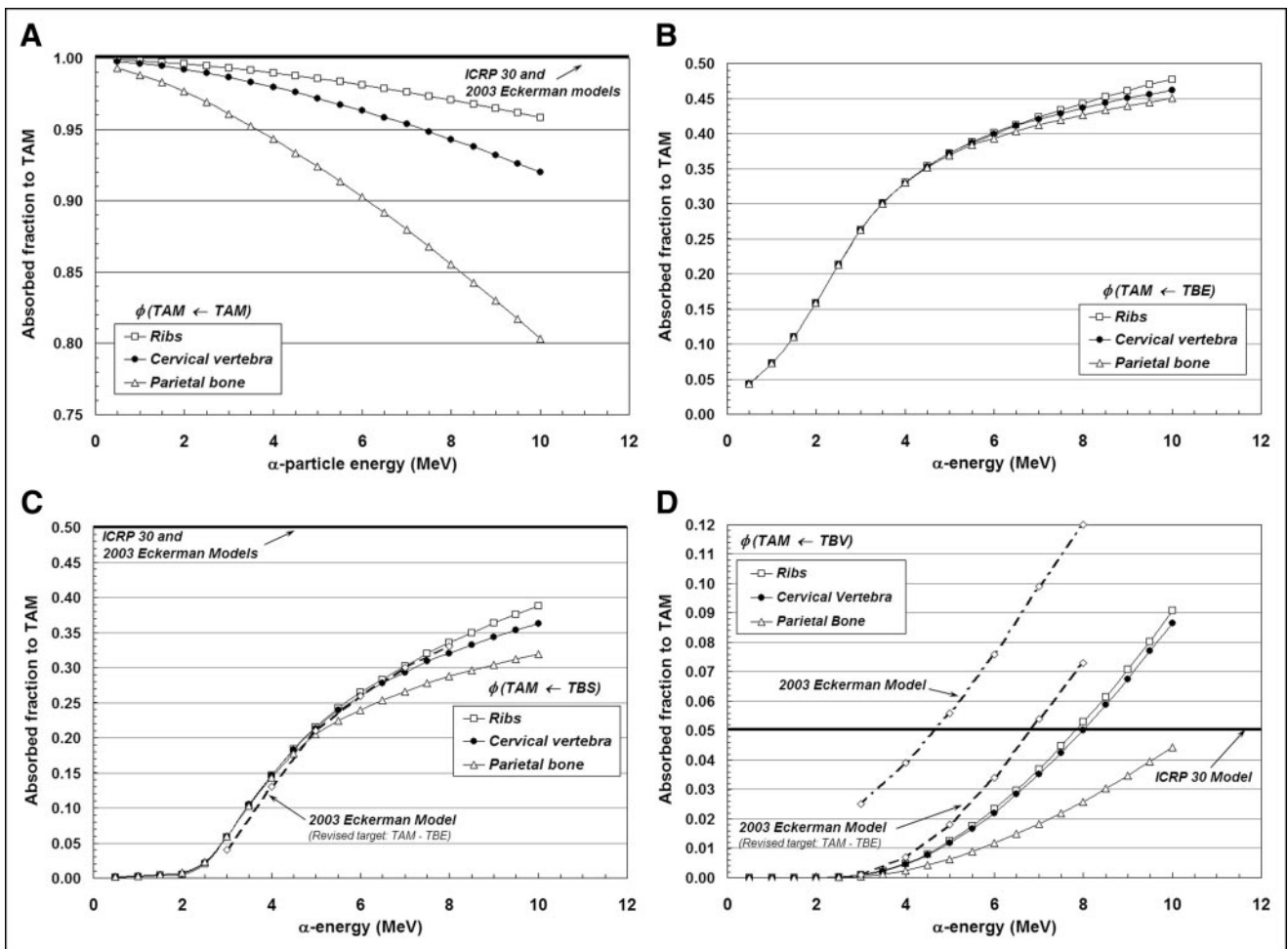


FIGURE 3. Absorbed fractions for an active marrow target (100% cellularity) from active marrow source (TAM) (A), trabecular bone endosteum source (TBE) (B), trabecular bone surface source (TBS) (C), and trabecular bone volume source (TBV) (D).

ered. Improved agreement is seen between energy-dependent values of the present study (for the ribs and cervical vertebra) and those from the 2003 Eckerman model provided that their target definition is again revised to exclude the endosteal layer—that is, the difference between $\phi(\text{TAM} \leftarrow \text{TBS})_{2003\text{Eckerman}}$ and $\phi(\text{TBE} \leftarrow \text{TBS})_{2003\text{Eckerman}}$.

Absorbed Fractions to Bone Endosteum

Figures 4A–4D display values of absorbed fraction to the trabecular endosteum as a function of α -particle energy at 3 of the 7 skeletal sites in the Leeds 44-y male subject. In each case, the marrow cellularity is set to 100% and, thus, differences in energy dependence are strictly related to differences in trabecular microstructure.

The fraction of α -particle energy deposited within the endosteal layers of trabecular bone is shown in Figure 4A for emissions within the marrow space. Transport results given by the 3D-CBIST skeletal model show values of absorbed fraction to endosteal tissues that begin at ~ 0.001 – 0.007 (500 keV) and increase to values of 0.074, 0.032, and 0.018 (10 MeV) for the parietal bone, cervical vertebra, and ribs, respectively. This particular source–target combination is not discussed in ICRP Publication 30, while an energy-

and bone-independent value of 0.09 is assigned for $\phi(\text{TBE} \leftarrow \text{TAM})$ in the 2003 Eckerman model. At 6 MeV, the 2003 Eckerman value is 1.56, 3.88, and 7.50 times higher than those given by the present model in the parietal bone, cervical vertebra, and ribs, respectively. If one additionally permits α -emissions in the endosteal layer itself (as is done in the 2003 Eckerman model), revised estimates of $\phi(\text{TBE} \leftarrow \text{TAM} + \text{TBE})$ from the 3D-CBIST model are given as shown by dot-dashed lines in Figure 4A. Here, we see that the additional contributions from endosteal self-dose increase estimates of $\phi(\text{TBE} \leftarrow \text{TAM})$ at very low α -energies for the ribs and parietal bone (where TBE accounts for 0.7% and 0.8% of the revised source mass), but negligibly impact their values at clinically relevant energies (5.5–8 MeV). In contrast, the endosteal layer in the cervical vertebrae accounts for up to 8.5% of the combined source mass and, thus, the endosteal self-dose is more prominent, even at the higher α -energies, although still smaller than predicted under the 2003 Eckerman model.

Values of $\phi(\text{TBE} \leftarrow \text{TBE})$ and $\phi(\text{TBE} \leftarrow \text{TBS})$ are given in Figures 4B and 4C, respectively. For these source–target combinations, the 3D-CBIST model predicts that the ab-

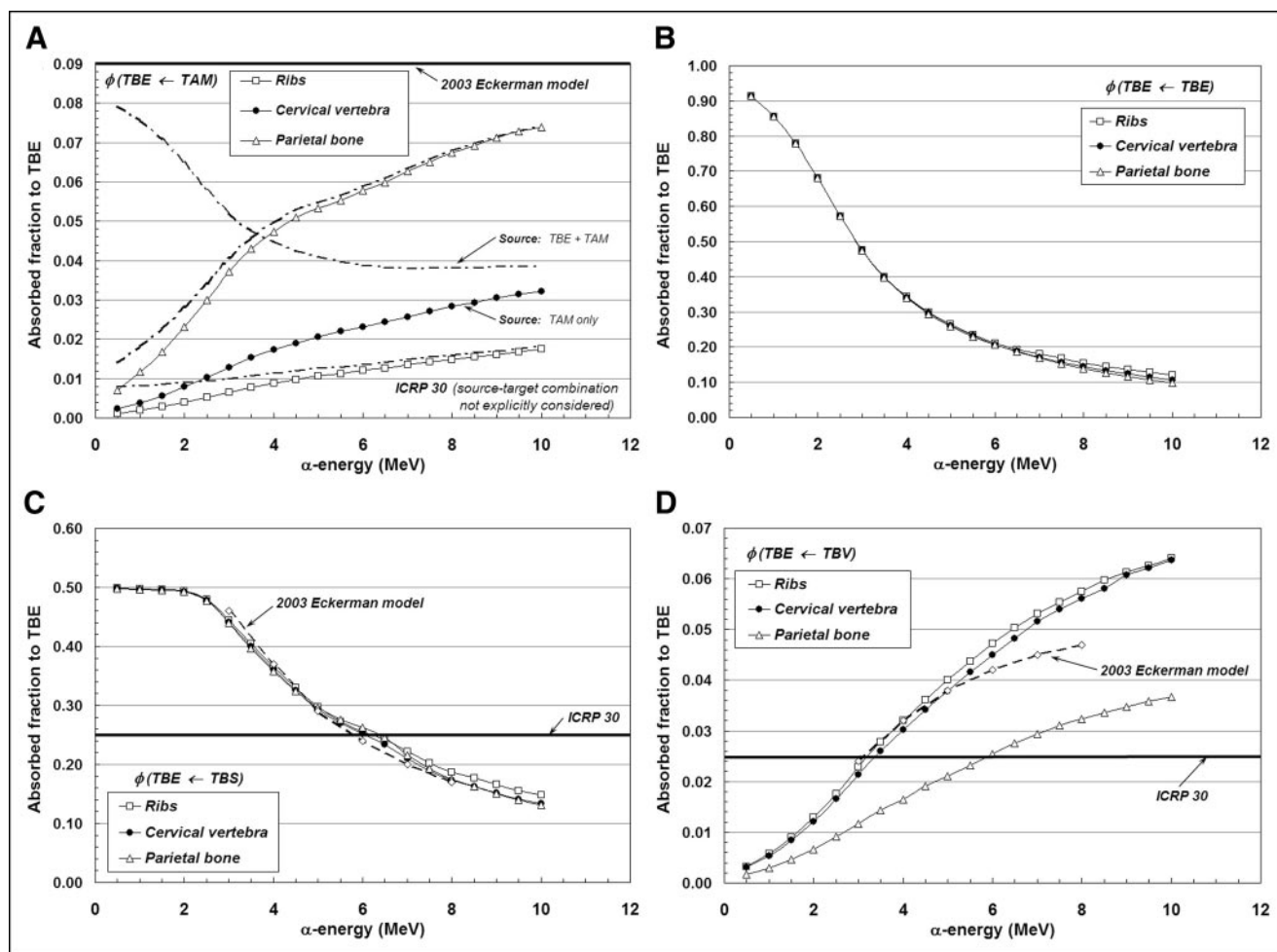


FIGURE 4. Absorbed fractions for endosteum target from α -sources emitted within the TAM (A), TBE (B), TBS (C), and TBV (D).

sorbed fraction is negligibly influenced by differences in trabecular microarchitecture across different skeletal sites. In Figure 4B, the absorbed fraction for the self-irradiation of the trabecular endosteum is shown to approach unity for very low-energy α -emissions and to approach values of ~ 0.10 – 0.12 at 10 MeV. When the source of α -emissions is localized to the surfaces of the bone trabeculae (Fig. 4C), the half-space assumption is shown to be valid for α -particles less than ~ 2 MeV, above which the absorbed fraction to trabecular endosteum declines to values of ~ 0.13 to 0.15 at 10 MeV. These values are compared with the energy-independent assignment of $\phi(\text{TBE} \leftarrow \text{TBS}) = 0.25$ under the ICRP Publication 30 bone model. Consequently, for low-energy α -emitters, the dose to trabecular endosteum is underestimated within the ICRP Publication 30 model according to our calculations. Comparisons with the 2003 Eckerman model, on the other hand, demonstrate excellent agreement over the energy range 3–8 MeV.

Finally, Figure 4D displays absorbed fractions to TBE for α -sources localized uniformly within the bone trabeculae. For α -energies exceeding ~ 3.0 MeV, the ICRP Publication

30 assumption of $\phi(\text{TBE} \leftarrow \text{TBV}) = 0.025$ is shown to underestimate the energy deposited within the trabecular endosteum of the ribs and cervical vertebra. This same model is shown to overestimate energy deposition to TBE within the parietal bone at α -particle energies up to ~ 6 MeV. Values of $\phi(\text{TBE} \leftarrow \text{TBV})$ given by the 2003 Eckerman model show good agreement with those of the present study in 2 of the 3 skeletal sites shown (ribs and cervical vertebra).

Influence of Marrow Cellularity on α -Particle Absorbed Fractions

In Figures 5A–5D, the same 4 source–target combinations shown in Figures 3A–3D are again considered. In this case, however, we focus on a single bone site (lumbar vertebra) and allow the marrow cellularity to range from 100% to 20%. For the self-irradiation of the active marrow (Fig. 5A), the ICRP Publication 30 and 2003 Eckerman bone models are shown to closely approximate values of $\phi(\text{TAM} \leftarrow \text{TAM})$ given by the 3D-CBIST model only for marrow that is 100% cellular. As adipocyte concentrations

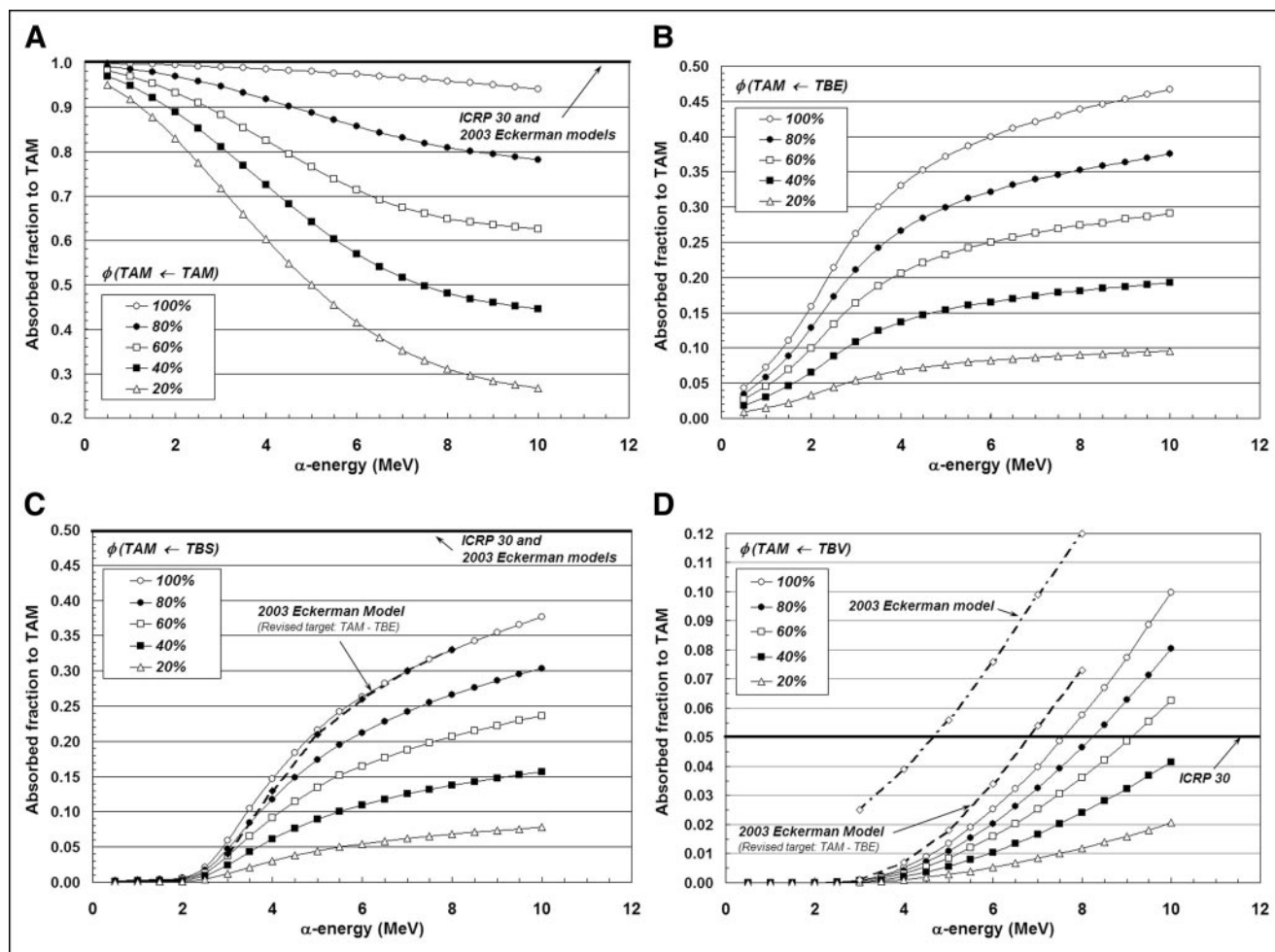


FIGURE 5. Dependence of active marrow absorbed fraction with changes in marrow cellularity within lumbar vertebrae: TAM source (A), TBE source (B), TBS source (C), and TBV source (D).

increase (marrow cellularities decrease), less α -particle energy is deposited within active marrow, and a greater divergence of $\phi(\text{TAM} \leftarrow \text{TAM})$ from the unity assumption is noted at all energies. Furthermore, at a given α -energy below 10 MeV, values of $\phi(\text{TAM} \leftarrow \text{TAM})$ at different marrow cellularities are shown not to scale as simple ratios of their corresponding cellularities; consequently, full 3D transport is thus required to accurately report values of α -particle absorbed fraction.

Shielding effects of increased adipocyte concentration are noticeably demonstrated in Figures 5B and 5C for α -sources localized within the bone endosteum or on the bone sur-

faces, respectively. As marrow cellularity decreases, α -particles emerging from the endosteal layer increasingly encounter adipocytes along the endosteal surface; values of both $\phi(\text{TAM} \leftarrow \text{TBE})$ and $\phi(\text{TAM} \leftarrow \text{TBS})$ thus decline in value at all energies. Consequently, energy deposition to active marrow is increasingly overestimated in the ICRP Publication 30 and 2003 Eckerman bone models as the marrow becomes less and less cellular. At 6 MeV, for example, the ICRP Publication 30 model overestimates the energy deposited to active marrow for TBS emissions by factors of 1.9, 3.0, and 9.2 at marrow cellularities of 100%, 60%, and 20%, respectively.

TABLE 4
Ratios of α -Particle Absorbed Fractions in Skeletal Tissues of Lumbar Vertebra

Energy (MeV)	44-y male $\phi(\text{TAM} \leftarrow \text{TAM})$	Absorbed fraction ratio					44-y male $\phi(\text{TBE} \leftarrow \text{TAM})$	Absorbed fraction ratio					
		25 M	55 F	70 F	85 F	Average		25 M	55 F	70 F	85 F	Average	
		44 M	44 M	44 M	44 M			44 M	44 M	44 M	44 M		44 M
3.0	9.90E-01	0.998	0.997	0.999	0.997	0.998	9.11E-03	1.177	0.997	1.125	1.261	1.140	
4.0	9.86E-01	0.997	0.996	0.998	0.996	0.997	1.23E-02	1.190	0.987	1.109	1.255	1.135	
5.0	9.80E-01	0.996	0.995	0.998	0.995	0.996	1.47E-02	1.183	0.983	1.094	1.245	1.126	
6.0	9.74E-01	0.995	0.993	0.997	0.993	0.995	1.68E-02	1.189	0.996	1.082	1.246	1.128	
7.0	9.67E-01	0.993	0.990	0.997	0.991	0.993	1.89E-02	1.191	1.013	1.074	1.251	1.132	
8.0	9.59E-01	0.992	0.989	0.996	0.989	0.991	2.07E-02	1.187	1.015	1.071	1.239	1.128	
9.0	9.50E-01	0.990	0.987	0.996	0.987	0.990	2.26E-02	1.178	1.041	1.060	1.234	1.128	
10.0	9.41E-01	0.988	0.984	0.996	0.985	0.988	2.41E-02	1.186	1.062	1.060	1.225	1.133	
Average:						0.994	Average:						1.131

Energy (MeV)	44-y male $\phi(\text{TAM} \leftarrow \text{TBS})$	Absorbed fraction ratio					44-y male $\phi(\text{TBE} \leftarrow \text{TBS})$	Absorbed fraction ratio					
		25 M	55 F	70 F	85 F	Average		25 M	55 F	70 F	85 F	Average	
		44 M	44 M	44 M	44 M			44 M	44 M	44 M	44 M		44 M
3.0	5.91E-02	1.013	1.010	1.001	1.012	1.009	4.42E-01	0.999	0.997	1.001	0.999	0.999	
4.0	1.46E-01	1.010	1.007	1.001	1.006	1.006	3.60E-01	0.986	0.987	0.998	0.992	0.991	
5.0	2.16E-01	0.998	0.996	0.993	0.997	0.996	2.93E-01	0.981	0.983	1.001	0.991	0.989	
6.0	2.63E-01	0.999	0.990	0.987	0.993	0.992	2.49E-01	0.982	0.996	1.012	1.001	0.998	
7.0	2.99E-01	0.996	0.990	0.984	0.990	0.990	2.10E-01	0.983	1.013	1.016	1.003	1.004	
8.0	3.30E-01	0.995	0.993	0.985	0.991	0.991	1.76E-01	0.986	1.015	1.016	1.010	1.007	
9.0	3.54E-01	0.993	0.997	0.985	0.993	0.992	1.57E-01	0.978	1.041	1.011	1.018	1.012	
10.0	3.76E-01	0.990	1.007	0.984	0.997	0.995	1.39E-01	0.977	1.062	1.021	1.041	1.025	
Average:						0.996	Average:						1.003

Energy (MeV)	44-y male $\phi(\text{TAM} \leftarrow \text{TBV})$	Absorbed fraction ratio					44-y male $\phi(\text{TBE} \leftarrow \text{TBV})$	Absorbed fraction ratio					
		25 M	55 F	70 F	85 F	Average		25 M	55 F	70 F	85 F	Average	
		44 M	44 M	44 M	44 M			44 M	44 M	44 M	44 M		44 M
3.0	9.75E-04	1.011	1.181	1.110	1.316	1.154	2.43E-02	0.983	1.155	1.073	1.234	1.111	
4.0	5.24E-03	0.986	1.139	1.068	1.231	1.106	3.42E-02	0.993	1.170	1.084	1.247	1.123	
5.0	1.36E-02	0.986	1.143	1.059	1.224	1.103	4.34E-02	0.984	1.149	1.066	1.227	1.106	
6.0	2.53E-02	0.995	1.162	1.077	1.242	1.119	5.10E-02	0.987	1.162	1.084	1.237	1.117	
7.0	3.97E-02	1.005	1.168	1.075	1.254	1.126	5.78E-02	0.989	1.157	1.079	1.237	1.116	
8.0	5.76E-02	0.996	1.156	1.064	1.238	1.113	6.31E-02	0.993	1.156	1.073	1.238	1.115	
9.0	7.74E-02	1.001	1.156	1.063	1.238	1.114	6.75E-02	0.992	1.152	1.074	1.232	1.112	
10.0	9.98E-02	0.999	1.149	1.057	1.225	1.108	7.10E-02	0.992	1.152	1.076	1.229	1.112	
Average:						1.118	Average:						1.114

Comparisons are made between values using the skeletal microstructure of the Leeds 44-y male (44 M) reference subject and 4 other individuals of the Leeds studies: 25-y male (25 M), 55-y female (55 F), 70-y female (70 F), and 85-y female (85 F).

The influence of marrow cellularity on values of $\phi(\text{TAM} \leftarrow \text{TBV})$ is demonstrated in Figure 5D for the lumbar vertebra. At marrow cellularities of 100%, 80%, and 60%, the ICRP Publication 30 bone model value of $\phi(\text{TAM} \leftarrow \text{TBV}) = 0.05$ is not reached until α -emission energies approach ~ 7.5 , 8.3, and 9.3 MeV, respectively. At lower marrow cellularities (e.g., 40% and 20%), the ICRP Publication 30 bone model conservatively estimates the energy deposited to active marrow at all energies considered (≤ 10 MeV). The 2003 Eckerman model is shown to closely match results from the 3D-CBIST model at 100% cellularity, if one accounts for energy lost to the TBE in their definition of the active marrow target.

Intersubject Variability in α -Particle Absorbed Fractions

Chord-length distributions for the 44-y male subject in the Leeds studies form the basis for both the present model and that of the 2003 Eckerman model of the OLINDA code. It is of clinical interest to explore the degree to which α -particle absorbed fractions can potentially vary with corresponding changes in trabecular microstructure seen in different patients. Four additional chord-length distributions are available from the Leeds studies of the lumbar vertebra, which can be used for just such a comparison: those from a 25-y male, a 55-y female, a 70-y female, and an 85-y female (19). Table 4 displays 3D-CBIST values of absorbed fractions of both active marrow and endosteum for the 44-y male subject at 100% cellularity. Ratios of these same values are then shown between each subject and the Leeds 44-y male. For TAM targets (left side of Table 4), variations of $<1\%$ are noted for α -emissions in the TAM and on the TBS, whereas

$\sim 12\%$ intersubject variations are seen for TBV sources. These variations are reasonable considering the short ranges of α -particles in the skeletal tissues and the fixed nature of the endosteal layer chord-length algorithm in the 3D-CBIST model. Intersubject variations in bone trabeculae thickness thus translate to increased intersubject variations in values of $\phi(\text{TAM} \leftarrow \text{TBV})$ over $\phi(\text{TAM} \leftarrow \text{TAM})$ or $\phi(\text{TAM} \leftarrow \text{TBS})$. For the TBE as the target tissue, $<1\%$ variations in values of $\phi(\text{TBE} \leftarrow \text{TBS})$ are noted, whereas $\sim 11\%$ – 13% intersubject variations in $\phi(\text{TBE} \leftarrow \text{TAM})$ or $\phi(\text{TBE} \leftarrow \text{TBV})$ are seen.

Skeletal-Averaged Absorbed Fractions for ICRP Reference Male (RM)

An application of the 3D-CBIST model is presented in Tables 5–7. In Table 5, site-specific reference marrow cellularities for the ICRP Reference Male (RM) at ages 25 and 40 y are shown as given in ICRP Publication 70 (10). In addition, the fractional tissue masses within the ICRP RM for active marrow, bone endosteum, and bone trabeculae (f_{TAM} , f_{TBS} , f_{TBV} , respectively) are given as published previously by Eckerman and Stabin (17). In this example, the fractional distribution of active marrow is given at both reference ages (25 and 40 y), as the latter more closely approximates the age of the Leeds individual from which reference absorbed fractions are given in the 2003 Eckerman bone model. As the Leeds data permit α -particle transport in only 7 skeletal sites, weighted combinations must be used to represent all skeletal regions of the body. Using the data of Table 5, and the site- and cellularity-dependent α -particle absorbed fractions of Appendix B (either directly or via interpolation), skeletal-averaged α -particle absorbed fractions, ϕ_{Skel} , for the ICRP RM can be calculated as given

TABLE 5
Marrow Cellularities and Fractional Tissue Distributions in Skeleton of ICRP Reference Male

Skeletal region	Bone groups*	ICRP 70 cellularity (age, 25 y)	ICRP 70 cellularity (age, 40 y)	f_{TAM} (age, 25 y)	f_{TAM} (age, 40 y)	f_{TBS}	f_{TBV}	Average cellularity (age, 25 y)	Average cellularity (age, 40 y)
Legs, upper	80% FH, 20% FN	0.30	0.25	0.033	0.030	0.167	0.163	0.010	0.008
Legs, middle	50% FH, 50% FN	0.00	0.00	0.000	0.000	0.169	0.165	0.000	0.000
Legs, lower	50% FH, 50% FN	0.00	0.00	0.000	0.000	0.040	0.040	0.000	0.000
Arms, upper	80% FH, 20% FN	0.30	0.25	0.023	0.021	0.031	0.030	0.007	0.005
Arms, middle	50% FH, 50% FN	0.00	0.00	0.000	0.000	0.026	0.025	0.000	0.000
Arms, lower	50% FH, 50% FN	0.00	0.00	0.000	0.000	0.026	0.026	0.000	0.000
Pelvis	60% IC, 40% LV	0.58	0.48	0.333	0.303	0.018	0.018	0.193	0.146
Spine, upper	100% CV	0.72	0.70	0.027	0.029	0.110	0.107	0.019	0.020
Spine, middle	50% CV, 50% LV	0.72	0.70	0.174	0.186	0.282	0.276	0.125	0.130
Spine, lower	100% LV	0.72	0.70	0.098	0.105	0.071	0.069	0.071	0.073
Skull, cranium	100% PB	0.42	0.38	0.056	0.056	0.012	0.026	0.024	0.021
Skull, facial	100% PB	0.42	0.38	0.028	0.028	0.006	0.013	0.012	0.011
Ribs	100% RB	0.72	0.70	0.192	0.206	0.031	0.030	0.138	0.144
Clavicles	60% IC, 40% LV	0.37	0.33	0.008	0.008	0.002	0.002	0.003	0.003
Scapulae	60% IC, 40% LV	0.42	0.38	0.028	0.028	0.009	0.009	0.012	0.011
Totals:				1.000	1.000	1.000	0.999	61.3%	57.1%
				Total active marrow mass:				1,170 g	1,090 g

*FH = femur head; FN = femur neck; IC = iliac crest; LV = lumbar vertebrae; CV = cervical vertebrae; PB = parietal bone; RB = ribs.

TABLE 6
Skeletal-Averaged α -Particle Absorbed Fractions in ICRP Reference Male with Explicit Consideration
of Reference Marrow Cellularities (Age, 25 Years)

Energy (MeV)	Target: Trabecular active marrow				
	$\phi(\text{TAM} \leftarrow \text{TAM})$	$\phi(\text{TAM} \leftarrow \text{TBE})$	$\phi(\text{TAM} \leftarrow \text{TBE} + \text{TAM})$	$\phi(\text{TAM} \leftarrow \text{TBS})$	$\phi(\text{TAM} \leftarrow \text{TBV})$
3.0	8.84E-01	1.37E-01	8.55E-01	3.10E-02	4.72E-04
3.5	8.57E-01	1.57E-01	8.29E-01	5.46E-02	1.24E-03
4.0	8.28E-01	1.72E-01	8.03E-01	7.67E-02	2.52E-03
4.5	7.99E-01	1.84E-01	7.76E-01	9.61E-02	4.31E-03
5.0	7.72E-01	1.94E-01	7.50E-01	1.13E-01	6.52E-03
5.5	7.45E-01	2.02E-01	7.25E-01	1.26E-01	9.21E-03
6.0	7.21E-01	2.09E-01	7.02E-01	1.38E-01	1.23E-02
6.5	7.00E-01	2.15E-01	6.82E-01	1.47E-01	1.57E-02
7.0	6.81E-01	2.19E-01	6.64E-01	1.57E-01	1.94E-02
7.5	6.66E-01	2.24E-01	6.50E-01	1.65E-01	2.35E-02
8.0	6.54E-01	2.28E-01	6.39E-01	1.72E-01	2.79E-02
8.5	6.45E-01	2.32E-01	6.30E-01	1.78E-01	3.26E-02
9.0	6.37E-01	2.36E-01	6.22E-01	1.84E-01	3.77E-02
9.5	6.30E-01	2.39E-01	6.17E-01	1.90E-01	4.30E-02
10.0	6.25E-01	2.42E-01	6.12E-01	1.95E-01	4.86E-02

Energy (MeV)	Target: Trabecular bone endosteum				
	$\phi(\text{TBE} \leftarrow \text{TAM})$	$\phi(\text{TBE} \leftarrow \text{TBE})$	$\phi(\text{TBE} \leftarrow \text{TBE} + \text{TAM})$	$\phi(\text{TBE} \leftarrow \text{TBS})$	$\phi(\text{TBE} \leftarrow \text{TBV})$
3.0	1.12E-02	4.75E-01	3.02E-02	4.42E-01	2.26E-02
3.5	1.29E-02	3.99E-01	2.88E-02	3.99E-01	2.75E-02
4.0	1.43E-02	3.41E-01	2.78E-02	3.59E-01	3.20E-02
4.5	1.53E-02	2.97E-01	2.69E-02	3.23E-01	3.63E-02
5.0	1.59E-02	2.61E-01	2.60E-02	2.92E-01	4.02E-02
5.5	1.63E-02	2.31E-01	2.52E-02	2.66E-01	4.40E-02
6.0	1.67E-02	2.07E-01	2.46E-02	2.47E-01	4.76E-02
6.5	1.70E-02	1.88E-01	2.41E-02	2.30E-01	5.08E-02
7.0	1.72E-02	1.72E-01	2.36E-02	2.08E-01	5.40E-02
7.5	1.73E-02	1.58E-01	2.32E-02	1.89E-01	5.65E-02
8.0	1.74E-02	1.45E-01	2.27E-02	1.74E-01	5.89E-02
8.5	1.74E-02	1.34E-01	2.23E-02	1.64E-01	6.11E-02
9.0	1.73E-02	1.26E-01	2.19E-02	1.53E-01	6.33E-02
9.5	1.72E-02	1.17E-01	2.14E-02	1.43E-01	6.50E-02
10.0	1.70E-02	1.09E-01	2.08E-02	1.35E-01	6.67E-02

Data taken from ICRP Publication 70 (10).

in Table 6 (age, 25 y) and Table 7 (age, 40 y) using the following expression:

$$\phi_{Skel}(r_T \leftarrow r_S) = \sum_j f_{S,j} \phi(r_T \leftarrow r_S; CF)_j, \quad \text{Eq. 7}$$

where r_S and r_T denote the source and target tissues, respectively, and $f_{S,j}$ and CF are the fractional mass of source tissue and reference cellularity at bone site j , respectively. When estimating skeletal-average radionuclide S values, however, values of ϕ_{Skel} cannot be used directly within the MIRD schema, as both the absolute target tissue mass ($m_{T,j}$) and its fractional distribution in the skeleton ($f_{T,j}$) must also be considered:

$$S_{Skel}(r_T \leftarrow r_S) = \sum_j f_{S,j} f_{T,j} \left[\sum_i \frac{\Delta_i \phi(r_T \leftarrow r_S)_{i,j}}{m_{T,j}} \right] = \sum_j f_{S,j} f_{T,j} S(r_T \leftarrow r_S)_j. \quad \text{Eq. 8}$$

CONCLUSION

A radiation transport model (3D-CBIST) has been developed that combines (a) chord-based techniques for tracking α -particles across bone trabeculae and marrow cavities and (b) a spatial model of the marrow tissues that explicitly considers the presence of marrow adipose tissue across a broad range of marrow cellularities. ICRP Publication 30 absorbed fractions are found to significantly overestimate α -particle energy deposition to active marrow as compared with values given by the 3D-CBIST model for all source regions. A single exception is high-energy α -particles emitted from within the bone trabeculae, irradiating marrow at high cellularity. These deviations become more prominent as marrow cellularity progressively decreases below 100%. In contrast, the ICRP Publication 30 bone model significantly underestimates energy deposition to skeletal endosteum as predicted under the 3D-CBIST model. Excep-

TABLE 7
Skeletal-Averaged α -Particle Absorbed Fractions in ICRP Reference Male with Explicit Consideration
of Reference Marrow Cellularities (Age, 40 Years)

Energy (MeV)	Target: Trabecular active marrow				
	$\phi(\text{TAM} \leftarrow \text{TAM})$	$\phi(\text{TAM} \leftarrow \text{TBE})$	$\phi(\text{TAM} \leftarrow \text{TBE} + \text{TAM})$	$\phi(\text{TAM} \leftarrow \text{TBS})$	$\phi(\text{TAM} \leftarrow \text{TBV})$
3.0	8.70E-01	1.28E-01	8.40E-01	2.90E-02	4.40E-04
3.5	8.39E-01	1.47E-01	8.12E-01	5.12E-02	1.17E-03
4.0	8.08E-01	1.61E-01	7.83E-01	7.18E-02	2.36E-03
4.5	7.77E-01	1.73E-01	7.53E-01	9.00E-02	4.03E-03
5.0	7.47E-01	1.82E-01	7.25E-01	1.06E-01	6.09E-03
5.5	7.18E-01	1.90E-01	6.98E-01	1.18E-01	8.60E-03
6.0	6.92E-01	1.95E-01	6.73E-01	1.29E-01	1.15E-02
6.5	6.69E-01	2.01E-01	6.52E-01	1.38E-01	1.47E-02
7.0	6.49E-01	2.06E-01	6.33E-01	1.46E-01	1.81E-02
7.5	6.33E-01	2.10E-01	6.18E-01	1.54E-01	2.20E-02
8.0	6.20E-01	2.14E-01	6.05E-01	1.61E-01	2.61E-02
8.5	6.10E-01	2.18E-01	5.96E-01	1.67E-01	3.05E-02
9.0	6.01E-01	2.21E-01	5.88E-01	1.72E-01	3.53E-02
9.5	5.95E-01	2.24E-01	5.82E-01	1.78E-01	4.02E-02
10.0	5.89E-01	2.27E-01	5.76E-01	1.83E-01	4.55E-02

Energy (MeV)	Target: Trabecular bone endosteum				
	$\phi(\text{TBE} \leftarrow \text{TAM})$	$\phi(\text{TBE} \leftarrow \text{TBE})$	$\phi(\text{TBE} \leftarrow \text{TBE} + \text{TAM})$	$\phi(\text{TBE} \leftarrow \text{TBS})$	$\phi(\text{TBE} \leftarrow \text{TBV})$
3.0	1.10E-02	4.75E-01	3.01E-02	4.42E-01	2.26E-02
3.5	1.27E-02	3.99E-01	2.86E-02	3.99E-01	2.75E-02
4.0	1.39E-02	3.41E-01	2.74E-02	3.59E-01	3.20E-02
4.5	1.48E-02	2.97E-01	2.65E-02	3.23E-01	3.63E-02
5.0	1.54E-02	2.61E-01	2.55E-02	2.92E-01	4.02E-02
5.5	1.57E-02	2.31E-01	2.47E-02	2.66E-01	4.40E-02
6.0	1.60E-02	2.07E-01	2.39E-02	2.47E-01	4.76E-02
6.5	1.62E-02	1.88E-01	2.33E-02	2.30E-01	5.08E-02
7.0	1.64E-02	1.72E-01	2.28E-02	2.08E-01	5.40E-02
7.5	1.63E-02	1.58E-01	2.22E-02	1.89E-01	5.65E-02
8.0	1.64E-02	1.45E-01	2.17E-02	1.74E-01	5.89E-02
8.5	1.63E-02	1.34E-01	2.12E-02	1.64E-01	6.11E-02
9.0	1.62E-02	1.26E-01	2.08E-02	1.53E-01	6.33E-02
9.5	1.61E-02	1.17E-01	2.03E-02	1.43E-01	6.50E-02
10.0	1.57E-02	1.09E-01	1.97E-02	1.35E-01	6.67E-02

tions are noted for $\phi(\text{TBE} \leftarrow \text{TBS})$ at high energies (>6 MeV) and for $\phi(\text{TBE} \leftarrow \text{TBV})$ at low energies (~ 3 MeV for ribs and cervical vertebra).

In cases of high marrow cellularity ($\sim 100\%$), good agreement in values of $\phi(\text{TAM} \leftarrow \text{TBS})$ and $\phi(\text{TAM} \leftarrow \text{TBV})$ are noted between the 3D-CBIST and 2003 Eckerman models, but only for an equivalent definition of the active marrow (e.g., exclusive of the endosteal layer). In contrast, the energy-independent assumption of unity for $\phi(\text{TAM} \leftarrow \text{TAM})$ in the 2003 Eckerman model is seen to be overly conservative in regard to its dependence on both skeletal site (Fig. 3A) and marrow cellularity (Fig. 5A). Excellent model agreement is also seen for values of $\phi(\text{TBE} \leftarrow \text{TBS})$ and $\phi(\text{TBE} \leftarrow \text{TBV})$. Energy-dependent values of $\phi(\text{TBE} \leftarrow \text{TAM})$ given by the 3D-CBIST code, however, are found to be very much lower than $\phi(\text{TBE} \leftarrow \text{TAM}) = 0.09$ assumed under the 2003 Eckerman model.

It has been shown that invasive or noninvasive measurements of marrow cellularity can be clinically impor-

tant to improvements in patient-specific dose estimates to active bone marrow (16,24,29). Explicit consideration of marrow cellularity and its role in modifying values of absorbed fraction under the MIRD schema has been made for β -particle emitters either by use of reference cellularity values by skeletal site (17,30) or by permitting marrow cellularity to be a running variable in the dosimetry model (24). Results presented here provide a firmer basis for patient-specific dosimetry in α -emitter radionuclide therapies through the explicit consideration of absorbed fraction variations with particle energy, skeletal site, and marrow cellularity. Although results given here use the University of Leeds chord-length distributions for a single 44-y male subject (ICRP RM), the 3D-CBIST code can be easily extended to other individuals (i.e., cadavers) for which chord-length distributions are available from 3D microimaging of sectioned samples of trabecular spongiosa (31,32).

APPENDIX A

A Revised Algorithm for Maximum Endosteal Chord-Length

Trajectories of electrons and α -particles across the near and far endosteal layers of a marrow cavity (d_{E1} and d_{E2} , respectively) must be considered in tandem with random sampling of the marrow-cavity chord-length d_{MC} as given in Equations 3–6. As shown in Equation 4, individual values of d_{E1} or d_{E2} can initially take on large and physically unrealistic values (values of $\eta \rightarrow 0$), and, thus, the total endosteal chord-length ($d_{E1} + d_{E2}$) must be limited to some maximum value d_E^{max} . In the skeletal models of Bouchet et al. (18) and of Eckerman and Stabin (17), d_E^{max} is set equal to the sampled marrow-cavity chord d_{MC} . Recent studies by Derek W. Jokisch (unpublished data, December 2004) and Shah (33), however, indicate that this approach tends to overestimate particle trajectories across the endosteal layer (e.g., electron endosteal doses are higher in the chord-based models by a factor of ~ 2 in comparison with those from image-based skeletal models). In the present study, a revised algorithm for d_E^{max} is thus adopted.

For each marrow-cavity chord d_{MC} sampled in the 3D-CBIST code, a hypothetical spheric marrow cavity is briefly established with radius R_{MC} such that a distribution of μ -random chords across it would yield a mean chord-length equal to this sampled chord d_{MC} :

$$\langle d_{MC} \rangle = \frac{4}{3} R_{MC}, \text{ and, thus, } R_{MC} = \frac{3}{4} \langle d_{MC} \rangle. \quad \text{Eq. 1A}$$

Interior to the surface of this sphere is placed a 10- μm -thick shell of endosteal tissue, thus defining an interior cocentric sphere of marrow space with radius $R_{MC} - 10 \mu\text{m}$. The value of d_E^{max} is then defined as the maximum chord-length within the endosteal layer tangent to the interior marrow-space sphere. Its value is given by the Pythagorean theorem and can be expressed as a function of the sampled marrow-cavity chord, d_{MC} :

$$d_E^{max} = 2 \sqrt{R_{MC}^2 - (R_{MC} - 10)^2} = 2 \sqrt{20R_{MC} - 100} = 2 \sqrt{15d_{MC} - 100}. \quad \text{Eq. 2A}$$

Note that this spheric marrow cavity is referenced only in Eq. 2A for the calculation of d_E^{max} and is not related to the spatial model of the marrow tissues shown in Figure 2. For values of $d_{MC} \geq 52.4 \mu\text{m}$, $d_E^{max} \leq d_{MC}$ and, thus, the revised algorithm is more restrictive than existing algorithms in skeletal dosimetry. The additional restriction in Equation 5 (that $d_{MS} \geq 0$) is applicable for those cases in which the sampled marrow-cavity chord $d_{MC} < 52.4 \mu\text{m}$ (first bin in the Leeds chord-length distributions), where d_E^{max} is slightly greater than d_{MC} . The algorithm given in Eq. A.2 is to be considered a phenomenological correction to the existing algorithm ($d_E^{max} = d_{MC}$), and future studies are suggested for improving our ability to accurately model the endosteal tissue layer while accounting for the full 3D microstructure of trabecular spongiosa.

ACKNOWLEDGMENTS

This work was supported in part by grant CA96441 from the National Cancer Institute and Grant DE-FG07-02ID14327 from the U.S. Department of Energy with the University of Florida.

REFERENCES

1. Zalutsky MR, Bigner DD. Radioimmunotherapy with alpha-particle emitting radioimmunoconjugates. *Acta Oncol.* 1996;35:373–379.
2. McDevitt MR, Barendswaard E, Ma D, et al. An alpha-particle emitting antibody (^{213}Bi J591) for radioimmunotherapy of prostate cancer. *Cancer Res.* 2000;60:6095–6100.
3. Sgouros G, Ballangrud AM, Jurcic JG, et al. Pharmacokinetics and dosimetry of an alpha-particle emitter labeled antibody: ^{213}Bi -HuM195 (anti-CD33) in patients with leukemia. *J Nucl Med.* 1999;40:1935–1946.
4. Henriksen G, Breistol K, Bruland OS, Fodstad O, Larsen RH. Significant antitumor effect from bone-seeking, alpha-particle-emitting ^{223}Ra demonstrated in an experimental skeletal metastases model. *Cancer Res.* 2002;62:3120–3125.
5. McDevitt MR, Sgouros G, Finn RD, et al. Radioimmunotherapy with alpha-emitting nuclides. *Eur J Nucl Med.* 1998;25:1341–1351.
6. Loevinger R, Budinger TF, Watson EE. *MIRD Primer for Absorbed Dose Calculations*. Revised. New York, NY: Society of Nuclear Medicine; 1991.
7. ICRP. *Limits for Intakes of Radionuclides by Workers*. ICRP Publication 30 (Part 1). Oxford, UK: International Commission on Radiological Protection; 1979.
8. Stabin MG, Siegel JA. Physical models and dose factors for use in internal dose assessment. *Health Phys.* 2003;85:294–310.
9. Stabin M, Sparks R. OLINDA: PC-based software for biokinetic analysis and internal dose calculations in nuclear medicine [abstract]. *J Nucl Med.* 2003; 44(suppl):103P.
10. ICRP. *Basic Anatomical and Physiological Data for Use in Radiological Protection: The Skeleton*. ICRP Publication 70. Oxford, UK: International Commission on Radiological Protection; 1995.
11. ICRP. *Basic Anatomical and Physiological Data for Use in Radiological Protection: Reference Values*. Publication 89. New York, NY: International Commission on Radiological Protection; 2002.
12. Thorne MC. Aspects of the dosimetry of plutonium in bone. *Nature.* 1976;259:539–541.
13. Thorne MC. Aspects of the dosimetry of alpha-emitting radionuclides in bone with particular emphasis on ^{226}Ra and ^{239}Pu . *Phys Med Biol.* 1977;22:36–46.
14. Mays C, Sears K. *Determination of Localized Alpha Dose. III. From Surface and Volume Deposits of Pu-230, Th-228, and Ra-226*. Report COO-226. Salt Lake City, UT: University of Utah; 1962.
15. Whitwell JR, Spiers FW. Calculated beta-ray dose factors for trabecular bone. *Phys Med Biol.* 1976;21:16–38.
16. Ballon D, Jakubowski AA, Graham MC, Schneider E, Koutcher JA. Spatial mapping of the percentage cellularity in human bone marrow using magnetic resonance imaging. *Med Phys.* 1996;23:243–250.
17. Eckerman KF, Stabin MG. Electron absorbed fractions and dose conversion factors for marrow and bone by skeletal regions. *Health Phys.* 2000;78:199–214.
18. Bouchet LG, Jokisch DW, Bolch WE. A three-dimensional transport model for determining absorbed fractions of energy for electrons in trabecular bone. *J Nucl Med.* 1999;40:1947–1966.
19. Whitwell JR. *Theoretical Investigations of Energy Loss by Ionizing Particles in Bone* [thesis]. Leeds, U.K.: Department of Medical Physics, University of Leeds; 1973.
20. Patton PW, Rajon DA, Shah AP, Jokisch DW, Inglis B, Bolch WE. Site-specific variability in trabecular bone dosimetry: considerations of energy loss to cortical bone. *Med Phys.* 2002;29:6–14.
21. ICRU. *Photon, Electron, Proton and Neutron Interaction Data for Body Tissues*. Report 46. Bethesda, MD: International Commission on Radiation Units and Measurements; 1992.
22. Knoll G. *Radiation Detection and Measurement*. 3rd ed. New York, NY: John Wiley & Sons, Inc.; 2000.
23. ICRU. *Stopping Powers and Ranges for Protons and Alpha Particles*. Report 49. Bethesda, MD: International Commission on Radiation Units and Measurements; 1993.
24. Bolch WE, Patton PW, Rajon DA, Shah AP, Jokisch DW, Inglis B. Considerations of marrow cellularity in 3D dosimetric models of the trabecular skeleton. *J Nucl Med.* 2002;43:97–108.
25. Reverter J, Feliu E, Climent C, Rozman M, Berga L, Rozman C. Stereological study of human bone marrow adipocytes: a comparison of four methods for estimating size distributions. *Path Res Pract.* 1993;189:1215–1220.

26. Shah AP, Patton PW, Rajon DA, Bolch WE. Adipocyte spatial distributions in bone marrow: implications for skeletal dosimetry models. *J Nucl Med.* 2003;44: 774–783.
27. Eckerman KF, Ryman JC, Taner AC, Kerr GD. Traversal of cells by radiation and absorbed fraction estimates for electrons and alpha particles. In: Schlafke-Stelson AT, Watson EE, eds. *Proceedings of the Fourth International Radiopharmaceutical Dosimetry Symposium.* Oak Ridge, Tennessee; Oak Ridge Associated Universities; 1985:67–81.
28. Beddoe AH, Darley PJ, Spiers FW. Measurements of trabecular bone structure in man. *Phys Med Biol.* 1976;21:589–607.
29. Ballon D, Jakubowski AA, Tulipano PK, et al. Quantitative assessment of bone marrow hematopoiesis using parametric magnetic resonance imaging. *Magn Reson Med.* 1998;39:789–800.
30. Stabin MG, Eckerman KF, Bolch WE, Bouchet LG, Patton PW. Evolution and status of bone and marrow dose models. *Cancer Biother Radiopharm.* 2002;17: 427–445.
31. Jokisch DW, Patton PW, Rajon DA, Inglis BA, Bolch WE. Chord distributions across 3D digital images of a human thoracic vertebra. *Med Phys.* 2001;28:1493–1504.
32. Shah A, Rajon D, Jokisch D, Patton P, Bolch W. A comparison of skeletal chord-length distributions between the ICRP Reference Male and the UF adult male radionuclide therapy patient. *Health Phys.* In press.
33. Shah A. *Reference Skeletal Dosimetry Model for an Adult Male Radionuclide Therapy Patient Based on 3D Imaging and Paired-Image Radiation Transport* [dissertation]. Gainesville, FL: Department of Biomedical Engineering, University of Florida; 2004.



APPENDIX B
Data Tables of α -Particle Absorbed Fraction to Skeletal Tissues

TABLE 1B
Absorbed Fractions to TBE and TBV for α -Emissions Within TBE of Leeds 44-Year Male

$\phi(\text{TBE} \leftarrow \text{TBE})$							
For all cellularities							
Energy (MeV)	Cervical Vertebrae	Femur Head	Femur Neck	Iliac Crest	Lumbar Vertebrae	Parietal Bone	Ribs
3.0	4.76E-01	4.75E-01	4.75E-01	4.75E-01	4.75E-01	4.75E-01	4.75E-01
3.5	4.00E-01	3.98E-01	3.99E-01	4.00E-01	3.99E-01	3.98E-01	4.00E-01
4.0	3.41E-01	3.40E-01	3.41E-01	3.42E-01	3.42E-01	3.39E-01	3.43E-01
4.5	2.97E-01	2.95E-01	2.97E-01	2.98E-01	2.97E-01	2.94E-01	2.99E-01
5.0	2.62E-01	2.59E-01	2.62E-01	2.63E-01	2.62E-01	2.58E-01	2.64E-01
5.5	2.32E-01	2.29E-01	2.32E-01	2.33E-01	2.32E-01	2.30E-01	2.35E-01
6.0	2.08E-01	2.04E-01	2.08E-01	2.09E-01	2.08E-01	2.07E-01	2.11E-01
6.5	1.88E-01	1.85E-01	1.90E-01	1.90E-01	1.89E-01	1.87E-01	1.93E-01
7.0	1.71E-01	1.68E-01	1.75E-01	1.73E-01	1.73E-01	1.68E-01	1.81E-01
7.5	1.57E-01	1.54E-01	1.62E-01	1.59E-01	1.60E-01	1.53E-01	1.68E-01
8.0	1.44E-01	1.42E-01	1.49E-01	1.47E-01	1.47E-01	1.39E-01	1.55E-01
8.5	1.33E-01	1.31E-01	1.39E-01	1.36E-01	1.37E-01	1.27E-01	1.45E-01
9.0	1.24E-01	1.22E-01	1.30E-01	1.27E-01	1.29E-01	1.16E-01	1.37E-01
9.5	1.15E-01	1.14E-01	1.22E-01	1.18E-01	1.21E-01	1.07E-01	1.28E-01
10.0	1.07E-01	1.06E-01	1.14E-01	1.10E-01	1.13E-01	9.78E-02	1.20E-01
$\phi(\text{TBV} \leftarrow \text{TBE})$							
For all cellularities							
Energy (MeV)	Cervical Vertebrae	Femur Head	Femur Neck	Iliac Crest	Lumbar Vertebrae	Parietal Bone	Ribs
3.0	2.62E-01	2.62E-01	2.62E-01	2.62E-01	2.62E-01	2.63E-01	2.62E-01
3.5	2.99E-01	3.01E-01	2.99E-01	3.00E-01	3.00E-01	3.01E-01	2.99E-01
4.0	3.28E-01	3.29E-01	3.28E-01	3.27E-01	3.27E-01	3.30E-01	3.26E-01
4.5	3.50E-01	3.52E-01	3.50E-01	3.48E-01	3.50E-01	3.54E-01	3.47E-01
5.0	3.66E-01	3.70E-01	3.66E-01	3.65E-01	3.66E-01	3.72E-01	3.63E-01
5.5	3.80E-01	3.84E-01	3.80E-01	3.78E-01	3.80E-01	3.86E-01	3.77E-01
6.0	3.92E-01	3.95E-01	3.92E-01	3.90E-01	3.92E-01	3.99E-01	3.87E-01
6.5	4.00E-01	4.05E-01	3.99E-01	3.98E-01	3.99E-01	4.10E-01	3.94E-01
7.0	4.08E-01	4.12E-01	4.02E-01	4.04E-01	4.05E-01	4.19E-01	3.96E-01
7.5	4.14E-01	4.18E-01	4.07E-01	4.10E-01	4.10E-01	4.28E-01	3.98E-01
8.0	4.20E-01	4.23E-01	4.10E-01	4.13E-01	4.14E-01	4.34E-01	4.01E-01
8.5	4.23E-01	4.28E-01	4.13E-01	4.17E-01	4.17E-01	4.40E-01	4.02E-01
9.0	4.25E-01	4.30E-01	4.14E-01	4.19E-01	4.18E-01	4.44E-01	4.02E-01
9.5	4.28E-01	4.33E-01	4.16E-01	4.21E-01	4.19E-01	4.48E-01	4.02E-01
10.0	4.31E-01	4.35E-01	4.17E-01	4.24E-01	4.20E-01	4.51E-01	4.02E-01

TABLE 2B

Absorbed Fractions to TBE and TBV for α -Emissions on TBS of Leeds 44-Year Male

Energy (MeV)	$\phi(\text{TBE} \leftarrow \text{TBS})$						
	For all cellularities						
	Cervical Vertebrae	Femur Head	Femur Neck	Iliac Crest	Lumbar Vertebrae	Parietal Bone	Ribs
3.0	4.42E-01	4.41E-01	4.43E-01	4.42E-01	4.42E-01	4.40E-01	4.44E-01
3.5	4.00E-01	3.97E-01	4.01E-01	4.00E-01	4.01E-01	3.96E-01	4.05E-01
4.0	3.61E-01	3.55E-01	3.61E-01	3.61E-01	3.60E-01	3.57E-01	3.65E-01
4.5	3.25E-01	3.18E-01	3.24E-01	3.24E-01	3.24E-01	3.24E-01	3.30E-01
5.0	2.94E-01	2.87E-01	2.93E-01	2.93E-01	2.93E-01	2.96E-01	2.98E-01
5.5	2.70E-01	2.60E-01	2.66E-01	2.68E-01	2.68E-01	2.76E-01	2.72E-01
6.0	2.52E-01	2.40E-01	2.48E-01	2.47E-01	2.49E-01	2.63E-01	2.56E-01
6.5	2.34E-01	2.22E-01	2.32E-01	2.29E-01	2.32E-01	2.45E-01	2.42E-01
7.0	2.10E-01	2.01E-01	2.12E-01	2.08E-01	2.10E-01	2.15E-01	2.22E-01
7.5	1.89E-01	1.83E-01	1.94E-01	1.90E-01	1.92E-01	1.92E-01	2.03E-01
8.0	1.74E-01	1.68E-01	1.79E-01	1.75E-01	1.76E-01	1.75E-01	1.87E-01
8.5	1.63E-01	1.59E-01	1.68E-01	1.65E-01	1.67E-01	1.63E-01	1.77E-01
9.0	1.52E-01	1.48E-01	1.58E-01	1.54E-01	1.57E-01	1.50E-01	1.66E-01
9.5	1.41E-01	1.38E-01	1.47E-01	1.43E-01	1.46E-01	1.40E-01	1.55E-01
10.0	1.33E-01	1.30E-01	1.39E-01	1.35E-01	1.39E-01	1.31E-01	1.48E-01

Energy (MeV)	$\phi(\text{TBV} \leftarrow \text{TBS})$						
	For all cellularities						
	Cervical Vertebrae	Femur Head	Femur Neck	Iliac Crest	Lumbar Vertebrae	Parietal Bone	Ribs
3.0	4.99E-01	4.99E-01	4.99E-01	4.98E-01	4.99E-01	5.00E-01	4.97E-01
3.5	4.95E-01	4.98E-01	4.95E-01	4.94E-01	4.95E-01	5.01E-01	4.92E-01
4.0	4.93E-01	4.97E-01	4.93E-01	4.91E-01	4.93E-01	4.99E-01	4.88E-01
4.5	4.92E-01	4.96E-01	4.91E-01	4.89E-01	4.92E-01	4.98E-01	4.86E-01
5.0	4.92E-01	4.96E-01	4.90E-01	4.88E-01	4.90E-01	4.99E-01	4.86E-01
5.5	4.90E-01	4.97E-01	4.90E-01	4.87E-01	4.90E-01	4.99E-01	4.85E-01
6.0	4.88E-01	4.94E-01	4.87E-01	4.85E-01	4.87E-01	4.97E-01	4.79E-01
6.5	4.89E-01	4.94E-01	4.83E-01	4.83E-01	4.85E-01	5.01E-01	4.75E-01
7.0	4.97E-01	4.97E-01	4.84E-01	4.87E-01	4.90E-01	5.19E-01	4.76E-01
7.5	5.01E-01	5.00E-01	4.85E-01	4.89E-01	4.92E-01	5.30E-01	4.77E-01
8.0	5.05E-01	5.00E-01	4.86E-01	4.90E-01	4.94E-01	5.37E-01	4.77E-01
8.5	5.04E-01	4.99E-01	4.82E-01	4.88E-01	4.90E-01	5.41E-01	4.73E-01
9.0	5.04E-01	4.98E-01	4.81E-01	4.88E-01	4.89E-01	5.46E-01	4.70E-01
9.5	5.05E-01	4.98E-01	4.79E-01	4.85E-01	4.88E-01	5.48E-01	4.69E-01
10.0	5.04E-01	4.95E-01	4.77E-01	4.84E-01	4.84E-01	5.49E-01	4.64E-01

TABLE 3BAbsorbed Fractions to TBE and TBV for α -Emissions Within TBV of Leeds 44-Year Male

Energy (MeV)	$\phi(\text{TBE} \leftarrow \text{TBV})$						
	For all cellularities						
	Cervical Vertebrae	Femur Head	Femur Neck	Iliac Crest	Lumbar Vertebrae	Parietal Bone	Ribs
3.0	2.14E-02	2.57E-02	1.91E-02	2.47E-02	2.43E-02	1.17E-02	2.29E-02
3.5	2.60E-02	3.13E-02	2.32E-02	2.99E-02	2.96E-02	1.43E-02	2.78E-02
4.0	3.03E-02	3.68E-02	2.69E-02	3.49E-02	3.42E-02	1.65E-02	3.20E-02
4.5	3.41E-02	4.18E-02	3.05E-02	3.92E-02	3.91E-02	1.92E-02	3.61E-02
5.0	3.78E-02	4.62E-02	3.38E-02	4.35E-02	4.34E-02	2.11E-02	4.01E-02
5.5	4.15E-02	5.06E-02	3.71E-02	4.75E-02	4.74E-02	2.32E-02	4.38E-02
6.0	4.50E-02	5.46E-02	4.01E-02	5.12E-02	5.10E-02	2.55E-02	4.72E-02
6.5	4.82E-02	5.81E-02	4.26E-02	5.47E-02	5.45E-02	2.76E-02	5.03E-02
7.0	5.15E-02	6.19E-02	4.48E-02	5.77E-02	5.78E-02	2.93E-02	5.32E-02
7.5	5.39E-02	6.48E-02	4.70E-02	6.11E-02	6.04E-02	3.10E-02	5.54E-02
8.0	5.61E-02	6.79E-02	4.88E-02	6.37E-02	6.31E-02	3.23E-02	5.75E-02
8.5	5.81E-02	7.05E-02	5.06E-02	6.57E-02	6.53E-02	3.35E-02	5.97E-02
9.0	6.08E-02	7.31E-02	5.21E-02	6.80E-02	6.75E-02	3.47E-02	6.13E-02
9.5	6.21E-02	7.52E-02	5.39E-02	6.95E-02	6.88E-02	3.58E-02	6.25E-02
10.0	6.37E-02	7.74E-02	5.50E-02	7.17E-02	7.10E-02	3.67E-02	6.41E-02

Energy (MeV)	$\phi(\text{TBV} \leftarrow \text{TBV})$						
	For all cellularities						
	Cervical Vertebrae	Femur Head	Femur Neck	Iliac Crest	Lumbar Vertebrae	Parietal Bone	Ribs
3.0	9.78E-01	9.73E-01	9.80E-01	9.74E-01	9.75E-01	9.88E-01	9.76E-01
3.5	9.72E-01	9.66E-01	9.75E-01	9.67E-01	9.68E-01	9.84E-01	9.70E-01
4.0	9.65E-01	9.58E-01	9.69E-01	9.60E-01	9.61E-01	9.81E-01	9.63E-01
4.5	9.58E-01	9.49E-01	9.63E-01	9.52E-01	9.52E-01	9.77E-01	9.56E-01
5.0	9.50E-01	9.39E-01	9.56E-01	9.43E-01	9.43E-01	9.73E-01	9.47E-01
5.5	9.42E-01	9.29E-01	9.48E-01	9.33E-01	9.34E-01	9.68E-01	9.39E-01
6.0	9.33E-01	9.18E-01	9.40E-01	9.23E-01	9.24E-01	9.63E-01	9.29E-01
6.5	9.23E-01	9.07E-01	9.32E-01	9.12E-01	9.13E-01	9.58E-01	9.20E-01
7.0	9.13E-01	8.94E-01	9.23E-01	9.01E-01	9.02E-01	9.52E-01	9.10E-01
7.5	9.04E-01	8.82E-01	9.15E-01	8.89E-01	8.91E-01	9.47E-01	9.00E-01
8.0	8.94E-01	8.69E-01	9.06E-01	8.77E-01	8.79E-01	9.42E-01	8.89E-01
8.5	8.83E-01	8.55E-01	8.96E-01	8.65E-01	8.67E-01	9.36E-01	8.79E-01
9.0	8.72E-01	8.42E-01	8.87E-01	8.52E-01	8.55E-01	9.31E-01	8.68E-01
9.5	8.61E-01	8.27E-01	8.76E-01	8.40E-01	8.42E-01	9.25E-01	8.57E-01
10.0	8.50E-01	8.12E-01	8.66E-01	8.26E-01	8.29E-01	9.19E-01	8.45E-01

TABLE 4B

Absorbed Fractions to Active Bone Marrow (TAM) for α -Emissions within
Cervical Vertebrae of Leeds 44-Year Male for Various Source Tissues and Marrow Cellularities

Energy (MeV)	Cervical Vertebrae									
	$\phi(\text{TAM} \leftarrow \text{TAM})$									
	Cellularity									
	100%	90%	80%	70%	60%	50%	40%	30%	20%	10%
3.0	9.87E-01	9.68E-01	9.43E-01	9.16E-01	8.80E-01	8.44E-01	8.08E-01	7.61E-01	7.15E-01	6.42E-01
3.5	9.83E-01	9.60E-01	9.28E-01	8.94E-01	8.50E-01	8.08E-01	7.65E-01	7.09E-01	6.57E-01	5.75E-01
4.0	9.80E-01	9.51E-01	9.12E-01	8.72E-01	8.20E-01	7.70E-01	7.21E-01	6.59E-01	6.00E-01	5.12E-01
4.5	9.76E-01	9.42E-01	8.96E-01	8.50E-01	7.90E-01	7.33E-01	6.78E-01	6.10E-01	5.47E-01	4.55E-01
5.0	9.72E-01	9.33E-01	8.80E-01	8.28E-01	7.59E-01	6.98E-01	6.37E-01	5.63E-01	4.96E-01	4.03E-01
5.5	9.67E-01	9.23E-01	8.64E-01	8.05E-01	7.32E-01	6.65E-01	6.00E-01	5.21E-01	4.52E-01	3.56E-01
6.0	9.63E-01	9.13E-01	8.48E-01	7.84E-01	7.06E-01	6.34E-01	5.65E-01	4.83E-01	4.12E-01	3.18E-01
6.5	9.58E-01	9.04E-01	8.33E-01	7.66E-01	6.84E-01	6.08E-01	5.35E-01	4.50E-01	3.78E-01	2.85E-01
7.0	9.54E-01	8.95E-01	8.20E-01	7.49E-01	6.66E-01	5.86E-01	5.11E-01	4.23E-01	3.49E-01	2.57E-01
7.5	9.48E-01	8.86E-01	8.08E-01	7.35E-01	6.52E-01	5.69E-01	4.91E-01	4.00E-01	3.26E-01	2.34E-01
8.0	9.43E-01	8.78E-01	7.96E-01	7.23E-01	6.40E-01	5.54E-01	4.74E-01	3.83E-01	3.08E-01	2.16E-01
8.5	9.38E-01	8.70E-01	7.88E-01	7.14E-01	6.31E-01	5.44E-01	4.62E-01	3.69E-01	2.92E-01	2.01E-01
9.0	9.32E-01	8.63E-01	7.79E-01	7.05E-01	6.24E-01	5.36E-01	4.53E-01	3.57E-01	2.80E-01	1.90E-01
9.5	9.26E-01	8.55E-01	7.72E-01	6.99E-01	6.18E-01	5.29E-01	4.45E-01	3.49E-01	2.71E-01	1.80E-01
10.0	9.20E-01	8.49E-01	7.66E-01	6.94E-01	6.13E-01	5.22E-01	4.37E-01	3.40E-01	2.63E-01	1.71E-01
Energy (MeV)	$\phi(\text{TAM} \leftarrow \text{TBE})$									
	Cellularity									
	100%	90%	80%	70%	60%	50%	40%	30%	20%	10%
3.0	2.62E-01	2.37E-01	2.11E-01	1.87E-01	1.63E-01	1.35E-01	1.09E-01	7.78E-02	5.38E-02	2.69E-02
3.5	3.01E-01	2.73E-01	2.42E-01	2.15E-01	1.87E-01	1.55E-01	1.24E-01	8.93E-02	6.19E-02	3.10E-02
4.0	3.30E-01	2.98E-01	2.66E-01	2.36E-01	2.06E-01	1.70E-01	1.36E-01	9.78E-02	6.80E-02	3.41E-02
4.5	3.52E-01	3.20E-01	2.84E-01	2.53E-01	2.20E-01	1.82E-01	1.46E-01	1.05E-01	7.25E-02	3.64E-02
5.0	3.71E-01	3.36E-01	2.98E-01	2.66E-01	2.32E-01	1.91E-01	1.54E-01	1.11E-01	7.64E-02	3.81E-02
5.5	3.87E-01	3.50E-01	3.11E-01	2.78E-01	2.42E-01	1.99E-01	1.60E-01	1.15E-01	7.96E-02	3.99E-02
6.0	3.99E-01	3.62E-01	3.22E-01	2.86E-01	2.50E-01	2.06E-01	1.65E-01	1.19E-01	8.20E-02	4.11E-02
6.5	4.12E-01	3.71E-01	3.30E-01	2.95E-01	2.57E-01	2.12E-01	1.70E-01	1.22E-01	8.45E-02	4.23E-02
7.0	4.20E-01	3.81E-01	3.38E-01	3.00E-01	2.63E-01	2.17E-01	1.73E-01	1.25E-01	8.62E-02	4.33E-02
7.5	4.29E-01	3.88E-01	3.45E-01	3.07E-01	2.68E-01	2.21E-01	1.77E-01	1.28E-01	8.87E-02	4.42E-02
8.0	4.36E-01	3.96E-01	3.51E-01	3.13E-01	2.73E-01	2.24E-01	1.81E-01	1.30E-01	8.98E-02	4.49E-02
8.5	4.43E-01	4.02E-01	3.57E-01	3.18E-01	2.77E-01	2.28E-01	1.83E-01	1.32E-01	9.09E-02	4.54E-02
9.0	4.50E-01	4.08E-01	3.62E-01	3.22E-01	2.81E-01	2.31E-01	1.86E-01	1.33E-01	9.23E-02	4.63E-02
9.5	4.56E-01	4.13E-01	3.67E-01	3.27E-01	2.84E-01	2.35E-01	1.88E-01	1.35E-01	9.35E-02	4.67E-02
10.0	4.62E-01	4.18E-01	3.71E-01	3.31E-01	2.89E-01	2.37E-01	1.90E-01	1.37E-01	9.46E-02	4.72E-02

TABLE 4B (Continued)

Energy (MeV)	Cervical Vertebrae $\phi(\text{TAM} \leftarrow \text{TBS})$									
	Cellularity									
	100%	90%	80%	70%	60%	50%	40%	30%	20%	10%
3.0	5.91E-02	5.37E-02	4.77E-02	4.25E-02	3.72E-02	3.07E-02	2.46E-02	1.77E-02	1.23E-02	6.05E-03
3.5	1.05E-01	9.45E-02	8.39E-02	7.48E-02	6.47E-02	5.39E-02	4.32E-02	3.10E-02	2.13E-02	1.08E-02
4.0	1.46E-01	1.33E-01	1.18E-01	1.05E-01	9.14E-02	7.53E-02	6.03E-02	4.32E-02	3.01E-02	1.49E-02
4.5	1.83E-01	1.65E-01	1.48E-01	1.32E-01	1.14E-01	9.43E-02	7.55E-02	5.43E-02	3.77E-02	1.91E-02
5.0	2.14E-01	1.94E-01	1.72E-01	1.54E-01	1.34E-01	1.11E-01	8.87E-02	6.38E-02	4.45E-02	2.21E-02
5.5	2.39E-01	2.17E-01	1.93E-01	1.72E-01	1.50E-01	1.24E-01	9.94E-02	7.17E-02	4.95E-02	2.47E-02
6.0	2.59E-01	2.35E-01	2.09E-01	1.86E-01	1.63E-01	1.35E-01	1.08E-01	7.81E-02	5.39E-02	2.69E-02
6.5	2.77E-01	2.52E-01	2.24E-01	1.99E-01	1.74E-01	1.44E-01	1.15E-01	8.35E-02	5.78E-02	2.90E-02
7.0	2.93E-01	2.67E-01	2.38E-01	2.12E-01	1.85E-01	1.53E-01	1.23E-01	8.86E-02	6.09E-02	3.07E-02
7.5	3.09E-01	2.81E-01	2.49E-01	2.22E-01	1.94E-01	1.60E-01	1.28E-01	9.26E-02	6.41E-02	3.21E-02
8.0	3.20E-01	2.92E-01	2.60E-01	2.32E-01	2.02E-01	1.67E-01	1.34E-01	9.67E-02	6.67E-02	3.33E-02
8.5	3.32E-01	3.02E-01	2.68E-01	2.40E-01	2.10E-01	1.73E-01	1.39E-01	1.00E-01	6.90E-02	3.46E-02
9.0	3.44E-01	3.11E-01	2.78E-01	2.48E-01	2.17E-01	1.78E-01	1.43E-01	1.03E-01	7.11E-02	3.55E-02
9.5	3.54E-01	3.21E-01	2.85E-01	2.54E-01	2.22E-01	1.83E-01	1.48E-01	1.06E-01	7.29E-02	3.70E-02
10.0	3.63E-01	3.30E-01	2.92E-01	2.62E-01	2.28E-01	1.88E-01	1.51E-01	1.08E-01	7.52E-02	3.76E-02
Energy (MeV)	$\phi(\text{TAM} \leftarrow \text{TBV})$									
	Cellularity									
	100%	90%	80%	70%	60%	50%	40%	30%	20%	10%
3.0	8.80E-04	7.96E-04	7.22E-04	6.12E-04	5.28E-04	4.49E-04	3.61E-04	2.52E-04	1.88E-04	9.00E-05
3.5	2.28E-03	2.05E-03	1.79E-03	1.65E-03	1.43E-03	1.20E-03	9.40E-04	6.89E-04	5.06E-04	2.30E-04
4.0	4.54E-03	4.12E-03	3.70E-03	3.29E-03	2.86E-03	2.34E-03	1.91E-03	1.38E-03	9.12E-04	4.59E-04
4.5	7.77E-03	7.14E-03	6.36E-03	5.67E-03	4.80E-03	4.02E-03	3.24E-03	2.28E-03	1.61E-03	8.11E-04
5.0	1.19E-02	1.06E-02	9.53E-03	8.51E-03	7.37E-03	6.11E-03	4.93E-03	3.49E-03	2.38E-03	1.20E-03
5.5	1.66E-02	1.50E-02	1.35E-02	1.20E-02	1.04E-02	8.60E-03	6.89E-03	5.03E-03	3.42E-03	1.70E-03
6.0	2.20E-02	1.99E-02	1.78E-02	1.59E-02	1.38E-02	1.13E-02	9.22E-03	6.64E-03	4.58E-03	2.25E-03
6.5	2.84E-02	2.55E-02	2.28E-02	2.03E-02	1.77E-02	1.45E-02	1.18E-02	8.44E-03	5.76E-03	2.91E-03
7.0	3.52E-02	3.14E-02	2.82E-02	2.50E-02	2.19E-02	1.81E-02	1.45E-02	1.04E-02	7.28E-03	3.63E-03
7.5	4.24E-02	3.83E-02	3.43E-02	3.04E-02	2.64E-02	2.20E-02	1.76E-02	1.27E-02	8.75E-03	4.44E-03
8.0	5.01E-02	4.55E-02	4.02E-02	3.59E-02	3.15E-02	2.60E-02	2.09E-02	1.50E-02	1.05E-02	5.20E-03
8.5	5.87E-02	5.33E-02	4.73E-02	4.21E-02	3.69E-02	3.04E-02	2.43E-02	1.77E-02	1.22E-02	6.11E-03
9.0	6.76E-02	6.14E-02	5.45E-02	4.84E-02	4.25E-02	3.50E-02	2.83E-02	2.04E-02	1.40E-02	6.96E-03
9.5	7.70E-02	7.00E-02	6.21E-02	5.54E-02	4.85E-02	4.01E-02	3.23E-02	2.30E-02	1.60E-02	8.05E-03
10.0	8.65E-02	7.87E-02	6.99E-02	6.29E-02	5.44E-02	4.52E-02	3.62E-02	2.60E-02	1.81E-02	9.00E-03

TABLE 5B

Absorbed Fractions to Active Bone Marrow (TAM) for α -Emissions Within
Femur Head of Leeds 44-Year Male for Various Source Tissues and Marrow Cellularities

Energy (MeV)	Femur Head $\phi(\text{TAM} \leftarrow \text{TAM})$									
	Cellularity									
	100%	90%	80%	70%	60%	50%	40%	30%	20%	10%
3.0	9.91E-01	9.72E-01	9.46E-01	9.19E-01	8.83E-01	8.47E-01	8.12E-01	7.64E-01	7.18E-01	6.45E-01
3.5	9.88E-01	9.65E-01	9.33E-01	8.99E-01	8.55E-01	8.11E-01	7.69E-01	7.13E-01	6.59E-01	5.78E-01
4.0	9.85E-01	9.57E-01	9.18E-01	8.77E-01	8.24E-01	7.75E-01	7.25E-01	6.62E-01	6.04E-01	5.14E-01
4.5	9.83E-01	9.48E-01	9.03E-01	8.56E-01	7.94E-01	7.38E-01	6.81E-01	6.13E-01	5.49E-01	4.57E-01
5.0	9.79E-01	9.40E-01	8.87E-01	8.33E-01	7.66E-01	7.02E-01	6.42E-01	5.67E-01	5.00E-01	4.04E-01
5.5	9.76E-01	9.31E-01	8.71E-01	8.12E-01	7.37E-01	6.69E-01	6.04E-01	5.24E-01	4.55E-01	3.59E-01
6.0	9.72E-01	9.23E-01	8.57E-01	7.92E-01	7.13E-01	6.40E-01	5.70E-01	4.87E-01	4.15E-01	3.20E-01
6.5	9.69E-01	9.13E-01	8.43E-01	7.73E-01	6.91E-01	6.14E-01	5.40E-01	4.55E-01	3.81E-01	2.87E-01
7.0	9.65E-01	9.06E-01	8.29E-01	7.58E-01	6.73E-01	5.92E-01	5.16E-01	4.27E-01	3.53E-01	2.59E-01
7.5	9.61E-01	8.98E-01	8.19E-01	7.44E-01	6.60E-01	5.75E-01	4.96E-01	4.05E-01	3.29E-01	2.37E-01
8.0	9.56E-01	8.91E-01	8.08E-01	7.33E-01	6.48E-01	5.62E-01	4.80E-01	3.87E-01	3.10E-01	2.18E-01
8.5	9.52E-01	8.83E-01	7.99E-01	7.24E-01	6.40E-01	5.52E-01	4.68E-01	3.73E-01	2.96E-01	2.03E-01
9.0	9.48E-01	8.77E-01	7.92E-01	7.17E-01	6.33E-01	5.44E-01	4.58E-01	3.62E-01	2.84E-01	1.91E-01
9.5	9.43E-01	8.71E-01	7.86E-01	7.11E-01	6.28E-01	5.37E-01	4.51E-01	3.53E-01	2.74E-01	1.82E-01
10.0	9.39E-01	8.65E-01	7.80E-01	7.06E-01	6.24E-01	5.32E-01	4.44E-01	3.45E-01	2.66E-01	1.74E-01
Energy (MeV)	$\phi(\text{TAM} \leftarrow \text{TBE})$									
	Cellularity									
	100%	90%	80%	70%	60%	50%	40%	30%	20%	10%
3.0	2.63E-01	2.37E-01	2.11E-01	1.88E-01	1.64E-01	1.36E-01	1.08E-01	7.82E-02	5.41E-02	2.71E-02
3.5	3.00E-01	2.72E-01	2.42E-01	2.15E-01	1.88E-01	1.55E-01	1.25E-01	8.94E-02	6.21E-02	3.09E-02
4.0	3.30E-01	2.99E-01	2.65E-01	2.36E-01	2.05E-01	1.70E-01	1.36E-01	9.79E-02	6.76E-02	3.38E-02
4.5	3.53E-01	3.20E-01	2.84E-01	2.53E-01	2.20E-01	1.82E-01	1.46E-01	1.05E-01	7.25E-02	3.64E-02
5.0	3.70E-01	3.37E-01	2.99E-01	2.66E-01	2.32E-01	1.92E-01	1.54E-01	1.10E-01	7.60E-02	3.84E-02
5.5	3.86E-01	3.50E-01	3.11E-01	2.76E-01	2.41E-01	2.00E-01	1.60E-01	1.15E-01	7.93E-02	3.99E-02
6.0	3.99E-01	3.62E-01	3.21E-01	2.86E-01	2.49E-01	2.06E-01	1.65E-01	1.18E-01	8.19E-02	4.09E-02
6.5	4.09E-01	3.72E-01	3.30E-01	2.93E-01	2.56E-01	2.11E-01	1.69E-01	1.22E-01	8.42E-02	4.21E-02
7.0	4.19E-01	3.80E-01	3.37E-01	3.00E-01	2.61E-01	2.16E-01	1.73E-01	1.24E-01	8.64E-02	4.32E-02
7.5	4.27E-01	3.87E-01	3.43E-01	3.06E-01	2.67E-01	2.20E-01	1.76E-01	1.27E-01	8.73E-02	4.39E-02
8.0	4.35E-01	3.94E-01	3.50E-01	3.11E-01	2.72E-01	2.24E-01	1.79E-01	1.29E-01	8.92E-02	4.47E-02
8.5	4.41E-01	4.00E-01	3.55E-01	3.16E-01	2.76E-01	2.27E-01	1.82E-01	1.31E-01	9.05E-02	4.52E-02
9.0	4.47E-01	4.06E-01	3.60E-01	3.21E-01	2.79E-01	2.30E-01	1.85E-01	1.33E-01	9.17E-02	4.60E-02
9.5	4.53E-01	4.11E-01	3.65E-01	3.24E-01	2.83E-01	2.33E-01	1.87E-01	1.35E-01	9.28E-02	4.64E-02
10.0	4.59E-01	4.16E-01	3.68E-01	3.29E-01	2.86E-01	2.36E-01	1.89E-01	1.36E-01	9.42E-02	4.70E-02

TABLE 5B (Continued)

Energy (MeV)	Femur Head $\phi(\text{TAM} \leftarrow \text{TBS})$									
	Cellularity									
	100%	90%	80%	70%	60%	50%	40%	30%	20%	10%
3.0	5.96E-02	5.41E-02	4.79E-02	4.27E-02	3.71E-02	3.07E-02	2.46E-02	1.79E-02	1.22E-02	6.15E-03
3.5	1.05E-01	9.50E-02	8.46E-02	7.52E-02	6.56E-02	5.42E-02	4.38E-02	3.13E-02	2.16E-02	1.08E-02
4.0	1.48E-01	1.34E-01	1.19E-01	1.06E-01	9.23E-02	7.66E-02	6.11E-02	4.40E-02	3.05E-02	1.51E-02
4.5	1.86E-01	1.68E-01	1.49E-01	1.33E-01	1.16E-01	9.55E-02	7.65E-02	5.50E-02	3.79E-02	1.91E-02
5.0	2.16E-01	1.97E-01	1.75E-01	1.56E-01	1.35E-01	1.12E-01	8.96E-02	6.47E-02	4.48E-02	2.24E-02
5.5	2.43E-01	2.21E-01	1.96E-01	1.75E-01	1.53E-01	1.26E-01	1.01E-01	7.24E-02	5.02E-02	2.52E-02
6.0	2.65E-01	2.41E-01	2.14E-01	1.90E-01	1.66E-01	1.37E-01	1.10E-01	7.91E-02	5.46E-02	2.75E-02
6.5	2.84E-01	2.57E-01	2.28E-01	2.04E-01	1.78E-01	1.47E-01	1.18E-01	8.50E-02	5.85E-02	2.93E-02
7.0	3.01E-01	2.74E-01	2.43E-01	2.17E-01	1.88E-01	1.56E-01	1.25E-01	9.06E-02	6.22E-02	3.12E-02
7.5	3.17E-01	2.88E-01	2.55E-01	2.27E-01	1.99E-01	1.64E-01	1.32E-01	9.46E-02	6.55E-02	3.28E-02
8.0	3.31E-01	2.99E-01	2.67E-01	2.38E-01	2.07E-01	1.71E-01	1.37E-01	9.89E-02	6.82E-02	3.41E-02
8.5	3.42E-01	3.10E-01	2.76E-01	2.45E-01	2.15E-01	1.77E-01	1.43E-01	1.02E-01	7.09E-02	3.54E-02
9.0	3.54E-01	3.21E-01	2.85E-01	2.54E-01	2.22E-01	1.83E-01	1.47E-01	1.05E-01	7.29E-02	3.67E-02
9.5	3.64E-01	3.30E-01	2.94E-01	2.62E-01	2.29E-01	1.89E-01	1.52E-01	1.09E-01	7.51E-02	3.75E-02
10.0	3.74E-01	3.39E-01	3.01E-01	2.69E-01	2.35E-01	1.94E-01	1.55E-01	1.11E-01	7.70E-02	3.84E-02
Energy (MeV)	$\phi(\text{TAM} \leftarrow \text{TBV})$									
	Cellularity									
	100%	90%	80%	70%	60%	50%	40%	30%	20%	10%
3.0	1.08E-03	9.80E-04	8.57E-04	7.46E-04	6.54E-04	5.78E-04	4.25E-04	3.16E-04	2.14E-04	1.05E-04
3.5	2.73E-03	2.47E-03	2.24E-03	2.03E-03	1.70E-03	1.44E-03	1.13E-03	7.93E-04	5.64E-04	2.95E-04
4.0	5.55E-03	5.06E-03	4.51E-03	4.06E-03	3.44E-03	2.92E-03	2.33E-03	1.69E-03	1.16E-03	5.67E-04
4.5	9.63E-03	8.59E-03	7.80E-03	6.92E-03	5.95E-03	4.89E-03	3.99E-03	2.85E-03	1.96E-03	1.02E-03
5.0	1.46E-02	1.33E-02	1.16E-02	1.04E-02	9.05E-03	7.54E-03	5.98E-03	4.34E-03	2.95E-03	1.50E-03
5.5	2.05E-02	1.87E-02	1.66E-02	1.47E-02	1.27E-02	1.06E-02	8.46E-03	6.13E-03	4.24E-03	2.16E-03
6.0	2.74E-02	2.47E-02	2.20E-02	1.95E-02	1.70E-02	1.43E-02	1.14E-02	8.25E-03	5.69E-03	2.83E-03
6.5	3.49E-02	3.19E-02	2.84E-02	2.53E-02	2.23E-02	1.82E-02	1.46E-02	1.04E-02	7.34E-03	3.63E-03
7.0	4.36E-02	3.96E-02	3.52E-02	3.16E-02	2.75E-02	2.25E-02	1.81E-02	1.30E-02	8.96E-03	4.54E-03
7.5	5.29E-02	4.81E-02	4.27E-02	3.81E-02	3.31E-02	2.76E-02	2.20E-02	1.58E-02	1.09E-02	5.54E-03
8.0	6.31E-02	5.73E-02	5.08E-02	4.53E-02	3.96E-02	3.26E-02	2.63E-02	1.89E-02	1.30E-02	6.56E-03
8.5	7.42E-02	6.72E-02	5.95E-02	5.34E-02	4.62E-02	3.83E-02	3.06E-02	2.22E-02	1.53E-02	7.61E-03
9.0	8.52E-02	7.75E-02	6.94E-02	6.14E-02	5.34E-02	4.44E-02	3.57E-02	2.57E-02	1.75E-02	8.84E-03
9.5	9.78E-02	8.85E-02	7.85E-02	7.03E-02	6.10E-02	5.03E-02	4.05E-02	2.91E-02	2.01E-02	1.00E-02
10.0	1.10E-01	9.99E-02	8.91E-02	7.93E-02	6.91E-02	5.73E-02	4.59E-02	3.31E-02	2.29E-02	1.14E-02

TABLE 6B

Absorbed Fractions to Active Bone Marrow (TAM) for α -Emissions Within
Femur Neck of Leeds 44-Year Male for Various Source Tissues and Marrow Cellularities

Energy (MeV)	Femur Neck									
	$\phi(\text{TAM} \leftarrow \text{TAM})$									
	Cellularity									
	100%	90%	80%	70%	60%	50%	40%	30%	20%	10%
3.0	9.93E-01	9.74E-01	9.49E-01	9.21E-01	8.85E-01	8.50E-01	8.13E-01	7.66E-01	7.20E-01	6.47E-01
3.5	9.92E-01	9.68E-01	9.36E-01	9.02E-01	8.58E-01	8.14E-01	7.71E-01	7.16E-01	6.62E-01	5.79E-01
4.0	9.90E-01	9.61E-01	9.22E-01	8.81E-01	8.29E-01	7.78E-01	7.28E-01	6.65E-01	6.05E-01	5.16E-01
4.5	9.88E-01	9.53E-01	9.07E-01	8.60E-01	7.98E-01	7.41E-01	6.86E-01	6.16E-01	5.52E-01	4.58E-01
5.0	9.86E-01	9.46E-01	8.93E-01	8.39E-01	7.70E-01	7.07E-01	6.45E-01	5.69E-01	5.03E-01	4.07E-01
5.5	9.83E-01	9.38E-01	8.78E-01	8.18E-01	7.43E-01	6.74E-01	6.07E-01	5.28E-01	4.57E-01	3.62E-01
6.0	9.81E-01	9.30E-01	8.64E-01	7.98E-01	7.19E-01	6.45E-01	5.74E-01	4.91E-01	4.18E-01	3.22E-01
6.5	9.78E-01	9.23E-01	8.51E-01	7.81E-01	6.97E-01	6.19E-01	5.45E-01	4.58E-01	3.84E-01	2.89E-01
7.0	9.76E-01	9.16E-01	8.38E-01	7.65E-01	6.80E-01	5.98E-01	5.20E-01	4.31E-01	3.56E-01	2.61E-01
7.5	9.73E-01	9.09E-01	8.28E-01	7.53E-01	6.66E-01	5.81E-01	5.02E-01	4.08E-01	3.32E-01	2.38E-01
8.0	9.70E-01	9.03E-01	8.19E-01	7.43E-01	6.56E-01	5.68E-01	4.86E-01	3.90E-01	3.13E-01	2.19E-01
8.5	9.67E-01	8.97E-01	8.11E-01	7.34E-01	6.48E-01	5.58E-01	4.74E-01	3.77E-01	2.98E-01	2.05E-01
9.0	9.64E-01	8.91E-01	8.04E-01	7.27E-01	6.43E-01	5.51E-01	4.65E-01	3.66E-01	2.87E-01	1.94E-01
9.5	9.61E-01	8.87E-01	7.99E-01	7.22E-01	6.38E-01	5.44E-01	4.57E-01	3.58E-01	2.78E-01	1.84E-01
10.0	9.57E-01	8.82E-01	7.95E-01	7.18E-01	6.35E-01	5.40E-01	4.51E-01	3.51E-01	2.70E-01	1.76E-01
Energy (MeV)	$\phi(\text{TAM} \leftarrow \text{TBE})$									
	Cellularity									
	100%	90%	80%	70%	60%	50%	40%	30%	20%	10%
3.0	2.62E-01	2.37E-01	2.11E-01	1.88E-01	1.64E-01	1.35E-01	1.08E-01	7.80E-02	5.41E-02	2.70E-02
3.5	3.01E-01	2.72E-01	2.42E-01	2.15E-01	1.87E-01	1.55E-01	1.25E-01	8.93E-02	6.16E-02	3.11E-02
4.0	3.30E-01	2.99E-01	2.66E-01	2.37E-01	2.06E-01	1.70E-01	1.36E-01	9.82E-02	6.77E-02	3.40E-02
4.5	3.52E-01	3.19E-01	2.84E-01	2.53E-01	2.20E-01	1.81E-01	1.47E-01	1.05E-01	7.26E-02	3.64E-02
5.0	3.71E-01	3.37E-01	2.99E-01	2.66E-01	2.32E-01	1.92E-01	1.54E-01	1.10E-01	7.64E-02	3.83E-02
5.5	3.87E-01	3.51E-01	3.12E-01	2.78E-01	2.43E-01	2.00E-01	1.60E-01	1.15E-01	7.97E-02	4.01E-02
6.0	4.00E-01	3.63E-01	3.22E-01	2.87E-01	2.50E-01	2.06E-01	1.66E-01	1.19E-01	8.24E-02	4.11E-02
6.5	4.11E-01	3.73E-01	3.31E-01	2.95E-01	2.58E-01	2.12E-01	1.70E-01	1.23E-01	8.45E-02	4.21E-02
7.0	4.22E-01	3.82E-01	3.39E-01	3.02E-01	2.63E-01	2.17E-01	1.74E-01	1.25E-01	8.63E-02	4.33E-02
7.5	4.31E-01	3.90E-01	3.46E-01	3.08E-01	2.68E-01	2.21E-01	1.79E-01	1.28E-01	8.81E-02	4.43E-02
8.0	4.40E-01	3.98E-01	3.53E-01	3.15E-01	2.74E-01	2.26E-01	1.81E-01	1.30E-01	9.02E-02	4.52E-02
8.5	4.48E-01	4.06E-01	3.60E-01	3.21E-01	2.80E-01	2.30E-01	1.85E-01	1.33E-01	9.21E-02	4.59E-02
9.0	4.56E-01	4.12E-01	3.67E-01	3.26E-01	2.84E-01	2.34E-01	1.88E-01	1.35E-01	9.34E-02	4.67E-02
9.5	4.62E-01	4.19E-01	3.72E-01	3.31E-01	2.89E-01	2.38E-01	1.90E-01	1.37E-01	9.44E-02	4.75E-02
10.0	4.69E-01	4.25E-01	3.77E-01	3.36E-01	2.93E-01	2.41E-01	1.93E-01	1.39E-01	9.59E-02	4.80E-02

TABLE 6B (Continued)

Energy (MeV)	Femur Neck $\phi(\text{TAM} \leftarrow \text{TBS})$									
	Cellularity									
	100%	90%	80%	70%	60%	50%	40%	30%	20%	10%
3.0	5.83E-02	5.28E-02	4.71E-02	4.19E-02	3.64E-02	3.01E-02	2.43E-02	1.73E-02	1.20E-02	6.11E-03
3.5	1.04E-01	9.43E-02	8.36E-02	7.43E-02	6.51E-02	5.34E-02	4.32E-02	3.11E-02	2.13E-02	1.07E-02
4.0	1.47E-01	1.33E-01	1.18E-01	1.05E-01	9.17E-02	7.59E-02	6.08E-02	4.36E-02	3.02E-02	1.52E-02
4.5	1.84E-01	1.67E-01	1.48E-01	1.32E-01	1.15E-01	9.51E-02	7.63E-02	5.44E-02	3.79E-02	1.91E-02
5.0	2.17E-01	1.97E-01	1.74E-01	1.56E-01	1.35E-01	1.12E-01	9.00E-02	6.45E-02	4.47E-02	2.26E-02
5.5	2.43E-01	2.21E-01	1.96E-01	1.74E-01	1.52E-01	1.26E-01	1.01E-01	7.24E-02	5.03E-02	2.52E-02
6.0	2.65E-01	2.41E-01	2.14E-01	1.91E-01	1.66E-01	1.37E-01	1.11E-01	7.93E-02	5.51E-02	2.77E-02
6.5	2.85E-01	2.59E-01	2.30E-01	2.05E-01	1.79E-01	1.47E-01	1.19E-01	8.54E-02	5.88E-02	2.95E-02
7.0	3.03E-01	2.75E-01	2.44E-01	2.18E-01	1.90E-01	1.57E-01	1.26E-01	9.10E-02	6.28E-02	3.14E-02
7.5	3.20E-01	2.90E-01	2.59E-01	2.30E-01	2.01E-01	1.66E-01	1.33E-01	9.59E-02	6.64E-02	3.34E-02
8.0	3.34E-01	3.04E-01	2.71E-01	2.42E-01	2.10E-01	1.74E-01	1.40E-01	1.00E-01	6.94E-02	3.48E-02
8.5	3.50E-01	3.18E-01	2.81E-01	2.51E-01	2.19E-01	1.81E-01	1.45E-01	1.04E-01	7.23E-02	3.63E-02
9.0	3.61E-01	3.28E-01	2.92E-01	2.60E-01	2.27E-01	1.87E-01	1.50E-01	1.08E-01	7.46E-02	3.73E-02
9.5	3.74E-01	3.39E-01	3.01E-01	2.69E-01	2.35E-01	1.93E-01	1.55E-01	1.12E-01	7.70E-02	3.86E-02
10.0	3.84E-01	3.49E-01	3.10E-01	2.77E-01	2.41E-01	1.99E-01	1.60E-01	1.15E-01	7.90E-02	3.95E-02
Energy (MeV)	$\phi(\text{TAM} \leftarrow \text{TBV})$									
	Cellularity									
	100%	90%	80%	70%	60%	50%	40%	30%	20%	10%
3.0	7.57E-04	6.64E-04	5.56E-04	5.47E-04	4.63E-04	3.99E-04	3.02E-04	2.11E-04	1.55E-04	7.70E-05
3.5	1.99E-03	1.79E-03	1.61E-03	1.42E-03	1.27E-03	1.04E-03	8.42E-04	6.04E-04	4.05E-04	1.99E-04
4.0	4.04E-03	3.72E-03	3.17E-03	2.91E-03	2.53E-03	2.11E-03	1.67E-03	1.21E-03	8.28E-04	4.17E-04
4.5	6.94E-03	6.35E-03	5.58E-03	4.99E-03	4.31E-03	3.59E-03	2.84E-03	2.08E-03	1.44E-03	7.28E-04
5.0	1.06E-02	9.61E-03	8.49E-03	7.46E-03	6.52E-03	5.48E-03	4.43E-03	3.15E-03	2.20E-03	1.07E-03
5.5	1.49E-02	1.36E-02	1.21E-02	1.07E-02	9.33E-03	7.59E-03	6.15E-03	4.49E-03	3.09E-03	1.59E-03
6.0	1.98E-02	1.80E-02	1.61E-02	1.44E-02	1.24E-02	1.03E-02	8.14E-03	5.90E-03	4.15E-03	2.09E-03
6.5	2.56E-02	2.30E-02	2.03E-02	1.82E-02	1.60E-02	1.31E-02	1.05E-02	7.63E-03	5.23E-03	2.58E-03
7.0	3.18E-02	2.88E-02	2.57E-02	2.28E-02	1.99E-02	1.62E-02	1.31E-02	9.42E-03	6.46E-03	3.31E-03
7.5	3.84E-02	3.48E-02	3.10E-02	2.75E-02	2.40E-02	1.99E-02	1.59E-02	1.15E-02	7.92E-03	3.99E-03
8.0	4.56E-02	4.13E-02	3.66E-02	3.28E-02	2.85E-02	2.36E-02	1.89E-02	1.35E-02	9.45E-03	4.78E-03
8.5	5.29E-02	4.83E-02	4.27E-02	3.84E-02	3.34E-02	2.74E-02	2.22E-02	1.58E-02	1.10E-02	5.57E-03
9.0	6.12E-02	5.56E-02	4.93E-02	4.41E-02	3.84E-02	3.18E-02	2.53E-02	1.82E-02	1.28E-02	6.34E-03
9.5	6.97E-02	6.34E-02	5.63E-02	5.01E-02	4.39E-02	3.61E-02	2.90E-02	2.09E-02	1.43E-02	7.20E-03
10.0	7.88E-02	7.17E-02	6.31E-02	5.66E-02	4.97E-02	4.08E-02	3.27E-02	2.35E-02	1.63E-02	8.15E-03

TABLE 7B

Absorbed Fractions to Active Bone Marrow (TAM) for α -Emissions Within
Iliac Crest of Leeds 44-Year Male for Various Source Tissues and Marrow Cellularities

Energy (MeV)	Iliac Crest									
	$\phi(\text{TAM} \leftarrow \text{TAM})$									
	Cellularity									
	100%	90%	80%	70%	60%	50%	40%	30%	20%	10%
3.0	9.87E-01	9.69E-01	9.43E-01	9.16E-01	8.80E-01	8.45E-01	8.08E-01	7.62E-01	7.16E-01	6.43E-01
3.5	9.84E-01	9.60E-01	9.29E-01	8.95E-01	8.52E-01	8.08E-01	7.66E-01	7.10E-01	6.58E-01	5.76E-01
4.0	9.80E-01	9.52E-01	9.13E-01	8.73E-01	8.20E-01	7.71E-01	7.22E-01	6.59E-01	6.00E-01	5.13E-01
4.5	9.77E-01	9.43E-01	8.97E-01	8.50E-01	7.90E-01	7.34E-01	6.78E-01	6.10E-01	5.46E-01	4.54E-01
5.0	9.73E-01	9.33E-01	8.81E-01	8.28E-01	7.60E-01	6.99E-01	6.38E-01	5.64E-01	4.96E-01	4.03E-01
5.5	9.68E-01	9.24E-01	8.65E-01	8.06E-01	7.32E-01	6.65E-01	6.00E-01	5.22E-01	4.52E-01	3.57E-01
6.0	9.64E-01	9.14E-01	8.49E-01	7.85E-01	7.07E-01	6.35E-01	5.66E-01	4.84E-01	4.13E-01	3.18E-01
6.5	9.59E-01	9.05E-01	8.34E-01	7.66E-01	6.85E-01	6.08E-01	5.35E-01	4.50E-01	3.78E-01	2.85E-01
7.0	9.54E-01	8.95E-01	8.20E-01	7.49E-01	6.66E-01	5.87E-01	5.11E-01	4.23E-01	3.50E-01	2.58E-01
7.5	9.49E-01	8.86E-01	8.08E-01	7.35E-01	6.51E-01	5.69E-01	4.90E-01	4.00E-01	3.26E-01	2.35E-01
8.0	9.43E-01	8.78E-01	7.97E-01	7.23E-01	6.40E-01	5.55E-01	4.75E-01	3.83E-01	3.07E-01	2.16E-01
8.5	9.37E-01	8.70E-01	7.87E-01	7.13E-01	6.32E-01	5.44E-01	4.63E-01	3.68E-01	2.92E-01	2.02E-01
9.0	9.31E-01	8.62E-01	7.79E-01	7.05E-01	6.23E-01	5.35E-01	4.53E-01	3.57E-01	2.80E-01	1.90E-01
9.5	9.25E-01	8.55E-01	7.72E-01	6.99E-01	6.19E-01	5.29E-01	4.45E-01	3.48E-01	2.71E-01	1.80E-01
10.0	9.19E-01	8.49E-01	7.66E-01	6.93E-01	6.13E-01	5.22E-01	4.38E-01	3.41E-01	2.63E-01	1.72E-01
Energy (MeV)	$\phi(\text{TAM} \leftarrow \text{TBE})$									
	Cellularity									
	100%	90%	80%	70%	60%	50%	40%	30%	20%	10%
3.0	2.62E-01	2.37E-01	2.11E-01	1.88E-01	1.64E-01	1.35E-01	1.09E-01	7.79E-02	5.40E-02	2.70E-02
3.5	3.00E-01	2.72E-01	2.42E-01	2.15E-01	1.88E-01	1.55E-01	1.24E-01	8.93E-02	6.18E-02	3.09E-02
4.0	3.30E-01	2.99E-01	2.65E-01	2.36E-01	2.05E-01	1.70E-01	1.37E-01	9.81E-02	6.78E-02	3.39E-02
4.5	3.53E-01	3.20E-01	2.85E-01	2.53E-01	2.20E-01	1.82E-01	1.46E-01	1.05E-01	7.27E-02	3.65E-02
5.0	3.72E-01	3.37E-01	3.00E-01	2.67E-01	2.32E-01	1.92E-01	1.54E-01	1.11E-01	7.62E-02	3.82E-02
5.5	3.88E-01	3.51E-01	3.12E-01	2.77E-01	2.42E-01	2.00E-01	1.60E-01	1.15E-01	7.97E-02	3.97E-02
6.0	4.01E-01	3.62E-01	3.23E-01	2.87E-01	2.51E-01	2.07E-01	1.66E-01	1.19E-01	8.26E-02	4.15E-02
6.5	4.12E-01	3.74E-01	3.32E-01	2.95E-01	2.58E-01	2.12E-01	1.70E-01	1.23E-01	8.47E-02	4.24E-02
7.0	4.22E-01	3.82E-01	3.39E-01	3.02E-01	2.63E-01	2.18E-01	1.75E-01	1.26E-01	8.67E-02	4.35E-02
7.5	4.31E-01	3.90E-01	3.47E-01	3.09E-01	2.69E-01	2.22E-01	1.79E-01	1.28E-01	8.83E-02	4.43E-02
8.0	4.40E-01	3.98E-01	3.53E-01	3.15E-01	2.74E-01	2.26E-01	1.82E-01	1.30E-01	9.03E-02	4.53E-02
8.5	4.47E-01	4.05E-01	3.59E-01	3.20E-01	2.79E-01	2.30E-01	1.84E-01	1.33E-01	9.16E-02	4.59E-02
9.0	4.54E-01	4.11E-01	3.65E-01	3.24E-01	2.84E-01	2.33E-01	1.87E-01	1.35E-01	9.33E-02	4.66E-02
9.5	4.60E-01	4.18E-01	3.69E-01	3.30E-01	2.87E-01	2.37E-01	1.90E-01	1.37E-01	9.45E-02	4.72E-02
10.0	4.66E-01	4.23E-01	3.75E-01	3.34E-01	2.92E-01	2.40E-01	1.92E-01	1.39E-01	9.56E-02	4.79E-02

TABLE 7B (Continued)

Energy (MeV)	Iliac Crest $\phi(\text{TAM} \leftarrow \text{TBS})$ Cellularity									
	100%	90%	80%	70%	60%	50%	40%	30%	20%	10%
3.0	6.00E-02	5.47E-02	4.85E-02	4.31E-02	3.74E-02	3.10E-02	2.48E-02	1.79E-02	1.25E-02	6.12E-03
3.5	1.05E-01	9.56E-02	8.49E-02	7.54E-02	6.60E-02	5.44E-02	4.37E-02	3.16E-02	2.16E-02	1.09E-02
4.0	1.48E-01	1.34E-01	1.19E-01	1.06E-01	9.27E-02	7.63E-02	6.13E-02	4.42E-02	3.07E-02	1.52E-02
4.5	1.86E-01	1.68E-01	1.50E-01	1.33E-01	1.16E-01	9.63E-02	7.69E-02	5.50E-02	3.81E-02	1.93E-02
5.0	2.19E-01	1.98E-01	1.76E-01	1.57E-01	1.37E-01	1.13E-01	9.02E-02	6.50E-02	4.50E-02	2.26E-02
5.5	2.46E-01	2.23E-01	1.98E-01	1.76E-01	1.54E-01	1.27E-01	1.01E-01	7.32E-02	5.08E-02	2.53E-02
6.0	2.68E-01	2.43E-01	2.16E-01	1.92E-01	1.68E-01	1.38E-01	1.11E-01	8.00E-02	5.58E-02	2.77E-02
6.5	2.88E-01	2.61E-01	2.32E-01	2.06E-01	1.80E-01	1.48E-01	1.19E-01	8.61E-02	5.93E-02	3.00E-02
7.0	3.05E-01	2.77E-01	2.45E-01	2.19E-01	1.91E-01	1.58E-01	1.27E-01	9.14E-02	6.30E-02	3.16E-02
7.5	3.21E-01	2.91E-01	2.59E-01	2.30E-01	2.01E-01	1.66E-01	1.34E-01	9.63E-02	6.62E-02	3.32E-02
8.0	3.35E-01	3.04E-01	2.70E-01	2.41E-01	2.10E-01	1.73E-01	1.39E-01	1.00E-01	6.89E-02	3.46E-02
8.5	3.47E-01	3.16E-01	2.81E-01	2.50E-01	2.18E-01	1.81E-01	1.44E-01	1.04E-01	7.19E-02	3.58E-02
9.0	3.59E-01	3.26E-01	2.90E-01	2.58E-01	2.26E-01	1.86E-01	1.49E-01	1.07E-01	7.42E-02	3.72E-02
9.5	3.71E-01	3.37E-01	2.99E-01	2.66E-01	2.32E-01	1.92E-01	1.54E-01	1.11E-01	7.63E-02	3.82E-02
10.0	3.81E-01	3.46E-01	3.07E-01	2.74E-01	2.39E-01	1.97E-01	1.58E-01	1.14E-01	7.89E-02	3.92E-02
Energy (MeV)	$\phi(\text{TAM} \leftarrow \text{TBV})$ Cellularity									
	100%	90%	80%	70%	60%	50%	40%	30%	20%	10%
3.0	1.02E-03	9.21E-04	8.37E-04	7.50E-04	6.38E-04	5.19E-04	4.19E-04	3.26E-04	1.96E-04	1.10E-04
3.5	2.65E-03	2.41E-03	2.04E-03	1.89E-03	1.67E-03	1.35E-03	1.08E-03	8.04E-04	5.39E-04	2.71E-04
4.0	5.32E-03	4.92E-03	4.31E-03	3.88E-03	3.31E-03	2.74E-03	2.22E-03	1.60E-03	1.10E-03	5.62E-04
4.5	8.95E-03	8.24E-03	7.35E-03	6.47E-03	5.71E-03	4.63E-03	3.71E-03	2.69E-03	1.88E-03	9.63E-04
5.0	1.37E-02	1.25E-02	1.11E-02	9.86E-03	8.64E-03	7.09E-03	5.66E-03	4.19E-03	2.84E-03	1.39E-03
5.5	1.95E-02	1.76E-02	1.57E-02	1.39E-02	1.21E-02	9.95E-03	8.15E-03	5.83E-03	4.02E-03	2.04E-03
6.0	2.58E-02	2.36E-02	2.08E-02	1.85E-02	1.63E-02	1.33E-02	1.07E-02	7.65E-03	5.30E-03	2.71E-03
6.5	3.31E-02	2.99E-02	2.69E-02	2.37E-02	2.07E-02	1.70E-02	1.36E-02	9.84E-03	6.79E-03	3.43E-03
7.0	4.10E-02	3.72E-02	3.32E-02	2.93E-02	2.56E-02	2.13E-02	1.71E-02	1.23E-02	8.46E-03	4.26E-03
7.5	4.97E-02	4.55E-02	4.01E-02	3.57E-02	3.11E-02	2.57E-02	2.06E-02	1.49E-02	1.03E-02	5.14E-03
8.0	5.89E-02	5.36E-02	4.73E-02	4.24E-02	3.70E-02	3.06E-02	2.43E-02	1.78E-02	1.22E-02	6.10E-03
8.5	6.93E-02	6.27E-02	5.60E-02	4.94E-02	4.34E-02	3.59E-02	2.86E-02	2.06E-02	1.44E-02	7.19E-03
9.0	7.99E-02	7.25E-02	6.43E-02	5.71E-02	5.00E-02	4.11E-02	3.29E-02	2.37E-02	1.65E-02	8.17E-03
9.5	9.06E-02	8.20E-02	7.26E-02	6.49E-02	5.70E-02	4.70E-02	3.78E-02	2.71E-02	1.87E-02	9.46E-03
10.0	1.02E-01	9.31E-02	8.29E-02	7.37E-02	6.42E-02	5.32E-02	4.25E-02	3.06E-02	2.10E-02	1.07E-02

TABLE 8B

Absorbed Fractions to Active Bone Marrow (TAM) for α -Emissions Within
Lumbar Vertebrae of Leeds 44-Year Male for Various Source Tissues and Marrow Cellularities

Energy (MeV)	Lumbar Vertebrae									
	$\phi(\text{TAM} \leftarrow \text{TAM})$									
	Cellularity									
	100%	90%	80%	70%	60%	50%	40%	30%	20%	10%
3.0	9.90E-01	9.72E-01	9.46E-01	9.19E-01	8.83E-01	8.47E-01	8.11E-01	7.65E-01	7.18E-01	6.45E-01
3.5	9.88E-01	9.64E-01	9.33E-01	8.99E-01	8.54E-01	8.12E-01	7.69E-01	7.13E-01	6.60E-01	5.77E-01
4.0	9.86E-01	9.57E-01	9.18E-01	8.78E-01	8.25E-01	7.75E-01	7.25E-01	6.62E-01	6.03E-01	5.15E-01
4.5	9.83E-01	9.49E-01	9.02E-01	8.55E-01	7.94E-01	7.38E-01	6.82E-01	6.13E-01	5.49E-01	4.57E-01
5.0	9.80E-01	9.40E-01	8.87E-01	8.34E-01	7.66E-01	7.03E-01	6.42E-01	5.67E-01	5.00E-01	4.05E-01
5.5	9.77E-01	9.32E-01	8.72E-01	8.13E-01	7.38E-01	6.69E-01	6.04E-01	5.25E-01	4.55E-01	3.59E-01
6.0	9.74E-01	9.23E-01	8.57E-01	7.93E-01	7.14E-01	6.40E-01	5.70E-01	4.87E-01	4.15E-01	3.20E-01
6.5	9.70E-01	9.14E-01	8.43E-01	7.75E-01	6.91E-01	6.15E-01	5.41E-01	4.55E-01	3.82E-01	2.87E-01
7.0	9.67E-01	9.07E-01	8.31E-01	7.59E-01	6.74E-01	5.93E-01	5.16E-01	4.27E-01	3.53E-01	2.60E-01
7.5	9.62E-01	8.99E-01	8.19E-01	7.45E-01	6.61E-01	5.76E-01	4.96E-01	4.05E-01	3.30E-01	2.37E-01
8.0	9.59E-01	8.93E-01	8.09E-01	7.34E-01	6.49E-01	5.63E-01	4.81E-01	3.87E-01	3.10E-01	2.18E-01
8.5	9.55E-01	8.85E-01	8.01E-01	7.25E-01	6.41E-01	5.52E-01	4.69E-01	3.74E-01	2.96E-01	2.03E-01
9.0	9.50E-01	8.79E-01	7.94E-01	7.18E-01	6.35E-01	5.44E-01	4.60E-01	3.63E-01	2.84E-01	1.92E-01
9.5	9.46E-01	8.74E-01	7.88E-01	7.13E-01	6.30E-01	5.38E-01	4.52E-01	3.54E-01	2.75E-01	1.82E-01
10.0	9.41E-01	8.68E-01	7.82E-01	7.08E-01	6.26E-01	5.33E-01	4.45E-01	3.47E-01	2.67E-01	1.74E-01
Energy (MeV)	$\phi(\text{TAM} \leftarrow \text{TBE})$									
	Cellularity									
	100%	90%	80%	70%	60%	50%	40%	30%	20%	10%
3.0	2.62E-01	2.38E-01	2.10E-01	1.87E-01	1.64E-01	1.35E-01	1.09E-01	7.79E-02	5.42E-02	2.70E-02
3.5	3.01E-01	2.72E-01	2.42E-01	2.15E-01	1.88E-01	1.54E-01	1.24E-01	8.94E-02	6.14E-02	3.09E-02
4.0	3.30E-01	2.98E-01	2.66E-01	2.37E-01	2.06E-01	1.70E-01	1.36E-01	9.80E-02	6.80E-02	3.38E-02
4.5	3.52E-01	3.20E-01	2.84E-01	2.52E-01	2.21E-01	1.81E-01	1.46E-01	1.05E-01	7.24E-02	3.62E-02
5.0	3.72E-01	3.36E-01	2.99E-01	2.66E-01	2.32E-01	1.92E-01	1.53E-01	1.11E-01	7.60E-02	3.84E-02
5.5	3.87E-01	3.52E-01	3.12E-01	2.77E-01	2.42E-01	2.00E-01	1.61E-01	1.15E-01	7.99E-02	3.99E-02
6.0	4.00E-01	3.62E-01	3.21E-01	2.86E-01	2.50E-01	2.07E-01	1.65E-01	1.19E-01	8.22E-02	4.13E-02
6.5	4.12E-01	3.73E-01	3.32E-01	2.95E-01	2.57E-01	2.12E-01	1.70E-01	1.22E-01	8.45E-02	4.23E-02
7.0	4.21E-01	3.81E-01	3.39E-01	3.01E-01	2.63E-01	2.17E-01	1.74E-01	1.25E-01	8.63E-02	4.31E-02
7.5	4.29E-01	3.89E-01	3.45E-01	3.08E-01	2.69E-01	2.22E-01	1.78E-01	1.28E-01	8.84E-02	4.42E-02
8.0	4.39E-01	3.98E-01	3.53E-01	3.14E-01	2.74E-01	2.26E-01	1.81E-01	1.30E-01	9.01E-02	4.50E-02
8.5	4.45E-01	4.05E-01	3.59E-01	3.19E-01	2.78E-01	2.29E-01	1.84E-01	1.33E-01	9.16E-02	4.60E-02
9.0	4.53E-01	4.10E-01	3.64E-01	3.24E-01	2.83E-01	2.33E-01	1.87E-01	1.35E-01	9.29E-02	4.64E-02
9.5	4.60E-01	4.17E-01	3.69E-01	3.30E-01	2.86E-01	2.37E-01	1.90E-01	1.36E-01	9.42E-02	4.72E-02
10.0	4.66E-01	4.23E-01	3.75E-01	3.35E-01	2.92E-01	2.41E-01	1.93E-01	1.39E-01	9.56E-02	4.79E-02

TABLE 8B (Continued)

Energy (MeV)	Lumbar Vertebrae									
	$\phi(\text{TAM} \leftarrow \text{TBS})$									
	Cellularity									
	100%	90%	80%	70%	60%	50%	40%	30%	20%	10%
3.0	5.91E-02	5.34E-02	4.76E-02	4.25E-02	3.70E-02	3.07E-02	2.44E-02	1.77E-02	1.21E-02	6.16E-03
3.5	1.05E-01	9.46E-02	8.41E-02	7.50E-02	6.52E-02	5.40E-02	4.31E-02	3.10E-02	2.15E-02	1.07E-02
4.0	1.46E-01	1.33E-01	1.18E-01	1.05E-01	9.18E-02	7.55E-02	6.11E-02	4.37E-02	3.04E-02	1.52E-02
4.5	1.84E-01	1.67E-01	1.48E-01	1.32E-01	1.15E-01	9.48E-02	7.60E-02	5.48E-02	3.83E-02	1.89E-02
5.0	2.16E-01	1.96E-01	1.74E-01	1.55E-01	1.35E-01	1.12E-01	8.96E-02	6.45E-02	4.45E-02	2.21E-02
5.5	2.42E-01	2.19E-01	1.95E-01	1.74E-01	1.52E-01	1.26E-01	1.01E-01	7.24E-02	5.02E-02	2.49E-02
6.0	2.63E-01	2.39E-01	2.12E-01	1.89E-01	1.65E-01	1.37E-01	1.10E-01	7.90E-02	5.42E-02	2.73E-02
6.5	2.82E-01	2.56E-01	2.28E-01	2.03E-01	1.77E-01	1.47E-01	1.18E-01	8.42E-02	5.84E-02	2.93E-02
7.0	2.99E-01	2.71E-01	2.42E-01	2.15E-01	1.88E-01	1.56E-01	1.25E-01	8.95E-02	6.24E-02	3.11E-02
7.5	3.16E-01	2.86E-01	2.55E-01	2.27E-01	1.98E-01	1.64E-01	1.31E-01	9.50E-02	6.55E-02	3.28E-02
8.0	3.30E-01	2.99E-01	2.66E-01	2.37E-01	2.07E-01	1.71E-01	1.38E-01	9.88E-02	6.80E-02	3.41E-02
8.5	3.42E-01	3.10E-01	2.76E-01	2.47E-01	2.15E-01	1.78E-01	1.42E-01	1.03E-01	7.09E-02	3.53E-02
9.0	3.54E-01	3.21E-01	2.86E-01	2.55E-01	2.22E-01	1.84E-01	1.47E-01	1.06E-01	7.31E-02	3.66E-02
9.5	3.66E-01	3.32E-01	2.95E-01	2.63E-01	2.30E-01	1.90E-01	1.53E-01	1.09E-01	7.56E-02	3.75E-02
10.0	3.76E-01	3.42E-01	3.03E-01	2.70E-01	2.36E-01	1.95E-01	1.57E-01	1.13E-01	7.79E-02	3.89E-02
Energy (MeV)	$\phi(\text{TAM} \leftarrow \text{TBV})$									
	Cellularity									
	100%	90%	80%	70%	60%	50%	40%	30%	20%	10%
3.0	9.75E-04	8.49E-04	7.90E-04	6.99E-04	6.09E-04	5.09E-04	3.91E-04	3.10E-04	1.97E-04	1.03E-04
3.5	2.52E-03	2.32E-03	2.09E-03	1.85E-03	1.61E-03	1.31E-03	1.08E-03	7.68E-04	5.25E-04	2.53E-04
4.0	5.24E-03	4.73E-03	4.14E-03	3.72E-03	3.19E-03	2.64E-03	2.14E-03	1.57E-03	1.07E-03	5.51E-04
4.5	8.96E-03	8.11E-03	7.11E-03	6.34E-03	5.51E-03	4.58E-03	3.59E-03	2.62E-03	1.81E-03	9.05E-04
5.0	1.36E-02	1.22E-02	1.08E-02	9.58E-03	8.36E-03	7.06E-03	5.59E-03	4.00E-03	2.81E-03	1.43E-03
5.5	1.90E-02	1.72E-02	1.54E-02	1.35E-02	1.19E-02	9.82E-03	7.93E-03	5.71E-03	3.90E-03	1.94E-03
6.0	2.53E-02	2.30E-02	2.03E-02	1.81E-02	1.59E-02	1.31E-02	1.05E-02	7.55E-03	5.22E-03	2.63E-03
6.5	3.23E-02	2.95E-02	2.62E-02	2.35E-02	2.03E-02	1.69E-02	1.36E-02	9.64E-03	6.75E-03	3.36E-03
7.0	3.97E-02	3.64E-02	3.24E-02	2.88E-02	2.52E-02	2.06E-02	1.67E-02	1.20E-02	8.37E-03	4.18E-03
7.5	4.86E-02	4.40E-02	3.93E-02	3.48E-02	3.05E-02	2.53E-02	2.02E-02	1.46E-02	1.00E-02	5.04E-03
8.0	5.76E-02	5.24E-02	4.66E-02	4.16E-02	3.62E-02	2.99E-02	2.41E-02	1.72E-02	1.18E-02	6.05E-03
8.5	6.71E-02	6.10E-02	5.42E-02	4.83E-02	4.21E-02	3.46E-02	2.81E-02	2.02E-02	1.40E-02	7.06E-03
9.0	7.74E-02	7.07E-02	6.29E-02	5.61E-02	4.87E-02	4.03E-02	3.23E-02	2.33E-02	1.59E-02	8.01E-03
9.5	8.87E-02	8.02E-02	7.13E-02	6.39E-02	5.55E-02	4.62E-02	3.69E-02	2.66E-02	1.82E-02	9.24E-03
10.0	9.98E-02	9.10E-02	8.05E-02	7.17E-02	6.27E-02	5.19E-02	4.14E-02	2.99E-02	2.06E-02	1.04E-02

TABLE 9B

Absorbed Fractions to Active Bone Marrow (TAM) for α -Emissions Within
Parietal Bone of Leeds 44-Year Male for Various Source Tissues and Marrow Cellularities

Energy (MeV)	Parietal Bone $\phi(\text{TAM} \leftarrow \text{TAM})$									
	Cellularity									
	100%	90%	80%	70%	60%	50%	40%	30%	20%	10%
3.0	9.61E-01	9.43E-01	9.18E-01	8.92E-01	8.57E-01	8.23E-01	7.89E-01	7.44E-01	6.98E-01	6.28E-01
3.5	9.52E-01	9.30E-01	8.99E-01	8.67E-01	8.24E-01	7.84E-01	7.42E-01	6.89E-01	6.37E-01	5.60E-01
4.0	9.43E-01	9.16E-01	8.79E-01	8.41E-01	7.91E-01	7.44E-01	6.96E-01	6.37E-01	5.81E-01	4.96E-01
4.5	9.34E-01	9.01E-01	8.58E-01	8.14E-01	7.57E-01	7.04E-01	6.51E-01	5.86E-01	5.25E-01	4.39E-01
5.0	9.24E-01	8.87E-01	8.38E-01	7.88E-01	7.24E-01	6.66E-01	6.09E-01	5.39E-01	4.76E-01	3.87E-01
5.5	9.14E-01	8.72E-01	8.17E-01	7.63E-01	6.93E-01	6.30E-01	5.70E-01	4.96E-01	4.31E-01	3.42E-01
6.0	9.02E-01	8.57E-01	7.97E-01	7.39E-01	6.66E-01	5.98E-01	5.35E-01	4.58E-01	3.92E-01	3.04E-01
6.5	8.92E-01	8.42E-01	7.77E-01	7.15E-01	6.41E-01	5.70E-01	5.04E-01	4.24E-01	3.58E-01	2.71E-01
7.0	8.80E-01	8.26E-01	7.59E-01	6.95E-01	6.19E-01	5.47E-01	4.78E-01	3.97E-01	3.30E-01	2.44E-01
7.5	8.68E-01	8.12E-01	7.42E-01	6.77E-01	6.02E-01	5.26E-01	4.56E-01	3.74E-01	3.06E-01	2.22E-01
8.0	8.56E-01	7.98E-01	7.26E-01	6.61E-01	5.87E-01	5.10E-01	4.38E-01	3.55E-01	2.87E-01	2.04E-01
8.5	8.43E-01	7.84E-01	7.11E-01	6.48E-01	5.75E-01	4.97E-01	4.24E-01	3.40E-01	2.72E-01	1.89E-01
9.0	8.30E-01	7.71E-01	6.99E-01	6.35E-01	5.64E-01	4.86E-01	4.12E-01	3.27E-01	2.59E-01	1.77E-01
9.5	8.17E-01	7.58E-01	6.87E-01	6.24E-01	5.55E-01	4.77E-01	4.02E-01	3.18E-01	2.49E-01	1.67E-01
10.0	8.03E-01	7.46E-01	6.75E-01	6.14E-01	5.47E-01	4.68E-01	3.93E-01	3.08E-01	2.39E-01	1.59E-01
Energy (MeV)	$\phi(\text{TAM} \leftarrow \text{TBE})$									
	Cellularity									
	100%	90%	80%	70%	60%	50%	40%	30%	20%	10%
3.0	2.62E-01	2.37E-01	2.11E-01	1.88E-01	1.64E-01	1.35E-01	1.08E-01	7.77E-02	5.37E-02	2.70E-02
3.5	3.00E-01	2.73E-01	2.42E-01	2.15E-01	1.88E-01	1.55E-01	1.24E-01	8.94E-02	6.19E-02	3.09E-02
4.0	3.30E-01	2.99E-01	2.65E-01	2.36E-01	2.06E-01	1.70E-01	1.36E-01	9.82E-02	6.78E-02	3.40E-02
4.5	3.52E-01	3.19E-01	2.83E-01	2.52E-01	2.20E-01	1.81E-01	1.46E-01	1.05E-01	7.27E-02	3.63E-02
5.0	3.69E-01	3.35E-01	2.97E-01	2.64E-01	2.31E-01	1.91E-01	1.53E-01	1.10E-01	7.58E-02	3.80E-02
5.5	3.84E-01	3.47E-01	3.08E-01	2.75E-01	2.40E-01	1.98E-01	1.59E-01	1.14E-01	7.89E-02	3.95E-02
6.0	3.93E-01	3.57E-01	3.18E-01	2.82E-01	2.46E-01	2.03E-01	1.64E-01	1.18E-01	8.13E-02	4.06E-02
6.5	4.03E-01	3.66E-01	3.25E-01	2.89E-01	2.54E-01	2.09E-01	1.67E-01	1.21E-01	8.35E-02	4.16E-02
7.0	4.12E-01	3.74E-01	3.32E-01	2.95E-01	2.58E-01	2.14E-01	1.71E-01	1.23E-01	8.50E-02	4.25E-02
7.5	4.19E-01	3.81E-01	3.38E-01	3.01E-01	2.63E-01	2.17E-01	1.74E-01	1.25E-01	8.65E-02	4.34E-02
8.0	4.26E-01	3.87E-01	3.44E-01	3.06E-01	2.68E-01	2.20E-01	1.77E-01	1.27E-01	8.80E-02	4.41E-02
8.5	4.33E-01	3.92E-01	3.49E-01	3.12E-01	2.72E-01	2.24E-01	1.80E-01	1.29E-01	8.93E-02	4.46E-02
9.0	4.39E-01	3.98E-01	3.53E-01	3.16E-01	2.75E-01	2.27E-01	1.82E-01	1.31E-01	9.06E-02	4.53E-02
9.5	4.45E-01	4.04E-01	3.58E-01	3.20E-01	2.78E-01	2.30E-01	1.84E-01	1.32E-01	9.15E-02	4.58E-02
10.0	4.50E-01	4.08E-01	3.63E-01	3.24E-01	2.83E-01	2.32E-01	1.87E-01	1.34E-01	9.24E-02	4.61E-02

TABLE 9B (Continued)

Energy (MeV)	Parietal Bone $\phi(\text{TAM} \leftarrow \text{TBS})$									
	Cellularity									
	100%	90%	80%	70%	60%	50%	40%	30%	20%	10%
3.0	5.98E-02	5.43E-02	4.80E-02	4.28E-02	3.71E-02	3.08E-02	2.47E-02	1.78E-02	1.22E-02	6.15E-03
3.5	1.03E-01	9.32E-02	8.29E-02	7.40E-02	6.42E-02	5.33E-02	4.25E-02	3.06E-02	2.11E-02	1.05E-02
4.0	1.43E-01	1.30E-01	1.16E-01	1.03E-01	8.98E-02	7.40E-02	5.93E-02	4.26E-02	2.95E-02	1.48E-02
4.5	1.78E-01	1.61E-01	1.43E-01	1.27E-01	1.11E-01	9.18E-02	7.31E-02	5.33E-02	3.66E-02	1.86E-02
5.0	2.05E-01	1.85E-01	1.66E-01	1.47E-01	1.28E-01	1.06E-01	8.56E-02	6.16E-02	4.24E-02	2.14E-02
5.5	2.24E-01	2.04E-01	1.81E-01	1.62E-01	1.42E-01	1.17E-01	9.42E-02	6.75E-02	4.69E-02	2.34E-02
6.0	2.39E-01	2.18E-01	1.94E-01	1.73E-01	1.52E-01	1.26E-01	1.01E-01	7.30E-02	5.04E-02	2.54E-02
6.5	2.54E-01	2.30E-01	2.05E-01	1.83E-01	1.60E-01	1.33E-01	1.07E-01	7.68E-02	5.35E-02	2.68E-02
7.0	2.66E-01	2.42E-01	2.16E-01	1.93E-01	1.69E-01	1.40E-01	1.13E-01	8.09E-02	5.60E-02	2.80E-02
7.5	2.78E-01	2.52E-01	2.25E-01	2.00E-01	1.76E-01	1.46E-01	1.17E-01	8.49E-02	5.85E-02	2.92E-02
8.0	2.88E-01	2.62E-01	2.33E-01	2.08E-01	1.83E-01	1.51E-01	1.21E-01	8.77E-02	6.05E-02	3.02E-02
8.5	2.96E-01	2.70E-01	2.41E-01	2.15E-01	1.89E-01	1.56E-01	1.25E-01	9.05E-02	6.22E-02	3.12E-02
9.0	3.04E-01	2.78E-01	2.47E-01	2.22E-01	1.94E-01	1.60E-01	1.29E-01	9.28E-02	6.42E-02	3.18E-02
9.5	3.12E-01	2.85E-01	2.54E-01	2.28E-01	1.99E-01	1.64E-01	1.32E-01	9.50E-02	6.53E-02	3.27E-02
10.0	3.20E-01	2.91E-01	2.60E-01	2.33E-01	2.03E-01	1.68E-01	1.35E-01	9.74E-02	6.70E-02	3.34E-02
Energy (MeV)	$\phi(\text{TAM} \leftarrow \text{TBV})$									
	Cellularity									
	100%	90%	80%	70%	60%	50%	40%	30%	20%	10%
3.0	4.94E-04	4.54E-04	4.07E-04	3.72E-04	3.72E-04	2.48E-04	2.15E-04	1.49E-04	1.06E-04	5.40E-05
3.5	1.25E-03	1.16E-03	1.01E-03	9.07E-04	9.07E-04	6.52E-04	5.25E-04	3.55E-04	2.61E-04	1.48E-04
4.0	2.49E-03	2.25E-03	2.00E-03	1.82E-03	1.82E-03	1.26E-03	1.04E-03	7.62E-04	5.07E-04	2.40E-04
4.5	4.30E-03	3.82E-03	3.48E-03	3.04E-03	3.04E-03	2.16E-03	1.72E-03	1.29E-03	8.34E-04	4.29E-04
5.0	6.37E-03	5.78E-03	5.07E-03	4.61E-03	4.61E-03	3.33E-03	2.64E-03	1.91E-03	1.30E-03	6.57E-04
5.5	8.87E-03	8.01E-03	7.25E-03	6.33E-03	6.33E-03	4.63E-03	3.74E-03	2.64E-03	1.78E-03	9.01E-04
6.0	1.18E-02	1.07E-02	9.38E-03	8.55E-03	8.55E-03	6.16E-03	4.87E-03	3.52E-03	2.39E-03	1.26E-03
6.5	1.48E-02	1.35E-02	1.21E-02	1.07E-02	1.07E-02	7.66E-03	6.24E-03	4.52E-03	3.03E-03	1.56E-03
7.0	1.83E-02	1.67E-02	1.49E-02	1.33E-02	1.33E-02	9.59E-03	7.67E-03	5.55E-03	3.81E-03	1.90E-03
7.5	2.19E-02	1.98E-02	1.77E-02	1.59E-02	1.59E-02	1.15E-02	9.20E-03	6.65E-03	4.64E-03	2.35E-03
8.0	2.58E-02	2.37E-02	2.11E-02	1.89E-02	1.89E-02	1.37E-02	1.09E-02	7.83E-03	5.46E-03	2.74E-03
8.5	3.02E-02	2.75E-02	2.47E-02	2.19E-02	2.19E-02	1.57E-02	1.26E-02	9.31E-03	6.36E-03	3.19E-03
9.0	3.47E-02	3.16E-02	2.80E-02	2.51E-02	2.51E-02	1.82E-02	1.45E-02	1.05E-02	7.26E-03	3.62E-03
9.5	3.94E-02	3.57E-02	3.17E-02	2.87E-02	2.87E-02	2.07E-02	1.67E-02	1.19E-02	8.23E-03	4.04E-03
10.0	4.43E-02	4.03E-02	3.57E-02	3.20E-02	3.20E-02	2.33E-02	1.87E-02	1.35E-02	9.37E-03	4.65E-03

TABLE 10B

Absorbed Fractions to Active Bone Marrow (TAM) for α -Emissions Within
Ribs of Leeds 44-Year Male for Various Source Tissues and Marrow Cellularities

Energy (MeV)	Ribs									
	$\phi(\text{TAM} \leftarrow \text{TAM})$									
	Cellularity									
	100%	90%	80%	70%	60%	50%	40%	30%	20%	10%
3.0	9.93E-01	9.74E-01	9.49E-01	9.22E-01	8.85E-01	8.50E-01	8.13E-01	7.66E-01	7.20E-01	6.46E-01
3.5	9.91E-01	9.68E-01	9.36E-01	9.02E-01	8.57E-01	8.14E-01	7.71E-01	7.15E-01	6.61E-01	5.79E-01
4.0	9.90E-01	9.61E-01	9.22E-01	8.81E-01	8.28E-01	7.78E-01	7.27E-01	6.65E-01	6.06E-01	5.16E-01
4.5	9.88E-01	9.53E-01	9.07E-01	8.59E-01	7.99E-01	7.42E-01	6.85E-01	6.16E-01	5.52E-01	4.58E-01
5.0	9.86E-01	9.46E-01	8.93E-01	8.38E-01	7.70E-01	7.07E-01	6.45E-01	5.70E-01	5.02E-01	4.07E-01
5.5	9.84E-01	9.38E-01	8.78E-01	8.18E-01	7.43E-01	6.74E-01	6.07E-01	5.27E-01	4.58E-01	3.61E-01
6.0	9.81E-01	9.30E-01	8.63E-01	7.98E-01	7.18E-01	6.45E-01	5.74E-01	4.90E-01	4.18E-01	3.23E-01
6.5	9.79E-01	9.23E-01	8.50E-01	7.81E-01	6.97E-01	6.19E-01	5.45E-01	4.58E-01	3.84E-01	2.89E-01
7.0	9.76E-01	9.15E-01	8.38E-01	7.65E-01	6.80E-01	5.98E-01	5.21E-01	4.31E-01	3.55E-01	2.61E-01
7.5	9.73E-01	9.09E-01	8.28E-01	7.53E-01	6.67E-01	5.81E-01	5.00E-01	4.09E-01	3.32E-01	2.38E-01
8.0	9.71E-01	9.03E-01	8.19E-01	7.43E-01	6.56E-01	5.68E-01	4.86E-01	3.91E-01	3.13E-01	2.20E-01
8.5	9.68E-01	8.98E-01	8.12E-01	7.35E-01	6.49E-01	5.59E-01	4.74E-01	3.77E-01	2.99E-01	2.05E-01
9.0	9.65E-01	8.92E-01	8.05E-01	7.28E-01	6.43E-01	5.51E-01	4.66E-01	3.67E-01	2.87E-01	1.93E-01
9.5	9.62E-01	8.87E-01	8.00E-01	7.23E-01	6.39E-01	5.45E-01	4.58E-01	3.59E-01	2.78E-01	1.84E-01
10.0	9.58E-01	8.84E-01	7.95E-01	7.19E-01	6.35E-01	5.40E-01	4.52E-01	3.51E-01	2.70E-01	1.76E-01
Energy (MeV)	$\phi(\text{TAM} \leftarrow \text{TBE})$									
	Cellularity									
	100%	90%	80%	70%	60%	50%	40%	30%	20%	10%
3.0	2.62E-01	2.37E-01	2.11E-01	1.88E-01	1.64E-01	1.35E-01	1.08E-01	7.78E-02	5.39E-02	2.73E-02
3.5	3.01E-01	2.72E-01	2.41E-01	2.15E-01	1.88E-01	1.55E-01	1.25E-01	8.94E-02	6.18E-02	3.10E-02
4.0	3.30E-01	2.98E-01	2.65E-01	2.37E-01	2.06E-01	1.70E-01	1.36E-01	9.84E-02	6.78E-02	3.39E-02
4.5	3.53E-01	3.19E-01	2.84E-01	2.53E-01	2.20E-01	1.82E-01	1.47E-01	1.05E-01	7.26E-02	3.63E-02
5.0	3.72E-01	3.36E-01	2.99E-01	2.66E-01	2.32E-01	1.92E-01	1.54E-01	1.11E-01	7.65E-02	3.85E-02
5.5	3.88E-01	3.52E-01	3.12E-01	2.79E-01	2.43E-01	2.00E-01	1.60E-01	1.16E-01	8.03E-02	4.02E-02
6.0	4.01E-01	3.64E-01	3.23E-01	2.88E-01	2.51E-01	2.07E-01	1.66E-01	1.19E-01	8.25E-02	4.13E-02
6.5	4.12E-01	3.74E-01	3.32E-01	2.96E-01	2.58E-01	2.13E-01	1.71E-01	1.23E-01	8.49E-02	4.25E-02
7.0	4.23E-01	3.84E-01	3.41E-01	3.02E-01	2.64E-01	2.18E-01	1.75E-01	1.26E-01	8.64E-02	4.36E-02
7.5	4.34E-01	3.93E-01	3.49E-01	3.10E-01	2.70E-01	2.23E-01	1.80E-01	1.29E-01	8.90E-02	4.45E-02
8.0	4.43E-01	4.02E-01	3.56E-01	3.17E-01	2.77E-01	2.28E-01	1.83E-01	1.32E-01	9.10E-02	4.56E-02
8.5	4.52E-01	4.10E-01	3.63E-01	3.24E-01	2.83E-01	2.32E-01	1.87E-01	1.34E-01	9.29E-02	4.65E-02
9.0	4.61E-01	4.18E-01	3.71E-01	3.31E-01	2.88E-01	2.37E-01	1.90E-01	1.37E-01	9.48E-02	4.73E-02
9.5	4.69E-01	4.24E-01	3.78E-01	3.35E-01	2.93E-01	2.42E-01	1.93E-01	1.39E-01	9.61E-02	4.82E-02
10.0	4.77E-01	4.32E-01	3.84E-01	3.42E-01	2.98E-01	2.45E-01	1.96E-01	1.41E-01	9.77E-02	4.90E-02

TABLE 10B (Continued)

Energy (MeV)	Ribs									
	$\phi(\text{TAM} \leftarrow \text{TBS})$									
	Cellularity									
	100%	90%	80%	70%	60%	50%	40%	30%	20%	10%
3.0	5.83E-02	5.27E-02	4.70E-02	4.20E-02	3.65E-02	2.99E-02	2.42E-02	1.74E-02	1.19E-02	6.00E-03
3.5	1.03E-01	9.35E-02	8.32E-02	7.40E-02	6.48E-02	5.34E-02	4.29E-02	3.09E-02	2.12E-02	1.06E-02
4.0	1.46E-01	1.32E-01	1.18E-01	1.04E-01	9.13E-02	7.56E-02	6.03E-02	4.34E-02	2.98E-02	1.51E-02
4.5	1.84E-01	1.66E-01	1.48E-01	1.32E-01	1.14E-01	9.48E-02	7.59E-02	5.46E-02	3.76E-02	1.89E-02
5.0	2.16E-01	1.96E-01	1.74E-01	1.54E-01	1.35E-01	1.11E-01	8.96E-02	6.43E-02	4.45E-02	2.24E-02
5.5	2.42E-01	2.20E-01	1.95E-01	1.74E-01	1.52E-01	1.26E-01	1.01E-01	7.22E-02	5.02E-02	2.52E-02
6.0	2.64E-01	2.40E-01	2.13E-01	1.90E-01	1.66E-01	1.37E-01	1.10E-01	7.93E-02	5.48E-02	2.75E-02
6.5	2.83E-01	2.57E-01	2.29E-01	2.04E-01	1.78E-01	1.47E-01	1.18E-01	8.51E-02	5.89E-02	2.94E-02
7.0	3.02E-01	2.74E-01	2.44E-01	2.17E-01	1.90E-01	1.57E-01	1.25E-01	9.08E-02	6.26E-02	3.13E-02
7.5	3.20E-01	2.90E-01	2.58E-01	2.30E-01	2.01E-01	1.65E-01	1.33E-01	9.63E-02	6.60E-02	3.31E-02
8.0	3.36E-01	3.05E-01	2.71E-01	2.42E-01	2.11E-01	1.74E-01	1.40E-01	1.01E-01	6.95E-02	3.49E-02
8.5	3.50E-01	3.17E-01	2.82E-01	2.51E-01	2.20E-01	1.82E-01	1.45E-01	1.05E-01	7.22E-02	3.63E-02
9.0	3.64E-01	3.29E-01	2.94E-01	2.61E-01	2.28E-01	1.89E-01	1.51E-01	1.09E-01	7.52E-02	3.77E-02
9.5	3.75E-01	3.42E-01	3.03E-01	2.71E-01	2.36E-01	1.95E-01	1.56E-01	1.13E-01	7.77E-02	3.88E-02
10.0	3.88E-01	3.52E-01	3.13E-01	2.79E-01	2.43E-01	2.01E-01	1.61E-01	1.16E-01	8.00E-02	4.01E-02
Energy (MeV)	$\phi(\text{TAM} \leftarrow \text{TBV})$									
	Cellularity									
	100%	90%	80%	70%	60%	50%	40%	30%	20%	10%
3.0	8.84E-04	7.99E-04	7.15E-04	6.46E-04	5.49E-04	4.46E-04	3.63E-04	2.74E-04	1.71E-04	8.50E-05
3.5	2.35E-03	2.13E-03	1.88E-03	1.68E-03	1.44E-03	1.23E-03	9.81E-04	7.11E-04	4.98E-04	2.50E-04
4.0	4.79E-03	4.33E-03	3.88E-03	3.50E-03	3.01E-03	2.44E-03	2.00E-03	1.44E-03	9.89E-04	4.80E-04
4.5	8.02E-03	7.48E-03	6.57E-03	5.89E-03	5.11E-03	4.25E-03	3.39E-03	2.41E-03	1.75E-03	8.55E-04
5.0	1.26E-02	1.15E-02	9.95E-03	9.03E-03	7.83E-03	6.47E-03	5.12E-03	3.78E-03	2.60E-03	1.31E-03
5.5	1.75E-02	1.59E-02	1.41E-02	1.26E-02	1.09E-02	9.05E-03	7.29E-03	5.22E-03	3.57E-03	1.80E-03
6.0	2.34E-02	2.12E-02	1.90E-02	1.69E-02	1.47E-02	1.21E-02	9.79E-03	7.01E-03	4.75E-03	2.42E-03
6.5	2.97E-02	2.71E-02	2.42E-02	2.15E-02	1.87E-02	1.55E-02	1.25E-02	8.90E-03	6.19E-03	3.11E-03
7.0	3.69E-02	3.35E-02	2.99E-02	2.65E-02	2.33E-02	1.92E-02	1.54E-02	1.11E-02	7.65E-03	3.77E-03
7.5	4.47E-02	4.08E-02	3.61E-02	3.21E-02	2.80E-02	2.32E-02	1.87E-02	1.34E-02	9.19E-03	4.69E-03
8.0	5.29E-02	4.83E-02	4.29E-02	3.79E-02	3.32E-02	2.76E-02	2.19E-02	1.59E-02	1.10E-02	5.43E-03
8.5	6.15E-02	5.59E-02	4.97E-02	4.44E-02	3.87E-02	3.19E-02	2.58E-02	1.85E-02	1.29E-02	6.40E-03
9.0	7.08E-02	6.43E-02	5.72E-02	5.09E-02	4.44E-02	3.68E-02	2.93E-02	2.12E-02	1.46E-02	7.43E-03
9.5	8.03E-02	7.31E-02	6.49E-02	5.80E-02	5.04E-02	4.17E-02	3.35E-02	2.42E-02	1.66E-02	8.38E-03
10.0	9.07E-02	8.22E-02	7.33E-02	6.53E-02	5.72E-02	4.71E-02	3.77E-02	2.71E-02	1.88E-02	9.46E-03

TABLE 11B

Absorbed Fractions to TBE from α -Emissions Within TAM of Leeds 44-Year Male
Within Various Skeletal Sites and as Function of Marrow Cellularity

Energy (MeV)	$\phi(\text{TBE} \leftarrow \text{TAM})$									
	Cervical Vertebrae									
	Cellularity									
	100%	90%	80%	70%	60%	50%	40%	30%	20%	10%
3.0	1.29E-02	1.29E-02	1.25E-02	1.23E-02	1.21E-02	1.19E-02	1.15E-02	1.11E-02	1.07E-02	1.01E-02
3.5	1.53E-02	1.49E-02	1.49E-02	1.47E-02	1.41E-02	1.35E-02	1.30E-02	1.24E-02	1.19E-02	1.09E-02
4.0	1.74E-02	1.71E-02	1.68E-02	1.61E-02	1.53E-02	1.49E-02	1.43E-02	1.33E-02	1.27E-02	1.15E-02
4.5	1.90E-02	1.87E-02	1.81E-02	1.73E-02	1.67E-02	1.59E-02	1.49E-02	1.38E-02	1.31E-02	1.15E-02
5.0	2.06E-02	2.00E-02	1.92E-02	1.82E-02	1.71E-02	1.63E-02	1.53E-02	1.41E-02	1.29E-02	1.14E-02
5.5	2.20E-02	2.11E-02	2.02E-02	1.91E-02	1.77E-02	1.66E-02	1.54E-02	1.42E-02	1.27E-02	1.09E-02
6.0	2.32E-02	2.23E-02	2.11E-02	1.97E-02	1.80E-02	1.70E-02	1.55E-02	1.36E-02	1.24E-02	1.04E-02
6.5	2.44E-02	2.31E-02	2.19E-02	2.01E-02	1.84E-02	1.69E-02	1.55E-02	1.36E-02	1.20E-02	1.00E-02
7.0	2.57E-02	2.44E-02	2.25E-02	2.10E-02	1.89E-02	1.68E-02	1.51E-02	1.32E-02	1.17E-02	9.36E-03
7.5	2.71E-02	2.54E-02	2.34E-02	2.12E-02	1.87E-02	1.68E-02	1.51E-02	1.29E-02	1.13E-02	8.94E-03
8.0	2.84E-02	2.63E-02	2.40E-02	2.15E-02	1.89E-02	1.68E-02	1.49E-02	1.25E-02	1.08E-02	8.55E-03
8.5	2.93E-02	2.73E-02	2.44E-02	2.17E-02	1.87E-02	1.65E-02	1.43E-02	1.21E-02	1.03E-02	8.09E-03
9.0	3.05E-02	2.80E-02	2.48E-02	2.19E-02	1.88E-02	1.61E-02	1.41E-02	1.17E-02	9.99E-03	7.67E-03
9.5	3.14E-02	2.87E-02	2.51E-02	2.20E-02	1.83E-02	1.58E-02	1.35E-02	1.13E-02	9.51E-03	7.44E-03
10.0	3.22E-02	2.92E-02	2.53E-02	2.17E-02	1.83E-02	1.55E-02	1.33E-02	1.09E-02	9.14E-03	7.19E-03
Energy (MeV)	Femur Head									
	Cellularity									
	100%	90%	80%	70%	60%	50%	40%	30%	20%	10%
3.0	9.08E-03	8.99E-03	8.93E-03	8.64E-03	8.57E-03	8.35E-03	8.04E-03	7.83E-03	7.36E-03	6.90E-03
3.5	1.11E-02	1.07E-02	1.05E-02	1.02E-02	1.00E-02	9.68E-03	9.28E-03	8.77E-03	8.43E-03	7.74E-03
4.0	1.26E-02	1.23E-02	1.19E-02	1.16E-02	1.12E-02	1.07E-02	1.02E-02	9.71E-03	9.13E-03	8.14E-03
4.5	1.40E-02	1.37E-02	1.32E-02	1.27E-02	1.22E-02	1.17E-02	1.09E-02	1.04E-02	9.46E-03	8.35E-03
5.0	1.54E-02	1.50E-02	1.43E-02	1.35E-02	1.27E-02	1.22E-02	1.13E-02	1.03E-02	9.58E-03	8.25E-03
5.5	1.64E-02	1.59E-02	1.50E-02	1.43E-02	1.33E-02	1.26E-02	1.14E-02	1.05E-02	9.48E-03	7.96E-03
6.0	1.78E-02	1.68E-02	1.59E-02	1.51E-02	1.38E-02	1.27E-02	1.17E-02	1.04E-02	9.24E-03	7.76E-03
6.5	1.88E-02	1.79E-02	1.66E-02	1.56E-02	1.40E-02	1.27E-02	1.16E-02	1.03E-02	9.18E-03	7.48E-03
7.0	1.97E-02	1.87E-02	1.73E-02	1.58E-02	1.42E-02	1.29E-02	1.17E-02	1.00E-02	8.72E-03	6.98E-03
7.5	2.07E-02	1.96E-02	1.79E-02	1.64E-02	1.44E-02	1.27E-02	1.13E-02	9.80E-03	8.44E-03	6.64E-03
8.0	2.20E-02	2.02E-02	1.85E-02	1.65E-02	1.43E-02	1.26E-02	1.10E-02	9.56E-03	8.05E-03	6.33E-03
8.5	2.27E-02	2.09E-02	1.89E-02	1.66E-02	1.43E-02	1.25E-02	1.08E-02	9.12E-03	7.78E-03	6.01E-03
9.0	2.35E-02	2.16E-02	1.92E-02	1.68E-02	1.44E-02	1.22E-02	1.05E-02	8.84E-03	7.37E-03	5.71E-03
9.5	2.45E-02	2.22E-02	1.93E-02	1.68E-02	1.43E-02	1.22E-02	1.02E-02	8.42E-03	7.18E-03	5.44E-03
10.0	2.51E-02	2.27E-02	1.94E-02	1.70E-02	1.39E-02	1.19E-02	1.00E-02	8.16E-03	6.85E-03	5.17E-03
Energy (MeV)	Femur Neck									
	Cellularity									
	100%	90%	80%	70%	60%	50%	40%	30%	20%	10%
3.0	6.51E-03	6.44E-03	6.23E-03	6.13E-03	6.12E-03	5.83E-03	5.75E-03	5.67E-03	5.29E-03	4.84E-03
3.5	7.67E-03	7.55E-03	7.36E-03	7.17E-03	7.01E-03	6.79E-03	6.65E-03	6.27E-03	6.03E-03	5.53E-03
4.0	8.80E-03	8.66E-03	8.48E-03	8.22E-03	7.88E-03	7.37E-03	7.25E-03	6.74E-03	6.38E-03	5.72E-03
4.5	9.80E-03	9.57E-03	9.27E-03	8.87E-03	8.61E-03	8.14E-03	7.66E-03	7.15E-03	6.68E-03	5.91E-03
5.0	1.08E-02	1.04E-02	1.00E-02	9.62E-03	8.89E-03	8.49E-03	8.00E-03	7.35E-03	6.57E-03	5.82E-03
5.5	1.15E-02	1.11E-02	1.04E-02	1.00E-02	9.27E-03	8.63E-03	8.00E-03	7.36E-03	6.60E-03	5.66E-03
6.0	1.21E-02	1.17E-02	1.11E-02	1.04E-02	9.49E-03	8.76E-03	8.11E-03	7.26E-03	6.51E-03	5.32E-03
6.5	1.30E-02	1.24E-02	1.15E-02	1.07E-02	9.69E-03	8.99E-03	8.04E-03	7.13E-03	6.33E-03	5.15E-03
7.0	1.37E-02	1.29E-02	1.20E-02	1.11E-02	9.86E-03	9.02E-03	7.99E-03	7.09E-03	6.19E-03	4.91E-03
7.5	1.45E-02	1.36E-02	1.25E-02	1.14E-02	1.00E-02	8.88E-03	7.87E-03	6.71E-03	5.96E-03	4.81E-03
8.0	1.53E-02	1.41E-02	1.28E-02	1.16E-02	1.01E-02	8.89E-03	7.96E-03	6.64E-03	5.62E-03	4.45E-03
8.5	1.58E-02	1.46E-02	1.33E-02	1.17E-02	1.02E-02	8.77E-03	7.72E-03	6.59E-03	5.52E-03	4.30E-03
9.0	1.63E-02	1.53E-02	1.35E-02	1.18E-02	9.97E-03	8.82E-03	7.59E-03	6.35E-03	5.30E-03	4.21E-03
9.5	1.71E-02	1.56E-02	1.37E-02	1.21E-02	1.00E-02	8.65E-03	7.47E-03	6.17E-03	5.13E-03	4.02E-03
10.0	1.77E-02	1.60E-02	1.38E-02	1.21E-02	9.99E-03	8.54E-03	7.23E-03	5.94E-03	5.04E-03	3.90E-03

TABLE 11B (Continued)

Energy (MeV)	$\phi(\text{TBE} \leftarrow \text{TAM})$									
	Iliac Crest									
	Cellularity									
	100%	90%	80%	70%	60%	50%	40%	30%	20%	10%
3.0	1.23E-02	1.21E-02	1.18E-02	1.17E-02	1.14E-02	1.11E-02	1.09E-02	1.06E-02	1.01E-02	9.33E-03
3.5	1.47E-02	1.45E-02	1.41E-02	1.39E-02	1.33E-02	1.30E-02	1.27E-02	1.18E-02	1.14E-02	1.04E-02
4.0	1.68E-02	1.65E-02	1.59E-02	1.56E-02	1.51E-02	1.43E-02	1.38E-02	1.29E-02	1.23E-02	1.09E-02
4.5	1.86E-02	1.84E-02	1.76E-02	1.70E-02	1.62E-02	1.53E-02	1.47E-02	1.37E-02	1.27E-02	1.11E-02
5.0	2.02E-02	1.98E-02	1.90E-02	1.80E-02	1.70E-02	1.59E-02	1.50E-02	1.38E-02	1.26E-02	1.11E-02
5.5	2.18E-02	2.11E-02	2.00E-02	1.89E-02	1.78E-02	1.65E-02	1.53E-02	1.38E-02	1.26E-02	1.08E-02
6.0	2.33E-02	2.24E-02	2.11E-02	2.00E-02	1.82E-02	1.68E-02	1.55E-02	1.39E-02	1.24E-02	1.03E-02
6.5	2.49E-02	2.38E-02	2.22E-02	2.05E-02	1.87E-02	1.72E-02	1.55E-02	1.37E-02	1.21E-02	9.80E-03
7.0	2.64E-02	2.48E-02	2.30E-02	2.11E-02	1.89E-02	1.72E-02	1.54E-02	1.34E-02	1.18E-02	9.48E-03
7.5	2.76E-02	2.62E-02	2.38E-02	2.19E-02	1.92E-02	1.69E-02	1.52E-02	1.29E-02	1.12E-02	9.04E-03
8.0	2.90E-02	2.70E-02	2.45E-02	2.22E-02	1.94E-02	1.70E-02	1.51E-02	1.29E-02	1.11E-02	8.57E-03
8.5	3.02E-02	2.82E-02	2.51E-02	2.25E-02	1.92E-02	1.69E-02	1.47E-02	1.25E-02	1.07E-02	8.24E-03
9.0	3.15E-02	2.87E-02	2.58E-02	2.26E-02	1.93E-02	1.67E-02	1.44E-02	1.20E-02	1.04E-02	8.04E-03
9.5	3.25E-02	2.97E-02	2.58E-02	2.25E-02	1.90E-02	1.64E-02	1.42E-02	1.17E-02	9.90E-03	7.70E-03
10.0	3.35E-02	3.02E-02	2.63E-02	2.27E-02	1.89E-02	1.59E-02	1.38E-02	1.14E-02	9.55E-03	7.54E-03
Energy (MeV)	Lumbar Vertebrae									
	Cellularity									
	100%	90%	80%	70%	60%	50%	40%	30%	20%	10%
3.0	9.11E-03	9.10E-03	8.85E-03	8.70E-03	8.47E-03	8.32E-03	8.13E-03	7.85E-03	7.53E-03	6.94E-03
3.5	1.10E-02	1.07E-02	1.05E-02	1.03E-02	9.95E-03	9.75E-03	9.25E-03	8.91E-03	8.35E-03	7.73E-03
4.0	1.23E-02	1.21E-02	1.18E-02	1.14E-02	1.11E-02	1.05E-02	1.01E-02	9.74E-03	9.07E-03	8.18E-03
4.5	1.37E-02	1.34E-02	1.31E-02	1.25E-02	1.20E-02	1.14E-02	1.06E-02	9.93E-03	9.42E-03	8.26E-03
5.0	1.47E-02	1.43E-02	1.39E-02	1.32E-02	1.25E-02	1.18E-02	1.10E-02	1.02E-02	9.31E-03	8.00E-03
5.5	1.59E-02	1.51E-02	1.46E-02	1.39E-02	1.28E-02	1.20E-02	1.13E-02	9.98E-03	9.12E-03	7.75E-03
6.0	1.68E-02	1.63E-02	1.53E-02	1.44E-02	1.32E-02	1.22E-02	1.12E-02	1.01E-02	8.95E-03	7.47E-03
6.5	1.80E-02	1.72E-02	1.60E-02	1.48E-02	1.37E-02	1.23E-02	1.13E-02	9.94E-03	8.66E-03	7.12E-03
7.0	1.89E-02	1.79E-02	1.65E-02	1.52E-02	1.37E-02	1.23E-02	1.11E-02	9.66E-03	8.49E-03	6.75E-03
7.5	2.00E-02	1.88E-02	1.71E-02	1.56E-02	1.38E-02	1.23E-02	1.10E-02	9.44E-03	8.19E-03	6.52E-03
8.0	2.07E-02	1.93E-02	1.76E-02	1.59E-02	1.39E-02	1.23E-02	1.08E-02	9.24E-03	7.85E-03	6.17E-03
8.5	2.16E-02	2.02E-02	1.80E-02	1.61E-02	1.39E-02	1.21E-02	1.05E-02	8.92E-03	7.61E-03	5.92E-03
9.0	2.26E-02	2.09E-02	1.84E-02	1.62E-02	1.39E-02	1.20E-02	1.04E-02	8.69E-03	7.37E-03	5.75E-03
9.5	2.34E-02	2.10E-02	1.86E-02	1.63E-02	1.37E-02	1.18E-02	1.01E-02	8.43E-03	7.09E-03	5.52E-03
10.0	2.41E-02	2.16E-02	1.88E-02	1.62E-02	1.35E-02	1.15E-02	9.82E-03	8.17E-03	6.85E-03	5.40E-03
Energy (MeV)	Parietal Bone									
	Cellularity									
	100%	90%	80%	70%	60%	50%	40%	30%	20%	10%
3.0	3.72E-02	3.67E-02	3.61E-02	3.53E-02	3.50E-02	3.41E-02	3.29E-02	3.17E-02	3.04E-02	2.89E-02
3.5	4.30E-02	4.24E-02	4.15E-02	4.06E-02	3.96E-02	3.81E-02	3.67E-02	3.52E-02	3.40E-02	3.11E-02
4.0	4.74E-02	4.65E-02	4.57E-02	4.42E-02	4.26E-02	4.10E-02	3.92E-02	3.72E-02	3.51E-02	3.21E-02
4.5	5.10E-02	4.99E-02	4.83E-02	4.72E-02	4.44E-02	4.23E-02	4.04E-02	3.80E-02	3.56E-02	3.17E-02
5.0	5.33E-02	5.20E-02	5.00E-02	4.80E-02	4.55E-02	4.26E-02	4.06E-02	3.75E-02	3.46E-02	3.04E-02
5.5	5.53E-02	5.36E-02	5.12E-02	4.85E-02	4.56E-02	4.25E-02	3.99E-02	3.63E-02	3.29E-02	2.84E-02
6.0	5.77E-02	5.51E-02	5.22E-02	4.92E-02	4.55E-02	4.22E-02	3.89E-02	3.50E-02	3.16E-02	2.68E-02
6.5	5.99E-02	5.73E-02	5.36E-02	5.04E-02	4.60E-02	4.20E-02	3.85E-02	3.40E-02	3.01E-02	2.53E-02
7.0	6.27E-02	5.97E-02	5.51E-02	5.09E-02	4.60E-02	4.16E-02	3.75E-02	3.30E-02	2.90E-02	2.37E-02
7.5	6.51E-02	6.13E-02	5.63E-02	5.16E-02	4.58E-02	4.11E-02	3.67E-02	3.20E-02	2.75E-02	2.22E-02
8.0	6.74E-02	6.30E-02	5.73E-02	5.19E-02	4.55E-02	4.03E-02	3.59E-02	3.05E-02	2.63E-02	2.10E-02
8.5	6.93E-02	6.45E-02	5.82E-02	5.20E-02	4.49E-02	3.92E-02	3.47E-02	2.92E-02	2.50E-02	1.97E-02
9.0	7.11E-02	6.52E-02	5.84E-02	5.19E-02	4.43E-02	3.82E-02	3.35E-02	2.82E-02	2.36E-02	1.85E-02
9.5	7.28E-02	6.61E-02	5.82E-02	5.13E-02	4.34E-02	3.71E-02	3.22E-02	2.67E-02	2.24E-02	1.75E-02
10.0	7.39E-02	6.67E-02	5.82E-02	5.07E-02	4.21E-02	3.56E-02	3.08E-02	2.53E-02	2.14E-02	1.66E-02

TABLE 11B (Continued)

Energy (MeV)	$\phi(\text{TBE} \leftarrow \text{TAM})$									
	Ribs									
	Cellularity									
	100%	90%	80%	70%	60%	50%	40%	30%	20%	10%
3.0	6.49E-03	6.52E-03	6.37E-03	6.27E-03	6.27E-03	6.01E-03	5.81E-03	5.58E-03	5.28E-03	4.97E-03
3.5	7.76E-03	7.67E-03	7.43E-03	7.30E-03	7.23E-03	6.85E-03	6.65E-03	6.24E-03	6.04E-03	5.50E-03
4.0	8.83E-03	8.68E-03	8.57E-03	8.28E-03	8.01E-03	7.58E-03	7.29E-03	6.99E-03	6.52E-03	5.87E-03
4.5	9.79E-03	9.53E-03	9.17E-03	8.94E-03	8.56E-03	8.09E-03	7.73E-03	7.15E-03	6.71E-03	5.88E-03
5.0	1.07E-02	1.04E-02	1.00E-02	9.46E-03	8.78E-03	8.31E-03	7.92E-03	7.21E-03	6.62E-03	5.82E-03
5.5	1.12E-02	1.10E-02	1.04E-02	9.89E-03	9.28E-03	8.48E-03	7.94E-03	7.21E-03	6.57E-03	5.65E-03
6.0	1.20E-02	1.16E-02	1.09E-02	1.03E-02	9.49E-03	8.76E-03	8.13E-03	7.19E-03	6.44E-03	5.40E-03
6.5	1.27E-02	1.24E-02	1.16E-02	1.07E-02	9.63E-03	8.86E-03	8.02E-03	7.16E-03	6.26E-03	5.03E-03
7.0	1.36E-02	1.28E-02	1.18E-02	1.10E-02	9.85E-03	8.81E-03	7.97E-03	6.97E-03	6.09E-03	4.91E-03
7.5	1.43E-02	1.35E-02	1.23E-02	1.11E-02	9.81E-03	8.91E-03	7.86E-03	6.79E-03	5.96E-03	4.72E-03
8.0	1.48E-02	1.39E-02	1.27E-02	1.15E-02	9.92E-03	8.96E-03	7.73E-03	6.78E-03	5.81E-03	4.64E-03
8.5	1.56E-02	1.44E-02	1.30E-02	1.16E-02	1.00E-02	8.95E-03	7.68E-03	6.41E-03	5.60E-03	4.35E-03
9.0	1.61E-02	1.48E-02	1.33E-02	1.18E-02	1.01E-02	8.58E-03	7.65E-03	6.37E-03	5.31E-03	4.24E-03
9.5	1.67E-02	1.55E-02	1.36E-02	1.20E-02	1.01E-02	8.71E-03	7.57E-03	6.33E-03	5.27E-03	4.28E-03
10.0	1.75E-02	1.57E-02	1.38E-02	1.19E-02	1.02E-02	8.54E-03	7.43E-03	6.21E-03	5.29E-03	4.23E-03

TABLE 12B

Absorbed Fractions to TBV from α -Emissions Within TAM of Leeds 44-Year Male
Within Various Skeletal Sites and as Function of Marrow Cellularity

Energy (MeV)	ϕ (TBV \leftarrow TAM)									
	Cervical Vertebrae									
	Cellularity									
	100%	90%	80%	70%	60%	50%	40%	30%	20%	10%
3.0	5.89E-04	5.99E-04	5.83E-04	6.09E-04	5.86E-04	5.93E-04	6.02E-04	5.79E-04	5.72E-04	5.57E-04
3.5	1.55E-03	1.52E-03	1.53E-03	1.55E-03	1.52E-03	1.47E-03	1.46E-03	1.47E-03	1.42E-03	1.34E-03
4.0	3.05E-03	3.02E-03	3.04E-03	3.06E-03	2.97E-03	2.89E-03	2.87E-03	2.77E-03	2.78E-03	2.65E-03
4.5	5.08E-03	5.08E-03	5.04E-03	4.90E-03	4.87E-03	4.84E-03	4.62E-03	4.61E-03	4.41E-03	4.12E-03
5.0	7.65E-03	7.65E-03	7.54E-03	7.39E-03	7.25E-03	7.11E-03	6.87E-03	6.73E-03	6.47E-03	5.91E-03
5.5	1.06E-02	1.04E-02	1.05E-02	1.02E-02	1.00E-02	9.67E-03	9.43E-03	8.91E-03	8.56E-03	7.91E-03
6.0	1.37E-02	1.36E-02	1.34E-02	1.31E-02	1.27E-02	1.25E-02	1.20E-02	1.14E-02	1.08E-02	1.00E-02
6.5	1.71E-02	1.69E-02	1.67E-02	1.62E-02	1.61E-02	1.59E-02	1.52E-02	1.46E-02	1.42E-02	1.32E-02
7.0	2.07E-02	2.07E-02	2.04E-02	2.02E-02	2.03E-02	1.96E-02	1.98E-02	1.91E-02	1.89E-02	1.84E-02
7.5	2.45E-02	2.44E-02	2.44E-02	2.42E-02	2.45E-02	2.42E-02	2.44E-02	2.44E-02	2.42E-02	2.41E-02
8.0	2.90E-02	2.85E-02	2.89E-02	2.88E-02	2.90E-02	2.92E-02	2.93E-02	2.93E-02	2.96E-02	3.01E-02
8.5	3.28E-02	3.31E-02	3.31E-02	3.33E-02	3.36E-02	3.40E-02	3.44E-02	3.47E-02	3.53E-02	3.56E-02
9.0	3.77E-02	3.79E-02	3.83E-02	3.81E-02	3.86E-02	3.94E-02	3.98E-02	4.04E-02	4.06E-02	4.14E-02
9.5	4.25E-02	4.28E-02	4.25E-02	4.29E-02	4.40E-02	4.43E-02	4.47E-02	4.57E-02	4.64E-02	4.68E-02
10.0	4.76E-02	4.81E-02	4.79E-02	4.81E-02	4.90E-02	5.00E-02	5.09E-02	5.18E-02	5.24E-02	5.33E-02
Energy (MeV)	Femur Head									
	Cellularity									
	100%	90%	80%	70%	60%	50%	40%	30%	20%	10%
3.0	3.86E-04	4.21E-04	4.20E-04	3.99E-04	3.93E-04	4.00E-04	4.03E-04	3.90E-04	3.84E-04	3.67E-04
3.5	1.06E-03	1.05E-03	9.93E-04	1.04E-03	1.03E-03	1.02E-03	1.03E-03	9.65E-04	9.63E-04	9.58E-04
4.0	2.08E-03	2.04E-03	2.03E-03	2.04E-03	2.02E-03	1.97E-03	1.96E-03	1.89E-03	1.86E-03	1.79E-03
4.5	3.50E-03	3.48E-03	3.46E-03	3.39E-03	3.45E-03	3.37E-03	3.21E-03	3.14E-03	3.06E-03	2.80E-03
5.0	5.25E-03	5.23E-03	5.24E-03	5.11E-03	5.04E-03	4.94E-03	4.82E-03	4.53E-03	4.44E-03	4.20E-03
5.5	7.34E-03	7.35E-03	7.12E-03	7.01E-03	6.95E-03	6.82E-03	6.57E-03	6.35E-03	6.05E-03	5.46E-03
6.0	9.73E-03	9.51E-03	9.40E-03	9.33E-03	9.14E-03	8.79E-03	8.42E-03	8.09E-03	7.67E-03	6.95E-03
6.5	1.22E-02	1.22E-02	1.20E-02	1.19E-02	1.14E-02	1.11E-02	1.11E-02	1.05E-02	1.02E-02	9.54E-03
7.0	1.49E-02	1.49E-02	1.49E-02	1.46E-02	1.47E-02	1.44E-02	1.42E-02	1.39E-02	1.39E-02	1.34E-02
7.5	1.80E-02	1.79E-02	1.80E-02	1.83E-02	1.80E-02	1.78E-02	1.80E-02	1.80E-02	1.79E-02	1.81E-02
8.0	2.16E-02	2.12E-02	2.15E-02	2.14E-02	2.16E-02	2.18E-02	2.17E-02	2.20E-02	2.23E-02	2.24E-02
8.5	2.50E-02	2.48E-02	2.49E-02	2.49E-02	2.53E-02	2.55E-02	2.59E-02	2.62E-02	2.66E-02	2.70E-02
9.0	2.86E-02	2.85E-02	2.89E-02	2.89E-02	2.94E-02	2.94E-02	3.03E-02	3.06E-02	3.12E-02	3.13E-02
9.5	3.22E-02	3.24E-02	3.25E-02	3.30E-02	3.37E-02	3.42E-02	3.46E-02	3.50E-02	3.55E-02	3.60E-02
10.0	3.63E-02	3.64E-02	3.65E-02	3.72E-02	3.74E-02	3.83E-02	3.93E-02	3.98E-02	4.04E-02	4.12E-02
Energy (MeV)	Femur Neck									
	Cellularity									
	100%	90%	80%	70%	60%	50%	40%	30%	20%	10%
3.0	2.88E-04	2.60E-04	2.57E-04	2.72E-04	2.86E-04	2.77E-04	2.76E-04	2.75E-04	2.80E-04	2.66E-04
3.5	6.91E-04	7.22E-04	7.26E-04	7.12E-04	6.89E-04	7.49E-04	7.23E-04	6.95E-04	6.75E-04	6.76E-04
4.0	1.44E-03	1.46E-03	1.49E-03	1.44E-03	1.44E-03	1.37E-03	1.38E-03	1.33E-03	1.30E-03	1.25E-03
4.5	2.49E-03	2.52E-03	2.43E-03	2.37E-03	2.36E-03	2.34E-03	2.31E-03	2.26E-03	2.17E-03	2.04E-03
5.0	3.68E-03	3.80E-03	3.61E-03	3.60E-03	3.62E-03	3.50E-03	3.43E-03	3.23E-03	3.13E-03	2.90E-03
5.5	5.17E-03	5.18E-03	5.08E-03	5.03E-03	4.90E-03	4.77E-03	4.65E-03	4.40E-03	4.12E-03	3.90E-03
6.0	6.80E-03	6.86E-03	6.75E-03	6.55E-03	6.34E-03	6.25E-03	6.02E-03	5.74E-03	5.42E-03	4.84E-03
6.5	8.57E-03	8.48E-03	8.36E-03	8.28E-03	8.18E-03	7.84E-03	7.71E-03	7.28E-03	7.14E-03	6.62E-03
7.0	1.03E-02	1.05E-02	1.05E-02	1.03E-02	1.02E-02	1.00E-02	9.85E-03	9.75E-03	9.62E-03	9.46E-03
7.5	1.25E-02	1.25E-02	1.27E-02	1.24E-02	1.24E-02	1.23E-02	1.24E-02	1.24E-02	1.26E-02	1.25E-02
8.0	1.47E-02	1.48E-02	1.47E-02	1.49E-02	1.49E-02	1.51E-02	1.52E-02	1.52E-02	1.53E-02	1.55E-02
8.5	1.71E-02	1.71E-02	1.70E-02	1.71E-02	1.76E-02	1.78E-02	1.78E-02	1.82E-02	1.83E-02	1.84E-02
9.0	1.94E-02	1.98E-02	1.95E-02	1.96E-02	2.02E-02	2.04E-02	2.08E-02	2.09E-02	2.10E-02	2.16E-02
9.5	2.21E-02	2.22E-02	2.23E-02	2.26E-02	2.27E-02	2.34E-02	2.36E-02	2.40E-02	2.44E-02	2.43E-02
10.0	2.50E-02	2.49E-02	2.48E-02	2.53E-02	2.54E-02	2.62E-02	2.66E-02	2.69E-02	2.73E-02	2.78E-02

TABLE 12B (Continued)

Energy (MeV)	ϕ (TBV←TAM)									
	Iliac Crest									
	Cellularity									
	100%	90%	80%	70%	60%	50%	40%	30%	20%	10%
3.0	5.65E-04	5.60E-04	5.59E-04	5.75E-04	5.74E-04	5.80E-04	5.37E-04	5.56E-04	5.39E-04	5.39E-04
3.5	1.45E-03	1.45E-03	1.40E-03	1.43E-03	1.43E-03	1.37E-03	1.38E-03	1.36E-03	1.31E-03	1.29E-03
4.0	2.88E-03	2.83E-03	2.81E-03	2.76E-03	2.80E-03	2.73E-03	2.70E-03	2.58E-03	2.54E-03	2.41E-03
4.5	4.79E-03	4.80E-03	4.59E-03	4.70E-03	4.66E-03	4.45E-03	4.44E-03	4.29E-03	4.20E-03	3.85E-03
5.0	7.08E-03	7.04E-03	7.12E-03	6.90E-03	6.68E-03	6.55E-03	6.44E-03	6.23E-03	5.88E-03	5.62E-03
5.5	9.88E-03	9.89E-03	9.67E-03	9.56E-03	9.34E-03	9.04E-03	8.69E-03	8.39E-03	7.90E-03	7.52E-03
6.0	1.29E-02	1.29E-02	1.28E-02	1.25E-02	1.21E-02	1.17E-02	1.12E-02	1.07E-02	1.02E-02	9.40E-03
6.5	1.65E-02	1.60E-02	1.60E-02	1.58E-02	1.55E-02	1.49E-02	1.46E-02	1.41E-02	1.35E-02	1.25E-02
7.0	2.00E-02	1.97E-02	1.98E-02	1.94E-02	1.95E-02	1.90E-02	1.89E-02	1.85E-02	1.82E-02	1.77E-02
7.5	2.38E-02	2.37E-02	2.36E-02	2.37E-02	2.37E-02	2.35E-02	2.35E-02	2.36E-02	2.37E-02	2.36E-02
8.0	2.79E-02	2.78E-02	2.82E-02	2.79E-02	2.83E-02	2.85E-02	2.88E-02	2.90E-02	2.92E-02	2.95E-02
8.5	3.26E-02	3.26E-02	3.27E-02	3.28E-02	3.32E-02	3.33E-02	3.38E-02	3.43E-02	3.47E-02	3.55E-02
9.0	3.73E-02	3.72E-02	3.73E-02	3.75E-02	3.84E-02	3.88E-02	3.91E-02	3.97E-02	4.04E-02	4.12E-02
9.5	4.20E-02	4.21E-02	4.20E-02	4.25E-02	4.31E-02	4.42E-02	4.46E-02	4.56E-02	4.63E-02	4.67E-02
10.0	4.73E-02	4.71E-02	4.72E-02	4.77E-02	4.87E-02	4.96E-02	5.02E-02	5.16E-02	5.24E-02	5.29E-02
Energy (MeV)	Lumbar Vertebrae									
	Cellularity									
	100%	90%	80%	70%	60%	50%	40%	30%	20%	10%
3.0	4.16E-04	4.30E-04	4.15E-04	4.29E-04	4.12E-04	4.08E-04	4.34E-04	3.95E-04	4.11E-04	3.87E-04
3.5	1.06E-03	1.06E-03	1.05E-03	1.06E-03	1.05E-03	1.06E-03	1.03E-03	1.01E-03	9.79E-04	9.47E-04
4.0	2.10E-03	2.06E-03	2.11E-03	2.04E-03	2.07E-03	2.00E-03	1.97E-03	1.93E-03	1.91E-03	1.78E-03
4.5	3.52E-03	3.51E-03	3.55E-03	3.46E-03	3.46E-03	3.32E-03	3.34E-03	3.14E-03	3.06E-03	2.92E-03
5.0	5.32E-03	5.29E-03	5.27E-03	5.19E-03	4.98E-03	4.96E-03	4.74E-03	4.67E-03	4.45E-03	4.12E-03
5.5	7.55E-03	7.19E-03	7.29E-03	7.12E-03	7.01E-03	6.73E-03	6.70E-03	6.25E-03	6.06E-03	5.54E-03
6.0	9.58E-03	9.54E-03	9.43E-03	9.26E-03	9.07E-03	8.81E-03	8.40E-03	8.08E-03	7.63E-03	6.98E-03
6.5	1.21E-02	1.19E-02	1.18E-02	1.18E-02	1.15E-02	1.12E-02	1.08E-02	1.03E-02	9.96E-03	9.42E-03
7.0	1.46E-02	1.47E-02	1.44E-02	1.44E-02	1.42E-02	1.40E-02	1.38E-02	1.38E-02	1.36E-02	1.31E-02
7.5	1.76E-02	1.76E-02	1.75E-02	1.73E-02	1.75E-02	1.72E-02	1.74E-02	1.74E-02	1.73E-02	1.74E-02
8.0	2.04E-02	2.05E-02	2.04E-02	2.06E-02	2.09E-02	2.10E-02	2.09E-02	2.12E-02	2.14E-02	2.15E-02
8.5	2.38E-02	2.40E-02	2.38E-02	2.42E-02	2.44E-02	2.46E-02	2.48E-02	2.51E-02	2.55E-02	2.56E-02
9.0	2.72E-02	2.72E-02	2.73E-02	2.75E-02	2.77E-02	2.84E-02	2.87E-02	2.91E-02	2.93E-02	2.98E-02
9.5	3.06E-02	3.05E-02	3.09E-02	3.09E-02	3.16E-02	3.22E-02	3.24E-02	3.31E-02	3.35E-02	3.40E-02
10.0	3.45E-02	3.43E-02	3.44E-02	3.46E-02	3.52E-02	3.61E-02	3.67E-02	3.73E-02	3.82E-02	3.87E-02
Energy (MeV)	Parietal Bone									
	Cellularity									
	100%	90%	80%	70%	60%	50%	40%	30%	20%	10%
3.0	1.90E-03	1.96E-03	1.93E-03	1.96E-03	1.87E-03	1.90E-03	1.87E-03	1.77E-03	1.80E-03	1.73E-03
3.5	4.78E-03	4.71E-03	4.68E-03	4.68E-03	4.58E-03	4.59E-03	4.62E-03	4.44E-03	4.38E-03	4.16E-03
4.0	9.22E-03	9.19E-03	9.10E-03	9.12E-03	9.06E-03	8.69E-03	8.59E-03	8.51E-03	8.20E-03	7.87E-03
4.5	1.54E-02	1.53E-02	1.50E-02	1.50E-02	1.46E-02	1.44E-02	1.40E-02	1.38E-02	1.33E-02	1.24E-02
5.0	2.27E-02	2.25E-02	2.24E-02	2.20E-02	2.19E-02	2.11E-02	2.04E-02	1.99E-02	1.91E-02	1.78E-02
5.5	3.11E-02	3.09E-02	3.04E-02	2.98E-02	2.92E-02	2.85E-02	2.77E-02	2.65E-02	2.52E-02	2.34E-02
6.0	3.99E-02	3.90E-02	3.87E-02	3.79E-02	3.70E-02	3.60E-02	3.45E-02	3.30E-02	3.15E-02	2.92E-02
6.5	4.83E-02	4.79E-02	4.71E-02	4.68E-02	4.54E-02	4.45E-02	4.30E-02	4.14E-02	3.98E-02	3.76E-02
7.0	5.74E-02	5.74E-02	5.66E-02	5.58E-02	5.57E-02	5.47E-02	5.39E-02	5.29E-02	5.20E-02	5.09E-02
7.5	6.69E-02	6.68E-02	6.63E-02	6.64E-02	6.65E-02	6.57E-02	6.61E-02	6.54E-02	6.52E-02	6.52E-02
8.0	7.71E-02	7.69E-02	7.72E-02	7.70E-02	7.78E-02	7.79E-02	7.81E-02	7.86E-02	7.84E-02	7.94E-02
8.5	8.80E-02	8.77E-02	8.85E-02	8.80E-02	8.92E-02	8.97E-02	9.06E-02	9.14E-02	9.18E-02	9.34E-02
9.0	9.86E-02	9.91E-02	9.91E-02	9.99E-02	1.01E-01	1.02E-01	1.03E-01	1.05E-01	1.06E-01	1.07E-01
9.5	1.10E-01	1.10E-01	1.10E-01	1.12E-01	1.13E-01	1.14E-01	1.16E-01	1.18E-01	1.19E-01	1.20E-01
10.0	1.23E-01	1.22E-01	1.23E-01	1.24E-01	1.25E-01	1.28E-01	1.30E-01	1.32E-01	1.33E-01	1.34E-01

TABLE 12B (Continued)

Energy (MeV)	$\phi(\text{TBV} \leftarrow \text{TAM})$									
	Ribs									
	Cellularity									
	100%	90%	80%	70%	60%	50%	40%	30%	20%	10%
3.0	2.98E-04	2.93E-04	2.87E-04	2.85E-04	2.76E-04	2.87E-04	2.87E-04	2.73E-04	2.83E-04	2.63E-04
3.5	7.78E-04	7.60E-04	7.35E-04	7.37E-04	7.39E-04	7.37E-04	7.27E-04	6.99E-04	7.19E-04	6.76E-04
4.0	1.54E-03	1.47E-03	1.49E-03	1.45E-03	1.47E-03	1.45E-03	1.45E-03	1.42E-03	1.35E-03	1.31E-03
4.5	2.53E-03	2.43E-03	2.48E-03	2.47E-03	2.45E-03	2.43E-03	2.36E-03	2.26E-03	2.17E-03	2.08E-03
5.0	3.79E-03	3.76E-03	3.68E-03	3.64E-03	3.60E-03	3.56E-03	3.46E-03	3.34E-03	3.21E-03	3.02E-03
5.5	5.24E-03	5.23E-03	5.23E-03	5.08E-03	5.07E-03	4.77E-03	4.83E-03	4.50E-03	4.32E-03	3.93E-03
6.0	6.98E-03	6.78E-03	6.84E-03	6.61E-03	6.49E-03	6.28E-03	6.07E-03	5.71E-03	5.38E-03	5.00E-03
6.5	8.55E-03	8.58E-03	8.25E-03	8.33E-03	8.20E-03	7.96E-03	7.81E-03	7.47E-03	7.08E-03	6.57E-03
7.0	1.05E-02	1.06E-02	1.03E-02	1.03E-02	1.01E-02	1.00E-02	9.95E-03	9.77E-03	9.63E-03	9.33E-03
7.5	1.24E-02	1.25E-02	1.24E-02	1.23E-02	1.22E-02	1.24E-02	1.25E-02	1.23E-02	1.23E-02	1.25E-02
8.0	1.43E-02	1.46E-02	1.46E-02	1.46E-02	1.48E-02	1.47E-02	1.48E-02	1.51E-02	1.53E-02	1.53E-02
8.5	1.68E-02	1.67E-02	1.69E-02	1.68E-02	1.70E-02	1.74E-02	1.73E-02	1.77E-02	1.79E-02	1.82E-02
9.0	1.90E-02	1.91E-02	1.93E-02	1.92E-02	1.95E-02	1.98E-02	2.02E-02	2.04E-02	2.06E-02	2.09E-02
9.5	2.14E-02	2.18E-02	2.17E-02	2.18E-02	2.21E-02	2.26E-02	2.27E-02	2.34E-02	2.33E-02	2.39E-02
10.0	2.41E-02	2.37E-02	2.39E-02	2.42E-02	2.48E-02	2.52E-02	2.56E-02	2.61E-02	2.65E-02	2.68E-02

Chord-based versus voxel-based methods of electron transport in the skeletal tissues

Amish P. Shah

Department of Biomedical Engineering, University of Florida, Gainesville, Florida 32611-8300

Derek W. Jokisch

Department of Physics and Astronomy, Francis Marion University, Florence, South Carolina 29501-0547

Didier A. Rajon

Department of Neurosurgery, University of Florida, Gainesville, Florida 32610-0265

Christopher J. Watchman

Department of Nuclear & Radiological Engineering, University of Florida, Gainesville, Florida, 32611-8300

Phillip W. Patton

Department of Health Physics, University of Nevada-Las Vegas, Las Vegas, Nevada 89154-3037

Wesley E. Bolch^{a)}

Departments of Nuclear & Radiological and Biomedical Engineering, University of Florida, Gainesville, Florida, 32611-8300

(Received 1 February 2005; revised 17 July 2005; accepted for publication 20 July 2005; published 29 September 2005)

Anatomic models needed for internal dose assessment have traditionally been developed using mathematical surface equations to define organ boundaries, shapes, and their positions within the body. Many researchers, however, are now advocating the use of tomographic models created from segmented patient computed tomography (CT) or magnetic resonance (MR) scans. In the skeleton, however, the tissue structures of the bone trabeculae, marrow cavities, and endosteal layer are exceedingly small and of complex shape, and thus do not lend themselves easily to either stylistic representations or in-vivo CT imaging. Historically, the problem of modeling the skeletal tissues has been addressed through the development of chord-based methods of radiation particle transport, as given by studies at the University of Leeds (Leeds, UK) using a 44-year male subject. We have proposed an alternative approach to skeletal dosimetry in which excised sections of marrow-intact cadaver spongiosa are imaged directly via microCT scanning. The cadaver selected for initial investigation of this technique was a 66-year male subject of nominal body mass index (22.7 kg m^{-2}). The objectives of the present study were to compare chord-based versus voxel-based methods of skeletal dosimetry using data from the UF 66-year male subject. Good agreement between chord-based and voxel-based transport was noted for marrow irradiation by either bone surface or bone volume sources up to 500–1000 keV (depending upon the skeletal site). In contrast, chord-based models of electron transport yielded consistently lower values of the self-absorbed fraction to marrow tissues than seen under voxel-based transport at energies above 100 keV, a feature directly attributed to the inability of chord-based models to account for nonlinear electron trajectories. Significant differences were also noted in the dosimetry of the endosteal layer (for all source tissues), with chord-based transport predicting a higher fraction of energy deposition than given by voxel-based transport (average factor of about 1.6). The study supports future use of voxel-based skeletal models which (1) permit nonlinear electron trajectories across the skeletal tissues, (2) do not rely on mathematical algorithms for treating the endosteal tissue layer, and (3) do not implicitly assume independence of marrow and bone trajectories as is the case for chord-based skeletal models. © 2005 American Association of Physicists in Medicine. [DOI: 10.1118/1.2040712]

Key words: skeletal dosimetry, bone marrow, absorbed fraction, voxel-based radiation transport, chord-based radiation transport

I. INTRODUCTION

Current models of skeletal dosimetry in both radiation protection^{1,2} and medical dosimetry³ track radiation particles (α particles, β particles, and secondary electrons) through an infinite region of trabecular spongiosa, thus neglecting ef-

fects introduced by the three-dimensional (3D) macrostructure of the bone site. These infinite spongiosa transport (or IST) models use as their input either (1) linear chord-length distributions measured across the trabeculae and marrow cavities,^{4,5} or (2) 3D digital images of that microstructure.^{6,7}

TABLE I. Acronyms and terms used in the present study.

Symbol	Definition	Description
Radiation transport methodologies for skeletal dosimetry		
IST	Infinite spongiosa transport	Class of skeletal dosimetry models in which particle energy is tracked within the tissues of spongiosa, with no accounting for energy escape to the cortical bone cortex. Spongiosa is defined as the combined tissues of the bone trabeculae, bone endosteum, and marrow tissues (active and inactive).
CBIST	Chord-based IST	Skeletal dosimetry model in which linear chord-length distributions through bone trabeculae and marrow cavities are used to track particle energy deposition. In CBIST, particle energy escape from trabecular spongiosa is not considered.
VBIST	Voxel-based IST	Skeletal dosimetry model in which particles are followed within the 3D microstructure of trabecular spongiosa as defined by either a microCT or NMR microscopy image. In VBIST, particle energy escape from trabecular spongiosa is not considered.
VBRST	Voxel-based restricted spongiosa transport	Skeletal dosimetry model that is equivalent to VBIST with the exception that the radiation particle is additionally tracked within a stylized (mathematical) model of the cortical bone cortex, and thus energy escape from trabecular spongiosa is accounted for.
PIRT	Paired-image radiation transport	Skeletal dosimetry model in which radiation particles are tracked simultaneously within an ex-vivo CT image of the skeletal site (cortical bone and spongiosa) and an ex-vivo microCT image of the trabecular spongiosa.
Terms defining source and target regions during radiation transport		
TAM	Trabecular active marrow	All soft tissues within the marrow cavities exclusive of both marrow adipocytes (TIM) and the cells immediately adjacent to the bone surfaces (TBE).
TIM	Trabecular inactive marrow	Generally defined as the marrow adipocytes and representative of the component of marrow tissues designated as “yellow” marrow.
TBE	Trabecular bone endosteum	Single-cell layer encompassing all surfaces of the bone trabeculae. The current ICRP definition of this region is adopted (10- μ m thickness).
TBS	Trabecular bone surfaces	Surfaces of all bone trabeculae, and thus equivalent to the bone-marrow interface of spongiosa
TBV	Trabecular bone volume	The region of the spongiosa defining the bone trabeculae.
TMS	Trabecular marrow space	Defined as the combined tissues of active marrow (TAM) and inactive marrow (TIM). Equivalent to total marrow for each bone site.
TMC	Trabecular marrow cavity	Defined as all tissues of spongiosa exclusive of the bone trabeculae, $TMC = TAM + TIM + TBE = TMS + TBE$.

These two transport approaches can thus be referred to as chord-based IST (CBIST) or voxel-based IST (VBIST) skeletal models, respectively (see Table I). The skeletal dosimetry models used in current clinical practice—the 2000 Eckerman model³ of MIRDOSE 3 (Ref. 8) and the 2003 Eckerman model⁹ of OLINDA 1.0 (Refs. 10 and 11)—belong to the CBIST model classification. Chord-length distributions used in both Eckerman models are taken from

studies conducted at the University of Leeds (Leeds, UK) in the early 1970s on a single 44-year old male subject.^{4,5,12} Furthermore, the Leeds chord-length distribution data provide the basic framework for many of the tissue and dosimetry features of Reference Man as published by the International Commission on Radiological Protection (ICRP).^{2,13}

With an ever increasing use of voxelized images for medical dosimetry, it is of interest to compare and contrast CBIST

and VBIST estimates of electron absorbed fractions to the skeletal tissues utilizing identical specimens of skeletal microstructure. The Leeds data are provided only in the form of chord-length distributions; consequently, such a comparison cannot be made using the Leeds 44-year old male. Recent studies in our laboratory have yielded trabecular microstructural data for a 66-year old male subject in both CBIST and VBIST input formats: (1) 3D omni-directional chord-length distributions, and (2) 3D voxelized images of spongiosa from (microCT) scans across several skeletal sites.

The objective of the present study was thus to use the University of Florida (UF) (Gainesville, FL) microstructural data to explore the impact of the transport technique (CBIST and VBIST) on values of electron absorbed fraction to both active bone marrow and trabecular endosteum at several skeletal sites. In both CBIST and VBIST models, it is acknowledged that values of absorbed fraction will not account for energy loss to cortical bone, and thus they will overestimate tissue doses at high electron energies. Energy loss to cortical bone has been previously documented by Patton *et al.*¹⁴ and Shah *et al.*¹⁵ using VBRST (voxel-based restricted spongiosa transport) simulations and more recently by Shah *et al.*^{16,17} using PIRT (paired-image radiation transport) simulations. Nevertheless, this comparison of CBIST and VBIST electron dosimetry methodologies is of critical interest as both the health physics^{18,19} and medical physics^{20,21} fields move toward more image-based (and thus voxel-based) approaches to internal dosimetry.²²

II. MATERIALS AND METHODS

A. UF trabecular microstructure acquisition

For details regarding cadaver selection, skeletal site harvesting, and microCT scanning trabecular spongiosa, the reader is referred to Shah *et al.*¹⁷ Only a brief summary is provided below. Microtomographic imaging of cuboidal samples of marrow-intact spongiosa was performed on desktop cone-beam μ CT40 or μ CT80 scanners (Scanco Medical AG, Bassersdorf, Switzerland) yielding isotropic image data sets at a voxel resolution of $60\ \mu\text{m} \times 60\ \mu\text{m} \times 60\ \mu\text{m}$. The value of $60\ \mu\text{m}$ was selected to represent an upper, but acceptable, limit on image resolution needed to resolve bone trabeculae features typically 100 to $150\ \mu\text{m}$ in thickness, while simultaneously permitting as large a section of spongiosa to be scanned by the microCT system. Post-acquisition image processing steps included (1) selection of a volume of interest for radiation transport (e.g., avoidance of cortical regions), (2) gray-level thresholding, (3) voxel segmentation, and (4) 3D median filtering, all of which have been previously reported in Jokisch *et al.*²³ and Patton *et al.*⁷ Figure 1 provides a 3D representation of the microCT image of the L₂ lumbar vertebra, as well as a cross-sectional slice through that data set.

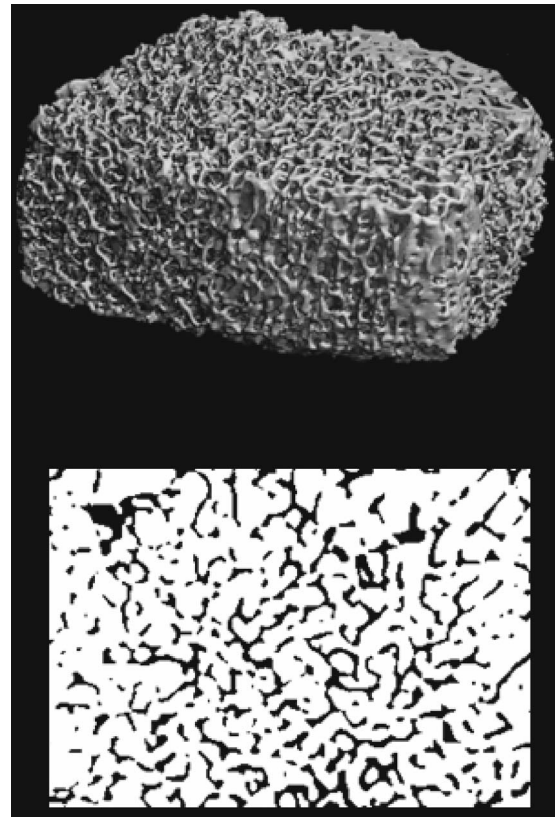


FIG. 1. Representative vertebral images used in the voxel-based transport model. A reconstruction of a microCT image of spongiosa is given as well as a transverse slice through the data set showing bone trabecula (black) and bone marrow (white).

B. Chord length distributions for the UF 66-year old male

Accurate techniques for both the generation and measurement of omnidirectional μ -random chords through trabecular spongiosa were previously investigated by Rajon and Bolch.^{24,25} In the present study, the trilinear interpolation marching cube algorithm was used to smoothly represent the bone-marrow interface during 3D ray tracing and assembly of the chord-length distribution across both bone trabeculae and marrow cavities of spongiosa sections of the UF 66-year old male. Further details are given in Shah *et al.*²⁶

C. Chord-based infinite spongiosa transport (CBIST) model

Calculations of electron absorbed fraction were performed using chord-length distributions digitally measured from imaging data on the UF 66-year old male.²⁶ In general, three fundamental types of random chord distributions exist: μ —mean free path, I —interior radiator, and S —surface radiator.^{27–29} Coleman²⁷ further explains that I -random distributions (used for volume source simulations) can be derived from μ -random distributions for regular convex bodies (used for tissue region traversals). However, for S -random distributions (used for surface sources), no corresponding mathematical correlation exists, and thus S -random distribu-

tions must be measured directly within the sample. Radial, or r randomness, has also been suggested to be appropriate for simulations of beta particle emissions originating from within complex structures such as trabecular bone (with interconnected convex/concave geometries). Studies by Spiers and Beddoe³⁰ suggest that small, but significant differences exist between derived I -random distributions and measured r -random distributions in trabecular bone. Nevertheless, since tabular I -random distribution are unavailable at present, only μ -random, and their derived I -random, distributions were used in the present study for the UF subject.

In a CBIST simulation, the bone and marrow chord-length distributions are randomly and alternately sampled with each selected chord representing the potential path length of an electron in the current tissue. This method thus assumes statistical independence of the bone and marrow distributions, a feature that previous work has questioned.³¹ Range-energy data are then used to calculate residual energies at tissue interfaces, and thus energy loss within each traversed tissue region. In the present study, electron range-energy relationships for active (red) marrow and endosteum were derived through the use of the Bragg additivity rule³² and elemental tissue compositions from ICRU Publication 46.³³ Three source tissues were used in this study: trabecular marrow space (TMS), the trabecular bone volume (TBV), and trabecular bone surfaces (TBS). Target tissues included the trabecular marrow space (marrow at 100% cellularity) and the trabecular bone endosteum (TBE).

The CBIST transport methodology is best described by first considering an electron-emitter uniformly distributed within the tissues of the bone trabeculae (i.e., TBV source). The transport code first randomly samples a bone chord-length d_T^{\max} from the I -random cumulative density function $CDF_I(d_T^{\max})$ for the skeletal site of interest (e.g., cervical vertebra). This sampled chord length is treated as the maximum possible distance that an electron may travel within its bone trabecula prior to entering the endosteal layer. The transport distance actually taken d_T is thus uniformly sampled across the interval $[0, d_T^{\max}]$. The range-energy relationship for electrons in bone tissue is then used to determine the total energy expended by the particle within that bone trabecula. If residual kinetic energy remains, the particle is further transported into (and potentially across) the adjacent endosteal layer.

Chord lengths across the endosteal layer must be considered in tandem with random sampling of the Leeds or UF marrow-cavity chord length d_{MC} . For an electron emerging from a bone trabecula, a random marrow-cavity chord length d_{MC} is sampled under μ randomness (CDF_μ) for the same skeletal site. The value of d_{MC} is at most composed of two endosteal chord lengths (near and far side of the marrow cavity) and an intervening chord length across the marrow space

$$d_{MC} = d_{E1} + d_{MS} + d_{E2}. \quad (1)$$

Values for d_{E1} and d_{E2} are determined through uniform sampling of the cosine of the entry angle (η) across each en-

dosteal layer (note that a half-space geometry is implicitly assumed here)

$$\eta_1 \in [0:1] \text{ with } d_{E1} = (10 \mu\text{m})/\eta_1 \text{ and} \quad (2)$$

$$\eta_2 \in [0:1] \text{ with } d_{E2} = (10 \mu\text{m})/\eta_2.$$

If $d_{E1} + d_{E2} \geq d_{MC}$, then

$$d_{E1} = d_{E2} = d_{MC}/2 \text{ and } d_{MS} = 0 \quad (3)$$

(the electron travels fully within the endosteal layer roughly parallel to the surface of the bone trabecula, and does not enter the marrow space). If, however, $d_{E1} + d_{E2} < d_{MC}$, then

$$d_{MS} = d_{MC} - (d_{E1} + d_{E2}). \quad (4)$$

The electron range-energy function in endosteal tissues is then used to determine the kinetic energy lost within the first endosteal layer. If residual kinetic energy still exists, and $d_{MS} > 0$, the electron is further transported within the tissues of the marrow space. Emission sites within the marrow (TMS source) or on the bone surfaces (TBS source) are considered in a similar fashion. For the latter, μ -random chord distributions are employed as an approximation of S -random distributions.

Absorbed fractions were calculated with sufficient histories to reduce the coefficient of variance to below 1% for primary targets and for most secondary (adjacent) targets. Coefficients of variation were less than 3% (exhibited at energies below 20 keV) for tertiary targets (TMS target for a TBV source with TBE as the intervening tissue).

D. Voxel-based infinite spongiosa transport (VBIST) model

In addition to acquiring chord distributions within the segmented microCT images, these images were also directly imported into the EGSNRC code for voxel-based electron transport. Although the voxel-based models allow for the inclusion of marrow cellularity as outlined previously,^{15,34} the present study only considered marrow at 100% cellularity so as to allow direct comparisons to CBIST results. The trabecular bone endosteum (TBE) is defined in ICRP Publications 11 (Ref. 35) and 26 (Ref. 36) as a 10- μm thick tissue layer at the bone-marrow interface. Its presence within a voxelized image of spongiosa has been described previously by Jokisch *et al.*⁶ The resulting 3D image was coupled to the EGSNRC radiation transport code³⁷ for electron (beta particle) transport simulations. Source tissues in this study included the trabecular marrow space (TMS), the trabecular bone surfaces (TBS), and the trabecular bone volume (TBV) (see Table I). TBS sources were approximated as a 0.1- μm layer on the marrow side of the bone-marrow voxel interface. Target tissues included both the marrow space and bone endosteum. Once a given electron reaches the physical edge of the 3D microimage, that particle was reintroduced within the image at its opposing edge within the same tissue medium (bone or marrow). The processes of particle transport within the image of spongiosa and its reintroduction were continued until all initial kinetic energy was expended. Particle histories

TABLE II. Mean values of trabecular and marrow cavity chord lengths as given by the present UF study and those published from the University of Leeds Ref. 12. Values of mean chord lengths across the endosteal layer and the marrow space (which in combination define the marrow cavity) are shown as well based upon the CBIST algorithm presented in this study. Values for source-independent absorbed fractions at high electron energies (convergence limits) are given for TBE, TMS, and TBV targets in both the Leeds and UF bone sites. At the bottom of the table, corresponding values of convergence limits under VBIST simulations are shown.

		Values from measured chord distributions		Values from CBIST algorithm		CBIST convergence limits [Eqs. (5)–(7)]		
Source	Skeletal site	Mean trabecular chord (μm)	Mean marrow cavity chord (μm)	Mean endosteal chord (μm)	Mean marrow space chord (μm)	$\phi(\text{TMS} \leftarrow r_S)$	$\phi(\text{TBE} \leftarrow r_S)$	$\phi(\text{TBV} \leftarrow r_S)$
Leeds	Femur head	231.7	1156.6	52.4	1051.8	0.681	0.068	0.251
Leeds	Femur neck	314.1	1655.4	55.1	1545.2	0.709	0.051	0.241
Leeds	Parietal bone	511.4	388.9	40.4	308.1	0.248	0.065	0.687
Leeds	Ribs	265.6	1703.3	54.3	1594.7	0.743	0.051	0.207
Leeds	Iliac crest	242.1	903.9	50.2	803.5	0.614	0.077	0.309
Leeds	Cervical vertebra	279.2	910.7	49.0	812.7	0.590	0.071	0.339
Leeds	Lumbar vertebra	245.5	1233.2	51.6	1130.0	0.688	0.063	0.250
UF	Femur head (right)	348.5	866.8	38.5	789.8	0.545	0.053	0.402
UF	Femur neck (right)	354.4	1551.8	40.2	1471.4	0.686	0.038	0.276
UF	Parietal bone (left)	503.6	806.5	37.4	731.7	0.444	0.045	0.510
UF	Rib (7th left)	329.2	1702.6	40.0	1622.6	0.720	0.036	0.244
UF	Os coxae (iliac crest)	245.2	1507.9	40.1	1427.7	0.745	0.042	0.214
UF	Cervical vertebra (C6)	279.2	1046.2	38.4	969.4	0.641	0.051	0.308
UF	Lumbar vertebra (L4)	288.3	1056.5	38.6	979.3	0.637	0.050	0.313
		Bone trabeculae mass (g)		Endosteal layer mass (g)	Marrow space mass (g)	VBIST convergence limits [Eqs. (8)–(10)]		
UF	Femur head (right)	45.2		3.7	54.5	0.552	0.038	0.410
UF	Femur neck (right)	45.7		3.6	108.6	0.709	0.023	0.268
UF	Parietal bone (left)	90.5		4.9	67.8	0.440	0.032	0.528
UF	Rib (7th left)	20.9		1.5	87.4	0.812	0.014	0.175
UF	Os coxae (iliac crest)	157.5		19.3	471.4	0.746	0.031	0.224
UF	Cervical vertebra (C6)	22.8		2.3	45.0	0.664	0.034	0.302
UF	Lumbar vertebra (L4)	96.9		9.9	182.6	0.653	0.035	0.311

were continued (50 000 to 2 000 000) until coefficients of variation on the absorbed fraction was below 1%.

III. RESULTS

As previously described by Eckerman³⁸ and Bouchet *et al.*,³⁹ values of absorbed fraction under CBIST converge to a single source-independent value at high electron emission energies. These convergence limits correspond to the fractional track length in the target tissue and are given by the following expressions, where r_S is any source within or around the marrow cavity:

$$\phi(\text{TMS} \leftarrow r_S)_{\text{CBIST}} = \frac{\langle d_{\text{MC}} \rangle - 2\langle d_E \rangle}{\langle d_{\text{MC}} \rangle + \alpha \langle d_T \rangle}, \quad (5)$$

$$\phi(\text{TBE} \leftarrow r_S)_{\text{CBIST}} = \frac{2\langle d_E \rangle}{\langle d_{\text{MC}} \rangle + \alpha \langle d_T \rangle}, \quad \text{and} \quad (6)$$

$$\phi(\text{TBV} \leftarrow r_S)_{\text{CBIST}} = \frac{\alpha \langle d_T \rangle}{\langle d_{\text{MC}} \rangle + \alpha \langle d_T \rangle}, \quad (7)$$

where $\langle d_T \rangle$, $\langle d_{\text{MC}} \rangle$, and $\langle d_E \rangle$ are the mean chord lengths across the bone trabeculae, marrow cavities, and endosteal

layer, respectively, for the bone site of interest, and α is the ratio of CSDA (or continuous slowing-down approximation) ranges in marrow to those in bone tissue at high electron energy.³⁹ Values of $\langle d_T \rangle$ and $\langle d_{\text{MC}} \rangle$ are shown in Table II for the seven Leeds skeletal sites as given by their published distributions.¹² Below these values are mean trabecular and marrow cavity chord lengths for seven of the corresponding skeletal sites in the UF 66-year old male subject. The next two columns of Table II show tabulated mean chord lengths across the endosteal layer and marrow space—two tissue regions which in combination define the marrow cavity. The values for the mean endosteal chord lengths are obtained from derivations based on the endosteum chord algorithm and the sampled marrow chord distribution. For example, while the endosteal layer is uniformly considered to be a 10- μm tissue layer on the bone surfaces at all skeletal sites, Eqs. (1)–(4) show that the maximum endosteal chord is directly limited by the sampled marrow cavity chord length. In the final three columns of Table II, we display the convergence limits on the absorbed fraction at high particle energy as given by Eqs. (5)–(7). The variable r_S denotes any of the various electron source regions within the skeletal site.

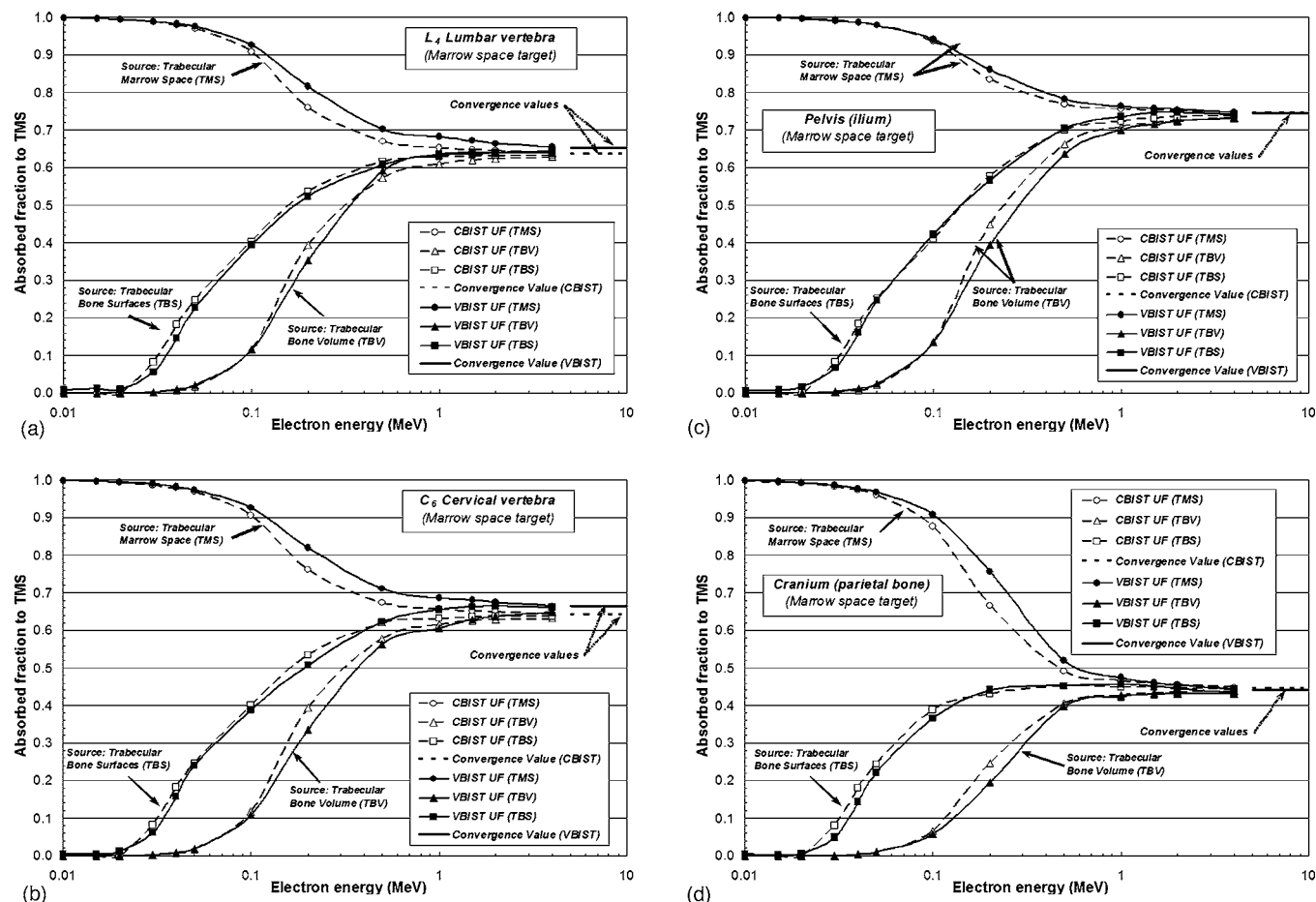


FIG. 2. Electron absorbed fractions to the active bone marrow within the (a) L_4 lumbar vertebra, (b) C_6 cervical vertebra, (c) ilium, and (d) cranium of the UF male. Two simulation methods are compared: voxel-based (solid lines) and chord-based (dashed lines) simulations, along with their respective convergence values.

Jokisch *et al.*⁶ derived corresponding convergence limits for infinite spongiosa transport within voxel-based models of the trabecular microstructure. These expressions are given as

$$\phi(\text{TMS} \leftarrow S)_{\text{VBIST}} = \frac{m_{\text{TMS}}}{m_{\text{TMS}} + m_{\text{TBE}} + \beta m_{\text{TBV}}}, \quad (8)$$

$$\phi(\text{TBE} \leftarrow S)_{\text{VBIST}} = \frac{m_{\text{TBE}}}{m_{\text{TMS}} + m_{\text{TBE}} + \beta m_{\text{TBV}}}, \quad \text{and} \quad (9)$$

$$\phi(\text{TBV} \leftarrow S)_{\text{VBIST}} = \frac{\beta m_{\text{TBV}}}{m_{\text{TMS}} + m_{\text{TBE}} + \beta m_{\text{TBV}}}, \quad (10)$$

where m_{TMS} , m_{TBE} , and m_{TBV} are the tissue masses for the marrow space, bone endosteum, and bone trabeculae within the physical sections of spongiosa used for microCT imaging, and β is the ratio of mean mass collisional stopping powers in bone and marrow tissues evaluated at high

electron energy. As derived by Jokisch *et al.*,⁶ Eqs. (5)–(7) yield equivalent convergence limits on the absorbed fraction as given by Eqs. (8)–(10) for similar targets provided that

$$\alpha = \frac{N_T}{N_{\text{MC}}} \frac{\overline{(dT/dx)}_{\text{TBV}}}{\overline{(dT/dx)}_{\text{TMS}}}, \quad (11)$$

where N_T and N_{MC} are the cumulative number of electron tracks through the bone trabeculae and marrow cavities, respectively. Under the assumption that $N_T \approx N_{\text{MC}}$ and that for 4-MeV electrons, the ratio of mean linear stopping powers in bone and in marrow is ~ 1.67 , the authors conclude that CBIST and VBIST should (in principle) produce equivalent convergence results at high source energies. This agreement would then follow only if the chord distribution data are consistent with the volume (or mass) fractions displayed within the 3D voxelized model of the skeletal sample. In the lower portion of Table II, mass estimates are given for the three tissue regions for each of the physical sections of spongiosa taken from the UF 66-year old male. Values of absorbed fraction convergence under VBIST are then given as defined in Eqs. (8)–(10) above.

IV. DISCUSSION

A. Comparison of CBIST and VBIST for marrow space targets

In this study, chord-length distributions from the UF 66-year old male subject were used to compare chord-based (CBIST) and voxel-based (VBIST) methods for infinite spongiosa transport in the skeletal tissues. In Figs. 2(a)–2(d), absorbed fractions to the marrow space (TMS) are shown for three source regions (TMS, TBS, and TBV) and four skeletal sites: lumbar vertebra, cervical vertebra, os coxae, and cranium, respectively. At electron energies below 50–100 keV, values of $\phi(\text{TMS} \leftarrow \text{TMS})$ are approximately equivalent under the two transport methodologies at all skeletal sites considered. At high energies (1–4 MeV), values of $\phi(\text{TMS} \leftarrow \text{TMS})$ approach their theoretically derived convergence values for both CBIST and VBIST simulations in these skeletal sites. As shown by Jokisch *et al.*,⁶ convergence values are expressed in terms of fractional masses for voxel-based infinite spongiosa transport models [see Eqs. (8)–(10) and values given in Table II]. For all bone sites (with the exception of the parietal bone), CBIST convergence falls slightly below that seen for VBIST convergence. The mean ratio of VBIST to CBIST convergence limits was found to be 0.97 ± 0.04 for all skeletal sites.

At electron energies exceeding 50–100 keV, Figs. 6(a)–6(d) indicate that, for the four bone sites considered, the chord-based IST model consistently predicts smaller values of $\phi(\text{TMS} \leftarrow \text{TMS})$ than given by the voxel-based IST model. This difference is most likely attributed to the fact that, under a CBIST simulation, sampled chord-lengths in the marrow space are directly equated to electron path lengths within the marrow tissues. As a result, nonlinear trajectories resulting from elastic and inelastic collisions are not properly accounted for under CBIST, and the marrow space is thus traversed with lower energy loss than seen under full 3D voxel-based transport. As the electron energy increases, however, the assumption of a linear path length under CBIST become less and less in error, and both approaches (if applied to the same skeletal microstructure) yield similar values of $\phi(\text{TMS} \leftarrow \text{TMS})$ within the agreement of their convergence limits.

Conversely, values of $\phi(\text{TMS} \leftarrow \text{TBS})$ and $\phi(\text{TMS} \leftarrow \text{TBV})$ at 500 keV to 1 MeV are noted to be slightly higher under CBIST transport than under VBIST transport for the same reason. In this case, electrons under CBIST travel straight-line trajectories through the bone trabeculae and endosteal layer, thus entering the marrow tissues with slightly more energy than under nonlinear trajectories seen under VBIST transport. The smaller tissue volumes of the bone trabeculae compared to the marrow cavities, however, tend to suppress these differences to a greater extent than for the case of marrow self-irradiation. At high energies (exceeding 1 MeV), both models approach their respective convergence limits. While minimal differences are seen for CBIST and VBIST convergence limits for the pelvis and cranium, slight differences are noticed for the lumbar and cervical vertebrae, for reasons discussed below.

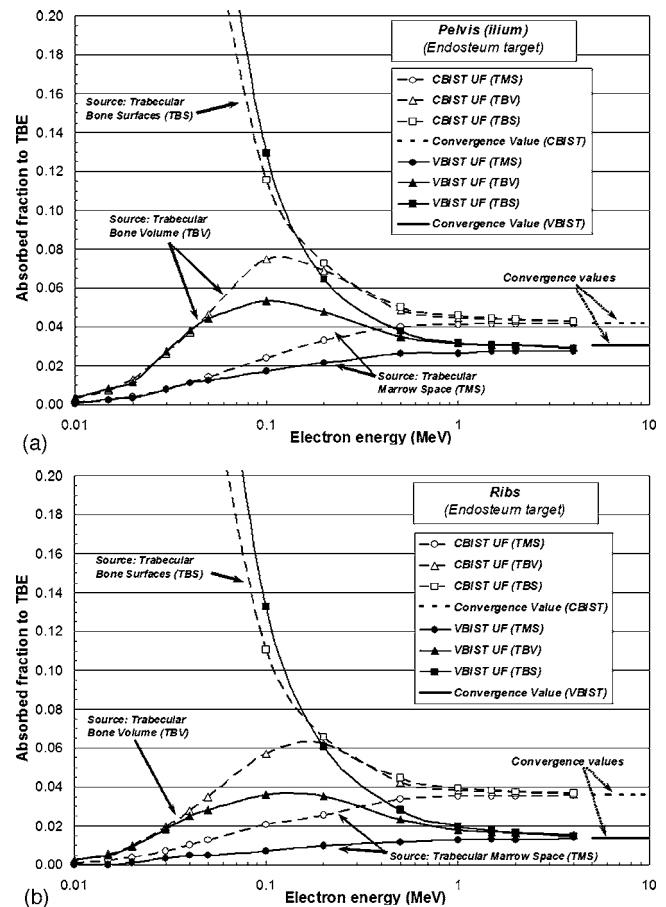


FIG. 3. Electron absorbed fractions to the trabecular endosteum within the (a) ilium and (b) ribs of the UF male. Two simulation methods are compared: voxel-based (solid lines) and chord-based (dashed lines) simulations, along with their respective convergence values.

B. Comparison of CBIST and VBIST for bone endosteum targets

In Figs. 3(a) and 3(b), we show values of $\phi(\text{TBE} \leftarrow \text{TMS})$, $\phi(\text{TBE} \leftarrow \text{TBS})$, and $\phi(\text{TBE} \leftarrow \text{TBV})$ for electron sources in the pelvis and ribs, respectively. Similar results are noted at other skeletal sites. As the electron energy increases, CBIST and VBIST values of $\phi(\text{TBE} \leftarrow r_s)$ begin to increasingly diverge, and approach different convergence limits under the two transport methodologies. In both Figs. 3(a) (pelvis) and 3(b) (ribs), a higher convergence value is given under chord-based transport than under voxel-based transport. In fact, ratios of CBIST to VBIST convergence limits for TBE targets range from a low of 1.37 in the iliac crest to a high of 2.58 in the ribs (skeletal mean ratio of 1.6 ± 0.4). This separation of convergence values at high electron energy was previously demonstrated by Jokisch *et al.*,⁶ who further noted that CBIST and VBIST convergence values should, in theory, be identical (independent of the transport technique).

The problem lies within the CBIST endosteum chord sampling method described in this work and used in previous CBIST computations.^{3,39} These methods [described in Eqs. (1)–(4)] sample an endosteum chord length for inclusion in-

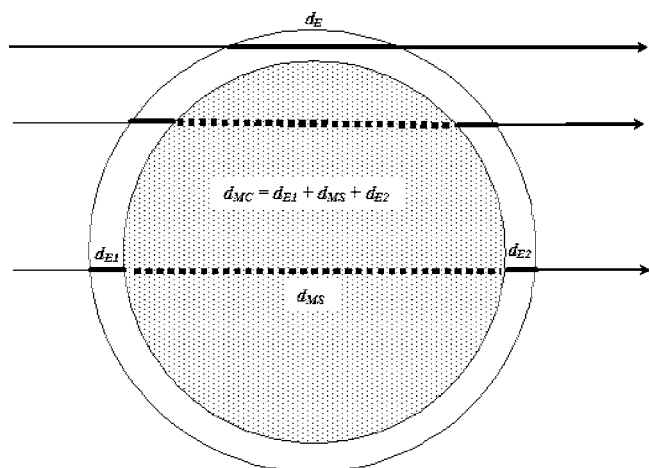


FIG. 4. Illustration of external (μ -random) chord lengths traversing a spherical marrow cavity lined with a 10- μm endosteal layer. Large marrow cavity chords (d_{MC}) are associated with small endosteal chords (d_{E1} and d_{E2}) and vice versa.

side an independently sampled marrow cavity chord. If one considers straight-line traversals of a marrow cavity, it is reasonable to assume that the longer the sampled marrow chord, the shorter the sampled endosteal chords as demonstrated in Fig. 4. In fact, a numerical analysis of a 750- μm diameter spherical marrow cavity surrounded by a 10 μm thick endosteum shell indicates that the current endosteal sampling algorithm would overestimate the mean endosteum chord length by a factor of 2.75. This would correspondingly lead to an overestimate of the endosteal dose by the same magnitude. This side calculation was simply done by using expressions to determine the mean marrow space and marrow cavity chord lengths in an ideal spherical geometry and comparing to results from the current CBIST endosteum model. Figures 3(a) and 3(b) indicate that CBIST endosteal doses are in fact ~ 1.3 to 2.6 times higher than those seen under VBIST. Similar results were observed for the other skeletal sites. This overestimate in endosteal pathlengths also leads to an underestimate of the marrow space pathlength [Eq. (4)]. This is observed in Figs. 2(a)–2(d) and in Table II where the VBIST marrow space absorbed fractions exceed those given by CBIST in all cases.

V. CONCLUSIONS

The present study was conducted to compare chord-based versus voxel-based methods of skeletal dosimetry using imaging data obtained from the same anatomical source. Several observations can be made from this investigation. First, chord-based IST models of electron transport typically yield lower values of $\phi(\text{TMS} \leftarrow \text{TMS})$ than given by voxel-based IST models at energies above 100 keV as the former does not account for nonlinear electron paths within the marrow tissues. Second, generally good agreement is seen between CBIST and VBIST values of $\phi(\text{TMS} \leftarrow \text{TBS})$, especially for electrons of energies below 500 keV. This finding is particularly significant in that the CBIST model in this study approximates the trajectories of surface-source emissions by

sampling μ -random chord distributions as an approximation to sampling S -random distributions. The agreement seen here lends strong support to the conclusion that μ -random chord sampling is an approximate, yet reasonable, substitute when S -random chord distributions are not available. Future efforts in image-based skeletal dosimetry studies should investigate this issue further through direct acquisition of S -random chord distributions within the 3D digital images of spongia. Third, excellent agreement is also seen between CBIST and VBIST values of $\phi(\text{TMS} \leftarrow \text{TBV})$, especially for electrons of energies below 500 keV. In the cervical vertebra and cranium, the CBIST-VBIST agreement in $\phi(\text{TMS} \leftarrow \text{TBV})$ extends to even higher energies (1 MeV). Finally, at high electron energies, values of $\phi(\text{TMS} \leftarrow r_s)$ under CBIST are noted to consistently fall below corresponding convergence limits as seen under VBIST ($\sim 3.2\%$ on average), while values of $\phi(\text{TBE} \leftarrow r_s)$ given by CBIST are shown to exceed those given by VBIST by an average of a factor of 1.6. Values of $\phi(\text{TMS} \leftarrow r_s)$ at high energy shown in Figs. 2(a)–2(d) confirm that the transport calculations are valid and do indeed converge to values predicted under either Eqs. (5)–(7) (CBIST) or Eqs. (8)–(10) (VBIST); consequently, these two discrepancies are coupled and the overestimate of energy deposition to TBE is attributed to limitations in the CBIST algorithm used to simulate electron traversal of this tissue layer (e.g., half-space geometry with linear electron trajectories).

This study supports the future use of voxel-based skeletal dosimetry models which circumvent three fundamental limitations of chord-based models. First, VBIST skeletal models explicitly define the microanatomy of the endosteal tissue layer, and thus they do not need to rely on mathematical algorithms for particle transport across this tissue layer. Second, VBIST skeletal models directly use the image of the trabecular microstructure to trace radiation particle paths across tissue regions; consequently, these voxel-based models do not rely on assumptions of statistical independence of the measured bone trabeculae and marrow chord-length distributions. Finally, VBIST skeletal models permit explicit treatment of nonlinear electron trajectories in the skeletal tissues, thus avoiding the assumption of straight-line electron paths as required of CBIST skeletal models.

ACKNOWLEDGMENTS

This work was supported in part by Grant No. CA96441 from the National Cancer Institute and Grant No. DE-FG07-02ID14327 from the U.S. Department of Energy with the University of Florida. We would also like to thank Scanco Medical AG for their assistance with the use of their commercial scanning service.

^aElectronic mail: wboleh@ufl.edu

¹ICRP, *Limits for Intakes of Radionuclides by Workers*, ICRP Publication 30 (Part 1). (International Commission on Radiological Protection, Oxford, UK, 1979).

²ICRP, *Basic Anatomical and Physiological Data for Use in Radiological Protection: The Skeleton*, ICRP Publication 70. (International Commission on Radiological Protection, Oxford, UK, 1995).

- ³K. F. Eckerman and M. G. Stabin, "Electron absorbed fractions and dose conversion factors for marrow and bone by skeletal regions," *Health Phys.* **78**, 199–214 (2000).
- ⁴J. R. Whitwell and F. W. Spiers, "Calculated beta-ray dose factors for trabecular bone," *Phys. Med. Biol.* **21**, 16–38 (1976).
- ⁵A. H. Beddoe, P. J. Darley, and F. W. Spiers, "Measurements of trabecular bone structure in man," *Phys. Med. Biol.* **21**, 589–607 (1976).
- ⁶D. W. Jokisch, L. G. Bouchet, P. W. Patton, D. A. Rajon, and W. E. Bolch, "Beta-particle dosimetry of the trabecular skeleton using Monte Carlo transport within 3D digital images," *Med. Phys.* **28**, 1505–1518 (2001).
- ⁷P. W. Patton, D. W. Jokisch, D. A. Rajon, A. P. Shah, S. L. Myers, and W. E. Bolch, "Skeletal dosimetry via NMR microscopy: investigations of sample reproducibility and signal source," *Health Phys.* **82**, 316–326 (2002).
- ⁸M. G. Stabin, "MIRDose: Personal computer software for internal dose assessment in nuclear medicine," *J. Nucl. Med.* **37**, 538–546 (1996).
- ⁹M. G. Stabin and J. A. Siegel, "Physical models and dose factors for use in internal dose assessment," *Health Phys.* **85**, 294–310 (2003).
- ¹⁰M. G. Stabin, R. B. Sparks, and E. Crowe, "OLINDA/EXM: the second-generation personal computer software for internal dose assessment in nuclear medicine," *J. Nucl. Med.* **46**, 1023–1027 (2005).
- ¹¹M. Stabin and R. Sparks, "OLINDA-PC-based software for biokinetic analysis and internal dose calculations in nuclear medicine [Abstract]," *J. Nucl. Med.* **44**, 103 (2003).
- ¹²J. R. Whitwell, "Theoretical investigations of energy loss by ionizing particles in bone," Thesis, (Department of Medical Physics, University of Leeds, Leeds, UK, 1973).
- ¹³ICRP, *Basic Anatomical and Physiological Data for Use in Radiological Protection: Reference Values*, Publication 89. (International Commission on Radiological Protection, New York, New York, 2002).
- ¹⁴P. W. Patton, D. A. Rajon, A. P. Shah, D. W. Jokisch, B. Inglis, and W. E. Bolch, "Site-specific variability in trabecular bone dosimetry: considerations of energy loss to cortical bone," *Med. Phys.* **29**, 6–14 (2002).
- ¹⁵A. P. Shah, P. W. Patton, D. A. Rajon, and W. E. Bolch, "Adipocyte spatial distributions in bone marrow: Implications for skeletal dosimetry models," *J. Nucl. Med.* **44**, 774–783 (2003).
- ¹⁶A. P. Shah, W. E. Bolch, D. A. Rajon, P. W. Patton, and D. W. Jokisch, "A paired-image radiation transport model for skeletal dosimetry," *J. Nucl. Med.* **46**, 344–353 (2005).
- ¹⁷A. Shah, D. Rajon, P. Patton, D. Jokisch, and W. Bolch, "Accounting for beta-particle energy loss to cortical bone via Paired-Image Radiation Transport (PIRT)," *Med. Phys.* **32**, 1354–1366 (2005).
- ¹⁸N. Petoussi-Henss, M. Zankl, U. Fill, and D. Regulla, "The GSF family of voxel phantoms," *Phys. Med. Biol.* **47**, 89–106 (2002).
- ¹⁹X. G. Xu, T. C. Chao, and A. Bozkurt, "VIP-Man: An image-based whole-body adult male model constructed from color photographs of the Visible Human Project for multi-particle Monte Carlo calculations," *Health Phys.* **78**, 476–486 (2000).
- ²⁰I. G. Zubal and C. H. Harell, "Voxel based Monte Carlo calculations of nuclear medicine images and applied variance reduction techniques," *Image Vis. Comput.* **10**, 342–348 (1992).
- ²¹H. Yoriyaz, A. dos Santos, M. G. Stabin, and R. Cabezas, "Absorbed fractions in a voxel-based phantom calculated with the MCNP-4B code," *Med. Phys.* **27**, 1555–1562 (2000).
- ²²M. Caon, "Voxel-based computational models of real human anatomy: a review," *Radiat. Environ. Biophys.* **42**, 229–235 (2004).
- ²³D. W. Jokisch, P. W. Patton, B. A. Inglis, L. G. Bouchet, D. A. Rajon, J. Rifkin, and W. E. Bolch, "NMR microscopy of trabecular bone and its role in skeletal dosimetry," *Health Phys.* **75**, 584–596 (1998).
- ²⁴D. A. Rajon and W. E. Bolch, "Interactions within 3D isotropic and homogeneous radiation fields: A Monte Carlo simulation algorithm," *Comput. Methods Programs Biomed.* **70**, 167–177 (2003).
- ²⁵D. Rajon and W. Bolch, "Marching cube algorithm: Review and trilinear interpolation adaptation for image-based dosimetric models," *Comput. Med. Imaging Graph.* **27**, 411–435 (2003).
- ²⁶A. Shah, D. Rajon, D. Jokisch, P. Patton, and W. Bolch, "A comparison of skeletal chord-length distributions in the adult male," *Health Phys.* **89**, 199–215 (2005).
- ²⁷R. Coleman, "Random paths through convex bodies," *J. Appl. Probab.* **6**, 430–441 (1969).
- ²⁸K. F. Eckerman, J. C. Ryman, A. C. Taner, and G. D. Kerr, "Traversal of cells by radiation and absorbed fraction estimates for electrons and alpha particles," in *Proceedings of the Fourth International Radiopharmaceutical Dosimetry Symposium*, edited by A. T. Schlatke-Stelson, and E. E. Watson (ORAU, Oak Ridge, Tennessee, 1985), pp. 67–81.
- ²⁹A. M. Kellerer, "Considerations on the random traversal of convex bodies and solutions for general cylinders," *Radiat. Res.* **47**, 359–376 (1971).
- ³⁰F. W. Spiers and A. H. Beddoe, "'Radial' scanning of trabecular bone: consideration of the probability distributions of path lengths through cavities and trabeculae," *Phys. Med. Biol.* **22**, 670–680 (1977).
- ³¹D. W. Jokisch, P. W. Patton, D. A. Rajon, B. A. Inglis, and W. E. Bolch, "Chord distributions across 3D digital images of a human thoracic vertebra," *Med. Phys.* **28**, 1493–1504 (2001).
- ³²ICRU, *Stopping Powers for Electrons and Positrons*, Report 37 (International Commission on Radiation Units and Measurements, Bethesda, MD, 1984).
- ³³ICRU, *Photon, Electron, Proton and Neutron Interaction Data for Body Tissues*, Report 46 (International Commission on Radiation Units and Measurements, Bethesda, MD, 1992).
- ³⁴W. E. Bolch, P. W. Patton, D. A. Rajon, A. P. Shah, D. W. Jokisch, and B. Inglis, "Considerations of marrow cellularity in 3D dosimetric models of the trabecular skeleton," *J. Nucl. Med.* **43**, 97–108 (2002).
- ³⁵ICRP, *A Review of the Radiosensitivity of the Tissues of Bone*, ICRP Publication 11 (International Commission on Radiological Protection, Oxford, UK, 1967).
- ³⁶ICRP, *Recommendations of the International Commission on Radiological Protection*, Publication 26 (Pergamon, Oxford, 1977).
- ³⁷I. Kawrakow, "Accurate condensed history Monte Carlo simulation of electron transport. I: EGSnrc, the new EGS4 version," *Med. Phys.* **27**, 485–498 (2000).
- ³⁸K. F. Eckerman, "Aspects of the dosimetry of radionuclides within the skeleton with particular emphasis on the active marrow," in *Proceedings of the Fourth International Radiopharmaceutical Dosimetry Symposium*, edited by A. T. Schlatke-Stelson and E. E. Watson (Oak Ridge Associated Universities, Oak Ridge, Tennessee, 1985), pp. 514–534.
- ³⁹L. G. Bouchet, D. W. Jokisch, and W. E. Bolch, "A three-dimensional transport model for determining absorbed fractions of energy for electrons in trabecular bone," *J. Nucl. Med.* **40**, 1947–1966 (1999).

Journal Articles – In Preparation

Absorbed Fractions for Alpha Particles in Tissues of Cortical Bone

Christopher J. Watchman, PhD¹ and Wesley E. Bolch, PhD^{2,3}

¹*Department of Radiation Oncology, University of Arizona, Tucson, AZ;*

²*Department of Nuclear & Radiological Engineering, University of Florida, Gainesville, FL;*

³*Department of Biomedical Engineering, University of Florida, Gainesville, FL*

For reprints and correspondence contact:

Wesley E. Bolch, PhD, PE, CHP

Director, Advanced Laboratory for Radiation Dosimetry Studies (ALRADS)

Department of Nuclear and Radiological Engineering

University of Florida, Gainesville, Florida 32611-8300

Phone: (352) 846-1361 Fax: (352) 392-3380 Email: wbolch@ufl.edu

SHORT TITLE:

Alpha Absorbed Fractions in Cortical Bone

This work was supported by the

U.S. Department of Energy and the National Cancer Institute

Word Count (Text and Refs): **4243** (no abstract)

Word Count (Figure Captions): **262**

Word Count (Table Captions): **163**

Word Count (Total): **4668**

INTRODUCTION

Beta-particle emitters have been traditionally used in radionuclide therapies for cancer treatment.¹⁻³ In many cases, toxicities to normal non-target organs such as the active bone marrow and tissues of the kidneys have been dose-limiting for these therapies. An attractive alternative is the use of shorter-ranged alpha particles. Examples of alpha emitters under clinical investigation include ^{213}Bi , ^{212}Bi , ^{211}At , ^{225}Ac , and ^{223}Ra .⁴⁻¹¹ Alpha particles emitted from these radionuclides have initial energies in the range of ~5.0 to 8.8 MeV – an energy range substantially higher than those from longer-lived radionuclides of general interest in radiation protection (~3.9 to 5.5 MeV). Consequently, skeletal dosimetry methods developed historically for health physics applications may not be totally appropriate as applied to alpha-emitters of interest in radionuclide therapy. We have recently developed a radiation transport model for alpha particles in the tissues of trabecular bone that makes use of stochastic sampling of chord-length distributions across the bone trabeculae and marrow cavities.¹² This model explicitly considers changes alpha particle absorbed fractions with variations in both alpha-particle energy and patient marrow cellularity. In the present study, we extend this modeling strategy to the study of alpha-particle dosimetry in cortical bone.

Previous Dosimetric Models for Alpha Particles in Cortical Bone

The majority of modeling strategies for radiation transport in cortical bone come from the health physics community. Consequently, these models have investigated alpha emitters commonly found in the production of nuclear power or as a result of nuclear weapons testing. The alpha emitters associated with these studies have energies typically below 5.5 MeV. Different methods of calculating endosteal dose from alpha particles have been presented in the literature. These methods began with analytical models, later to geometric models, and have since evolved to chord-based geometric models as described in this paper.

In 1953, Spiers presented an analytical methodology to calculate the alpha-particle dose to bone tissues from ^{226}Ra and ^{222}Rn .¹³ His model entailed methods for calculating the dose rate in soft tissue adjacent to bone surfaces and soft tissues enclosed in bone tissue. For the tissues adjacent to bone, he developed a relationship describing the dose in soft tissue as a function of distance from the bone surface. Similar information was obtained for the soft tissue enclosed case, which was an analytical relationship for the dose rate as a function of distance from the cavity center. Using this model, Spiers also obtained values for the maximum permissible body burden in the skeleton for ^{226}Ra . This work was later followed by a study by Charlton and Cormack who developed a method to calculate alpha-particle absorbed dose to bone cavities filled with soft tissue.¹⁴ This model consisted of calculating the absorbed dose at a point in space within a cylindrical cavity as a function of the particle's linear energy transfer. Geometrical dose factors were then calculated and tabulated for use in dosimetry calculations for ^{226}Ra .

A new method for describing the structure of cortical bone was developed by Beddoe using chord length distributions.¹⁵ In this model, Beddoe obtained samples of three cortical bones: femur, tibia, and humerus. Sections of bone were taken in 20-30 μm slices perpendicular to the longitudinal axis of the bone diaphysis. These sections were stained and then viewed using an optical scanning system developed previous for chord-length measurements in cancellous bone. Consequently, only chord lengths in the transverse direction were obtained. This method also described how a transverse chord data set could be transformed into an omni-directional data set. The transformation adjustments accounted for ~1% changes for chord-lengths through the mineralized portion of cortical bone, but they resulted in increases of ~40% for chord-lengths across the haversian cavities. Chord lengths obtained from this study were later used by Beddoe as the structural background for Monte Carlo radiation dose calculations in cortical bone.

Another series of dose factors was presented by Polig.¹⁶ In this model, a Monte Carlo approach was used to calculate doses to different soft tissue target volumes located within a cylindrical osteonal shell. Dose factors were obtained for alpha particles being emitted from shells of different distances from the soft tissue targets. Different diameter haversian canal diameters for a human and a beagle were used in the calculations, specifically 70 μm for the human and 30 μm for the beagle. Two radionuclides were studied in their model: ^{226}Ra and ^{239}Pu . These radionuclides reflect the traditional focus on radiological protection for alpha emitters.

Currently, the cortical bone model given in ICRP Publication 30¹⁷ is used in health physics applications. Simple geometries consisting of planes are used in the ICRP 30 bone model. ICRP Publication 30 assumes that the short range of alpha particles in human tissues allows for such geometries to be appropriate approximations. Values for absorbed fractions are given for two different targets: the active (or red) bone marrow and bone surface cells lining the haversian canals (cortical endosteum). No other source target combinations are identified. Active marrow targets are given absorbed fraction values of 0.0 for both cortical bone volume and surface sources. For the cortical endosteum target, alpha particle absorbed fraction values for volume and surface sources are 0.01 and 0.25, respectively. In medical internal dosimetry, absorbed fractions for alpha-particles in cortical bone from the 2003 Eckerman skeletal model¹⁸ are used within the OLINDA code for nuclear medicine dosimetry.¹⁹ This code improves on previous modeling strategies used in the ICRP 30 bone model in that it allows for energy dependence in alpha particle absorbed fraction. Values of alpha particle absorbed fractions in cortical bone for the ICRP 30 and 2003 Eckerman models are given in Tables 1 and 2, respectively.

MATERIALS AND METHODS

In this study, particle transport in cortical bone is accomplished using techniques similar to those developed for microstructural electron transport in the model published by Bouchet and Bolch.²⁰ The microstructure of individual osteons within cortical bone are taken directly from transverse chord-length distributions (perpendicular to the long axis of the bone) published by Beddoe for the femur, humerus, and tibia.^{15, 21} These distributions are shown in Figure 1, while average chord lengths across and between the haversian cavities are given in Table 3. Figure 1A shows the distribution of chord lengths found between individual haversian cavities in the transverse plane of each bone site, while Figure 1B gives the probability distribution of chord lengths across the haversian cavities themselves. Through the use of range-energy relationships, absorbed fractions to cortical endosteum and to the tissues of the haversian canal are calculated for alpha-particle emissions between 0.5 and 10 MeV and over an energy range of 0.01 to 4 MeV for electrons.

As given in Bouchet and Bolch²⁰, we adopt the following nomenclature for the various source and target tissues: CBV – cortical bone volume, CBE – cortical bone endosteum, CBS – cortical bone surface, and CHS – cortical haversian space. The CBV is further defined as the composite of all osseous tissues of cortical bone including that found in circumferential lamellae, inter-osteon lamellae, and intra-osteon (interstitial) lamellae. Further subdivision of the CBV is broken down into long bones (CBV_{long}) and the cortical cortex (CBV_{cortex}) surrounding spongiosa (as in the proximal and distal ends of long bones, and at all other skeletal sites of the axial skeleton). Unless otherwise specified in this paper, CBV will be used interchangeably with CBV_{long} . Two additional tissues are also defined as the inactive (or yellow) marrow of the medullary cavity (CIM) and the medullary cavity endosteum (CME).

Calculations of particle transport are performed under the assumption of an infinite region of cortical bone, thus ignoring cross-dose contributions to active marrow in the adjacent trabecular spongiosa. While this assumption is rarely valid for higher-energy beta particles in the skeleton²², the model is quite adequate for alpha particles even at energies approaching 10 MeV which correlate in linear range to beta particles of ~100 keV. The model described below are termed CBICT (Chord-Based Infinite Cortical Transport) model for charged particle transport in the cortical bone microstructure.

Tissue Composition and Range/Energy Data

Range-energy relationships needed for alpha-particle transport in cortical bone were taken from data tabulated in ICRU Report 49.²³ Elemental data for both endosteal tissue, cortical bone and blood were taken from Appendix A of ICRU Report 46²⁴ and are listed in Table 4. Range-energy relationships for these specific tissue compositions and densities are not given in ICRU Report 49, and thus they were calculated using the Bragg-Kleeman rule with liquid water as the reference media for scaling to blood and cortical endosteum, while the ICRU compact bone was used as the reference media for scaling to cortical bone. The Bragg-Kleeman scaling rule is,

$$R_T = R_{Ref} \frac{\rho_{Ref}}{\rho_T} \sqrt{\frac{A_T}{A_{Ref}}}, \quad (\text{Eq. 1})$$

where R_T is the linear CSDA range in the desired tissue (CBE or CHS), R_{Ref} is the corresponding linear range in the reference tissue, and ρ_T and ρ_{Ref} are the mass densities of these media. In Eq. 1, the effective atomic number of each tissue, A_T (as well as A_{Ref}), is calculated as:

$$\sqrt{A_T} = \left(\sum_i \frac{w_i}{\sqrt{A_i}} \right)^{-1}, \quad (\text{Eq. 2})$$

where w_i is the mass fraction for the i^{th} element within that tissue. Tabular data for CSDA range versus particle energy were thus created for all tissues for use by the transport code.

Chord-Based Model for Particle Transport in Cortical Bone

Particle transport in the present study is performed through random and alternate sampling of the University of Leeds cumulative density functions (CDFs) for μ -random transverse chord lengths across the bone matrix (d_B^T) and the haversian cavities (d_{HC}^T) of cortical bone. The T superscript indicates chords lying within the plane transverse to the long axis of the osteons. Corresponding distributions under I-randomness are applied in regions of alpha-particle source emissions. For consistency with the sample preparation and scanning methods of the Leeds studies, we make a distinction between the haversian cavity (HC) (inclusive of the cortical endosteal layer) and the haversian space (HS) (exclusive of the cortical endosteal layer). Owing to the short ranges of alpha particle relative to the macroscopic structure of cortical bone, all osteons are treated as infinite in their longitudinal extent. For electrons this assumption does not hold up as well at high energies and modifications to this model are described later in this study.

The transport methodology is best described by first considering an alpha-emitter uniformly distributed within the osseous tissues of the cortical bone matrix (e.g., CBV source) as shown in Figure 3. Here, we see four representative osteons, with different haversian cavity diameters, within the transverse plane of the bone site. The transport code first randomly samples a bone matrix chord $(d_{B1}^T)^{max}$ from the I-random cumulative density function for the skeletal site of interest (e.g, humerus). This sample chord thus represents the maximum possible distance - in the transverse plane - that an alpha particle may travel within the bone matrix prior to its potential entry into the endosteal layer of an adjacent haversian cavity. In the example of Figure 3, the value of $(d_{B1}^T)^{max}$ is given as chord A→B. The transverse transport distance actually taken by the particle, d_{B1}^T , is thus uniformly sampled across the interval $[0, (d_{B1}^T)^{max}]$. In this example, the site of particle emission in Figure 3 is taken as point A^* , a

location within the inter-osteon regions of cortical bone (e.g., interstitial lamellae). To account for the 3D pathlength of the particle, a polar angle ϕ is randomly sampled across the interval $[1 \leq \cos \phi \leq 0]$ as shown in Figure 4. The particle is thus physically transported across the chord $d_{B1} = (d_{B1}^T)^{max} / \cos \phi$. The range-energy function for alpha particles in bone matrix is used to determine the energy expended by the particle during its trajectory across chord length d_{B1} . If the particle retains residual kinetic energy following trajectory d_{B1} , the particle is further transported into (and potentially across) the endosteal layer of the intersected osteon (see Fig. 4).

Chord lengths across the endosteal layer must be considered in tandem with random sampling of the transverse haversian cavity chord length, d_{HC}^T , as described by Bouchet al.²⁰ In their method, the value of d_{HC}^T is given as:

$$d_{HC}^T = d_{E1}^T + d_{HS}^T + d_{E2}^T, \quad (\text{Eq. 3})$$

with values for d_{E1}^T and d_{E2}^T being equal (owing to the circular geometry of the osteon) and are determined through uniform sampling of the cosine of the entry angle (η) in the transverse plane:

$$\eta \in [0 : 1] \text{ with } d_{E1}^T = d_{E2}^T = (10 \mu m) / \eta \quad (\text{Eq. 4})$$

If $d_{E1}^T + d_{E2}^T \geq d_{HC}^T$, then

$$d_{E1}^T = d_{E2}^T = d_{HC}^T / 2 \text{ and } d_{HS}^T = 0 \quad (\text{Eq. 5})$$

(the particle travels fully within the endosteal layer of the haversian cavity). If, however, $d_{E1}^T + d_{E2}^T < d_{HC}^T$, then

$$d_{HS}^T = d_{HC}^T - (d_{E1}^T + d_{E2}^T). \quad (\text{Eq. 6})$$

In this algorithm (which is adopted from that used in trabecular bone), curvature of the Haversian cavity is insufficiently accounted for (see Fig. 5B) since the cortical endosteum is modeled as two infinite planes. Problems with this sampling algorithm were described in

Watchman et al¹² and a modification was subsequently applied. To correct for this issue, the modification mentioned is adopted and described below. We begin by first sampling the Haversian chord d_{HC}^T . We assume that this sampled chord is the average chord length through the cavity and generate the radius of the Haversian cavity using the following formula from Coleman²⁵:

$$\langle d_{HC}^T \rangle = \pi \frac{Area}{Perimeter} = \frac{\pi}{2} R_{HC}^T \quad (\text{Eq. 7})$$

$$R_{HC}^T = \frac{2 \langle d_{HC}^T \rangle}{\pi} \quad (\text{Eq. 8})$$

Once the R_{HC}^T is calculated, the maximum distance the particle may travel in the transverse plane is calculated as,

$$dE_{max} = 2 \sqrt{(R_{HC}^T)^2 - (R_{HC}^T - 10)^2} \quad (\text{Eq. 9})$$

The value of dE_{max} is then replaced in the conditional statements before Eqs. 5 and 6 which results in: if $d_{E1}^T + d_{E2}^T \geq dE_{max}^T$, then $d_{E1}^T = d_{E2}^T = dE_{HC}^T / 2$ and $d_{HS}^T = 0$ the particle travels fully within the endosteal layer of the haversian cavity. However if, $d_{E1}^T + d_{E2}^T < dE_{max}^T$, then $d_{HS}^T = d_{HC}^T - (d_{E1}^T + d_{E2}^T)$.

As before, all transverse distances are trigonometrically transformed to potential particle trajectories through the polar emission angle ϕ as shown in Figure 4 (e.g., $d_{HS} = d_{HS}^T / \cos \phi$). The particle range-energy functions in endosteal tissues (CBE) are then used to determine the kinetic energy lost within the near endosteal layer. If the particle has residual kinetic energy and d_{HS}^T (and d_{HS}) > 0 , the alpha particle is further transported within the tissues (e.g, blood) of the haversian space (distance d_{HS}) and potentially through the endosteal layer of the opposite side (distance d_{E2}). Under the condition that the alpha particle continues to retain kinetic energy upon exiting the entire haversian cavity (point C in Fig. 3), another transverse bone matrix chord d_{B2}^T is selected, and the particle is further transported (using the range-energy relationship in

bone tissue) through the chord $d_{B2} = d_{B2}^T / \cos \phi$. The entire process is repeated until all initial particle energy is fully expended.

Emission sites within the haversian space (CHS source) are also considered in a similar fashion. For a CHS source of alpha-particle emissions, transport calculations begin with the selection of a maximum transverse chord length $(d_{HC}^T)^{max}$ as given by chord A→D in Figure 5A. Emission site A* is then selected randomly across chord A→D taking into account transverse endosteal thicknesses d_{E1}^T and d_{E2}^T . Particle tracking is then followed along the haversian space chord $d_{HS} = d_{HS}^T / \cos \phi$, through the endosteal layer chord $d_{E2} = d_{E2}^T / \cos \phi$, and potentially into the bone matrix of the osteon along another sampled chord $d_B = d_B^T / \cos \phi$. Transport across tissue boundaries is, of course, dependent upon residual energy of the particle at that point along its trajectory. In the case of a cortical bone surface source (CBS), an approximate radius of a haversian cavity cylinder containing the endosteal source layer is first derived as previously described (see Fig. 5B). A random sampling of the emission direction is then used to determine if the particle enters the CBV or the CBE.

RESULTS

Absorbed fractions for alpha particles and electrons were obtained for several target (CHS, CBE, and CBV) and source (CHS, CBS, and CBV) tissues as a function of particle emission energy and skeletal site. The tissues of the bone matrix are not traditionally considered as a radiosensitive target for internal dosimetry; however, the CBV may be used as a surrogate for bone lesions within cortical bone instead of site-specific information on tumor micro-morphometry.

Absorbed fractions to the cortical bone endosteum are shown in Figures 6A to 6C for alpha particles emitted uniformly within the CHS, CBS, and CBV source regions of cortical bone, respectively. Solid horizontal lines indicate current energy-independent absorbed fractions recommended in the ICRP 30 bone model for alphas and electrons in cortical bone.

Dashed lines designate results from the 2003 Eckerman model. Tabulated values of absorbed fraction are presented in the Appendix to this paper (Tables A1 to A3). For each source-target combination, energy deposition was tracked within the primary tissue (self-irradiation), secondary tissue (tissue adjacent to the source tissue), or tertiary tissue (third or greater tissue encountered) depending on the emission energy (and resulting CSDA range) of the alpha particle. Coefficients of variation (COVs) for alpha particles are $\leq 1\%$ for self-irradiation of cortical bone tissues, and $\leq 3\%$ for cross-irradiations at energies exceeding 2.5 MeV. At very low energy particles, COVs on the absorbed fraction for cross-irradiation can approach 25%. For cortical bone surface (CBS) sources, absorbed fractions had COVs below 1% at energies exceeding 2.5 MeV, and COVs below 5% for alpha energies less than 2.5 MeV.

DISCUSSION

Alpha Particle Absorbed Fractions to the Cortical Bone Endosteum

The energy-dependent values of alpha-particle absorbed fractions to the endosteal tissues of cortical bone are shown in Figures 6A to 6C for emission sites uniformly localized in the haversian space, bone surfaces, and osseous tissues of cortical bone, respectively. Of the three source tissues considered, the greatest bone-site dependence is shown in Fig. 6A for α -particles emitted uniformly within the haversian spaces of the femur, humerus, and tibia. As shown in Figure 1B, the tibia was shown in the Leeds studies to have haversian cavity sizes which are relatively large compared to those of the femur and humerus, and thus more alpha-particle source energy is expended in the source tissue, with less energy available for deposition to the CBE (see corresponding Fig. 6A).

Using the average chord length argument it would be expected that the humerus would exhibit the highest absorbed fraction, yet this is not the case. The differences observed are due to variations in the chord length distribution, and the alpha-particle stopping powers. In Fig. 6A the absorbed fraction profile for the femur and humerus demonstrates little divergence until

about 4 MeV. At this energy the range of an alpha particle (Fig. 2A) is $\sim 25 \mu\text{m}$. Ranges on this order would only effect energy deposition in the smallest of haversian cavities sampled from the chord length distribution (i.e. those sampled from the first chord-length bin). Thus the differences between the femur and humerus are small. As the energy increases beyond 4 MeV the influence of the differences in chord length distribution become more apparent. At $50 \mu\text{m}$ ($\sim 6 \text{ MeV}$), the chord lengths within the humerus begins to drop in probability with respect to larger chord lengths. This results in smaller chords being sampled in the calculation for the humerus as opposed to the femur. Consequently, the humerus profile begins to drop as the alpha particles have sufficient energy to cross through the endosteum and begin to deposit energy in the bone volume. The femur conversely samples a greater number of larger chords. Thus, despite the alpha particle having the same energy, a greater distance must be traversed in the endosteum of the femur.

Figure 6B shows values of $\phi(\text{CBE} \leftarrow \text{CBS})$ for alpha particles emitted on the bone surfaces. As expected, values of $\phi(\text{CBE} \leftarrow \text{CBS})$ begin at ~ 0.5 (where approximately one-half of the particles are emitted in the direction of the endosteal layer). In Watchman et al.,¹² a very similar energy-dependence was seen for values of $\phi(\text{TBE} \leftarrow \text{TBS})$ for lower-energy alpha particles in trabecular bone (TBS – trabecular bone surfaces) (see Figure 7). However, at the highest alpha energy considered (10 MeV), the $\phi(\text{CBE} \leftarrow \text{CBS})$ in femoral cortical bone is 0.33 while corresponding values of $\phi(\text{TBE} \leftarrow \text{TBS})$ in the same bone site significantly lower ~ 0.15 . This difference is expected since in the trabecular bone the distance a particle nominally travels in the endosteum will be much smaller than in cortical bone. Discrepancies are due to the cylindrical geometry of cortical bone osteons in comparison to the complex micro-architecture of trabecular bone.

In the ICRP 30 bone model, a value of 0.25 is assigned for both $\phi(\text{CBE} \leftarrow \text{CBS})$ and $\phi(\text{TBE} \leftarrow \text{TBS})$. As given by the values from our CBICT model, the ICRP 30 bone model is

shown to underestimate the alpha-particle dose to cortical endosteum by a range of ~2 to 1.6 over the entire energy range for emissions on the bone surfaces. The values obtained from the 2003 Eckerman model, as shown by the dashed line (also see Table 3), are significantly lower than those we have calculated. These differences can be, at least in part, attributed to the modeling of curvature in our model. Since full details of the 2003 Eckerman model are unavailable, a full comparison is not possible. Further comparisons to this model will be made later in this work accompanied by additional details.

Figure 6C shows values of $\phi(\text{CBE} \leftarrow \text{CBV})$ for alpha particles uniformly distributed in the osseous tissues of cortical bone. Again, very little bone-site dependence is seen among values for the femur, humerus, and tibia. This finding is consistent with the rather uniform pattern of bone matrix chord lengths shown in Figure 1A. Values given by the CBICT model are furthermore shown to be strongly energy dependent in contrast to the single-valued estimate of $\phi(\text{CBE} \leftarrow \text{CBV}) = 0.01$ assigned within the ICRP 30 bone model. For alpha energies exceeding ~7.5 MeV, the ICRP 30 model underestimates cortical endosteal dose as given by the CBICT model, while it overestimates the dose at energies below ~7.5 MeV. At very low energies, the CBICT model correctly predicts very little energy absorption to the CBE tissues. This is expected for a CBV source as the majority of energy is deposited in the bone volume due to the decrease range of alpha particles in bone as compared to the other tissues (see Fig. 2A). We also see differences absorbed fractions in comparison to 2003 Eckerman model. At 8 MeV they give an absorbed fraction of 0.0012 for this source/target combination. Our value at 8 MeV is ~0.017 occurs due to a greater fraction of alpha particle tracks passing through only endosteum and not into the haversian space due to the curvature associated with our model. Additionally, our modeling of the longitudinal component of the particles path further explains these differences.

Absorbed Fractions to Other Cortical Tissues

Tabulated values for the CHS target and CBV target are listed in Appendix A of this paper. The CHS target tissue is not considered in the ICRP 30 bone model. As expected, the model predicts that values of $\phi(\text{CHS} \leftarrow \text{CHS})$ approach unity at lower and lower particle emission energies. Self-absorbed fractions to the CSH tissues are shown to be highest in the tibia, where chord distributions in Figure 1B show this bone site to have the larger haversian cavity sizes. Values for the $\phi(\text{CHS} \leftarrow \text{CBV})$ for alpha particles have absorbed fractions of <0.006 which is insignificant for dosimetry purposes.

Values of $\phi(\text{CSH} \leftarrow \text{CBS})$ for alpha particles begin near zero for the absorbed fraction and then approaches absorbed fractions between 0.08 and 0.19 at 10 MeV. The CBV target, as noted earlier, may be used as a representative bone lesion target. Absorbed fraction values obtained for alpha particles demonstrate very little bone site dependence. As with the other sources described earlier, the CHS source also demonstrates the most significant differences. Data for the CME target were found to be <0.001 for all six long bone sites. Accordingly, these results were not tabulated.

CONCLUSION

A chord-based model for charged-particle transport in the cortical bone has been presented that incorporates microstructural data (individual target energy deposition). The model incorporates the transverse chord-length distributions obtained by Beddoe for three cortical bone sites. This data set is limited to three long bone sites for microstructural data. Absorbed fractions obtained in this model provide an improved data set for alpha emitters and may be used in therapeutic applications as well as health physics applications. Over the energy range studied, the effective alpha particle ranges are less than a maximum of $\sim 120 \mu\text{m}$ and thus cross-osteon irradiation and bone volume escape are negligible. For therapeutic applications, use of these absorbed fractions, especially the CHS source, may lead to a better

estimate of endosteal dose due to the short-lived nature of the alpha emitters proposed for therapy. In radiation protection applications, an improved dose estimate will also be achieved since the current ICRP 30 values are energy independent and values given in the 2003 Eckerman model do not account for the relative fraction of the haversian cavity associated with the endosteal layer.

ACKNOWLEDGMENTS

This work was supported in part by Grant CA96441 from the National Cancer Institute and Grant DE-FG07-02ID14327 from the U.S. Department of Energy with the University of Florida.

REFERENCES

- 1 J. L. Humm, Dosimetric aspects of radiolabeled antibodies for tumor therapy J Nucl Med 27, 1490 (1986).
- 2 V. K. Langmuir, Radioimmunotherapy: Clinical results and dosimetric considerations Nucl. Med. Biol. 19, 213 (1992).
- 3 V. K. Langmuir, J. F. Fowler, S. J. Knox, et al., Radiobiology of radiolabeled antibody therapy as applied to tumor dosimetry Med. Phys. 20, 601 (1993).
- 4 M. R. Zalutsky and G. Vaidyanathan, Astatine-211-labeled radiotherapeutics: an emerging approach to targeted alpha-particle radiotherapy Curr Pharm Des 6, 1433 (2000).
- 5 M. R. Zalutsky, R. E. McLendon, P. K. Garg, et al., Radioimmunotherapy of neoplastic meningitis in rats using an alpha- particle-emitting immunoconjugate Cancer Res 54, 4719 (1994).
- 6 M. R. McDevitt, E. Barendswaard, D. Ma, et al., An alpha-particle emitting antibody ([213Bi]J591) for radioimmunotherapy of prostate cancer Cancer Res 60, 6095 (2000).
- 7 M. R. McDevitt, G. Sgouros, R. D. Finn, et al., Radioimmunotherapy with alpha-emitting nuclides Eur J Nucl Med 25, 1341 (1998).
- 8 G. Sgouros, Long-lived alpha emitters in radioimmunotherapy: the mischievous progeny Cancer Biother Radiopharm 15, 219 (2000).
- 9 R. M. Macklis, B. M. Kinsey, A. I. Kassis, et al., Radioimmunotherapy with alpha-particle-emitting immunoconjugates Science 240, 1024 (1988).
- 10 R. M. Macklis, J. Y. Lin, B. Beresford, et al., Cellular kinetics, dosimetry, and radiobiology of a-particle radioimmunotherapy: Induction of apoptosis Radiat. Res. 130, 220 (1992).
- 11 G. Henriksen, D. R. Fisher, J. C. Roeske, et al., Targeting of osseous sites with alpha-emitting 223Ra: comparison with the beta-emitter 89Sr in mice J Nucl Med 44, 252 (2003).
- 12 C. J. Watchman, D. W. Jokisch, P. W. Patton, et al., Absorbed fractions for alpha-particles in tissues of trabecular bone: considerations of marrow cellularity within the ICRP reference male J Nucl Med 46, 1171 (2005).
- 13 F. W. Spiers, Alpha-Ray Dosage in Bone Containing Radium British Journal of Radiology 26, 296 (1953).
- 14 D. E. Charlton and D. V. Cormack, A method for calculating the alpha-ray dosage to soft tissue-filled cavities in bone Br J Radiol 35, 473 (1962).
- 15 A. H. Beddoe, Measurements of the microscopic structure of cortical bone Phys. Med. Biol. 22, 298 (1977).
- 16 E. Polig, The localized dosimetry of internally deposited alpha-emitters Curr. Top. Radiat. Res. 13, 189 (1978).
- 17 I. C. o. R. P. ICRP, (International Commission on Radiological Protection, Oxford, 1978).
- 18 M. G. Stabin and J. A. Siegel, Physical models and dose factors for use in internal dose assessment Health Phys 85, 294 (2003).
- 19 M. G. Stabin, R. B. Sparks, and E. Crowe, OLINDA/EXM: the second-generation personal computer software for internal dose assessment in nuclear medicine J Nucl Med 46, 1023 (2005).
- 20 L. G. Bouchet and W. E. Bolch, A three-dimensional transport model for determining absorbed fractions of energy for electrons in cortical bone J. Nucl. Med. 40, 2115 (1999).
- 21 A. H. Beddoe, in *Department of Medical Physics* (University of Leeds, Leeds, UK, 1976), p. 165.
- 22 W. E. Bolch, P. W. Patton, D. A. Rajon, et al., Considerations of marrow cellularity in 3D dosimetric models of the trabecular skeleton J Nucl Med 43, 97 (2002).

- ²³ ICRU, (International Commission on Radiation Units and Measurements, Bethesda, MD, 1993).
- ²⁴ ICRU, (International Commission on Radiation Units and Measurements, Bethesda, MD, 1992).
- ²⁵ R. Coleman, Random paths through convex bodies J. Appl. Prob. 6, 430 (1969).

Table 1 – Reference alpha and beta particle absorbed fractions from ICRP 30.

ICRP 30	AF
$\phi (CBE \leftarrow CBV)$	0.01
$\phi (CBE \leftarrow CBS)$	0.25

Table 2 – Absorbed fractions for alpha and beta particles
used in the OLINDA code

Energy (MeV)	α	
	$\phi (CBE \leftarrow CBS)$	$\phi (CBE \leftarrow CBV)$
3.0	0.43	0.0060
4.0	0.34	0.0072
5.0	0.28	0.0086
6.0	0.25	0.0100
7.0	0.26	0.0110
8.0	0.23	0.0120

Table 3 - Average transverse chord length distributions through haversian cavities and through cortical bone matrix of three difference skeletal sites.

Cortical bone site	Average transverse chord (μm)[*]		% volume of bone matrix[†]
	Haversian cavities	Bone matrix	
Femur cortex	68	711	93.4
Tibia cortex	84	730	95.4
Humerus cortex	63	730	94.6

* Original transverse chord length data were not available. Consequently, these distribution were graphically estimated from figures given in the original thesis (3).

For these reasons, average values given here differ slightly from published values (2,3).

[†] Percent bone volume calculated by Beddoe (2,3).

Table 4 - Elemental composition of the tissues of cortical bone. Data taken from ICRU Publication 46.

Element	Tissues of Cortical Bone		
	Haversian Space (CHS) ^a	Endosteum (CBE) ^b	Bone Matrix (CBV) ^c
H	10.2	10.5	3.4
C	11	25.6	15.5
N	3.3	2.7	4.2
O	74.5	60.2	43.5
Na	0.1	0.1	0.1
Mg	----	----	0.2
P	0.1	0.2	10.3
S	0.2	0.3	0.3
Cl	0.3	0.2	----
K	0.2	0.2	----
Ca	----	----	22.5
Fe	0.1	----	----
Mass Density (g cm ⁻³)	1.06	1.03	1.92

Source: ICRU Report 46 - Appendix A

^a CHS - "adult whole blood"

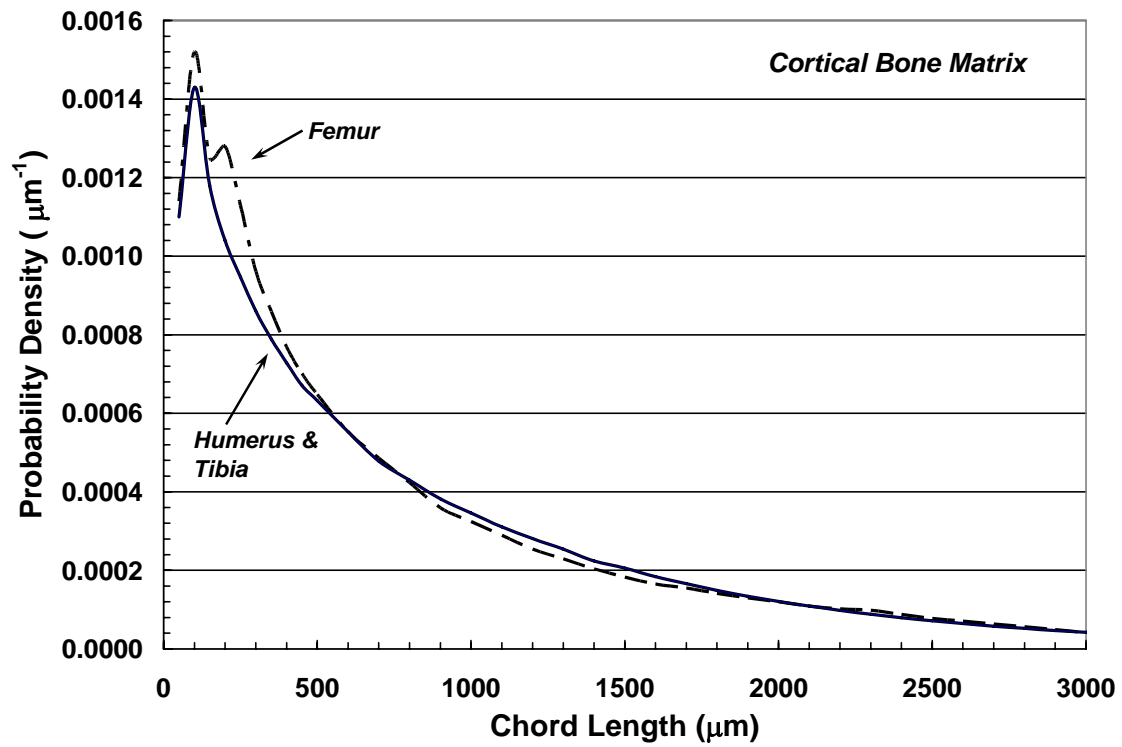
^c CBE - "adult ICRU-44 soft tissue (male)"

^d CBV - "adult cortical bone"

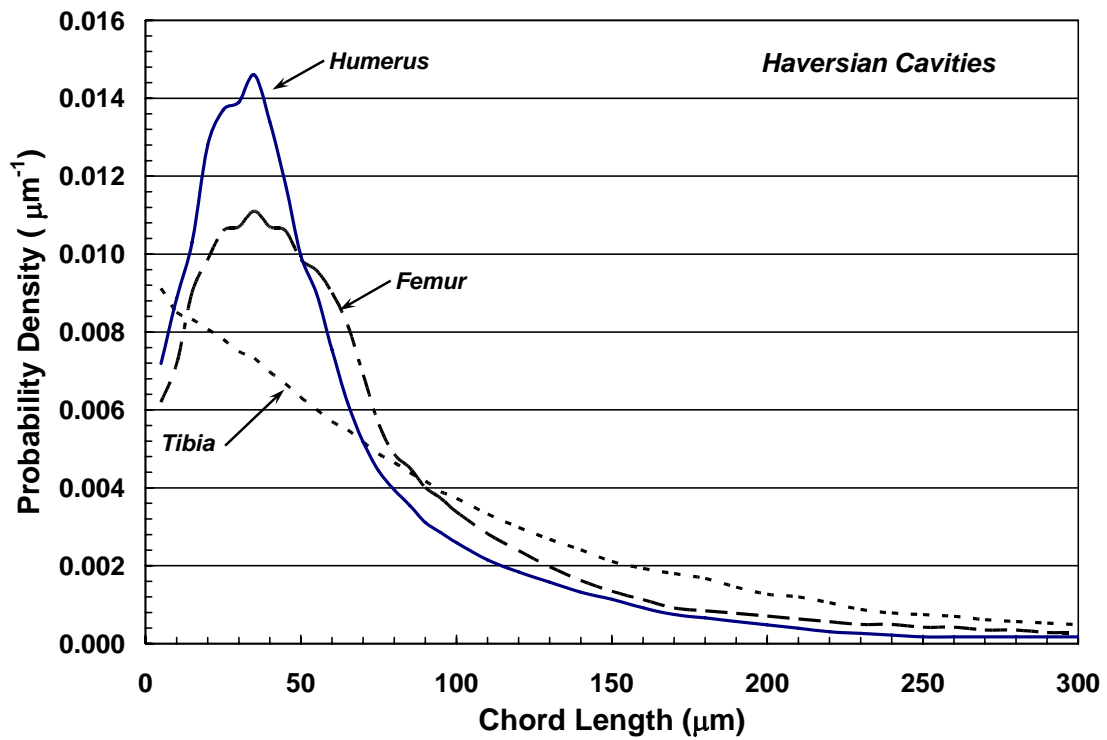
FIGURES

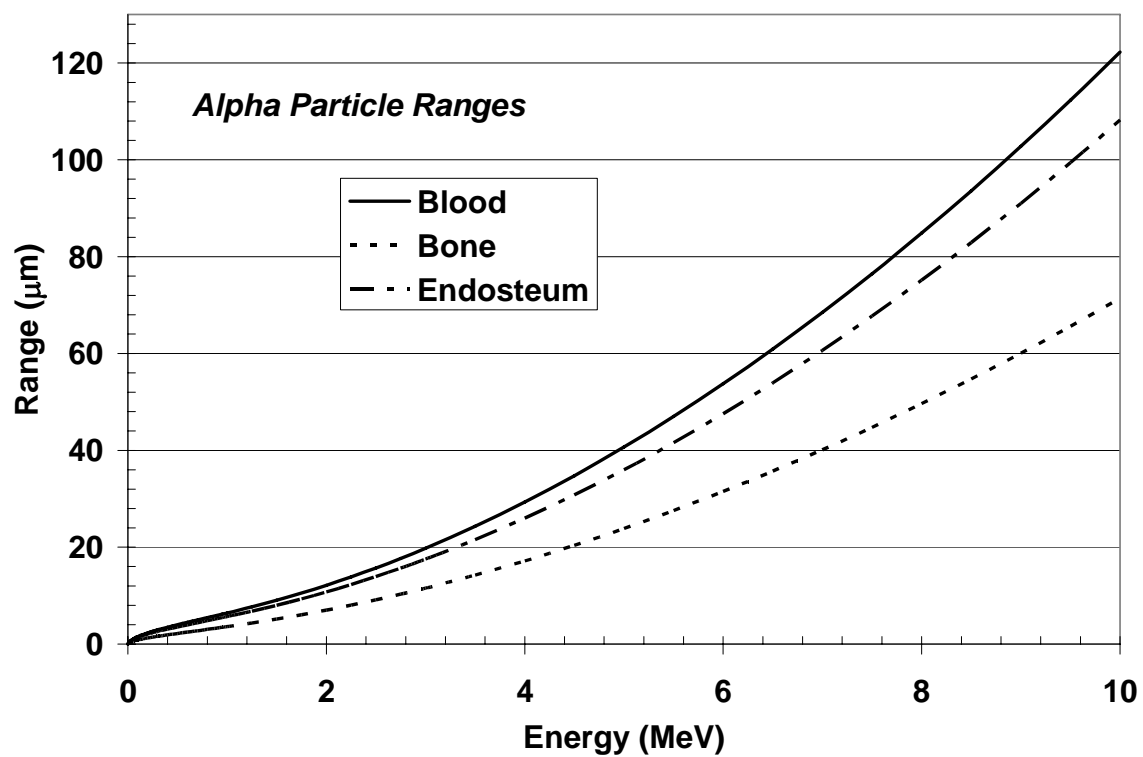
- Figure 1.** Traverse chord-length distributions across (A) the osseous tissues (distances between haversian cavities), and (B) the haversian cavities (haversian space and endosteal layer) within the cortex of the femur, tibia, and humerus of a 50-year male subject.
- Figure 2.** Range-energy plots for alpha particles.
- Figure 3.** Transverse view of the cortical bone microstructure showing four representative osteons and sampled transverse chords for a cortical bone volume (CBV) source of alpha particle emissions.
- Figure 4.** Diagram illustrating the transport method used for alpha particle tracking across a given osteon. A representative cylindrical geometry is shown with cross sections in the transverse and coronal planes. Distinctions are made between sampled chord lengths in the transverse plane (d_{B1}^T , d_{HC}^T , and d_{B2}^T) and the corresponding α -particle trajectories along the emission direction ϕ (d_{B1} , d_{HC} , and d_{B2}). The figures in the lower half of Fig. 3 illustrate the partitioning of the sampled haversian cavity chord d_{HC} into component chords across the endosteal layer, d_{E1} and d_{E2} , and the haversian space, d_{HS} .
- Figure 5.** Diagram illustrating different source geometries the in transverse plane. (A) CHS volume source and (B) CBS source.
- Figure 6.** Alpha particle absorbed fractions to the cortical bone endosteum from (A) an cortical haversian source, (B) a cortical bone surface source and (C) a cortical bone volume source. For comparison, ICRP 30 values are indicated by solid horizontal (energy-independent) lines with the Eckerman 2003 model specified by a dashed line.
- Figure 7.** A comparison of the endosteum absorbed fraction from sources of the trabecular bone surface (TBS) and the cortical bone surface (CBV).

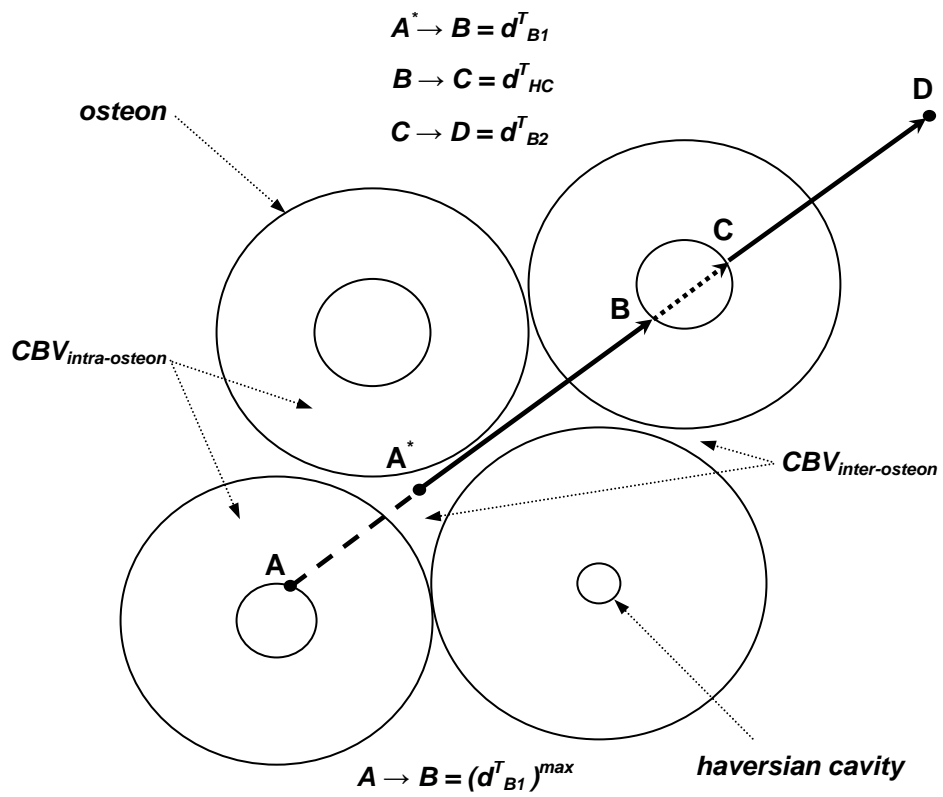
A

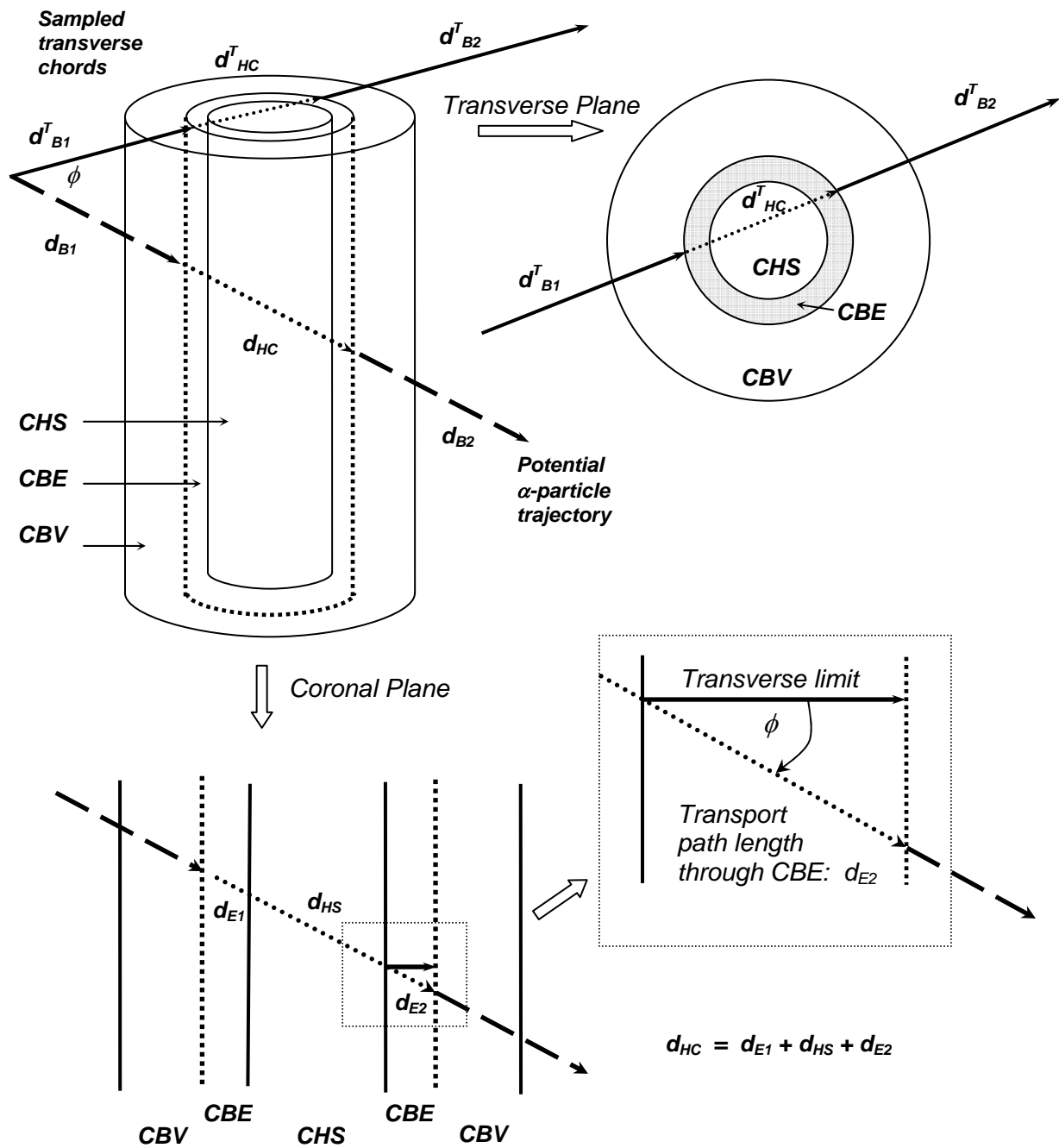


B



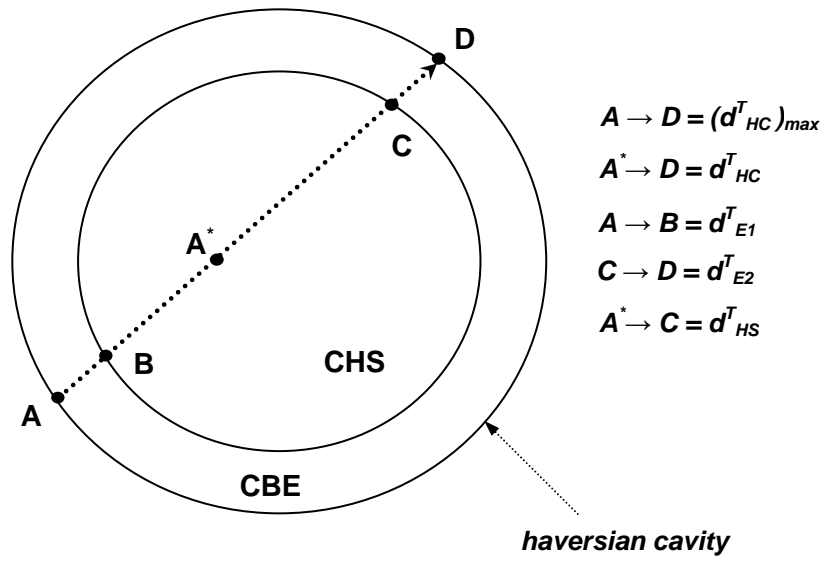






Watchman and Bolch
Figure 4

A



B

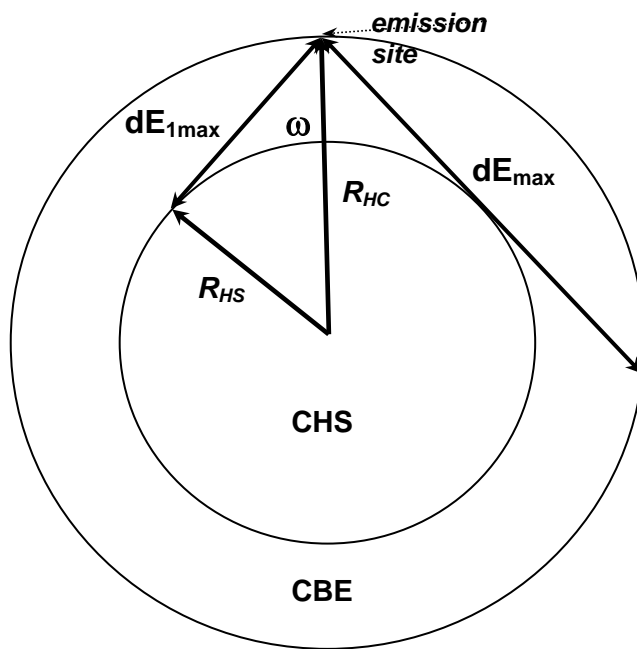


Fig. 5

A

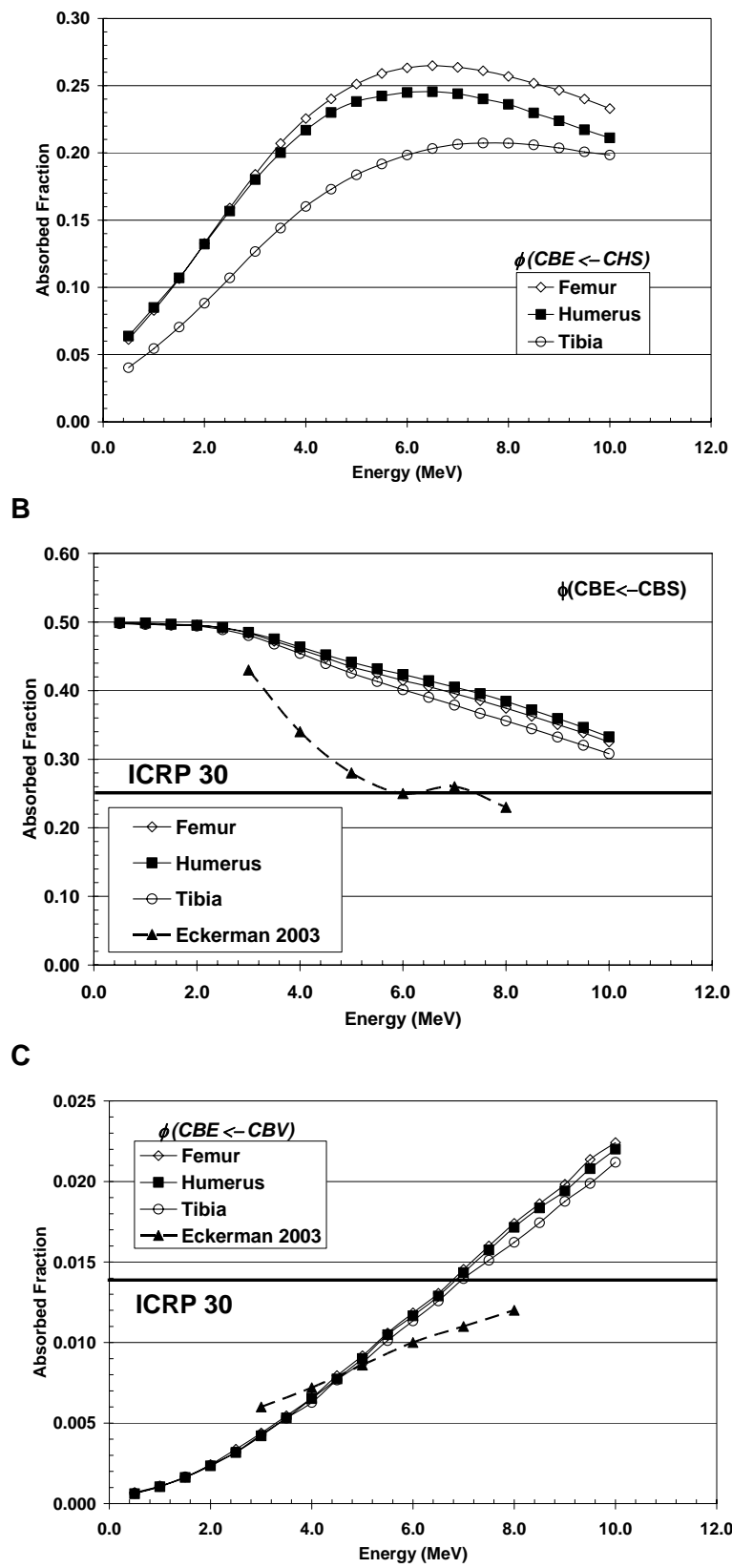


Fig. 6

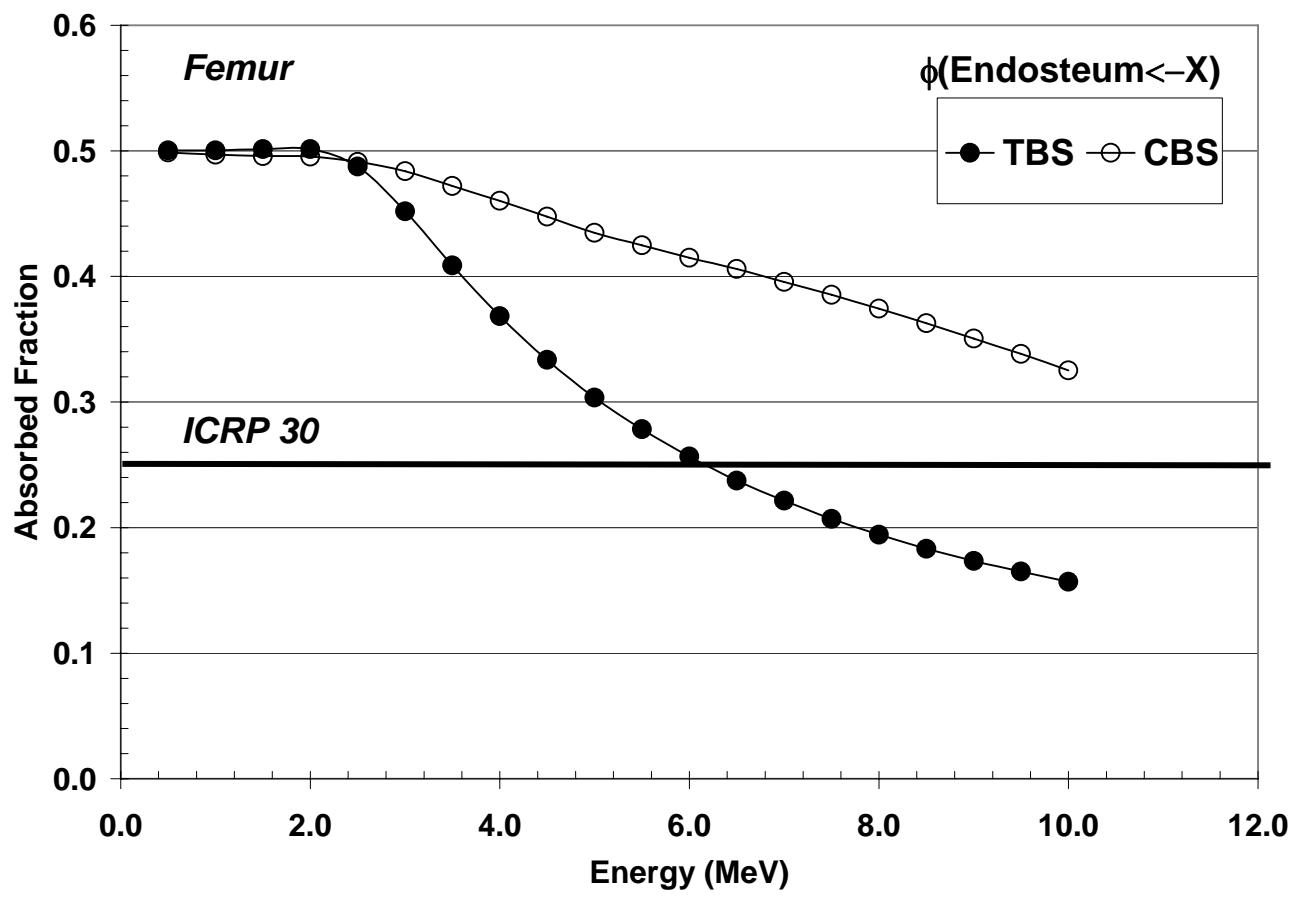


Fig. 7

Table A1 - Absorbed fractions to the cortical bone endosteum (CBE) for α -emissions within various source tissues of the femoral, humeral, and tibial cortex in a 50-year male subject.

$\phi(\text{CBE} \leftarrow \text{CHS})$				
Energy (MeV)	Femur	Humerus	Tibia	Average
0.5	6.13E-02	6.38E-02	4.02E-02	5.51E-02
1.0	8.29E-02	8.50E-02	5.45E-02	7.41E-02
1.5	1.06E-01	1.07E-01	7.05E-02	9.46E-02
2.0	1.33E-01	1.32E-01	8.82E-02	1.18E-01
2.5	1.59E-01	1.57E-01	1.07E-01	1.41E-01
3.0	1.84E-01	1.80E-01	1.27E-01	1.64E-01
3.5	2.07E-01	2.00E-01	1.44E-01	1.84E-01
4.0	2.26E-01	2.17E-01	1.60E-01	2.01E-01
4.5	2.40E-01	2.30E-01	1.73E-01	2.14E-01
5.0	2.51E-01	2.38E-01	1.84E-01	2.24E-01
5.5	2.59E-01	2.42E-01	1.92E-01	2.31E-01
6.0	2.63E-01	2.45E-01	1.98E-01	2.36E-01
6.5	2.65E-01	2.45E-01	2.03E-01	2.38E-01
7.0	2.64E-01	2.44E-01	2.06E-01	2.38E-01
7.5	2.61E-01	2.40E-01	2.07E-01	2.36E-01
8.0	2.57E-01	2.36E-01	2.07E-01	2.33E-01
8.5	2.52E-01	2.30E-01	2.06E-01	2.29E-01
9.0	2.47E-01	2.24E-01	2.04E-01	2.25E-01
9.5	2.40E-01	2.17E-01	2.01E-01	2.19E-01
10.0	2.33E-01	2.11E-01	1.98E-01	2.14E-01
$\phi(\text{CBE} \leftarrow \text{CBS})$				
Energy (MeV)	Femur	Humerus	Tibia	Average
0.5	4.99E-01	4.99E-01	4.98E-01	4.98E-01
1.0	4.97E-01	4.99E-01	4.96E-01	4.97E-01
1.5	4.96E-01	4.97E-01	4.96E-01	4.96E-01
2.0	4.96E-01	4.95E-01	4.94E-01	4.95E-01
2.5	4.91E-01	4.92E-01	4.89E-01	4.91E-01
3.0	4.84E-01	4.85E-01	4.80E-01	4.83E-01
3.5	4.72E-01	4.75E-01	4.68E-01	4.72E-01
4.0	4.60E-01	4.64E-01	4.54E-01	4.59E-01
4.5	4.48E-01	4.52E-01	4.39E-01	4.46E-01
5.0	4.35E-01	4.41E-01	4.26E-01	4.34E-01
5.5	4.25E-01	4.32E-01	4.13E-01	4.23E-01
6.0	4.15E-01	4.23E-01	4.01E-01	4.13E-01
6.5	4.06E-01	4.14E-01	3.90E-01	4.03E-01
7.0	3.96E-01	4.05E-01	3.79E-01	3.93E-01
7.5	3.85E-01	3.95E-01	3.67E-01	3.83E-01
8.0	3.74E-01	3.84E-01	3.56E-01	3.72E-01
8.5	3.63E-01	3.72E-01	3.44E-01	3.60E-01
9.0	3.51E-01	3.59E-01	3.32E-01	3.47E-01
9.5	3.38E-01	3.46E-01	3.20E-01	3.35E-01
10.0	3.25E-01	3.32E-01	3.08E-01	3.22E-01

Table A1 - (continued) $\phi(\text{CBE} \leftarrow \text{CBV})$

Energy (MeV)	Femur	Humerus	Tibia	Average
0.5	6.96E-04	6.13E-04	6.43E-04	6.51E-04
1.0	1.09E-03	1.05E-03	1.08E-03	1.07E-03
1.5	1.64E-03	1.63E-03	1.67E-03	1.64E-03
2.0	2.43E-03	2.35E-03	2.37E-03	2.38E-03
2.5	3.38E-03	3.18E-03	3.21E-03	3.25E-03
3.0	4.38E-03	4.21E-03	4.28E-03	4.29E-03
3.5	5.45E-03	5.32E-03	5.30E-03	5.36E-03
4.0	6.58E-03	6.52E-03	6.28E-03	6.46E-03
4.5	7.94E-03	7.74E-03	7.67E-03	7.78E-03
5.0	9.18E-03	9.01E-03	8.78E-03	8.99E-03
5.5	1.06E-02	1.05E-02	1.01E-02	1.04E-02
6.0	1.18E-02	1.17E-02	1.14E-02	1.16E-02
6.5	1.31E-02	1.29E-02	1.26E-02	1.28E-02
7.0	1.45E-02	1.43E-02	1.40E-02	1.43E-02
7.5	1.60E-02	1.58E-02	1.51E-02	1.56E-02
8.0	1.74E-02	1.72E-02	1.62E-02	1.69E-02
8.5	1.86E-02	1.84E-02	1.74E-02	1.81E-02
9.0	1.98E-02	1.94E-02	1.88E-02	1.93E-02
9.5	2.14E-02	2.08E-02	1.99E-02	2.07E-02
10.0	2.24E-02	2.20E-02	2.12E-02	2.19E-02

Table A2 - Absorbed fractions to the cortical haversian space (CHS) for α -emissions within various source tissues of the femoral, humeral, and tibial cortex in a 50-year male subject.

$\phi(\text{CHS} \leftarrow \text{CHS})$				
Energy (MeV)	Femur	Humerus	Tibia	Average
0.5	9.38E-01	9.35E-01	9.59E-01	9.44E-01
1.0	9.15E-01	9.13E-01	9.44E-01	9.24E-01
1.5	8.91E-01	8.90E-01	9.27E-01	9.02E-01
2.0	8.62E-01	8.63E-01	9.08E-01	8.77E-01
2.5	8.33E-01	8.35E-01	8.86E-01	8.51E-01
3.0	8.03E-01	8.07E-01	8.64E-01	8.25E-01
3.5	7.73E-01	7.80E-01	8.41E-01	7.98E-01
4.0	7.44E-01	7.53E-01	8.18E-01	7.72E-01
4.5	7.16E-01	7.26E-01	7.95E-01	7.46E-01
5.0	6.89E-01	7.02E-01	7.73E-01	7.21E-01
5.5	6.62E-01	6.80E-01	7.51E-01	6.97E-01
6.0	6.37E-01	6.57E-01	7.29E-01	6.74E-01
6.5	6.13E-01	6.36E-01	7.07E-01	6.52E-01
7.0	5.91E-01	6.15E-01	6.86E-01	6.31E-01
7.5	5.70E-01	5.96E-01	6.66E-01	6.11E-01
8.0	5.50E-01	5.78E-01	6.47E-01	5.92E-01
8.5	5.30E-01	5.63E-01	6.28E-01	5.73E-01
9.0	5.10E-01	5.46E-01	6.10E-01	5.55E-01
9.5	4.93E-01	5.31E-01	5.93E-01	5.39E-01
10.0	4.77E-01	5.16E-01	5.75E-01	5.23E-01
$\phi(\text{CHS} \leftarrow \text{CBS})$				
Energy (MeV)	Femur	Humerus	Tibia	Average
0.5	1.67E-03	1.44E-03	2.00E-03	1.70E-03
1.0	2.55E-03	2.35E-03	3.12E-03	2.67E-03
1.5	3.63E-03	3.15E-03	4.29E-03	3.69E-03
2.0	5.03E-03	4.25E-03	5.75E-03	5.01E-03
2.5	7.08E-03	5.84E-03	7.98E-03	6.96E-03
3.0	1.26E-02	1.07E-02	1.38E-02	1.24E-02
3.5	2.20E-02	1.88E-02	2.33E-02	2.14E-02
4.0	3.31E-02	2.88E-02	3.50E-02	3.23E-02
4.5	4.44E-02	3.85E-02	4.69E-02	4.32E-02
5.0	5.51E-02	4.72E-02	5.85E-02	5.36E-02
5.5	6.42E-02	5.51E-02	6.91E-02	6.28E-02
6.0	7.18E-02	6.16E-02	7.83E-02	7.06E-02
6.5	7.90E-02	6.64E-02	8.70E-02	7.75E-02
7.0	8.44E-02	7.06E-02	9.43E-02	8.31E-02
7.5	8.85E-02	7.42E-02	9.99E-02	8.75E-02
8.0	9.23E-02	7.75E-02	1.06E-01	9.18E-02
8.5	9.45E-02	7.94E-02	1.10E-01	9.46E-02
9.0	9.72E-02	8.15E-02	1.14E-01	9.77E-02
9.5	9.85E-02	8.25E-02	1.17E-01	9.94E-02
10.0	9.91E-02	8.37E-02	1.19E-01	1.01E-01

Table A2 - (continued) $\phi(\text{CHS} \leftarrow \text{CBV})$

Energy (MeV)	Femur	Humerus	Tibia	Average
0.5	1.00E-06	2.00E-06	2.00E-06	1.67E-06
1.0	5.00E-06	4.00E-06	2.00E-06	3.67E-06
1.5	8.00E-06	8.00E-06	9.00E-06	8.33E-06
2.0	1.50E-05	1.70E-05	2.70E-05	1.97E-05
2.5	3.30E-05	3.20E-05	3.30E-05	3.27E-05
3.0	7.00E-05	6.20E-05	7.90E-05	7.03E-05
3.5	1.11E-04	1.14E-04	1.34E-04	1.20E-04
4.0	2.19E-04	1.85E-04	2.62E-04	2.22E-04
4.5	3.82E-04	3.28E-04	4.08E-04	3.73E-04
5.0	6.22E-04	4.96E-04	6.00E-04	5.73E-04
5.5	8.66E-04	7.60E-04	9.40E-04	8.55E-04
6.0	1.20E-03	9.90E-04	1.26E-03	1.15E-03
6.5	1.62E-03	1.33E-03	1.64E-03	1.53E-03
7.0	2.05E-03	1.70E-03	2.15E-03	1.96E-03
7.5	2.49E-03	2.13E-03	2.65E-03	2.42E-03
8.0	3.11E-03	2.55E-03	3.20E-03	2.95E-03
8.5	3.61E-03	3.02E-03	3.90E-03	3.51E-03
9.0	4.22E-03	3.45E-03	4.60E-03	4.09E-03
9.5	4.88E-03	3.99E-03	5.19E-03	4.69E-03
10.0	5.50E-03	4.55E-03	6.05E-03	5.37E-03

Table A3 - Absorbed fractions to the cortical bone volume (CBV) for α -emissions within various source tissues of the femoral, humeral, and tibial cortex in a 50-year male subject.

$\phi(\text{CBV} \leftarrow \text{CHS})$				
Energy (MeV)	Femur	Humerus	Tibia	Average
0.5	7.23E-04	7.85E-04	5.63E-04	6.90E-04
1.0	1.65E-03	1.72E-03	1.27E-03	1.54E-03
1.5	3.07E-03	3.10E-03	2.47E-03	2.88E-03
2.0	5.32E-03	5.30E-03	4.21E-03	4.94E-03
2.5	8.23E-03	8.34E-03	6.51E-03	7.69E-03
3.0	1.30E-02	1.27E-02	9.79E-03	1.18E-02
3.5	2.02E-02	2.00E-02	1.46E-02	1.83E-02
4.0	3.05E-02	3.00E-02	2.22E-02	2.76E-02
4.5	4.42E-02	4.39E-02	3.16E-02	3.99E-02
5.0	6.02E-02	6.03E-02	4.36E-02	5.47E-02
5.5	7.92E-02	7.82E-02	5.74E-02	7.16E-02
6.0	9.97E-02	9.81E-02	7.26E-02	9.01E-02
6.5	1.22E-01	1.19E-01	8.92E-02	1.10E-01
7.0	1.46E-01	1.41E-01	1.07E-01	1.31E-01
7.5	1.69E-01	1.63E-01	1.26E-01	1.53E-01
8.0	1.93E-01	1.86E-01	1.46E-01	1.75E-01
8.5	2.18E-01	2.08E-01	1.66E-01	1.97E-01
9.0	2.43E-01	2.30E-01	1.87E-01	2.20E-01
9.5	2.66E-01	2.51E-01	2.06E-01	2.41E-01
10.0	2.90E-01	2.72E-01	2.26E-01	2.63E-01
$\phi(\text{CBV} \leftarrow \text{CBS})$				
Energy (MeV)	Femur	Humerus	Tibia	Average
0.5	5.00E-01	5.00E-01	5.00E-01	5.00E-01
1.0	5.01E-01	4.99E-01	5.00E-01	5.00E-01
1.5	5.01E-01	5.00E-01	5.00E-01	5.00E-01
2.0	4.99E-01	5.01E-01	5.00E-01	5.00E-01
2.5	5.02E-01	5.02E-01	5.03E-01	5.02E-01
3.0	5.03E-01	5.05E-01	5.06E-01	5.05E-01
3.5	5.06E-01	5.06E-01	5.09E-01	5.07E-01
4.0	5.07E-01	5.08E-01	5.11E-01	5.08E-01
4.5	5.08E-01	5.10E-01	5.14E-01	5.10E-01
5.0	5.10E-01	5.11E-01	5.16E-01	5.13E-01
5.5	5.11E-01	5.13E-01	5.18E-01	5.14E-01
6.0	5.13E-01	5.15E-01	5.20E-01	5.16E-01
6.5	5.15E-01	5.19E-01	5.23E-01	5.19E-01
7.0	5.20E-01	5.24E-01	5.27E-01	5.24E-01
7.5	5.26E-01	5.30E-01	5.33E-01	5.30E-01
8.0	5.33E-01	5.38E-01	5.38E-01	5.37E-01
8.5	5.43E-01	5.49E-01	5.46E-01	5.46E-01
9.0	5.52E-01	5.59E-01	5.53E-01	5.55E-01
9.5	5.63E-01	5.71E-01	5.63E-01	5.66E-01
10.0	5.76E-01	5.84E-01	5.73E-01	5.77E-01

Table A3 - (continued)

$\phi(\text{CBV} < \text{CBV})$				
Energy (MeV)	Femur	Humerus	Tibia	Average
0.5	9.99E-01	9.99E-01	9.99E-01	9.99E-01
1.0	9.99E-01	9.99E-01	9.99E-01	9.99E-01
1.5	9.98E-01	9.98E-01	9.98E-01	9.98E-01
2.0	9.98E-01	9.98E-01	9.98E-01	9.98E-01
2.5	9.97E-01	9.97E-01	9.97E-01	9.97E-01
3.0	9.96E-01	9.96E-01	9.96E-01	9.96E-01
3.5	9.94E-01	9.95E-01	9.95E-01	9.95E-01
4.0	9.93E-01	9.93E-01	9.93E-01	9.93E-01
4.5	9.92E-01	9.92E-01	9.92E-01	9.92E-01
5.0	9.90E-01	9.90E-01	9.91E-01	9.90E-01
5.5	9.89E-01	9.89E-01	9.89E-01	9.89E-01
6.0	9.87E-01	9.87E-01	9.87E-01	9.87E-01
6.5	9.85E-01	9.86E-01	9.86E-01	9.86E-01
7.0	9.83E-01	9.84E-01	9.84E-01	9.84E-01
7.5	9.82E-01	9.82E-01	9.82E-01	9.82E-01
8.0	9.79E-01	9.80E-01	9.81E-01	9.80E-01
8.5	9.78E-01	9.79E-01	9.79E-01	9.78E-01
9.0	9.76E-01	9.77E-01	9.77E-01	9.77E-01
9.5	9.74E-01	9.75E-01	9.75E-01	9.75E-01
10.0	9.72E-01	9.73E-01	9.73E-01	9.73E-01

Absorbed Fractions for Electrons in Tissues of Cortical Bone

Christopher J. Watchman, PhD^{1*} and Wesley E. Bolch, PhD^{1,2}

¹*Department of Nuclear & Radiological Engineering, University of Florida, Gainesville, FL;*

²*Department of Biomedical Engineering, University of Florida, Gainesville, FL*

**Current address, Department of Radiation Oncology, University of Arizona, Tucson, AZ*

For reprints and correspondence contact:

Wesley E. Bolch, PhD, PE, CHP

Director, Advanced Laboratory for Radiation Dosimetry Studies (ALRADs)

Department of Nuclear and Radiological Engineering

University of Florida, Gainesville, Florida 32611-8300

Phone: (352) 846-1361 Fax: (352) 392-3380 Email: wbolch@ufl.edu

SHORT TITLE:

Electron Absorbed Fractions in Cortical Bone

This work was supported by the

U.S. Department of Energy and the National Cancer Institute

Word Count (Text and Refs): **4883 (no abstract)**

Word Count (Figure Captions): **281**

Word Count (Table Captions): **294**

Word Count (Total): **5458**

INTRODUCTION

The use of beta-particle emitting radionuclides has been the standard in radionuclide therapies for cancer treatment.¹⁻³ In many cases, toxicities to normal non-target organs such as the active bone marrow and tissues of the kidneys have been dose limiting for these therapies. In the companion paper to this article a chord based infinite cortical transport model was presented for alpha particle transport. In this present work this model has been modified for electron dosimetry in cortical bone to explicitly account for electron escape to surrounding tissues both in and outside the skeleton.

Previous Dosimetric Model for Electrons in Cortical Bone

Dosimetry models for electrons in cortical bone were also developed by Beddoe using the same chord-based techniques applied for alpha particles.⁴ A limited number of radionuclides, of interest to health physics, were included in this study including ^{14}C , ^{18}F , ^{22}Na , ^{32}P , ^{45}Ca , ^{90}Sr , and ^{90}Y . The use of this chord-length data set was also extended by Eckerman in 2000⁵ and in again in 2003⁶ in the tabulation of electron absorbed fractions to in cortical bone for the MIRDOSE3 and OLINDA codes, respectively. Standardized absorbed fraction data using the Beddoe data, as shown in Table 1, has been adopted by the ICRP. Values from the 2003 Eckerman model for electrons in cortical bone are given in Table 2.

A model for electron absorbed fractions in cortical bone has been published by Bouchet and Bolch.⁷ In this model, transverse chord-length distributions from Beddoe were used in conjunction with the EGS4-PRESTA radiation transport code to calculate absorbed fractions for a cortical bone volume source, a cortical haversian space source, and a cortical endosteum volume source. Transverse chord lengths were used to create a hemi-spherical cylinder representing the limiting distance an electron may travel in the transverse plane. This model allowed for electrons to follow a non-linear track as generated by the EGS4-PRESTA code. An algorithm to account for energy deposition in endosteum was slightly modified from that

developed previously for trabecular model. This algorithm takes the sampled chord length and then assigns a fraction of the chord to two endosteal chords, one for the particle entering the endosteum in the haversian cavity and then one for the particle exiting. This algorithm seems to inaccurately reflect the angular component of an electron path through cortical bone. This inaccuracy leads to an overestimation of endosteum doses, as we will be discussed later in the present study. Additionally, their model only presented a cortical bone endosteum volume source and not a true surface source. Comparisons of the cortical endosteum source to the ICRP 30 surface source leads to an unfair comparison of the ICRP default values for electron-absorbed fractions in cortical bone.

Recently, Shah et al⁸ has demonstrated the need for calculating beta-particle escape from the trabecular spongiosa. In their study, a Paired Image Radiation Transport (PIRT) model was developed using both a macroscopic image of an individual bone site and a microscopic image of interior spongiosa structure. Results for spongiosa tissue irradiating cortical bone as well as cortical self-dose were presented in their study. Data obtained for the cortical bone cortex in this study showed that significant overestimation of beta particle absorbed fractions to the spongiosa tissues occurs when using high-energy beta emitters. Absorbed fractions using PIRT were, for most bone sites, shown to be smaller than those under infinite spongiosa transport (IST) for energies greater than 100 keV at marrow cellularities of 100%. Reduced differences in the two methods were seen with decreasing marrow cellularity. Shah et al demonstrated that beta-particle escape issues are greatest in bone sites that have spongiosa dimensions that are comparable to the beta-particle range in those tissues. For example, differences seen in comparison of PIRT with IST for the femur head demonstrate IST results ~1.41 times greater than PIRT results at 4 MeV. In contrast, results of the same comparison in the L₄ lumbar vertebrae resulted in PIRT data ~1.95 times greater than IST results in the spongiosa tissues. Similar data for beta particle escape in cortical bone of the long bones is not available in the literature.

MATERIALS AND METHODS

In this study, particle transport in cortical bone is accomplished using the CBICT methodology described in previously and a PIRT like calculation to account for macrostructural particle escape. Full details of the CBICT calculation may be found in the companion alpha emitter article. As was previously mentioned, calculations of particle transport are performed under the assumption of an infinite region of cortical bone is rarely valid for higher-energy beta particles in the skeleton⁹. Modifications of this method for beta particle at energies exceeding 100 keV are accomplished by combining these results with those of calculations that incorporate particle escape from the cortical bone. The revised model described below is known as SBoRT (Stylized Bone Radiation Transport) for macroscopic transport of beta particles in the long bones. The combination of the two models, which results in PIRT like results, is defined as SBoRT-CBICT.

As given in the previous alpha-particle article, the following nomenclature is used for the various source and target tissues: CBV – cortical bone volume, CBE – cortical bone endosteum, CBS – cortical bone surface, and CHS – cortical haversian space. The CBV is further defined as the composite of all osseous tissues of cortical bone including that found in circumferential lamellae, inter-osteon lamellae, and intra-osteon (interstitial) lamellae. Further subdivision of the CBV is broken down into long bones (CBV_{long}) and the cortical cortex (CBV_{cortex}) surrounding spongiosa (as in the proximal and distal ends of long bones, and at all other skeletal sites of the axial skeleton). Unless otherwise specified in this paper, CBV will be used interchangeably with CBV_{long} . Two additional tissues are also defined as the inactive (or yellow) marrow of the medullary cavity (CIM) and the medullary cavity endosteum (CME).

Tissue Composition and Range/Energy Data

Range-energy data for electron calculations was also based upon ICRU 46 tissue compositions and the range-energy data in ICRU Report 37.¹⁰ Calculation of the range-energy tables was performed using the National Institute for Standards and Technology ESTAR database,¹¹ which uses ICRU 37 data. The ESTAR database website allows for the calculation of elemental specific data using scaling techniques listed in ICRU 37. A plot of the calculated range-energy tables is presented in Figure 1 for electrons. Ranges at intermediate energies (between data points) were assessed via interpolation of tabular values.

Stylized Bone Radiation Transport (SBoRT)

As previously noted, the use of infinite chord-based methods for beta-particle dosimetry in cortical bone will potentially overestimate the absorbed fraction to target tissues due to lack of consideration of particle escape. The escape fraction is particularly high for the proximal ends of long bone and all other bones of the axial skeleton (e.g., vertebrae, ribs, etc.). In the shafts of the long bones, data regarding escape fraction is not available in the literature. To obtain information regarding cortical thickness and medullary cavity diameters, a study was conducted using a series of 12 cadavers imaged using a Siemens Sensation 16 multi-slice CT scanner. Each cadaver was scanned with a slice thickness of 2 mm and in a 512 x 512 image matrix at ~1 mm in-plane resolution. Cadaver selection was limited to those individuals whose pathologies or cause of death did not result in significant skeletal deterioration prior to death. Subject ages ranged from 35 years to 82 years with an average age of 67 years. Figure 2 illustrates two examples of the CT data for the femur (Fig. 2A), and radius and ulna (Fig. 2B). On the right side of the figure a single cross-sectional slice of the CT image is shown at a reference position in the transverse plane. Measurements of the cortical thickness and medullary cavity thickness were made using the PACScubeTM software (DatCard Systems Incorporated, Irvine, CA). The mid-shaft distance was taken as the measuring level in the

longitudinal plane. Determination of the mid-shaft slice was made by taking the average of the slice numbers at the proximal and distal ends of the bones. For bones in the upper extremity, particularly the radius and ulna, this was not always possible. Visual inspection of the midpoints was used to determine the measurement slice. In cases where the bones were not aligned with the scan axis, such as the radius and ulna shown in Fig. 2B, measurements were done only in the short axis of the cut. This method was confirmed to be consistent with an alternate method where the measurements along the long axis of the cut were corrected, using trigonometry, based upon the angle of bone. Three to seven measurements were made for each bone site, for both the medullary cavity and cortical shell, and the averages were then determined. Table 4 presents results of these measurements with their corresponding standard deviations.

Calculation of the escape of high-energy beta particles within long bones was performed using a series of cylindrical models representing the long bones of dimension given by the data of Table 4. Radiation transport calculations were performed using the Monte Carlo radiation transport code MCNP5 and will be referred to as the SBoRT (stylized bone radiation transport) model. Tissues of the long bones consist of soft tissue surrounding the bone (CST), cortical bone (CBV), and the medullary cavity tissues of endosteum (CME) and inactive (or yellow) marrow (CIM). The thickness of soft tissue surrounding the bone was taken as 1 cm larger than the diameter of the bone. Inspection of the images found in Figure 2 demonstrated different thicknesses of soft tissue surrounding the long bones. The choice of 1 cm was chosen to allow for backscatter into the bone while simultaneously minimizing computation time. Since the purpose of these calculations was to determine the energy escape fraction within the long bones, a larger soft tissue region was unnecessary. Figure 3 illustrates this model. Each bone cylinder model was taken with a length of 5 cm above and below a source plane. This distance was greater than the maximum distance a beta particle may travel in bone, thus no end effects were present. A donut shaped disk source at the center plane was modeled to simulate a CBV source in each of the six long bones of Table 4.

Beta Particle Absorbed Fraction Calculation

Once absorbed fractions were calculated in SBoRT, absorbed fractions were also calculated for electrons using CBICT. The corresponding absorbed fractions for the cortical microstructure were then determined for the humerus, femur, and tibia as given by the transverse chord-length distributions measured by Beddoe. An average absorbed fraction for all three bone sites was also calculated and is used to represent the micro-structural absorbed fraction data for cortical bone sites not given in the Beddoe studies. To incorporate beta particle escape from the cortical bone volume the results of SBoRT and CBICT were combined (SBoRT-CBICT) together to obtain absorbed fractions in cortical tissues. This method was also applied to the data obtained by Shah et al⁸ for the CBV_{cortex} in bone sites and bone regions surrounding spongiosa. Details of the process are derived in Appendix A.

RESULTS

Absorbed fractions for alpha particles and electrons were obtained for several target (CHS, CBE, CBV and CBV_{cortex}) and source (CHS, CBS, CBV, CBV_{cortex} , and spongiosa tissues) tissues as a function of particle emission energy and skeletal site. The tissues of the bone matrix are not traditionally considered as a radiosensitive target for internal dosimetry; however, the CBV may be used as a surrogate for bone lesions within cortical bone instead of site-specific information on tumor micro-morphometry.

Absorbed fractions obtained using SboRT are shown in Figure 4, while absorbed fractions to the cortical bone endosteum are shown in Figures 5A to 5C for alpha particles emitted uniformly within the CHS, CBS, and CBV source regions of cortical bone, respectively. Solid horizontal lines indicate current energy-independent absorbed fractions recommended in the ICRP 30 bone model for alphas and electrons in cortical bone. Dashed lines designate results from the 2003 Eckerman model. Tabulated values of absorbed fraction are presented in the Appendix to this paper (Tables B1 to B5). For electrons all coefficients of variance (COVs) were

less than 1% except at very low energies in the tertiary targets. In these tissues the COV could be as high as 20%, but only for very low energies (i.e. <40 keV). Results generated for the SBoRT calculations were less than 1% for the CBV.

DISCUSSION

Electron Absorbed Fractions to the Cortical Bone Endosteum

An absorbed fraction profile illustrating the relative energies where particle escape becomes important are shown for the SBoRT calculation in Figure 4A. At electron energies above 100 keV, values of $\phi(\text{CBE} \leftarrow \text{CBV})_{\text{SBoRT}}$ indicate electron escape from cortical bone in the humerus. As particle energy increases, the effects of particle escape become significantly larger and the absorbed fraction approaches a minimum of 0.49 at 4 MeV in the humerus. Results from changes in the cortical shell thickness and bone diameter (see Table 4) on the macroscopic absorbed fraction are shown in Fig. 4B. In Table 4, the femur is shown to have the largest diameter, while the ulna has the smallest. Consequently, one would expect the femur to have the greatest amount of self-dose to the cortical bone matrix. This proves to be the case while the converse is also true for the ulna. As stated earlier, macroscopic SBoRT results were combined with microscopic CBICT results to give geometrically more accurate absorbed fraction estimations for electron sources in cortical bone.

The energy-dependent values of electron absorbed fractions to the endosteal tissues of cortical bone are shown in Figures 5A to 5C for emission sites uniformly localized in the haversian space, bone surfaces, and osseous tissues of cortical bone, respectively. Within these plots, average values for infinite cortical transport (ICT) are also presented (solid lines) along with the values from the 2003 Eckerman model (dashed line). Similar to the alpha particle absorbed fractions, little bone site dependence is seen between sources, but the CHS source once again demonstrates the greatest degree of bone site dependence as shown in Fig. 5A. In this figure, we see a build up of energy in the endosteum, which begins to drop at 0.05 MeV.

This decrease continues up to energies of 0.2 MeV and then starts to flatten out at higher energies. This behavior is expected since at energies up to 0.2 MeV the electron encounters only one Haversian cavity due to the shorter electron ranges ($< 500 \mu\text{m}$). Similar results were seen for alphas. At the highest energies the absorbed fraction profile begins to flatten out as since the fraction of energy absorbed in the endosteum, as a function of initial energy, becomes constant.

Differences in the femur, humerus and tibia profiles are similar to the alpha particle case. Once again the tibia demonstrates the lowest absorbed fraction and the same average chord length argument holds at low energies ($< 50 \text{ keV}$). The same argument also holds for the femoral and humeral differences at lower energies ($< 200 \text{ keV}$). Unlike the alpha particles, higher energy electrons have sufficient range to enter a second haversian cavity. The tibia which has the largest average haversian cavity shows less of a drop in endosteal dose over the 50 keV to 200 keV range than does the two other bone sites. Energy deposition differences occur due to a larger fraction of energy being deposited in a larger relative bone volume. The values for the humerus and the femur begin to diverge at 200 keV with the absorbed fraction in the femur beginning to level off while values in the humerus increase. Differences in these two are ascribed to the fractional energy available to deposit energy in the second endosteal layer. In the humerus, we see that a smaller fraction of energy is deposited in the first endosteal layer than in the femur. Hence the residual electron energy is greater in the humerus and therefore when the electron passes through the bone volume it is likely to be more energetic than in the femoral case. Thus a greater fraction of energy can be deposited in the second and third endosteal layers as will be fully explained in the following sections.

In Figure 6A, we show values of $\phi(\text{CBE} \leftarrow \text{CHS})$ in the humerus broken down into successive endosteal layers. These layers include the first layer encountered as the particle escapes the haversian cavity, then the entry layer of the next osteon, and finally the exit layer of this next osteon. For the purposes of this illustration, layers E2 and E3 were tallied multiple

times if more osteons were encountered beyond the second osteon. At ~50 keV, the electron begins to have sufficient energy to escape the haversian cavity of the source osteon and deposit energy into the bone volume (see E1 in Fig. 6A). At approximately 200 keV electrons have sufficient energy to begin to deposit energy in the endosteum of an adjacent osteon's haversian space (E2 and E3).

Results for the second and third endosteal layers for each of the bone sites used are shown in Fig. 6B. This profile demonstrates this model's ability to simulate multiple osteon crossfire, which is necessary to correctly account for beta particle absorbed fractions in cortical bone. Data for the femur and tibia demonstrate a greater drop off at high energies as compared to the humerus. Combination of the macro and micro structural data sets results in a greater weighting of the cross osteon microstructural data in the humerus when compared to the other two bone sites. In the femur and tibia, which have greater diameters, a greater fraction of the emission energy will be deposited within the bone volume than in the humerus. Consequently, energy that is deposited in the humeral endosteum is a greater fraction of the emission energy compared to the other bone sites. Thus the cross-osteon endosteal dose in the humerus does not drop off to the same extent as does the femur and tibia.

Figure 5B shows values of $\phi(\text{CBE} \leftarrow \text{CBS})$ for beta particles emitted on the bone surfaces. Very little bone-site dependence is seen as was the case with alpha particles. Lines representing the energy dependant ICRP 30 values are also shown. Differences are seen in our absorbed fractions when compared to the ICRP 30 and 2003 Eckerman values. Our model estimates greater energy deposition in the target tissue over the entire energy range. Differences with respect to the 2003 Eckerman model are due to the additional longitudinal parameter included in our model that results in a greater volume of endosteum. Changes in the endosteum sampling algorithm also contribute to these observed differences.

In this model, one may more accurately take into account the curvature associated with the Haversian cavity. The energy deposition in the Haversian space is dependant upon the

entry angle of the particle into the Haversian cavity. This leads to differences in the probability of that the particle will enter the Haversian space. Thus with greater Haversian cavity sizes, the greater the probability that the endosteum will be the only tissue encountered by the electron. Figure 7 further illustrates this point graphically with four representative haversian cavities. The radii of the four cavities represent four randomly chosen transverse chords, which we then use to represent the diameter of the haversian cavity. As we noted earlier, a 10- μm layer is taken from the outer diameter and represents the endosteal layer (as shown by the double pointed arrows in Fig. 7). Notice that as the sampled diameter increases the fraction of the total volume occupied by the endosteal layer decrease. This leads to a decreasing value of dE_{max} , which results in an increased probability of a particle track entering the haversian space by passing through the endosteum. As was shown in our previous article, haversian cavity chords are shown to have higher probabilities of short chords ($< \sim 75 \mu\text{m}$) for all bone sites. This means that for the most probable sampled chords the endosteal layer will take up a larger fraction of the total haversian cavity area (75% at $R_{HC} = 20 \mu\text{m}$ and 25% at $R_{HC} = 75 \mu\text{m}$). Thus you have a greater probability that the particle will only pass through the endosteum. Consequently, it is expected that our method differ in comparison to that of the ICRP 30 model and the 2003 Eckerman model.

The CBS source data also seem to be more consistent with the physical geometry than does the ICRP 30 values. Figure 5B shows that for low energies the surface source deposits 50% of its energy in the endosteum up to $\sim 0.05 \text{ MeV}$. At these low energies the half space nature of the geometry holds since the effective range of electrons below 0.05 MeV are less than $\sim 50 \mu\text{m}$. As the energy increases, particles that enter the endosteum have sufficient energy to cross the endosteum and enter either the Haversian space or into the bone. As was previously mentioned, the values calculated in the CBICT model are greater than the ICRP default values for reasons described earlier.

The cortical bone volume source for $\phi(\text{CBE} \leftarrow \text{CBV})$ for a beta particles is shown in Figure 5C. Similar to the CBS source, the ICRP 30 default value of 0.01 is significantly less than the energy-dependent values given by the CBICT model. For energies less than 40 keV, the ICRP value overestimates the CBICT values. At energies greater than 40 keV, the deviation from the ICRP 30 value becomes greater. The absorbed fraction differences are a result of the geometric differences in modeling. In the present model, each time a bone chord terminates at the boundary of the haversian cavity, it must enter the cortical endosteum. Consequently, each beta particle that has sufficient energy to escape the bone volume deposits some energy into the endosteum. As the electron energy increases, a greater number of particles have sufficient energy to enter the haversian cavity, and thus the endosteum. Inter-osteal crossfire also becomes more of a factor with increasing energy. This leads to more particles with greater residual energy entering the cortical endosteum. This is supported by the tibial absorbed fractions being smaller than those found for the other bone sites. In Table 3, we show that the tibia has the largest average cortical bone chord length. This means that there are greater distances between osteons in the tibia. Consequently, a smaller fraction of electrons emitted within the bone volume will have sufficient energy to escape the bone volume. Those that do will have lower residual energy than those particles emitted in the bone volume of the humerus and femur.

The 2003 Eckerman model demonstrates similar behavior with respect to the ICRP reference value. Although absorbed fractions in the 2003 Eckerman model are lower than those presented by the SBoRT-CBICT combination. Differences are also seen in comparison of the shapes of the curves. A very mild down turn is seen for the Eckerman data that most closely resembles the average ICT results. SBoRT-CBICT results demonstrate a significant down turn starting at 200 keV as a result of electrons escaping from the cortical bone regions of the diaphysis, a feature that is not considered in the 2003 Eckerman model. Despite this,

differences in the magnitude of the absorbed fractions are a result of differences in the modeling of endosteum layer itself (see Fig. 7) and the longitudinal particle path component.

Absorbed Fractions to Other Cortical Tissues

Tabulated values for the CHS target and CBV target are listed in Appendix B of this paper. The CHS target tissue is not considered in the ICRP 30 bone model. As expected, the model predicts that values of $\phi(\text{CHS} \leftarrow \text{CHS})$ approach unity at lower and lower particle emission energies. Self-absorbed fractions to the CSH tissues are shown to be highest in the tibia, where chord distributions in this bone site tend to have the larger haversian cavity sizes. Differences do occur between the alpha source and the electron source. Although electrons exhibit unity behavior at low energies, the effective range of the higher energy electrons allows for the absorbed fraction to drop to a convergence value while the alpha source does not. Electron results also demonstrate effects from the SBoRT-CBIC combination. Values for the $\phi(\text{CHS} \leftarrow \text{CBV})$ for electrons are as high as 0.03 at 50 keV but drop over the energy range of 50-200 keV at which point they rise and level off to values between 0.005 and ~0.01.

For an electron $\phi(\text{CSH} \leftarrow \text{CBS})$ significant differences are seen. The $\phi(\text{CSH} \leftarrow \text{CBS})$ results are dominated by the macrostructural restriction and demonstrates cross osteon irradiation. Maximum absorbed fraction values are ~0.14. The CBV target, as noted earlier, may be used as a representative bone lesion target. Absorbed fraction values obtained for both alpha particles and electrons demonstrate very little bone site dependence. As with the other sources described earlier, the CHS source also demonstrates the most significant differences. Data for the CME target were found to be <0.001 for all six long bone sites. Accordingly, these results were not tabulated.

Data for cortical bone surrounding spongiosa ($\text{CBV}_{\text{cortex}}$) are presented in Table B4 of Appendix B (spongiosa sources - r_s) and in Table B5 ($\text{CBV}_{\text{cortex}}$ source). Values for $\phi(\text{CBE}_{\text{cortex}} \leftarrow r_s)$ have values of <0.01 for all bone sites except for the cranium, ribs and mandible where

they may be as high as 0.0182. For the $\phi(\text{CBE}_{\text{cortex}} \leftarrow \text{CBV}_{\text{cortex}})$ results show a peak in the absorbed fraction at 500 keV after which a decrease is seen. The maximum value seen in all bone sites was found in the right humerus at a value of 0.041. Note that the absorbed fractions were dominated by the macrostructural results of the PIRT calculation.

CONCLUSION

A chord-based model for charged-particle transport in the cortical bone has been presented that incorporates microstructural data (individual target energy deposition) and macrostructural (particle escape) data. The model incorporates the transverse chord-length distributions obtained by Beddoe for three cortical bone sites. This data set is limited to three long bone sites for microstructural data. The primary limitation of this model with respect to electrons lies in the assumption of linear pathlengths in cortical bone. Electrons as they travel through a medium undergo angular deflections that result in different amounts of energy along their tracks when compared to our CSDA range methodology. While the cortical model of Bouchet and Bolch does take these nonlinear pathlengths into account, this model also does not allow for irradiation of neighboring osteons, and thus neither model fully accounts for all factors relevant for high-energy emitters in the cortical bone microstructure. It is recommended that perhaps microCT images of cortical bone may be used in future to construct a more accurate transport geometry for cortical bone similar to that providing by the PIRT model for trabecular bone.^{8, 12}

Absorbed fractions obtained in this model provide an improved data set that may be used in therapeutic applications as well as health physics applications. With respect to electrons, this method more effectively accounts for electron escape from the diaphysis of the long bones. For therapeutic applications, use of absorbed fractions, especially the CHS source, should lead to a better estimate of endosteal dose due to the short-lived nature of the alpha emitters proposed for therapy. In radiation protection applications, an improved dose

estimate will also be achieved since the ICRP 30 model presents only two absorbed fraction values and values given in the 2003 Eckerman model do not account for the relative fraction of the haversian cavity associated with the endosteal layer.

ACKNOWLEDGMENTS

This work was supported in part by Grant CA96441 from the National Cancer Institute and Grant DE-FG07-02ID14327 from the U.S. Department of Energy with the University of Florida.

APPENDIX A

Combining transport results for microscopic and macroscopic data was performed by the following method. Absorbed fractions for the self dose to the CBV in the SBoRT macroscopic model is calculated as,

$$\phi(CBV \leftarrow CBV)_{SBoRT} = \frac{T_o - T_{CBV}^{macro} - T_{ESC}}{T_o}, \quad (A1)$$

where T_o is the initial particle energy, T_{CBV} is the energy deposited in the cortical bone volume and T_{ESC} is the energy not deposited within the CBV. Absorbed fractions for a specific tissue within the microstructure of the cortical bone volume (i.e., CBE) may be similarly calculated as,

$$\phi(CBE \leftarrow CBV)_{CBICT} = \frac{T_o - T_{CBV}^{micro} - T_{CHS}}{T_o} \quad (A2)$$

where T_{CHS} is the energy deposited in the blood of the CHS and the other parameters are previously defined. Within the macrostructure of the simulated bone is contained the microstructure such that $T_{CBV}^{macro} = T_{CHS} + T_{CBV}^{micro} + T_{CBE}$. Therefore, Eq. A2 may be rewritten to relate both the microscopic and macroscopic situations as,

$$\phi(CBE \leftarrow CBV)_{CBICT} = \frac{T_o - (T_{CBV}^{micro} + T_{CHS}) - T_{ESC}}{T_o} \quad (A3)$$

This means that the energy deposited in CBE is a fraction of $\phi(CBV \leftarrow CBV)_{SBoRT}$, thus we obtain the following,

$$\begin{aligned}\phi(CBE \leftarrow CBV)_{CBICT} &= \phi(CBV \leftarrow CBV)_{SBoRT} - \frac{T_{CBV} + T_{CHS}}{T_o} \\ \phi(CBV \leftarrow CBV)_{SBoRT} &= F_{Bone} \frac{T_{CBV} + T_{CHS} + T_{CBE}}{T_o} \\ F_{Bone} &= \frac{\phi(CBV \leftarrow CBV)_{SBoRT}}{\left[\frac{T_{CBV} + T_{CHS} + T_{CBE}}{T_o} \right]}\end{aligned}\tag{A4}$$

with F_{Bone} being a factor relating the SBoRT absorbed fraction to the CBICT absorbed fraction in a specific bone site. Therefore, energy deposition in a specific microstructural target as it relates to the macroscopic target is,

$$\phi_i^{SBoRT} = F_{Bone} \phi_i^{CBICT}\tag{A5}$$

In Eq. A5 ϕ_i represents the specific microscopic target in CBICT and SBoRT. Since the sum of all energy deposited in the CBICT method results in unity, the results in Eq. A1-A5 allow for,

$$\phi_i = \phi_{CBV}^{SBoRT} \phi_i^{CBICT}.\tag{A6}$$

Eq. A6 may be more simply stated as the convolution/multiplication of the results from a macroscopic transport calculation with those of a microscopic transport calculation result in the absorbed fraction that accounts for both geometries.

REFERENCES

- 1 J. L. Humm, Dosimetric aspects of radiolabeled antibodies for tumor therapy J Nucl Med 27, 1490 (1986).
- 2 V. K. Langmuir, Radioimmunotherapy: Clinical results and dosimetric considerations Nucl. Med. Biol. 19, 213 (1992).
- 3 V. K. Langmuir, J. F. Fowler, S. J. Knox, et al., Radiobiology of radiolabeled antibody therapy as applied to tumor dosimetry Med. Phys. 20, 601 (1993).
- 4 A. H. Beddoe, in *Department of Medical Physics* (University of Leeds, Leeds, UK, 1976), p. 165.
- 5 M. G. Stabin and J. A. Siegel, Physical models and dose factors for use in internal dose assessment Health Phys 85, 294 (2003).
- 6 K. F. Eckerman and M. G. Stabin, Electron absorbed fractions and dose conversion factors for marrow and bone by skeletal regions Health Phys. 78, 199 (2000).
- 7 L. G. Bouchet and W. E. Bolch, A three-dimensional transport model for determining absorbed fractions of energy for electrons in cortical bone J. Nucl. Med. 40, 2115 (1999).
- 8 A. P. Shah, D. A. Rajon, P. W. Patton, et al., Accounting for beta-particle energy loss to cortical bone via paired-image radiation transport (PIRT) Med Phys 32, 1354 (2005).
- 9 W. E. Bolch, P. W. Patton, D. A. Rajon, et al., Considerations of marrow cellularity in 3D dosimetric models of the trabecular skeleton J Nucl Med 43, 97 (2002).
- 10 ICRU, (International Commission on Radiation Units and Measurements, Bethesda, MD, 1984).
- 11 FDA, (US Food and Drug Administration, Washington, DC, Vol. 2005).
- 12 A. P. Shah, W. E. Bolch, D. A. Rajon, et al., A paired-image radiation transport model for skeletal dosimetry J Nucl Med 46, 344 (2005).

Table 1 – Reference alpha and beta particle absorbed fractions from ICRP 30.

ICRP 30	AF
$\phi (CBE \leftarrow CBV)$	0.015
$\phi (CBE \leftarrow CBS) E \geq 0.2 \text{ MeV}$	0.015
$\phi (CBE \leftarrow CBS) E < 0.2 \text{ MeV}$	0.25

Table 2 – Absorbed fractions for alpha and beta particles used in the OLINDA code

Energy (MeV)	β	
	$\phi(CBE \leftarrow CBS)$	$\phi(CBE \leftarrow CBV)$
0.01	0.4910	0.0007
0.02	0.4820	0.0014
0.02	0.4670	0.0022
0.03	0.3720	0.0044
0.05	0.2380	0.0081
0.10	0.0704	0.0130
0.20	0.0469	0.0190
0.50	0.0318	0.0214
1.00	0.0287	0.0211
2.00	0.0209	0.0209
4.00	0.0205	0.0205

Table 3 - Elemental composition of the tissues of cortical bone. Data taken from ICRU Publication 46.

Element	Tissues of Cortical Bone		
	Haversian Space (CHS) ^a	Endosteum (CBE) ^b	Bone Matrix (CBV) ^c
H	10.2	10.5	3.4
C	11	25.6	15.5
N	3.3	2.7	4.2
O	74.5	60.2	43.5
Na	0.1	0.1	0.1
Mg	----	----	0.2
P	0.1	0.2	10.3
S	0.2	0.3	0.3
Cl	0.3	0.2	----
K	0.2	0.2	----
Ca	----	----	22.5
Fe	0.1	----	----
Mass Density (g cm ⁻³)	1.06	1.03	1.92

Source: ICRU Report 46 - Appendix A

^a CHS - "adult whole blood"

^c CBE - "adult ICRU-44 soft tissue (male)"

^d CBV - "adult cortical bone"

Table 4 – Measured long bone diameters and thicknesses.

Bone Site	<i>Average Diameter or Thickness (cm)</i>					
	Medulary Cavity	σ	Cortical Shell	σ	Total Bone Diameter	σ
Humerus	1.26	0.02	0.39	0.02	2.04	0.07
Radius	0.63	0.06	0.30	0.01	1.23	0.04
Ulna	0.52	0.04	0.29	0.02	1.09	0.03
Femur	1.48	0.07	0.62	0.02	2.72	0.11
Tibia	1.36	0.05	0.55	0.02	2.47	0.09
Fibula	0.60	0.02	0.30	0.02	1.20	0.02

Table 1 – Reference alpha and beta particle absorbed fractions from ICRP 30.

ICRP 30	AF
$\phi (CBE \leftarrow CBV)$	0.015
$\phi (CBE \leftarrow CBS) E \geq 0.2 \text{ MeV}$	0.015
$\phi (CBE \leftarrow CBS) E < 0.2 \text{ MeV}$	0.25

Table 2 – Absorbed fractions for alpha and beta particles used in the OLINDA code

Energy (MeV)	β	
	$\phi(CBE \leftarrow CBS)$	$\phi(CBE \leftarrow CBV)$
0.01	0.4910	0.0007
0.02	0.4820	0.0014
0.02	0.4670	0.0022
0.03	0.3720	0.0044
0.05	0.2380	0.0081
0.10	0.0704	0.0130
0.20	0.0469	0.0190
0.50	0.0318	0.0214
1.00	0.0287	0.0211
2.00	0.0209	0.0209
4.00	0.0205	0.0205

Table 3 - Elemental composition of the tissues of cortical bone. Data taken from ICRU Publication 46.

Element	Tissues of Cortical Bone		
	Haversian Space (CHS) ^a	Endosteum (CBE) ^b	Bone Matrix (CBV) ^c
H	10.2	10.5	3.4
C	11	25.6	15.5
N	3.3	2.7	4.2
O	74.5	60.2	43.5
Na	0.1	0.1	0.1
Mg	----	----	0.2
P	0.1	0.2	10.3
S	0.2	0.3	0.3
Cl	0.3	0.2	----
K	0.2	0.2	----
Ca	----	----	22.5
Fe	0.1	----	----
Mass Density (g cm ⁻³)	1.06	1.03	1.92

Source: ICRU Report 46 - Appendix A

^a CHS - "adult whole blood"

^c CBE - "adult ICRU-44 soft tissue (male)"

^d CBV - "adult cortical bone"

Table 4 – Measured long bone diameters and thicknesses.

Bone Site	<i>Average Diameter or Thickness (cm)</i>					
	Medulary Cavity	σ	Cortical Shell	σ	Total Bone Diameter	σ
Humerus	1.26	0.02	0.39	0.02	2.04	0.07
Radius	0.63	0.06	0.30	0.01	1.23	0.04
Ulna	0.52	0.04	0.29	0.02	1.09	0.03
Femur	1.48	0.07	0.62	0.02	2.72	0.11
Tibia	1.36	0.05	0.55	0.02	2.47	0.09
Fibula	0.60	0.02	0.30	0.02	1.20	0.02

Table B1 - Absorbed fractions to the cortical bone endosteum (CBE) for β -emissions within various source tissues of the femoral, humeral, and tibial cortex in a 50-year male subject.

$\phi(\text{CBE} \leftarrow \text{CHS})$						
Energy (MeV)	Femur	Humerus	Tibia	Radius	Ulna	Fibula
0.010	5.80E-02	6.07E-02	3.76E-02	5.21E-02	5.21E-02	5.21E-02
0.015	9.88E-02	1.01E-01	6.49E-02	8.82E-02	8.82E-02	8.82E-02
0.020	1.37E-01	1.37E-01	9.10E-02	1.22E-01	1.22E-01	1.22E-01
0.030	2.02E-01	1.97E-01	1.40E-01	1.80E-01	1.80E-01	1.80E-01
0.040	2.44E-01	2.32E-01	1.76E-01	2.18E-01	2.18E-01	2.18E-01
0.050	2.63E-01	2.44E-01	1.97E-01	2.35E-01	2.35E-01	2.35E-01
0.100	2.07E-01	1.87E-01	1.83E-01	1.92E-01	1.88E-01	1.92E-01
0.200	1.33E-01	1.21E-01	1.25E-01	1.25E-01	1.23E-01	1.25E-01
0.500	9.25E-02	8.45E-02	8.74E-02	8.51E-02	8.38E-02	8.51E-02
1.000	7.13E-02	6.34E-02	6.68E-02	6.14E-02	6.06E-02	6.14E-02
1.500	6.04E-02	5.24E-02	5.68E-02	4.84E-02	4.78E-02	4.85E-02
2.000	5.30E-02	4.38E-02	4.92E-02	4.01E-02	4.00E-02	4.03E-02
4.000	3.58E-02	2.83E-02	3.32E-02	2.56E-02	2.46E-02	2.56E-02
$\phi(\text{CBE} \leftarrow \text{CBS})$						
Energy (MeV)	Femur	Humerus	Tibia	Radius	Ulna	Fibula
0.010	4.98E-01	4.99E-01	4.99E-01	4.98E-01	4.98E-01	4.98E-01
0.015	4.96E-01	4.96E-01	4.96E-01	4.96E-01	4.96E-01	4.96E-01
0.020	4.95E-01	4.95E-01	4.94E-01	4.95E-01	4.95E-01	4.95E-01
0.030	4.77E-01	4.77E-01	4.71E-01	4.75E-01	4.75E-01	4.75E-01
0.040	4.43E-01	4.48E-01	4.35E-01	4.42E-01	4.42E-01	4.42E-01
0.050	4.17E-01	4.24E-01	4.05E-01	4.15E-01	4.15E-01	4.15E-01
0.100	2.81E-01	2.86E-01	2.68E-01	2.78E-01	2.73E-01	2.78E-01
0.200	1.57E-01	1.56E-01	1.50E-01	1.53E-01	1.51E-01	1.53E-01
0.500	9.66E-02	9.11E-02	9.14E-02	8.98E-02	8.85E-02	8.99E-02
1.000	7.20E-02	6.58E-02	6.74E-02	6.25E-02	6.18E-02	6.26E-02
1.500	6.04E-02	5.32E-02	5.66E-02	4.86E-02	4.79E-02	4.87E-02
2.000	5.30E-02	4.42E-02	4.96E-02	4.03E-02	4.03E-02	4.06E-02
4.000	3.56E-02	2.84E-02	3.32E-02	2.56E-02	2.46E-02	2.55E-02
$\phi(\text{CBE} \leftarrow \text{CBV})$						
Energy (MeV)	Femur	Humerus	Tibia	Radius	Ulna	Fibula
0.010	6.06E-04	5.46E-04	5.73E-04	5.75E-04	5.75E-04	5.75E-04
0.015	1.34E-03	1.30E-03	1.32E-03	1.32E-03	1.32E-03	1.32E-03
0.020	2.31E-03	2.23E-03	2.28E-03	2.27E-03	2.27E-03	2.27E-03
0.030	4.77E-03	4.58E-03	4.57E-03	4.64E-03	4.64E-03	4.64E-03
0.040	7.36E-03	7.26E-03	7.14E-03	7.25E-03	7.25E-03	7.25E-03
0.050	1.03E-02	1.04E-02	9.64E-03	1.01E-02	1.01E-02	1.01E-02
0.100	2.38E-02	2.34E-02	2.23E-02	2.31E-02	2.27E-02	2.31E-02
0.200	3.69E-02	3.58E-02	3.51E-02	3.56E-02	3.51E-02	3.56E-02
0.500	4.64E-02	4.44E-02	4.37E-02	4.33E-02	4.26E-02	4.33E-02
1.000	4.68E-02	4.30E-02	4.42E-02	4.08E-02	4.03E-02	4.09E-02
1.500	4.43E-02	3.94E-02	4.18E-02	3.59E-02	3.54E-02	3.59E-02
2.000	4.08E-02	3.45E-02	3.82E-02	3.12E-02	3.11E-02	3.14E-02
4.000	3.03E-02	2.43E-02	2.81E-02	2.18E-02	2.09E-02	2.17E-02

Table B2 - Absorbed fractions to the cortical haversian space (CHS) for β -emissions within various source tissues of the femoral, humeral, and tibial cortex in a 50-year male subject.

$\phi(\text{CHS} \leftarrow \text{CHS})$						
Energy (MeV)	Femur	Humerus	Tibia	Radius	Ulna	Fibula
0.010	9.41E-01	9.39E-01	9.62E-01	9.47E-01	9.47E-01	9.47E-01
0.015	8.99E-01	8.97E-01	9.33E-01	9.10E-01	9.10E-01	9.10E-01
0.020	8.58E-01	8.57E-01	9.05E-01	8.73E-01	8.73E-01	8.73E-01
0.030	7.80E-01	7.87E-01	8.47E-01	8.05E-01	8.05E-01	8.05E-01
0.040	7.09E-01	7.20E-01	7.90E-01	7.40E-01	7.40E-01	7.40E-01
0.050	6.44E-01	6.64E-01	7.34E-01	6.81E-01	6.81E-01	6.81E-01
0.100	4.23E-01	4.69E-01	5.17E-01	4.68E-01	4.60E-01	4.68E-01
0.200	2.41E-01	3.02E-01	3.02E-01	2.79E-01	2.75E-01	2.79E-01
0.500	1.41E-01	1.67E-01	1.73E-01	1.55E-01	1.53E-01	1.55E-01
1.000	1.23E-01	1.23E-01	1.47E-01	1.20E-01	1.18E-01	1.20E-01
1.500	1.17E-01	1.06E-01	1.40E-01	1.04E-01	1.02E-01	1.04E-01
2.000	1.13E-01	9.41E-02	1.34E-01	9.36E-02	9.34E-02	9.41E-02
4.000	9.80E-02	7.31E-02	1.15E-01	7.49E-02	7.20E-02	7.48E-02
$\phi(\text{CHS} \leftarrow \text{CBS})$						
Energy (MeV)	Femur	Humerus	Tibia	Radius	Ulna	Fibula
0.010	1.52E-03	1.37E-03	1.82E-03	1.57E-03	1.57E-03	1.57E-03
0.015	3.28E-03	2.93E-03	3.94E-03	3.38E-03	3.38E-03	3.38E-03
0.020	5.37E-03	4.40E-03	5.98E-03	5.25E-03	5.25E-03	5.25E-03
0.030	1.88E-02	1.59E-02	1.97E-02	1.81E-02	1.81E-02	1.81E-02
0.040	4.80E-02	4.17E-02	5.07E-02	4.68E-02	4.68E-02	4.68E-02
0.050	7.14E-02	6.08E-02	7.65E-02	6.96E-02	6.96E-02	6.96E-02
0.100	9.88E-02	8.35E-02	1.23E-01	1.02E-01	9.98E-02	1.02E-01
0.200	7.95E-02	6.84E-02	1.04E-01	8.30E-02	8.18E-02	8.31E-02
0.500	8.26E-02	6.92E-02	1.02E-01	8.16E-02	8.04E-02	8.16E-02
1.000	9.42E-02	7.48E-02	1.13E-01	8.58E-02	8.47E-02	8.58E-02
1.500	9.85E-02	7.57E-02	1.18E-01	8.31E-02	8.19E-02	8.32E-02
2.000	9.99E-02	7.28E-02	1.19E-01	7.95E-02	7.94E-02	8.00E-02
4.000	9.27E-02	6.43E-02	1.09E-01	6.94E-02	6.67E-02	6.93E-02
$\phi(\text{CHS} \leftarrow \text{CBV})$						
Energy (MeV)	Femur	Humerus	Tibia	Radius	Ulna	Fibula
0.010	1.00E-06	1.00E-06	1.00E-06	1.00E-06	1.00E-06	1.00E-06
0.015	9.00E-06	6.00E-06	9.00E-06	8.00E-06	8.00E-06	8.00E-06
0.020	2.10E-05	1.30E-05	2.30E-05	1.90E-05	1.90E-05	1.90E-05
0.030	8.20E-05	6.30E-05	1.06E-04	8.37E-05	8.37E-05	8.37E-05
0.040	3.95E-04	3.15E-04	4.00E-04	3.70E-04	3.70E-04	3.70E-04
0.050	1.04E-03	7.52E-04	1.04E-03	9.44E-04	9.44E-04	9.44E-04
0.100	7.13E-03	5.83E-03	7.94E-03	6.95E-03	6.82E-03	6.95E-03
0.200	2.16E-02	1.78E-02	2.60E-02	2.16E-02	2.13E-02	2.16E-02
0.500	5.09E-02	4.20E-02	6.11E-02	4.95E-02	4.87E-02	4.95E-02
1.000	7.32E-02	5.88E-02	8.92E-02	6.72E-02	6.64E-02	6.72E-02
1.500	8.35E-02	6.48E-02	1.02E-01	7.11E-02	7.01E-02	7.12E-02
2.000	8.79E-02	6.42E-02	1.06E-01	7.04E-02	7.02E-02	7.08E-02
4.000	8.59E-02	6.02E-02	1.02E-01	6.48E-02	6.22E-02	6.47E-02

Table B3 - Absorbed fractions to the cortical bone volume (CBV) for β -emissions within various source tissues of the femoral, humeral, and tibial cortex in a 50-year male subject.

$\phi(\text{CBV} \leftarrow \text{CHS})$						
Energy (MeV)	Femur	Humerus	Tibia	Radius	Ulna	Fibula
0.010	5.99E-04	6.56E-04	4.90E-04	5.82E-04	5.82E-04	5.82E-04
0.015	2.29E-03	2.40E-03	1.79E-03	2.16E-03	2.16E-03	2.16E-03
0.020	5.40E-03	5.62E-03	4.23E-03	5.08E-03	5.08E-03	5.08E-03
0.030	1.75E-02	1.68E-02	1.26E-02	1.56E-02	1.56E-02	1.56E-02
0.040	4.74E-02	4.73E-02	3.41E-02	4.29E-02	4.29E-02	4.29E-02
0.050	9.34E-02	9.23E-02	6.86E-02	8.48E-02	8.48E-02	8.48E-02
0.100	3.67E-01	3.39E-01	2.96E-01	3.33E-01	3.27E-01	3.33E-01
0.200	6.15E-01	5.63E-01	5.61E-01	5.73E-01	5.65E-01	5.73E-01
0.500	7.24E-01	7.00E-01	6.95E-01	6.77E-01	6.67E-01	6.77E-01
1.000	7.04E-01	7.00E-01	6.78E-01	6.23E-01	6.15E-01	6.23E-01
1.500	6.59E-01	6.61E-01	6.30E-01	5.40E-01	5.32E-01	5.41E-01
2.000	6.12E-01	6.18E-01	5.82E-01	4.75E-01	4.74E-01	4.78E-01
4.000	4.62E-01	4.72E-01	4.36E-01	3.39E-01	3.25E-01	3.38E-01
$\phi(\text{CBV} \leftarrow \text{CBS})$						
Energy (MeV)	Femur	Humerus	Tibia	Radius	Ulna	Fibula
0.010	5.00E-01	5.00E-01	5.00E-01	5.00E-01	5.00E-01	5.00E-01
0.015	5.00E-01	5.01E-01	5.00E-01	5.00E-01	5.00E-01	5.00E-01
0.020	4.99E-01	5.00E-01	5.00E-01	5.00E-01	5.00E-01	5.00E-01
0.030	5.05E-01	5.07E-01	5.09E-01	5.07E-01	5.07E-01	5.07E-01
0.040	5.09E-01	5.10E-01	5.14E-01	5.11E-01	5.11E-01	5.11E-01
0.050	5.12E-01	5.15E-01	5.19E-01	5.15E-01	5.15E-01	5.15E-01
0.100	6.16E-01	6.26E-01	6.05E-01	6.14E-01	6.03E-01	6.14E-01
0.200	7.53E-01	7.63E-01	7.35E-01	7.42E-01	7.31E-01	7.42E-01
0.500	7.78E-01	7.94E-01	7.62E-01	7.46E-01	7.34E-01	7.46E-01
1.000	7.32E-01	7.49E-01	7.11E-01	6.55E-01	6.47E-01	6.55E-01
1.500	6.78E-01	6.94E-01	6.53E-01	5.60E-01	5.53E-01	5.61E-01
2.000	6.25E-01	6.42E-01	5.97E-01	4.89E-01	4.88E-01	4.91E-01
4.000	4.67E-01	4.82E-01	4.42E-01	3.44E-01	3.31E-01	3.43E-01
$\phi(\text{CBV} \leftarrow \text{CBV})$						
Energy (MeV)	Femur	Humerus	Tibia	Radius	Ulna	Fibula
0.010	9.99E-01	9.99E-01	9.99E-01	9.99E-01	9.99E-01	9.99E-01
0.015	9.99E-01	9.99E-01	9.99E-01	9.99E-01	9.99E-01	9.99E-01
0.020	9.98E-01	9.98E-01	9.98E-01	9.98E-01	9.98E-01	9.98E-01
0.030	9.95E-01	9.95E-01	9.95E-01	9.95E-01	9.95E-01	9.95E-01
0.040	9.92E-01	9.92E-01	9.92E-01	9.92E-01	9.92E-01	9.92E-01
0.050	9.89E-01	9.89E-01	9.89E-01	9.89E-01	9.89E-01	9.89E-01
0.100	9.66E-01	9.67E-01	9.66E-01	9.63E-01	9.46E-01	9.63E-01
0.200	9.31E-01	9.35E-01	9.27E-01	9.21E-01	9.07E-01	9.21E-01
0.500	8.60E-01	8.69E-01	8.50E-01	8.24E-01	8.12E-01	8.24E-01
1.000	7.78E-01	7.90E-01	7.59E-01	6.96E-01	6.87E-01	6.96E-01
1.500	7.09E-01	7.22E-01	6.84E-01	5.85E-01	5.77E-01	5.86E-01
2.000	6.49E-01	6.63E-01	6.22E-01	5.07E-01	5.06E-01	5.10E-01
4.000	4.79E-01	4.92E-01	4.54E-01	3.53E-01	3.39E-01	3.52E-01

Table B4 - Absorbed fractions to the cortical bone cortex tissues for β -emissions within spongiosa tissues. Values for the long bones are only for the proximal ends which contain spongiosa.

$\phi(CBE_{cortex} \leftarrow r_s)$ Skeletal Site																	
Energy (MeV)	Right Femur	Left Femur	Right Humerus	Left Humerus	Cervical Vert	Thoracic Vert	Lumbar Vert	Sacrum	Os Coxae	Cranium	Mandible	Ribs	Sternum	Right Clavicle	Left Clavicle	Right Scapula	Left Scapula
0.010	0.0000	0.0000	0.0000	0.0000	0.0000	0.0000	0.0000	0.0000	0.0000	0.0000	0.0000	0.0000	0.0000	0.0000	0.0000	0.0000	0.0000
0.015	0.0000	0.0000	0.0000	0.0000	0.0000	0.0000	0.0000	0.0000	0.0000	0.0000	0.0000	0.0000	0.0000	0.0000	0.0000	0.0000	0.0000
0.02	0.0000	0.0000	0.0000	0.0000	0.0000	0.0000	0.0000	0.0000	0.0000	0.0000	0.0000	0.0000	0.0000	0.0000	0.0000	0.0000	0.0000
0.03	0.0000	0.0000	0.0000	0.0000	0.0000	0.0000	0.0000	0.0000	0.0000	0.0000	0.0000	0.0000	0.0000	0.0000	0.0000	0.0000	0.0000
0.04	0.0000	0.0000	0.0000	0.0000	0.0000	0.0000	0.0000	0.0000	0.0000	0.0000	0.0000	0.0000	0.0000	0.0000	0.0000	0.0000	0.0000
0.05	0.0000	0.0000	0.0000	0.0000	0.0000	0.0000	0.0000	0.0000	0.0000	0.0001	0.0000	0.0000	0.0000	0.0000	0.0000	0.0000	0.0000
0.1	0.0001	0.0001	0.0001	0.0001	0.0003	0.0001	0.0001	0.0002	0.0001	0.0003	0.0003	0.0003	0.0001	0.0002	0.0002	0.0002	0.0002
0.2	0.0002	0.0002	0.0003	0.0003	0.0013	0.0005	0.0005	0.0007	0.0005	0.0015	0.0014	0.0015	0.0006	0.0007	0.0007	0.0009	0.0009
0.5	0.0010	0.0011	0.0013	0.0013	0.0051	0.0020	0.0020	0.0029	0.0022	0.0060	0.0059	0.0065	0.0028	0.0031	0.0031	0.0037	0.0036
1.0	0.0023	0.0024	0.0029	0.0027	0.0099	0.0040	0.0039	0.0056	0.0047	0.0123	0.0126	0.0127	0.0059	0.0070	0.0071	0.0074	0.0070
1.5	0.0030	0.0032	0.0039	0.0038	0.0115	0.0047	0.0046	0.0068	0.0064	0.0157	0.0167	0.0136	0.0075	0.0090	0.0096	0.0088	0.0082
2.0	0.0034	0.0036	0.0047	0.0045	0.0112	0.0048	0.0046	0.0069	0.0071	0.0164	0.0182	0.0123	0.0080	0.0096	0.0105	0.0090	0.0084
4.0	0.0039	0.0041	0.0059	0.0054	0.0078	0.0038	0.0037	0.0058	0.0072	0.0125	0.0146	0.0069	0.0070	0.0073	0.0078	0.0070	0.0066
$\phi(CBV_{cortex} \leftarrow r_s)$ Skeletal Site																	
Energy (MeV)	Right Femur	Left Femur	Right Humerus	Left Humerus	Cervical Vert	Thoracic Vert	Lumbar Vert	Sacrum	Os Coxae	Cranium	Mandible	Ribs	Sternum	Right Clavicle	Left Clavicle	Right Scapula	Left Scapula
0.010	0.0001	0.0001	0.0001	0.0001	0.0003	0.0002	0.0002	0.0002	0.0002	0.0008	0.0003	0.0005	0.0001	0.0003	0.0001	0.0003	0.0002
0.015	0.0001	0.0001	0.0002	0.0001	0.0007	0.0003	0.0002	0.0004	0.0004	0.0012	0.0008	0.0008	0.0004	0.0006	0.0003	0.0003	0.0005
0.02	0.0002	0.0002	0.0003	0.0003	0.0010	0.0005	0.0003	0.0005	0.0004	0.0016	0.0011	0.0012	0.0005	0.0005	0.0005	0.0007	0.0007
0.03	0.0003	0.0005	0.0004	0.0004	0.0016	0.0008	0.0007	0.0010	0.0007	0.0025	0.0020	0.0021	0.0009	0.0010	0.0009	0.0013	0.0013
0.04	0.0005	0.0006	0.0007	0.0006	0.0027	0.0011	0.0010	0.0014	0.0011	0.0035	0.0032	0.0033	0.0012	0.0018	0.0014	0.0019	0.0019
0.05	0.0007	0.0008	0.0008	0.0011	0.0040	0.0016	0.0014	0.0021	0.0015	0.0050	0.0043	0.0048	0.0020	0.0025	0.0023	0.0027	0.0028
0.1	0.0022	0.0023	0.0027	0.0023	0.0114	0.0044	0.0042	0.0069	0.0047	0.0145	0.0125	0.0143	0.0055	0.0074	0.0070	0.0087	0.0080
0.2	0.0059	0.0060	0.0070	0.0077	0.0326	0.0123	0.0117	0.0180	0.0129	0.0395	0.0370	0.0393	0.0150	0.0184	0.0178	0.0234	0.0228
0.5	0.0194	0.0197	0.0240	0.0250	0.0978	0.0382	0.0375	0.0552	0.0423	0.1152	0.1117	0.1242	0.0534	0.0596	0.0584	0.0712	0.0695
1.0	0.0379	0.0393	0.0502	0.0471	0.1679	0.0680	0.0663	0.0961	0.0805	0.2096	0.2148	0.2162	0.1008	0.1199	0.1214	0.1267	0.1199
1.5	0.0486	0.0504	0.0641	0.0633	0.1873	0.0773	0.0755	0.1117	0.1042	0.2567	0.2724	0.2226	0.1220	0.1461	0.1573	0.1434	0.1339
2.0	0.0548	0.0567	0.0779	0.0752	0.1811	0.0781	0.0740	0.1114	0.1156	0.2658	0.2962	0.1992	0.1300	0.1552	0.1709	0.1460	0.1364
4.0	0.0615	0.0652	0.0981	0.0902	0.1270	0.0613	0.0595	0.0941	0.1162	0.2017	0.2372	0.1115	0.1127	0.1183	0.1265	0.1129	0.1071
$\phi(CHS_{cortex} \leftarrow r_s)$ Skeletal Site																	
Energy (MeV)	Right Femur	Left Femur	Right Humerus	Left Humerus	Cervical Vert	Thoracic Vert	Lumbar Vert	Sacrum	Os Coxae	Cranium	Mandible	Ribs	Sternum	Right Clavicle	Left Clavicle	Right Scapula	Left Scapula
0.010	0.0000	0.0000	0.0000	0.0000	0.0000	0.0000	0.0000	0.0000	0.0000	0.0000	0.0000	0.0000	0.0000	0.0000	0.0000	0.0000	0.0000
0.015	0.0000	0.0000	0.0000	0.0000	0.0000	0.0000	0.0000	0.0000	0.0000	0.0000	0.0000	0.0000	0.0000	0.0000	0.0000	0.0000	0.0000
0.02	0.0000	0.0000	0.0000	0.0000	0.0000	0.0000	0.0000	0.0000	0.0000	0.0000	0.0000	0.0000	0.0000	0.0000	0.0000	0.0000	0.0000
0.03	0.0000	0.0000	0.0000	0.0000	0.0000	0.0000	0.0000	0.0000	0.0000	0.0000	0.0000	0.0000	0.0000	0.0000	0.0000	0.0000	0.0000
0.04	0.0000	0.0000	0.0000	0.0000	0.0000	0.0000	0.0000	0.0000	0.0000	0.0000	0.0000	0.0000	0.0000	0.0000	0.0000	0.0000	0.0000
0.05	0.0000	0.0000	0.0000	0.0000	0.0000	0.0000	0.0000	0.0000	0.0000	0.0000	0.0000	0.0000	0.0000	0.0000	0.0000	0.0000	0.0000
0.1	0.0000	0.0000	0.0000	0.0000	0.0001	0.0000	0.0000	0.0000	0.0000	0.0001	0.0001	0.0001	0.0000	0.0001	0.0001	0.0001	0.0001
0.2	0.0001	0.0001	0.0001	0.0001	0.0008	0.0003	0.0003	0.0004	0.0003	0.0009	0.0009	0.0009	0.0004	0.0004	0.0004	0.0005	0.0005
0.5	0.0011	0.0012	0.0012	0.0012	0.0059	0.0023	0.0022	0.0033	0.0025	0.0069	0.0067	0.0075	0.0032	0.0036	0.0035	0.0043	0.0042
1.0	0.0036	0.0037	0.0040	0.0037	0.0162	0.0066	0.0064	0.0093	0.0078	0.0203	0.0208	0.0209	0.0097	0.0116	0.0117	0.0122	0.0116
1.5	0.0057	0.0059	0.0064	0.0063	0.0228	0.0094	0.0092	0.0136	0.0127	0.0312	0.0331	0.0271	0.0148	0.0178	0.0191	0.0174	0.0163
2.0	0.0074	0.0077	0.0088	0.0085	0.0252	0.0109	0.0103	0.0155	0.0161	0.0369	0.0411	0.0277	0.0180	0.0216	0.0237	0.0203	0.0189
4.0	0.0110	0.0117	0.0147	0.0135	0.0233	0.0113	0.0109	0.0173	0.0214	0.0371	0.0436	0.0205	0.0207	0.0217	0.0233	0.0207	0.0197

Table B5 - Absorbed fractions to the cortical bone cortex tissues for β -emissions within cortical bone cortex volume. Values for long bones are only for the proximal ends containing spongiosa.

$$\phi(CBE_{cortex} \leftarrow CBV_{cortex})$$

Skeletal Site

Energy (MeV)	Right Femur	Left Femur	Right Humerus	Left Humerus	Cervical Vert	Thoracic Vert	Lumbar Vert	Sacrum	Os Coxae	Cranium	Mandible	Ribs	Sternum	Right Clavicle	Left Clavicle	Right Scapula	Left Scapula
0.010	0.0006	0.0006	0.0005	0.0005	0.0006	0.0006	0.0006	0.0006	0.0006	0.0006	0.0006	0.0006	0.0006	0.0006	0.0006	0.0006	0.0006
0.015	0.0013	0.0013	0.0013	0.0013	0.0013	0.0013	0.0013	0.0013	0.0013	0.0013	0.0013	0.0013	0.0013	0.0013	0.0013	0.0013	0.0013
0.02	0.0023	0.0023	0.0022	0.0022	0.0023	0.0023	0.0023	0.0023	0.0023	0.0023	0.0023	0.0023	0.0023	0.0023	0.0023	0.0023	0.0023
0.03	0.0048	0.0048	0.0046	0.0046	0.0046	0.0046	0.0046	0.0046	0.0046	0.0046	0.0046	0.0046	0.0046	0.0046	0.0046	0.0046	0.0046
0.04	0.0073	0.0073	0.0072	0.0072	0.0072	0.0072	0.0072	0.0072	0.0072	0.0072	0.0072	0.0072	0.0072	0.0072	0.0072	0.0072	0.0072
0.05	0.0102	0.0102	0.0104	0.0104	0.0100	0.0100	0.0100	0.0100	0.0100	0.0101	0.0101	0.0100	0.0100	0.0100	0.0100	0.0100	0.0100
0.1	0.0234	0.0234	0.0231	0.0231	0.0226	0.0226	0.0226	0.0226	0.0228	0.0228	0.0229	0.0225	0.0226	0.0227	0.0227	0.0226	0.0226
0.2	0.0350	0.0351	0.0349	0.0347	0.0335	0.0333	0.0334	0.0335	0.0341	0.0346	0.0348	0.0329	0.0336	0.0340	0.0342	0.0335	0.0333
0.5	0.0389	0.0393	0.0410	0.0404	0.0349	0.0345	0.0344	0.0351	0.0375	0.0393	0.0404	0.0326	0.0351	0.0370	0.0377	0.0346	0.0339
1.0	0.0313	0.0319	0.0362	0.0353	0.0256	0.0250	0.0248	0.0263	0.0301	0.0340	0.0359	0.0219	0.0252	0.0285	0.0299	0.0252	0.0243
1.5	0.0249	0.0255	0.0315	0.0301	0.0194	0.0190	0.0189	0.0202	0.0235	0.0285	0.0305	0.0166	0.0184	0.0218	0.0232	0.0189	0.0183
2.0	0.0199	0.0207	0.0266	0.0254	0.0156	0.0152	0.0151	0.0165	0.0189	0.0244	0.0261	0.0137	0.0144	0.0175	0.0189	0.0150	0.0145
4.0	0.0117	0.0121	0.0166	0.0154	0.0091	0.0088	0.0089	0.0094	0.0112	0.0157	0.0169	0.0079	0.0088	0.0109	0.0120	0.0088	0.0087

$$\phi(CBV_{cortex} \leftarrow CBV_{cortex})$$

Skeletal Site

Energy (MeV)	Right Femur	Left Femur	Right Humerus	Left Humerus	Cervical Vert	Thoracic Vert	Lumbar Vert	Sacrum	Os Coxae	Cranium	Mandible	Ribs	Sternum	Right Clavicle	Left Clavicle	Right Scapula	Left Scapula
0.010	0.9991	0.9990	0.9991	0.9991	0.9989	0.9990	0.9988	0.9989	0.9990	0.9990	0.9990	0.9988	0.9989	0.9991	0.9989	0.9989	0.9988
0.015	0.9978	0.9979	0.9979	0.9982	0.9975	0.9976	0.9975	0.9977	0.9979	0.9981	0.9983	0.9974	0.9975	0.9979	0.9979	0.9975	0.9975
0.02	0.9962	0.9964	0.9967	0.9966	0.9960	0.9958	0.9958	0.9960	0.9965	0.9966	0.9966	0.9958	0.9963	0.9963	0.9962	0.9962	0.9958
0.03	0.9925	0.9928	0.9935	0.9934	0.9920	0.9916	0.9918	0.9917	0.9927	0.9931	0.9934	0.9911	0.9918	0.9921	0.9925	0.9918	0.9916
0.04	0.9880	0.9880	0.9892	0.9891	0.9867	0.9864	0.9866	0.9867	0.9881	0.9887	0.9894	0.9853	0.9864	0.9872	0.9879	0.9863	0.9866
0.05	0.9824	0.9825	0.9842	0.9837	0.9802	0.9801	0.9802	0.9808	0.9825	0.9838	0.9844	0.9787	0.9804	0.9821	0.9819	0.9803	0.9799
0.1	0.9485	0.9490	0.9566	0.9554	0.9429	0.9415	0.9418	0.9436	0.9493	0.9526	0.9546	0.9375	0.9446	0.9470	0.9489	0.9430	0.9412
0.2	0.8845	0.8857	0.9072	0.9027	0.8656	0.8623	0.8631	0.8662	0.8835	0.8947	0.9001	0.8504	0.8704	0.8807	0.8846	0.8654	0.8616
0.5	0.7215	0.7296	0.7867	0.7753	0.6649	0.6579	0.6550	0.6681	0.7139	0.7494	0.7700	0.6211	0.6696	0.7054	0.7175	0.6590	0.6463
1.0	0.5201	0.5308	0.6280	0.6119	0.4360	0.4252	0.4227	0.4475	0.5119	0.5782	0.6117	0.3731	0.4288	0.4849	0.5100	0.4287	0.4147
1.5	0.3994	0.4091	0.5220	0.4984	0.3168	0.3105	0.3089	0.3301	0.3840	0.4648	0.4979	0.2712	0.3006	0.3556	0.3779	0.3075	0.2987
2.0	0.3171	0.3299	0.4406	0.4199	0.2540	0.2470	0.2453	0.2678	0.3070	0.3968	0.4236	0.2219	0.2335	0.2844	0.3072	0.2429	0.2361
4.0	0.1845	0.1914	0.2752	0.2551	0.1468	0.1430	0.1439	0.1528	0.1810	0.2535	0.2731	0.1272	0.1424	0.1767	0.1943	0.1432	0.1401

$$\phi(CHS_{cortex} \leftarrow CBV_{cortex})$$

Skeletal Site

Energy (MeV)	Right Femur	Left Femur	Right Humerus	Left Humerus	Cervical Vert	Thoracic Vert	Lumbar Vert	Sacrum	Os Coxae	Cranium	Mandible	Ribs	Sternum	Right Clavicle	Left Clavicle	Right Scapula	Left Scapula
0.010	0.0000	0.0000	0.0000	0.0000	0.0000	0.0000	0.0000	0.0000	0.0000	0.0000	0.0000	0.0000	0.0000	0.0000	0.0000	0.0000	0.0000
0.015	0.0000	0.0000	0.0000	0.0000	0.0000	0.0000	0.0000	0.0000	0.0000	0.0000	0.0000	0.0000	0.0000	0.0000	0.0000	0.0000	0.0000
0.02	0.0000	0.0000	0.0000	0.0000	0.0000	0.0000	0.0000	0.0000	0.0000	0.0000	0.0000	0.0000	0.0000	0.0000	0.0000	0.0000	0.0000
0.03	0.0001	0.0001	0.0001	0.0001	0.0001	0.0001	0.0001	0.0001	0.0001	0.0001	0.0001	0.0001	0.0001	0.0001	0.0001	0.0001	0.0001
0.04	0.0004	0.0004	0.0003	0.0003	0.0004	0.0004	0.0004	0.0004	0.0004	0.0004	0.0004	0.0004	0.0004	0.0004	0.0004	0.0004	0.0004
0.05	0.0010	0.0010	0.0007	0.0007	0.0009	0.0009	0.0009	0.0009	0.0009	0.0009	0.0009	0.0009	0.0009	0.0009	0.0009	0.0009	0.0009
0.1	0.0070	0.0070	0.0058	0.0058	0.0068	0.0068	0.0068	0.0068	0.0068	0.0069	0.0069	0.0068	0.0068	0.0068	0.0068	0.0068	0.0068
0.2	0.0205	0.0205	0.0174	0.0173	0.0203	0.0202	0.0202	0.0203	0.0207	0.0210	0.0211	0.0199	0.0204	0.0206	0.0207	0.0203	0.0202
0.5	0.0427	0.0431	0.0389	0.0383	0.0399	0.0395	0.0393	0.0401	0.0429	0.0450	0.0462	0.0373	0.0402	0.0424	0.0431	0.0396	0.0388
1.0	0.0489	0.0499	0.0495	0.0483	0.0421	0.0411	0.0408	0.0432	0.0495	0.0559	0.0591	0.0360	0.0414	0.0469	0.0493	0.0414	0.0401
1.5	0.0471	0.0482	0.0518	0.0494	0.0385	0.0377	0.0375	0.0401	0.0467	0.0565	0.0605	0.0330	0.0365	0.0432	0.0459	0.0374	0.0363
2.0	0.0430	0.0447	0.0496	0.0472	0.0353	0.0343	0.0341	0.0372	0.0426	0.0551	0.0588	0.0308	0.0324	0.0395	0.0427	0.0337	0.0328
4.0	0.0330	0.0343	0.0411	0.0381	0.0270	0.0263	0.0265	0.0281	0.0333	0.0466	0.0502	0.0234	0.0262	0.0325	0.0357	0.0263	0.0257

Age and Individual Variability in Alpha-Particle Absorbed Fractions to the Skeletal Tissues

Christopher J. Watchman, MS

Department of Nuclear & Radiological Engineering, University of Florida, Gainesville, FL 32611

Wesley E. Bolch, PhD

Departments of Nuclear & Radiological and Biomedical Engineering, University of Florida,
Gainesville, FL 32611

For reprints and correspondence contact:

Wesley E. Bolch, PhD, PE, CHP

Director, Advanced Laboratory for Radiation Dosimetry Studies (ALRADS)

Department of Nuclear and Radiological Engineering

University of Florida, Gainesville, Florida 32611-8300

Phone: (352) 846-1361 Fax: (352) 392-3380 Email: wbolch@ufl.edu

SHORT TITLE:

Individual variability in α -particle absorbed fractions

This work was supported by the

The U.S. Department of Energy

Submitted to Medical Physics

Abstract

Introduction: A previous study of α -particle absorbed fractions using chord distribution data from the ICRP reference male (Leeds 44-year male) demonstrated their dependence on marrow cellularity, skeletal site, and particle energy. In this study, we extend our analysis to include a series of 6 adults and 2 pediatric subjects. Currently, there are no published values of α -particle absorbed fractions in the skeletal tissues that account marrow cellularity by skeletal site. **Methods:** Using the 3D-CBIST computer code published by Watchman et al. [JNM **46** 1171-1185 (2005)], absorbed fractions were calculated for the Leeds 1.7-y male (5 bone sites) and 9-y male (6 bone sites) in the iliac crest and ribs. Lumbar vertebrae sites were also investigated for a 55-y, 70-y and 85-y female, as well as a 25-y and 66-y male. Each calculation was performed over the energy range of 3 – 10 MeV for marrow cellularities ranging from 10% to 100%, and for α -emitting radiopharmaceuticals localized to the active marrow (TAM), bone surfaces (TBS) and bone trabeculae volumes (TBV). Comparisons of absorbed fractions were made at 100% cellularity and at an age-dependant reference cellularity for active marrow and endosteum targets. **Results:** Variations in $\phi(\text{active marrow} \leftarrow \text{active marrow})$ are less than 1% among the six adults in the lumbar vertebrae at 100% marrow cellularity, but are between 12-15% for values of $\phi(\text{endosteum} \leftarrow \text{active marrow})$. While observable differences were seen α -particle absorbed fractions as a function of age at 100% cellularity, significantly higher age variations were seen when age-dependent marrow cellularity was explicitly considered during particle transport. For example, at an energy of 7 MeV, the ratio of $\phi(\text{active marrow} \leftarrow \text{active marrow})$ and $\phi(\text{endosteum} \leftarrow \text{active marrow})$ in the iliac crest of the 1.7-y to their corresponding values in the 66-y male are 1.87 and 0.32, respectively. **Conclusion:** The largest source of uncertainty in patient-specific α -particle dosimetry in molecular radiotherapy continues to be the neglect of marrow cellularity in the assignment of absorbed fractions to the skeletal tissues. The assumption of unity for values of $\phi(\text{TAM} \leftarrow \text{TAM})$ as given in existing skeletal dosimetry models can lead to significant errors in marrow dose assessment, particularly in older patients with high skeletal fat fractions and high α -particle energies (5 to 9 MeV).

Keywords: Radionuclide therapy; alpha particles; absorbed fraction; marrow cellularity; individual variability; pediatric dosimetry

I. Introduction

With renewed interest in alpha-particle emitters for use in therapy nuclear medicine, the assessment of patient variability in marrow tissue dosimetry becomes an important issue in current and proposed clinical trials.¹⁻⁹ Currently, the skeletal dosimetry model of Publication 30¹⁰ from the International Commission on Radiological Protection (ICRP) assigns values of the absorbed fraction to skeletal tissues that are constant and do not vary with either particle energy, skeletal site, subject age, or marrow cellularity – all potentially important features in clinical assessments of active marrow dose to individual therapy patients. An energy dependence was introduced in the 2003 Eckerman skeletal dosimetry model¹¹ for some source-target tissue combinations, while for others values from the ICRP 30 model were adopted without revision.

In the present study, published information on the skeletal microstructure of the lumbar vertebrae in six adult subjects, and of the iliac crest and ribs in two pediatric and in two adults subjects, were used to explore both the age and individual variability of α -particle absorbed fraction in the skeleton tissues. The clinical importance of these findings is then discussed with specific suggestions of how to improve the patient-specificity of skeletal tissue dosimetry in molecular radiotherapies that utilize short-lived, high-energy α -emitting radionuclides.

II. Materials and Methods

Absorbed fractions were calculated for alpha-particles emitted within the skeletal tissues of a various individuals and skeletal sites as permitted by published data on their trabecular microstructure. Alpha particle energies of 3 to 10 MeV were considered in 0.5 MeV increments. This energy range covers that of interest both in occupational radiation protection (~3 to 4.5 MeV) and in molecular radiotherapy (~4.5 to 9 MeV). Target tissues included the trabecular active (or red) marrow (TAM) and the trabecular bone endosteum (TBE). The latter is defined by the ICRP as a 10- μ m layer of soft tissue covering all interior bone surfaces of cancellous

bone.¹² In this study, the active bone marrow is considered to include all soft tissues within the marrow cavity exclusive of the endosteal layer and marrow adipocytes (e.g., inactive or yellow marrow). Tissue sources for radiopharmaceutical localization included the trabecular active marrow, the trabecular bone surfaces (TBS), and the trabecular bone volume (TBV). Values of the absorbed fraction for alpha-emissions at partial depth within in the bone trabeculae would thus be intermediate to those given for the TBS (surface only) and TBV (uniform throughout) sources.

A. Chord-Length Distributional Data

The most comprehensive series of microstructural studies on cancellous bone was conducted at the University of Leeds in the late 1960s to late 1970s. These studies report probability density functions of linear chord lengths across both the marrow cavities and bone trabeculae as determined via optical scanning of contact radiographs of thin physical sections of cancellous bone. Table 1 summarizes this data set in terms of distributional-averaged values of the marrow cavity chord-length (upper section) and the bone trabeculae chord-length (lower section). The Leeds series includes two male pediatric subjects of 1.7 years and 9 years (5 skeletal sites each), one 44-year male (7 skeletal sites), and four additional adults (3rd lumbar vertebra only). In the present study, numerical values of these chord-length distributions were taken directly from the dissertation of Whitwell¹³ for all individuals except the 9-year male. For this latter individual, the bone and marrow chord distributions were estimated from data given in graphical format within the dissertation of Beddoe.¹⁴ Finally, recent microCT-based imaging studies by Shah et al.¹⁵ have provided a comprehensive series of bone and marrow chord-length distributions across multiples skeletal sites in a 66-year male. For the latter, cord-length distributions assembled from segmented microCT scans of individual cores of spongiosa were used for alpha-particle transport (see below). The resulting energy profiles of alpha-particle absorbed fraction were then volume-averaged to report a single set of absorbed fractions for a

given skeletal site. For example, absorbed fractions for tissues within the lumbar vertebrae of the UF 66-year male were taken as the volume-weighted average of those found within spongiosa cores from the L₂ and L₄ vertebrae. Similarly, alpha-particle absorbed fractions determined within spongiosa cores from the ilium, ischium, and pubic bone were used to report a single set of absorbed fractions for the pelvis of the UF 66-year male.

B. Radiation Transport Methodology

Values of alpha-particle absorbed fraction to the skeletal tissues were determined using the 3D chord-based infinite spongiosa transport (or 3D-CBIST) code of Watchman et al.¹⁶ The code's transport algorithm alternately and randomly samples bone trabeculae and marrow cavity chord-lengths for the individual of interest, and applies range-energy relationships to report energy loss to traversed tissue regions in cancellous bone. Energy loss to bone marrow is further treated using a supplemental 3D spatial model of the marrow tissues in which alpha-particle traversals across individual marrow adipocytes are explicitly considered. As such, the 3D-CBIST code permits one to report alpha-particle absorbed fractions as a function of marrow cellularity – the fractional volume of bone marrow that is hematopoietically active. Table 2 summarizes mean values of marrow cellularity as a function of age as reported in ICRP Publication 70.¹² In the present study, site-specific marrow cellularities for the Leeds 1.7-year male, 9-year male, and 44-year male were approximated by ICRP 70 reference cellularities for the ICRP 1-year-old, 10-year-old, and 40-year-old, respectively. Values for the UF 66-year male are taken from the graphical age-dependent data of Custer et al.¹⁷ as available for the vertebral column, sternum, ribs, and os coxae. For all other skeletal sites in the UF 66-year male, the 40-year reference data of Table 2 was assumed. Particle histories were run so that the coefficient of variation (COV) was less than 1% for self-irradiation of target tissues, and <3% for all other targets.

III. RESULTS

A. Individual Variations with Trabecular Microstructure in the Adult

Alpha-particle absorbed fractions to the skeletal tissues of the lumbar vertebrae are given in Figures 1A to 1F for six different source-target combinations and for all six adult subjects listed in Table 2. Figures 1A and 1B display values for active marrow sources irradiating the active marrow and bone endosteum, respectively. Similarly, Figures 1C and 1D show corresponding values for bone surface sources to these same target tissues, while Figures 1E and 1F give values for bone volume sources. For visual consistency, the ordinate is kept at a constant range for each source tissue. Statistical summaries of these data are shown in Table 3. In all cases, the 3D-CBIST code was run at 100% marrow cellularity so that variations in alpha-particle absorbed fraction will reflect only those differences attributed to individual variations in the spongiosa microstructure among the adult subjects.

Absolute variations in the absorbed fraction are noted to be small for α -particles among the six individuals of the study. In all but two of the six of the source-target combinations, the range of values is noted to increase with increasing particle energy (longer ranged particles are increasingly impacted by differences in the trabecular microstructure). When the endosteal layer is irradiated by alpha-emitters localized within the active marrow (Fig. 1B) or on the bone surfaces (Fig. 1D), the range of absorbed fraction values is noted to be essentially constant with particle energy. The last two columns of Table 3 for each source-target combination give the average and coefficient of variation of the absorbed fraction among the six subjects of the study. As anticipated, individual variations in values of $\phi(\text{TAM} \leftarrow \text{TAM})$ are very small (less than 1%). For alpha-particle emitters localized on the bone surfaces, individual variations in $\phi(\text{TAM} \leftarrow \text{TBS})$ and $\phi(\text{TBE} \leftarrow \text{TBS})$ are typically between 2 – 6%. The source-target combinations with the

largest individual variations (~12-15%) are seen for bone volume sources irradiating the active marrow and endosteal layer (Figs. 1E and 1F, respectively), as well as active marrow sources irradiating the endosteal layer (Fig. 1B). Variations in values of $\phi(\text{TAM} \leftarrow \text{TBV})$ and $\phi(\text{TBE} \leftarrow \text{TBV})$ among the six individuals are directly attributed to variations in trabeculae thicknesses as seen through in their corresponding bone chord-length distributions. Thicker trabeculae result in more self-absorption of α -particle energy with concomitantly lower amounts of energy available for deposition to the endosteal layer or surrounding marrow tissues. Similarly, variations in values of $\phi(\text{TBE} \leftarrow \text{TAM})$ are influenced by individual variations in marrow cavity sizes among the study subjects, with smaller marrow cavities permitting increased opportunity for alpha particles to reach and deposit energy to the endosteal layer.

B. Age Variations with both Trabecular Microstructure and Marrow Cellularity

As shown in Table 1, chord-length distributions characterizing the pediatric skeletal microstructure are only available at two ages in the Leeds studies, and at only three skeletal sites at both ages: the femoral head and neck, iliac crest, and ribs. For the latter two bone sites, adult chord-length distributions are also available for the 44-year and 66-year males. In the femur, separate distributions are obtained in the femoral head and neck of the adults, owing to their different biomechanical loadings. Separate femoral distributions are not available in the Leeds pediatric subjects, and thus this skeletal site was excluded from the present study.

Figures 2A and 2B show both age- and energy-dependent values of the alpha-particle absorbed fraction for self-irradiation of the active bone marrow at 100% cellularity within the iliac crest and ribs, respectively. The variation with subject age follows directly with differences in marrow cavity sizes (see mean chord-lengths in Table 1), where these differences become increasingly evident at the higher particle energies. At 10 MeV, for example, the value of $\phi(\text{TAM} \leftarrow \text{TAM})$ in the iliac crest is 0.96 for the 66-year male, but only 0.86 for the 1.7-year male.

In the ribs, the mean marrow chord-lengths are relatively large in both adults (1703 μm in the 44-year male and 1630 μm in the 66-year male), and thus values of $\phi(\text{TAM} \leftarrow \text{TAM})$ are almost identical (very few alpha particles reach the trabeculae of the ribs in either subject).

While Figures 2A and 2B show a clear age-dependence in values of the marrow self-absorbed fraction linked to corresponding changes in the expansion of the marrow cavities with increasing age, Figures 2C and 3D shown an even greater variation when age-dependent marrow cellularity is also considered. As the marrow fat content increases with subject age, less and less alpha-particle energy is deposited to the hematopoietically active tissues of the bone marrow. Consequently, the age-dependent order of the absorbed fraction profiles at 100% cellularity (where the lowest values occur at the youngest ages - Figs. 2A and 2B) are then reversed when reference marrow cellularities are factored into the radiation transport calculations (lowest values are now associated with the oldest subject in Figs. 2C and 2D).

An important observation is that values of $\phi(\text{TAM} \leftarrow \text{TAM})$ at reference cellularities in Figures 2C and 2D cannot be predicted from values at 100% cellularity (Figs. 1A and 1B) through a simple scaling by the reference cellularity, at least at energies below 10 MeV. As the fat fraction of bone marrow increases with subject age, the rather linear energy dependency seen at 100% cellularity gives rise to an increasingly curvilinear profile with increasing particle energy. Simple cellularity scaling would, of course, incorrectly preserve the linear slopes seen at 100% cellularity, and would not permit convergence of $\phi(\text{TAM} \leftarrow \text{TAM})$ to unity at very low alpha-particle energies. This same issue was addressed for electron and beta sources in the skeleton by Bolch et al.¹⁸ and by Stabin et al.¹⁹

Figures 3A and 3B display values of $\phi(\text{TAM} \leftarrow \text{TBS})$ for bone surface emissions within the iliac crest and ribs, respectively, as a function of alpha energy and subject age at 100% cellularity. Interestingly, the age variation of the absorbed fraction for this source-target combination in these bone sites (Fig. 3A and 3B) is less than the inter-subject variation seen in

the adult lumbar vertebrae (Fig. 1C). When calculations are performed at their respective reference cellularities, values of $\phi(\text{TAM} \leftarrow \text{TBS})$ disperse as noted in Figures 3C (iliac crest) and 3D (ribs). Unlike similar values of $\phi(\text{TAM} \leftarrow \text{TAM})$, values of $\phi(\text{TAM} \leftarrow \text{TBS})$ are indeed noted to scale in nearly direct proportion to the marrow cellularity. This feature of the data is consistent with the findings of Shah et al.²⁰ who found that the fractional surface area of the bone trabeculae in contact with marrow adipocytes was directly proportional to the marrow fat fraction ($\sim 1 - \text{marrow cellularity}$).

Absorbed fractions to active bone marrow (100% cellularity) for α -particles emitted uniformly within the bone trabeculae are shown in Figures 4A (iliac crest) and 4B (ribs) as a function of subject age and particle energy. While values of $\phi(\text{TAM} \leftarrow \text{TBV})$ were noted to be higher for the 44-year male than for the 66-year male within the lumbar vertebrae (see Fig. 1E), these two individuals display very similar values of $\phi(\text{TAM} \leftarrow \text{TBV})$ in both the iliac crest and ribs at 100% marrow cellularity. While both pediatric subjects show very similar values of $\phi(\text{TAM} \leftarrow \text{TBV})$ within the iliac crest (Fig. 4A), more energy escape to the active bone marrow is noted for in the 9-year male than in the 1.7-year male within the ribs (Fig. 4B) (mean bone chord-lengths are 183 μm and 189 μm , respectively). However, when reference marrow cellularities are factored into the transport model (Figs. 4C and 4D), the pediatric values for $\phi(\text{TAM} \leftarrow \text{TBV})$ in the ribs are then brought into agreement as the greater α -particle energy escape within the 9-year-old ribs is deposited to marrow that is only 80% cellular in comparison to that which is 95% cellular in the 1.7-year-old.

IV. DISCUSSION

The absorbed fraction for α -particles in the skeletal tissues is a key physical / anatomical parameter needed in both the ICRP and MIRD systems of skeletal internal dosimetry. In radiological protection, dose coefficients used in prospective studies of worker exposures to

bone-seeking radionuclides are based upon separate assignments of (1) skeletal tissue masses in reference individuals, (2) absorbed fractions for various source-target combinations, and (3) other factors (e.g., w_R and w_T). Current estimates reference skeletal tissues masses are given in ICRP Publications 70¹² and 89²¹ where explicit consideration is given to age-dependent marrow cellularity by skeletal site. Currently adopted values of α -particle absorbed fractions, however, are based upon those published in ICRP Publication 30¹⁰ which are independent of particle energy, skeletal site, and marrow cellularity. For example, values of $\phi(\text{TAM} \leftarrow \text{TAM})$, $\phi(\text{TAM} \leftarrow \text{TBS})$, and $\phi(\text{TAM} \leftarrow \text{TBV})$ are fixed in the ICRP 30 bone model at constant values of 1.0, 0.5, and 0.05, respectively. The data reviewed in this and a previous study¹⁶ indicates that these values (at α -particle energies of 4 to 5.5 MeV) are overly conservative even for radiological protection purposes. In particular, reference values of skeletal absorbed fractions for α -particles should be adjusted to consider age-dependent reference marrow cellularity in manner consistent with that used to assign the reference skeletal masses.

In α -emitter molecular radiotherapy, the objective of a skeletal tissue dose assessment is to accurately predict (or reconstruct) the absorbed dose to target tissues within skeletal regions of a given patient. In concept, therefore, one should explicitly use alpha-particle absorbed fractions that are uniquely matched to (1) the energies of the α -particles employed in the therapy, (2) the marrow cellularity of the patient at the skeletal site of treatment, and (3) the patient's trabecular microstructure in that same skeletal region. The absorbed fractions given in Supplement B of Watchman et al.¹⁶ provide, at least for the Leeds 44-year male, values of α -particle absorbed fractions as a function of particle energy, skeletal site, and marrow cellularity. In a given therapy, the particle energies and skeletal sites of treatment are clearly known, and proper adjustment of the skeletal tissue doses can thus be made. Information on marrow cellularity is typically limited to core biopsies in the iliac crest, although non-invasive MR techniques are also possible across the skeletal regions.²² One possible approach is to assess

the patient's marrow cellularity via iliac crest biopsy, compare that value to ICRP 70 reference values (58% at 25 years and 48% at 40 years) and then linearly scale reference cellularities to all other skeletal sites. Clearly, further research on the distribution of marrow cellularity by skeletal site in both normal and therapy patient populations is warranted to justify this or other approaches. The importance of making marrow cellularity adjustments in α -particle dosimetry, however, is clearly highlighted in the data of Figures 2-4.

Perhaps the most challenging adjustment for patient-specific dosimetry in α -emitter molecular radiotherapy is the assessment of the trabecular microstructure unique to a given patient. Clearly, in-vivo imaging will not permit visualization of individual marrow cavities and bone trabeculae, and thus reliance on cadaver-based reference models must continue. Fortunately, of the various source-target tissue combinations summarized in Table 3, individual variations in α -emitter absorbed fractions were noted to be less than 1% for marrow self-dose, and less than ~5-6% for bone surface sources irradiating either skeletal target tissue. Absorbed fractions for TBV sources were seen to display individual variations upwards of 12-15%; nevertheless, uniform localization of α -emitters within the bone trabeculae, while an important scenario in radiation protection dosimetry, is not a very relevant source region for short-lived α -emitters of interest in molecular radiotherapy. Still, the data of the present study indicated a 11-15% individual variation in values of $\phi(\text{TBE} \leftarrow \text{TAM})$, which can be a potential source-target combination of clinical interest. One possible approach would be to seek correlations of the trabecular microstructure (via quantities such as the spongiosa marrow volume fraction) with parameters measurable in a given patient (e.g., CT-based volumetric bone mineral density). Such correlations could conceivably be developed through cadaver studies using pre-bone harvesting CT images and post-bone harvesting microCT images of cored spongiosa. A library of microCT-based images of the cadaver bone microstructure could then be used to establish a database of α -particle absorbed fractions as a function of bone-mineral status by skeletal site.

This database would further reduce dosimetry uncertainties given by reference values of α -particle absorbed fraction taken from one single individual (e.g., the Leeds 44-year male).

V. CONCLUSIONS

An investigation into the age and individual variability of α -particle absorbed fractions in the human skeleton was presented. A study of the skeletal microstructure within the lumbar vertebrae in six adult subjects (ages 25 to 85 years) indicated that individual variations in the skeletal absorbed fractions for α -emitters was below 1% for marrow self-dose, and was less than ~5-6% bone surface emissions irradiating both the active marrow and bone endosteum. Higher variability was noted for marrow sources irradiating the trabecular endosteum and for bone volume sources irradiating the both target tissues (~12-15%). Based upon a very limited set of only two pediatric subjects (ages 1.7 and 9 years), a clear age-dependence was noted in the ribs and iliac crest showing that the smaller sizes of both the marrow cavities and bone trabeculae at younger patient ages translate to smaller values of $\phi(\text{TAM} \leftarrow \text{TAM})$ and larger values of $\phi(\text{TAM} \leftarrow \text{TBV})$ than seen in two adult subjects (ages 44 and 66 years). Clearly, further research into the pediatric skeletal microstructure as a function of patient age and skeletal site is warranted to support therapy treatments of childhood skeletal disease.

The largest and most easily corrected source of uncertainty in patient-specific α -particle dosimetry in molecular radiotherapy, however, continues to be the neglect of marrow cellularity in the assignment of absorbed fractions to the skeletal tissues. The assumption of unity for values of $\phi(\text{TAM} \leftarrow \text{TAM})$ given in existing skeletal dosimetry models^{10,11} can lead to significant errors in marrow dose assessment, particularly in older patients with high skeletal fat fractions and at high α -particle energies (5 to 9 MeV). While direct in-vivo assessment of marrow cellularity by skeletal site would be ideal, simple linear scaling of age- and site-dependent reference cellularities using patient measurements in an iliac crest core biopsy would permit a

significant improvement in the assignment of cellularity-dependent α -particle absorbed fractions for marrow dose assessment in patient trials and clinical studies.

ACKNOWLEDGMENTS

This work was supported in part by Grant CA96441 from the National Cancer Institute and Grant DE-FG07-02ID14327 from the U.S. Department of Energy with the University of Florida.

REFERENCES

- ¹G. P. Adams, C. C. Shaller, L. L. Chappell, C. Wu, E. M. Horak, H. H. Simmons, S. Litwin, J. D. Marks, L. M. Weiner, and M. W. Brechbiel, "Delivery of the alpha-emitting radioisotope bismuth-213 to solid tumors via single-chain Fv and diabody molecules," *Nucl Med Biol* **27**, 339-346 (2000).
- ²B. J. Allen, S. Rizvi, Y. Li, Z. Tian, and M. Ranson, "In vitro and preclinical targeted alpha therapy for melanoma, breast, prostate and colorectal cancers," *Crit Rev Oncol Hematol* **39**, 139-146 (2001).
- ³B. J. Allen, S. M. Rizvi, and Z. Tian, "Preclinical targeted alpha therapy for subcutaneous melanoma," *Melanoma Res* **11**, 175-182 (2001).
- ⁴K. A. Hamacher, R. B. Den, E. I. Den, and G. Sgouros, "Cellular dose conversion factors for alpha-particle--emitting radionuclides of interest in radionuclide therapy," *J Nucl Med* **42**, 1216-1221 (2001).
- ⁵Y. Kvinnsland, T. Stokke, and E. Aurlen, "Radioimmunotherapy with alpha-particle emitters: microdosimetry of cells with a heterogeneous antigen expression and with various diameters of cells and nuclei," *Radiat Res* **155**, 288-296 (2001).
- ⁶M. R. McDevitt, E. Barendswaard, D. Ma, L. Lai, M. J. Curcio, G. Sgouros, A. M. Ballangrud, W. H. Yang, R. D. Finn, V. Pellegrini, M. W. Geerlings, Jr., M. Lee, M. W. Brechbiel, N. H. Bander, C. Cordon-Cardo, and D. A. Scheinberg, "An alpha-particle emitting antibody ([²¹³Bi]J591) for radioimmunotherapy of prostate cancer," *Cancer Res* **60**, 6095-6100 (2000).
- ⁷M. Ranson, Z. Tian, N. M. Andronicos, S. Rizvi, and B. J. Allen, "In vitro cytotoxicity of bismuth-213 (²¹³Bi)-labeled-plasminogen activator inhibitor type 2 (alpha-PAI-2) on human breast cancer cells," *Breast Cancer Res Treat* **71**, 149-159 (2002).
- ⁸J. C. Roeske, G. T. Y. Chen, and A. B. Brill, "Dosimetry of intraperitoneally administered radiolabeled antibodies," *Med. Phys.* **20**, Pt. 2, 593-600 (1993).
- ⁹G. Sgouros, "Long-lived alpha emitters in radioimmunotherapy: the mischievous progeny," *Cancer Biother Radiopharm* **15**, 219-221 (2000).
- ¹⁰ICRP, *Limits for intakes of radionuclides by workers*, ICRP Publication 30 (Part 1). (International Commission on Radiological Protection, Oxford, UK, 1979).
- ¹¹M. G. Stabin, and J. A. Siegel, "Physical models and dose factors for use in internal dose assessment," *Health Phys* **85**, 294-310 (2003).
- ¹²ICRP, *Basic anatomical and physiological data for use in radiological protection: the skeleton*, ICRP Publication 70. (International Commission on Radiological Protection, Oxford, UK, 1995).
- ¹³J. R. Whitwell, "Theoretical investigations of energy loss by ionizing particles in bone," Thesis, *Department of Medical Physics* (University of Leeds, Leeds, UK, 1973), pp. 268.
- ¹⁴A. H. Beddoe, "The microstructure of mammalian bone in relation to the dosimetry of bone-seeking radionuclides," Thesis, *Department of Medical Physics* (University of Leeds, Leeds, UK, 1976), pp. 165.
- ¹⁵A. Shah, D. Rajon, D. Jokisch, P. Patton, and W. Bolch, "A comparison of skeletal chord-length distributions in the adult male," *Health Phys* **89**, 199-215 (2005).
- ¹⁶C. Watchman, D. W. Jokisch, P. Patton, D. Rajon, G. Sgouros, and W. Bolch, "Absorbed fractions for alpha-particles in tissues of trabecular bone: Considerations of marrow cellularity within the ICRP reference male," *J Nucl Med* **46**, 1171-1185 (2005).
- ¹⁷R. Custer, *An atlas of the blood and bone marrow*, (W.B. Saunders, Philadelphia, PA, 1974).
- ¹⁸W. E. Bolch, P. W. Patton, D. A. Rajon, A. P. Shah, D. W. Jokisch, and B. Inglis, "Considerations of marrow cellularity in 3D dosimetric models of the trabecular skeleton," *J Nucl Med* **43**, 97-108 (2002).
- ¹⁹M. G. Stabin, K. F. Eckerman, W. E. Bolch, L. G. Bouchet, and P. W. Patton, "Evolution and status of bone and marrow dose models," *Cancer Biother Radiopharm* **17**, 427-445 (2002).

²⁰A. P. Shah, P. W. Patton, D. A. Rajon, and W. E. Bolch, "Adipocyte spatial distributions in bone marrow: Implications for skeletal dosimetry models," J Nucl Med **44**, 774-783 (2003).

²¹ICRP, *Basic anatomical and physiological data for use in radiological protection: reference values*, Publication 89. (International Commission on Radiological Protection, New York, New York, 2002).

²²D. Ballon, A. A. Jakubowski, M. C. Graham, E. Schneider, and J. A. Koutcher, "Spatial mapping of the percentage cellularity in human bone marrow using magnetic resonance imaging," Med Phys **23**, 243-250 (1996).

Table 1. Mean chord-lengths for marrow cavities and bone trabeculae for all subjects.

<i>Skeletal Site</i>	<i>Subject Age and Gender</i>							
	<i>Leeds 1.7-y Male</i>	<i>Leeds 9-y Male</i>	<i>Leeds 25-y Male</i>	<i>Leeds 44-y Male</i>	<i>Leeds 55-y Female</i>	<i>UF 66-y Male</i>	<i>Leeds 70-y Female</i>	<i>Leeds 85-y Female</i>
<i>Mean Marrow Cavity Chord Length (μm)</i>								
<i>Cervical Vertebrae</i>	*	770	*	910	*	1038	*	*
<i>Femur Head and Neck</i>	765	631	*	*	*	*	*	*
<i>Femoral Head</i>	*	*	*	1157	*	1043	*	*
<i>Femoral Neck</i>	*	*	*	1655	*	1454	*	*
<i>Humerus</i>	*	766	*	*	*	1169	*	*
<i>Iliac Crest</i>	541	698	*	904	*	1508	*	*
<i>Lumbar Vertebrae</i>	736	*	1048	1233	993	1479	1155	1013
<i>Parietal Bone</i>	255	*	*	389	*	812	*	*
<i>Ribs</i>	619	835	*	1703	*	1630	*	*
<i>Mean Bone Trabeculae Chord Length (μm)</i>								
<i>Cervical Vertebrae</i>	*	149	*	279	*	282	*	*
<i>Femur Head and Neck</i>	203	200	*	*	*	*	*	*
<i>Femoral Head</i>	*	*	*	232	*	348	*	*
<i>Femoral Neck</i>	*	*	*	314	*	347	*	*
<i>Humerus</i>	*	155	*	*	*	357	*	*
<i>Iliac Crest</i>	179	189	*	242	*	245	*	*
<i>Lumbar Vertebrae</i>	188	*	250	246	198	316	229	199
<i>Parietal Bone</i>	112	*	*	511	*	469	*	*
<i>Ribs</i>	189	183	*	266	*	302	*	*

Table 2. Reference bone marrow cellularities as a function of age.

Skeletal Site	Age (years)							
	0	1	5	10	15	25	40	66
Cranium and Mandible	1.00	0.95	0.80	0.65	0.55	0.42	0.38	0.38
Vertebral Column*	1.00	0.95	0.85	0.80	0.75	0.72	0.70	0.40
Sternum*	1.00	0.95	0.85	0.80	0.75	0.72	0.70	0.45
Ribs*	1.00	0.95	0.85	0.80	0.75	0.72	0.70	0.40
Scapula	1.00	0.95	0.80	0.65	0.55	0.42	0.38	0.38
Clavicles	1.00	0.95	0.79	0.63	0.52	0.37	0.33	0.33
Os coxae*	1.00	0.95	0.79	0.72	0.64	0.58	0.48	0.35
Sacrum	1.00	0.95	0.79	0.72	0.64	0.58	0.48	0.35
Humeri, upper half	1.00	0.95	0.77	0.60	0.45	0.30	0.25	0.25
Humeri, lower half	1.00	0.89	0.71	0.39	0.10	0.00	0.00	0.00
Radii and Ulni	1.00	0.89	0.57	0.23	0.00	0.00	0.00	0.00
Wrist and Hands	1.00	0.50	0.20	0.00	0.00	0.00	0.00	0.00
Femora, upper half	1.00	0.95	0.77	0.60	0.45	0.30	0.25	0.25
Femora, lower half	1.00	0.89	0.71	0.39	0.10	0.00	0.00	0.00
Patellae, Tibiae, Fibulae	1.00	0.89	0.57	0.23	0.00	0.00	0.00	0.00
Ankles and Feet	1.00	0.50	0.20	0.00	0.00	0.00	0.00	0.00

*Data for the 66-year male are taken from Custer et al.¹⁷ For all other skeletal sites, ICRP 70 values for the 40-year male are assumed.

Table 3. Inter-subject variations in alpha-particle absorbed fractions at 100% marrow cellularity.

Energy (MeV)	ϕ (TAM \leftarrow TAM) [Fig. 1A]					ϕ (TBE \leftarrow TAM) [Fig. 1B]				
	Min	Max	Range^a	Ave	COV	Min	Max	Range^a	Ave	COV
3.0	9.87E-01	9.92E-01	3%	9.89E-01	0.19%	7.71E-03	1.17E-02	2%	1.01E-02	15.05%
4.0	9.80E-01	9.88E-01	4%	9.83E-01	0.27%	1.07E-02	1.58E-02	3%	1.36E-02	13.91%
5.0	9.72E-01	9.82E-01	5%	9.76E-01	0.37%	1.33E-02	1.84E-02	3%	1.63E-02	12.84%
6.0	9.64E-01	9.76E-01	6%	9.69E-01	0.46%	1.55E-02	2.11E-02	3%	1.86E-02	12.25%
7.0	9.55E-01	9.69E-01	7%	9.61E-01	0.56%	1.77E-02	2.38E-02	3%	2.07E-02	11.84%
8.0	9.45E-01	9.62E-01	9%	9.52E-01	0.67%	1.95E-02	2.60E-02	3%	2.25E-02	11.67%
9.0	9.35E-01	9.54E-01	10%	9.43E-01	0.78%	2.12E-02	2.81E-02	3%	2.40E-02	11.62%
10.0	9.24E-01	9.45E-01	11%	9.33E-01	0.90%	2.26E-02	3.00E-02	4%	2.54E-02	11.86%

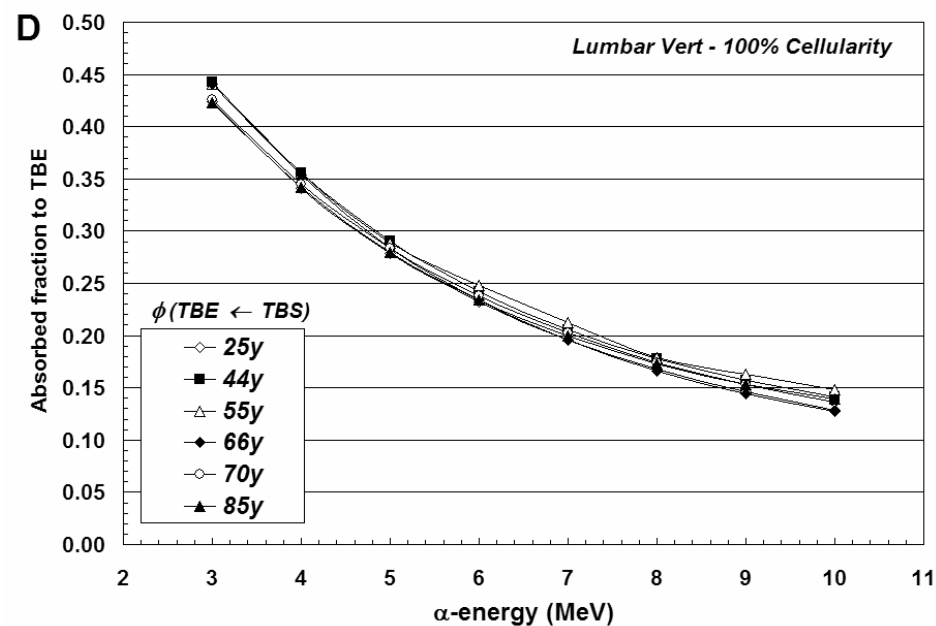
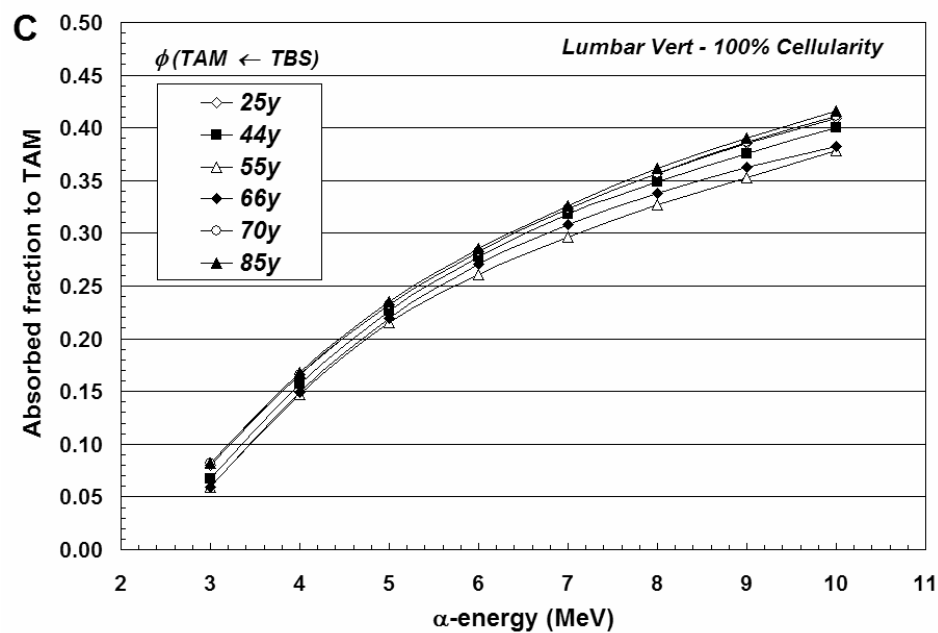
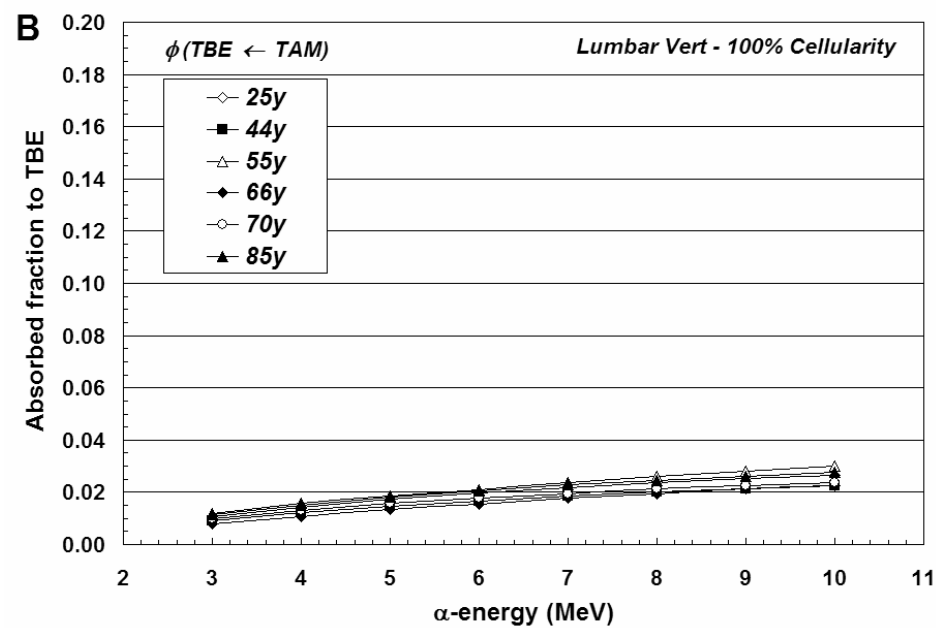
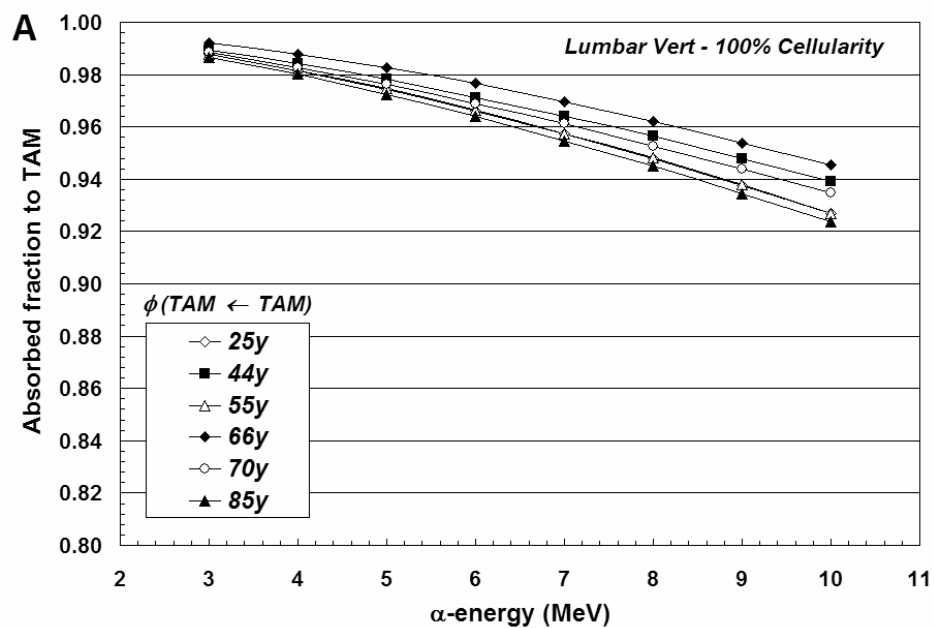
Energy (MeV)	ϕ (TAM \leftarrow TBS) [Fig. 1C]					ϕ (TBE \leftarrow TBS) [Fig. 1D]				
	Min	Max	Range^a	Ave	COV	Min	Max	Range^a	Ave	COV
3.0	5.96E-02	8.24E-02	5%	7.18E-02	15.24%	4.23E-01	4.43E-01	4%	4.33E-01	2.23%
4.0	1.47E-01	1.68E-01	4%	1.59E-01	5.69%	3.41E-01	3.56E-01	3%	3.49E-01	2.00%
5.0	2.15E-01	2.35E-01	4%	2.27E-01	3.50%	2.78E-01	2.91E-01	3%	2.84E-01	1.68%
6.0	2.61E-01	2.85E-01	5%	2.77E-01	3.43%	2.33E-01	2.48E-01	3%	2.38E-01	2.47%
7.0	2.96E-01	3.26E-01	6%	3.16E-01	3.62%	1.96E-01	2.13E-01	3%	2.02E-01	3.27%
8.0	3.27E-01	3.61E-01	7%	3.48E-01	3.77%	1.66E-01	1.79E-01	3%	1.73E-01	3.15%
9.0	3.53E-01	3.90E-01	7%	3.75E-01	3.95%	1.45E-01	1.63E-01	4%	1.53E-01	4.61%
10.0	3.79E-01	4.16E-01	7%	3.99E-01	3.91%	1.27E-01	1.48E-01	4%	1.37E-01	5.85%

Energy (MeV)	ϕ (TAM \leftarrow TBV) [Fig. 1E]					ϕ (TBE \leftarrow TBV) [Fig. 1F]				
	Min	Max	Range^a	Ave	COV	Min	Max	Range^a	Ave	COV
3.0	8.01E-04	1.28E-03	0%	1.06E-03	15.27%	1.94E-02	2.99E-02	5%	2.56E-02	14.35%
4.0	4.18E-03	6.45E-03	1%	5.48E-03	14.11%	2.73E-02	4.26E-02	8%	3.64E-02	14.63%
5.0	1.08E-02	1.66E-02	3%	1.41E-02	13.97%	3.43E-02	5.33E-02	9%	4.56E-02	14.42%
6.0	2.07E-02	3.14E-02	5%	2.67E-02	13.83%	4.04E-02	6.31E-02	11%	5.39E-02	14.66%
7.0	3.31E-02	4.98E-02	8%	4.23E-02	13.56%	4.58E-02	7.15E-02	13%	6.09E-02	14.52%
8.0	4.82E-02	7.13E-02	12%	6.07E-02	13.09%	5.02E-02	7.81E-02	14%	6.65E-02	14.40%
9.0	6.53E-02	9.59E-02	15%	8.17E-02	12.87%	5.40E-02	8.31E-02	15%	7.11E-02	14.09%
10.0	8.46E-02	1.22E-01	19%	1.05E-01	12.44%	5.74E-02	8.73E-02	15%	7.49E-02	13.75%

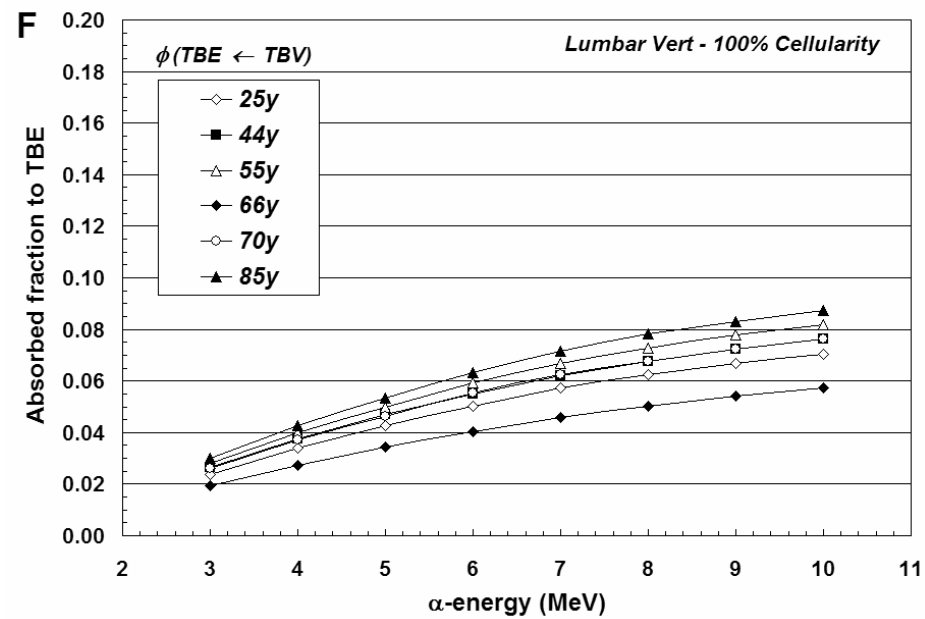
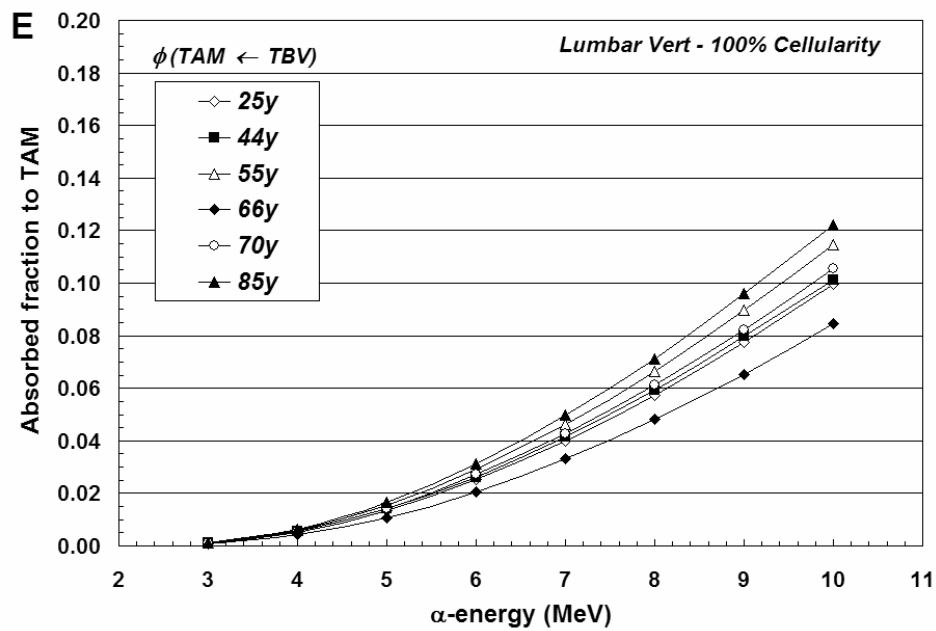
^aRange of values expressed as a fraction of the ordinate scale

Figure Captions

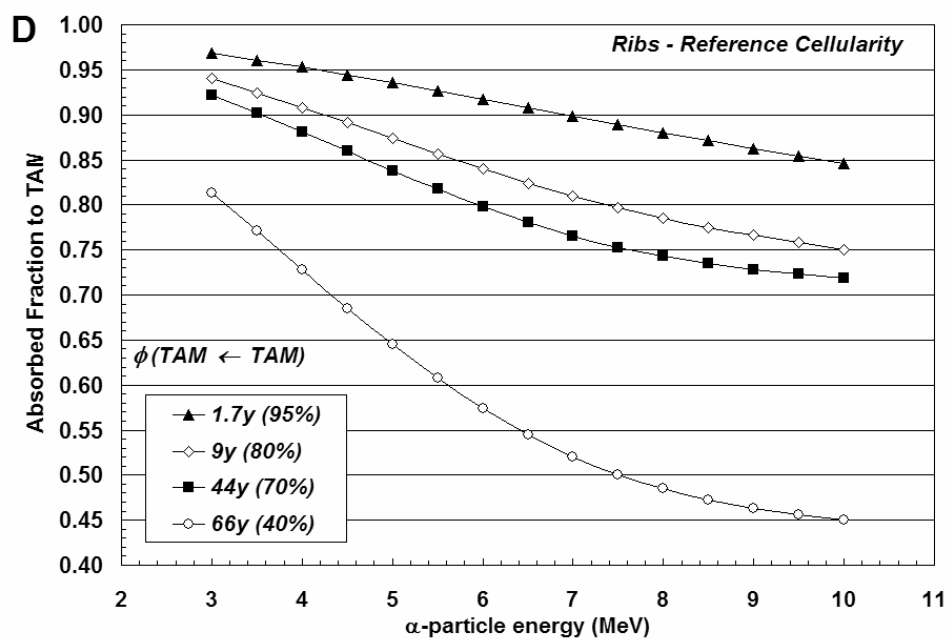
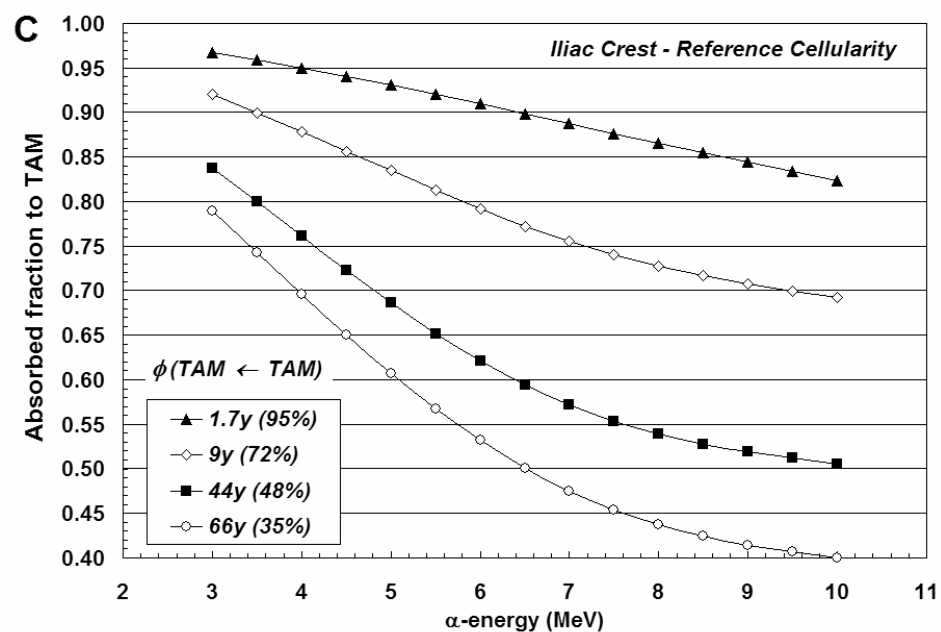
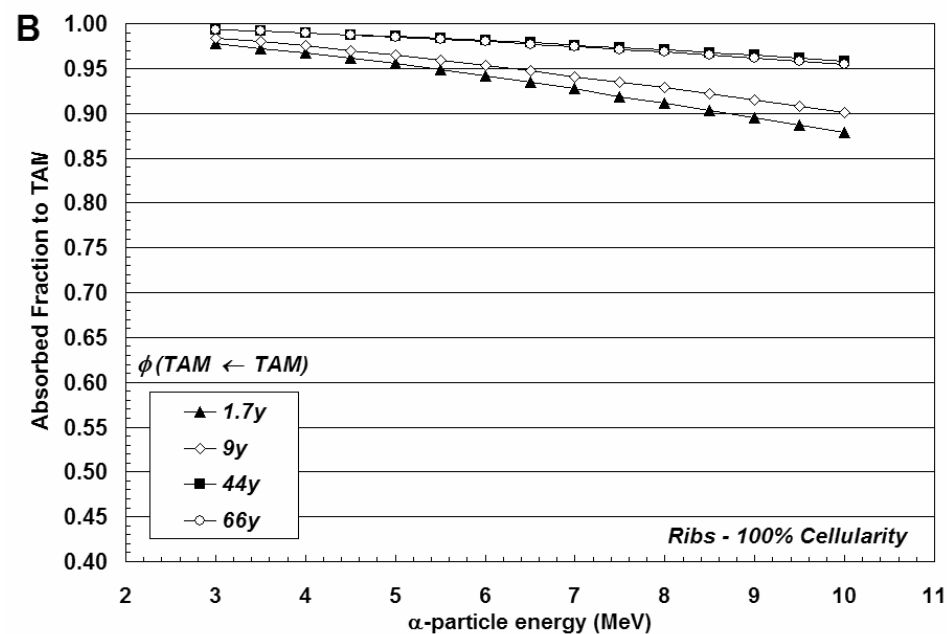
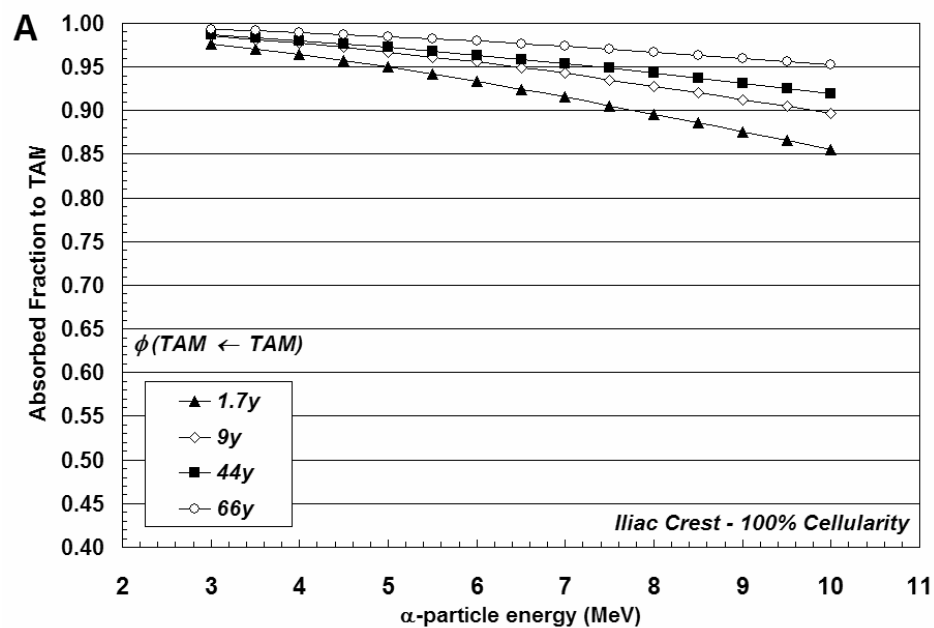
- Figure 1.** Inter-subject variations in alpha-particle absorbed fractions within the lumbar vertebrae at 100% marrow cellularity. Source-target tissue combinations include (A) TAM \leftarrow TAM, (B) TBE \leftarrow TAM, (C) TAM \leftarrow TBS, (D) TBE \leftarrow TBS, (E) TAM \leftarrow TBV, and (F) and TBE \leftarrow TBS, where TAM = trabecular active marrow, TBE = trabecular bone endosteum, TBS = trabecular bone surfaces, and TBV = trabecular bone volume.
- Figure 2.** Inter-subject variations in values of $\phi(\text{TAM} \leftarrow \text{TAM})$ for alpha particles emitted within the iliac crest (A at 100% cellularity, C at reference cellularities) and ribs (B at 100% cellularity, D at reference cellularities).
- Figure 3.** Inter-subject variations in values of $\phi(\text{TAM} \leftarrow \text{TBS})$ for alpha particles emitted within the iliac crest (A at 100% cellularity, C at reference cellularities) and ribs (B at 100% cellularity, D at reference cellularities).
- Figure 4.** Inter-subject variations in values of $\phi(\text{TAM} \leftarrow \text{TBV})$ for alpha particles emitted within the iliac crest (A at 100% cellularity, C at reference cellularities) and ribs (B at 100% cellularity, D at reference cellularities).



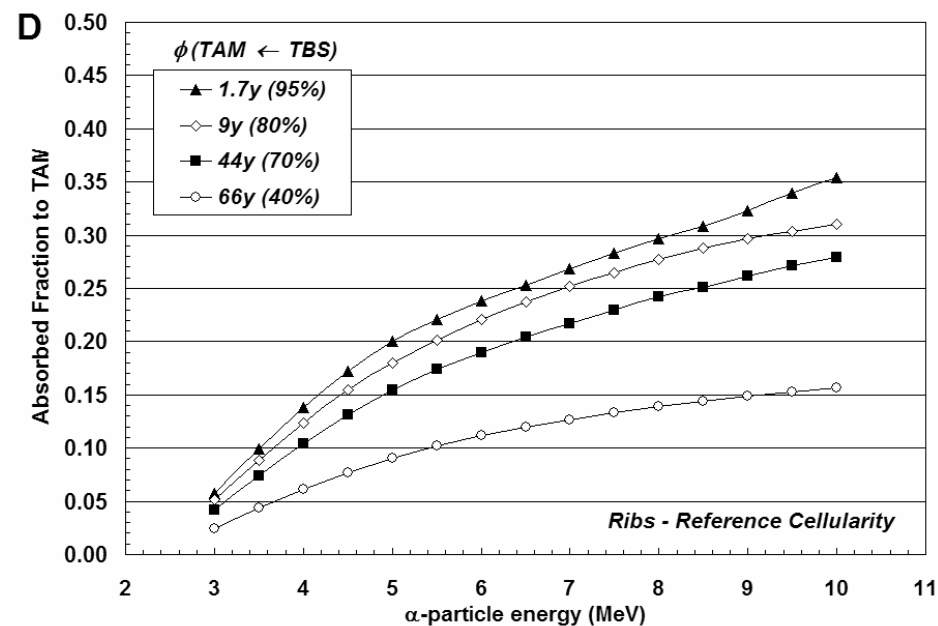
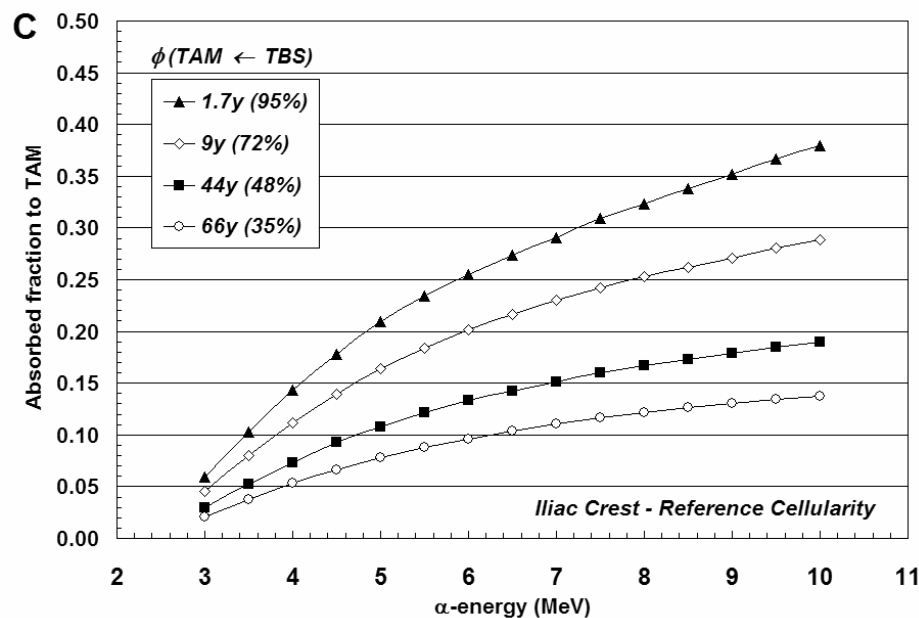
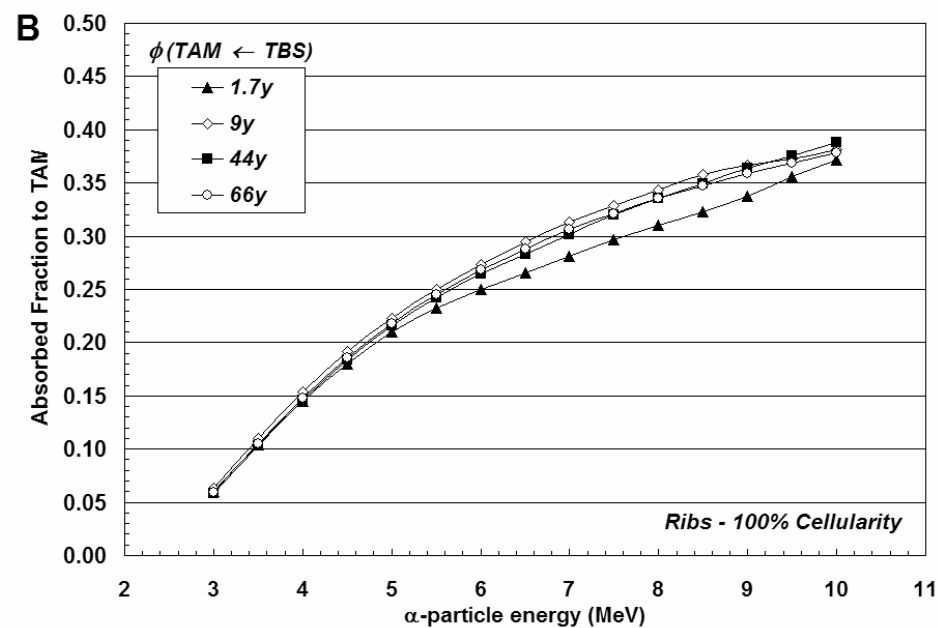
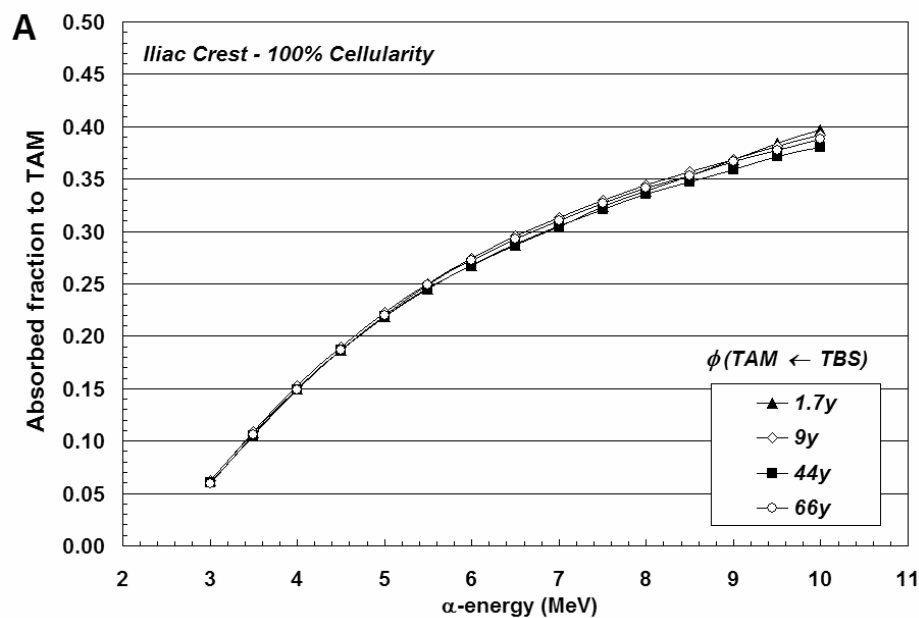
Watchman and Bolch
Figure 1



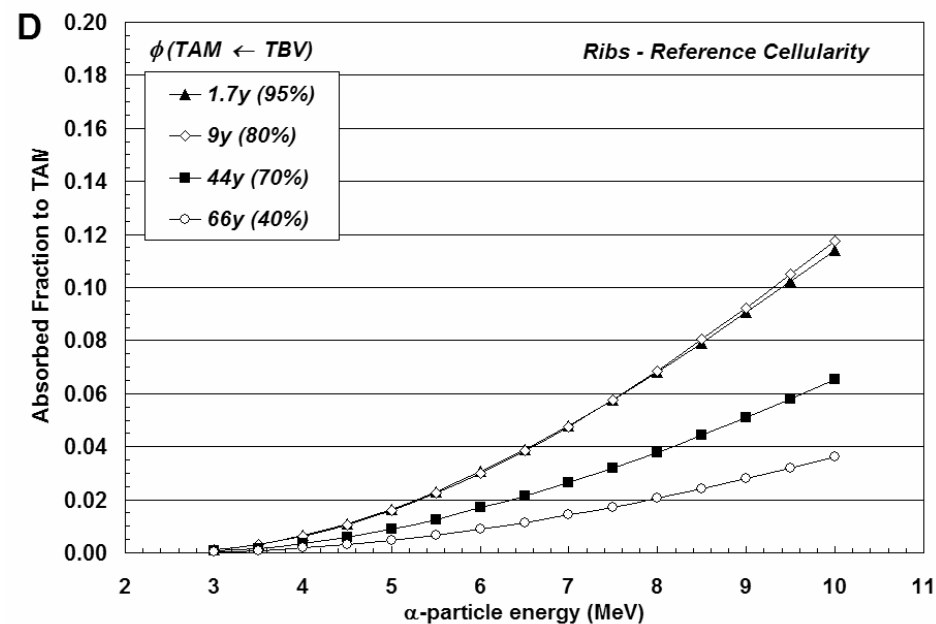
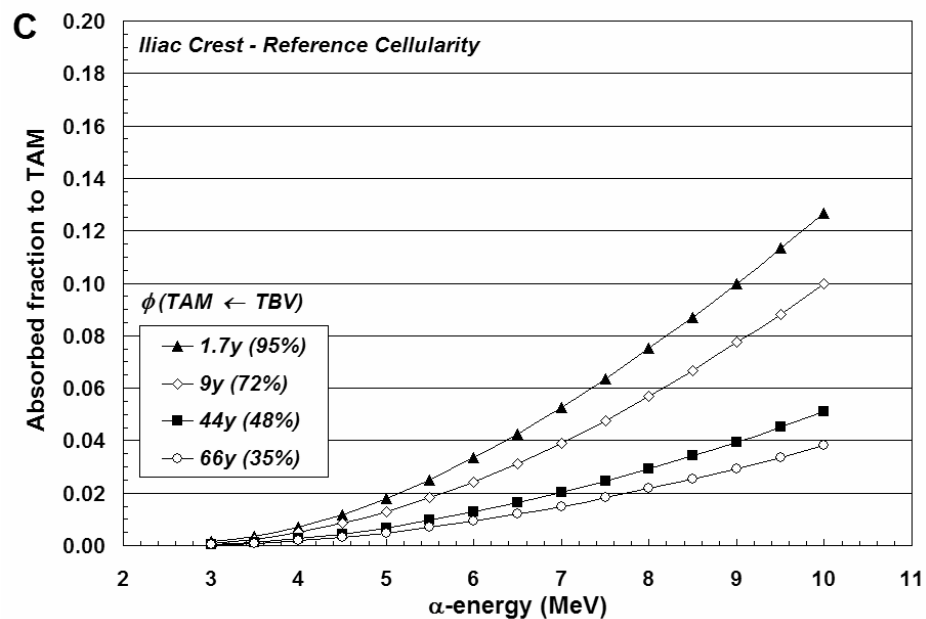
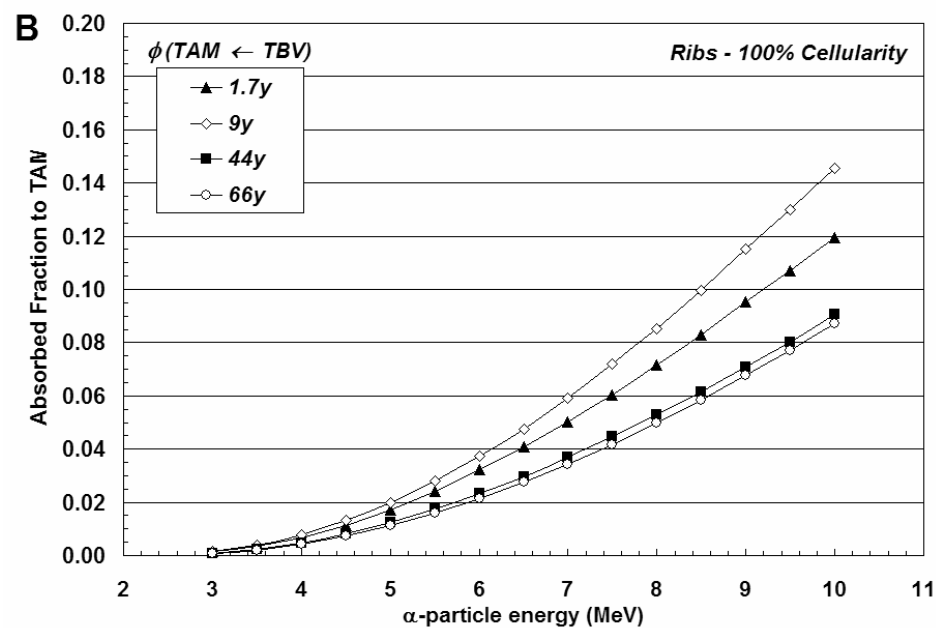
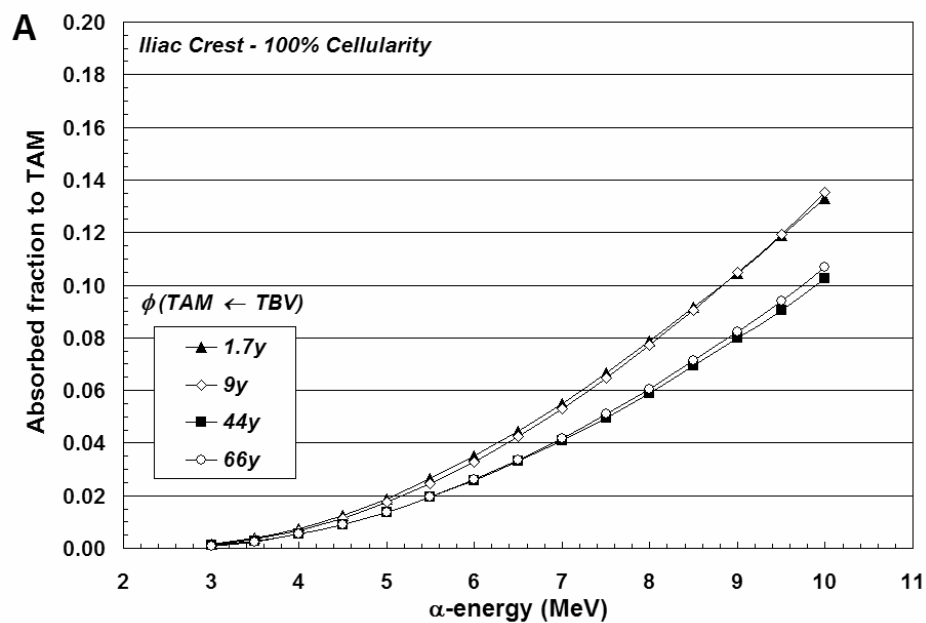
Watchman and Bolch
Figure 1



Watchman and Bolch
Figure 2



Watchman and Bolch
Figure 3



Watchman and Bolch
Figure 4

Derivation of Skeletal Masses within the Current ICRP Age Series: Considerations of a 10- μ m and 50- μ m Endosteum

Christopher J. Watchman, MS

*Department of Nuclear & Radiological Engineering,
University of Florida, Gainesville, FL 32611-8300*

Wesley E. Bolch, PhD^a

Department of Nuclear & Radiological Engineering and Department of Biomedical Engineering, University of Florida, Gainesville, FL 32611-8300

^aFor reprints and correspondence contact:

Wesley E. Bolch, PhD, PE, CHP

*Director, Advanced Laboratory for Radiation Dosimetry Studies (ALRADS)
Department of Nuclear and Radiological Engineering
University of Florida, Gainesville, Florida 32611-8300
Phone: (352) 846-1361 Fax: (352) 392-3380 Email: wbolch@ufl.edu*

RUNNING TITLE:

Reference Skeletal Tissue Masses

This work was supported by the

U.S. Department of Energy and the National Cancer Institute

Submitted to *Physics Medicine and Biology*

Word Count (Text and Refs):	5319	
Word Count (Figure Captions):		43
Word Count (Table Captions):		69
Word Count (Total):	5431	

Abstract

Dosimetry calculations in skeletal tissues are routinely performed using tissue masses provided in publications from the International Commission on Radiological Protection. These values include gross tissue masses as a function of age, and are not generally broken down by individual skeletal site. Recent studies have demonstrated site-specific variations in absorbed fraction calculations. Consequently, site-specific bone tissue masses are required to properly determine skeletal-averaged absorbed fractions and specific absorbed fractions. Assignment of values for these reference masses is based upon several different data sources. These sources are not necessarily be consistent with one another. To asses the validity and limitations of the ICRP values, a methodology has been developed, using data from the various ICRP publications, to determine bone-site-specific skeletal tissue masses for the entire ICRP age series. Active marrow masses have been calculated and differences have been shown with respect to ICRP Publication 70 and ICRP Publication 89 values. Mineral bone and endosteal masses have also been calculated and shown to follow similar growth patterns. A series of tables are provided with age-dependant and bone-site-specific masses for all members of the ICRP age series other than the newborn.

Keywords: bone, marrow, dosimetry, ICRP age series, skeletal masses

INTRODUCTION

Using the ICRP 30 or MIRD methodologies for internal dosimetry calculations requires knowledge of the fraction of energy deposited in a target tissue, the physical properties of the radionuclide (yield, energy), the number of transformations in the source organ, and the mass of the target tissue. The ICRP has provided reference values for each of these factors. In bone dosimetry applications, different mass values have been used for the different tissues in bone. These tissues include cortical bone, trabecular bone, cortical endosteum, trabecular endosteum, and active bone marrow. These reference masses are based upon several different studies that reflect the biological diversity of the skeletal tissues. At the present time, only gross tissue masses are given as reference values for dosimetry applications. Recently, studies have been performed at the University of Florida to more accurately determine the fractional energy deposition in bone for alpha- and beta-emitters as a function of skeletal site¹. Knowledge of bone-site specific skeletal tissue masses are necessary for proper calculation of skeletal-averaged values of the specific effective energy (ICRP schema) and the radionuclide S value (MIRD schema).

In Equation 1, the definition of a skeletal-averaged specific absorbed fraction is presented:

$$\Phi_{Skel}(r_T \leftarrow r_S)_i = \sum_j f_{s,j} f_{T,j} \Phi(r_T \leftarrow r_S)_{i,j} , \quad (\text{Eq. 1})$$

Where the subscript j denotes the individual skeletal site, while s denotes the source tissue and T the target tissue. The energy emission index is presented by the subscript i , and thus the skeletal-averaged specific absorbed fraction is given as a doubly weighted average of the specific absorbed fraction where $f_{s,j}$ and $f_{T,j}$ are the fractional masses of the source and target tissue, respectively. Site-specific values of the specific

absorbed fraction require knowledge of both the site-specific absorbed fraction ϕ_{ij} and the site-specific tissue mass m_j :

$$\Phi(r_T \leftarrow r_S)_{i,j} = \frac{\phi(r_T \leftarrow r_S)_{i,j}}{m_j} \quad (\text{Eq. 2})$$

As was previously stated, data are available for absorbed fractions in specific bone sites. Thus to correctly assess the skeletal-averaged specific absorbed fraction, each bone sites absorbed fraction must be associated with site-specific tissue masses. If the calculation is performed with a total skeletal mass (m_{total}) the results are not equivalent as shown in Eq. 3.

$$S_{\text{Skel}}(r_T \leftarrow r_S)_i = \sum_j f_{S,j} f_{T,j} \frac{\phi(r_T \leftarrow r_S)_{i,j}}{(m_T)_j} \neq \frac{1}{m_{\text{total}}} \sum_j f_{S,j} f_{T,j} \phi(r_T \leftarrow r_S)_{i,j} \quad (\text{Eq. 3})$$

This necessitates having data regarding skeletal-site-specific tissue masses.

The objective of this paper is to present a methodology where the information referenced in ICRP documents can be used to compile a list of age-dependant, skeletal site-specific mass values for use in skeletal dosimetry applications. We begin with a brief history of the current reference masses.

Marrow Masses

Bone marrow consists of two tissue types: (1) active (or red) marrow that includes all of the hematopoietically active elements, and (2) inactive (or yellow) marrow. Certain bone marrow pathologies can occur where fluid build up occurs in the marrow space, but for the purposes of radiological protection and non-medical dosimetry these cases are of little relevance. In the International Commission on Radiological Protection (ICRP) Publication 23,² a reference mass for red marrow is given as 1500 g for adult males and 1300 g for adult females. These values were used in ORNL5000³ and MIRD 11⁴ to calculate radionuclide S-values for the skeletal tissues. Note that the S-value in the

MIRD schema is equivalent to the specific effective energy (SEE) used in the ICRP dosimetry schema. A review of the tabular information in ICRP Publication 23, demonstrates that the reference male red marrow mass was in fact only 1045.7 g while the 1500 g value referred to the mass of total marrow (red and yellow combined). Other estimates of marrow mass were given by Cristy and Eckerman⁵ as 1120 g for the adult reference male. More recently, the ICRP revised the Cristy and Eckerman estimate to 1170 g in ICRP Publication 70⁶ and this value is retained in ICRP Publication 89⁷. In ICRP 89, marrow values are also listed for the newborn, 1-year-old, 5-year-old, 10-year-old, 15-year-old (male and female), and the adult (male and female).

Bone and Endosteum Masses

Reference masses for mineralized bone were given in ICRP Publication 23² as 5000 g, while separate masses for cortical and trabecular components were given as 4000 g and 1000 g, respectively. In ICRP 70,⁸ total bone volumes were given for cortical bone (2130 cm³) and trabecular bone (530 cm³). Using a bone density of 1.92 g/cm³, masses are obtained for each as 4090 g and 1114 g, respectively. In ICRP 89,⁷ further refinement of the mass of the total skeleton was changed to 5500 g. The reference percentage of cortical bone is now given as 80% (4400 g) with trabecular bone comprising the remaining 20% (1100 g). Reference masses at other ages and for the adult female are given in ICRP Publication 89 (pg. 185). A reference mass for endosteum is given in ICRP Publication 30⁹ as 120 g. Age-dependant endosteal masses, however, were not presented (even for the reference adult male) in ICRP Publication 70 or Publication 89.

Recent studies have demonstrated that the target tissues for bone cancer induction are more likely located further from the bone surfaces than is given in the current definition of ICRP Publication 30 which is 10- μ m.¹¹ These studies indicate that a 50- μ m

layer of soft tissue may be a more appropriate target for radiation dosimetry. Revising this definition would necessitate changes to the current ICRP suggested mass for the trabecular endosteum.

Bouchet and Bolch (1999)

In Bouchet and Bolch,¹² a methodology was developed to calculate tissue masses for active marrow, bone (cortical and trabecular), and endosteum (cortical and trabecular) in the adult male for 22 bone sites in the adult skeleton. Using ICRP 70 Table 41⁸ they calculated active marrow masses for each of 22 bone sites. Adipose marrow masses were calculated using the reference total marrow mass of 3650 g and ICRP 23 Table 30², which gives the fraction of total body marrow space for each bone. These authors calculated cellularity factors from their calculated masses which were in good agreement with values given in ICRP 89 Table 9.4⁷. The masses obtained were then applied for all adults despite the differences in the reference cellularities between the reference 25 year old and 40 year old. Nevertheless, differences in the mass densities of red and yellow marrow were not accounted for in their method.

These authors calculated cortical and trabecular bone mass using Table 8 from ICRP 70⁶ which gives the relative fraction of dry bones to the total mass of the dry skeleton in the adult. Using the reference mass of 5500 g, the bone mass of individual skeletal sites were then calculated. The percentage of bone attributed to cortical and trabecular bone from ICRP 70 Table 10⁶ was then used to calculate the mass of trabecular and cortical bone in each of the 22 bone sites chosen. Endosteal masses were then calculated using the individual mass and surface-to-volume ratios for each skeletal site. These ratios were taken from ICRP 70 Table 11 (cortical) and 12 (trabecular), the ICRP 70 reference value (ICRP 70 pg. 23) and from Beddoe¹³. Once these data were calculated then the bone density was used to calculate the volume of

bone. Endosteal volumes were calculated by combining the bone volume, surface-to-volume ratio and multiplying this value by a 10- μ m endosteal layer thickness. The endosteal volume was then converted to its equivalent mass by using a soft tissue density of 1.03 g/cm³.

MATERIALS AND METHODS

Calculation of tissue masses for active marrow, trabecular bone, cortical bone and endosteum (cortical and trabecular) was accomplished using data from ICRP Publications 23, 70, and 89, and studies by Beddoe. The methods of Bouchet and Bolch have been extended to reference ages and both genders. Their methods for mineral bone and endosteum have been directly applied to the ICRP reference ages. A modification of their adult male marrow calculations has been applied and then used to calculate reference masses for both the reference adult male and female. The calculation of marrow masses for children is performed using a method described below. All calculations were made for 22 different sites within the skeleton.

In this study, we adopt the following tissue definitions. The trabecular active marrow (TAM) is defined as all non-fatty tissues located within the marrow cavity. All non-fat soft tissues within a distance of 50- μ m from the bone surface are delineated as trabecular bone endosteum (TBE₅₀), while all tissues within 10- μ m from the bone surface are denoted as TBE₁₀. Note that the definition of TAM includes the endosteum, which for radiation dosimetry is a sub-target tissue. Cortical bone endosteum (CBE) is identified as the soft tissue located within 10- μ m from the cortical bone surfaces of the long bones. Adipocyte tissues within the marrow cavity are classified as trabecular inactive marrow (TIM). Cortical bone volume (CBV) and trabecular bone volume (TBV) are then defined as all osseous tissues within the skeleton.

Marrow Masses

Modification of the Bouchet and Bolch methodology was made for the inactive marrow by using a ratio of the red marrow to fat mass densities. In using their methodology, we began by taking the percentage of active marrow from ICRP Publication 70 Table 40 for the 40 year old and then multiplying this value by the reference mass of active marrow (1170 g). This calculation gives the mass of active marrow in each of the skeletal sites. Values for the distribution of the percentage of the marrow space in each bone site (ICRP 23 Table 30) were multiplied by the 3650 g reference mass of total marrow (active + inactive). Thus we obtained the mass associated with the marrow space in each skeletal site. The next step involved taking the difference of the marrow space mass and the active marrow mass in each bone site, which gave the mass of inactive marrow.

In Bouchet and Bolch the cellularity factor (CF) was computed as the ratio of the active marrow mass divided by the total marrow space mass. As mentioned earlier their data was most reminiscent of the ICRP 40 year old cellularities as given in ICRP 70 Table 41. Here is where our method differs from theirs. Once we obtained the cellularity factor and the marrow space mass, we then calculated the fat fraction (FF = 1-CF). The following equation was then used to calculate the marrow space mass, in each bone site, if the marrow space contained 100% active marrow.

$$MS_{100\%} = MS \times \left(CF + FF \times \frac{\rho_{marrow}}{\rho_{fat}} \right) \quad (\text{Eq. 4})$$

In Eq. 4, MS is the marrow space, while $MS_{100\%}$ is the marrow space containing 100% active marrow. Densities of active and inactive marrow are ρ_{marrow} and ρ_{fat} , respectively.

In this calculation, we take the previously calculated marrow mass and reapportion the masses with regard to the density of fat (0.98 g/cm³) and the density of marrow (1.03 g/cm³). By doing this, the mass of the marrow space is obtained for only active marrow.

Now, the calculation of age dependant, hence cellularity dependant, masses can be made by multiplying the 100% AM marrow space mass by either the 25 or 40 year old cellularity factors from ICRP 70 Table 40.

Unfortunately, this method is not applicable to children as no pediatric values are given for the individual bone marrow space as a fraction of total marrow space. In the literature, it has generally been assumed that one can assign the values found in ICRP 23 Table 30 to children.² Cristy noted that this method does not account for the change in bone site volume with respect to total body volume as one ages.¹⁴ Consequently, assuming the adult values will insufficiently estimate their values for children.

To account for these body volume changes, the values obtained by Cristy for age dependant cellularity factors have been used in the calculation of marrow masses. The following series of equations demonstrate our method for calculating pediatric marrow masses (active AM and inactive IM). We begin by taking the ICRP 70 Table 40 values of percent active marrow (%AM) in each bone site and multiply these by the ICRP reference marrow value ($M_{reference}$).

$$AM = \%AM * M_{reference} \quad (Eq. 5)$$

The mass of the marrow space is then calculated by using the CF from ICRP 70 Table 41 as shown in the following equation.

$$MS = AM/CF \quad (Eq. 6)$$

This mass calculation gives a marrow space with 100% cellularity (no inactive marrow). To properly assess the content of the marrow space, we need to calculate the inactive marrow mass as well. This is done by subtracting the total marrow space mass from the active marrow mass and then by applying a correction for the density of fat as shown in Equation 7.

$$IM = (MS - AM) * \frac{\rho_{fat}}{\rho_{marrow}} \quad (Eq. 7)$$

Once the density correction is applied to the inactive marrow mass, the total mass of the marrow space needs to be corrected by taking the sum of the active marrow and the inactive marrow. The fraction of marrow space assigned to each bone was also calculated for comparison with ICRP 23 Table 30. This was done by taking the density corrected marrow space mass and dividing it by the ICRP reference mass for the total marrow space.

Bone and Endosteum Masses

To calculate the site-specific bone and endosteum masses, two pieces of information are required, as shown by Bouchet and Bolch. The first piece of information is the surface-to-volume ratios (S/V) of both cortical and trabecular bone. In cortical bone, the S/V represents the ratio of the Haversian canal and the Volkmann canal surfaces to their volume. Trabecular bone on the other hand relates the surface of the bone trabeculae to the volume of the spongiosa. Values for S/V are presented in ICRP 70 in Tables 11 (cortical) and 12 (trabecular). In ICRP Publication 89, guidance is given in regards to S/V in bone where it is suggested that $3\text{-mm}^2/\text{mm}^3$ be used as a reference value for cortical bone. A value $18\text{-mm}^2/\text{mm}^3$ is given for trabecular bone. For the purposes of these calculations, the values obtained by Beddoe are used since they provide a more comprehensive data set and give information for specific bone sites at various ages. Table 1 presents the values used in our calculations. Note that the values for the 5 year old and 15 year old were obtained by linear interpolation between the 1.7 year, 9 year, and adult values. Where other data was not available, the ICRP Publication 89 defaults were used in the calculation.

The second data set required is the fraction of the skeletal mass in each bone site as relation to the whole skeleton. In Table 8 of ICRP 70, the percentage of mass of each bone site relative the whole dry skeleton is given for the adult. Corresponding

values in each bone site are not given in the literature for children. Consequently, we have derived a method to estimate their pediatric values. Using the data from Cristy for the percentage of body region per body volume and Table 8 of ICRP 70, calculations of age-dependant skeletal mass fraction were calculated. In Cristy's data, volumes for the following body regions were calculated: the Head (cranium and mandible), Trunk (vertebrae, sternum, ribs, scapula, clavicles and os coxae), Upper legs (femora), Lower legs (tibia, fibula and patella), Feet (ankle and foot bones), Upper arms (humeri), forearms (ulna and radius), and hands (wrist and hand bones). These values are listed in Table 2 for ages 1, 5, 10 and 15 years old. Using this data, it was assumed that the relative fractional distribution of bone mass was the same within each body region regardless of age. Using the adult values in column 1 of Table 2, the relative distribution of body volume in each bone region was calculated. Next, a ratio of the adult mass and volumes were taken and are shown in column 12 of Table 2. These ratios were then multiplied by the age dependant volumes to obtain age-dependant masses. These mass calculations were then renormalized as the calculated values were greater than unity. It was assumed that mass-to-volume ratios would be different at younger ages and thus the calculated values would not be exactly unity. The renormalization of the calculated values was done to account for this and these fractional masses are listed in Columns 13-16 of Table 2.

Calculation of cortical bone masses was then done using the data in Tables 1 and 2. To obtain the cortical bone mass, we take the fraction of total bone in each bone site and multiply it by the reference skeletal mass (ICRP 70 and 89) to obtain the total skeletal mass in each bone site. The mass of cortical bone in each bone is then obtained by multiplying the total bone site mass by the fraction of cortical bone found in ICRP 70 Table 10. This calculation assumes that the fraction of cortical and trabecular bone is constant at all ages. This assumption is made since no corresponding values for

each bone site for children are found in the literature. Values for trabecular bone masses are calculated similarly using the trabecular values from ICRP 70 Table 10.

Once the bone matrix masses are calculated, the endosteum masses may be calculated. The bone masses for cortical bone are calculated using the density of bone, the S/V ratio (Table 1), the thickness of endosteum (10 μm) and the density of endosteum (soft tissue 1.03 g/cm^3). Equation 8 demonstrates this calculation.

$$M_{CBE_i} = M_{CBV_i} \times \left(\frac{S}{V} \right)_{i,age}^{CBV} \times T_C \times \left(\frac{\rho_{endosteum}}{\rho_{bone}} \right) \quad (\text{Eq. 8})$$

In Eq. 8, the subscript i is used to represent the specific bone site where site specific values are needed to calculate the solution. T_C is the endosteum thickness used i.e. 10 μm . Modification of the method is applied to trabecular endosteum as shown in Eq. 9.

$$M_{TBE_i} = M_{TBV_i} * \left(\frac{S}{V} \right)_{i,age}^{TBV} * (1 - FF) * T_E * \left(\frac{\rho_{endosteum}}{\rho_{bone}} \right) \quad (\text{Eq. 9})$$

The fat fraction (FF) is included to accommodate the space occupied by adipocytes within the endosteum. When calculating the 10 μm endosteum (T_E), the fat fraction was assumed to be zero since this is the assumption upon which the ICRP definition is made. If a 50- μm endosteum is considered, this assumption is not valid and consequently, the marrow cellularity must be accounted for using the fat fraction volume.

Using this method does introduce a potential error to the endosteum thickness calculation. This error is best described by considering two concentric spheres of different diameters. Exact calculation of the volume difference between these two spheres is accomplished by taking the difference of the two volumes as shown in Figure 1A. Unfortunately, this is not possible when considering marrow cavities due to their irregular shape, which is not spherical. The sphere example then illustrates the worst case scenario for calculation of volume differences. Application of our method to a

sphere results in an error of $\pm 1\%$ for a $10\ \mu\text{m}$ shell and $\pm 5\%$ for a $50\ \mu\text{m}$ shell. This error is due to the concavity differences between the two spheres. For a real marrow cavity, bone trabeculae may be plate like structures as well as rod structures. The above endosteum calculation method assumes a flat surface from which to calculate the endosteum volume. Plate like structures in the spongiosa are well approximated by planes (see Figure 1B). Thus the total error in our calculation of the $50\ \mu\text{m}$ endosteum mass is $\leq 5\%$.

Density differences in bone as a function of age were also accounted for in our calculation. The densities used in our calculations were $1.66\ \text{g/cm}^3$ for the one year old, $1.70\ \text{g/cm}^3$ for the 5 year old, $1.75\ \text{g/cm}^3$ for the 10 year old and $1.80\ \text{g/cm}^3$ for the fifteen year olds⁷. The incorporation of these density differences is essential for the calculation of the proper bone volume, which is then used to calculate the volume of endosteum. Using these age dependant densities, the above equations were applied to each bone site for each reference age and gender allowed for the development of a database of cortical and trabecular endosteum masses.

RESULTS AND DISCUSSION

Marrow Masses

Age dependant active marrow masses are listed in Table 3. Here we demonstrate differences as compared to the ICRP reference masses for the total marrow mass. Note that for the adults, the density corrected Bouchet and Bolch method was used while the marrow cellularity based calculation developed in the paper was used for children. Masses developed using the cellularity method are shown to be $\sim 98\%$ of the reference values given for children. This is attributed to the density difference between inactive and active marrow. If the cellularity method were applied to the adults the same 2%

difference would also occur. This demonstrates an issue with regard to the method and the ICRP values with respect to the accounting of fatty tissues of the bone marrow in individual bone sites. By using the cellularity method, we see that ICRP value assumes the active and inactive marrow to be of the same mass density which is not the case. This situation further justifies our density corrected Bouchet and Bolch methodology. Calculation of site-specific marrow masses is not a trivial procedure. The data listed in the ICRP publications is a compilation of many different data sets. These data sets are not always consistent with one another. One example of this is seen in the marrow mass for an adult male is given as a constant value, 1170 g, despite the differences in cellularity between the 25 and 40 year olds. Results from Table 2 demonstrate that the 1170 g marrow mass gives an average value for the two ages. This seems inconsistent with the inclusion of cellularity factors given in ICRP 70 Table 41, which have also been included in ICRP 89. Consistency would dictate that two different reference masses should be included. For the 25 year old our method gives a total marrow mass of 1266 g while the 40 year old has a total marrow mass of 1151 g. The reference marrow mass is closer to the value obtained for the 40 year old. This seems consistent as the computed cellularity factors in Table 2 are more reminiscent of ICRP 70 values for the 40 year old. From this we can assume that the 1170 g is most appropriately used in conjunction with an older adult male. The opposite situation occurs with the adult females as shown in Table 7. Here calculated masses are 916 g and 866 g for the 25 year old and 40 year old respectively. The reference mass more closely resembles the 25 year old female. Not only does this demonstrate age dependant gender differences but it also demonstrates an inconsistency in the data provided in the ICRP documents.

Another issue involved in complicating these calculations is found in the lack of data with regard to children. For example, the method proposed by Bouchet and Bolch seems to be very consistent with regard to the calculation of adult marrow masses from

literature data. In Column 3 of Table 2 values for the percentage of the total marrow space (active and inactive marrow) in each bone site from ICRP 23 Table 30 is listed. These values allow for the calculation of the total marrow space. Regrettably, similar data is not available for children and this necessitated the method we have used in this paper. Here the underlying assumption is that the reference masses, cellularity factors and the fraction of active marrow in the bone site are all consistent with one another. In Table 3 we have shown that this is not the case as density differences between marrow and fat were not adequately accounted for in the calculation of the reference marrow space mass (active + inactive marrow). We see an increasing disparity between the marrow space reference mass and the calculated MS mass with the density correction as age increases. The marrow space mass was not included in Table 3 as the inactive marrow dose need not be calculated. As previously mentioned, the inactive marrow mass shows greater disparity with the ICRP reference values as does active marrow masses.

Bone Masses

Tables 4 lists age-dependant masses for bone tissue within the body. In these data, we continue to see consistent increases in masses as age increases. We also see gender differences consistent with the above mentioned findings. It should also be pointed out that when using these methodologies, the differences in gender are wholly attributed to the different reference bone masses. A plot of the total cortical bone mass (Fig. 2A) and the total trabecular bone mass (Fig. 2B) demonstrates a sigmoidal growth pattern where the slope transition occurs between 10 years and 15 years. This seems consistent with changes associated with puberty, its associated body changes, and the data provided in ICRP 23 Fig. 41.

Changes in female bone masses were very small when comparing the 15 year old and the adult female. Male differences over this age range were greater. Gender differences in these masses can be ascribed to the fact that reference mass for the 15 year female is 93% of adult female while the 15 year male is 74% of the adult male. While it is not explicitly stated in ICRP 70 or 89, it can be assumed that these differences are due to normal growth pattern differences in males and females.

From the data, we also see that as age increases there is a decrease in the fraction of the previous ages mass to the current age. This is expected as one grows the size of the skeleton begins to approach its adult size. Consequently the relative differences from age to age should decrease. Another interesting result seen in the data is that the fraction of trabecular bone to total bone increases only ~1-2% as one grows older.

Endosteum Masses

Table 5 presents results for cortical endosteum at each of the references ages, while Table 6 shows results for trabecular endosteum for both its 10 μm and 50 μm definition. Calculated masses for cortical endosteum demonstrate similar properties to the calculated bone masses with the values increasing with age. Differences in the 15 year and adult females demonstrated negligible differences (0.1 g). Larger differences were seen with the two male masses at similar ages (13.7 g). As noted earlier, in ICRP Publication 30,⁹ an endosteal reference mass of 120 g is given for the adult. Our results for the cortical endosteum and TBE₁₀ demonstrate a larger value, 156.1 g, in the male and a female endosteum mass of 113.3 g for the 10 μm endosteum. For children, total TBE₁₀ masses of 17.9 g, 41.0 g, and 81.3 g were obtained for the 1, 5 and 10 year olds respectively. Male and female 10 μm endosteum masses at 15 years were 127.7 g and

116.6 g. Our data differs significantly from the reference value for the adult male. The differences can be attributed to the use of the same S/V ratios for both cortical and trabecular bone, by the ICRP in Publication 23.

Comparison of the TBE masses demonstrates significant changes in the masses due to the two endosteum thickness. As expected, the 50 μm masses are larger than the 10 μm masses. The relative difference between the total mass of the two data sets decreases with increasing age. Increasing mass values are seen for the 10 μm data set as a function of age. Mass values for the 50 μm data set do not show this same relationship. Age dependency is seen among the pediatric ages with the 15 year old male and female having the greatest masses. Adult values are less than the 15 year old data for both the male and female data. In contrast to the pediatric ages, the adult demonstrate a decreasing TBE₅₀ mass with increasing age. Changes in bone marrow cellularity with age are the source of this relationship. Note that the 15 year olds have the largest masses and also have the highest cellularity values. As one ages the fat fraction increasing resulting in more of the 50 μm endosteum layer being occupied by marrow adipocytes. Under the 10 μm endosteum definition, this is not the case and consequently this data follows an increasing age-dependant trend.

CONCLUSION

A set of marrow, bone and endosteum masses for 22 bone sites has been developed using ICRP reference values. Skeletal tissue masses were obtained for each of the ICRP reference ages. Despite this being an encompassing data set, the referenced data are quite old, with some of the data dating back to the 1920s. This data found in the ICRP documents also demonstrates areas of inconsistency with respect to their reference values (i.e., one marrow mass for adults despite different reference

cellularities at 25 years and 40 years). For the purposes radiation protection, these values may be used as they relate the reference person at each age and gender category. Additionally, the reference masses provided by the ICRP tend to be used in dose calculations looking for long-term effects where the inconsistencies may not necessarily affect the results significantly.

For purposes of nuclear medicine dosimetry, these mass values would most likely be very ineffectual in the assessment of patient doses due to the differences in physiological variability between people. Mass values that are tied to the specific subject are necessary to correctly determine a total skeletal dose as shown in Eqs. 1-3. Work by Shah et al¹⁵ in determining skeletal tissue masses in a reference patient when used in conjunction with absorbed fraction values for alphas and betas obtained using the reference model allow for a basis from which patient specific dosimetry calculations may be made. Additional research into the scalability of this model is under investigation.

Issues with respect to skeletal masses for dosimetry of children are of great interest since irradiation of a child allows for a greater time frame in which radiation induced effects may occur. The current use of the ICRP age series masses does not seem to apply as well to children as it does to the adult. Once again, this is due to significant lack of published information on the skeletal tissues of children. Consequently, more research is needed in developing consistent and broad-based skeletal masses values for use in the dosimetry of pediatric patients.

REFERENCES

- 1 A. P. Shah, W. E. Bolch, D. A. Rajon et al., J Nucl Med 46 (2), 344 (2005); C J
2 Watchman, D W Jokisch, P W Patton et al., J Nucl Med in press (2005).
3 International Commission on Radiological Protection ICRP, 1974.
4 WS Ford Snyder, MR Warner, GG Watson, SB, 1974.
5 R. Budinger Leovinger, R.F. Watson, E.E., *MIRD Primer for Absorbed Dose*
6 *Calculations*. (Society of Nuclear Medicine, New York, 1991).
7 M. Cristy, Eckerman, K.F., 1987.
8 International Commission on Radiological Protection ICRP, 1994.
9 International Commission on Radiological Protection ICRP, 2003.
10 ICRP, Report No. ICRP Publication 70, 1995.
11 ICRP, Report No. ICRP Publication 30, 1979.
12 M. G. Stabin, VisualBasic MIRDOSE3 (Oak Ridge Institute for Science and
13 Education, Oak Ridge, 1994); M. G. Stabin, J Nucl Med 37 (3), 538 (1996).
14 W. Gossner, R Masse, and JW Stather, Radiat Prot Dosim 92 (1-3), 209 (2000);
15 W. Gossner, Radiat Prot Dosimetry 105 (1-4), 39 (2003).
L. G. Bouchet, W. E. Bolch, R. W. Howell et al., J Nucl Med 41 (1), 189 (2000).
A. H. Beddoe, J Anat 122, 190 (1976).
J. L. Coffey, M. Cristy, and G. G. Warner, J Nucl Med 22 (1), 65 (1981).
A P Shah, Dissertation, University of Florida, 2004.

Table 1. Surface to Volume Ratios Used in Trabecular Bone Calculation*

Skeletal Site	S/V (mm²/mm³)				
	1.7	5	9	15	Adult
Cranium	3.8	5.1	6.4	7.1	7.8
Mandible	3.8	5.1	6.4	7.1	7.8
Cervical	23.5	24.7	25.8	21.9	18.0
Thoracic	23.5	24.7	25.8	21.9	18.0
Lumbar	23.5	24.7	25.8	22.8	19.7
Sternum	23.7	21.8	19.8	19.2	18.5
Ribs	23.7	21.8	19.8	19.2	18.5
Scapula#	26.6	25.4	24.3	21.4	18.5
Clavicles#	26.6	25.4	24.3	21.4	18.5
Os coxae#	29.6	26.2	22.8	20.0	17.2
Sacrum#	29.6	26.2	22.8	21.3	19.7
Humeri, upper half	18.0	18.0	18.0	18.0	18.0
Humeri, lower half	18.0	18.0	18.0	18.0	18.0
Radius	18.0	18.0	18.0	18.0	18.0
Ulna	18.0	18.0	18.0	18.0	18.0
Hands	18.0	18.0	18.0	18.0	18.0
Femora, upper half	23.0	20.7	18.4	17.9	17.3
Femora, lower half	23.0	20.7	18.4	17.9	17.3
Patella	18.0	18.0	18.0	18.0	18.0
Tibia	18.0	18.0	18.0	18.0	18.0
Fibula	18.0	18.0	18.0	18.0	18.0
Ankles and Feet	18.0	18.0	18.0	18.0	18.0

*Linear interpolation of 5 Y and 15 Y from values obtained by Beddoe

#S/V ratios for these bone site were obtained by using 50% of the Iliac Crest value and 50% of the Lumbar vertebrae. This was done to account for difference in these bone sites trabecular structure

Table 2. Calculation of fraction of Total Skeleton Mass in Children

Skeletal Site	ADULT	Cristy (1981)					% Volume of					Ratio of	% Mass of Each Bone Site			
	% Mass of	Percentage of body region					each bone site					% Mass /	% Adult Skeletal Mass / % Adult Bone Site Volume			
	total dry skeleton	per body volume					within body region					% Volume	x % Bone Site Volume#			
	ICRP 70											for				
	Table 8	1 Y	5 Y	10 Y	15 Y	Adult	1 Y	5 Y	10 Y	15 Y	Adult	Adult	1 Y	5 Y	10 Y	15 Y
Cranium	15.7	25.20	15.70	10.50	7.70	7.20	22.87	14.25	9.53	6.99	6.53	2.40	44.28	30.49	21.33	16.48
Mandible	1.6						2.33	1.45	0.97	0.71	0.67	2.40	4.51	3.11	2.17	1.68
Cervical	1.5	50.60	52.30	51.00	53.00	52.70	2.59	2.68	2.61	2.71	2.70	0.56	1.16	1.33	1.35	1.48
Thoracic	3.8						6.56	6.78	6.61	6.87	6.83	0.56	2.94	3.36	3.43	3.75
Lumbar	3.2						5.53	5.71	5.57	5.79	5.76	0.56	2.48	2.83	2.89	3.16
Sternum	0.5						0.86	0.89	0.87	0.90	0.90	0.56	0.39	0.44	0.45	0.49
Ribs	6.0						10.36	10.71	10.44	10.85	10.79	0.56	4.64	5.30	5.41	5.92
Scapula	3.1						5.35	5.53	5.40	5.61	5.58	0.56	2.40	2.74	2.79	3.06
Clavicles	1.0						1.73	1.78	1.74	1.81	1.80	0.56	0.77	0.88	0.90	0.99
Os coxae	8.3						14.33	14.82	14.45	15.01	14.93	0.56	6.42	7.34	7.48	8.19
Sacrum	1.9						3.28	3.39	3.31	3.44	3.42	0.56	1.47	1.68	1.71	1.88
Humeri, upper half	3.4	4.69	4.66	4.70	6.17	6.37	2.35	2.33	2.35	3.09	3.19	1.07	2.02	2.22	2.34	3.23
Humeri, lower half	3.4						2.35	2.33	2.35	3.09	3.19	1.07	2.01	2.21	2.33	3.23
Radii	2.3	2.90	2.94	2.95	3.12	3.32	1.28	1.30	1.30	1.38	1.47	1.57	1.62	1.81	1.90	2.12
Ulna	2.9						1.62	1.64	1.65	1.74	1.85	1.57	2.04	2.29	2.40	2.68
Hands	2.6	1.41	1.40	1.84	1.30	1.20	1.41	1.40	1.84	1.30	1.20	2.17	2.46	2.70	3.71	2.77
Femora, upper half	9.5	7.00	12.20	16.20	16.40	16.90	3.50	6.10	8.10	8.20	8.45	1.12	3.17	6.11	8.48	9.05
Femora, lower half	9.5						3.50	6.10	8.10	8.20	8.45	1.12	3.17	6.11	8.48	9.05
Patella	0.6	5.60	7.80	8.80	9.40	9.40	0.24	0.33	0.38	0.40	0.42	1.43	0.28	0.42	0.50	0.56
Tibia	11.1						4.44	6.18	6.98	7.45	7.79	1.43	5.10	7.85	9.27	10.43
Fibula	2.3						0.92	1.28	1.45	1.54	1.61	1.43	1.06	1.63	1.92	2.16
Ankles and Feet	5.6	2.60	3.00	3.50	2.90	2.90	2.60	3.00	3.50	2.90	2.09	2.68	5.61	7.16	8.74	7.63
Total	99.8	100.0	100.0	99.5	100.0	100.0	100.0	100.0	99.5	100.0	99.6	1.00	100.00	100.00	100.00	100.00

*Assuming that the relative distribution within each bone set is the same as the relative distribution of the mass within the Adult i.e. ICRP 70 Table 8

#These values are all renormalized due to the relative differences in the ratio of mass to volume with respect to age

Table3. Active Marrow Masses for All Ages Using Cellularity Method and Density Corrected Bouchet and Bolch

Skeletal Site	Age (years)					Age (years)			
	Cellularity Method					Density Corrected Bouchet and Bolch			
	1	5	10	15 Male	15 Female	25 Male	25 Female	40 Male	40 Female
Cranium	37.6	53.5	71.8	97.2	90.0	100.1	74.0	90.6	66.9
Mandible	3.6	5.4	6.8	9.5	8.8	9.5	7.0	8.6	6.3
Cervical	4.2	7.4	16.8	35.2	32.6	47.5	35.1	46.2	34.1
Thoracic	12.6	30.0	68.0	146.2	135.3	194.4	143.6	189.0	139.6
Lumbar	6.4	23.0	52.4	112.0	103.7	149.7	110.6	145.5	107.5
Sternum	1.2	5.7	13.1	28.8	26.7	36.8	27.2	35.8	26.4
Ribs	13.3	29.7	68.0	145.1	134.3	195.8	144.6	190.4	140.6
Scapula	4.0	9.1	18.0	34.9	32.3	37.6	27.8	34.1	25.2
Clavicles	1.2	3.0	5.6	10.5	9.8	10.6	7.8	9.5	7.0
Os coxae	16.6	44.1	96.9	196.3	181.8	225.3	166.5	186.5	137.8
Sacrum	3.6	18.5	41.6	89.1	82.5	127.8	94.5	105.8	78.2
Humeri, upper half	3.6	8.1	15.4	32.6	30.2	34.1	25.2	28.4	21.0
Humeri, lower half	3.4	7.4	9.8	7.2	6.7	0.0	0.0	0.0	0.0
Radii	1.9	3.3	3.3	0.0	0.0	0.0	0.0	0.0	0.0
Ulna	1.9	3.3	3.3	0.0	0.0	0.0	0.0	0.0	0.0
Wrist and Hands	2.8	2.9	0.0	0.0	0.0	0.0	0.0	0.0	0.0
Femora, upper half	6.1	22.9	58.1	96.7	89.5	96.6	71.4	80.5	59.5
Femora, lower half	5.8	21.1	37.3	20.7	19.1	0.0	0.0	0.0	0.0
Patella	1.0	6.7	6.1	0.0	0.0	0.0	0.0	0.0	0.0
Tibia	9.9	13.3	21.2	0.0	0.0	0.0	0.0	0.0	0.0
Fibula	1.3	8.3	9.1	0.0	0.0	0.0	0.0	0.0	0.0
Ankles and Feet	6.9	8.2	0.0	0.0	0.0	0.0	0.0	0.0	0.0
Total	149	335	623	1062	983	1266	935	1151	850
Reference Total	150	340	630	1080	1000	1170	900	1170	900

Table 4. Summary of Bone Masses for All Ages

Skeletal Site	Cortical (g)							Trabecular (g)						
	Age (years)							Age (years)						
	1	5	10	15 Male	15 Female	Adult Male	Adult Female*	1	5	10	15 Male	15 Female	Adult Male	Adult Female*
Cranium	248.2	365.0	466.1	634.2	579.4	822.0	597.8	13.1	19.2	24.5	33.4	30.5	43.3	31.5
Mandible	25.3	37.2	47.5	64.6	59.0	83.8	60.9	1.3	2.0	2.5	3.4	3.1	4.4	3.2
Cervical	1.7	4.2	7.8	15.0	13.7	20.7	15.0	5.1	12.5	23.3	45.0	41.1	62.0	45.1
Thoracic	4.3	10.6	19.7	38.0	34.7	52.4	38.1	13.0	31.7	59.1	114.0	104.1	157.1	114.2
Lumbar	5.0	12.1	22.6	43.5	39.7	60.0	43.6	9.6	23.5	43.8	84.5	77.2	116.4	84.6
Sternum	2.1	5.2	9.7	18.8	17.2	25.9	18.8	0.1	0.3	0.6	1.2	1.1	1.7	1.2
Ribs	25.7	62.8	117.0	225.5	206.0	310.8	226.1	1.6	4.0	7.5	14.4	13.2	19.8	14.4
Scapula	13.3	32.5	60.4	116.5	106.5	160.6	116.8	0.8	2.1	3.9	7.4	6.8	10.3	7.5
Clavicles	4.3	10.5	19.5	37.6	34.3	51.8	37.7	0.3	0.7	1.2	2.4	2.2	3.3	2.4
Os coxae	34.1	83.2	154.9	298.7	272.9	411.7	299.4	3.8	9.2	17.2	33.2	30.3	45.7	33.3
Sacrum	6.5	15.9	29.5	57.0	52.1	78.5	57.1	2.2	5.3	9.8	19.0	17.4	26.2	19.0
Humeri, upper half	10.7	25.1	48.4	117.8	107.7	168.6	122.6	1.2	2.8	5.4	13.1	12.0	18.7	13.6
Humeri, lower half	10.7	25.1	48.3	117.7	107.5	168.6	122.6	1.2	2.8	5.4	13.1	11.9	18.7	13.6
Radius	8.3	19.9	38.1	74.8	68.3	110.3	80.2	1.2	3.0	5.7	11.2	10.2	16.5	12.0
Ulna	10.5	25.1	48.0	94.3	86.1	139.0	101.1	1.6	3.7	7.2	14.1	12.9	20.8	15.1
Hands	13.8	32.3	81.2	106.4	97.2	136.1	99.0	0.7	1.7	4.3	5.6	5.1	7.2	5.2
Femora, upper half	14.4	59.3	150.2	282.2	257.9	403.1	293.2	4.3	17.7	44.9	84.3	77.0	120.4	87.6
Femora, lower half	14.4	59.3	150.2	282.2	257.9	403.1	293.2	4.3	17.7	44.9	84.3	77.0	120.4	87.6
Patella	1.3	4.3	9.2	18.3	16.7	26.5	19.2	0.3	1.1	2.3	4.6	4.2	6.6	4.8
Tibia	25.0	82.1	176.9	350.6	320.3	507.7	369.3	5.1	16.8	36.2	71.8	65.6	104.0	75.6
Fibula	5.5	18.2	39.3	77.9	71.2	112.8	82.0	0.7	2.3	4.9	9.6	8.8	13.9	10.1
Ankles and Feet	31.5	85.7	190.9	293.5	268.1	293.2	213.2	1.7	4.5	10.0	15.4	14.1	15.4	11.2
Total	516.7	1075.4	1935.4	3365.2	3074.3	4547.2	3307.1	73.3	184.6	364.6	684.9	625.7	952.8	692.9

Table 5. Summary of 10- μ m Endosteal Masses for All Ages

Skeletal Site	Cortical (g)						
	Age (years)						
	1	5	10	15 Male	15 Female	25 Male	Adult Female*
Cranium	4.6	6.6	8.7	10.9	9.9	13.23	9.60
Mandible	0.5	0.7	0.9	1.1	1.0	1.35	0.98
Cervical	0.03	0.1	0.5	0.3	0.2	0.33	0.24
Thoracic	0.1	0.2	1.4	0.7	0.6	0.84	0.61
Lumbar	0.1	0.2	1.2	0.7	0.7	0.96	0.70
Sternum	0.04	0.1	0.2	0.3	0.3	0.42	0.30
Ribs	0.5	1.1	2.2	3.9	3.5	5.00	3.63
Scapula	0.2	0.6	1.1	2.0	1.8	2.58	1.88
Clavicles	0.1	0.2	0.4	0.6	0.6	0.83	0.61
Os coxae	0.6	1.5	3.0	5.1	4.7	6.63	4.81
Sacrum	0.1	0.3	0.7	1.0	0.9	1.26	0.92
Humeri, upper half	0.2	0.4	0.7	1.6	1.4	2.08	1.51
Humeri, lower half	0.2	0.3	0.7	1.5	1.4	2.08	1.51
Radii	0.1	0.3	0.6	1.0	0.9	1.36	0.99
Ulna	0.1	0.3	0.7	1.2	1.1	1.72	1.25
Hands	0.2	0.5	1.2	1.4	1.3	1.68	1.22
Femora, upper half	0.3	1.0	3.3	4.7	4.3	6.27	4.55
Femora, lower half	0.3	1.0	3.3	4.7	4.3	6.27	4.55
Patella	0.02	0.1	0.2	0.3	0.3	0.43	0.31
Tibia	0.3	0.9	2.4	3.8	3.5	5.18	3.76
Fibula	0.1	0.2	0.5	0.8	0.8	1.15	0.83
Ankles and Feet	0.6	1.6	3.5	5.0	4.6	4.72	3.42
Total	9.2	18.3	37.5	52.7	48.1	66.4	48.2

*Female endosteal masses were obtained using the assumption that the % of dry skeleton was the same as the male of the same age

Table 6. Trabecular Endosteum Masses for both 10- μ m and 50- μ m Endosteum

Skeletal Site	10- μ m							50- μ m								
	Age (years)							Age (years)								
	1	5	10	15 Male	15 Female	Adult Male	Adult Female*	1	5	10	15 Male	15 Female	25 Male	40 Male	25 Female*	40 Female*
Cranium	0.31	0.6	0.9	1.4	1.2	1.81	1.3	1.5	2.4	3.0	3.1	3.4	3.8	3.4	2.8	2.5
Mandible	0.031	0.06	0.1	0.14	0.13	0.18	0.1	0.1	0.2	0.3	0.3	0.3	0.4	0.4	0.3	0.3
Cervical	0.7	1.9	3.5	5.6	5.2	5.99	4.3	3.6	8.0	14.2	7.0	19.3	21.6	21.0	15.7	15.2
Thoracic	1.9	4.7	9.0	14.3	13.0	15.17	11.0	9.0	20.1	35.9	17.9	48.9	54.6	53.1	39.7	38.6
Lumbar	1.4	3.5	6.7	11.0	10.0	12.30	8.9	6.7	14.9	26.6	13.7	37.7	44.3	43.1	32.2	31.3
Sternum	0.0	0.0	0.1	0.1	0.1	0.16	0.1	0.1	0.2	0.3	0.2	0.5	0.6	0.6	0.4	0.4
Ribs	0.2	0.5	0.9	1.6	1.4	1.97	1.4	1.1	2.2	3.5	2.0	5.4	7.1	6.9	5.2	5.0
Scapula	0.1	0.3	0.6	0.9	0.8	1.02	0.7	0.7	1.3	1.8	2.0	2.3	2.1	1.9	1.6	1.4
Clavicles	0.0	0.1	0.2	0.3	0.3	0.33	0.2	0.2	0.4	0.6	0.7	0.7	0.6	0.5	0.4	0.4
Os coxae	0.7	1.5	2.3	3.8	3.5	4.22	3.1	3.3	5.8	8.3	6.8	11.1	12.2	10.1	8.9	7.4
Sacrum	0.4	0.8	1.3	2.3	2.1	2.77	2.0	1.9	3.3	4.8	4.2	6.8	8.0	6.6	5.8	4.8
Humeri, upper half	0.1	0.3	0.6	1.3	1.2	1.81	1.3	0.6	1.2	1.7	3.7	2.8	2.7	2.3	2.0	1.6
Humeri, lower half	0.1	0.3	0.6	1.3	1.2	1.81	1.3	0.6	1.1	1.1	6.1	0.6	0.0	0.0	0.0	0.0
Radii	0.1	0.3	0.6	1.2	1.1	1.59	1.2	0.6	0.9	0.7	5.8	0.0	0.0	0.0	0.0	0.0
Ulna	0.2	0.4	0.8	1.5	1.3	2.01	1.5	0.8	1.2	0.9	7.3	0.0	0.0	0.0	0.0	0.0
Hands	0.1	0.2	0.5	0.6	0.5	0.69	0.5	0.2	0.2	0.0	2.9	0.0	0.0	0.0	0.0	0.0
Femora, upper half	0.6	2.2	4.9	8.6	7.9	11.18	8.1	2.9	8.5	14.6	23.7	17.7	16.8	14.0	12.2	10.2
Femora, lower half	0.6	2.2	4.9	8.6	7.9	11.18	8.1	2.7	7.9	9.5	38.8	3.9	0.0	0.0	0.0	0.0
Patella	0.0	0.1	0.2	0.5	0.4	0.64	0.5	0.2	0.3	0.3	2.4	0.0	0.0	0.0	0.0	0.0
Tibia	0.6	1.8	3.8	7.4	6.8	10.04	7.3	2.5	5.2	4.4	37.0	0.0	0.0	0.0	0.0	0.0
Fibula	0.1	0.2	0.5	1.0	0.9	1.35	1.0	0.3	0.7	0.6	5.0	0.0	0.0	0.0	0.0	0.0
Ankles and Feet	0.2	0.5	1.1	1.6	1.5	1.49	1.1	0.5	0.5	0.0	8.0	0.0	0.0	0.0	0.0	0.0
Total	8.7	22.7	43.8	75.0	68.5	89.7	65.1	40.2	86.6	132.9	198.2	161.4	174.8	163.8	127.1	119.1

*Female endosteal masses were obtained using the assumption that the % of dry skeleton was the same as the male of the same age

FIGURES

Figure 1. Illustration demonstrating the error associated with the endosteum calculation using two concentric spheres.

Figure 2. (A) Total cortical bone mass as a function of age in the male, (B) Total trabecular bone mass as a function of age in the male.

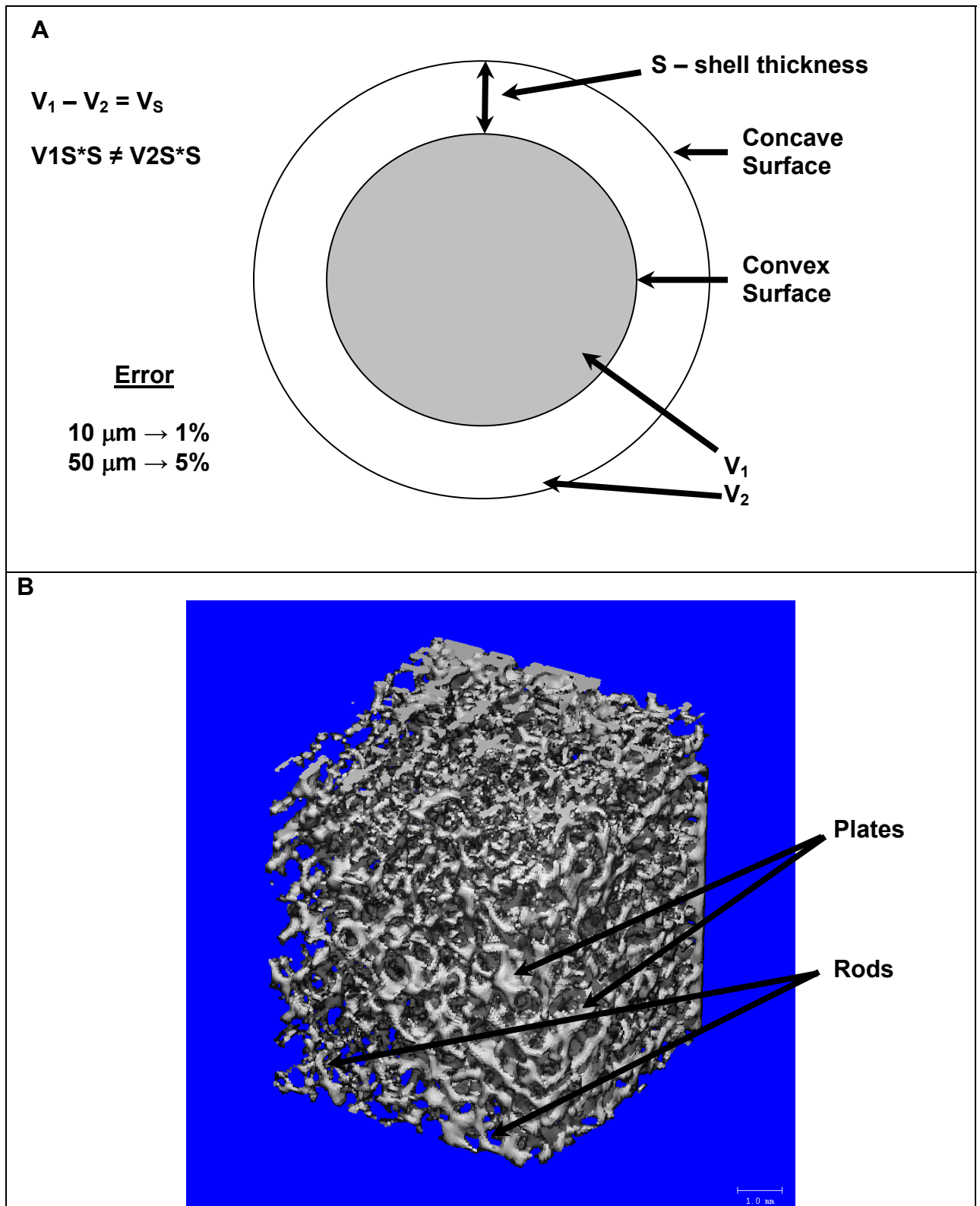


Figure 1

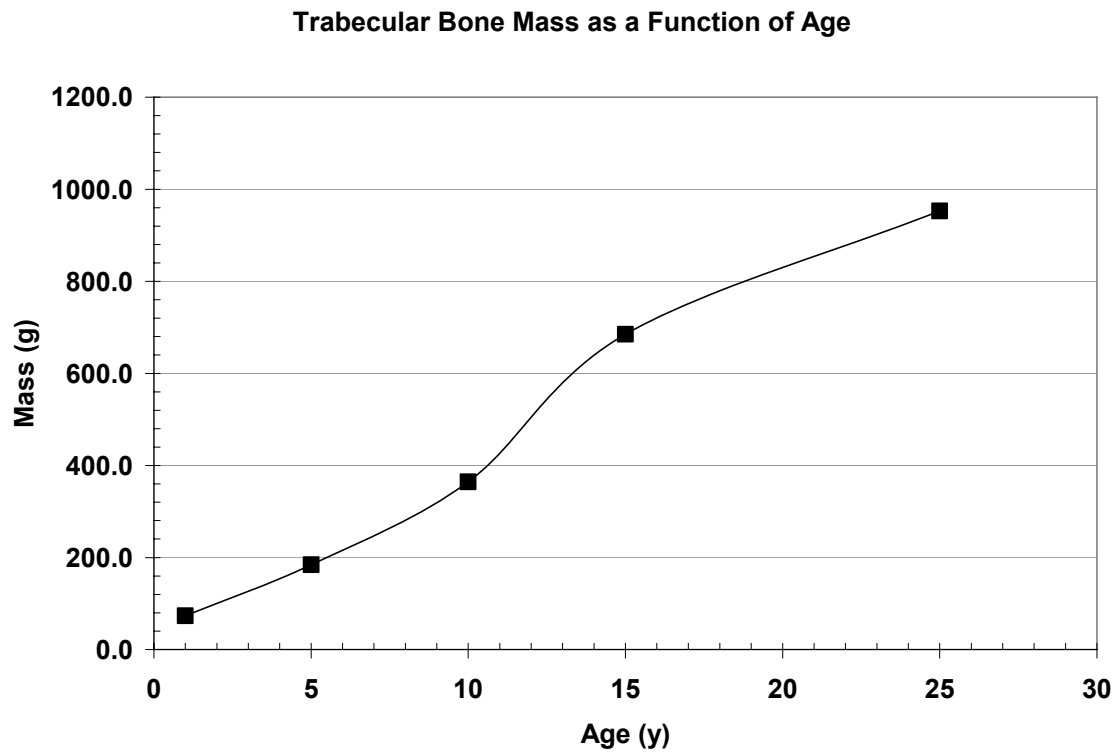
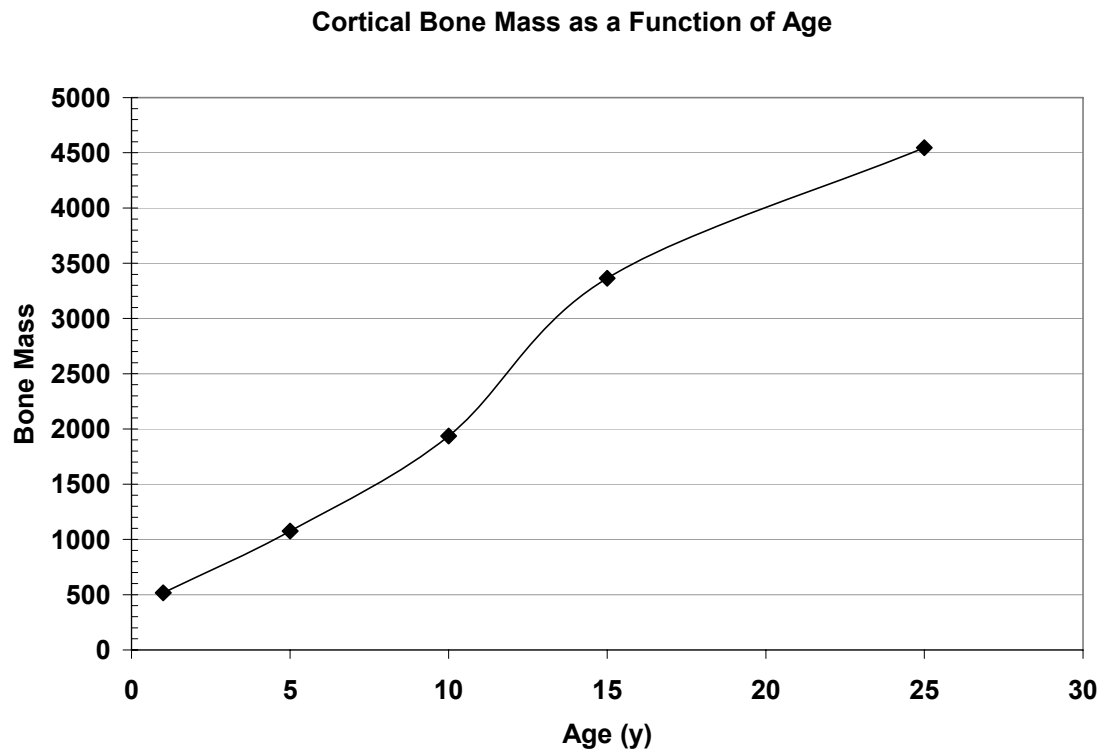


Figure 2

ALPHA PARTICLE ABSORBED FRACTIONS IN THE SKELETAL TISSUES: CONSIDERATION OF A 50- μ m ENDOSTEUM TARGET

Christopher J. Watchman, MS

*Department of Nuclear & Radiological Engineering,
University of Florida, Gainesville, FL 32611-8300*

Wesley E. Bolch, PhD^a

Department of Nuclear & Radiological Engineering and Department of Biomedical Engineering, University of Florida, Gainesville, FL 32611-8300

^aFor reprints and correspondence contact:

Wesley E. Bolch, PhD, PE, CHP

*Director, Advanced Laboratory for Radiation Dosimetry Studies (ALRADS)
Department of Nuclear and Radiological Engineering
University of Florida, Gainesville, Florida 32611-8300
Phone: (352) 846-1361 Fax: (352) 392-3380 Email: wbolch@ufl.edu*

RUNNING TITLE:

Alpha Absorbed Fractions: 50 μ m Endosteum

This work was supported by the

U.S. Department of Energy and the National Cancer Institute

Submitted to *Physics Medicine and Biology*

Word Count (Text and Refs): 5812

Word Count (Figure Captions): 214

Word Count (Table Captions): 77

Word Count (Total): **6103**

INTRODUCTION

Traditionally, two radiosensitive target tissues have been identified in skeletal dosimetry. The first is the active (or red) bone marrow defined as the hematopoietic stem cells and their progenitors within the marrow tissues of trabecular bone. The second target is the osteoprogenitor and mesenchymal stem cells lining the bone surfaces in either trabecular or cortical bone. This latter target tissue has been termed the bone endosteum and in Publication 11[1] of the International Commission on Radiological Protection (ICRP), it was specifically identified as osteogenic and epithelial tissues lining the bone surfaces. In Publication 26[2], the ICRP gave specific dosimetry guidance for the bone endosteum in which the absorbed dose is to be averaged across all soft tissues within 10 μm from the bone surfaces. While the active marrow target has been used to assess the risk of leukemia induction following radiation exposure of the skeletal tissues, the endosteum has been used as the target tissue relevant to the risk of bone cancer induction following skeletal irradiation. In cortical bone, the endosteal layer is thus defined as a 10- μm tissue layer aligning the Haversian cavities within the cortical osteons. In trabecular bone, the endosteum has been defined as a 10- μm tissue layer lining the surfaces of the bone trabeculae within the trabecular spongiosa. According to ICRP Publication 89,[Ref] trabecular bone accounts for 62% of the total bone endosteal surfaces, while cortical bone accounts for the remaining 38%. Recent radiation epidemiological studies, however, have indicated that radiogenic bone cancers originate in the trabecular spongiosa, and thus current proposals in the ICRP are to no longer consider cortical endosteum as a relevant target for risk assessment. As a result, all relevant targets (active marrow and trabecular endosteum) are now considered to reside in the trabecular bone regions of the skeleton, with cortical bone serving only as a potential source regions for dosimetry purposes.

Computational modeling of energy deposition in the skeletal tissues has customarily been performed using chord-based transport methods. Calculation of absorbed dose to the trabecular endosteum target has been accomplished using algorithms based upon the sampled marrow cavity chord and the assumption of a uniform 10- μm thickness on the bone surfaces. Studies by Eckerman[3], Bouchet et al[4], and Jokisch et al[5] have used this methodology to obtain electron absorbed fractions to the trabecular endosteum. Recently, a modification of this algorithm has been presented in Watchman et al[6] based upon work by Jokisch, in which the average endosteal chord length was shortened to more closely match the voxel-based transport results of Shah et al[7].

Questions regarding the validity of the ICRP assigned 10 μm thickness of endosteum has recently become of interest due to new information regarding tissues of interest in the development of bone tumors. Two review articles by Gössner[8] and Gössner et al[9] present overviews of the current research into which radiosensitive tissues are responsible for bone tumor induction. In these articles, specific examples from the literature are presented that indicate that osteoprogenitor cells as far as 50 μm from the endosteum surface are potentially the tissues of interest regarding bone tumor induction. Fifty micrometers is within the range of alpha particles of interest in not only radiological protection but also in molecular radiotherapy (MRT). In MRT, alpha-emitting radionuclides are chosen such that they have a short half life and high emission energies. Alpha emitters with energies of $\sim 5\text{-}9\text{ MeV}$, which corresponds to a range of 50-80 μm in soft tissue, are being investigated[10-31]. These issues indicate that modification of the current endosteum thickness is warranted and should be implemented in skeletal dosimetry modeling.

In this paper, an in depth investigation is made into alpha emitter dosimetry with the proposed change in the thickness of the trabecular endosteum from 10 μm to 50 μm from all trabecular surfaces. Using the 3D chord based infinite spongiosa transport methodology (3D-CBIST) previously described in Watchman et al[6], changes in absorbed fractions as function of bone site, energy, marrow cellularity and subject are investigated. Furthermore, additional information regarding how these changes may impact the magnitude of radionuclide S-values is explored.

MATERIALS AND METHODS

In this study, modifications were made to the methods used in Watchman et al[6] to allow for variations in the thickness of the trabecular endosteum. In this previous study, a series of tissue definitions were presented. Accommodation of a larger endosteum thickness requires revision to these definitions. Table 1 gives a comprehensive list of these revised definitions. Major revisions include partitioning the trabecular active marrow (TAM) into shallow active marrow (TAM_S) and deep active marrow (TAM_D). Similar definitions are applied to the trabecular inactive marrow (TIM_S and TIM_D). The trabecular bone endosteum is further defined as all non-adipose tissues within distance x (in μm) from the bone trabeculae surfaces and is given in the symbol TBE _{x} . Current ICRP definitions of the trabecular endosteum are thus given as TBE₁₀ defining a 10- μm layer, while the proposed definition would be TBE₅₀ defining a 50- μm layer on the bone trabeculae surfaces. When $x = 50 \mu\text{m}$, then the shallow active marrow and the trabecular bone endosteum define the same target tissue (TBE₅₀ is equivalent to TAM_S). In the previous dosimetry study by Watchman et al., the trabecular bone endosteum was defined as TBE₁₀ and was exclusive of the active bone marrow and did not include the presence of marrow adipocytes. In the current study, the trabecular active marrow is

now inclusive of the trabecular bone endosteum (since shallow active marrow is by definition TBE_{50}). Furthermore, the presence of marrow adipocytes is now explicitly considered within the revised definition of the trabecular bone endosteum, or TBE_{50} . In other words, the larger tissue region of TBE_{50} necessitates that one explicitly exclude energy deposition to marrow adipocytes located within 50 μm of the bone surfaces .

Changes to the 3DCBIST code (3D chord based radiation transport) were made to accommodate these modifications. Two major revisions included (1) allowing adipocytes within the TBE and (2) allowing for alpha particle emissions from within the entire TAM which is now inclusive of the TBE layer. Adipocytes were previously modeled, but changes to the endosteum transport algorithm were implemented to place the sampled endosteum chord within the marrow space. Thus, the alpha particle path is broken into sub-chords based upon the marrow cellularity and the sampled path. Prior to these revisions, this was only done for the TAM region. In Figure 1, we show how this modification is made where chord A-C represents an alpha emission in the TBE. Sub chord A-B represents the particle path through the endosteum layer. Another alteration to the transport algorithm occurs when the alpha particle leaves the endosteum and enters the deep marrow. Once the particle passes into the deep marrow, the sampled d_{MS} chord (B-C) is placed such that it starts, within the marrow sphere model, at the point where the endosteum chord (d_{E1} or A-B) ends. The same process is repeated when the marrow space chord ends and the exiting endosteum chord (d_{E2}) begins. Note that this may allow for the total path (sum of all three chords) to exit the marrow sphere model, which would not allow for energy deposition in fat once the chord exits the sphere. As a result of the short particle ranges of alpha particles at even the highest energy considered, this does not occur as the total energy deposited will always occur within the marrow sphere model due to the buffer region previously described[6]. Energy deposition is then tallied along the total particle path, regardless of which region

the alpha particle is traveling through, in both the active marrow and inactive marrow tissues of the marrow cavity.

A TAM source, as previously mentioned, allows for alpha particle emissions in the entire marrow cavity in regions outside the marrow adipocytes. To simulate this source region, the transport algorithm changes mentioned in the previous paragraph are slightly altered. Since the alpha particle may be emitted from d_{E1} , d_{MS} or d_{E2} , a correction must be made to the sampled source chord. Previous studies using chord-based transport have described methods for describing a volume source using an interior (I) random chord. Modifications to our tissue definitions require that the TAM source chord sampling of the I-random chord be limited to the sub-chord within the marrow cavity (d_{E1} , d_{MS} or d_{E2}). In Figure 2 this process is illustrated for emissions starting in (A) d_{E1} , (B) d_{MS} , and (C) d_{E2} . First, the total I-random chord length d_{MC} is sampled and then partitioned into sub-chords using the algorithm described in Watchman et al[6]. A random particle emission point along the total chord d_{MC} is then sampled as shown in Figure 2. A determination of which sub-chord the emission point occurs in is then made. The sub-chord is then revised, as the transport sub chord, based upon the emission point as illustrated in Figure 2. This algorithm allows for the alpha particle to be emitted uniformly within the TAM. Other source regions, TBV and TBS, are modeled as previously described.

Transport calculations were performed using chord length distributions from a 66-y old male and a series of third lumbar vertebrae obtained by the University of Leeds group for the following subjects; 25-y male, 44-y male, and three females 55-y, 70-y and 80-y. Details regarding the 66-y subject and chord acquisition methods are found in Shah et al.[ref – HP paper] Data regarding the lumbar vertebrae series can be found in Whitwell[32]. Three source regions, TAM, TBS and TBV were modeled along with five target regions ($TAM_{>50}$, TBE, $TIM_{<50}$, $TIM_{>50}$ and TBV). An endosteum thickness of 50

μm was used in the majority of simulations. Dosimetry changes in the endosteal dose were also investigated through a series of calculations in which the endosteum thickness was varied in 10 μm increments from 10 μm to 50 μm . Calculations were performed over the energy range of 0.5 MeV to 10.0 MeV with a marrow cellularity range of 100% to 10%. Each simulation was performed using one million histories to optimize data statistics. Simulations were made using 1-GHz Pentium V work stations in the Advanced Laboratory for Radiation Dosimetry Studies (ALRADS) located in Department of Nuclear and Radiological Engineering at the University of Florida. Maximum calculation times, for all source, of ~ 1.5 hours occurred for low marrow cellularity simulations of a TAM source. Once all absorbed fraction data were obtained, S-values were calculated for four α -emitting radionuclides of interest in MRT. Masses used to calculate the S-value were obtained by Shah[33] for the 10 μm endosteum thickness. For the 50 μm thick endosteum other data in Shah was used and modified using the methods of Watchman and Bolch[34] to calculate mass values at age specific marrow cellularities.

RESULTS

Absorbed fraction data were obtained for each of the bone sites listed in Shah[33] for the TAM, TBS and TBV sources over the energy range of 0.5 to 10 MeV. The lower energies were modeled to demonstrate the full behavior of alpha particles from radionuclides of interest in both medicine and radiological protection. Coefficients of variation (COV) were less than 1% for all targets irradiated by the TAM source. Primary targets also demonstrated COVs less than 1% for a TBV source. Secondary targets were $\leq 5\%$ for the same source. Greater variation in the COVs was seen for this source in the tertiary targets. COVs were largest at low energies, especially when the particle

range was less than the secondary target thickness and at low cellularities could vary by as much as 90% due to the reduced target volume. Except at the lowest energies (<2.5 MeV) COV values were $\leq 20\%$. Results for the TBS source also demonstrated very low COVs for primary targets (<1%). Secondary targets did have COVs of up to 10% at very low energy and low marrow cellularity. Note that when the secondary or tertiary target was TAM_D results for the TAM target combined the total results from TBE and TAM_{>50}. In these cases the COV was dominated by the TBE results and thus the TAM COV was low.

DISCUSSION

Variations in the Definition of the Trabecular Endosteum Thickness

The following results for each of the TAM, TBS and TBV sources are presented to demonstrate the effects of changes in the endosteum thickness on the energy deposition within the deep active marrow (TAM_D) and the trabecular endosteum (TBE). Following this section, results will only be presented for the TBE target as the radiation target. In Figure 3, results for a TAM source irradiating (A) the TAM_D and (B) the TBE are presented for the sixth cervical vertebrae at 100% marrow cellularity and are representative of other bone sites. The absorbed fraction profiles for the TAM_D demonstrate an increasing uniformity in the deep active marrow dose as a function of thickening endosteum. For a 10 μm endosteum, which is currently used, the absorbed fraction starts at ~ 0.93 (at 0.5 MeV) and falls off to ~ 0.89 (at 10 MeV). With the addition of the TBE results, the total TAM absorbed fraction starts at unity and decreases to 0.94. As the endosteum thickness is increased, the TAM_D results show a decrease in the degree to which the absorbed fraction falls off at increasing emission energies. At 50 μm , the deep marrow absorbed fraction profile is fairly uniform with a decrease of only

~0.01. Decreasing uniformity in the absorbed fraction, as a function of endosteum thickness, within the deep marrow is due to the fractional volume of active marrow encompassed by the endosteum. As the thickness of endosteum increases, fewer alpha particles emitted within the TAM_D region of the TAM have the ability to exit the marrow cavity. Those alpha particles emitted within the TBE region of the TAM, as a function of endosteum thickness, begin to reach a state of equilibrium where the relative number of particles exiting the deep marrow is balanced by those entering the deep marrow from the TBE.

In Figure 3B, this idea is further illustrated by the relative order of the absorbed fraction profiles. Data for the TAM_D show the 10 μm endosteum to have the highest absorbed fraction profile, while the 50- μm endosteum has the lowest. TBE results demonstrate the opposite relationship. Unlike the TAM_D results, the TBE results demonstrate a decrease in absorbed fraction over the entire energy range, although at 9-10 MeV the results for the 10- μm endosteum are relatively constant. Changes in the energy profiles are due to the fact that the endosteum is the region of the marrow cavity that is directly adjacent to the bone trabeculae. Consequently, this marrow region is where the alpha particle escape from the marrow cavity occurs. When the endosteum thickness is smallest, then the higher energy alpha particles have a greater probability of escaping the deep marrow region, as shown in Figure 3A. This results in a greater uniformity of the TBE results for the same endosteum thickness. Note that the summation of both the absorbed fraction to TAM_D and TBE at each endosteum thickness results in the same absorbed fraction profile. Thus, the absorbed fraction in the marrow cavity is the same and the sub-target absorbed fractions depend entirely upon the defined endosteum thickness.

Data for the TBS source as a function of endosteum thickness for the TAM_D and TBE are shown in Figure 4. At the top of each plot, values of $\phi(\text{TAM} \leftarrow \text{TBS})$ are included for comparison with each sub-target. Results for the TBE target demonstrate an increasing energy threshold for alpha particles to enter this tissue. Although a slight fraction of energy is deposited in this target as the thickness of endosteum increases, a distinct inflection point in the curves are seen for each thickness. The slight rise in the absorbed fraction to TAM_D is mirrored in the total TAM target and is a result of the increased probability for an alpha particle to enter the marrow cavity due to the marrow volume fraction in the spongiosa. In Fig. 4B the same inflection points are also seen for the TBE targets. Each of these inflection points coincide with the alpha particle energy dependant range and thickness of the endosteum. For example, the 50 μm endosteum curves demonstrate an inflection point at 6.5 MeV. An alpha particle of 6.5 MeV has a range of $\sim 52 \mu\text{m}$ in active bone marrow. At this energy the alpha particle has sufficient range to escape the endosteal layer (4B) and enter into the deep marrow (4A). These results mirror data in an unpublished report by Stather, Eckerman and Harrison[35].

Similar results to the TBS source are seen for the TBV source irradiating the deep marrow as shown in Figure 5A. Energy deposition into the deep marrow does not occur unless the alpha particle has sufficient energy to escape the TBE. Just as was the case with the TBS source the absorbed fraction is greatest in the 10 μm endosteum case due to the alpha particle range being greater than the endosteum thickness over the greatest range of energies. With the 50 μm endosteum, a significantly greater portion of the initial emission energy is deposited in the TBE as opposed to the TAM_D. Note that the total energy deposition in the marrow cavity stays the same for all endosteum thicknesses. Irradiation of the TBE from the TBV shows the opposite order of absorbed fraction profiles as compared to the deep marrow, as is expected.

Decreasing endosteum thickness (50 μm to 10 μm) shows an increasing separation between the relative thickness intervals. These differences are caused by the alpha particles having a greater relative fraction of their initial energy being deposited in the TBE as the endosteum thickens. For example, at 8 MeV, as a function of decreasing endosteum thickness, the fraction of the energy deposited in the next lower TBE thickness is 0.97, 0.92, 0.86 and 0.67.

Bone Site Variability

Variations in the TBE₅₀ dose as a function bone site are illustrated in Figure 6 for the cervical vertebrae, parietal bone and pelvis (os coxae) at 100% marrow cellularity. At this marrow cellularity, only microstructural differences determine differences in the absorbed fraction. Absorbed fraction profiles for the TAM source irradiating the TBE₅₀ target are shown in Fig 6A. An absolute variation of ~ 0.05 occurs between the parietal bone and the cervical vertebrae. The pelvis demonstrates a profile which is significantly lower than the other two bone sites. It also has a different shape along the energy range. A comparison of the average chord lengths or nominal cavity sizes, as presented by Shah[33], easily explains these differences. Marrow cavities in the parietal bone were shown to be smaller than both the cervical vertebrae and os coxae, with the latter having the largest cavities. The order of the absorbed fraction profiles mirrors the average chord lengths such that alpha particle energy deposition is highest in the parietal bone (smallest cavities) and lowest in the os coxae (largest cavities). As cavity size increases the relative volume of that cavity occupied by the endosteal space decreases. Consequently, fewer alpha particles are either emitted from or enter into the TBE₅₀, which results in a smaller absorbed fraction in this target. Conversely, the smaller cavities of the parietal bone result in a greater fraction of emissions occurring within the endosteum. Other differences in the absorbed fraction profiles, i.e. shape, are

attributable to the not only the size of the cavity but also to the shape of the chord length distribution from which the geometry was sampled.

Much less variation is seen between these three bone sites for the TBS source and TBE₅₀ target. Similar minor variations were also seen for results of the TBE₁₀ (10 μm thick endosteum) from Watchman et al[6]. Relative uniformity in the absorbed fraction is due to the fact that most marrow cavities in all bone sites tend to be larger than 100 μm (entry and exit endosteum layers). In fact an average marrow cavity is on the order of ~ 1000 μm and thus an alpha particle being emitted from the bone surface tends to only see the initial endosteal layer as it travels into the marrow cavity. Since the endosteum is modeled as a function of the marrow cavity chord length distribution, in general little to no variation in the absorbed fraction should occur. Differences in the parietal bone results occur because the secondary variable of the chord length distribution plays a larger role since the average chord in this bone site is significantly smaller than the others.

The TBV source also demonstrates bone site dependence in the absorbed fraction to the TBE₅₀ which is ~ 2.5 times greater than for the TBE₁₀ results of Watchman et al[6]. In Figure 6C the parietal bone is shown to have the lowest absorbed fraction due to this bone site having significantly thicker than average bone trabeculae as was measured by Shah et al.. The cervical vertebrae results were greater than those of the os coxae. Average bone trabeculae thickness does not account for the differences as the average chord length measured in both these bones was ~ 280 μm . Differences occur due to the marrow cavities sizes where the smaller cavities in the cervical vertebrae result in a greater fraction of the total energy deposited in the marrow cavity being deposited in the endosteum. The os coxae, on the other hand, has a significantly larger average marrow cavity chord (1523 μm vs. 1038 μm) that results in a greater fraction of the emitted

energy being deposited in the deep marrow. Consequently, the os coxae TBE₅₀ dose is less than the smaller cavity cervical vertebrae.

Variation Due to Marrow Cellularity

In Watchman et al[6], alpha-particle absorbed fractions in the skeletal tissues were shown to be highly dependant on bone marrow cellularity. No marrow cellularity dependence was demonstrated in the endosteum target for the TBV and TBS sources, which was due to the definition of TBE₁₀. When TBE₁₀ irradiation occurred from a TAM source marrow, a marrow cellularity dependence was seen. With the increased endosteum thickness, used in this study, TAM results will not be affected significantly but absorbed fractions for the TBE₅₀ are now shown to be marrow cellularity dependant for all sources. Figure 7 presents TBE absorbed fraction results from (A) TAM source, (B) TBE source and (C) TBV source in the cervical vertebrae. Data for the TAM source in Fig. 7A exhibits large variation in absorbed fraction as a function of marrow cellularity. At 8 MeV that absorbed fraction at 10% and 50% cellularity are respectively factors of 3.64 and 1.61 times smaller than at 100% marrow cellularity. Results from Watchman et al. for the same source/target combination demonstrated similar ratios as a function of energy. The major change resulting from the increased endosteum thickness is the magnitude of the absorbed fraction. In this study, a 5-MeV alpha particle has an absorbed fraction of 0.199 at 50% cellularity in the TBE₅₀ of the cervical vertebrae. The previously mentioned study reported a value of 0.0163 for a TBE₁₀ target in the same bone site. Note that the data were obtained using chord lengths from two different individuals and as such the value of the absorbed fractions will be different. Despite this, the major issue is that the 50 μ m endosteum has an absorbed fraction that is an order of magnitude larger than given by a 10- μ m endosteum for a TAM source.

As was previously mentioned, the original definition of the trabecular endosteum defined this target tissue as an adipose-free 10- μm layer on the bone trabeculae surfaces. Absorbed fractions were thus independent of marrow cellularity. In Figure 7B data for the TBS source and the TBE target are shown to vary with marrow cellularity. Several points of interest are illustrated in this plot. First, the absorbed fraction varies relatively linearly as a function of marrow cellularity over each energy within the energy spectrum. Second, at high cellularities ($\geq 60\%$) the absorbed fraction begins to decrease at 6.5 MeV and is due to the alpha particles having sufficient range to escape the 50 μm TBE. At lower marrow cellularities, this drop in absorbed fraction begins to disappear and the absorbed fraction profiles become more uniform across the energy range. Alpha particles traversing the endosteum at the lower marrow cellularities start to have a more homogeneous probability of depositing energy in adipocytes contained within the TBE₅₀. Even as the energy of the alpha particles is increasing, and consequently their range, the relative fraction of energy deposited in the TBE₅₀ is very similar. Comparison of the scale of the absorbed fraction axis in Fig. 7B with previous results demonstrates an order of magnitude difference at low marrow cellularities with the TBE₅₀ results being smaller than the TBE₁₀. At 100% cellularity, no significant difference is seen in the 50 μm vs. 10 μm endosteum doses until alpha particles are able to escape the TBE₁₀. The thicker endosteum of the TBE₅₀ allows for greater energy deposition and thus a higher absorbed fraction than does the TBE₁₀. A ratio of the TBE₅₀ and TBE₁₀ at 8 MeV shows the thicker endosteum target to have a dose 2.6 times greater than the other.

Unlike the TBS source, data for the TBV source do demonstrate noteworthy variations in absorbed fraction as both a function of energy and marrow cellularity. In Figure 7C, the absorbed fraction at 100% cellularity and at 10 MeV is 0.138 where as the TBE₁₀ from Watchman et al[6] is 0.0637. The thicker endosteum results in an

absorbed fraction that is ~2 times greater. When marrow cellularity is accounted for, the 10 MeV value at 10% cellularity is 0.0178 which is approximately an order of magnitude smaller than the 100% case and 3.6 times smaller than the TBE₁₀ scenario. Further variations in the absorbed fraction due to decreasing marrow cellularity are seen in Fig. 7C in the fact that the slope of the absorbed fractions as a function of energy decreases with decreasing marrow cellularity.

Inter Subject Variability

Table 2 presents ratios of the absorbed fraction to the TBE₅₀ for four subjects within the third lumbar vertebrae[32] with respect to their values in the ICRP 44-y reference male. This table is similar to Table 4 of Watchman et al except only the TBE₅₀ results are shown. Values in the table represent results at 100% marrow cellularity; therefore the differences in absorbed fractions are due only to microstructure. Data in this study showed almost identical results for the total average ratio of all three sources. Unlike the previous study results for the 10 μ m endosteum less diversity over the energy range was seen in each subject for the larger endosteum thickness. Greater uniformity is due to the larger endosteum thickness, which decreases the probability of alpha particle escape from the endosteum. Individual subject variations, as a function of energy, in absorbed fraction were lower for TBE₅₀ than for TBE₁₀ results previously reported for a TAM source. For the TBS and TBV sources, similar individual variations are seen over the energy range for both the TBE₅₀ and TBE₁₀ results.

Dosimetric Consequences of a 50 μ m Trabecular Endosteum

The implementation of a 50- μ m endosteum target is easily made and the data shown has demonstrated significant differences in the absorbed fractions as a function of energy, bone site, subject, and marrow cellularity. Absorbed fraction does not

illustrate the entire ramifications of a thicker endosteum. To fully understand the consequences with regards to the entire dose calculation of the S-value must be looked at. Using the absorbed fraction data and the decay schemes for several alpha emitters of interest in molecular radiotherapy, radionuclide S-values (mGy/MBq-s) are presented in Table 3 for three bone sites at ICRP reference marrow cellularities[36]. Mass terms used to generate these values were obtained for the UF 66-y male as listed in Shah[33]. S-values for the TAM, TBS and TBV sources are shown for both a 10 μm endosteum and a 50 μm endosteum at the ICRP reference marrow cellularities. Values of 0.7, 0.48 and 0.38 were used for the cervical vertebrae, os coxae and parietal bone respectively. For the 10- μm endosteum target, no adipocytes were allowed to be within the endosteum in concert with the current ICRP definition of the trabecular endosteum.

Inspection of Table 3 shows that in all cases, excluding the $\phi(\text{TBE} \leftarrow \text{TAM})$ in the parietal bone, the S-values are smaller for the thicker endosteum case. Both the increased thickness of the target and the inclusion of adipocytes in the TBE_{50} contribute to these results. Increased thickness in the endosteum produces a larger volume over which the dose is averaged. Despite the increased volume of the target region, the absorbed fraction does not increase in direct proportion. While the increased volume of the target region is evident, this volume is reduced due to the marrow cellularity factor. Consequently, target volume (mass) is smaller than the total volume of soft tissue 50 μm from the bone surface though the total mass over which the absorbed fraction is averaged is still significantly larger than that currently prescribed by the ICRP.

Differences in the parietal bone S-values as compared to the others are a result of the smaller marrow cavities seen in the parietal bone. Smaller cavities allow for a smaller total volume of soft tissue in the marrow cavities in general and specifically in the TBE_{50} space. Table 4 presents mass terms used in the calculation of these S-values.

Changes in the total mass in the parietal bone are much smaller than in the other two bone sites. Not only do the small marrow cavities contribute to this but the lower cellularity factor (0.38 vs. 0.48 or 0.7) further enhances this effect. Notwithstanding the thicker endosteum volume of the TBE₅₀, averaging the absorbed fraction across both TBE targets results in an S-value that is slightly larger ($\leq 6\%$) for the TBE₅₀ target.

Results found in these S-value calculations hold profound significance in dosimetry calculation and in the understanding of the effect alpha particles have to cause tissue damage. In determining the tissue weighting factor for endosteum, current estimates are based upon the ICRP definition of the endosteum target being a layer of cells 10 μm from the bone surfaces. Under the revised 50 μm definition the lower S-values result in a lower absorbed dose to the tissue of interest. As previously mentioned, there is increasing evidence for the thicker endosteum region being the site of bone cancer induction. This increased incidence means that the lower S-values calculated in this study result in smaller dose to these tissues. As a result, lower doses than previously calculated are resulting in bone cancer induction. If this is true, then the currently defined tissue weighting factor for endosteum of 0.01, from ICRP 60[37], might need to be re-addressed by the ICRP.

CONCLUSION

In response to the increasing body of evidence that irradiation of osteoprogenitor cells within a distance of 50 μm from bone surfaces is relevant to bone cancer induction, this study into the dosimetry consequences of this tissue definition has been presented. This study has shown results for absorbed fractions calculated using 3D-CBIST for a 50 μm endosteum target. Results obtained for both the UF 66-y male subject and five third lumbar vertebrae from the University of Leeds were presented. Data obtained in this

study has demonstrated significant differences in alpha particle absorbed fractions for the TBE_{50} in comparison to the TBE_{10} as a function of bone site, individual, marrow cellularity and changes endosteum thickness. Results from this study also show that using the current definition of endosteum results in over-estimates of the total dose to sensitive tissues with respect to bone cancer induction. Further research is warranted in better describing the spatial distribution of osteoprogenitor tissues within the marrow cavities.

REFERENCES

1. ICRP, *Publication 11: A Review of the Radiosensitivity of Tissues in Bone*. 1967, International Commission on Radiological Protection.
2. ICRP, *ICRP Publication 26: Recommendations of the International Commission on Radiological Protection*. 1977.
3. Eckerman, K.F. and M.G. Stabin, *Electron absorbed fractions and dose conversion factors for marrow and bone by skeletal regions*. Health Phys, 2000. 78(2): p. 199-214.
4. Bouchet, L.G., D.W. Jokisch, and W.E. Bolch, *A three-dimensional transport model for determining absorbed fractions of energy for electrons within trabecular bone*. J Nucl Med, 1999. 40(11): p. 1947-66.
5. Jokisch, D., *Beta particle dosimetry of the trabecular region of a thoracic vertebra utilizing NMR microscopy*, in *Nuclear and Radiological Engineering*. 1999, University of Florida: Gainesville, Florida. p. 235.
6. Watchman, C.J., et al., *Absorbed Fractions for Alpha Particles in Tissues of Trabecular Bone: Considerations of Marrow Cellularity within the ICRP Reference Male*. J Nucl Med, 2005. 46(7): p. 1171-85.
7. Shah, A.P., et al., *A paired-image radiation transport model for skeletal dosimetry*. J Nucl Med, 2005. 46(2): p. 344-53.
8. Gossner, W., *Target cells in internal dosimetry*. Radiat Prot Dosimetry, 2003. 105(1-4): p. 39-42.
9. Gossner, W., R. Masse, and J. Stather, *Cells at Risk For Dosimetric Modelling Relevant to Bone Tumor Induction*. Radiat Prot Dosim, 2000. 92(1-3): p. 209-213.
10. McDevitt, M.R., et al., *An $^{225}\text{Ac}/^{213}\text{Bi}$ generator system for therapeutic clinical applications: construction and operation*. Appl Radiat Isot, 1999. 50(5): p. 895-904.
11. McDevitt, M.R., et al., *An alpha-particle emitting antibody (^{213}Bi -J591) for radioimmunotherapy of prostate cancer*. Cancer Res, 2000. 60(21): p. 6095-100.
12. Ranson, M., et al., *In vitro cytotoxicity of bismuth-213 (^{213}Bi)-labeled-plasminogen activator inhibitor type 2 (alpha-PAI-2) on human breast cancer cells*. Breast Cancer Res Treat, 2002. 71(2): p. 149-59.
13. Sgouros, G., et al., *Pharmacokinetics and dosimetry of an alpha-particle emitter labeled antibody: ^{213}Bi -HuM195 (anti-CD33) in patients with leukemia*. J Nucl Med, 1999. 40(11): p. 1935-46.
14. Geerlings, M.W., et al., *The feasibility of ^{225}Ac as a source of α -particles in radioimmunotherapy*. Nucl. Med. Commun., 1993. 14: p. 121-125.
15. Henriksen, G., et al., *Targeting of osseous sites with alpha-emitting ^{223}Ra : comparison with the beta-emitter ^{89}Sr in mice*. J Nucl Med, 2003. 44(2): p. 252-9.
16. Humm, J.L., *A microdosimetric model of astatine-211 labeled antibodies for radioimmunotherapy*. Int. J. Radiation Oncology Biol. Phys., 1987. 13: p. 1767-1773.
17. Huneke, R.B., et al., *Effective α -particle-mediated radioimmunotherapy of murine leukemia*. Cancer Res., 1992. 52: p. 5818-5820.
18. Kotz, D., *Alpha particle therapy poised to become new line of cancer treatment*. J Nucl Med, 1998. 39(2): p. 17N-19N, 36N.
19. Kvinnsland, Y., T. Stokke, and E. Aurlien, *Radioimmunotherapy with alpha-particle emitters: microdosimetry of cells with a heterogeneous antigen expression and with various diameters of cells and nuclei*. Radiat Res, 2001. 155(2): p. 288-96.
20. Kurtzman, S.H., et al., *Bismuth-212 linked to an antipancreatic carcinoma antibody: Model for alpha-particle-emitter radioimmunotherapy*. J. Natl. Cancer. Inst., 1988. 80: p. 449-452.
21. Larsen, R.H., et al., *^{211}At - and ^{131}I -labeled bisphosphonates with high in vivo stability and bone accumulation*. J Nucl Med, 1999. 40(7): p. 1197-203.
22. Larsen, R.H., et al., *The cytotoxicity and microdosimetry of astatine-211-labeled chimeric monoclonal antibodies in human glioma and melanoma cells in vitro*. Radiat Res, 1998. 149(2): p. 155-62.

23. McDevitt, M.R., et al., *Radioimmunotherapy with alpha-emitting nuclides*. Eur J Nucl Med, 1998. 25(9): p. 1341-51.
24. Roeske, J.C. and T.G. Stinchcomb, *Dosimetric framework for therapeutic alpha-particle emitters*. J Nucl Med, 1997. 38(12): p. 1923-9.
25. Roeske, J.C. and T.G. Stinchcomb, *The use of microdosimetric moments in evaluating cell survival for therapeutic alpha-particle emitters*. Radiat Res, 1999. 151(1): p. 31-8.
26. Roeske, J.C. and T.G. Stinchcomb, *Tumor control probability model for alpha-particle-emitting radionuclides*. Radiat Res, 2000. 153(1): p. 16-22.
27. Sgouros, G., *Long-lived alpha emitters in radioimmunotherapy: the mischievous progeny*. Cancer Biother Radiopharm, 2000. 15(3): p. 219-21.
28. Stinchcomb, T.G. and J.C. Roeske, *Analytic microdosimetry for radioimmunotherapeutic alpha emitters*. Med Phys, 1992. 19(6): p. 1385-93.
29. Stinchcomb, T.G. and J.C. Roeske, *Values of "S," $\langle z_1 \rangle$, and $\langle (z_1)^2 \rangle$ for dosimetry using alpha-particle emitters*. Med Phys, 1999. 26(9): p. 1960-71.
30. Zalutsky, M.R., et al., *Radioimmunotherapy of neoplastic meningitis in rats using an alpha- particle-emitting immunoconjugate*. Cancer Res, 1994. 54(17): p. 4719-25.
31. Zalutsky, M.R. and G. Vaidyanathan, *Astatine-211-labeled radiotherapeutics: an emerging approach to targeted alpha-particle radiotherapy*. Curr Pharm Des, 2000. 6(14): p. 1433-55.
32. Whitwell, J.R., *Theroetical Investigations of Energy Loss by Ionizing Particles in Bone*. 1973, University of Leeds: Leeds.
33. Shah, A.P., *Reference Skeletal Dosimetry Model for an Adult Male Radionuclide Therapy Patient Based on 3D Imaging and Paired Image Radiation Transport*, in *Biomedical Engineering*. 2004, University of Florida: Gainesville.
34. Watchman, C. and W. Bolch, *Derivations of Skeletal Masses in the Current ICRP Age Series: Considerations of a 10 micrometer and 50 micrometer Endosteum*. Phys Med Biol, 2005. in preparation.
35. Stather, J., K.F. Eckerman, and J. Harrison, *Dosimetric Modeling Relevant to Stem Cells at Risk for Bone Tumor Induction*. 2003.
36. ICRP, *ICRP No. 89: Basic Anatomical and Physiological Data for Use In Radiological Protection: Reference Values*. 2003, International Commission on Radiological Protection: Oxford.
37. ICRP, *1990 Recommendations of the International Commission on Radiological Protection*. 1990, International Commission on Radiological Protection: Oxfore. p. 201.

Table 1. Descriptions and definitions of tissue used in this study.

Tissue	Acronym	Description
Trabecular Bone Endosteum	TBE_x	All non-adipose soft tissues within distance x (in mm) of the bone trabeculae surfaces. The current ICRP definition would thus be TBE_{10} defining a 10- μ m cell layer. The proposed definition would be TBE_{50} defining a 50- μ m layer of trabecular endosteum.
Deep Active Marrow	TAM_D	Hematopoietically active marrow at distances beyond x μ m of the bone trabeculae surfaces, where x defines the thickness of the trabecular bone endosteum.
Shallow Active Marrow	TAM_S	Hematopoietically active marrow at distances within x μ m of the bone trabeculae surfaces, where x defines the thickness of the trabecular bone endosteum. TAM_S is thus equivalent to TBE_x .
Trabecular Active Marrow	$TAM = TAM_D + TAM_S$	All non-adipose soft tissues of the marrow cavities. Equivalent to the dosimetry term "red marrow".
Deep Inactive Marrow	TIM_D	Marrow adipocytes at distances beyond x μ m of the bone trabeculae surfaces
Shallow Inactive Marrow	TIM_S	Marrow adipocytes at distances within x μ m of the bone trabeculae surfaces
Trabecular Inactive Marrow	$TIM = TIM_D + TIM_S$	All adipose tissue within the marrow cavities. Equivalent to the dosimetry term "yellow marrow"
Trabecular Bone Volume	TBV	Osseous tissues within the trabecular spongiosa (i.e., the trabeculae)

Table 2. Ratios of absorbed fractions from TAM, TBS and TBV sources irradiating the TBE of a 66-y male subject.

$\phi(\text{TBE} \leftarrow \text{TAM})$					
Energy (MeV)	25-y Male 44-y Male	55-y Female 44-y Male	70-y Female 44-y Male	85-y Female 44-y Male	Average
0.5	1.16	1.19	1.03	1.16	1.14
1	1.15	1.19	1.03	1.16	1.13
1.5	1.15	1.19	1.03	1.16	1.13
2	1.15	1.19	1.03	1.16	1.13
2.5	1.15	1.19	1.03	1.16	1.13
3	1.15	1.19	1.03	1.16	1.13
3.5	1.15	1.19	1.03	1.16	1.13
4	1.15	1.19	1.03	1.16	1.13
4.5	1.15	1.19	1.03	1.15	1.13
5	1.15	1.19	1.04	1.16	1.13
5.5	1.14	1.19	1.03	1.15	1.13
6	1.15	1.18	1.02	1.15	1.13
6.5	1.15	1.19	1.03	1.16	1.13
7	1.14	1.18	1.03	1.15	1.12
7.5	1.14	1.18	1.03	1.15	1.13
8	1.15	1.18	1.03	1.15	1.13
8.5	1.15	1.19	1.03	1.14	1.13
9	1.15	1.18	1.03	1.15	1.13
9.5	1.15	1.19	1.03	1.15	1.13
10	1.14	1.18	1.03	1.15	1.13
Average:					1.13
$\phi(\text{TBE} \leftarrow \text{TBV})$					
Energy (MeV)	25-y Male 44-y Male	55-y Female 44-y Male	70-y Female 44-y Male	85-y Female 44-y Male	Average
0.5	0.99	1.16	1.09	1.27	1.13
1	0.98	1.14	1.06	1.22	1.10
1.5	1.00	1.19	1.09	1.25	1.13
2	1.00	1.17	1.07	1.24	1.12
2.5	0.98	1.15	1.07	1.24	1.11
3	0.98	1.16	1.07	1.24	1.11
3.5	0.98	1.16	1.07	1.23	1.11
4	0.99	1.17	1.08	1.24	1.12
4.5	1.00	1.17	1.09	1.26	1.13
5	0.98	1.15	1.07	1.23	1.11
5.5	0.98	1.16	1.08	1.24	1.11
6	1.00	1.17	1.08	1.25	1.12
6.5	0.99	1.17	1.07	1.24	1.12
7	0.99	1.15	1.07	1.23	1.11
7.5	0.99	1.16	1.08	1.24	1.12
8	0.99	1.15	1.07	1.23	1.11
8.5	1.00	1.16	1.07	1.24	1.12
9	0.99	1.15	1.07	1.23	1.11
9.5	0.99	1.15	1.07	1.24	1.11
10	1.00	1.15	1.07	1.23	1.11
Average:					1.12

Table 2 (continued)

$\phi(\text{TBE} < -\text{TBS})$					
Energy (MeV)	<u>25-y Male</u> 44-y Male	<u>55-y Female</u> 44-y Male	<u>70-y Female</u> 44-y Male	<u>85-y Female</u> 44-y Male	Average
0.5	1.00	1.00	1.00	1.00	1.00
1	1.00	1.00	1.00	1.00	1.00
1.5	1.00	1.00	1.00	1.00	1.00
2	1.00	1.00	1.00	1.00	1.00
2.5	1.00	1.00	1.00	1.00	1.00
3	1.00	1.00	1.00	1.00	1.00
3.5	0.99	0.99	1.00	1.00	1.00
4	0.99	0.99	1.00	1.00	0.99
4.5	0.99	0.99	1.00	1.00	0.99
5	0.99	0.99	1.00	0.99	0.99
5.5	0.99	0.99	1.00	0.99	0.99
6	0.99	0.99	1.00	0.99	0.99
6.5	0.99	0.99	1.00	0.99	0.99
7	0.99	1.00	1.00	1.00	0.99
7.5	0.99	1.00	1.00	1.00	1.00
8	0.98	1.00	1.00	1.00	1.00
8.5	0.99	1.01	1.00	1.01	1.00
9	0.98	1.01	1.00	1.01	1.00
9.5	0.98	1.02	1.00	1.01	1.01
10	0.99	1.03	1.01	1.02	1.01
Average:					1.00

Table 3. S-values (mGy/MBq-s) for the cervical vertebrae, parietal bone and os coxae of a 66-y male subject for ^{211}At , ^{212}Bi , ^{213}Bi and ^{223}Ra .

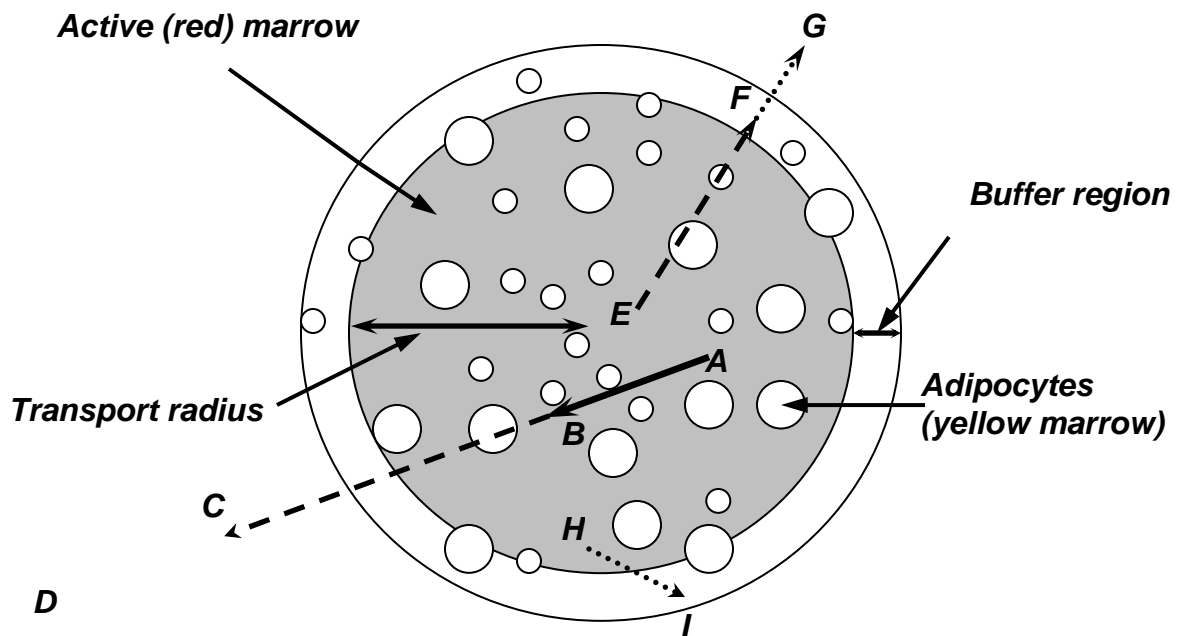
Cervical Vertebrae						
Radionuclide	10 μm			50 μm		
	$S(TBE \leftarrow TAM)$	$S(TBE \leftarrow TBS)$	$S(TBE \leftarrow TBV)$	$S(TBE \leftarrow TAM)$	$S(TBE \leftarrow TBS)$	$S(TBE \leftarrow TBV)$
^{211}At	2.68E-02	9.40E-02	2.43E-02	2.36E-03	4.03E-03	6.86E-04
^{212}Bi	3.00E-02	8.02E-02	3.09E-02	2.38E-03	4.46E-03	9.84E-04
^{213}Bi	3.14E-02	9.76E-02	3.48E-02	2.36E-03	4.73E-03	1.15E-03
^{223}Ra	1.06E-01	3.57E-01	9.34E-02	1.82E-03	9.67E-03	2.57E-03
Parietal Bone						
Radionuclide	10 μm			50 μm		
	$S(TBE \leftarrow TAM)$	$S(TBE \leftarrow TBS)$	$S(TBE \leftarrow TBV)$	$S(TBE \leftarrow TAM)$	$S(TBE \leftarrow TBS)$	$S(TBE \leftarrow TBV)$
^{211}At	1.32E-02	4.01E-02	1.32E-02	1.40E-02	1.70E-02	1.70E-02
^{212}Bi	1.47E-02	3.96E-02	7.59E-03	1.49E-02	1.89E-02	2.58E-03
^{213}Bi	1.54E-02	3.79E-02	8.69E-03	1.50E-02	2.01E-02	3.01E-03
^{223}Ra	5.23E-02	1.63E-01	2.29E-02	5.59E-02	6.69E-02	6.71E-03
Os Coxae						
Radionuclide	10 μm			50 μm		
	$S(TBE \leftarrow TAM)$	$S(TBE \leftarrow TBS)$	$S(TBE \leftarrow TBV)$	$S(TBE \leftarrow TAM)$	$S(TBE \leftarrow TBS)$	$S(TBE \leftarrow TBV)$
^{211}At	2.36E-03	4.10E+00	2.97E-03	1.26E-03	1.26E-03	1.80E-04
^{212}Bi	2.64E-03	1.22E-02	3.78E-03	5.50E-04	4.42E-03	2.60E-04
^{213}Bi	2.78E-03	1.19E-02	4.25E-03	5.63E-04	1.50E-03	3.03E-04
^{223}Ra	2.32E-02	4.96E-02	1.14E-02	2.03E-03	4.98E-03	6.75E-04

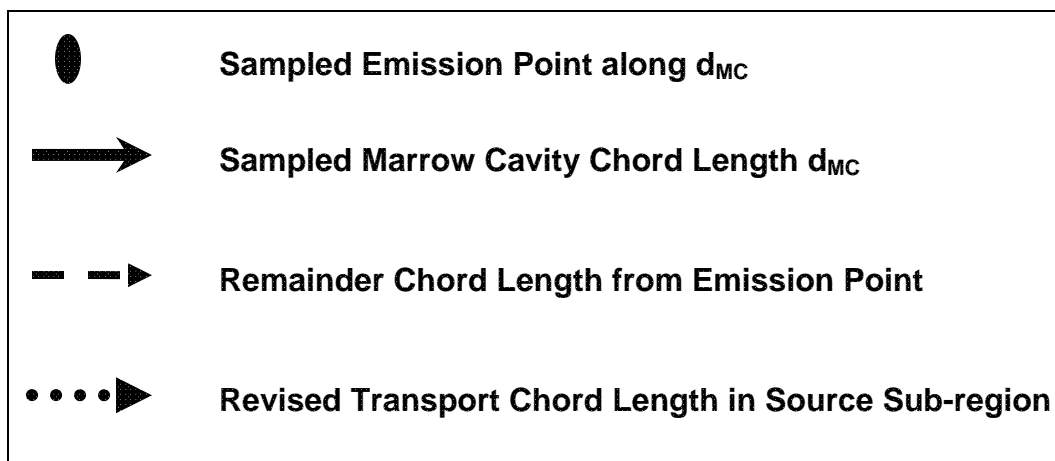
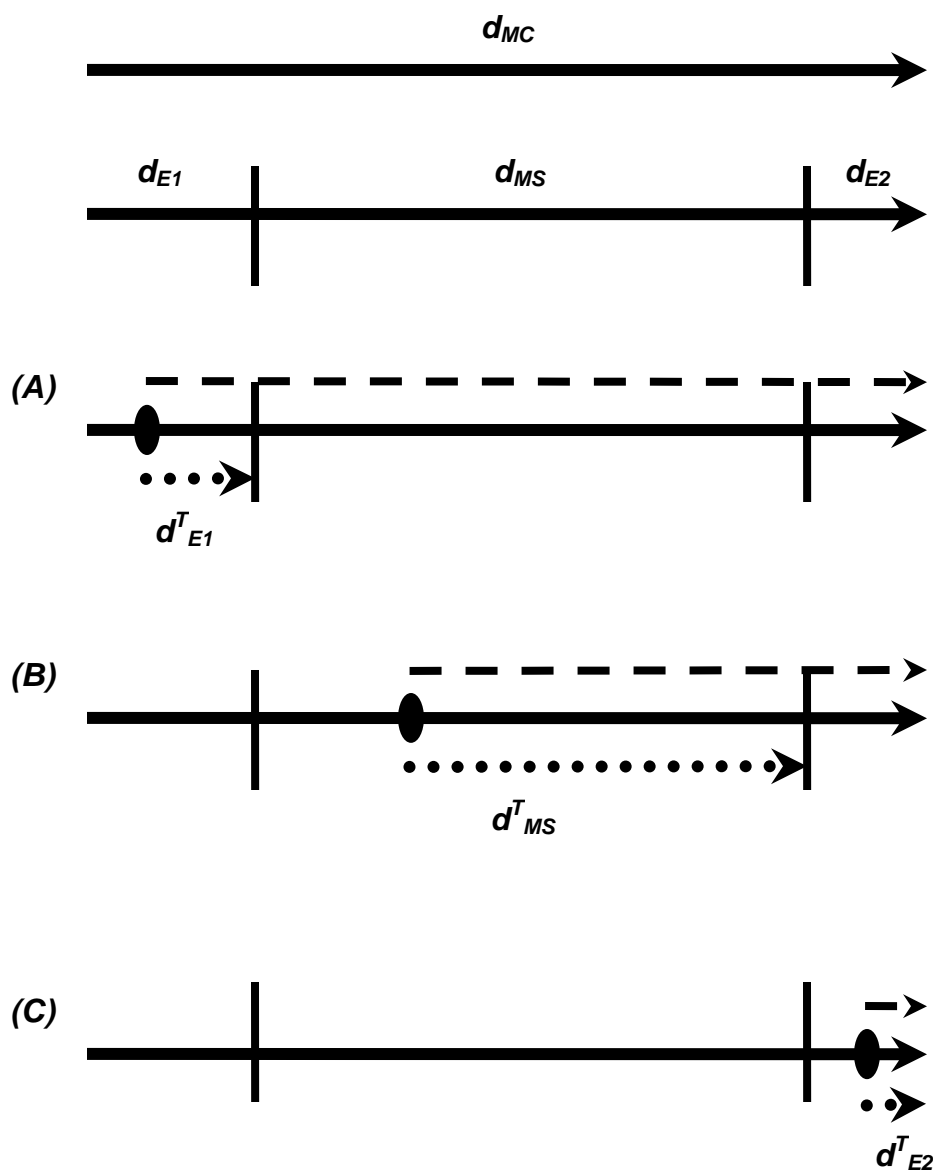
Table 4. Endosteum masses at 10 μm and 50 μm thickness in a 66-y male at reference marrow cellularities

<i>Mass (g)</i>			
TBE (μm)	CV	IC	PB
10	2.2	18.3	5.5
50	93.9	209.8	12.4

Figures

- Figure 1.** Diagram illustrating the placement of sampled chords occurring in the first endosteum region (A-C), deep marrow space (E-G) and second endosteum region (H-I).
- Figure 2.** Illustration of how the sampled marrow cavity chord (d_{MC}) is sampled for an active marrow source.
- Figure 3.** Plots showing the absorbed fraction in the sixth cervical vertebrae in a 66-y male for a TAM source as a function of endosteum thickness in (A) $TAM_{>50}$ and (B) TBE.
- Figure 4.** Plots showing the absorbed fraction in the sixth cervical vertebrae in a 66-y male for a TBS source as a function of endosteum thickness in (A) $TAM_{>50}$ and (B) TBE.
- Figure 5.** Plots showing the absorbed fraction in the sixth cervical vertebrae in a 66-y male for a TBV source as a function of endosteum thickness in (A) $TAM_{>50}$ and (B) TBE.
- Figure 6.** Diagrams illustrating the variation in TBE absorbed fractions as function of bone site in the cervical vertebrae, os coxae and parietal bone of a 66-y male for a (A) TAM source, (B) TBS source and (C) TBV source.
- Figure 7.** Diagrams illustrating the variation in TBE absorbed fractions as function of marrow cellularity in the cervical vertebrae of a 66-y male for a (A) TAM source, (B) TBS source and (C) TBV source.





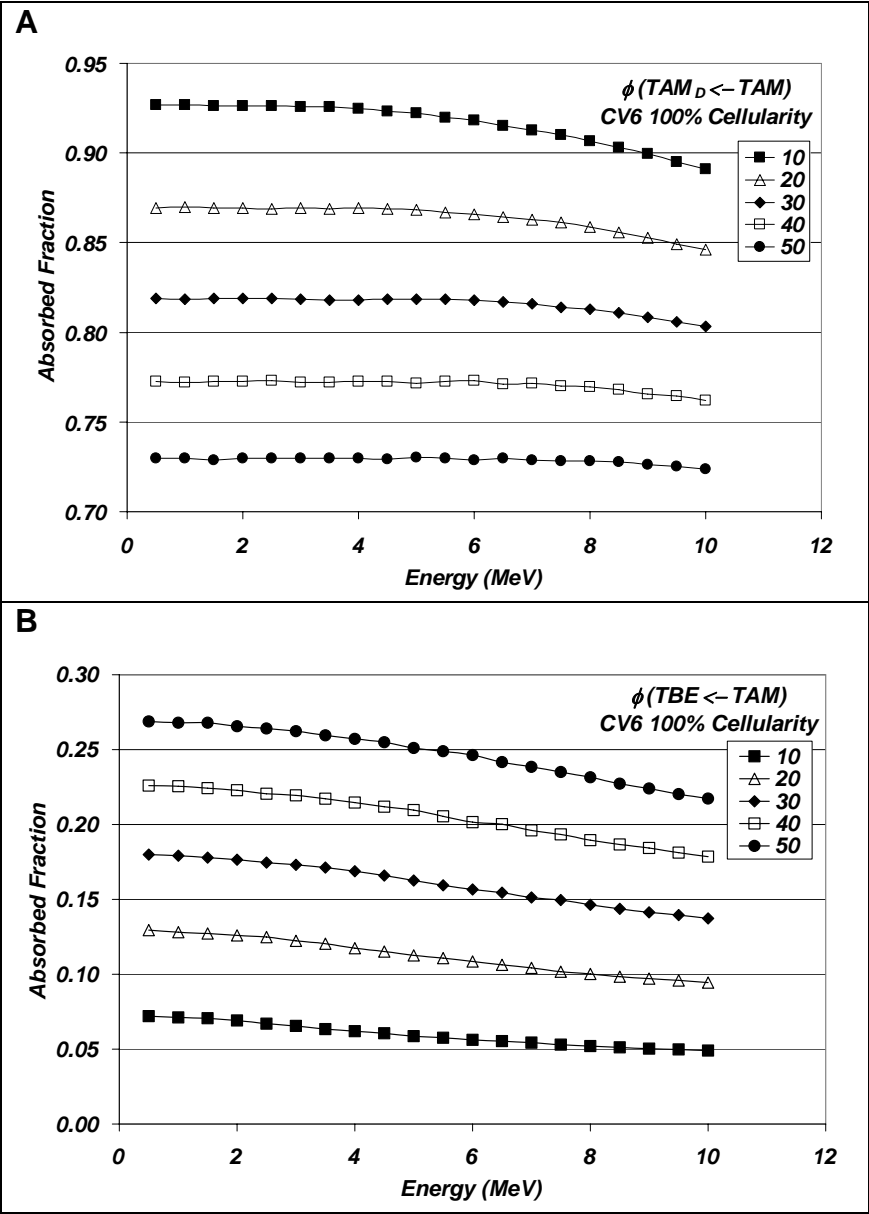


Figure 3

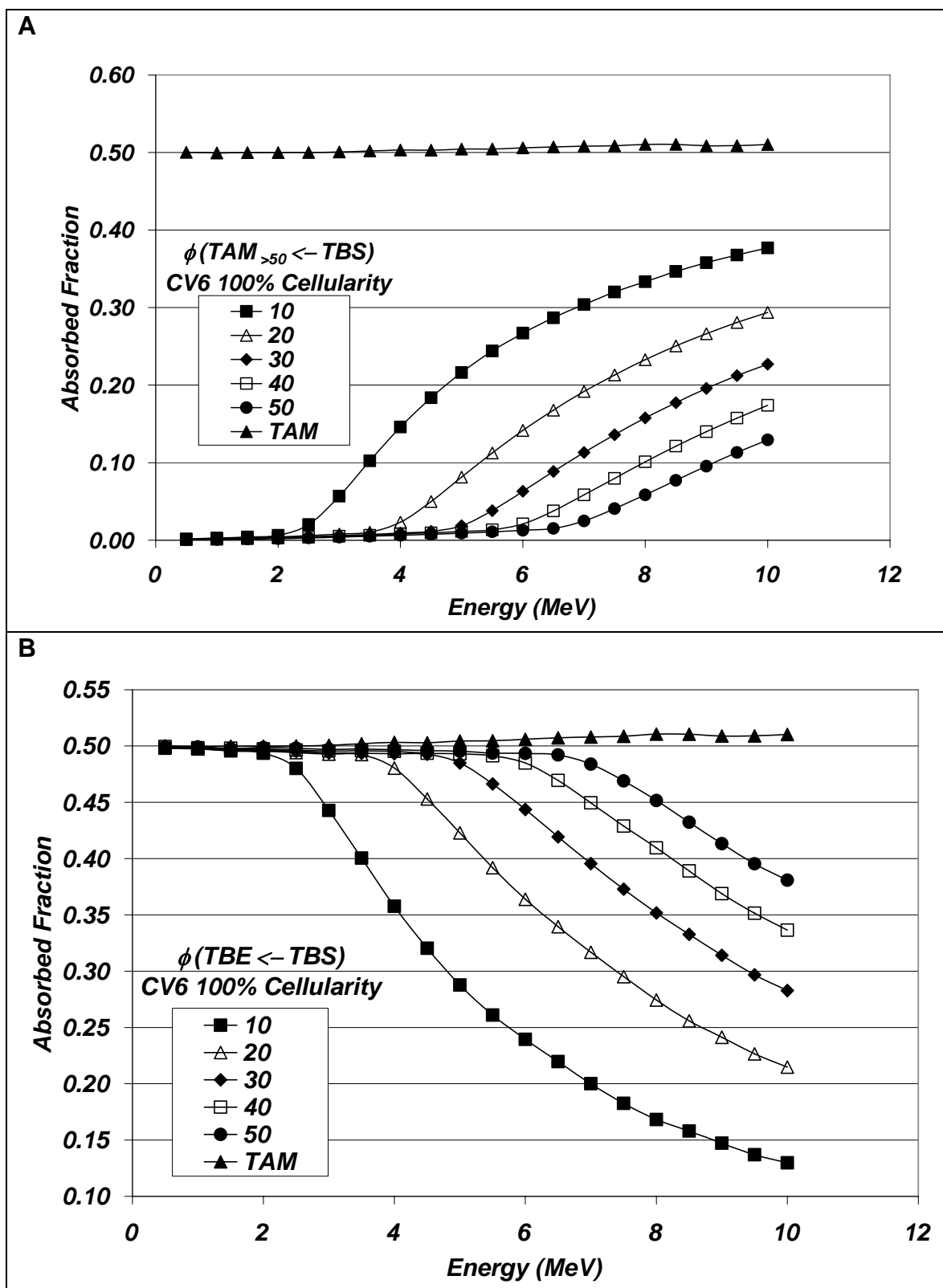


Figure 4

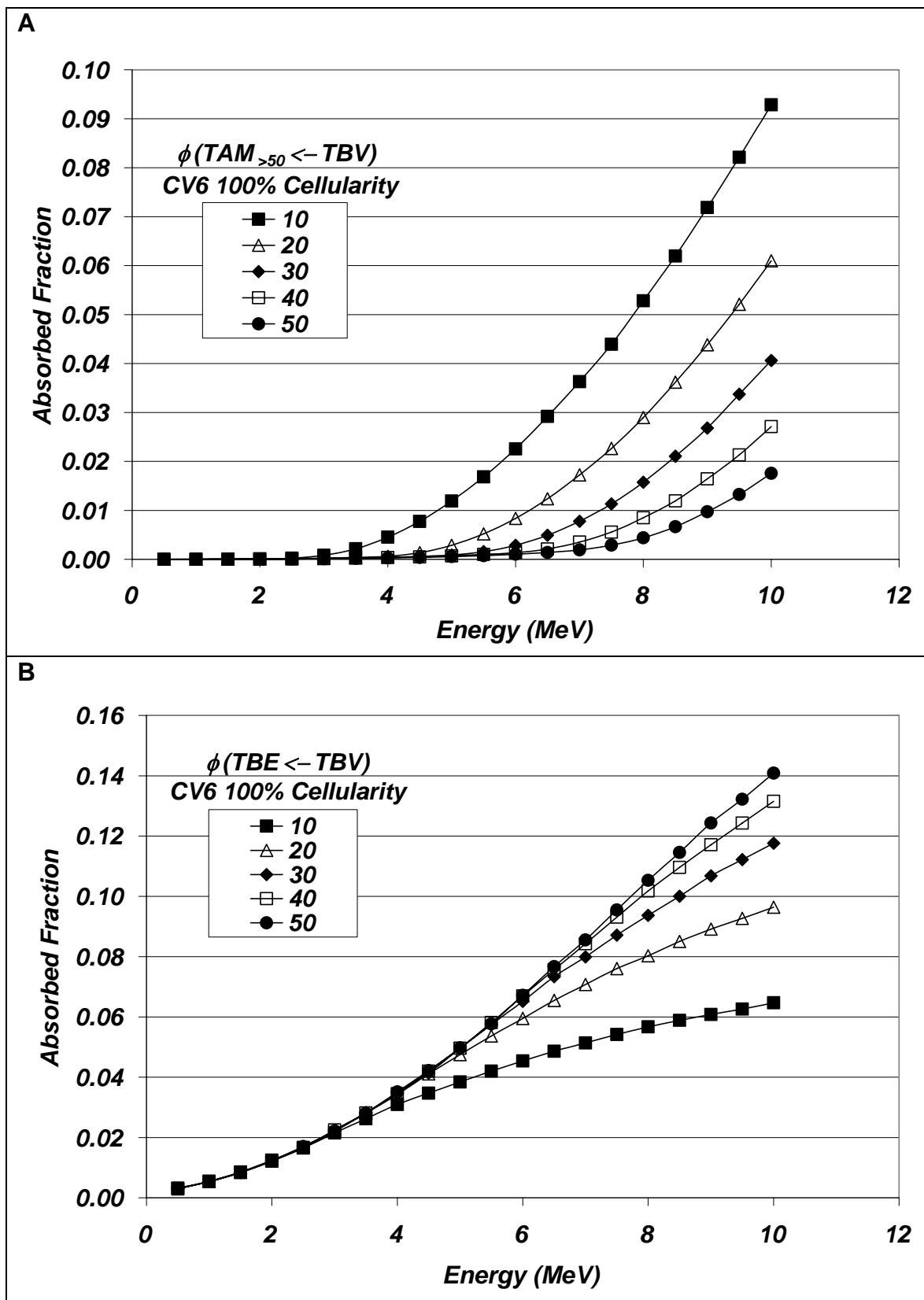


Figure 5

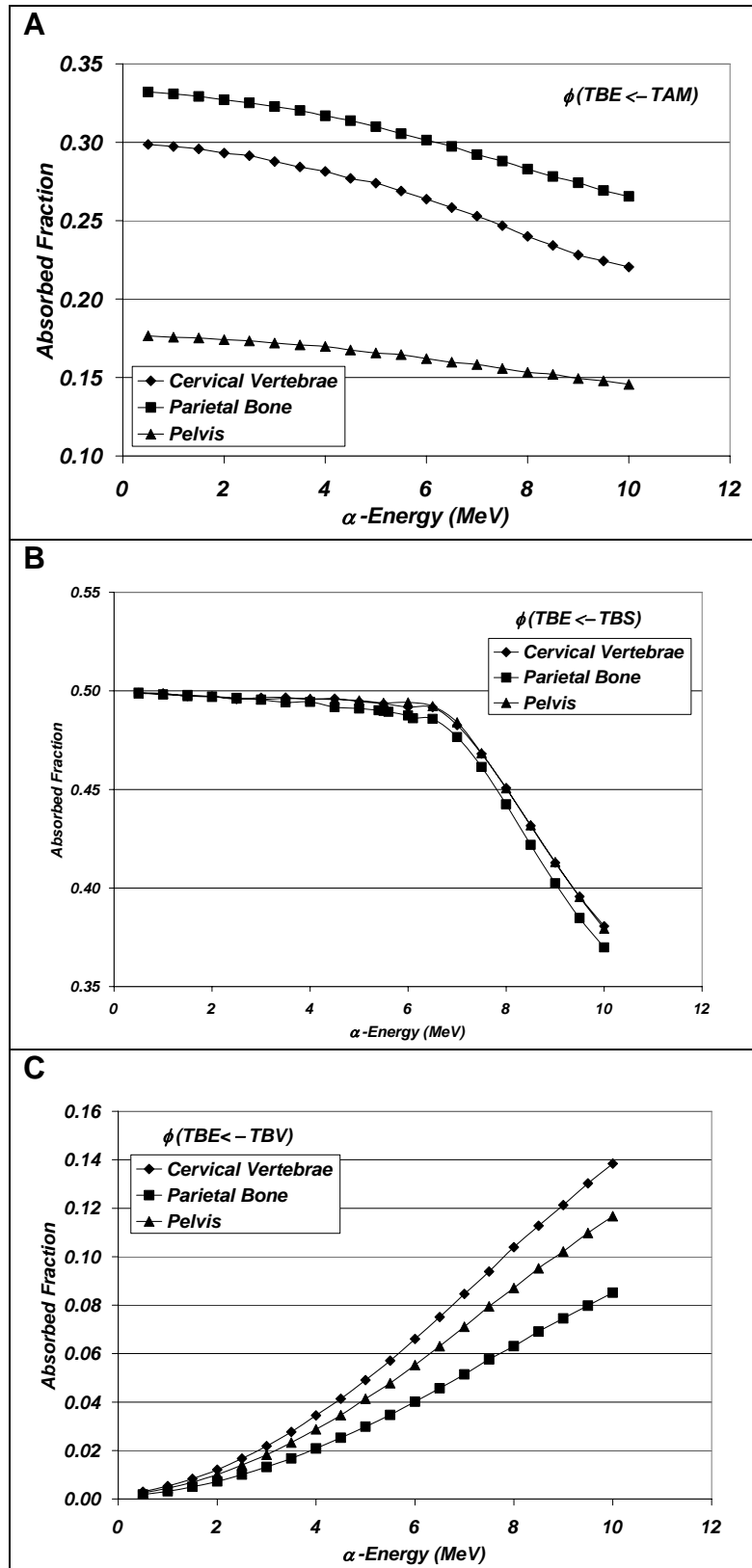


Figure 6

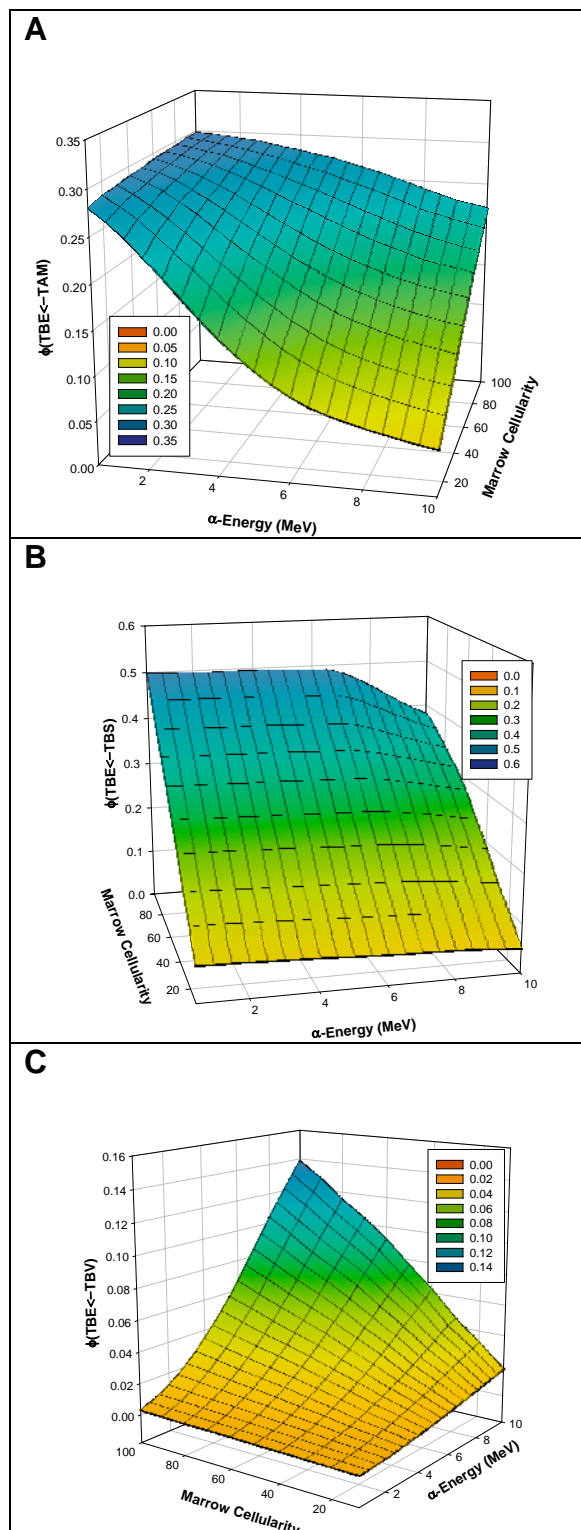


Figure 7

SPATIAL DISTRIBUTION OF CD34⁺ PRIMITIVE HEMATOPOEITIC CELLS AND BLOOD VESSELS WITH IN THE MARROW CAVITIES OF TRABECULAR BONE

Christopher J. Watchman¹, Vincent A. Bourke^{2,3}, Jared R. Lyon³,
Andrea E. Knowlton⁴, Samantha L. Butler⁵, David D. Grier⁵, John
Wingard⁶, Raul Braylan⁵ and Wesley E. Bolch^{2,3,7,a}

¹*Department of Radiation Oncology, Tucson, AZ,* ²*Department of Nuclear &
Radiological Engineering,* ³*Advanced Laboratory for Radiation Dosimetry
Studies,* ⁴*Department of Oral Biology,* ⁵*Department of Pathology,* ⁵*Department of
Medicine,* ⁷*Department of Biomedical Engineering, University of Florida,
Gainesville, FL*

^aFor reprints and correspondence contact:

Wesley E. Bolch, PhD, PE, CHP
*Director, Advanced Laboratory for Radiation Dosimetry Studies (ALRADS)
Department of Nuclear and Radiological Engineering
University of Florida, Gainesville, Florida 32611-8300
Phone: (352) 846-1361 Fax: (352) 392-3380 Email: wbolch@ufl.edu*

RUNNING TITLE:

Primitive Hematopoietic Cells Spatial Distribution in Spongiosa

This work was supported by the

U.S. Department of Energy and the National Cancer Institute

Submitted to Cancer Biotherapy and Radiopharmaceuticals

Word Count (Text and Refs):	4511
Word Count (Figure Captions):	162
Word Count (Table Captions):	21
Word Count (Total):	4694

INTRODUCTION

Current practice in internal radiation dosimetry is to average the dose to a target over the whole target of interest¹. This assumes uniformity in dose across the target which may or may not be the case. With the current interest and clinical implementation of molecular radiotherapy agents further data regarding the dose distributions and target cells at risk is needed to better assess the radiation absorbed dose and risks from irradiation. Of particular interest are the cells at risk in bone marrow (BM), which tends to be the dose-limiting organ in internal medical dosimetry. Within the bone marrow the cells considered to be at risk are the hematopoietic stem cell (HSC) and hematopoietic progenitor cells (HPC). Each of these cell types relates an increasing stage of differentiation with the HSC being the most primitive². Following the HSC in the hematopoietic lineage are the multilineage progenitor cells (HMPC), early progenitor cells (HEPC), late progenitor cells (HLPC), blasts and finally the mature hematopoietic cells in order of increasing differentiation³. Delineation of this HSC line is often done using immunohistochemistry with the CD34 immunophenotype. CD34 antigen sites are present on the HSC, HMPC, HEPC and HLPC³. Hematopoietic blasts may also exhibit the CD34 antigen site but do so but their expression is quite variable³. Other stem cells have also shown to be present in bone marrow, which may further add to the radiosensitivity of bone marrow⁴. These other tissue committed stem cells may include endothelial, skeletal, skeletal muscle and neural stem cells⁵⁻⁷. Recent studies have shown that osteoprogenitor and mesenchymal stem cells within the bone marrow may be the tissues at risk for bone cancers following irradiation⁸.

Under the frame work of most dosimetry methods, i.e. MIRD or ICRP, the dose to the bone marrow is taken as an average of the dose to bone marrow in each bone site divided by the sum total marrow mass. This macroscopic approach assumes that the distribution of primitive hematopoietic cells (PHC) is homogenous throughout the marrow cavities. Work by Charlton, Utteridge and Beddoe is used to support this hypothesis⁹. In this work they used CD34 and CD38 immunohistochemical staining to identify stem cells and measured their distances from adipocytes in bone marrow. Data obtained in this study indicated that HSC were uniformly

distributed from adipocytes within BM. Work by Shah et al has indicated that adipocytes are randomly distributed within BM¹⁰. Charlton et al's work was specifically used to determine radon dose to the stem cell population from accumulation in marrow adipocytes. Other data, coming from bone marrow biology, has indicated that HSC tend to be located closer to bone trabeculae surfaces^{11,12}. Work by Fassoni et al¹³, Lord¹⁴ and Cui et al¹⁵ in mice has found spatial dependence in the distribution of different cell lines, based upon cytokine expression, within mouse marrow. Data from these studies was used by Shah to modify dosimetry results to include a gradient weighting component based upon cytokine expression¹⁶ in different colony forming units (CFUs).

The objective of this study has been to challenge the homogenous hypothesis used in marrow dosimetry for human applications. Verification of the homogenous assumption would indicate that current dosimetry methods are appropriate for dosimetry studies and that using the average dose across the entire marrow give a good indication of PHC dose. If on the other hand a dose gradient is seen in the location of primitive hematopoietic cells (PHC i.e. CD34⁺ cells), this would suggest that our current inability to properly correlate BM dose with marrow toxicity may be the result of poor dosimetry caused by misidentification of the target cells. Furthermore, if a dose gradient does exist in human data then the weighting methods proposed by Shah¹⁶ for BM dosimetry may lead to a better correlation of absorbed dose with clinical effect and marrow toxicity in molecular radiotherapy.

MATERIALS AND METHODS

Bone marrow biopsies were obtained from the University of Florida Pathology tissue bank. Biopsies were obtained during regular clinical practice and stored in paraffin wax within the UF tissue bank for future use. SHANDS pathologists performed identification of specimens and specimens were identified as containing normal marrow (no pathology present). Twelve specimens were identified for the study with an age range of 2 to 80 years old. In Table 1 data regarding each subject is presented. Following specimen identification each specimen was prepared for immunohistochemical staining and slide placement.

Slide Preparation

Paraffin sections, 4- μm thick, were cut and placed on slides that were dried for 2 hours in a 60 degrees Celsius oven. The slides were placed on the Ventana Benchmark automated immunostainer where they were de-waxed and heat induced epitope retrieval was performed with Ventana CC1 retrieval solution. (Ventana Medical Systems Inc. Tucson AZ). CD34 (QBend/10 clone pre-diluted from Ventana) was applied to the paraffin sections for 32 minutes. The presence of the antigen was visualized with the Ventana Enhanced V red detection kit. Slides were removed from stainer and placed in reaction buffer (Ventana) and then placed in 95 degree Celsius Trilogy (Cell Marque Hot Springs Arkansas) for 10 minutes. Slides were placed in a reaction buffer and then placed on the Ventana Benchmark for staining with CD31 (Dako Corporation Carpinteria CA) at a dilution of 1:20. The antigen was visualized by using the i-view DAB detection kit (Ventana). Slides were counterstained with Hematoxylin (Ventana) and taken off the stainer and then were dehydrated through graded alcohols, cleared with xylene and mounted with permanent mounting media.

Image Acquisition and Processing

Following staining and slide preparation, each biopsy specimen was imaged. Images were taken at the University of Florida McKnight Brain Institute (MBI) Optical Microscopy (OM) facility (OM). Each specimen was imaged using the Zeiss Axioplan 2 Microscope (Zeiss, Germany) and a Hamamatsu C-4742 chilled CCD camera (Hamatsu Photonics, Japan) in bright field mode. A 20x objective lens was used in the imaging process. This magnification was determined to be the best compromise between image resolution and field of view. Image resolution was set to be 1 pixel/ μm in the software but in reality this translated to 1.2 pixels/ μm . Using the tile field mapping capabilities of the morphometric imaging lab in the MBI-OM facility a series of tile field maps were obtained for each specimen. The number of individual tile map images taken for each biopsy specimen varied depending of the length and width of the biopsy. Nominally five separate tile field images were taken per biopsy but as many as ten were possible. Each image field was processed using SPOT Advanced software (Diagnostic Instruments Inc, Sterling Heights, MI) with a sharpening filter. Once each biopsy image set was obtained,

individual images were stitched together using Adobe Photoshop 7.01 (Adobe Systems Inc, San Jose, CA) to give a total biopsy image. In Figure 1A this process is illustrated with a final biopsy image.

Stem Cell and Blood Vessel Measurements

Using the SPOT Advanced software a series of measurements were made using the measurement tool. This tool allows for linear measurements in units of pixels which may be converted to microns based upon our calibration measurement of 1.2 pixels/ μm . Distance measurements were referenced to the bone trabeculae for both stem cell and blood vessels. Each of these measurements was done so that the nearest distance from the structure of interest to the bone was measured. An additional set of measurements was performed to obtain the distance between the CD34⁺ cells and the blood vessels. In cases where a linear distance, along the line of measurement, was not able to be measured then no inter vessel/cell measurement was made. Identification of each structure was performed using an OM36LED contour microscope (Microscope Store, Rock Mount, VA) with a 40x objective. Note that the biopsy sample was only used to obtain identify PHC and blood vessels and not for spatial information. Measurements were also done for one or more sections on the slide depending on the inter section thickness which varied from 4 μm to 20 μm . For example if three sections were obtained on a single slide, sections where the thickness was 4- μm only one section would be used in the measurement process. If the 20- μm thickness was used two sections, at least 40 μm apart would be used in the counting process. This was done to minimize the potential for identifying and counting the same cells and vessels in multiple sections. See Figure 1B for an example of the above measurements.

To correctly assess the spatial distribution of structures with respect to the bone trabeculae in the spongiosa knowledge of the area (or volume in 3D) effects must be accounted for. Calculation of the area occupied by bone marrow was done by measuring concentric layers, extending 50 μm , from the surface of bone trabeculae. The original bone marrow biopsy image was manually segmented, using Adobe Photoshop, to exclude bone trabeculae in the region in which CD34⁺ cells were counted (Fig. 2A). The image was saved after this step, and then

converted to a grayscale image. Thresholding of the image was performed using a 2 pixel Gaussian blur to accomplish conversion to a black and white binary image (Fig. 2B). An edge dilation algorithm was then used to expand the binary trabeculae image in 50 μm increments, and each dilated image was saved for later use.

The original segmented color image was then further segmented to exclude all image pixels that were not active bone marrow within the measured area (Fig. 2C). The image was converted to grayscale, filtered, and re-thresholded using the previously described process. This created a binary black and white image displaying only the active marrow region (Fig. 2D). Final image sets depicting trabeculae dilation in 50 μm increments were obtained by merging the dilated trabeculae image and the original binary bone marrow image, using SPOT Image processing software (v4.04, Diagnostic Instruments Inc.)(Fig. 2E). Grey areas depict the dilated regions, and white pixels depict active marrow. Black pixels depict trabeculae regions that were dilated using the edge dilation algorithm, but were outside the measured active marrow area. ImageJ software (NIH, Bethesda MD) was then used to estimate marrow area in each merged by determining the number of white pixels in each subsequent image (Fig. 2E).

During the microtoming and staining process artifacts, such as tissue being pulled from the bone or displacement of the bone trabeculae occurred (Fig. 1A). Adjustments were made to deal with these issues. When the bone trabeculae appeared to be missing but a clearly defined anatomical trabecular space was present, measurements were made to the edge of the marrow and the trabecular space. Cases where the marrow was pulled from the bone trabeculae required measurements to be made from the structure of interest to the edge of the marrow. No measurements were made along the outer perimeter of the biopsy image unless specimen integrity lead to no question regarding the anatomical features.

RESULTS

In Figure 3, a scatter plot of all CD34⁺ cells counted and their distance from the bone surface is presented. Visual inspection of this plot would indicate a greater density of CD34⁺ cells near the bone surfaces as compared to increasing depth within the marrow cavity. Using the measured area data, from the binary image sets, the relative number of CD34⁺ cells or BV were

calculated per layer in each subject. These were then normalized to the total number of cells per total marrow area as shown in Equation 1.

$$\rho_S^i = \frac{N_i / A_i}{N_T / A_T} \quad (\text{Eq. 1})$$

In this equation, N_i is the number of cells in the area A_i in layer i and the total number of counted cells is N_T , A_T is the total marrow area and S is the subject. The cumulative data for each normalized tissue thickness layer over all patients was then calculated as shown in Equation 2.

$$\rho_T^i = \sum_S \rho_S^i \quad (\text{Eq. 2})$$

Data was then compiled into 50 μm bins as shown in Figure 4. Data for the CD34^+ measurements shows a log-normal gradient from the surface of the bone trabeculae and extends to 700 μm into the marrow cavities. Data presented here demonstrates that the CD34^+ cells have the highest probability of occurring at distances of 51-100 μm with the next highest probabilities occurring over the next 100 μm out from the bone trabeculae. A similar result was observed by Lord and collaborators in mice with a peak concentration at $\sim 110 \mu\text{m}^{13-15}$. Approximately 78% of the CD34^+ cells are shown to be located within the first 200 μm from the bone surfaces. A p value of <0.01 was found to indicate statistical significance of the distribution.

The same area weighting method was applied to the BV to TB data that is shown in Figure 5. The BS-TB data also shows a gradient which decreases from the bone surface into the marrow cavity. Similar to the results in Fig. 4, the BV also have their highest probability in the second bin depth. Measurements for the BV-TB distances also show a longer tail that extends out to 700 μm . Unlike the CD34^+ cell distribution the BV distribution demonstrates greater statistical fluctuation in the data. In the 101-150 μm bin a value which is less than the next bin is seen. Error bars shown in Fig. 5 show crossover in the confidence intervals of the data in this bin and the next three bins, which show statistical significance. The a similar p value of <0.01 was also found for this distribution. Greater statistical fluctuation in the BV data, as opposed to

the CD34⁺ data, was a result of counting statistics. Approximately 1.5 times more CD34⁺ cells were identified in comparison to the BV.

Unlike the two previously mentioned data sets, the CD34⁺-BV data did not require area weighting since these measurements are linear distances within the marrow cavities, thus area effects with respect to the bone trabeculae are not present. In Figure 6A a similar log-normal gradient was also found in for these measurements. The tail of this distribution also goes further with a maximum depth of 900 μm . In contrast the maximum values for the CD34⁺-TB and the BV-TB's maximum bin depth was 700 μm . These observed maximum depths tend to be less than the average iliac crest marrow cavity diameter ($\sim 1100 \mu\text{m}$)¹⁷. A comparison of the two distributions found in Figs. 4 and 5 are presented in Fig. 6B. Both distributions have similar shapes and locations throughout the marrow cavities, indicating a shared spatial niche.

DISCUSSION

Our methodology has allowed us to obtain data for the differential spatial location of CD34⁺ cells that are representative of the hematopoietic stem cells and hematopoietic progenitor cells. Using bone marrow biopsies from the iliac crest has certain advantages. Trabecular bone tends to have a preferential direction in the thickness of bone trabeculae. Anisotropy in the trabecular structure is a result of biomechanical loading of the bone. Wakamatsu and Sissons¹⁸ have shown that the iliac crest is the least anisotropic bone in terms of trabecular microstructure. Consequently, measurements made in this study will relate the spatial information that is least effected by a preferential direction in the bone trabeculae. If other bone sites were studied, the frequency distributions may potentially be different since thicker trabeculae in a preferential direction may result in a skewing of the distribution in Figures 4 and 5. Another advantage to the use of iliac crest biopsies is that they are regularly obtained in clinical practice. Accordingly this study could be expanded to include a much larger subject population.

Using bone marrow biopsies does lead to some limitations due to the field of view of the biopsy caused by limited size of the biopsy needle. In Figure 1A an example of the biopsy is shown. Along the outer edges of the biopsy core no information is found in regards to what tissues are near the edge. As a result, CD34⁺ cells or blood vessels near the outer edges result

in measurements from these structures being evaluated as being further from bone trabeculae than they really were in vivo. The following example illustrates the worst-case scenario of this edge effect. Consider the sample in Figure 1A and assume the edges of the samples are bone. The worst-case scenario would result in a shift in the frequency of cells or vessels towards the shorter distances in comparison to Figures 4 and 5. Thus the shift in the distribution would not affect the longer distances but would increase the frequency of shorter distance. The results we have obtained show little to no CD34⁺ cells or blood vessels beyond ~700 μm and thus this error would not affect this finding.

Another concern arises with respect to the biopsy samples in relationship to the 2D measurements we have obtained. The question becomes how much different does the 3D distribution look in comparison to the 2D distribution obtained from the biopsy slides. The general principle in sterology is that by taking a sufficient number of 2D samples from a structure you will approximate a 3D sample. Using the nearest distance measurements in this study we assume that along with the number of subjects and the total number of cells counted, we sufficiently account for the 3D structure. This is in part due to the degree of isotropy found in the iliac crest. Another potential source of error in the 2D sample occurs with respect to the vasculature. In the 2D samples used in this study a blood vessel may be passing in and out of the plane of the sample slice as opposed to its actual configuration in 3D. This can result in the same blood vessel being counted multiple times when in reality it is the same vessel. Consequently, the BV to CD34⁺ cell distance may in reality be different than the results we have obtained in 2D. If a 3D sample were obtained then not only would we be able to remove the edge effects but also decrease the reliance on the sterology assumption.

In spite of any limitations for this data set our results clearly indicate the presence of a spatial gradient. Thus dosimetry results using the homogenous assumption will incorrectly estimate the dose to hematopoietic cells of interest. Knowledge of where the PHC preferentially locate within the marrow cavity allows for the ability to weight the dose across the cavity. In Figure 7 this idea is illustrated for a hypothetical spherical marrow cavity. In the figure a series of concentric shells are presented from the surface of the cavity. Cavity layers L_1 and L_2 are given

an arbitrary thickness t . Layer L_3 represents the depth in the marrow cavity where $CD34^+$ cells have a very low probability of being located. Thus a decreasing gradient in the target cell population is seen as $L_1 > L_2 > L_3$. With in a transport simulation the energy deposition can be tallied in each of these layers for each source type, marrow, surface and volume. Once each dose is calculated a weighting factor may be applied proportional to the frequency of target cell density in that layer as shown in the following equation.

$$D = \sum_i^N \omega_i D_i = \tilde{A}_s \sum_i^N \omega_i \sum_j \Delta_j \frac{\phi(r_T \leftarrow r_s)_{i,j}}{m_{i,j}} \quad (\text{Eq. 3})$$

In Equation 3, D is the dose to the entire marrow, i is the layer of thickness t and N is the total number of layers in all marrow cavities resulting from the largest cavity. D_i is the dose calculated in tissue layer i , while ω_i is the target cell frequency factor obtained in Figure 4. The factor Δ_j is the mean energy emitted per nuclear transition, j is the energy emission index, $m_{i,j}$ is the layer mass, and $\phi(r_T \leftarrow r_s)_{i,j}$ is the fraction of energy absorbed as a function of initial particle energy.

Lastly, r_T is the radiation target, r_s is the radiation source and \tilde{A}_s is the accumulated activity. This method allows for the dose received in the region with the greatest density of target cells to be given more influence in the total dose across the marrow cavity. What this means is that the dose to the cells at greatest risk are assessed as being more meaningful to the cavity dose and hence total marrow dose.

For example, a trabecular bone surface source or bone volume source result in particle emissions, which for therapeutic alpha emitters, deposit energy in the regions of highest target cell density. In comparison a marrow volume source, emissions within the central part of the marrow cavity may not have sufficient range to enter the higher density regions of the cavity. On the other hand, emissions occurring within the higher density cell region may potentially escape the marrow cavity. Consequently the overall dose to the most sensitive tissues may be different than that of the entire cavity averaged dose. This issue is more prevalent depending upon the particle type and emission energy. For instance, alpha emitters and low energy beta emitters have relatively short transport ranges (approximately $<120 \mu\text{m}$ in soft tissue). In bone volume

and bone surface source the majority of energy deposition will occur in the most sensitive target regions. Alternately, emission from a marrow volume source located further away from the bone trabeculae will have insufficient energy to enter the higher target cell density region. Only those emissions emitted within or very near to the high-density region will contribute to PHC dose. Therefore the dose to the target cells should be lower than if the homogenous assumption methodology was used. Range effects become less important for intermediate and higher energy beta particles (~100 keV – 4 MeV) since each emitted particle has a better chance of depositing energy in the high HPC density regions. Thus regardless of which particle type is used the above described methodology should then result in a total marrow dose which better correlates with the specific target cells at risk and potentially clinical effect and marrow toxicity. Further investigation into this issue is required to fully validate this concept experimentally.

In addition to the dosimetric consequences the data regarding vascular distances and distances between CD34⁺ cells and blood vessels have clinical implications in both molecular radiotherapy and bone marrow transplantation. Data in Fig. 6B would indicate that blood vessels and CD34⁺ hematopoietic cells share a similar spatial niche in bone marrow. As a result irradiation affecting one also has a high likelihood of affecting the other. Additionally studies have demonstrated that hematopoietic stem cells develop from vascular endothelium in embryo/fetus¹⁹. This indicates a supportive interaction between these two tissues that seems to be supported by the close proximity of the CD34⁺ cells and the blood vessels (Fig. 6). In molecular therapy applications this shared spatial niche can play a role in the radiopharmaceutical chosen to treat a particular malignancy. For example, treating tumors which reside on bone trabeculae with a radiopharmaceutical that preferentially locates on bone surfaces would result in not only tumor dose but dose to the PHC and the vascular endothelium. A poor therapeutic ratio between tumor dose and marrow dose would occur. Thus tumor toxicity would likely result in marrow toxicity as well. On the other hand if a tumor were located near the central region of a marrow cavity and the radiopharmaceutical were targeted to attach to the tumor potential sparing of the marrow could be achieved, in particular if an alpha emitter, auger electron or low energy beta emitter was chosen. In bone marrow transplantation use of radioimmunotherapy for myeloablation has the

potential to spare non-target organs and improve efficacy of transplantation²⁰. Choosing a radiopharmaceutical, which has a range less than 700 μm in marrow tissue, could result in ablation of not only the PHC but also the vasculature. Further exploration is warranted to better correlate radiopharmaceutical choice and data obtained in this study with marrow toxicity

CONCLUSION

Data has been presented that contradicts the homogenous distribution of hematopoietic progenitor cells within the marrow cavities of trabecular bone. These results indicate that the current disparity between dose calculations and clinical response in molecular radiotherapy may be due in part to incorrectly estimating the dose to the most radiosensitive cells in bone marrow. A weighting method has been presented which will allow for incorporation of the PHC frequency data into current dosimetry methods. Use of this data in dosimetry modeling may result in improved dose-response relationships.

Further work is warranted due to the spatial limitations resulting from the use of bone marrow core biopsies. Development of 3D models that allow for multiple whole marrow cavities may further improve our knowledge of the location of PHC and the marrow vasculature. Potentially greater delineation of cell types is possible if additional immunohistochemical agents are used to directly differentiate between cell types, i.e. using CD34 and CD38 to distinguish between HSC (CD38⁻) and other progenitor cells (CD38⁺). Additional investigation is also merited in looking at how pathology may change the spatial distribution of PHC in the marrow. Improved description of each cell type, with respect to normal and pathological bone marrow, along the hematopoietic lineage may allow for other weighting schemes that further improve dose-response relationships with respect to marrow toxicity and clinical effect.

ACKNOWLEDGEMENTS

The authors would like to thank Tim Vaught at the UF McKnight Brain Institute for his assistance and expertise in conjunction with the use of the optical imaging facilities. We would also like to thank Elaine Dooley at the Shands Rocky Point hematology lab for her expertise and assistance in specimen preparation. This work was supported in part by grant CA96411 from the

National Cancer Institute and Grant DE-FG07-02ID14327 from the Department of Energy with the University of Florida.

REFERENCES

1. Leovinger RB, R.F. Watson, E.E. MIRDO Primer for Absorbed Dose Calculations. New York: Society of Nuclear Medicine; 1991.
2. Hall E. Radiobiology for the radiologist (ed 3rd Edition). Philadelphia: Lippincott Co.; 1988.
3. Foucar K. Bone marrow pathology. Chicago: American Society of Clinical Pathologists; 2001.
4. Kucia M, Reza R, Jala VR, Dawn B, Ratajczak J, Ratajczak MZ. Bone marrow as a home of heterogeneous populations of nonhematopoietic stem cells. *Leukemia*. 2005;19:1118-1127.
5. Kuznetsov SA, Mankani MH, Gronthos S, Satomura K, Bianco P, Robey PG. Circulating skeletal stem cells. *J Cell Biol*. 2001;153:1133-1140.
6. Rafii S, Shapiro F, Rimarich J, et al. Isolation and characterization of human bone marrow microvascular endothelial cells: hematopoietic progenitor cell adhesion. *Blood*. 1994;84:10-19.
7. Pituch-Noworolska A, Majka M, Janowska-Wieczorek A, et al. Circulating CXCR4-positive stem/progenitor cells compete for SDF-1-positive niches in bone marrow, muscle and neural tissues: an alternative hypothesis to stem cell plasticity. *Folia Histochem Cytobiol*. 2003;41:13-21.
8. Nekolla EA, Kreisheimer M, Kellerer AM, Kuse-Isingschulte M, Gossner W, Spiess H. Induction of malignant bone tumors in radium-224 patients: risk estimates based on the improved dosimetry. *Radiat Res*. 2000;153:93-103.
9. Charlton DE, Uttridge TD, Beddoe AH. Microdosimetry of haemopoietic stem cells irradiated by alpha particles from the short-lived products of ²²²Rn decays in fat cells and haemopoietic tissue. *Int J Radiat Biol*. 1996;69:585-592.
10. Shah AP, Patton PW, Rajon DA, Bolch WE. Adipocyte spatial distributions in bone marrow: implications for skeletal dosimetry models. *J Nucl Med*. 2003;44:774-783.
11. Taichman RS. Blood and bone: two tissues whose fates are intertwined to create the hematopoietic stem-cell niche. *Blood*. 2005;105:2631-2639.
12. Nilsson SK, Johnston HM, Coverdale JA. Spatial localization of transplanted hemopoietic stem cells: inferences for the localization of stem cell niches. *Blood*. 2001;97:2293-2299.
13. Frasson F, Testa NG, Lord BI. The relative spatial distribution of erythroid progenitor cells (BFUe and CFUe) in the normal mouse femur. *Cell Tissue Kinet*. 1982;15:447-455.
14. Lord BI. The architecture of bone marrow cell populations. *Int J Cell Cloning*. 1990;8:317-331.
15. Cui YF, Lord BI, Woolford LB, Testa NG. The relative spatial distribution of in vitro-CFCs in the bone marrow, responding to specific growth factors. *Cell Prolif*. 1996;29:243-257.
16. Shah AP, Rajon DA, Patton PW, Howell RW, Bolch WE. Skeletal dosimetry: Establishment of dose gradients for cellular components across the marrow cavity. *Medical Physics*. 2003;30:1400-1400.
17. Shah AP. Reference Skeletal Dosimetry Model for an Adult Male Radionuclide Therapy Patient Based on 3D Imaging and Paired Image Radiation Transport. Biomedical Engineering. Gainesville: University of Florida; 2004.
18. Wakamatsu E, Sissions H. The cancellous bone of the iliac crest. *Calcif Tiss Res*. 1969;147-161.
19. Tavani M, Zheng B, Oberlin E, et al. The vascular wall as a source of stem cells. *Ann N Y Acad Sci*. 2005;1044:41-50.
20. Nemecek ER, Hamlin DK, Fisher DR, et al. Biodistribution of yttrium-90-labeled anti-CD45 antibody in a nonhuman primate model. *Clin Cancer Res*. 2005;11:787-794.

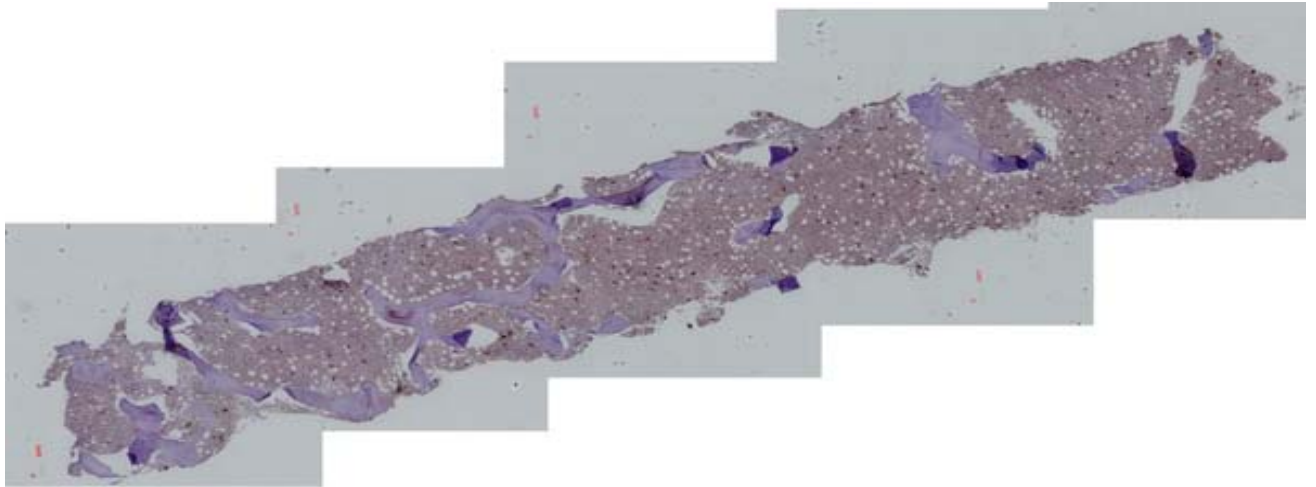
Table 1. Characteristics of specimens used in present study.

Gender	Age (y)	Patient Pathology
F	46	
F	80	
M	2	
M	11	ITP
F	35	Hodgkins
F	32	Hodgkins
F	69	Hodgkins
M	19	Liver Toxicity
F	32	
F	7	Abdominal Mass
F	68	
M	44	Seminoma

FIGURES

- Figure 1.** Images of bone marrow biopsies from iliac crest where (A) total biopsy imaged obtained by stitching individual images into a composite image, and (B) example of measurements obtained from biopsy image and slide.
- Figure 2.** Illustration of the imaged based area measurements of concentric layers from the bone surfaces.
- Figure 3.** Scatter plot illustrating the raw count data for CD34⁺ cells. Note the higher density of cells near the surface of the bone trabeculae.
- Figure 4.** Histogram relating the frequency of CD34⁺ cells with respect to the bone trabeculae with area correction applied.
- Figure 5.** Histogram relating the frequency of blood vessels with respect to the bone trabeculae with area correction applied.
- Figure 6.** Histogram relating the frequency of CD34⁺ cells to blood vessel distances.
- Figure 7.** Figure presenting a stylized representation of a marrow cavity. In the cavity multiple layers representing cell densities are shown (L1, L2 and L3). Arrow shown in figure represents possible emission point transport paths.

A



B

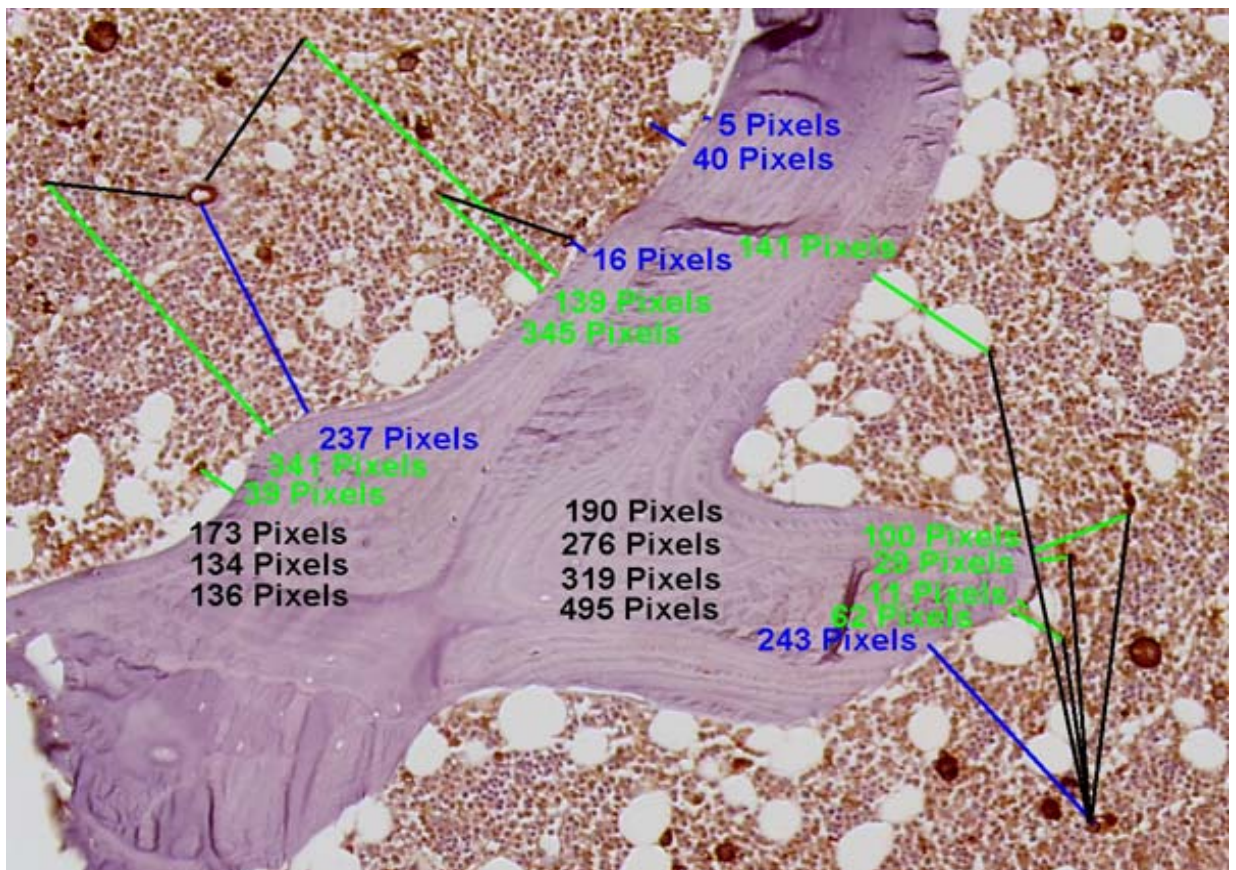
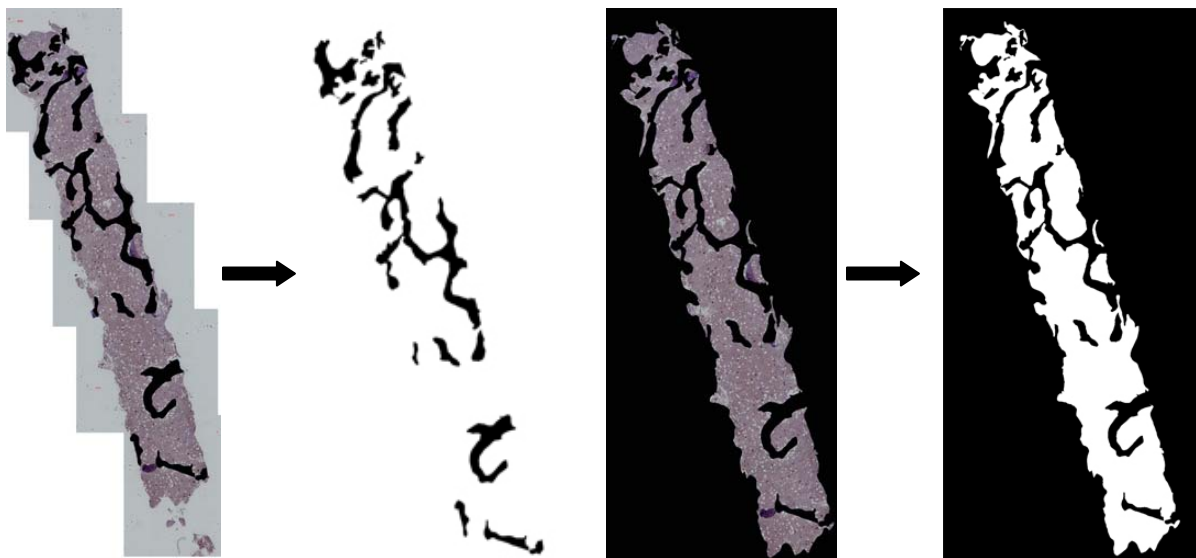


Fig. 1



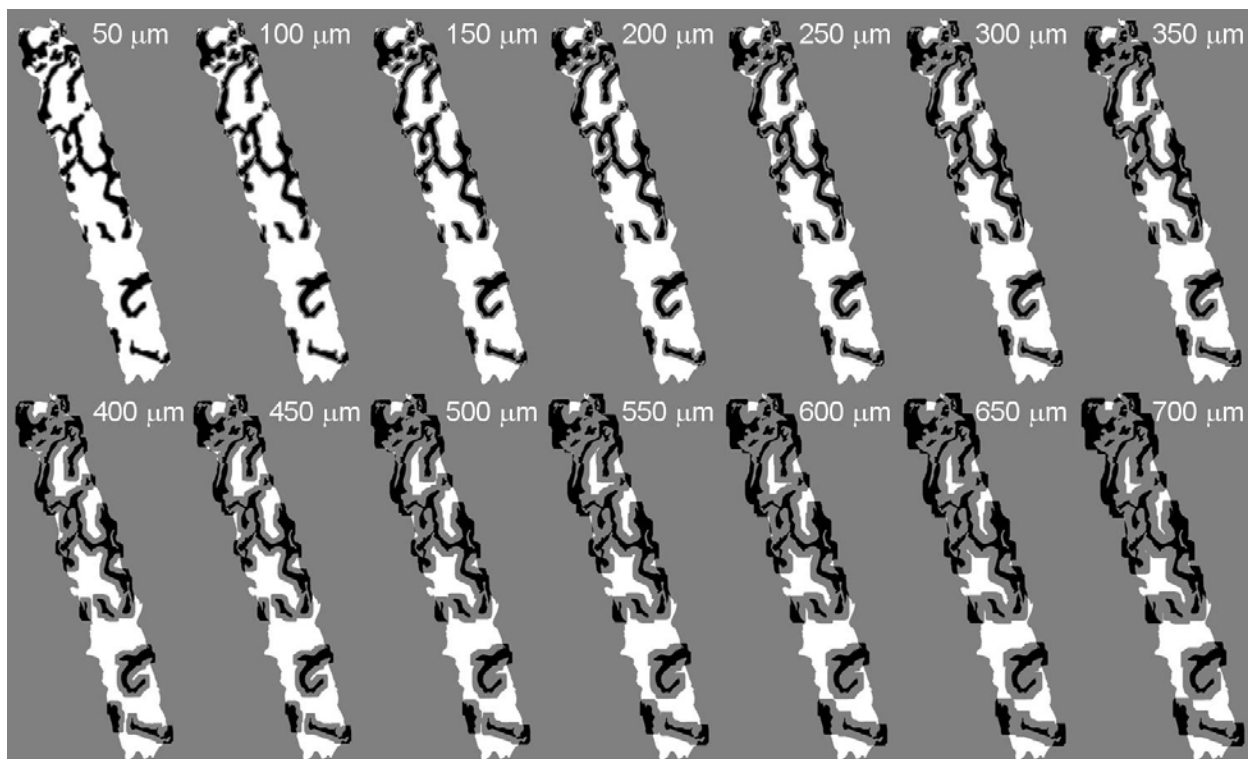
A

B

C

D

E



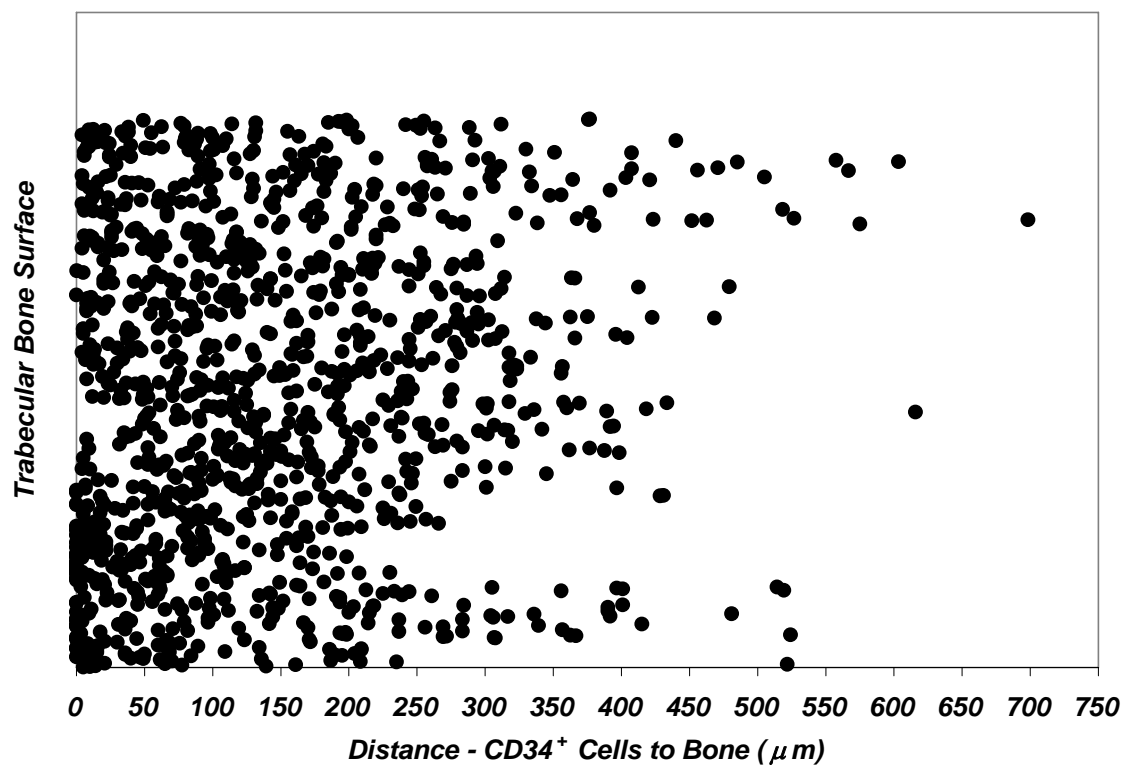


Fig. 3

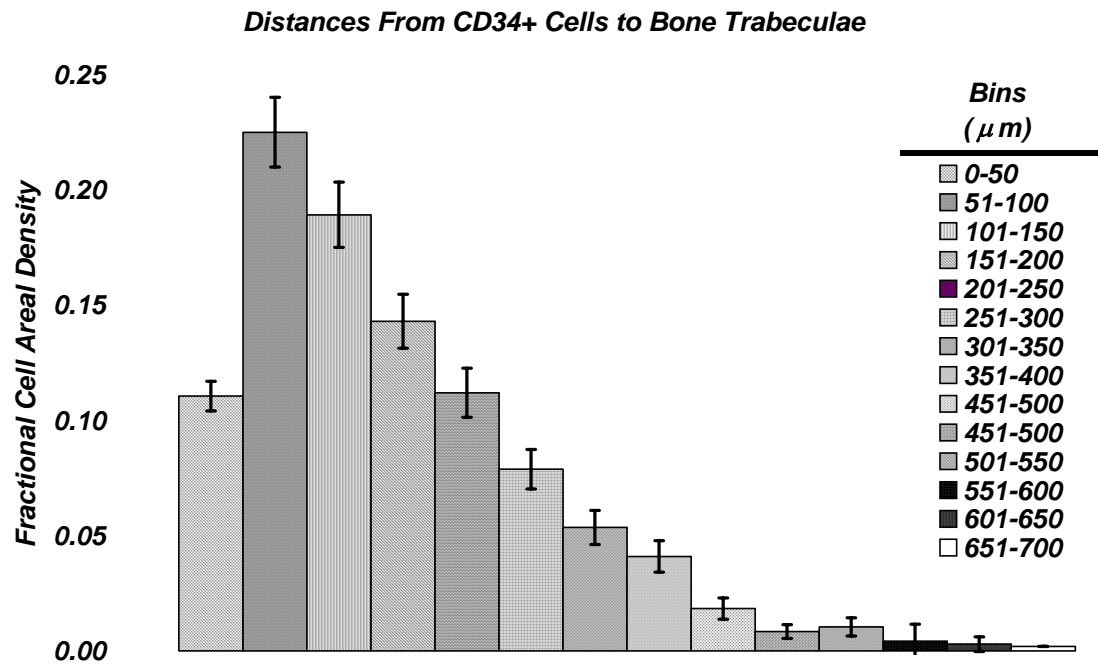


Fig 4

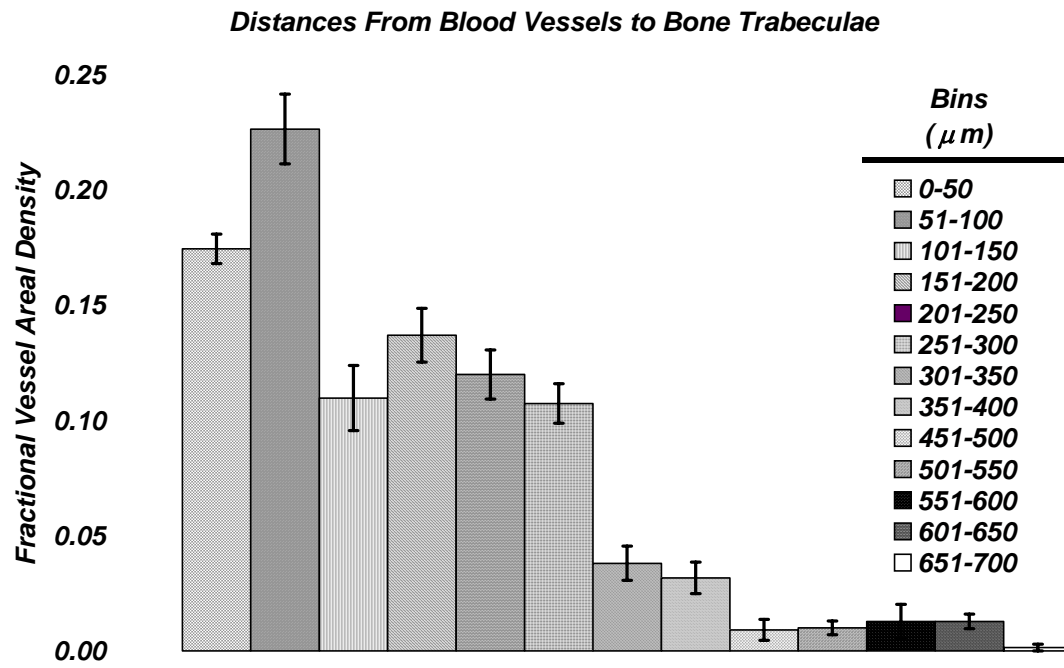


Fig. 5

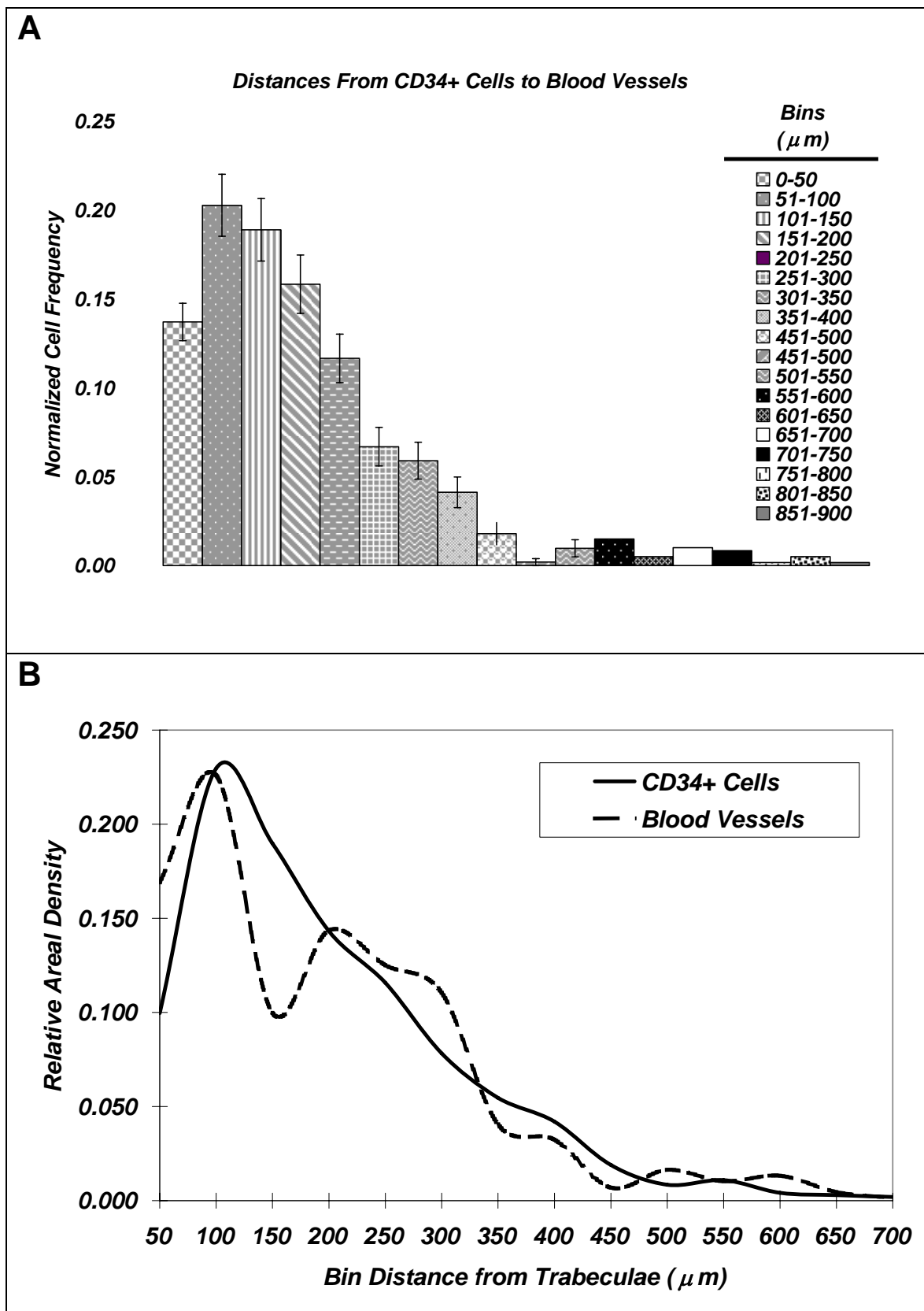


Fig 6

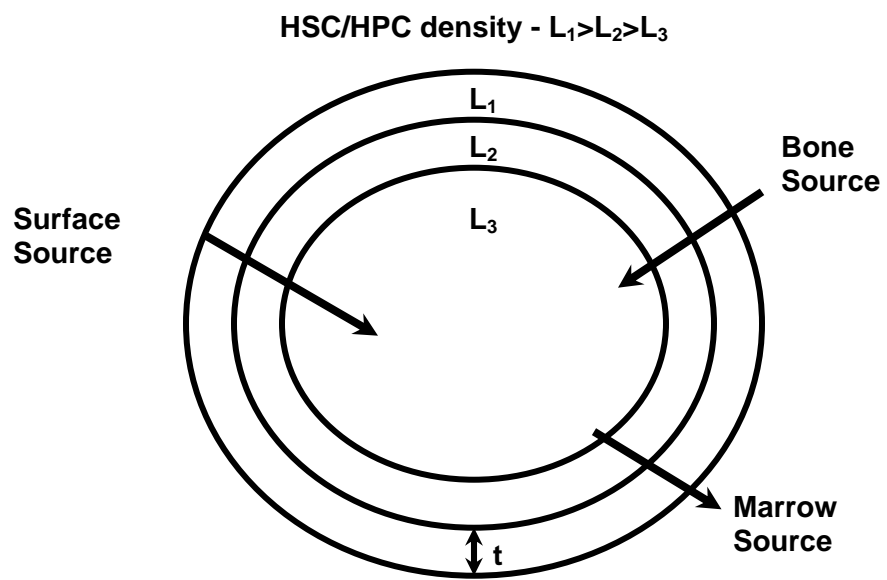


Fig. 7